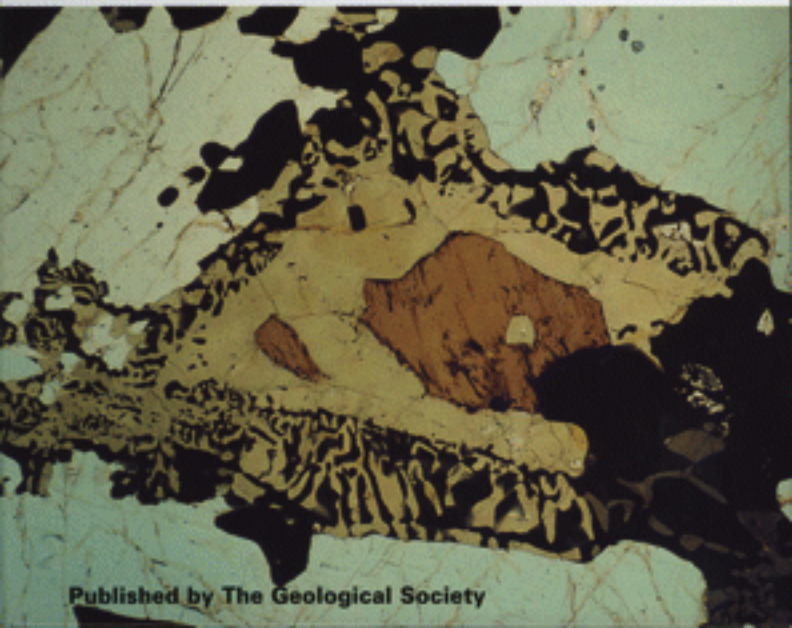


What Drives Metamorphism and Metamorphic Reactions?

edited by P. J. Treloar and P. J. O'Brien

Geological Society
Special Publication
No. 138



Published by The Geological Society

What Drives Metamorphism and Metamorphic Reactions?

Geological Society Special Publications

Series Editors

A. J. FLEET

A. C. MORTON

A. M. ROBERTS

It is recommended that reference to all or part of this book should be made in one of the following ways.

TRELOAR, P. J. & O'BRIEN, P. J. (eds) 1998. *What Drives Metamorphism and Metamorphic Reactions?* Geological Society, London, Special Publications, **138**.

JAMIESON, R. A., BEAUMONT, C., FULLSACK, P. & LEE, B. 1998. Barrovian regional metamorphism: where's the heat? In: TRELOAR, P. J. & O'BRIEN, P. J. (eds) 1998. *What Drives Metamorphism and Metamorphic Reactions?* Geological Society, London, Special Publications, **138**, 23–46.

GEOLOGICAL SOCIETY SPECIAL PUBLICATION NO. 138

What Drives Metamorphism and Metamorphic Reactions?

EDITED BY

PETER J. TRELOAR
Kingston University, UK

AND

PATRICK J. O'BRIEN
Universität Bayreuth, Germany

1998

Published by
The Geological Society
London

THE GEOLOGICAL SOCIETY

The Society was founded in 1807 as The Geological Society of London and is the oldest geological society in the world. It received its Royal Charter in 1825 for the purpose of 'investigating the mineral structure of the Earth'. The Society is Britain's national society for geology with a membership of around 8500. It has countrywide coverage and approximately 1500 members reside overseas. The Society is responsible for all aspects of the geological sciences including professional matters. The Society has its own publishing house, which produces the Society's international journals, books and maps, and which acts as the European distributor for publications of the American Association of Petroleum Geologists, SEPM and the Geological Society of America.

Fellowship is open to those holding a recognized honours degree in geology or cognate subject and who have at least two years' relevant postgraduate experience, or who have not less than six years' relevant experience in geology or a cognate subject. A Fellow who has not less than five years' relevant postgraduate experience in the practice of geology may apply for validation and, subject to approval, may be able to use the designatory letters C Geol (Chartered Geologist).

Further information about the Society is available from the Membership Manager, The Geological Society, Burlington House, Piccadilly, London W1V 0JU, UK. The Society is a Registered Charity, No. 210161.

Published by The Geological Society from:
The Geological Society Publishing House
Unit 7, Brassmill Enterprise Centre
Brassmill Lane
Bath BA1 3JN
UK.
(Orders: Tel. 01225 445046
Fax 01225 442836)

First published 1998

The publishers make no representation, express or implied, with regard to the accuracy of the information contained in this book and cannot accept any legal responsibility for any errors or omissions that may be made.

© The Geological Society 1996. All rights reserved.
No reproduction, copy or transmission of this publication may be made without written permission.
No paragraph of this publication may be reproduced, copied or transmitted save with the provisions of the Copyright Licensing Agency, 90 Tottenham Court Road, London W1P 9HE. Users registered with the Copyright Clearance Center, 27 Congress Street, Salem, MA 01970, USA: the item-fee code for this publication is 0305-8719/98/\$10.00.

British Library Cataloguing in Publication Data
A catalogue record for this book is available from the British Library.

ISBN 1-86239-009-6

Typeset by Aarontype Ltd, Unit 47, Easton Business Centre, Felix Road, Bristol BS5 0HE, UK

Printed by The Alden Press,
Osney Mead, Oxford, UK.

Distributors

USA
AAPG Bookstore
PO Box 979
Tulsa
OK 74101-0979
USA
(Orders: Tel. (918) 584-2555
Fax (918) 560-2652)

Australia

Australian Mineral Foundation
63 Conyngham Street
Glenside
South Australia 5065
Australia
(Orders: Tel. (08) 379-0444
Fax (08) 379-4634)

India

Affiliated East-West Press PVT Ltd
G-1/16 Ansari Road
New Delhi 110 002
India
(Orders: Tel. (11) 327-9113
Fax (11) 326-0538)

Japan

Kanda Book Trading Co.
Tanikawa Building
3-2 Kanda Surugadai
Chiyoda-Ku
Tokyo 101
Japan
(Orders: Tel. (03) 3255-3497
Fax (03) 3255-3495)

Contents

Acknowledgements	vi
Introduction	1
HODGES, K. V. The thermodynamics of Himalayan orogenesis	7
JAMIESON, R. A., BEAUMONT, C., FULLSACK, P. & LEE, B. Barrovian regional metamorphism: where's the heat?	23
WHITNEY, D. L. & DILEK, Y. Characterization and interpretation of <i>P-T</i> paths with multiple thermal peaks	53
RECHE, J., MARTÍNEZ, F. J. & ARBOLEYA, M. L. Low- to medium-pressure Variscan metamorphism in Galicia (NW Spain): evolution of a kyanite-bearing synform and associated bounding antiformal domains	61
HARLEY, S. L. On the occurrence and characterization of ultrahigh-temperature crustal metamorphism	81
SANDIFORD, M. & HAND, M. Australian Proterozoic high-temperature, low-pressure metamorphism in the conductive limit	109
GIBSON, R. L. & STEVENS, G. Regional metamorphism due to anorogenic intracratonic magmatism	121
BROWN, M. Ridge-trench interactions and high- <i>T</i> low- <i>P</i> metamorphism, with particular reference to the Cretaceous evolution of the Japanese Islands	137
HARRIS, N. & AYRES, M. The implications of Sr-isotope disequilibrium for rates of prograde metamorphism and melt extraction in anatexic terrains	171
WHITTINGTON, A., HARRIS, N. & BAKER, J. Low-pressure crustal anatexis: the significance of spinel and cordierite from metapelitic assemblages at Nanga Parbat, northern Pakistan	183
RUBIE, D. C. Disequilibrium during metamorphism: the role of nucleation kinetics	194
VERNON, R. H. Chemical and volume changes during deformation and prograde metamorphism of sediments	215
BARKER, A. J. & ZHANG, X. The role of microcracking and grain-boundary dilation during retrograde reactions	247
WORLEY, B. & POWELL, R. Making movies: phase diagrams changing in pressure, temperature, composition and time	269
Index	281

Acknowledgements

The papers in this volume arise from a meeting held at Kingston University on 11–13 September 1996 on the topic 'What Drives Metamorphism and Metamorphic Reactions'. The meeting was convened by Peter J. Treloar and Patrick J. O'Brien on behalf of the Metamorphic Studies Group, a specialist group of both the Geological Society of London and the Mineralogical Society of Great Britain and Ireland. The support of the Metamorphic Studies Group and of both its parent organizations is acknowledged. Peter Treloar wishes to express admiration to Pam Nieto for yet again permitting her home to be overrun by mountains of conference/volume related paperwork (cf. Geological Society of London Special Publication No. 74).

The editors wish to acknowledge reviews by the following geoscientists:

A. J. Barker	N. C. Hudson
M. J. Bickle	F. McDermott
A. P. Boyle	N. Petford
M. Bröker	T. Reischmann
D. P. Carrington	J. Reinhardt
S. Chakroborty	M. Riedel
J. D. Clemens	J. Rötzler
J. A. D. Connolly	C. Ruppell
T. Dempster	M. Sandiford
G. T. R. Droop	V. Schenk
T. F. Fliervoet	K. Schullmann
L. Franz	J. C. Schumacher
C. R. L. Friend	F. S. Spear
M. Guiraud	D. J. Waters
S. L. Harley	J. Wheeler
N. B. W. Harris	B. W. D. Yardley

Introduction

PETER J. TRELOAR¹ & PATRICK J. O'BRIEN²

¹ *School of Geological Sciences, Kingston University, Penrhyn Road, Kingston-upon-Thames, Surrey KT1 2EE, UK (e-mail: p.treloar@kingston.ac.uk)*
² *Bayerisches GeoInstitut, Universität Bayreuth, Postfach 101251, D-95440 Bayreuth, Germany (e-mail: Patrick.Obrien@uni-bayreuth.de)*

Although it has long been recognized that what ultimately drives metamorphism and metamorphic processes is heat, what was for long less certain is the distribution of heat within the crust, the type and location of the major heat sources and the rates of heat flux through crustal rocks. In early work a spatial link was established between the emplacement of igneous bodies and the metamorphism of their immediately adjacent country rocks. Widely described now as 'contact metamorphism' what needed addressing at that stage was the extent to which regional metamorphism itself might be a function of heat advected by igneous intrusions. Simply, are all 'regional' metamorphic terrains underlain by voluminous igneous plutons? In some of the earliest studied metamorphic terrains the highest temperature rocks are commonly associated with igneous rocks. Over a period of years, while George Barrow, Pentti Eskola and Cecil Tilley were developing the basis of modern metamorphic petrology (the facies concept and the concepts of metamorphic isograds, assemblages and zones) it became apparent that high-grade rocks are commonly spatially linked with igneous material, some of which would now be identified as former anatetic partial melts, but some of which, as in NE Scotland, include gabbroic plutons. In contrast, German petrologists in the early twentieth century developed an essentially baric approach to studies of regional metamorphism. Here, rather than invoking magmatic heat advection as the driving force for regional metamorphism, the classification of epizonal, mesozonal and katazonal divisions stressed the change in metamorphic grade with structural depth. The driving force for regional metamorphism was taken to be the internal heat flux from the Earth's core to its surface, with the important implication that higher metamorphic grades equated with greater depths. Subsequently, the term 'dynamothermal metamorphism' also began to appear in the literature and text-books as a synonym for regional metamorphism, implying that regional metamorphism was not simply a function of heat sources and thermal fluxes, but was commonly associated with crustal

deformation and orogenic processes. A simplistic understanding of these latter processes was that crustal thickening buried shallow-level rocks to depths where temperatures were, or would become, higher.

Hence, by the middle of the twentieth century the basic tenets of modern metamorphic petrology were already in place: heat advection through magma transport and emplacement, heat flux from below the crust, and the role of tectonic processes in localising heat sources and heating up rocks. Having said that, in the last quarter of the century our understanding of the role that these processes play has changed remarkably. This is probably due to two main lines of study, both of which have benefitted greatly from advances in analytical instrumentation. The first of these relates to the quantification of the intensive variables, particularly pressure (P) and temperature (T), within metamorphic terrains, more recently coupled with isotope dating and forward modelling of mineral chemical zonation patterns, to allow the construction of pressure-temperature-time paths of metamorphism. This approach depends heavily on the experimental and empirical derivation of thermodynamic data for metamorphic phases, along with the application of these data to the determination of equilibration conditions for the minerals or mineral assemblages of actual metamorphic rocks. The second advance in understanding relates to studies of heat distribution and radiogenic heat generation within the crust and the consequent modelling of the thermal evolution of the crust in a variety of tectonic settings, a procedure greatly enhanced by advances in computer technology.

What these studies have shown essentially is: firstly that, with the recognition of high-temperature low-pressure metamorphic terrains, temperature (and hence grade) is not simply a function of depth; secondly that metamorphic events can be long lived, as predicted by models of the conductive cooling of thickened crust, or short lived, as expected in contact aureoles; thirdly that post metamorphic peak $P-T-t$ paths can show evidence for isothermal decompression or for isobaric cooling; and, fourthly,

that regional metamorphism of the continental crust is not necessarily just a simple function of crustal thickening, but can alternatively be a product of intraplate magmatism generated by deep Earth or shallow Earth processes. An important point which comes out of a combination of these studies, and of studies into the melting of crustal rocks, is that metamorphic conditions are always anomalous. Calculated temperatures of mid- to lower-crustal metamorphism frequently exceed the granite minimum melting temperature, often by hundreds of degrees. Temperatures at the base of normal, c. 35 km thick continental crust in stable tectonic regions, which clearly is not melting are no greater than 500 to 600°C. This implies that regional metamorphism, in which temperatures are well in excess of the normal continental geotherm, represents a severe perturbation of the normal continental geothermal gradient. One of the questions that this volume aims to address can be summed up as 'What causes this perturbation?'

The seminal papers of Philip England and Stephen Richardson and of Philip England and Alan Thompson stressed the role of radiogenic isotopes in the heating of thickened continental crust (England & Richardson 1977; England & Thompson 1984; Thompson & England 1984). What they showed is that, given the concentration of radiogenic isotopes through crustal differentiation, in the upper crust, any crustal thickening will lead, over timescales of tens of millions of years, to enhanced surface heat flows, steeper geothermal gradients and hence the attaining of temperatures characteristic of regional metamorphism in the middle crust. The models presented in these studies suggest that orogenically thickened crust will reach a maximum temperature at some time after deformation and crustal thickening has finished, that cooling will accompany erosive exhumation along a clockwise P - T - t path with a positive, post peak metamorphic dP/dT slope, and that the temperature maximum will be attained during exhumation. The steepness of the clockwise P - T - t path will be a function either of the rate of erosion or, as has been increasingly recognised in orogenic belts such as the Himalaya, upper crustal extension and thinning accommodated along high-level, late-orogenic normal fault systems.

However, derived P - T - t path data document radically different P - T paths in diverse tectonic settings. Among features which the numerical models mentioned above do not readily account for are: firstly, the presence of high-temperature-low-pressure metamorphic terrains or of ultra-

high-temperature metamorphic terrains, both of which can only be generated through conductive heating models with extreme radiogenic heat distributions; secondly, anticlockwise or isobaric cooling post-peak-metamorphism paths; thirdly, short lived (>1 Ma and $\ll 10$ Ma) metamorphic events of regional extent; or fourthly, that in many regional metamorphic terrains microstructural fabric-porphyroblast relationships imply that peak metamorphism was synchronous with, rather than significantly post-dating, the cessation of crustal deformation and, hence, thickening. These observations suggest that, although conductive heating/cooling models may explain some aspects of the thermal evolution of thickened continental crust, there is a family of models with alternative heat source distributions and transfer patterns that can influence the nature of regional metamorphism.

One solution to the observation, in many regional metamorphic terrains, that fabric-porphyroblast relationships imply peak metamorphism to be synchronous with crustal deformation is that deformation itself is a potential heat source. The role of dissipative shear heating has been explored over the last few years by a number of authors especially in respect of the thermal evolution of the Himalayan orogen (Molnar & England 1990; England *et al.* 1992; England & Molnar 1993; Treloar 1997; but see also Royden 1993; Ruppel & Hodges 1994; Harris & Massey 1994 for an opposing view). Although not addressed in papers in this volume it remains a significant potential energy source, albeit one over which there remains significant debate about its efficiency in significantly elevating temperatures, even if only briefly. There is an arguable case that high initial convergence rates favour dissipative shear heating as a key element in the thermal budget at early stages of orogeny, but that this becomes less important as convergence rates and hence strain rates decrease with time. Ultimately, thermal equilibrium in continent-continent collisional settings becomes dominated by long time-scale conductive heating. Early stages of orogeny, where the thermal evolution within the active thrust zones is more strongly influenced by the balance between conductive and advective heat transfer as well as from the input of strain related energy, may become either modified or overprinted by longer time-scale thermal equilibration or removed by erosional processes.

For those of us brought up with the concept that regional metamorphism of crustal rocks is essentially a closed system involving crustal thickening and subsequent thermal evolution consequent on isotopic degradation of radiogenic

heat producing elements, a host of papers published since 1985 have forced a serious re-evaluation (e.g. Lux *et al.* 1986; Bohlen 1987, 1989; Bohlen & Mezger 1989; Ellis 1987; Wickham & Oxburgh 1987; Harley 1989; Looseveld 1989; De Yoreo *et al.* 1991; Sandiford & Powell 1991). High-temperature-low-pressure metamorphism is now often interpreted as the result of the transient advection of heat due to magma emplacement within the crust, with mantle derived magmas widely regarded as playing a major role in advecting heat into the crust. There are a number of potential causes of this, summarized in this volume by **Brown, Gibson & Stevens, Harley** and **Sandiford & Hand**. Most of these involve some form of decompressive partial melting of upwelling asthenospheric mantle. The causes of this upwelling can be divided into two major subsets. One involves deep Earth processes, probably core-mantle interface related, such as hot spots associated with mantle plumes, with basaltic magmas underplating and intruding, potentially thinned continental crust. The other relates to shallower plate tectonic processes that involve the removal of the lithospheric root due to delamination or extensional thinning consequent on earlier lithospheric thickening, slab breakoff in subduction zones, and voluminous supra-subduction zone magma emplacement. All of these involve advection of heat into the continental crust due to its underplating, or intrusion, by mantle derived basaltic magmas. Ironically, in some ways we ultimately come full circle back toward the views of the pioneers who identified a causal link between the emplacement of igneous bodies and metamorphism. **Brown** suggests that 'regional contact or pluton enhanced metamorphism' may result from the advection of heat due to the upward transfer of granodioritic or granitic magmas. We have to infer that these magmas were probably derived from partial melting of the lower crust in response to a basaltic underplate, itself dependent on melting of the mantle lithosphere.

Is there an arguable case, therefore, that the majority of regional metamorphism is a function of mantle processes? Certainly in this volume **Gibson & Stevens** argue that middle to lower crustal granulite-facies metamorphic rocks now exposed in the core of the Vredefort astrobleme Dome are a function of regional metamorphism of the lower crust in response to the initiation of a mantle plume related to emplacement of the Bushveld Complex. **Brown** argues that the low-pressure-high-temperature metamorphic belts in the classic Japanese paired metamorphic belt sequences are the result of ridge subduction with

asthenospheric mantle permitted to upwell through the widening, subducted spreading ridge centre. In contrast, **Sandiford & Hand** suggest that low-pressure-high-temperature metamorphism in some Australian Proterozoic terrains may be due to anomalous mid-crustal radiogenic heat production. **Whittington, Harris & Baker** show that in the Nanga Parbat region of the Himalayan orogen, low-pressure-high-temperature is a function of rapid, structurally controlled, exhumation of mid-crustal rocks already brought to amphibolite-facies temperatures by crustal thickening. **Whitney & Dilek** argue that, in metamorphic core complexes, complex $P-T$ trajectories, with short lived (≤ 1 Ma) thermal spikes, may be indicative of brief magmatic episodes probably temporally associated with exhumation. In this case, does the exhumation drive the magmatism and hence the short lived metamorphic spikes? **Jamieson, Beaumont, Fullsack & Lee** suggest that the heat source for Barrovian-type regional metamorphism may be an accretionary wedge underplated beneath the supra-subduction zone sequence.

It is thus clear that there is no simple model to explain regional metamorphism. Even where ultra high-temperature (UHT) metamorphism is concerned there remains a degree of ambivalence. If UHT metamorphism is simply a function of magma underplating and subsequent heat advection into normal thickness crust, then it should carry a characteristic $P-T$ path signature. However, **Harley** shows that UHT terrains are characterized by a variety of $P-T-t$ path trajectories, some typical of isobaric cooling and others of isothermal decompression. Hence, even in the highest temperature crustal rocks, we are faced with a variety of disparate tectonic settings for regional metamorphism.

Thus far we have spoken only about the driving force for metamorphism. Equally important for our understanding of lithospheric processes is a knowledge of the mechanisms of mineral deformation and transformation, and of the rates at which these processes take place. Although information about the amount of heat energy and the duration of heat availability during metamorphic events can be modelled or estimated, the transformation of mineral assemblages to those expected for the pertaining conditions, such as easily visualized in the 'video clips' presented by **Worley & Powell**, may be hindered due to spatial differences in kinetic factors. In other words, you can subject a gabbro to eclogite facies conditions but it may not react to form eclogite. Likewise, in a situation familiar to all petrologists, a metamorphic rock taken outside the stability

conditions of its mineral constituents during exhumation and cooling, need not necessarily transform to the mineral assemblage or mineral compositions required for the new conditions. The reports of preserved diamonds in metamorphic rocks and the ever increasing number of rocks with relict coesite are clear examples of this problem. As outlined by **Rubie**, and by **Barker & Zhang**, the simple presence or absence of a fluid phase can control whether a reaction takes place or not, independent of whether it is prograde or retrograde in type, even in rocks sometimes well outside their stability field. **Vernon** also emphasizes the importance of a fluid phase in changing grain boundary properties thus enhancing deformation and, ultimately, transformation rates. Importantly, the incomplete transformation of some of the rocks subducted to extreme depths, via their buoyancy, may provide us with a significant driving force for the apparent rapid uplift of such rocks.

All of us must come to terms with some degree of disequilibrium in order to reconstruct the pressure-temperature trajectories followed by our studied samples. Using disequilibrium to their advantage, **Harris & Ayres** combine experimentally determined diffusion rates for Sr with detailed measurement of spatial variations in Sr composition, to extract timescales for anatetic processes. Likewise, **Reche, Martinez & Aboleya** show how sequential mineral growth patterns can be used to provide a detailed picture of the relationship between metamorphism and local tectonic processes. Rather than being frightened away by samples showing strong disequilibrium features, we should be searching them out and subjecting them to detailed examination. With the ever increasing database of experimentally determined kinetic rate data it is becoming increasingly possible to constrain closely the temporal thermal and baric changes undergone by non-equilibrated rocks, during orogeny, as they passed through the crust. The results of such studies provide the fine detail as to how the lithosphere responds, tectonically and in terms of energy and material balance, to plate tectonic processes.

So, we can now demonstrate on the basis of a combination of P - T data, derived P - T - t paths, metamorphism-deformation analyses involving both fabric-porphyroblast relationships and field criteria, and numerical modelling that metamorphism of crustal rocks is a complex function of a mantle derived heat flux and crustal radiogenic heat production. In response to the question 'Do we know much more now than we did 25/50/75 years ago?' the answer is a resounding 'Yes'. Firstly, we are now able to quantify

metamorphic processes more accurately and more thoroughly, and secondly, we now understand more about the tectonic processes that influence metamorphic evolution and that contribute the heat needed to drive it.

What appears increasingly clear is that metamorphism is, in the phraseology of modern science, complex rather than chaotic. As explored by **Hedges**, albeit only in the context of continent-continent collision and crustal thickening, there is a clear sense of emerging order in this science with a complex interplay between input and output parameters. Whether, as implied by John Horgan in his recent book *The End of Science*, subtitled *Facing the Limits of Knowledge in the Twilight of the Scientific Age* metamorphic petrology has, like other scientific disciplines, already made its best and most exciting discoveries is a moot point. Is it possible that further research may yield no more great revelations but, rather, only incremental diminishing returns? What is interesting is that it is arguable, to an extent, that all of our major findings of the last 25 or so years, albeit based on analytical data and integrated into the modern Plate Tectonic paradigm, do not necessarily tell us more about 'What Controls Metamorphism' than our predecessors would have concluded.

We acknowledge comments on this introduction from Michael Brown, John Clemens, Gilcs Droop and Clark Friend.

References

- BOHLEN, S. R. 1987. Pressure-temperature-time paths and a tectonic model for the evolution of granulites. *Journal of Geology*, **95**, 617-632.
- 1989. On the formation of granulites. *Journal of Metamorphic Geology*, **9**, 223-229.
- & MEZGER, K. 1989. Origin of granulite terranes and the formation of the lowermost continental crust. *Science*, **244**, 326-329.
- DE YOREO, J. J., LUX, D. R. & GUIDOTTI, C. V. 1991. Thermal modelling in low-pressure/high-temperature metamorphic belts. *Tectonophysics*, **188**, 209-238.
- ELLIS, D. J. 1987. Origin and evolution of granulites in normal and thickened crust. *Geology*, **15**, 167-170.
- ENGLAND, P. C., LE FORT, P., MOLNAR, P. & PECHER, A. 1992. Heat sources for Tertiary metamorphism and anatexis in the Annapurna-Manaslu region, Central Nepal. *Journal of Geophysical Research*, **97**, 2107-2128.
- & MOLNAR, P. 1993. The interpretation of inverted metamorphic isograds using simple physical calculations. *Tectonics*, **12**, 145-157.
- & RICHARDSON, S. W. 1977. The influence of erosion upon the mineral facies of rocks from different metamorphic environments. *Journal of the Geological Society, London*, **134**, 201-213.

— & THOMPSON, A. B. 1984. Pressure-temperature-time paths of regional metamorphism. I: Heat transfer during the evolution of regions of thickened crust. *Journal of Petrology*, **25**, 894–925.

HARLEY, S. L. 1989. Granulites: a metamorphic perspective. *Geological Magazine*, **126**, 215–247.

HARRIS, N. B. W. & MASSEY, J. 1984. Decompression and anatexis of Himalayan metapelites. *Tectonics*, **13**, 1537–1546.

LOOSEVELD, R. 1989. The synchronism of crustal thickening and low-pressure facies metamorphism in the Mount Isa inlier, Australia. 2: Fast convective thinning of mantle lithosphere during thickening. *Tectonophysics*, **165**, 191–218.

LUX, D. R., DE YOREO, J. J., GUIDOTTI, C. V. & DECKER, E. R. 1986. Role of plutonism in low-pressure metamorphic belt formation. *Nature*, **323**, 797–797.

MOLNAR, P. & ENGLAND, P. C. 1990. Temperatures, heat flux and frictional stress near major thrust faults. *Journal of Geophysical Research*, **95**, 4833–4856.

ROYDEN, L. H. 1993. The steady state thermal structure of eroding orogenic belts and accretionary prisms. *Journal of Geophysical Research*, **98**, 4487–4507.

RUPPEL, C. & HODGES, K. V. 1994. Pressure-temperature-time paths from two-dimensional thermal models: prograde, retrograde and inverted metamorphism. *Tectonics*, **13**, 17–44.

SANDIFORD, M. & POWELL, R. 1991. Some remarks on high-temperature low-pressure metamorphism in convergent orogens. *Journal of Metamorphic Geology*, **9**, 333–340.

THOMPSON, A. B. & ENGLAND, P. C. 1984. Pressure-temperature-time paths of regional metamorphism. II: their influence and interpretation using mineral assemblages in metamorphic rocks. *Journal of Petrology*, **25**, 929–955.

TRELOAR, P. J. 1997. Thermal controls on early-Tertiary, short-lived, rapid regional metamorphism in the NW Himalaya, Pakistan. *Tectonophysics*, **273**, 77–104.

WICKHAM, S. R. & OXBURGH, E. R. 1987. Low pressure metamorphism in the Pyrenees and its implications for the thermal evolution of rifted continental crust. *Philosophical Transactions of the Royal Society of London*, **A321**, 219–242.

The thermodynamics of Himalayan orogenesis

K. V. HODGES

*Department of Earth, Atmospheric, and Planetary Sciences,
Massachusetts Institute of Technology, Cambridge, MA 02139, USA*

Abstract: Geological and geochemical research in the internal zone of the Himalayan orogen reveal evidence for complex relationships between regional metamorphism, anatexis, thrust faulting and normal faulting in Miocene time. Such interactions share many characteristics with those that define the behaviour of non-equilibrium thermodynamic systems, like chemical oscillators. The internal ordering of such systems arises spontaneously and is maintained by continual exchange of energy with the outside world. Mountain ranges are open thermodynamic systems, equally capable of displaying self-organized behaviour. They accumulate energy through a variety of mechanisms, particularly crustal thickening, but their non-equilibrium structure is maintained through compensating mechanisms of energy dissipation. The simultaneous operation of normal faults and thrust faults in the Himalayan system, ejecting a wedge of middle crust southward from the orogen towards the Indian foreland, was a remarkably efficient method of mass (and therefore energy) dissipation in Miocene time. Research in many branches of science suggests that thermodynamic systems forced far from equilibrium by their boundary conditions may evolve towards establishing the most efficient possible mechanisms for counteracting those conditions. For the Himalaya, one possible explanation for development of a process set characterized by simultaneous normal faulting and thrust faulting, linked through metamorphism and anatexis, is that simple physical erosion alone was inadequate to moderate the extraordinary crustal thickness and topographic gradients that characterized the southern flank of the range in Miocene time. The orogenic system may have adapted to this condition through a new and more efficient mechanism of energy dissipation that required the coordination of a variety of thermal and deformational processes.

One of the great success stories in the Earth sciences over the past quarter-century has been the integration of petrology, geochemistry, structural geology and geophysics to improve our understanding of the relationships between thermal and deformational processes in mountain belts. When faced with a question like 'What drives metamorphism?', physical chemistry tell us that the answer is largely 'Heat', but the metamorphic evolution of an orogen is dictated by complex interactions between heat and mass transfer processes that can only be fully appreciated from a multidisciplinary perspective. Though the more optimistic among us might argue that sophisticated numerical simulations, systematic structural studies, and a burgeoning petrologic and thermochronologic database have provided us with a good, basic understanding of *how* thermal, erosional and deformational processes are related in mountainous regions, a more difficult question is '*Why*?'.

The physics of orogeny requires no unique style of metamorphism. Metamorphic patterns that emerge from numerical models of orogeny (e.g. Barr & Dahlen 1989; Jamieson & Beaumont 1988; Huerta *et al.* 1996) depend heavily on assumptions about the structural and erosional evolution of mountain ranges in space

and time, not to mention the thermal characteristics of the rocks involved. Tectonics research and geomorphology tell us that there is no single way of building mountains or tearing them down, thermodynamics tells us that there is no single way of moving heat through an orogen, and real rocks cannot be characterized by a single set of physical and thermal constants. Numerical models thus provide a conceptual understanding of the many ways that thermal and deformational processes can relate to one another, but they cannot predict why the specific relationships observed in real mountain ranges developed instead of other relationships that are equally viable from a thermomechanical perspective. In fact, the thermal structure of mountain ranges is so dependent on parameters that can vary tremendously from place to place (e.g. erosion rate, accretion rate, and heat production) that we might expect significant changes in metamorphic history along strike in a single range and relatively little similarity between the metamorphic evolution of different ranges. Yet many orogens display similar, first-order spatial patterns of metamorphism and deformation despite their relatively dissimilar tectonic histories (e.g. Miyashiro 1961; Turner 1981), and a uniform pattern of metamorphism

characterizes the internal zone of mountain belts like the Himalaya over vast areas (Pêcher 1989). To understand why such patterns may develop and persist for millions of years, we may have to develop fresh perspectives on the relationships between metamorphism and other orogenic processes.

One possibility is to consider mountain ranges as *complex systems*. Such systems incorporate processes that, viewed independently, are governed by simple physical laws. However, the relationships between these processes are such that the collective behaviour of the system is not predictable from first principles. An important characteristic of complex systems is their ability to evolve towards specific patterns of process relationships known as *attractor states*; a familiar example to geologists is the self-organization of a uniformly heated fluid into a regular pattern of convection cells (Platten & Legros 1984). If orogens behave like other complex systems, we might expect them to exhibit ordered behaviour that emerges spontaneously from a seemingly random collection of thermal and deformational processes. Such ordering signifies a dynamic balance between fluxes of matter and energy into and out of the system; once achieved, these balances can be self-sustaining for long time periods. In this paper, a synergetic relationship between Miocene deformation, metamorphism and anatexis in Nepal is interpreted as evidence of the emergence of an attractor state for the Himalayan orogenic system.

Thermal and deformational history of the Himalayan orogen

Initiating with the collision of India and Eurasia in the early Cenozoic, the Himalayan orogen is one of our best natural laboratories for the study of active mountain-building processes. It can be divided into six lithotectonic zones that can be traced for hundreds of kilometres along strike (Fig. 1). The Transhimalayan zone includes numerous calc-alkaline batholiths that represent part of an Andean-type continental arc developed along the southern margin of Eurasia over the Cretaceous–early Tertiary interval (Honneger *et al.* 1982; Debon *et al.* 1986). Strongly deformed ophiolitic, volcanic and sedimentary rocks of the Indus suture zone mark the surface boundary between Eurasian crust to the north and Indian crust to the south (Le Fort 1975; Searle 1991). The Tibetan zone comprises a thick, passive margin sequence deposited along the northern margin of the

Indian plate (Gaetani & Garzanti 1991; Garzanti 1993). These predominantly unmetamorphosed strata contrast with high-grade gneisses and leucogranitic rocks exposed sporadically in Neogene metamorphic core complexes within the Tibetan zone and continuously along the crest of the Himalaya in the Greater Himalayan zone. This metamorphic package has been thrust southward over Neoproterozoic to Lower Eocene, predominantly low-grade meta-sedimentary strata of the Lesser Himalayan zone (Valdiya 1986). A foreland fold-and-thrust belt developed in Oligocene(?)–Pleistocene Siwalik molasse corresponds to the Subhimalayan zone (Johnson *et al.* 1979; Alam 1989; Najman *et al.* 1993).

With the exception of steeply dipping shear zones that occur along some margins of the Indus suture zone, the boundaries between Himalayan lithotectonic zones are defined by moderately N-dipping fault systems. Two of the most famous—the Main Central and Main Boundary thrust systems (Fig. 1)—accommodated hundreds of kilometres of shortening in Miocene to Pliocene time (Molnar 1984). The most recently recognized zone boundary is also the most unusual; the South Tibetan detachment system is a family of low-angle normal faults that dip northward beneath the Tibetan zone and were responsible for tens of kilometres of tectonic unroofing of the underlying Greater Himalayan sequence (Burchfiel *et al.* 1992). Geochronologic studies show that most strands initiated in Early or Middle Miocene time, while the structurally lower Main Central thrust system was enabling large-scale crustal thickening (Hubbard & Harrison 1989; Guillot *et al.* 1994; Hodges *et al.* 1996; Searle *et al.* 1997; Coleman 1996; Hodges *et al.* in press; Wu *et al.* 1998). The most likely explanation for the South Tibetan extensional structures is that they were triggered when the internal strength of the orogen was no longer capable of supporting the crustal thickness and topographic gradients that had developed during the Himalayan mountain-building process (Burchfiel & Royden 1985).

Metamorphism and anatexis in the Greater Himalayan zone

For the study of metamorphic processes, the most interesting part of the Himalayan orogen is the Greater Himalayan zone, which can be viewed as a northward-tapering prism bounded above by the South Tibetan detachment (STD)

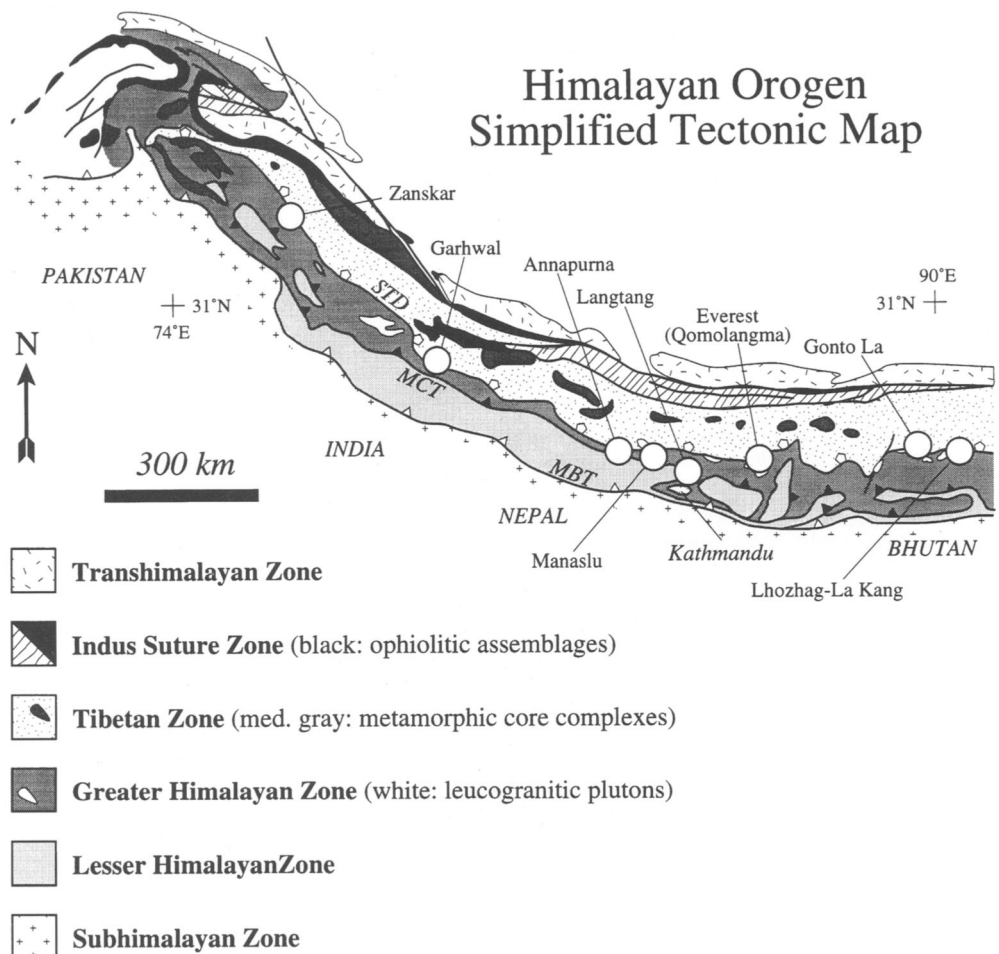


Fig. 1. Simplified tectonic map of the Himalayan orogen. Circles indicate localities mentioned in text. Major fault systems include the Main Boundary thrust (MBT), Main Central thrust (MCT) and South Tibetan detachment (STD).

system and below by the Main Central thrust (MCT) system. Petrologic studies of pelitic gneisses that dominate the lower half to two-thirds of the Greater Himalayan sequence suggest a two-phase metamorphic evolution: an early, high-pressure, intermediate-temperature 'Eohimalayan' event was overprinted by a later, lower-pressure, higher-temperature 'Neohimalayan' event (Hodges *et al.* 1988; Pêcher 1989). In the central and eastern Himalaya, the intensity of the Neohimalayan event was so great that it obliterated most evidence for the age of the Eohimalayan event. In the western Himalaya, where Neohimalayan effects are less severe, U-Pb and Sm-Nd thermochronology demonstrate an Early Oligocene age for the Eohimalayan metamorphic peak (Vance &

Harris 1996; Walker 1998). Similar U-Pb ages have been obtained for relict, presumably Eohimalayan metamorphic monazites from the Annapurna Range of central Nepal (Coleman 1996; Hodges *et al.* 1996). The age of Neohimalayan metamorphism is better constrained in the central and eastern Himalaya, where it culminated in the anatetic event responsible for a series of leucogranitic plutons emplaced near the top of the Greater Himalayan sequence. A growing U-Th-Pb database for the leucogranites implies a 24–12 Ma interval for Neohimalayan metamorphism and anatexis, with the greatest period of intensity at c. 20–23 Ma (Schärer 1984; Schärer *et al.* 1986; Parrish *et al.* 1992; Noble & Searle 1995; Harrison *et al.* 1995; Hodges *et al.* 1996; Edwards and

Harrison 1997; Searle *et al.* 1997; Coleman submitted; Hodges *et al.* submitted; Wu *et al.* submitted).

The Himalayan leucogranites have been the subject of numerous geological studies, but disagreements remain regarding their petrogenetic origins. They can be grouped loosely into two categories: centimetre- to decimetre-scale migmatitic leucosomes developed in pelitic gneisses; and discrete bodies that range from metre-scale sills and dykes to plutons with volumes of several tens of cubic kilometres (Le Fort *et al.* 1987). The migmatitic leucosomes typically contain the assemblage Qtz + Kfs + Pl + Ms \pm Bt \pm Tur \pm Grt \pm Sil (abbreviations after Kretz 1983), but kyanite-bearing leucosomes have been identified in at least one transect (Hodges *et al.* 1996). In many well-studied areas, two distinctively different types of discrete leucogranite bodies have been identified: an early phase with the characteristic sub-assemblage Qz + Kfs + Pg + Bt \pm Tur, and a later phase with Qtz + Kfs + Pl + Ms + Tur \pm Crd (Hodges *et al.* 1993; Inger & Harris 1993; Harris & Massey 1994; Guillot & Le Fort 1995; Scalliet *et al.* 1995; Searle *et al.* 1997). For many years, it was commonly assumed that both the leucosomes and leucogranites had a common origin – anatexis of the metapelitic parts of the Greater Himalayan sequence – and that the discrete bodies were simply coalesced and mobilized leucosome (e.g. Le Fort 1975; Gariépy *et al.* 1985; Deniel *et al.* 1987; Le Fort *et al.* 1987; France-Lanord *et al.* 1988). Some of the details of this model have been challenged recently on the basis of trace-element modelling of leucogranites in the Langtang area (Fig. 1), which suggests that the Greater Himalayan source region for those leucogranites is not the same as the part of the section displaying abundant migmatitic leucosomes (e.g. Harris & Massey 1994). Given such evidence for distinctive origins for the leucosomes and leucogranites, Inger & Harris (1993) even went so far as to suggest that the leucosomes may be pre-Himalayan. While subsequent U-Pb studies of the leucosomes at Langtang and elsewhere in the Himalaya yield ages that are indistinguishable from those of the oldest leucogranites in any single transect (e.g. Parrish *et al.* 1992; Hodges *et al.* 1996; Coleman 1996), it is true that most leucogranite bodies are somewhat younger than most leucosomes and the genetic relationships between the two remain controversial.

One of the most distinctive characteristics of the Greater Himalayan zone is the common occurrence of inverted metamorphic gradients. From Bhutan at least as far west as the

Zanskar Himalaya (Fig. 1), the basal Greater Himalayan sequence contains mineral assemblages characteristic of intermediate P-T metamorphism (Ky + Str grade). The grade of metamorphism increases structurally upward to upper-amphibolite facies, typically $\text{Sil} \pm \text{Crd}$ at the structural level of maximum *in situ* melting (Brunel & Kienast 1986; Hubbard 1989; Mohan *et al.* 1989; Swapp & Hollister 1991; Inger & Harris 1992; Macfarlane 1992; Hodges *et al.* 1993; Meier & Hiltner 1993; Pognante & Benna 1993; Coleman 1996; Vannay & Hodges 1996). At least some of the apparent inversion is now known to be the result of polymetamorphism (Brunel & Kienast 1986; Hodges & Silverberg 1988; Swapp & Hollister 1991; Inger & Harris 1992), but there are several transects for which thermobarometric data indicate an inversion of metamorphic isograds developed during a single metamorphic event (Hubbard 1989; Pêcher 1989). Four classes of models have been proposed to explain this phenomenon.

1. Late penetrative shearing or recumbent folding of pre-existing Neohimalayan isograds produced an apparent thermal inversion (Searle & Rex 1989; Jain & Manickavasagam 1993; Grujic *et al.* 1996). One variation envisages simple thrusting of the upper Greater Himalayan sequence over the lower after the early stages of Neohimalayan metamorphism but before final thermal equilibration (Swapp & Hollister 1991; Reddy *et al.* 1993; Davidson *et al.* 1995).
2. Local frictional heating in the highest-grade parts of the Greater Himalayan sequence produced an inverted thermal structure (England & Molnar 1993; Harris & Massey 1994).
3. Accretion of rocks with unusually high heat production to the base of the Himalayan orogenic wedge, coupled with the effects of surface erosion, produced a thermal high in the Greater Himalayan zone which was surrounded by lower-temperature regions (Royden 1993; Huerta *et al.* 1996).
4. Heat flowing through and generated within the Greater Himalayan sequence was concentrated near the top of the metamorphic core due to the thermal blanketing effect of the Tibetan sedimentary sequence, leading to an inverted temperature structure that could be preserved as metamorphic isograds (Jaupart & Provost 1985; Pinet & Jaupart 1987).

The first of these differs from the rest by requiring significant shearing within the Greater

Himalayan sequence, and furthermore this deformation largely post-dated the establishment of metamorphic isograds. For many years, the Greater Himalayan zone was regarded as a more or less intact crystalline slab that was thrust southward along the MCT with little internal deformation (e.g. Le Fort 1975). As more field data have become available, it is clear that the Greater Himalayan zone is more complicated structurally than previously believed. For example, major thrust faults within the Greater Himalayan zone have been documented in Bhutan (Gansser 1983; Davidson *et al.* 1995) and central Nepal (Hodges *et al.* 1996; Vannay & Hodges 1996). However, the metamorphic discontinuity created by these post-metamorphic faults is of minor geographic extent in both regions, and is always restricted to the upper part of the Greater Himalayan sequence. In contrast, the metamorphic inversions throughout much of the Greater Himalayan zone occur over 7 to 20 km thick sections of rocks that display a simple tectonostratigraphy which persists nearly 2000 km along strike from Bhutan to Zanskar. Given the monotonous lithostratigraphy of the Greater Himalayan pelitic gneisses, it might be difficult to recognize the abundant post-metamorphic shear zones required by models of inverted metamorphism such as that of Grujic *et al.* (1996), but there is as yet no evidence that all or even most of the inverted isograds in the Greater Himalayan sequence correspond to zones of significant shear displacement.

Fundamental relationships between anatexis, metamorphism and deformation in the Himalaya

Regardless of whether or not post-metamorphic shearing played an important role in the present-day distribution of metamorphic isograds in the Greater Himalayan zone, there is strong evidence that Neohimalayan metamorphism and anatexis were broadly coeval with the development of the MCT and STD fault systems. Detailed structural studies show that the earliest shearing fabrics related to the MCT were synmetamorphic with respect to Neohimalayan metamorphism in the Everest (Hubbard 1988; Hubbard & Harrison 1989), Langtang (Macfarlane *et al.* 1992), Annapurna (Parrish & Hodges 1993; Hodges *et al.* 1996; Coleman 1996), and Garhwal (Hodges & Silverberg 1988; Metcalfe 1993) regions of Nepal and India (Fig. 1). The exact age of MCT initiation seems likely to have

varied along strike in the Himalaya, but all existing quantitative constraints fall within a narrow time frame of 23–20 Ma (Hubbard & Harrison 1989; Hodges *et al.* 1996; Coleman 1996). The Annapurna Range is one of the few places where migmatitic gneisses can be traced down to the structural level at which MCT-related fabrics have been developed. There the earliest phases of anatexis predated MCT initiation, but only by 2–3 Ma at most, and melting persisted throughout the high-temperature phase of MCT movement (Hodges *et al.* 1996; Coleman 1996).

The discrete leucogranites have a similar relationship with the STD system. In most cases, the largest Himalayan leucogranites intruded to the approximate structural level occupied by the basal faults of the STD system. Some of these plutons and many leucogranite dykes and sills exhibit extensional fabrics associated with the basal detachments (e.g. Burg *et al.* 1984; Searle & Fryer 1986; Herren 1987; Burchfiel *et al.* 1992; Hodges *et al.* 1994), and some researchers have observed direct truncation of leucogranites by the basal detachments (e.g. Burchfiel *et al.* 1992; Searle *et al.* 1997). However, late-stage leucogranites intrude the basal STD detachment in at least four widely scattered areas (Fig. 1): Lhohag-La Kang (Burchfiel *et al.* 1992), Gonto La (Edwards *et al.* 1996), Everest or Qomolangma (Hodges *et al.* 1992; Hodges *et al.* 1996), Manaslu (Guillot *et al.* 1993) and Annapurna (Brown & Nazarchuk 1993; Coleman 1996; Hodges *et al.* 1996). In all of these instances, younger, structurally higher detachments of the STD either truncated or facilitated unroofing of the late-stage leucogranites. Thus, the anatexic event responsible for the discrete leucogranites predated initiation of the STD system and continued during extension, but the latest extensional structures of the STD system are younger than the youngest leucogranites. Given our current state of knowledge, these relationships loosely bracket the *onset* of extension between 23 and 16 Ma throughout the orogen. Since the oldest leucogranites are indistinguishable in age from the migmatitic leucosomes that slightly predate MCT initiation in well-studied areas like the Annapurna Range, it seems probable that the earliest stages of MCT and STD movement occurred at about the same time in any given transect and just after the earliest stages of anatexis in the Greater Himalayan sequence.

Two models have been proposed for the relationship between anatexis and deformation in the Himalayan metamorphic core. One hypothesis holds that anatexic melting at deep,

presently unexposed levels in the orogen triggered rheological changes that permitted the nucleation of discrete thrust structures within the Greater Himalayan sequence. Swapp & Hollister (1991) and Hollister *et al.* (1995) proposed that thrusting of this actively melting material to higher structural levels would serve as an efficient mechanism of heat transfer into the upper Greater Himalayan sequence and facilitate the production of the discrete leucogranites. This scenario implies a direct cause-and-effect relationship between anatetic melting and thrust displacement (Hollister & Crawford 1986; Hollister 1993). The second model (Hodges 1990; Hodges *et al.* 1993; Harris & Massey 1994) recognizes a probable relationship between migmatite genesis and thrusting, but attributes the discrete leucogranitic bodies to decompression melting associated with the STD system. In this case, deformation is the cause, rather than the effect, of widespread anatexis.

Geological relationships in the Himalaya support certain aspects of both models. The fact that leucogranites in several transects intrude the basal STD detachment is consistent with decompression melting. However, the early stages of melting and dyke emplacement predate the oldest STD detachment in all areas, implying that tectonic denudation cannot be the sole triggering mechanism for anatexis. Where major thrusts have been identified within the Greater Himalayan sequence, related shear fabrics are most intense in zones with the highest concentration of leucogranite dykes (Davidson *et al.* 1995; Hodges *et al.* 1996; Vannay & Hodges 1996), reinforcing the notion that rheological changes induced by melting influenced localization of thrusts. However, a large proportion of the leucogranites occur below these structures in the Annapurna Range and were not thrust into their present position relative to deeper parts of the Greater Himalayan sequence. The following model, derived from those previously proposed, seems consistent with all geological data currently available.

1. Underthrusting and accretion of Indian plate crust with elevated levels of radioactive heat production beneath the evolving orogen created a thermal environment in the Greater Himalayan zone that was conducive to limited anatexis by c. 23–24 Ma. The record of this earliest melting process includes disseminated migmatitic leucosomes and possibly one leucogranite, the Makalu pluton (Schärer 1984).
2. Initiation of the MCT and STD systems at c. 20–23 Ma coincided with widespread

melting in the Greater Himalayan sequence and produced sufficient melt volumes to feed numerous leucogranite plutons. It seems likely that the basal décollements of both systems developed at lithostratigraphic horizons that contained large volumes of melt and were therefore relatively weak. Movement on these structures could have been facilitated by melt lubrication (Hollister & Crawford 1986). At this time, a direct positive feedback relationship developed between MCT displacement and anatexis. While the presence of melt encouraged deformation, thrusting itself resulted in underplating of more material with high heat production (Huerta *et al.* 1996), limited shear heating (England *et al.* 1992), and the fluxing of metamorphic fluids from the Lesser Himalayan sequence into the MCT hanging wall (Le Fort 1981), all of which are processes that would have promoted melting in the Greater Himalayan sequence and thus melt-enhanced thrust displacement.

3. Several lines of petrologic evidence suggest that as much as 20 km of overburden was stripped off the Greater Himalayan zone over the c. 23–12 Ma interval, principally as a consequence of movement on the STD system (e.g. Burchfiel *et al.* 1992; Hodges *et al.* 1993; Harris & Massey 1994; Edwards and Harrison 1997; Hodges *et al.* in press). Adiabatic decompression related to tectonic denudation undoubtedly enhanced melting in the Greater Himalayan sequence and may have been exclusively responsible for the muscovite leucogranite magmas that produced many of the largest Himalayan plutons. Again, a kind of 'symbiosis' is apparent, with the STD system triggering anatexis and the consequent melts facilitating continued fault movement. Ultimately, the STD system achieved sufficient denudation of the metamorphic core to cool it below the temperature range appropriate for anatetic melting.

Autocatalytic processes and non-equilibrium thermodynamics

The mutual reinforcement of normal faulting, thrusting and anatetic melting in the Himalaya is reminiscent of special types of catalysis in complex chemical systems. A chemical catalyst is some species that modifies reaction rates in a chemical system without necessarily being one of the reactants. Autocatalysis occurs when the presence of a species increases the production

rate of that same species, through reactions like $X + Y \Rightarrow 2X$, for example. Such autocatalytic reactions are especially common in biological systems and are, in fact, of fundamental importance to the process of life (Kauffman 1995). Living systems survive by consuming and expending matter and energy, which is to say that, from a thermodynamic perspective, they are open systems whose behaviour is governed by non-equilibrium processes.

Why an ordered relationship between deformation and metamorphism should arise in the Himalaya, and why it should persist for several million years, may be understood by considering the implications of the Second Law of Thermodynamics for systems far from equilibrium, like orogenic belts. Most of us are familiar with a statement of the Second Law that describes the tendency towards increasing disorder or entropy (S) with time (t) in an isolated system:

$$\frac{dS}{dt} \geq 0 \quad (1)$$

with the equilibrium state defined as the situation at which $dS \Rightarrow 0$. If an isolated chemical system is perturbed from the equilibrium state, Le Châtelier's principle holds that it will naturally respond through spontaneous reactions towards equilibrium. Thus, equilibrium can be viewed as an attractor state for those isolated thermodynamic systems that can achieve it.

For open systems, we must distinguish between changes in entropy that occur through irreversible processes within the system (d_iS) and those that simply involve entropy transfer with the outside world (d_eS). In the general case,

$$\frac{dS}{dt} = \frac{d_iS}{dt} + \frac{d_eS}{dt} \quad (2)$$

The first term on the right-hand side of equation (2) describes entropy production due to irreversible processes in the system. The Second Law tells us that this term is either positive or zero, but it does not *dictate* increasing disorder in a non-isolated system; whether or not the total entropy of such a system increases or decreases with time depends on the nature of its interactions with its surroundings. In fact, an open system can exhibit spontaneous self-organization (implying $dS/dt < 0$) away from the equilibrium state by exchanging energy and matter with the rest of the universe such that its overall entropy change remains positive (Nicolis & Prigogine 1977). The collections of dynamic processes that permit such behaviour are referred to as *dissipative structures*.

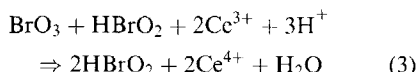
Not very far from equilibrium, in the realm of linear non-equilibrium thermodynamics, open systems naturally evolve towards an attractor state of minimum entropy production consistent with the boundary conditions imposed by their surroundings (Prigogine 1980). This stationary state is much like equilibrium insofar as the tendency of a system near equilibrium is still predictable from the nature of its externally dictated boundary conditions. However, in the far-from-equilibrium world of non-linear thermodynamics, system behaviour is not predictable in any simple way, and attraction to a variety of different organized states may be supported by a complex array of dissipative structures.

One of the most famous experiments used to illustrate non-linear chemical dynamics is the Belousov-Zhabotinsky (BZ) reaction (Gray & Scott 1990; Nicolis 1995). Stumbled upon quite by accident around 1950 by Russian biochemist Boris Belousov, the most widely studied form of this reaction involves the oxidation of malonic acid (CH_2COOH_2) by potassium bromate (KBrO_3) in the presence of sulphuric acid (H_2SO_4), a redox indicator (typically a Ce compound), and a chemical dye (ferroin) to facilitate viewing of chemical processes that take place. When continuously stirred, the BZ cocktail spontaneously oscillates between the colour red (indicating the presence of reduced Ce^{3+}) and the colour blue (indicating oxidation to Ce^{4+}). This self-imposed ordering of an unstructured chemical mixture into a pattern of oscillating reactions seems at odds with the Second Law of Thermodynamics, so much so that Belousov's results were written off by the scientific establishment as the result of incompetence or fraud. It took nearly 20 years for the research of Belousov and his intellectual descendants on oscillatory reactions to find its way to publication in the mainstream scientific literature (Winfree 1984). By that time, researchers had found that an unstirred BZ compound would display complex, three-dimensional patterns of red and blue chemical waves, corresponding to evolving and propagating reaction fronts that emerged spontaneously (Winfree 1987; Zaikin & Zhabotinsky 1970). Obviously, some physiochemical process must provide an exception to the rule that all systems evolve from order to disorder.

The problems that Belousov's reviewers had with his manuscripts stemmed from the belief that the BZ mixture's purported behaviour implied oscillation around equilibrium. At constant temperature and pressure, equilibrium thermodynamics dictates that the Gibbs free energy (G) of a system undergoing any set of

reactions must decrease monotonically to a minimum value corresponding to equilibrium (e.g. Anderson & Crerar 1993). If it was true that each oscillation of the BZ system passes through the equilibrium state, then the implication would be that G itself oscillates, a clear violation of thermodynamic precepts. We now know that an active BZ mixture is actually far from equilibrium, cycling about attractor sets through processes governed by non-equilibrium thermodynamics.

The complete set of processes responsible for the oscillatory behaviour of the BZ mixture is unknown – it probably involves more than 30 separate reactions – but a simplified model developed by Field *et al.* (1972) involves three stages: (1) relatively slow bromide consumption; (2) oxidation of Ce^{3+} to Ce^{4+} along with a rapid drop in Br^- ; and (3) reduction of Ce^{4+} back to Ce^{3+} with regeneration of Br^- . A crucial part of this process is the operation of intermediate autocatalytic reactions like the one principally responsible for cerium oxidation in the second step:



In addition, these autocatalytic processes must cooperate with one another to produce the structured behaviour of the system as a whole (Nicolis 1995).

In a closed system, with no addition of reactants or removal of products, the oscillatory

behaviour of a BZ mixture eventually stops as some of the reactants are consumed forever and the system approaches stable equilibrium. This observation confirms that G does indeed decrease monotonically throughout the evolution of the system while the concentrations of intermediate reactants and products oscillate. In effect, any transient decrease in entropy due to these concentration changes is overcompensated by other processes that produce entropy. However, in an open system that permits the introduction of new reactants, the BZ reaction can be maintained in an oscillatory state indefinitely. The longevity and stability of self-organized structures like the patterns shown by a BZ mixture are thus dependent on the transfer or energy and/or matter into and out of the system.

A non-equilibrium view of orogenic systems

Mountain ranges are open systems from a thermodynamic perspective inasmuch as they exchange both matter and energy with their surroundings, and it seems only reasonable to postulate that their behaviour is governed by non-equilibrium thermodynamics. From this perspective, the processes that constitute mountain evolution can be divided into those that add energy (ξ^+) to the orogenic system, those that store energy within it, and those that dissipate energy into the rest of the universe (Fig. 2). One of the most important mechanisms of energy storage is crustal shortening and thickening.

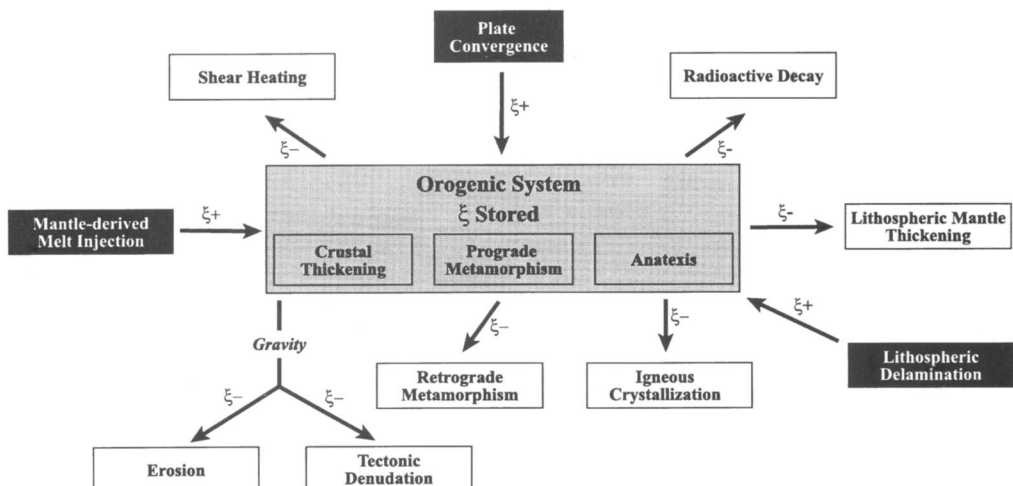


Fig. 2. Energy fluxes and the orogenic system. Processes that add energy to the system (ξ^+) are shown as black rectangles; those that dissipate energy into the surrounding environment (ξ^-) as white rectangles. The orogenic system (grey) stores energy temporarily through prograde metamorphism, anatexis, and crustal thickening and accretion.

While some of this energy is stored by elastic strain (Means 1976), most is simply gravitational potential energy (Artyushkov 1973). In regions of isostatic compensation, the potential energy per unit area stored in the system in this way ($\Delta\xi_{\text{pot}}$) is:

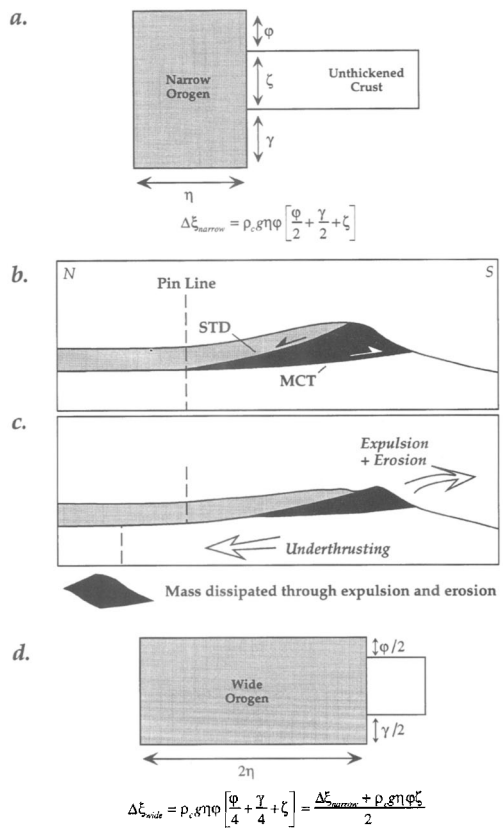
$$\Delta\xi_{\text{pot}} = \rho_c g \varphi \left(\frac{\varphi}{2} + \frac{\gamma}{2} + \zeta \right) \quad (4)$$

where the variables are as defined in Fig. 3 and the density of the additional crust (ρ_c) is assumed to be uniform (Molnar & Lyon-Caen 1988). Energy can also be stored by endothermic processes such as prograde metamorphic reactions and anatexis. Imbrication and accretion of upper crust in collisional mountain ranges tends to concentrate heat-producing elements, which are reservoirs of 'radiogenic' energy that may escape the system through dissipation or be retained through prograde metamorphism (Jaupart & Provost 1985; Huerta *et al.* 1996; Sandiford & Hand 1998). Other energy-dissipation mechanisms include some petrologic

processes (such as retrograde metamorphism and magma crystallization), some deformational processes (such as dynamic recrystallization, strain release during earthquakes, and shear heating), and processes such as erosion and tectonic denudation that reduce the thickness of the crust in an orogen and thus $\Delta\xi_{\text{pot}}$.

Some postulated or demonstrated orogenic processes have a mixed effect on the energy budget. For example, there is some evidence that collision tectonics results in thickening of the mantle lithosphere as well as the crust (Houseman *et al.* 1981; England & Houseman 1988; Seber *et al.* 1996). Colder and more dense than the asthenosphere it replaces, a lithospheric 'root' would resist the buoyancy forces associated with thickened crust (Molnar *et al.* 1993). Thickening of the mantle lithosphere is thus a dissipative process, while coeval thickening of the crust is energy accumulative. If the lithospheric root delaminates or is convectively removed (Bird 1979; Molnar *et al.* 1993), potential energy is added to the system. This

Fig. 3. The energetics of crustal thickening and expulsion: (a) and (c) are modified from Molnar & Lyon-Caen (1988). (a) Simple block diagram of a narrow orogen (grey) adjoining normal, unthickened lithosphere (white). The orogen, with width η , has a thickness which is the sum of the original thickness of the normal lithosphere (ζ), the elevation of the mountains above the adjacent surface of the normal lithosphere (φ), and the thickness of the compensating crustal root (γ). The difference in potential energy per unit length between the orogen and normal lithosphere ($\Delta\xi_{\text{narrow}}$) can be thought of as energy storage by crustal thickening; it is also the potential energy change per unit area ($\Delta\xi_{\text{pot}}$) multiplied by the width of the orogen (cf. equation 4). (b) Cartoon (not to scale) of the Himalayan orogenic system showing the geometric relationship between the STD and MCT systems, which separate the Tibetan zone (grey), the Greater Himalayan zone (black), and the Lesser Himalayan zone (white). Pin line is an arbitrary vertical line drawn to indicate the overall movement shown in the next frame. (c) Cartoon of the system after an increment of coordinated movement on the STD and MCT systems. Southward extrusion of the Greater Himalayan zone and simultaneous erosion removes material from the system in the amount shown by the freeform black polygon. (d) Block diagram indicating the energy dissipation that can occur through expulsion or crustal spreading. A wide orogen is constructed by permitting the excess crust in (a) ($\varphi + \gamma$) to flow towards the right of the diagram, so that the height of the mountains becomes $\varphi/2$, the thickness of the root becomes $\gamma/2$, and the width of the orogen becomes 2η . The new potential energy change per unit length, relative to unthickened lithosphere, for the wide orogen ($\Delta\xi_{\text{wide}}$) is substantially less than that for the narrow orogen.



reminds us that the deconstruction of orogenic systems is not synonymous with energy loss, just as building mountains is not simply a matter of adding potential energy. The orogenic process, from beginning to end, is a battle between energy accumulation and energy dissipation. The history of an orogenic belt thus records the flow of energy through the system and depends largely on how that energy was converted from one form to another during its stay.

Figure 4, a process network map for orogenic systems, illustrates many of the complicated feedback relationships that can arise. A process that enhances the probability of another occurring can be thought of as a catalyst, whereas one which does the opposite is an inhibitor. Circuits that involve both catalytic and inhibiting relationships imply negative feedback. A simple example is that crustal thickening encourages erosion through uplift, but erosional transport removes material from the system and thins the crust in an orogenic belt. Autocatalytic relationships are represented here as closed circuits of catalysis. These are the groups of processes that

can sustain non-equilibrium, but nonetheless stable, orogenic structures for significant lengths of time.

A 'systems approach' to understanding Himalayan orogeny helps explain thrusting on the MCT system, normal faulting on the STD system, prograde metamorphism, and anatexis in the Himalaya (Fig. 5). Although the relative importance of various heat sources for metamorphism and anatexis in the Greater Himalayan zone can be debated, there seems to be consensus that MCT movement helped trigger these thermal phenomena. At the same time, the presence of melt and other metamorphic fluids probably enhanced deformation on the fault system, such that metamorphism/anatexis and MCT thrusting constitute an autocatalytic circuit. The same is true of anatexis and STD normal faulting; anatexic melts facilitated movement on STD structures, while footwall decompression caused by movement on these faults encouraged further melting. As is the case for the Belousov–Zhabotinsky reaction and other chemical oscillators, these autocatalytic

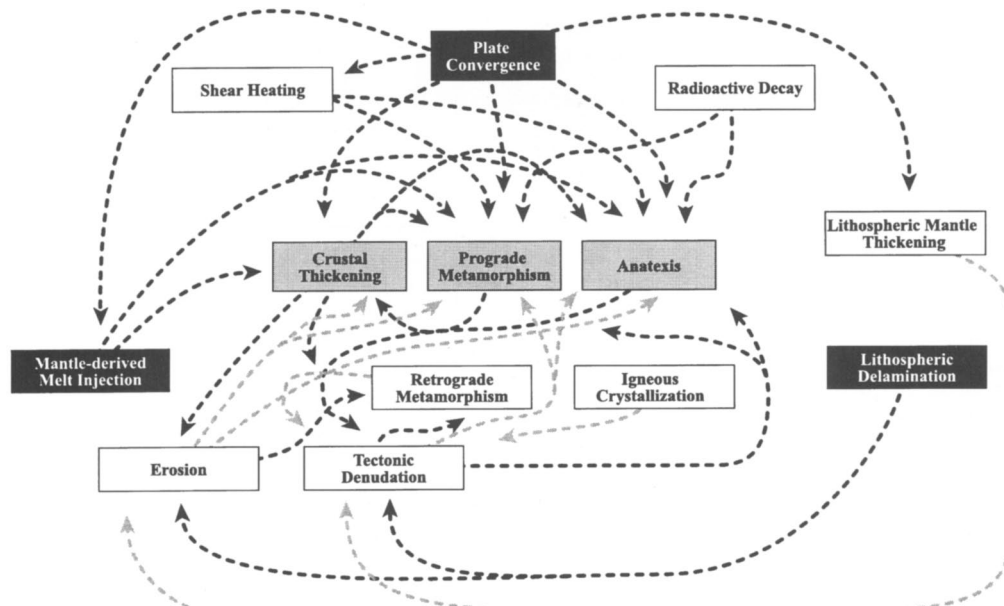


Fig. 4. Process network map for orogenic systems. As in Fig. 2, processes are divided into those that add energy to the system (black rectangles), those that store energy (grey), and those that dissipate energy (white). Black dashed lines with arrows indicate the encouragement of one process by another, whereas grey dashed lines indicate retardation. Bewildering arrays of process relationships, such as those shown here, are diagnostic of complex systems. They show why predicting the behaviour of such systems from simple physical models can be very difficult, if not impossible. The challenge is to determine which design factors control the collaboration of processes and the stabilization of certain system states.

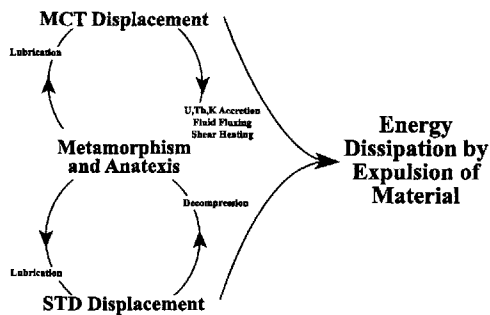


Fig. 5. Feedback relationships between deformational and thermal processes in the Greater Himalayan zone. The upper circle with arrows indicates positive feedback between MCT displacement and metamorphism and anatexis through various catalytic mechanisms. The lower circle indicates another autocatalytic relationship between STD movement and metamorphism and anatexis. Thermal processes thus provide a critical link for the coordination of thrust and normal faulting, ultimately resulting in extrusion of the Greater Himalayan zone southward towards the Indian foreland. The consequent mass dissipation lowers the potential energy of the orogenic system.

relationships alone are not sufficient to sustain the process structure illustrated in Fig. 5. *It is the coordination of thrust faulting and normal faulting, connected through anatexis and metamorphism, that defines the structure and reveals its purpose.*

The kinematics and synchronicity of the MCT and STD systems imply that the two moved in concert during the Middle Miocene to expel the wedge of material now represented by the Greater Himalayan zone southward towards the Indian foreland (Burchfiel & Royden 1985; Burchfiel *et al.* 1992; Grujic *et al.* 1996; Fig. 3b). The net effect of this was to convert a narrow, thick orogen into one which was substantially broader but thinner. As shown by Molnar & Lyon-Caen (1988), such spreading amounts to efficient dissipation of part of the potential energy stored in the orogen (Fig. 3c). While major thrust faults like the MCT are typically strictly regarded as agents of crustal shortening and thickening, a closer look at the Himalaya reveals that thrust faults and normal faults can cooperate when the result is evolution of the orogenic system as a whole towards a stable attractor state. In this instance, the attractor may have been a condition of balance between the rate of energy contribution to the system by plate convergence and the rate of energy dissipation.

The natural selection of orogenic processes

If process relationships develop for specific purposes in orogenic systems, then what favours one set over others that could achieve the same goals? In the Himalayan example, physical erosion and sediment transport provide a dissipation mechanism that is a simpler alternative to coordinated thrust and normal faulting. Why the complexity? The answer may lie in the relative efficiencies of different process sets.

In the course of their investigation of the implications of thermodynamics for living systems, Schneider & Kay (1994) suggested a corollary to the Zeroth, First and Second Laws of Thermodynamics. It can be paraphrased as follows:

'If systems are moved away from equilibrium by imposed gradients, they will use all available avenues to counter those gradients. As the applied gradients increase, so will the system's ability to oppose further movement from equilibrium.'

Implicit in this statement is the notion that systems far from equilibrium will evolve towards increasingly efficient sets of compensating processes. Could it be that a kind of 'natural selection' was responsible for development of a dissipative thrust-detachment combination in the Himalaya to complement simple erosion?

Numerical models of the pressure-temperature-time ($P-T-t$) evolution of metamorphic terrains require that regional trends of very rapid cooling and near-isothermal decompression require rapid unroofing (England & Jackson 1987; Ruppel & Hodges 1994; Ruppel *et al.* 1988). Evidence for such $P-T-t$ paths is very common in the Himalaya (e.g. Hodges *et al.* 1988, 1993; Metcalfe 1993; Pognante & Benna 1993; Vannay & Hodges 1996; Winslow *et al.* 1995; Zeitler *et al.* 1993), indicating fast denudation during the late stages of Neohimalayan metamorphism. While very rapid physical erosion may have occurred in some regions, it seems likely that STD movement played an important role in unroofing the Greater Himalayan sequence in most areas, because normal faulting is a more efficient mode of denudation than physical erosion. For example, estimates of physical erosion rates are generally much less than average plate motion rates or slip rates on major fault systems as measured by geodetic techniques (Bilham *et al.* 1997; King *et al.* 1997; Puntodewo *et al.* 1994; Summerfield 1991). At least one strand of the STD system accommodated unroofing at a rate of $\geq 8.4 \text{ mm a}^{-1}$,

a value that is higher than all but the highest estimates for physical erosion (Hodges *et al.* in press).

In light of such evidence, it seems reasonable that the STD–MCT system developed to provide a more efficient means of energy dissipation *c.* 20–23 Ma when erosion alone became insufficient to counteract the crustal thickness and topographic gradients imposed on the Himalayan system by plate convergence. However, the very existence of this dissipation mechanism may have been triggered by the presence of enough anatetic melt to sufficiently weaken the lithosphere and permit the development of appropriate deformational structures. Like other complex systems, orogenic belts may evolve towards certain stable configurations because of chance events, a little melting in this case. Once achieved, those attractor states might be maintained for millions of years by a continual flow of energy and/or matter through the system; in the central and eastern Himalaya, anatexis and displacement on the STD and MCT systems persisted from at least 23 to 12 Ma. Moreover, geophysical data from southern Tibet suggest that the middle crust there is substantially fluid, and it has been suggested that southward expulsion of this material continues today in similar fashion to the Miocene scenario in the Greater Himalayan zone (Nelson *et al.* 1996).

Conclusions

Temporal and spatial relationships between metamorphism, anatexis, thrusting and normal faulting in the Himalaya suggest that they were part of a cooperative set of processes with the net consequence of crustal spreading. Non-equilibrium thermodynamics provides a useful context for understanding this behaviour. We can speculate that by Early Miocene time, the Himalaya had achieved a high mean elevation, with steep topographic and crustal thickness gradients across the southern margin. At *c.* 23–24 Ma, the thermal structure of the Greater Himalayan zone became such that small amounts of anatetic melting could occur at deep crustal levels, reducing the strength of the crust to the point that it could no longer support the potential energy gradients imposed by India–Eurasia convergence. Once begun, melting triggered a cascade of other processes, including large displacements on both the MCT and STD systems. By encouraging more anatexis, both deformational processes became autocatalytic and the entire process set became self-sustaining through their cooperation. The fact that this particular process set persisted for so long – and

may still be operative – implies that it may be one of the most efficient possible energy dissipation mechanisms for orogenic systems.

If mountain ranges behave like other complex systems, there is no simple route to a unifying theory of orogenesis. All existing thermo-mechanical models of mountain building are fundamentally deterministic; a set of assumed boundary conditions uniquely constrains the evolution of the system through the simultaneous solution of simple equations describing processes like heat and mass transfer (e.g. England & Thompson 1984; Willett *et al.* 1993; Huerta *et al.* 1996; Batt & Braun 1997). However, complex systems are characteristically non-deterministic; a single set of boundary conditions can lead to a variety of outcomes. In my view, we will not fully understand the evolution of mountain ranges until we move beyond determinism to a new generation of models that are as fully adaptive as orogens themselves.

M. Bickle, P. O'Brien and P. Treloar provided much appreciated reviews of the submitted version of this paper. Earlier drafts benefited from comments by S. Bowring, M. Coleman, A. Friedrich and A. Huerta. My continuing work in the Himalayas and Tibet is supported by grants from the United States National Science Foundation.

References

- ALAM, M. 1989. Geology and depositional history of Cenozoic sediments of the Bengal Basin of Bangladesh. *Palaeogeography, Palaeoclimatology, Palaeoecology*, **69**, 125–13.
- ANDERSON, G. M. & CRERAR, D. A. 1993. *Thermodynamics in Geochemistry: The Equilibrium Model*. Oxford University Press, New York.
- ARTYUSHKOV, E. V. 1973. Stresses in the lithosphere caused by crustal thickness inhomogeneities. *Journal of Geophysical Research*, **78**, 7675–7708.
- BARR, T. D. & DAHLEN, F. A. 1989. Brittle frictional mountain building 2: Thermal structure and heat budget. *Journal of Geophysical Research*, **94**, 3923–3947.
- BATT, G. E. & BRAUN, J. 1997. On the thermomechanical evolution of compressional orogens. *Geophysical Journal International*, **128**, 364–382.
- BILHAM, R., LARSON, K., FREYMULLER, J. & PROJECT IDYLLHIM MEMBERS 1997. GPS measurements of present-day convergence across the Nepal Himalaya. *Nature*, **386**, 61–64.
- BIRD, P. 1979. Continental delamination and the Colorado Plateau. *Journal of Geophysical Research*, **84**, 7561–7571.
- BROWN, R. L. & NAZARCHUK, J. H. 1993. Annapurna detachment fault in the Greater Himalaya of central Nepal. In: TRELOAR, P. J. & SEARLE, M. P., (eds) *Himalayan Tectonics*. Geological Society, Special Publication, **74**, London, 461–473.

BRUNEL, M. & KIENAST, J. R. 1986. Etude petro-structurale des chevauchements ductile himalayens sur la transversale de L'Everest-Makalu Nepal oriental. *Canadian Journal of Earth Sciences*, **23**, 1117–1137.

BURCHFIELD, B. C. & ROYDEN, L. H. 1985. North-south extension within the convergent Himalayan region. *Geology*, **13**, 679–682.

—, CHEN, Z., HODGES, K. V., LIU, Y., ROYDEN, L. H., DENG, C. & XU, J. 1992. *The South Tibetan Detachment System, Himalayan Orogen: Extension Contemporaneous With and Parallel to Shortening in a Collisional Mountain Belt*. Geological Society of America, Boulder, CO.

BURG, J. P., BRUNEL, M., GAPAIS, D., CHEN, G. M. & LIU, G. H. 1984. Deformation of leucogranites of the crystalline Main Central Sheet in southern Tibet China. *Journal of Structural Geology*, **6**, 535–542.

COLEMAN, M. E. 1996. *The Tectonic Evolution of the Central Himalaya, Marsyandi Valley, Nepal*. PhD Thesis, Massachusetts Institute of Technology.

DAVIDSON, C., SCHMID, S., PAVLIS, T., GRUJIC, D., KUNDIG, R. & HOLLISTER, L. 1995. Intrusion of leucogranite into the High Himalayas of Bhutan during penetrative deformation: Evidence and consequences. In: SPENCER, D. A., BURG, J.-P. & SPENCER-CERVATO, C. (eds) *10th Himalaya-Karakoram-Tibet Workshop Abstract Volume*. Mitteilungen aus dem Geologischen Institut der ETH und der Universität Zürich, No. **298**, Zürich.

DEBON, F., LE FORT, P., SHEPPARD, S. M. F. & SONET, J. 1986. The four plutonic belts of the Transhimalaya-Himalaya; a chemical, mineralogical, isotopic, and chronological synthesis along a Tibet-Nepal section. *Journal of Petrology*, **27**, 219–250.

DENIEL, C., VIDAL, P., FERNANDEZ, A., LE FORT, P. & PEUCAT, J.-J. 1987. Isotopic study of the Manaslu granite Himalaya, Nepal: inferences on the age and source of the Himalayan leucogranites. *Contributions to Mineralogy and Petrology*, **96**, 78–92.

EDWARDS, M. A. & HARRISON, T. M. 1997. When did the roof collapse? Late Miocene north-south extension in the high Himalaya revealed by Th-Pb monazite dating of the Khula Kangri granite. *Geology*, **25**, 543–546.

—, KIDD, W. S. F., LI, J., YUE, Y. & CLARK, M. 1996. Multi-stage development of the southern Tibetan detachment system near Khula Kangri. New data from Gonto La. *Tectonophysics*, **260**, 1–19.

ENGLAND, P. C. & HOUSEMAN, G. A. 1988. The mechanics of the Tibetan Plateau. In: SHACKLETON, R. M., DEWEY, J. F. & WINDLEY, B. F. (eds) *Tectonic Evolution of the Himalayas and Tibet*. The Royal Society, London, 301–319.

— & JACKSON, J. 1987. Migration of the seismic-aseismic transition during uniform and nonuniform extension of the continental lithosphere. *Geology*, **15**, 291–294.

— & MOLNAR, P. 1993. The interpretation of inverted metamorphic isograds using simple physical calculations. *Tectonics*, **12**, 145–157.

& THOMPSON, A. B. 1984. Pressure-temperature-time paths of regional metamorphism I. Heat transfer during the evolution of regions of thickened continental crust. *Journal of Petrology*, **25**, 894–928.

—, LE FORT, P., MOLNAR, P. & PÉCHER, A. 1992. Heat sources for Tertiary metamorphism and anatexis in the Annapurna-Manaslu region, central Nepal. *Journal of Geophysical Research*, **97**, 2107–2128.

FIELD, R., KÓRÓS, E. & NOYES, R. 1972. Oscillations in chemical systems. II. Thorough analysis of temporal oscillation in the bromate-cerium-malonic acid system. *Journal of the American Chemical Society*, **94**, 8649–8664.

FRANCÉ-LANORD, C., SHEPPARD, S. M. F. & LE FORT, P. 1988. Hydrogen and oxygen isotope variations in the High Himalaya peraluminous leucogranite: Evidence for heterogeneous sedimentary source. *Geochimica et Cosmochimica Acta*, **52**, 513–526.

GAETANI, M. & GARZANTI, E. 1991. Multicyclic history of the northern India continental margin Northwestern Himalaya. *Bulletin of the American Association of Petroleum Geologists*, **75**, 1427–1446.

GANSSE, A. 1983. *Geology of the Bhutan Himalaya*. Birkhäuser Verlag, Basel.

GARIÉPY, C., ALLÉGRE, C. J. & XU, R.-H. 1985. The Pb-isotope geochemistry of granitoids from the Himalaya-Tibet collision zone: implications for crustal evolution. *Earth and Planetary Science Letters*, **74**, 220–234.

GARZANTI, E. 1993. Sedimentary evolution and drowning of a passive margin shelf Giumal Group; Zanskar Tethys Himalaya, India: paleoenvironmental changes during final break-up of Gondwanaland. In: TRELOAR, P. J. & SEARLE, M. P. (eds) *Himalayan Tectonics*. Geological Society, Special Publication, **74**, London, 277–298.

GRAY, P. & SCOTT, S. 1990. *Chemical Oscillations and Instabilities*. Oxford University Press, Oxford.

GRUJIC, D., CASEY, M., DAVIDSON, C., HOLLISTER, L. S., KUNDIG, R., PAVLIS, T. & SCHMID, S. 1996. Ductile extrusion of the Higher Himalayan crystalline in Bhutan: evidence from quartz microfabrics. *Tectonophysics*, **260**, 21–43.

GUILLOT, S. & LE FORT, P. 1995. Geochemical constraints on the bimodal origin of High Himalayan leucogranites. *Lithos*, **353–4**, 221–234.

—, HODGES, K. V., LE FORT, P. & PÉCHER, A. 1994. New constraints on the age of the Manaslu leucogranite: Evidence for episodic tectonic denudation in the central Himalayas. *Geology*, **22**, 559–562.

—, PÉCHER, A., ROCHE, P. & LE FORT, P. 1993. The emplacement of the Manaslu granite of Central Nepal: field and magnetic susceptibility constraints. In: TRELOAR, P. J. & SEARLE, M. P. (eds) *Himalayan Tectonics*. Geological Society, Special Publication, **74**, London, 413–428.

HARRIS, N. & MASSEY, J. 1994. Decompression and anatexis of Himalayan metapelites. *Tectonics*, **13**, 1537–1546.

HARRISON, T. M., McKEEGAN, K. D. & LE FORT, P. 1995. Detection of inherited monazite in the Manaslu leucogranite by $^{208}\text{Pb}/^{232}\text{Th}$ ion microprobe dating: Crystallization age and tectonic implications. *Earth and Planetary Science Letters*, **133**, 271–282.

HERREN, E. 1987. Zanskar shear zone: Northeast-southwest extension within the Higher Himalayas, Ladakh, India. *Geology*, **15**, 409–413.

HODGES, K., BOWRING, S., DAVIDEK, K., HAWKINS, D. & KROL, M. in press. Evidence for rapid displacement on Himalayan normal faults and the importance of tectonic denudation in the evolution of mountain ranges. *Geology*.

HODGES, K. V. 1990. Tectonic denudation and anatetic melting in compressional settings. *EOS*, **71**, 1618.

— & SILVERBERG, D. S. 1988. Thermal evolution of the Greater Himalaya, Garhwal, India. *Tectonics*, **7**, 583–600.

—, BURCHFIELD, B. C., ROYDEN, L. H., CHEN, Z. & LIU, Y. 1993. The metamorphic signature of contemporaneous extension and shortening in the central Himalayan orogen: Data from the Nyalam transect, southern Tibet. *Journal of Metamorphic Geology*, **11**, 721–737.

—, HAMES, W. E., OLSZEWSKI, W. J., BURCHFIELD, B. C., ROYDEN, L. H. & CHEN, Z. 1994. Thermobarometric and $^{40}\text{Ar}/^{39}\text{Ar}$ geochronologic constraints on Eohimalayan metamorphism in the Dinggyé area, southern Tibet. *Contributions to Mineralogy and Petrology*, **117**, 151–163.

—, HUBBARD, M. S. & SILVERBERG, D. S. 1988. Metamorphic constraints on the thermal evolution of the central Himalayan Orogen. *Philosophical Transactions of the Royal Society of London*, **A326**, 257–280.

—, PARRISH, R., HOUSH, T., LUX, D., BURCHFIELD, B. C., ROYDEN, L. & CHEN, Z. 1992. Simultaneous Miocene extension and shortening in the Himalayan orogen. *Science*, **258**, 1466–1470.

—, — & SEARLE, M. P. 1996. Tectonic evolution of the central Annapurna Range, Nepalese Himalayas. *Tectonics*, **15**, 1264–1291.

HOLLISTER, L. S. 1993. The role of melt in the uplift and exhumation of orogenic belts. *Chemical Geology*, **108**, 31–48.

HOLLISTER, L. S. & CRAWFORD, M. L. 1986. Melt-enhanced deformation: A major tectonic process. *Geology*, **14**, 558–561.

—, KUNDIG, R., SCHIMID, S., GRUJIC, D., PAVLIS, T. & DAVIDSON, C. 1995. Tectonic transport of heat and melt within the High Himalayan Crystallines of Bhutan. In: SPENCER, D. A., BURG, J.-P. & SPENCER-CERVATO, C. (eds) *10th Himalaya-Karakoram-Tibet Workshop Abstract Volume*. Mitteilungen aus dem Geologischen Institut der ETH und der Universität Zürich, No. **298**, Zürich.

HONNEGER, K., DIETRICH, V., FRANK, W., GANSSE, A., THONI, M. & TROMMSDORF, V. 1982. Magmatism and metamorphism in the Ladakh Himalayas the Indus-Tsangpo suture zone. *Earth and Planetary Science Letters*, **60**, 253–292.

HOUSEMAN, G. A., MCKENZIE, D. P. & MOLNAR, P. 1981. Convective instability of a thickened boundary layer and its relevance for the thermal evolution of continental convergence belts. *Journal of Geophysical Research*, **86**, 6115–6132.

HUBBARD, M. S. 1988. *Thermobarometry, $^{40}\text{Ar}/^{39}\text{Ar}$ geochronology, and structure of the Main Central Thrust zone and Tibetan Slab, eastern Nepal Himalaya*. PhD Thesis, Massachusetts Institute of Technology.

— 1989. Thermobarometric constraints on the thermal history of the Main Central Thrust Zone and Tibetan Slab, eastern Nepal Himalaya. *Journal of Metamorphic Geology*, **7**, 19–30.

— & HARRISON, T. M. 1989. $^{40}\text{Ar}/^{39}\text{Ar}$ age constraints on deformation and metamorphism in the Main Central thrust zone and Tibetan Slab, eastern Nepal Himalaya. *Tectonics*, **8**, 865–880.

HUBERTA, A. D., ROYDEN, L. H. & HODGES, K. V. 1996. The interdependence of deformational and thermal processes in mountain belts. *Science*, **273**, 637–639.

INGER, S. & HARRIS, N. 1993. Geochemical constraints on leucogranite magmatism in the Langtang Valley, Nepal Himalaya. *Journal of Petrology*, **34**, 345–368.

— & HARRIS, N. B. W. 1992. Tectono-thermal evolution of the High Himalayan crystalline sequence, Langtang Valley, northern Nepal. *Journal of Metamorphic Geology*, **10**, 439–452.

JAIN, A. K. & MANICKAVASAGAM, R. M. 1993. Inverted metamorphism in the intracontinental ductile shear zone during Himalayan collision tectonics. *Geology*, **21**, 407–410.

JAMIESON, R. A. & BEAUMONT, C. 1988. Orogeny and metamorphism: a model for deformation and pressure-temperature-time paths with applications to the central and southern Appalachians. *Tectonics*, **7**, 417–445.

JAUPART, C. & PROVOST, A. 1985. Heat focusing, granite genesis, and inverted metamorphic gradients in continental collision zones. *Earth and Planetary Science Letters*, **73**, 385–397.

JOHNSON, G. D., JOHNSON, N. M., OPDYKE, N. D. & TAHIRKHETI, R. A. K. 1979. Magnetic reversal stratigraphy and sedimentary tectonic history of the Upper Siwalik Group. In: FARAH, A. & DE JONG, K. A. (eds) *Geodynamics of Pakistan*. Geological Survey of Pakistan, Quetta, Pakistan, 149–165.

KAUFFMAN, S. 1995. *At Home in the Universe: The Search for Laws of Self-Organization and Complexity*. Oxford University Press, New York.

KING, R. W., SHEN, F., BURCHFIELD, B. C., ROYDEN, L. H., WANG, E., CHEN, Z., LIU, Y., ZHANG, X., ZHAO, J. & LI, Y. 1997. Geodetic measurement of crustal motion in southwest China. *Geology*, **25**, 179–182.

KRETZ, R. 1983. Symbols for rock-forming minerals. *American Mineralogist*, **68**, 277–279.

LE FORT, P. 1975. Himalayas: the collided range. Present knowledge of the continental arc. *American Journal of Science*, **275-A**, 1–44.

— 1981. Manaslu leucogranite: A collision signature in the Himalaya, a model for its genesis and emplacement. *Journal of Geophysical Research*, **86**, 10 545–10 568.

—, CUNIY, M., DENIEL, C., FRANCE-LANORD, C., SHEPPARD, S. M. F., UPRETI, B. N. & VIDAL, P. 1987. Crustal generation of Himalayan leucogranites. *Tectonophysics*, **134**, 39–57.

MACFARLANE, A., HODGES, K. V. & LUX, D. 1992. A structural analysis of the Main Central thrust zone, Langtang National Park, central Nepal Himalaya. *Geological Society of America Bulletin*, **104**, 1389–1402.

MACFARLANE, A. M. 1992. *The Tectonic Evolution of the Core of the Himalaya. Langtang National Park, Central Nepal*. PhD Thesis, Massachusetts Institute of Technology.

MEANS, W. D. 1976. *Stress and Strain: Basic Concepts of Continuum Mechanics for Geologists*. Springer-Verlag, New York.

MEIER, K. & HILTNER, E. 1993. Deformation and metamorphism within the Main Central Thrust zone, Arun Tectonic Window, eastern Nepal. In: TRELOAR, P. J. & SEARLE, M. P. (eds) *Himalayan Tectonics*. Geological Society, Special Publication, **74**, London, 511–524.

METCALFE, R. P. 1993. Pressure, temperature and time constraints on metamorphism across the Main Central Thrust zone and High Himalayan Slab in the Garhwal Himalaya. In: TRELOAR, P. J. & SEARLE, M. P. (eds) *Himalayan Tectonics*. Geological Society, Special Publication, **74**, London, 485–509.

MIYASHIRO, A. 1961. Evolution of metamorphic belts. *Journal of Petrology*, **2**, 227–311.

MOHAN, A., WINDLEY, B. F. & SEARLE, M. P. 1989. Geothermobarometry and development of inverted metamorphism in the Darjeeling-Sikkim region of the eastern Himalaya. *Journal of Metamorphic Geology*, **7**, 95–110.

MOLNAR, P. 1984. Structure and tectonics of the Himalaya: constraints and implications of geophysical data. *Annual Reviews of Earth and Planetary Science*, **12**, 489–518.

— & LYON-CAEN, H. 1988. Some simple physical aspects of the support, structure, and evolution of mountain belts. In: CLARK, S., BURCHFIELD, B. C. & SUPPE, J. (eds) *Processes in Continental Lithospheric Deformation*. Geological Society of America, Special Paper, **218**, Boulder, CO, 179–207.

—, ENGLAND, P. & MARTINOD, J. 1993. Mantle dynamics, uplift of the Tibetan Plateau, and the Indian monsoon. *Reviews of Geophysics*, **31**, 357–396.

NAJMAN, Y., CLIFT, P., JOHNSON, M. R. W. & ROBERTSON, A. H. F. 1993. Early stages of foreland basin evolution in the Lesser Himalaya, N. India. In: TRELOAR, P. J., & SEARLE, M. P. (eds) *Himalayan Tectonics*. Geological Society, Special Publication, **74**, London, 541–558.

NELSON, K. D., ZHAO, W., BROWN, L. D. *et al.* 1996. Partially molten middle crust beneath southern Tibet: Synthesis of Project INDEPTH Results. *Science*, **274**, 1684–1688.

NICOLIS, G. 1995. *Introduction to Nonlinear Science*. Cambridge University Press, Cambridge.

— & PRIGOGINE, I. 1977. *Self-Organization in Nonequilibrium Systems*. Wiley, New York.

NOBLE, S. R. & SEARLE, M. P. 1995. Age of crustal melting and leucogranite formation from U-Pb zircon and monazite dating in the western Himalaya, Zanskar, India. *Geology*, **23**, 1135–1138.

PARRISH, R. R. & HODGES, K. V. 1993. Miocene (22 ± 1 Ma) metamorphism and two-stage thrusting in the Greater Himalayan sequence, Annapurna Sanctuary, Nepal. *Geological Society of America Abstracts with Programs*, **25**, A174.

— & MACFARLANE, A. 1992. U-Pb geochronology of igneous and metamorphic rocks near the Main Central Thrust in the Langtang area, central Nepal Himalaya. In: SEARLE, M. P. & TRELOAR, P. J. (eds) *7th Himalaya-Tibet-Karakoram Workshop Abstracts*. Oxford, 67–68.

PÊCHER, A. 1989. The metamorphism in the central Himalaya. *Journal of Metamorphic Geology*, **7**, 31–41.

PINET, C. & JAUPART, C. 1987. A thermal model for the distribution in space and time of the Himalayan granites. *Earth and Planetary Science Letters*, **84**, 87–99.

PLATTEN, J. K. & LEGROS, J. C. 1984. *Convection in Liquids*. Springer Verlag, Berlin.

POGNANTE, U. & BENNA, P. 1993. Metamorphic zonation, migmatization and leucogranites along the Everest transect of eastern Nepal and Tibet: The record of an exhumation history. In: TRELOAR, P. J. & SEARLE, M. P. (eds) *Himalayan Tectonics*. Geological Society, London, Special Publication, **74**, 323–340.

PRIGOGINE, I. 1980. *From Being to Becoming: Time and Complexity in the Physical Sciences*. W. H. Freeman, San Francisco.

PUNTODEWO, S. S. O., MCCAFFREY, R., CALAIS, E. *et al.* 1994. GPS measurements of crustal deformation within the Pacific-Australia plate boundary zone in Irian Jaya, Indonesia. *Tectonophysics*, **237**, 141–153.

REDDY, S. M., SEARLE, M. P. & MASSEY, J. A. 1993. Structural evolution of the High Himalayan gneiss sequence, Langtang Valley, Nepal. In: TRELOAR, P. J. & SEARLE, M. P. (eds) *Himalayan Tectonics*. Geological Society, Special Publication, **74**, London, 375–389.

ROYDEN, L. H. 1993. The steady-state thermal structure of eroding orogenic belts and accretionary prisms. *Journal of Geophysical Research*, **98**, 4487–4507.

RUPPEL, C. & HODGES, K. V. 1994. Pressure-Temperature-Time paths from two-dimensional thermal models: Prograde, retrograde, and inverted metamorphism. *Tectonics*, **13**, 17–44.

—, ROYDEN, L. & HODGES, K. V. 1988. Thermal modeling of extensional tectonics: application to pressure-temperature-time histories of metamorphic rocks. *Tectonics*, **7**, 947–957.

SANDIFORD, M. & HAND, M. 1998. Australian Proterozoic high-temperature, low-pressure metamorphism in the conductive limit. *This volume*.

SCALLIET, B., PÊCHER, A., ROCHETTE, P. & CHAMPEANOIS, M. 1995. The Gangotri granite Garhwal Himalaya: Laccolithic emplacement in an extending orogenic belt. *Journal of Geophysical Research*, **100**, 585–607.

SCHÄRER, U. 1984. The effect of initial ^{230}Th disequilibrium on young U-Pb ages: the Makalu case, Himalaya. *Earth and Planetary Science Letters*, **67**, 191–204.

—, XU, R. & ALLEGRE, C. 1986. U-Th-Pb systematics and ages of Himalayan leucogranites, South Tibet. *Earth and Planetary Science Letters*, **77**, 35–48.

SCHNEIDER, E. D. & KAY, J. J. 1994. Life as a manifestation of the Second Law of Thermodynamics. *Mathematical and Computer Modeling*, **19**, 25–48.

SEARLE, M. P. 1991. *Geology and Tectonics of the Karakoram Mountains*. John Wiley & Sons, Chichester.

— & FRYER, B. J. 1986. Garnet, tourmaline, and muscovite-bearing leucogranites, gneisses and migmatites of the Higher Himalaya from Zanskar, Kulu, Lahoul and Kashmir. In: COWARD, M. P. & RIES, A. C. (eds) *Collision Tectonics*. Geological Society, Special Publication, **19**, London, 185–201.

— & REX, A. J. 1989. Thermal model for the Zanskar Himalaya. *Journal of Metamorphic Geology*, **7**, 127–134.

—, PARRISH, R. R., HODGES, K. V., HURFORD, A., AYERS, M. W. & WHITEHOUSE, M. J. 1997. Shisha Pangma leucogranite, South Tibetan Himalaya: Field relations, geochemistry, age, origin, and emplacement. *Journal of Geology*, **105**, 295–317.

SEBER, D., BARAZANGI, M., IBENBRAHIM, A. & DEMNATI, A. 1996. Geophysical evidence for lithospheric delamination beneath the Alboran Sea and Rif-Betic mountains. *Nature*, **379**, 785–790.

SUMMERFIELD, M. A. 1991. *Global Geomorphology*. Longman Scientific, New York.

SWAPP, S. M. & HOLLISTER, L. S. 1991. Inverted metamorphism within the Tibetan Slab of Bhutan: Evidence for a tectonically transported heat-source. *Canadian Mineralogist*, **29**, 1019–1041.

TURNER, F. J. 1981. *Metamorphic Petrology*. McGraw-Hill, New York.

VALDIYA, K. S. 1986. Correlation of Lesser Himalayan formations of Nepal and Kumaun. *Sciences de la Terre, Mémoire*, **47**, 361–383.

VANCE, D. & HARRIS, N. 1996. Precise Sm-Nd ages from Himalayan garnet: temporal controls on metamorphism. In: TRELOAR, P. & O'BRIEN, P. (eds) *What Drives Metamorphism and Metamorphic Reactions: Heat Production, Heat Transfer, Deformation and Kinetics?* Kingston University, Kingston.

VANNAY, J.-C. & HODGES, K. V. 1996. Tectonometamorphic evolution of the Himalayan metamorphic core between Annapurna and Dhaulagiri, central Nepal. *Journal of Metamorphic Geology*, **14**, 635–656.

WALKER, J. 1998. *Structural Evolution of the High Himalayan Slab in Northwest India*. DSc Thesis, University of Oxford.

WILLETT, S., BEAUMONT, C. & FULLSACK, P. 1993. Mechanical model for the tectonics of doubly vergent compressional orogens. *Geology*, **21**, 371–374.

WINFREE, A. T. 1984. The prehistory of the Belousov-Zhabotinsky reaction. *Journal of Chemical Education*, **61**, 661–663.

— 1987. *When Time Breaks Down: The Three-Dimensional Dynamics of Electrochemical Waves and Cardiac Arrhythmias*. Princeton University Press, Princeton, NJ.

WINSLOW, D. M., CHAMBERLAIN, C. P. & ZEITLER, P. K. 1995. Metamorphism and melting of the lithosphere due to rapid denudation, Nanga Parbat massif, Himalaya. *Journal of Geology*, **103**, 395–409.

WU, C., NELSON, K. D., WORTMAN, G., SAMSON, S., YUE, Y., LI, J., KIDD, W. S. F. & EDWARDS, M. 1998. Yadong cross structure and South Tibetan Detachment in the east central Himalaya (89°–90°E). *Tectonics*, **17**, 28–45.

ZAIKIN, A. N. & ZHABOTINSKY, A. M. 1970. Concentration wave propagation in two-dimensional liquid-phase self-oscillating systems. *Nature*, **225**, 535–537.

ZEITLER, P. K., CHAMBERLAIN, C. P. & SMITH, H. A. 1993. Synchronous anatexis, metamorphism, and rapid denudation at Nanga Parbat Pakistan Himalaya. *Geology*, **21**, 347–350.

Barrovian regional metamorphism: where's the heat?

R. A. JAMIESON¹, C. BEAUMONT², P. FULLSACK² & B. LEE²

¹ Department of Earth Sciences, Dalhousie University, Halifax, Nova Scotia B3H 3J5, Canada

² Department of Oceanography, Dalhousie University, Halifax, Nova Scotia B3H 4J1, Canada

Abstract: Coupled thermal–mechanical models of convergent orogens offer a novel way to investigate the interactions between heat and tectonics that lead to regional metamorphism. In this study, the effects of different distributions of heat-producing material in the crust and upper mantle on crustal thermal histories and deformation fields are investigated. The models involve subduction-driven collision with moderate convergence and erosion rates. For models involving standard continental crust, where heat production is initially concentrated in the upper crust, P – T – t paths do not intersect the field of typical Barrovian P – T conditions. However, heat-producing material can be tectonically redistributed, for example, by subduction of crustal rocks to upper mantle depths, or by formation of thick accretionary wedges or continental margin sequences during convergence. Models that include a wedge of heat-producing material in the upper mantle generate high temperatures in the lower crust and upper mantle that lead to a change in orogenic style; radioactive heating of partially subducted crustal material on time scales of 10–30 Ma yields temperatures high enough for partial melting. However, crustal P – T – t paths are unlikely to intersect the Barrovian field unless erosion or convergence rates change. Models that include a crustal-scale region with moderate, uniform heat production, simulating a large accretionary wedge or tectonically thickened continental margin sequence, generate P – T – t paths that intersect the Barrovian field. However, as convergence proceeds, the heat-producing region is deformed, eroded, and reduced in volume, so that the model orogen begins to cool down after about 20 Ma. The model results provide an explanation for many first-order tectonic and metamorphic features of small orogens, including metamorphic styles ranging from blueschists to the Barrovian series to granulites, late-orogenic granitoid magmatism, and the crustal-scale tectonic features associated with regional metamorphic belts. We conclude that the thermal state of an orogen is controlled by the evolving competition between cooling by subduction and radioactive heating within the deforming orogen.

The most common style of regional metamorphism in time and space is the ‘Barrovian’ metamorphic series, first described by Barrow (1893, 1912; Tilley 1925) from the Scottish Highlands. Barrovian sequences are associated with progressive metamorphism from chlorite through biotite, garnet, staurolite, kyanite and sillimanite zones. The isograds and bathograds associated with this style of metamorphism are well documented and in many cases experimentally calibrated, so that the general P – T range of Barrovian metamorphism is well known (Fig. 1). Numerous case studies of Barrovian metamorphic sequences ranging from Archean to Cenozoic in age have yielded precise P – T determinations, P – T – t paths, and space–time relationships between the various metamorphic zones and important episodes of regional deformation and plutonism. For example, metamorphic grade generally increases structurally up-section, with peak metamorphic assemblages post-dating the earliest fabrics but synchronous

with later thrust-related foliations. P – T – t paths generally form open loops in which an early pressure increase is followed by a pressure decrease at nearly constant or slightly increasing temperature (Fig. 1). Peak metamorphism generally predates the main stage of granite intrusion, although sillimanite-bearing assemblages may be synchronous with plutonism. While variations on this general pattern are common, these first-order observations clearly require explanation in any general orogenic model. However, a quantitative explanation for Barrovian metamorphism in thermal–tectonic models of orogenesis has proven elusive.

Although it is intuitively obvious that regional metamorphism is controlled by interactions between heat and tectonics, there is considerable latitude in how these are treated in geodynamic models. The temperature field within any model orogen is controlled by competition between heat production from crust and mantle sources, and cooling of the orogen from the surface and

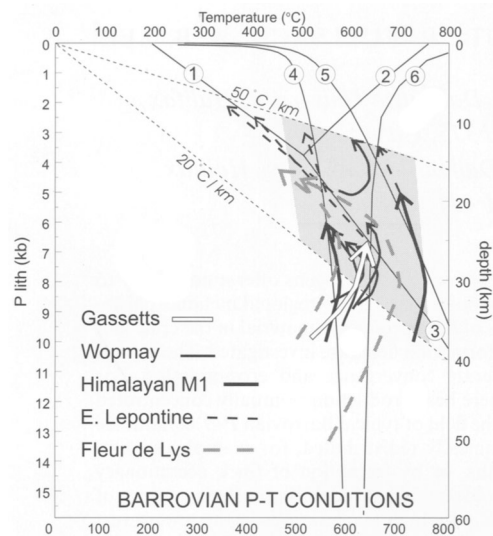


Fig. 1. Pressure (P)-temperature (T) grid used throughout this paper. Reactions shown are: 1, kyanite = andalusite; 2, andalusite = sillimanite; 3, kyanite = sillimanite; 4, chloritoid + quartz = staurolite + garnet + H_2O (staurolite-in isograd); 5, muscovite + quartz = K-feldspar + Al_2SiO_5 + H_2O (muscovite-out isograd); 6, fluid-saturated melting for granitoid rocks. The $20^\circ C \text{ km}^{-1}$ and $50^\circ C \text{ km}^{-1}$ geotherms bracket the range normally associated with Barrovian metamorphism. P - T - t paths are from the Gassetts Schist (Vance & Holland 1993), Wopmay orogen (St. Onge 1987), Main Central thrust zone of the Nepal Himalayas (Hodges *et al.* 1988), Eastern Lepontine Alps (Ring 1992; Engi *et al.* 1995), and Fleur de Lys Supergroup, Newfoundland (Jamieson 1990). The shaded area is the Barrovian P - T range used for comparison with model results.

by subduction or underthrusting of cool material. Because there is a tendency for geological processes to concentrate radioactive heat-producing elements (K, U, Th) in the upper continental crust relative to the lower crust and mantle, the 'standard' model of crustal heat production assumes high near-surface values that decrease with depth, so that the lower crust is assumed to contribute little to surface heat flux (e.g. McLennan & Taylor 1996). Figure 2 (column 1) illustrates an average model for thermally stable Phanerozoic crust which is used as a basis for discussion in this paper, although it is by no means unique. During convergence, increased heat production in any vertical column resulting from crustal thickening is partly offset by erosion and removal of the radioactive upper crust. Orogen models that use average values for crustal heat production, convergence rates and erosion tend to be 'too

cold'; that is, they fail to produce peak metamorphic temperatures of 600 – $700^\circ C$ at crustal depths of 20 – 30 km as typically inferred from the higher-grade parts of Barrovian sequences (Fig. 1). Most models for metamorphism therefore invoke some combination of increased radioactive heat production, increased crustal thickness, strain heating, or reduced convergence and/or erosion rates.

In an active orogen, the tectonic regime controls how heat-producing upper crustal material is distributed: it may be accreted and thickened within the crust, it may be accreted below the crust through partial subduction of continental material, or it may be eroded and either redistributed or lost to the system. Under stable conductive (non-orogenic) conditions, this distribution strongly affects the temperature of the lower crust, even among examples where surface and basal heat flux are identical (Fig. 2, columns 1, 2). For example, burial of heat-producing material in the lower crust as shown in Fig. 2 (column 2) increases the equilibrium temperature at the Moho by $200^\circ C$. Distributing upper crustal radioactive material uniformly through the whole crust (Fig. 2, column 3), with an average of half the near-surface heat production shown in column 1, increases the Moho temperature by an additional $120^\circ C$, and also increases the surface heat flux, although this value still lies within the observed range for orogenic continental crust.

A number of numerical experiments have shown that increased radioactive crustal heat production (rate per unit mass or volume and/or the total volume) can yield model crustal P - T conditions that approach those observed in Barrovian metamorphic sequences. For example, Chamberlain & Sonder (1990) showed that thickening of sedimentary basins enriched in heat-producing elements could account for Acadian high-grade metamorphism and plutonism in the New England Appalachians. Ruppel & Hodges (1994) considered the thermal consequences of tectonic thrusting that disrupts and duplicates a radioactive crustal layer. More recently, Huerta *et al.* (1996) analysed the effects of redistribution of heat-producing material through surface erosion and continuous tectonic accretion during underthrusting, and showed that temperatures above $600^\circ C$ at 20 – 40 km depth, accompanied by inverted upper-plate geotherms, could be reached after 25 – 35 Ma of convergence. However, these approaches did not consider how the changing thermal structure of the crust would affect the tectonic velocity field, and thus the subsequent thermal and tectonic evolution of the system. This thermal-mechanical coupling

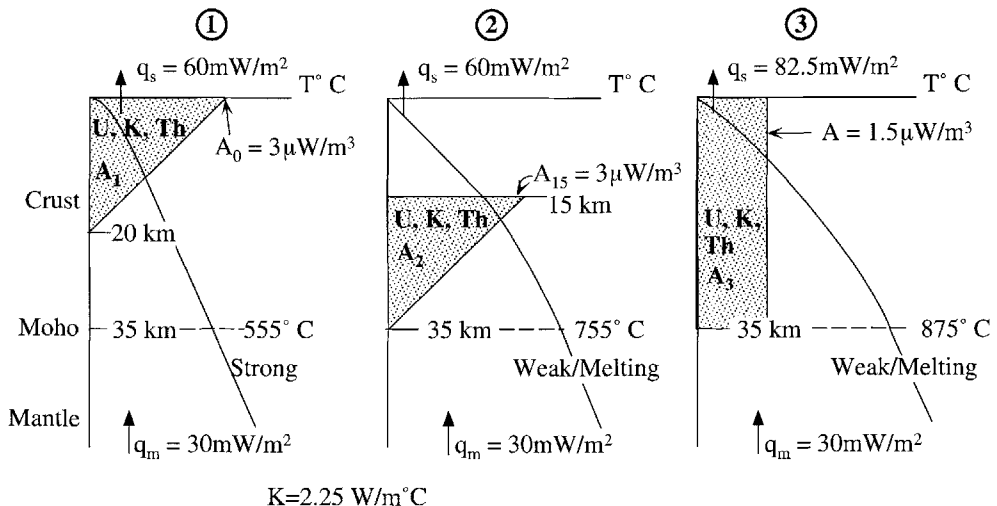


Fig. 2. Effect of distribution of heat-producing elements (U, K, Th) on 1D steady-state thermal structure of continental crust. Typical values of mantle heat flux ($q_m = 30 \text{ mW m}^{-2}$), and conductivity ($K = 2.25 \text{ W m}^{-1} \text{ C}^{-1}$) are used in all three panels. The thermal effects of three contrasting example distributions (A_1 , A_2 , A_3) for heat production with depth are shown. A_1 , the 'standard' distribution for continental crust (e.g. McLennan & Taylor 1996), results in an equilibrium temperature at the Moho of 555°C , and a relatively strong lower crust. A_2 , the same distribution but in the lower crust, results in a Moho temperature of 755°C . A_3 , which has the average heat production of A_1 uniformly distributed through the crust, results in a Moho temperature of 875°C . Both A_2 and A_3 result in hot, weak lower crust which is likely to undergo some partial melting. These contrasts in lower crustal strength would strongly affect orogenic style.

is important because the tectonic regime is controlled by crustal rheology, which has an exponential dependence on temperature in the ductile field.

Understanding the feedbacks between thermal and tectonic processes in orogens and their consequences for metamorphism requires a different approach. Previous quantitative investigations of metamorphism and melting have used one- and two-dimensional thermal-kinematic models, in which heat transport is modelled in a system where the styles and times of deformation and exhumation are specified (e.g. England & Thompson 1984; Ruppel & Hodges 1994; Thompson & Connolly 1995; Cermak & Bodri 1996; Huerta *et al.* 1996). Two-dimensional mechanical models of subduction-controlled convergent orogens (Willett *et al.* 1993; Beaumont *et al.* 1994) calculate deformation fields within model orogenic crust, but so far have not included the thermal effects associated with heat production and crustal thickening. Coupled thermal mechanical models, which calculate both deformation and thermal evolution of model orogens (Jamieson *et al.* 1996; Batt & Braun 1997), allow investigation of interactions between heat and tectonics in

simple convergent systems. This type of model is thus a potentially more powerful tool than either thermal-kinematic or mechanical models for investigating the factors controlling regional metamorphism.

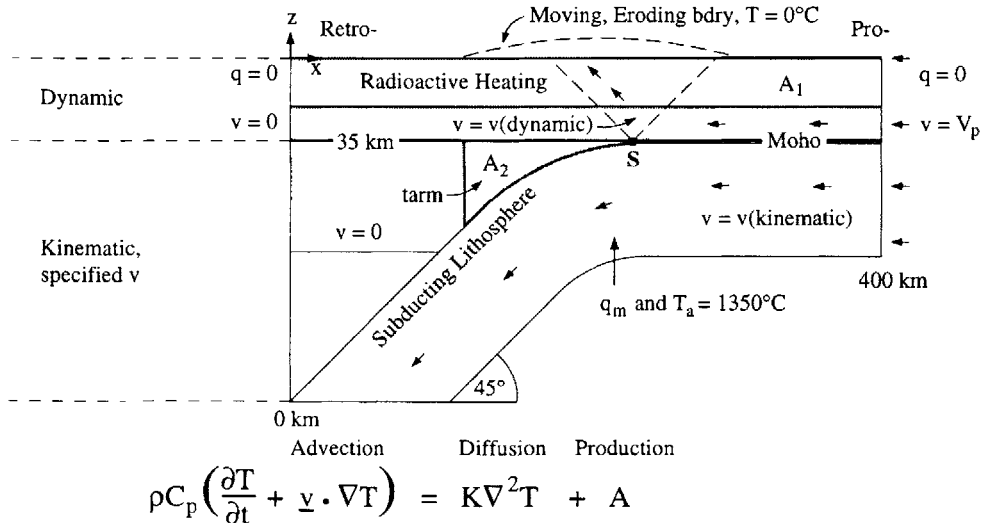
This paper uses a coupled thermal-mechanical model (Figs 3 and 4) for subduction-controlled orogenesis to investigate how the tectonic redistribution of heat-producing upper crustal material affects P - T - t paths, T - t histories, and crustal deformation within a model orogen. We refer to the heat-producing material as 'tectonically accreted radioactive material', or 'tarm', and distinguish between tarm accreted at crustal levels (e.g. by thickening of continental margin sediments during subduction and collision), and tarm accreted in the uppermost mantle (e.g. by partial subduction of upper crustal material).

Illustration of the problem using a reference model

A problem common to geodynamic models for regional metamorphism is that transport of cool material into the orogen by subduction or

Mechanical Model

Thermal Model



ρ = density, C_p = heat capacity, K = thermal conductivity

$\kappa = K/\rho C_p$ = thermal diffusivity (all constant)

$T = T(x, z, t)$ = temperature, t = time

$A = A(x, z, t)$ = rate of heat production / unit volume

$\underline{v} = \underline{v}(x, z, t)$ = tectonic (advective) velocity
dynamic (in crust), kinematic (in mantle)

$\nabla = \partial/\partial x + \partial/\partial z$ = gradient operator

Initial Conditions — conductive steady state, $v = 0$

Boundary Conditions Top surface $T = 0^\circ\text{C}$, $\underline{v} = \underline{v}(\text{dynamic})$

Left, Right $q = 0$, $v(x) = 0$, V_p

Base $q = q_m$ and $T_{\max} = T_a$, $\underline{v} = V_p$

Fig. 3. Thermal-mechanical model geometry and thermal parameters (see also Table 1). Models assume that orogenesis is controlled by convergence and subduction of pro-lithosphere (upstream) with velocity V_p . At S, pro-mantle lithosphere detaches and subducts beneath the retro-side (downstream) of the model. Retro-mantle is stationary ($v = V_R = 0$). This assumed (kinematic) behaviour of the mantle forces two conjugate, thrust-sense, step-up shear zones (pro- and retro-shears, initial positions shown as dashed lines) to develop in the dynamically modelled crust. Arrows show initial sense of motion in both the kinematic and dynamic regions of the model. The mechanical model calculates crustal deformation with the basal boundary conditions specified by the kinematic mantle velocity. Crustal material is uniform with brittle (frictional, non-cohesive Coulomb; see Fig. 4) and ductile (pyroxene-controlled power law rheology; see Fig. 4) properties. Brittle-ductile behaviour is determined dynamically within the model based on current temperature, stress and strain rate. The finite element numerics for the mechanical model are described by Fullsack (1995). Convergence (Δx) causes crustal thickening, isostatically compensated by two broken elastic beams (flexural rigidity 10^{22} Nm; crustal and mantle densities 2800 and 3300 kg m^{-3} , respectively), and uplift of the surface to elevation $h_i(x, t)$. Material is eroded at rate h_i/τ_e (τ_e = erosional time constant) and the surface temperature is maintained at 0°C . Thermal-mechanical coupling is as described by Jamieson *et al.* (1996) except for the values used for basal and surface heat flux (Figs 2 and 4, Table 1). The model is time-stepped by alternating mechanical and thermal steps. Thermal steps solve the time-dependent thermal advection diffusion-production equation (above) with the current velocity field determined dynamically within the crust and by the boundary conditions. Radioactive material (e.g. A_1 above) and the temperature field are advected and the updated temperature calculated for the entire model region. The current crustal temperature field modifies the mechanics through the ductile material behaviour (effective viscosity $\eta = B^*(\dot{\varepsilon})^{1/\tilde{n}-1} \exp(Q^*/nRT)$; where $T = ^\circ\text{K}$, R = gas constant, $\dot{\varepsilon}$ = strain rate; other parameters defined in Fig. 4 and Table 1). Initial thermal conditions for some models assume $v = 0$ ($t < 0$), whereas other models assume initial steady state with a finite thermal Peclet number ($\text{Pe} = vL/\kappa$; Figs 4, 14 and 17).

Table 1. Summary of model styles, parameters and significant results

Model	Style	Parameters (as for CA unless otherwise noted)	Results
CA	Reference model, no tarm, initial temperature field for $Pe = 0$.	$V_p = 1 \text{ cm a}^{-1} (0\text{--}37.5 \text{ Ma})$ $\eta = B^*(\dot{\varepsilon})^{1/n-1} \exp(Q^*/hRT)$, $n = 2.6$, $Q^* = 335 \text{ kJ mol}^{-1}$, $B^* = 1.05 \times 10^5 \text{ Pa s}^{1/26}$, $K = 2.25 \text{ W m}^{-1} \text{ K}^{-1}$; $\kappa = 7 \times 10^{-7} \text{ m}^2 \text{ s}^{-1}$; $q_m = 30 \text{ mW m}^{-2}$; $\tau_e = 1.75 \text{ Ma}$; $Pe = 14$ ($L = 35 \text{ km}$) or $Pe \approx 5$ ($L = 100 \text{ km}$); $d' = d/h$ = transport distance/crustal thickness; Δx = total convergence distance (km); $A_1 = 3 \mu \text{W m}^{-3}$, $h_t = 20 \text{ km}$; $A_2 = A_3 = 0$	Tight $P-T-t$ loops with lower crustal $T_{\max} \approx 600^\circ\text{C}$ at $c. 14.5 \text{ kb}$ (Fig. 8a); strongly asymmetric peak grade profile with exposed $T_{\max} \approx 550^\circ\text{C}$ (Fig. 6)
CB	Collision model, mantle tarm, initial temperature field for $Pe = 0$.	$A_2 = 3 \mu \text{W m}^{-3}$	Tight $P-T-t$ loops with lower crustal $T_{\max} \approx 740^\circ\text{C}$ at $c. 14 \text{ kb}$ (Fig. 8b); asymmetric peak grade profile with exposed $T_{\max} \approx 550^\circ\text{C}$ (Fig. 10)
CC	Collision model, mantle tarm, reduced convergence, initial temperature field for $Pe = 0$.	$V_p = 1 \text{ cm a}^{-1} (0\text{--}28 \text{ Ma})$, $0.033 \text{ cm a}^{-1} (28\text{--}238 \text{ Ma})$; $Pe = 14$ ($0\text{--}28 \text{ Ma}$), 0.42 ($28\text{--}238 \text{ Ma}$); $A_2 = 3 \mu \text{W m}^{-3}$	Open lower crustal $P-T-t$ loops with $T_{\max} \approx 740^\circ\text{C}$ at $c. 11 \text{ kb}$ (Fig. 8c); broad peak grade profile with exposed $T_{\max} \approx 550^\circ\text{C}$ (Figs 11 and 12)
CD	Collision model, mantle tarm, increased erosion, initial temperature field for $Pe = 0$.	$\tau_e = 1.75 \text{ Ma}$ ($0\text{--}28 \text{ Ma}$), 0.44 Ma ($28\text{--}38.5 \text{ Ma}$); $A_2 = 3 \mu \text{W m}^{-3}$	Open lower crustal $P-T-t$ loops with $T_{\max} \approx 740^\circ\text{C}$ at $c. 11 \text{ kb}$ (Fig. 8d); asymmetric peak grade profile with exposed $T_{\max} \approx 600^\circ\text{C}$ (Fig. 13).
CE	Collision model, crustal tarm, precursor 'steady-state' temperature field for $Pe = 14$.	$A_2 = 0$; $A_3 = 1.5 \mu \text{W m}^{-3}$, $h_r = 35 \text{ km}$	Mid-crustal $P-T-t$ paths in Barrovian field with $T_{\max} \approx 600^\circ\text{C}$ at 7.5 kb (Fig. 16a); strongly asymmetric peak grade profile with exposed $T_{\max} \approx 675^\circ\text{C}$ (Fig. 18)
CF	Collision model, crustal + mantle tarm, precursor 'steady-state' temperature field for $Pe = 14$.	$A_2 = 1.5 \mu \text{W m}^{-3}$, $A_3 = 1.5 \mu \text{W m}^{-3}$, $h_r = 35 \text{ km}$	Mid-crustal $P-T-t$ paths in Barrovian field with $T_{\max} \approx 600^\circ\text{C}$ at 7.5 kb (Fig. 16b); strongly asymmetric peak grade profile with exposed $T_{\max} \approx 675^\circ\text{C}$ (Fig. 19)
SA	Oceanic subduction model, tarm accreted from a 10 km moderately radioactive layer, initial temperature field for $Pe = 0$.	$A_2, A_3 = 0$; $A_4 = 1.5 \mu \text{W m}^{-3}$, $h_r = 10 \text{ km}$; $Pe = 49$ ($L = 10 \text{ km}$)	$P-T-t$ paths in blueschist field (Fig. 16); very low grade rocks at surface (Fig. 15)

C = collision; S = subduction: tarm = tectonically accreted radioactive material; V_p = convergence velocity from pro-side; η = effective viscosity; $\dot{\varepsilon}$ = calculated second invariant of deviatoric strain rate; K = thermal conductivity; q_m = mantle heat flux, constant for all models; $K/\rho C_p$; q_s = surface heat flux, varies with time and position as shown in figures illustrating model results; τ_e = erosional time constant, erosion rate = h_t/τ_e where h_t = surface uplift in timestep t ; Pe = thermal Peclet number = vL/κ , where v = velocity, L = characteristic length scale (35 km except where otherwise noted); A_1, A_2, A_3, A_4 = regions with contrasting radioactive heat production and geometries, as specified in the text and Figs 4, 14 and 17; h_t = initial thickness of heat-producing layer. Length of model timestep = 0.015 Ma . See Fullsack (1995) for details of mechanical model calculations. See also Figs 3 and 4.

Initial Configuration of Collision Models, CA – CD

Temperature and Velocity Fields

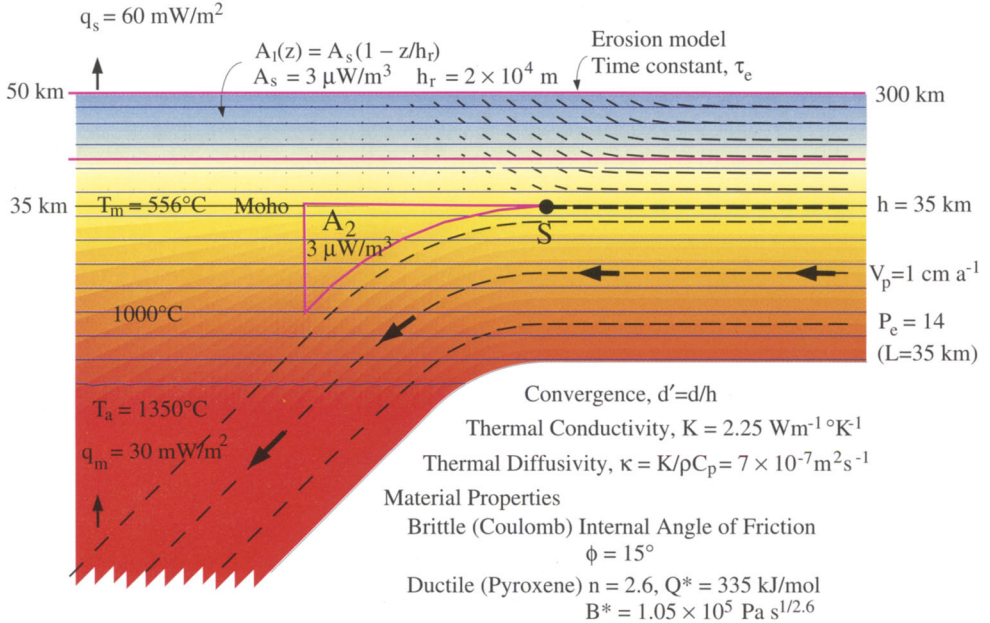


Fig. 4. Initial configuration of thermal-mechanical models CA to CD. Region A₁ has the standard heat production distribution for continental crust (Fig. 2). A₂ corresponds to tectonically accreted radioactive material (tarm) derived from upper crustal material that has been subducted to mantle depths below the orogen; this is not present in Model CA but is present in CB, CC and CD (Table 1). The mantle tarm forms a wedge of material sandwiched between the base of the crust and the top of the subducting slab. The kinematic velocity specified for the mantle lithosphere assumes that mantle tarm remains stationary during the model experiment. Thermal and material parameters shown in the diagram are constant for all models described in this paper. The initial temperature field corresponds to steady-state conductive conditions (Fig. 2, column 1) prior to rapid accretion of tarm. These initial thermal conditions are not designed to represent circumstances following a precursor phase of subduction. The results presented (Figs 5, 6, 9–13) represent conditions after decay of these initial transient conditions at a crustal scale.

underthrusting counteracts the effects of diffusional heating resulting from thermal relaxation during and after crustal thickening, i.e. at normal convergence rates ($c. 1 \text{ cm a}^{-1}$) advection dominates over diffusion. This effect is quantitatively expressed by the thermal Peclet number (Pe , Table 1); where $\text{Pe} > 1$, material is transported through a model orogen before it can heat up significantly. This problem can be illustrated by reference to a standard coupled thermal-mechanical model, Model CA, which has $\text{Pe} = 14$ (Fig. 4, Table 1). This model uses average thermal parameters for the crust and mantle, displays laterally uniform initial crustal properties including heat production (A_1) and an initially conductive temperature field, and involves moderate, uniform rates of convergence

and erosion (Figs 3 and 4, Table 1). Reference Model CA lacks tarm ($A_2, A_3 = 0$).

In the mechanical model, which is based on those described by Willett *et al.* (1993) and Beaumont *et al.* (1994), material converges from the pro-side of the system ($V_p = 1 \text{ cm a}^{-1}$) towards the fixed retro-side of the system (Fig. 3). The underlying pro-mantle lithosphere detaches and subducts at the detachment point, S. The crustal deformation field is characterized by two thrust-sense step-up shear zones, termed the pro-shear and the retro-shear, which dip in opposite directions and root at S. The model orogen is inherently asymmetric, with deformation and exhumation concentrated in the retro-shear. The thermal model (Fig. 3) calculates the temperature field in the model orogen in two

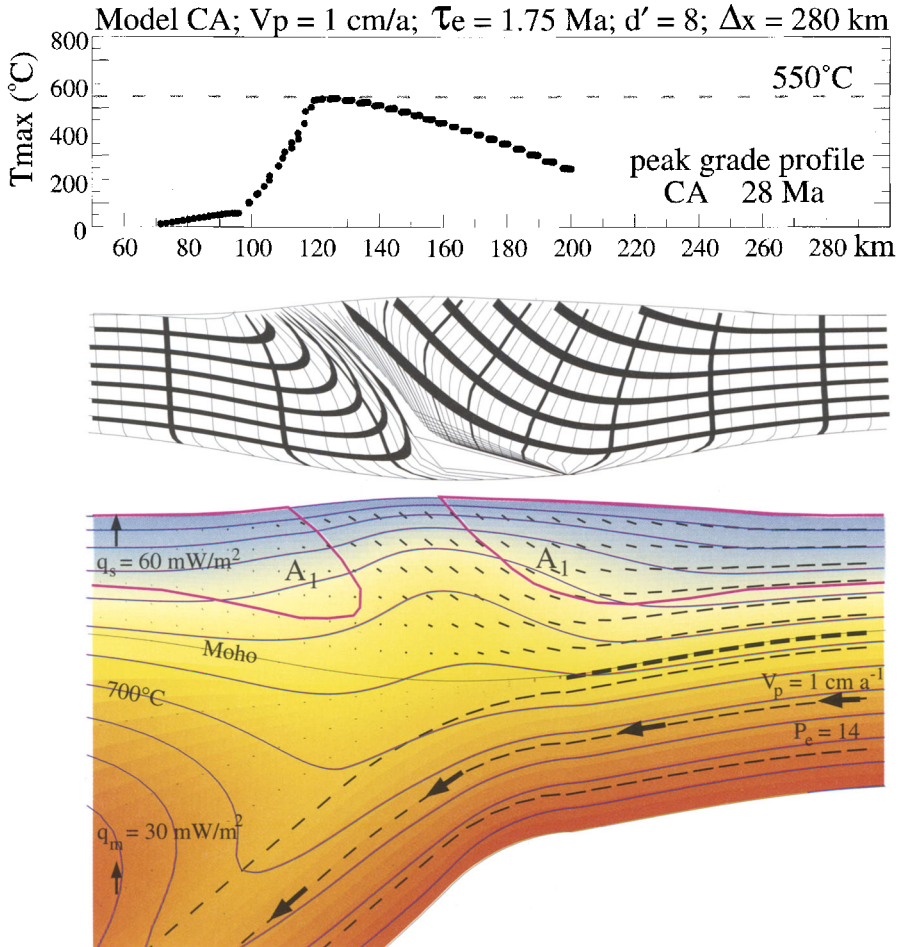


Fig. 5. Model CA at 28 Ma after the onset of convergence. Bottom panel shows the thermal structure of the orogenic lithosphere, with isotherms at 100°C intervals shown in blue and heat-producing region A_1 outlined in magenta. Heavy dashes are the instantaneous velocity vectors. Bold arrows show specified kinematic subduction of mantle lithosphere at velocity $V_p = 1 \text{ cm a}^{-1}$. Middle panel shows the calculated crustal deformation field at 28 Ma; grid lines and stripes were initially horizontal and vertical passive markers; they do not represent material variations. Top panel shows the distribution of maximum temperatures (T_{\max}) achieved by points reaching the model surface at this time; this corresponds to the distribution of peak metamorphic grade that would be observed in a transect across the model orogen. The 550°C reference line corresponds approximately to the staurolite-in isograd in pelites (Fig. 1), and also to the initial equilibrium Moho temperature. $d' = \text{normalized convergence} = \text{transport distance}/\text{crustal thickness} (d/h)$; Fig. 4); $\Delta x = \text{total convergence distance}$; τ_e is the surface erosion timescale (Table 1). Horizontal scale is identical in all three panels; there is no vertical exaggeration in the lower two panels. See text for further discussion.

dimensions using the parameters specified in Fig. 3. Crustal rheology responds to the changing thermal structure of the model orogen according to the temperature-dependent material properties listed in Fig. 4. These 'standard' thermal and tectonic parameters are held constant between models (Table 1) in order to focus on the effects of the specified distributions of

heat-producing material. The sensitivity of the model predictions to a broader parameter range has not been investigated in this study.

Figures 5 and 6 show the thermal structure and velocity field of Model CA at specified times (lower panel) and the crustal deformation field at the same times (middle panel). The maximum temperature achieved by points that reach the

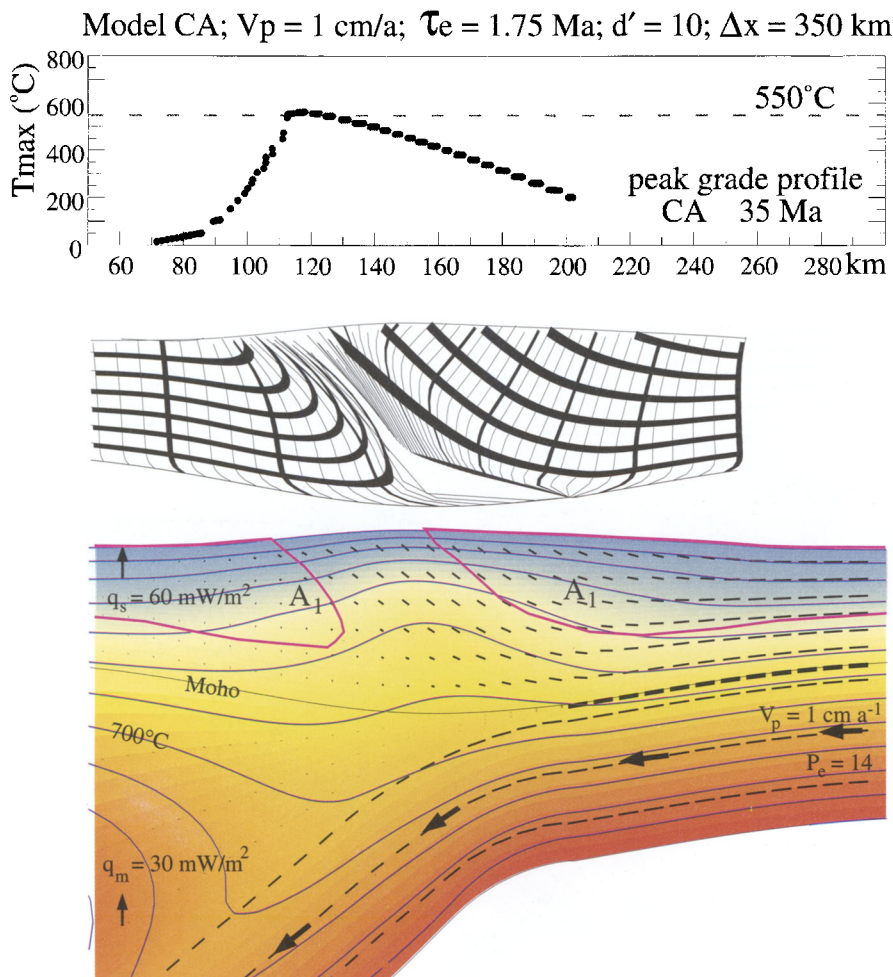


Fig. 6. Results from Model CA at 35 Ma. Panels, symbols, and parameters as for Fig. 5. Note that there has been very little change in the crustal isotherms or deformation field (as indicated by the position of the retro-shear zone) since 28 Ma, indicating that the model orogen is close to dynamic and thermal steady-state at the crustal scale.

model surface at the specified times, which correlates closely with peak metamorphic grade, is shown as a 'peak grade profile' (upper panel). The similarity between the results for 28 and 35 Ma suggests that the thermal and deformation fields approximate steady-state conditions within 30 Ma of the onset of convergence. The velocity and deformation fields show that material is transported into the orogen from the pro-side of the system, and is exhumed within and above the crustal-scale, thrust-sense retro-shear zone. Between 28 and 35 Ma this shear zone propagates into its footwall by about

10 km. Radioactive upper crust (region A₁) has been removed by erosion in the strongly deformed central part of the orogen. Isotherms are depressed in the upper mantle in the vicinity of the subducting lithosphere, and elevated in the lower crust at the base of the retro-shear zone. The maximum temperature in the lower crust is slightly above 600°C, an increase of about 60°C over the original Moho temperature of 555°C. The peak grade profiles are asymmetric, with maximum temperatures rising steeply across the retro-shear and declining gradually towards the pro-side of the system.

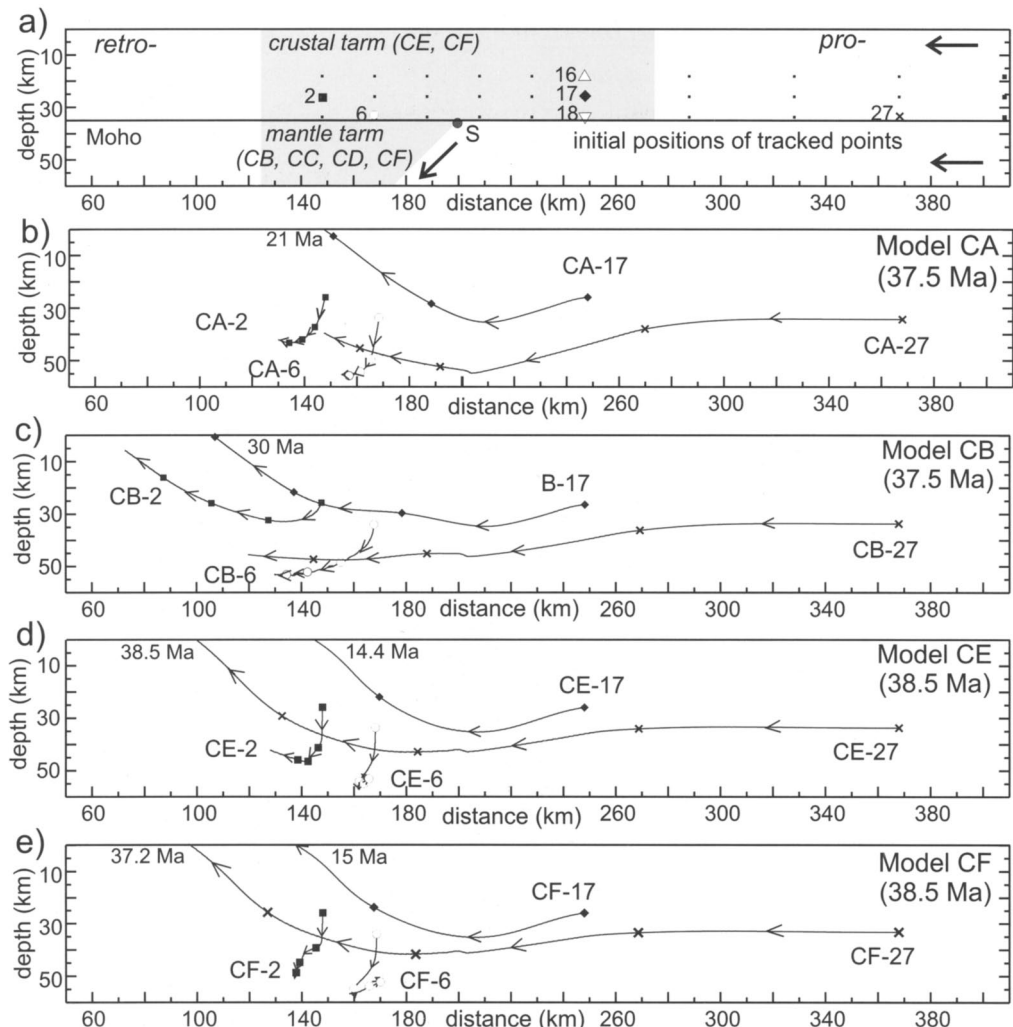


Fig. 7. (a) Initial positions of 30 points whose positions and P - T - t histories are tracked in these models. Numbered points are discussed in the text; symbols are consistent for all diagrams. Also shown are the initial positions of the crustal and mantle tarm. (b) Particle trajectories for four selected points, Model CA (ends at 37.5 Ma), which lacks tarm. Symbols appear at intervals of 10 Ma; arrowheads, which point in the transport direction, appear at intervening 5 Ma intervals. Also shown are times at which points reach the model surface. Note that points entering the model orogen from the pro-side experience substantially more lateral than vertical transport. (c) Particle trajectories for the same four points, Model CB (ends at 37.5 Ma), which has mantle tarm. The increased horizontal transport reflects heating of the lower crust by mantle tarm. (d) Particle trajectories for the same four points, Model CE (ends at 38.5 Ma), which has crustal tarm. (e) Particle trajectories for the same four points, Model CF (ends at 38.5 Ma), which has both crustal and mantle tarm. Note the similarity between model results from CE and CF (see also Fig. 20). Further discussion in text.

The maximum temperature of points reaching the surface, which increases slightly between 28 and 35 Ma, is about 550°C.

Particle trajectories and P - T - t paths for four selected points (2, 6, 17, 27; Fig. 7a) common to all the models described in this paper are shown

in Figs 7 and 8. Points CA-2 and CA-6, initially located on the retro-side of the model orogen, undergo substantial burial and some retro-ward motion (Fig. 7b) in response to crustal thickening and limited retro-ward propagation of the orogen (Figs 5 and 6). Points CA-17 and

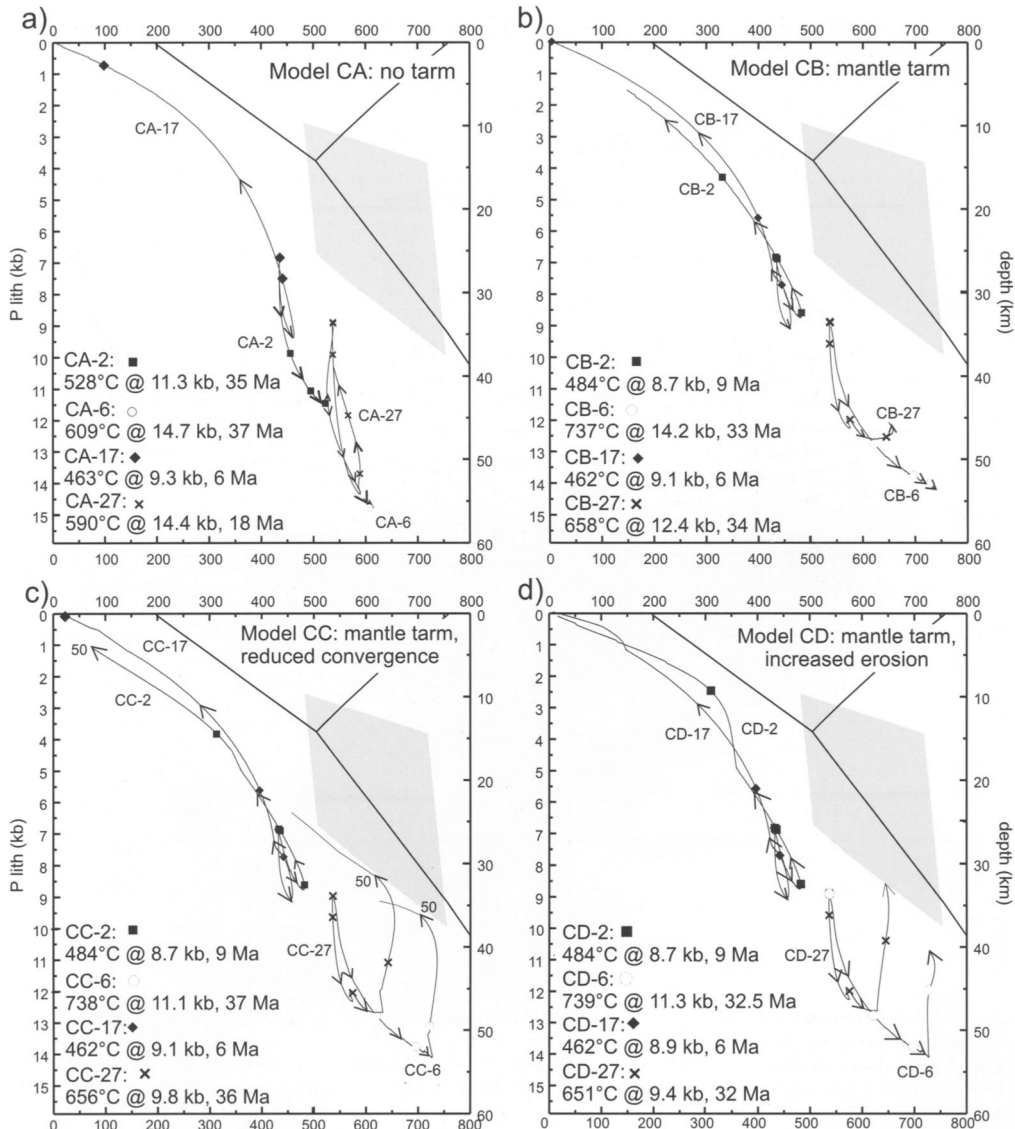


Fig. 8. P - T - t paths for the four selected points shown in Fig. 7, Models CA to CD. Symbols at 10 Ma intervals; arrowheads at intervening 5 Ma intervals. Also shown are the Al_2SiO_5 phase diagram and Barrovian reference P - T field from Fig. 1. The maximum temperature, the pressure at that temperature, and the time at which that temperature was first reached are listed for each point.

CA-27, initially on the pro-side of the system, are carried into the orogen and are exhumed (CA-17) or partly exhumed (CA-27) in the retro-shear zone; these points undergo far more lateral transport than vertical movement. Figure 8a shows that none of the corresponding P - T - t paths for these points passes through the peak P - T range typical of Barrovian sequences. The

model P - T - t paths all reach peak temperatures at too high a pressure and are either not exhumed (CA-2, CA-6), or follow exhumation paths that lie on the high- P , low- T side of the Barrovian field. The P - T - t loops are also much tighter than those normally inferred from Barrovian sequences, with exhumation paths lying within 50°C of the corresponding burial

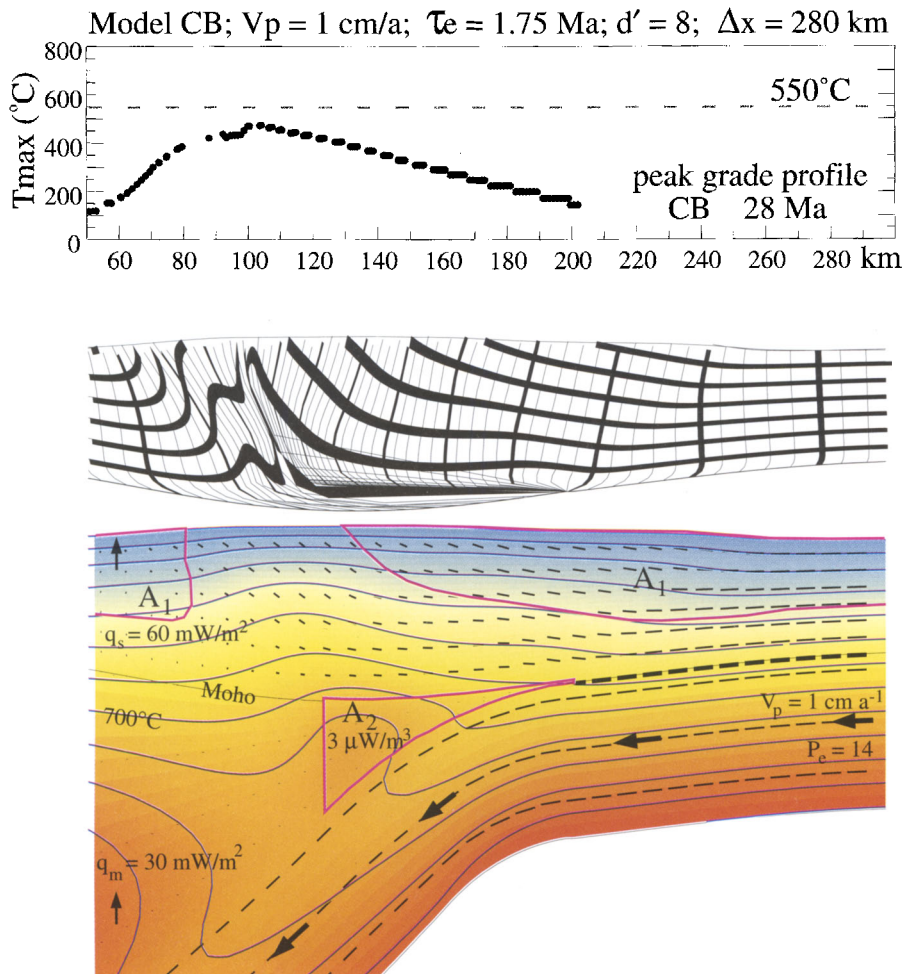


Fig. 9. Results from Model CB at 28 Ma; format and symbols as for Fig. 5. Note the presence of mantle tarm, and the corresponding deflection of mantle isotherms and change in crustal deformation field; in particular, the retro-shear zone has migrated to the retro-side of the mantle tarm wedge. The peak grade profile is broader and has lower maximum temperatures than the corresponding profile for Model CA.

paths (CA-17, CA-27, Fig. 8a). The model orogenic crust is too cold owing to continued subduction of mantle lithosphere beneath the orogen and preferential erosion of heat-producing upper crust in the active central part of the orogen (Figs 5 and 6). Although the crust thickens to more than 55 km, there is little syntectonic thermal relaxation because the Peclet number for this type of model is too high. Model CA therefore cannot be considered a viable general model for Barrovian regional metamorphism.

Effects of mantle ‘tarm’

Many orogens follow a tectonic progression from oceanic subduction through accretion of oceanic or sedimentary crustal material to collision with another continental block. Although the thermal effects associated with subduction-related magmatism prior to collision may be important, these are transient, difficult to quantify, and may not produce significant heating of the entire mantle wedge and crust above the subducting slab (e.g. Cermak & Bodri 1996).

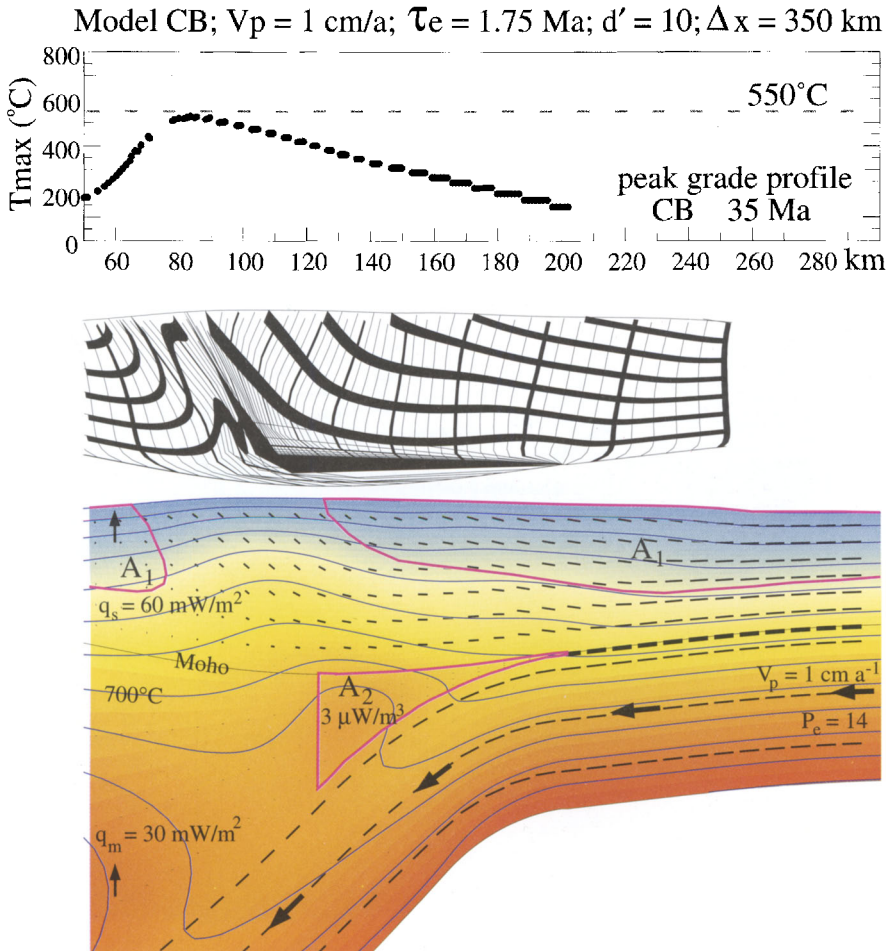


Fig. 10. Results from Model CB at 35 Ma. Although there is little change in crustal or mantle isotherms, there has been further retro-ward migration of the retro-shear, and the peak grade profile is somewhat steeper and reaches slightly higher temperatures, compared with 28 Ma. Note that most of the crustal deformation occurs retro-ward of the detachment point, located at 200 km.

Rigorous investigation of this problem is beyond the scope of the present model, which focuses instead on the effects of increased heat production in the crust or upper mantle. In some orogens like the Alps, where sub-crustal structure has been resolved by seismic methods (e.g. Schmid *et al.* 1996) and/or where ultra high-pressure crustal rocks are present, there is clear evidence that continental crustal rocks have been subducted to upper mantle depths. We have therefore investigated a series of models (CB, CC, CD; Table 1) where a wedge of tarm ($A_2 = 3 \mu\text{W m}^{-3}$) is embedded in the upper mantle; this represents partially subducted

upper crustal material accreted beneath an orogen immediately prior to collision.

Model CB (Figs 9 and 10) uses the same thermal and tectonic parameters as Model CA (Table 1), but includes a wedge of mantle tarm. The mantle tarm lies entirely below the deforming crust and remains fixed relative to the detachment point and subducting slab. At its early stages the model reflects the assumed initial stable conductive thermal conditions, i.e. tarm is assumed to have been accreted shortly before the model start and has not had time to evolve thermally. By 28 Ma, the effect of the initial conditions has been largely removed so that a

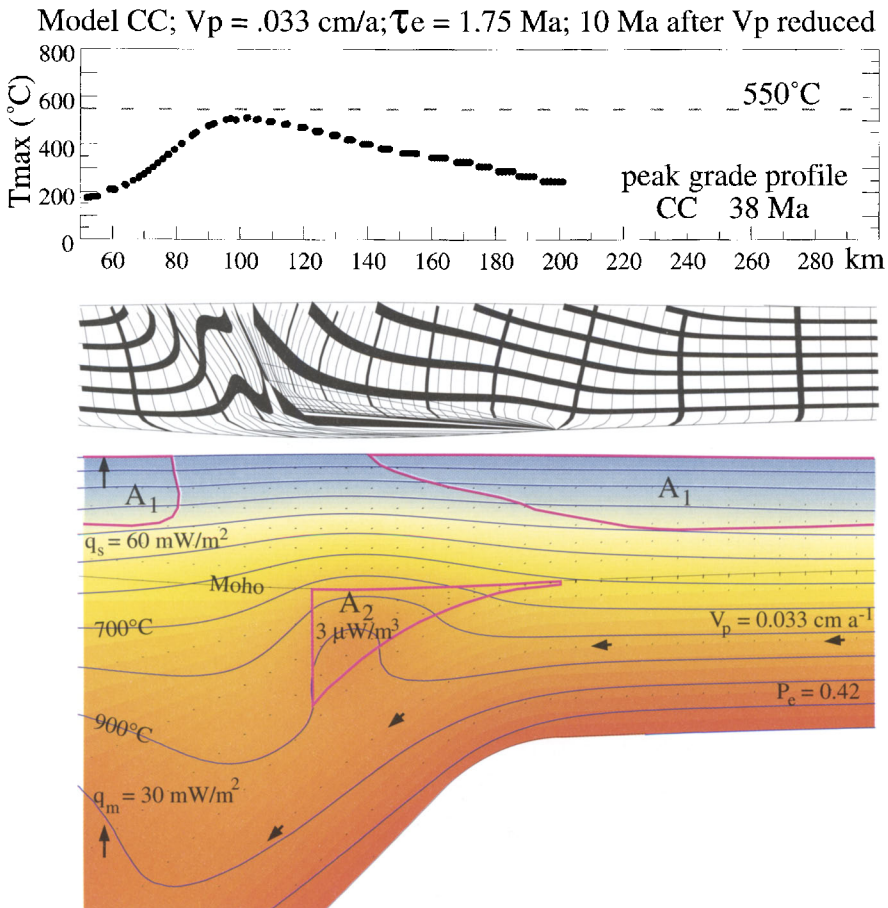


Fig. 11. Results from Model CC at 38 Ma; symbols and format as for Fig. 5. This model is identical to Model CB until 28 Ma ($\Delta x = 280$ km), when the convergence rate is reduced to 0.033 cm a^{-1} , i.e. convergence effectively stops. 10 Ma after the end of convergence, mantle isotherms are deflected strongly upward into the tarm zone, which exceeds 900°C at its base, but crustal isotherms have relaxed substantially (compare with Figs 9 and 10) during post-orogenic denudation and crustal thinning. The peak grade profile is somewhat broader than for Model CB at 35 Ma.

broad zone of lower crust has reached temperatures above 600°C , and a small zone directly above the mantle tarm exceeds 700°C . The 800°C mantle isotherm is drawn upward into the tarm wedge, demonstrating that for these conditions, heating by mantle tarm out-competes cooling by mantle subduction. Velocity vectors in the hot lower crust are nearly horizontal, indicating decoupling between the weak lower crust and the stronger middle and upper crust, which are detached and exhumed above this weak zone. This behaviour is a consequence of the thermal-mechanical coupling, in which there is an exponential decrease in viscosity with increased temperature. The lower crust above

the tarm is therefore much weaker than it was initially, and is also much weaker than lower crust on either side of the model orogen. This results in displacement of the retro-shear zone from its original position, rooted at the S-point at 200 km, to the retro-side of the mantle tarm zone at about 125 km. The pattern of deformation within the model orogen is correspondingly complex, and changes significantly between 28 and 35 Ma. The migration and re-establishment of the retro-shear zone is accompanied by focusing of deformation and exhumation, and steepening and retro-ward migration of the peak grade profile. Between 28 and 35 Ma peak temperatures recorded by rocks reaching the

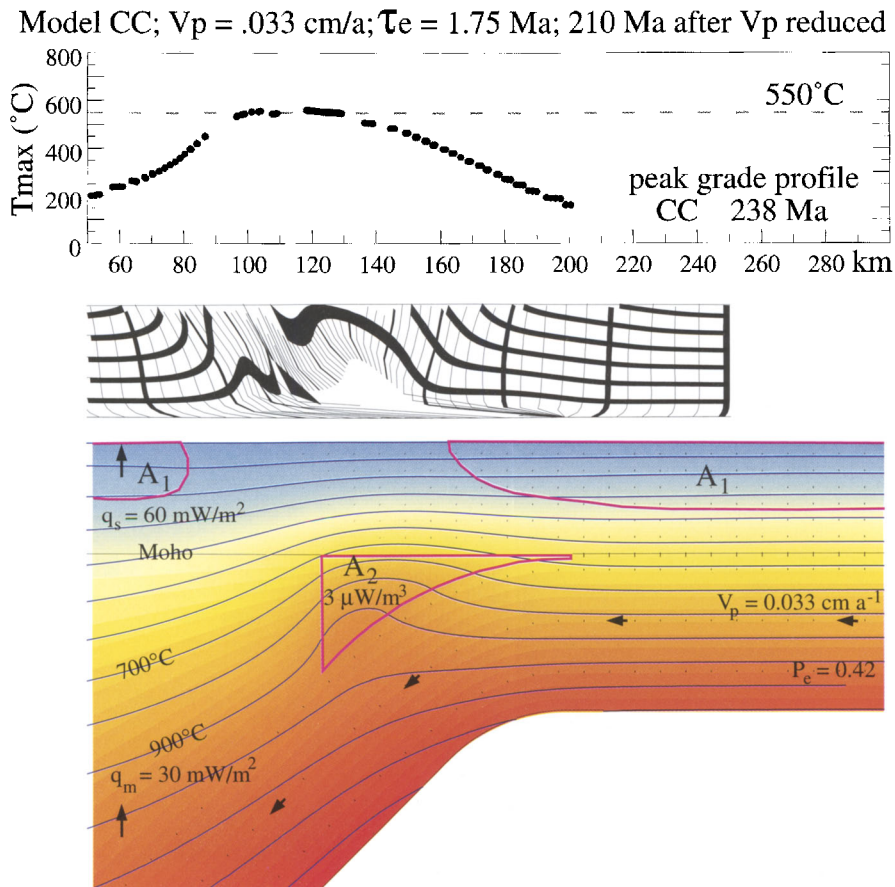


Fig. 12. Results from Model CC at 238 Ma, showing the effects of prolonged post-orogenic erosion. Except in the retro-region, crustal isotherms are almost completely relaxed to the conductive steady-state conditions. Mantle isotherms are still deflected upward into the tarm wedge, demonstrating the long-term capacity of mantle tarm to cause post-orogenic heating with little surface heat-flux anomaly. The deformation field shows the effect of long-term, mainly vertical displacement controlled by erosional unroofing, and the peak grade profile is much broader, and somewhat hotter, than at 38 Ma (Fig. 11).

surface rise from about 450°C to about 525°C. The 35 Ma peak grade profile is broader, and does not reach as high a temperature as the corresponding profile from Model CA.

Particle trajectories from Model CB (Fig. 7c) clearly show the effects of thermal weakening and detachment of the lower crust immediately above the wedge of mantle tarm. Points CB-2 and CB-6 migrate much further laterally than their equivalents in Model CA (Fig. 7b) in response to displacement of the retro-shear zone. Point CB-2 is first buried, then exhumed in the migrating retro-shear, while point CB-6 remains deeply buried. Points CB-17 and CB-27 initially follow similar paths to their equivalents in Model CA, but once they have been

incorporated into the orogen they are carried further laterally as the orogen propagates retro-ward. Consequently, CB-17 reaches the surface much later than CA-17, and CB-27 remains near its maximum burial depth as it migrates retro-ward. These results show that a region of weak, hot lower crust above the mantle tarm wedge is bypassed by the deforming orogen; particles that originate in, or are transported into, this tectonically stagnant zone are unlikely to be exhumed during the episode of convergence responsible for their burial.

P-T-t paths from Model CB (Fig. 8b) reflect these differences in burial and exhumation history, with the exception of CB-17 which follows a nearly identical path to CA-17. Point

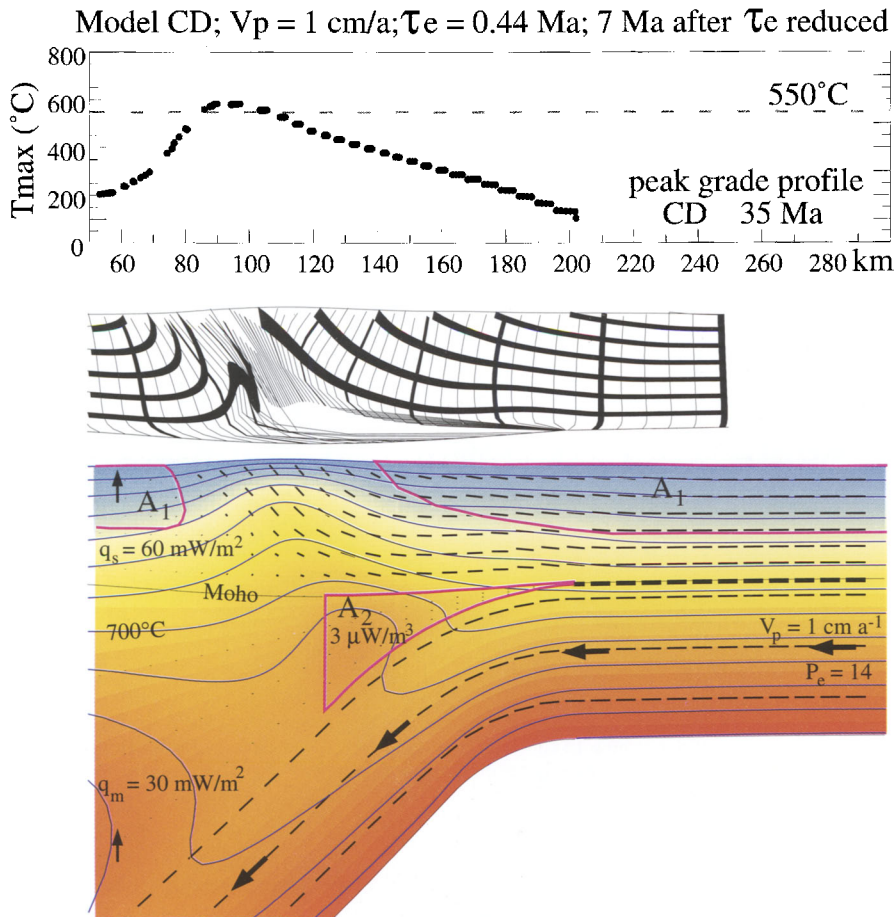


Fig. 13. Results from Model CD at 35 Ma. This model is identical to CB until 28 Ma ($\Delta x = 280$ km), when the erosion rate is increased through a reduction in τ_c by a factor of 4. Crustal isotherms are deflected upward in the vicinity of the retro-shear owing to more rapid tectonic and isostatic vertical transport of material. The peak grade profile is correspondingly hotter than for Model CB at the same time (Fig. 10).

CB-2 is exhumed, rather than buried, and follows a similar $P-T-t$ path to CB-17. Points CB-6 and CB-27 remain deeply buried, reaching maximum temperatures of 737°C and 658°C respectively. These high lower-crustal temperatures, 128 and 68°C higher than the corresponding points in Model CA, are the direct result of heating by the mantle tarm wedge. Results from Model CB suggest that the most important effect of accretion of radioactive material beneath an orogen is a substantially hotter lower crust and a consequent change in tectonic style. Thermal weakening of the lower crust leads to detachment and retro-ward propagation of the orogen, with the retro-shear zone re-established on the retro-ward side of the mantle tarm wedge. The

mid to upper orogenic crust is transported over the hot lower crust, which remains deeply buried and tectonically stagnant. The maximum temperatures in the lower crust and mantle tarm wedge are high enough to produce granulite assemblages in rocks of appropriate composition, and could induce dehydration-controlled partial melting, particularly in the tarm wedge, within 30 Ma after the onset of convergence.

Two additional models (CC, CD; Table 1) were run to test the effects of mantle tarm for different convergence and erosion rates. Model CC is identical to CB until 28 Ma, when the convergence rate is reduced to 0.033 cm a^{-1} , or, effectively, convergence stops. Reducing the convergence rate so that $P_e \ll 1$ allows the orogen

Initial Configuration of Subduction Model, SA

Temperature and Velocity Fields

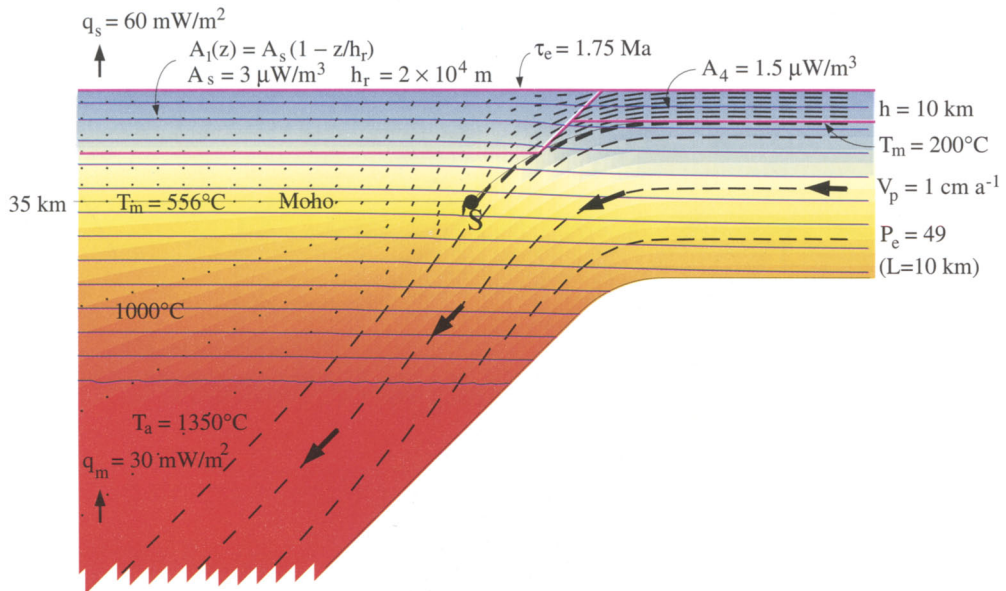


Fig. 14. Model SA starting conditions. This model simulates an ocean/continent subduction zone which will develop a tarm accretionary wedge from a 10 km thick layer of moderately radioactive sedimentary material (A_4). Initially, thermally stable oceanic lithosphere is assumed to be subducted. The adjoining continental crust has standard thickness and heat production (A_1). There is no mantle tarm. Other model properties are the same as those for Model CA.

to heat up by removing the cooling effect of subduction. Figure 11 shows Model CC at 38 Ma, 10 Ma after the the convergence rate is reduced. The hot lower-crustal region above the mantle tarm is wider than for Model CB, and both the 800°C and 900°C isotherms are drawn up into the mantle tarm. There has been some relaxation of crustal isotherms in the central part of the orogen. More than 200 Ma after the end of convergence (Fig. 12), crustal and mantle isotherms have relaxed substantially, and the mantle tarm region is still anomalously hot, exceeding 900°C at its base. Post-orogenic unroofing of the orogen affects the entire region of thickened crust, rather than being focused on the retro-side of the system, resulting in a broad, weakly asymmetric peak grade profile with maximum temperatures of about 550°C exposed over a central 30 km wide region.

$P-T-t$ paths from Model CC (Fig. 8c) show that mid-crustal points CC-2 and CC-17 are virtually identical to their equivalents in Model CB. Deep crustal points CC-6 and CC-27 reach approximately the same maximum temperatures as CB-6 and CB-17, but undergo some isother-

mal decompression during erosional unroofing. The maximum temperatures are therefore sustained to lower pressures. At about 50 Ma after the model start, or 22 Ma after the end of convergence, points CC-6 and CC-27 approach the high $T-P$ region of the Barrovian field, but cool at relatively high pressure thereafter.

Model CD tests the effect of increased erosion rate on the decompression paths. It is identical to Model CB until 28 Ma, when the erosion rate is increased by reducing the erosional time constant τ_e by a factor of 4 (Table 1). After 7 Ma of increased erosion (Fig. 13), crustal isotherms are drawn up in the vicinity of the retro-shear and are compressed near the surface in response to rapid exhumation of lower crustal rocks in the retro-shear zone. Crustal deformation is concentrated in the retro-shear, and maximum temperatures recorded in rocks reaching the surface approach 600°C in the hanging wall of the retro-shear zone.

Mid-crustal points CD-17 and CD-2 follow $P-T-t$ paths that are identical to those for CB-2 and CB-17, except for the last few million years when the decompression rate increases.

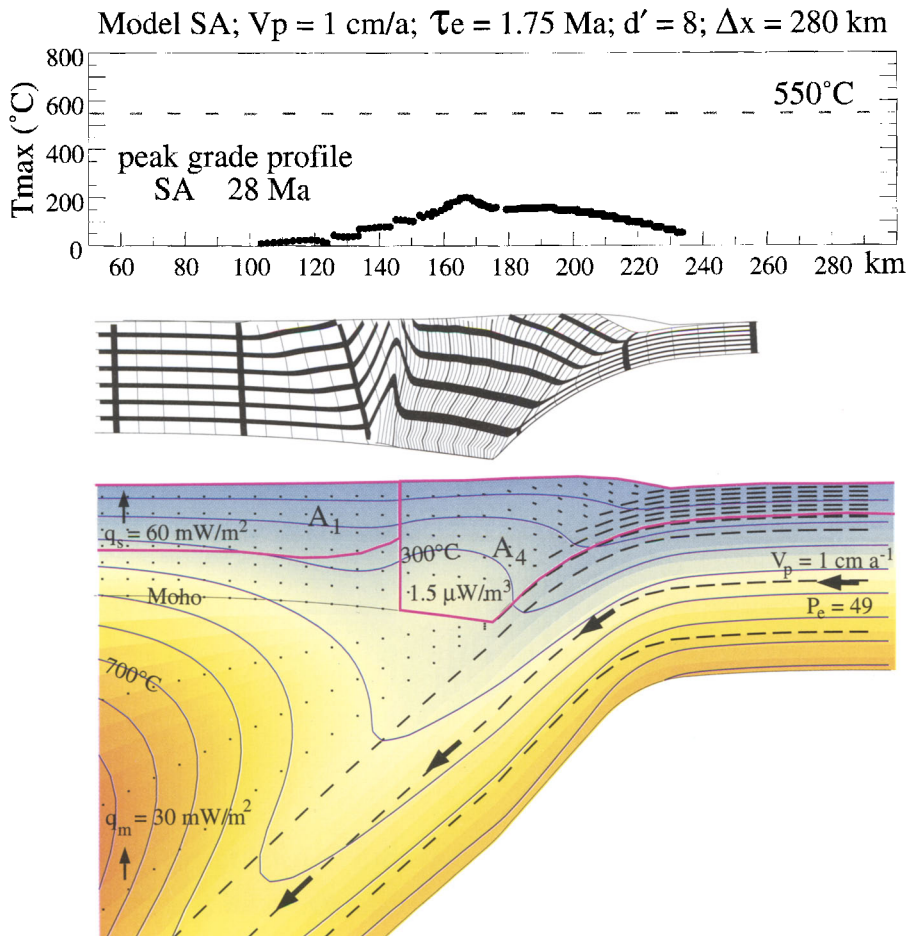


Fig. 15. Results from Model SA after 28 Ma of subduction. A broad crustal-scale accretionary wedge has been constructed from moderately radioactive material. Internal heating of the wedge has offset the cooling effect of subduction in the region immediately above the subduction zone. This model is approximately at steady-state conditions at this time. Similar results can be obtained for a thinner sedimentary layer, but the accretionary wedge accumulates more slowly.

Since these points are already near the surface at this time, the effect is minimal and unlikely to be recorded in mineral assemblages. Deep crustal points CD-6 and CD-27 follow isothermal decompression paths that would cross into the high P - T part of the Barrovian field if exhumation continued at the same rate beyond 35 Ma (Fig. 8d). However, rapid erosion-controlled decompression is a transient phenomenon, because the crust reaches a new equilibrium thickness in isostatic balance with the enhanced erosion rate. These particles would not be exhumed to the surface through the Barrovian P - T field unless the ensuing

tectonic exhumation rate were comparable to the isostatic rate.

In summary, in these models, burial of a wedge of tarm in the upper mantle beneath an active orogen heats the lower orogenic crust to temperatures of 650–750°C. This changes the tectonic style, so that the hot lower crust is bypassed by the active orogen, and remains deeply buried unless there is a change in the tectonic parameters. Both decreased convergence rate and increased erosion rate lead to near-isothermal decompression of lower crustal rocks, although at a much faster rate in the latter case. If decompression is sustained, the

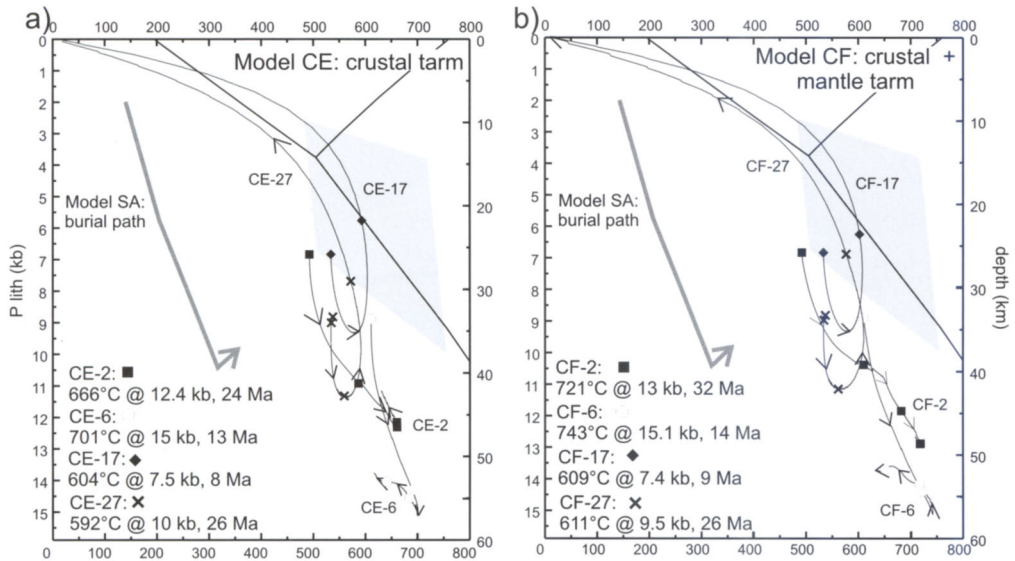
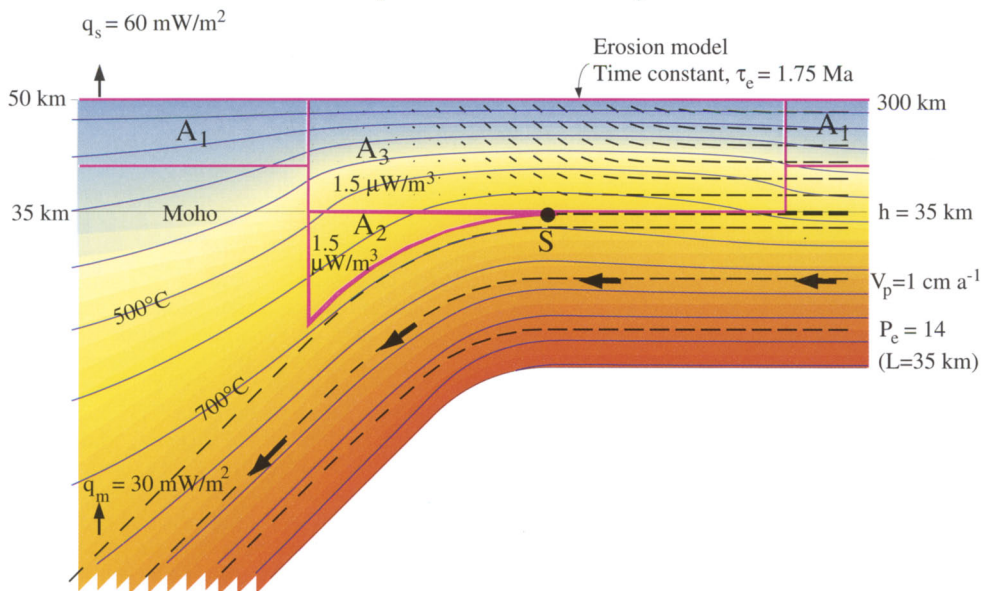


Fig. 16. P - T - t paths from crustal tarm Models CE and CF. Also shown is the burial path for points originating on the pro-side of Model SA that are incorporated into the growing accretionary wedge (Fig. 15). This burial path lies entirely within the blueschist field. P - T - t paths shown for Models CE and CF (see Figs 17, 18, 19 and Table 1 for model conditions and results) are for the same four points as shown in Figs 7 and 8; corresponding particle trajectories are shown in Fig. 7d,e. Note that points 17 and 27 follow P - T - t paths through the Barrovian field. In a model that combines subduction and collision, the initial SA burial path may evolve into CE-17, CE-2 or CE-6 style behaviour. Further discussion in text.

Initial Configuration of Collision Models with Crustal tarm, CE and CF

Temperature and Velocity Fields



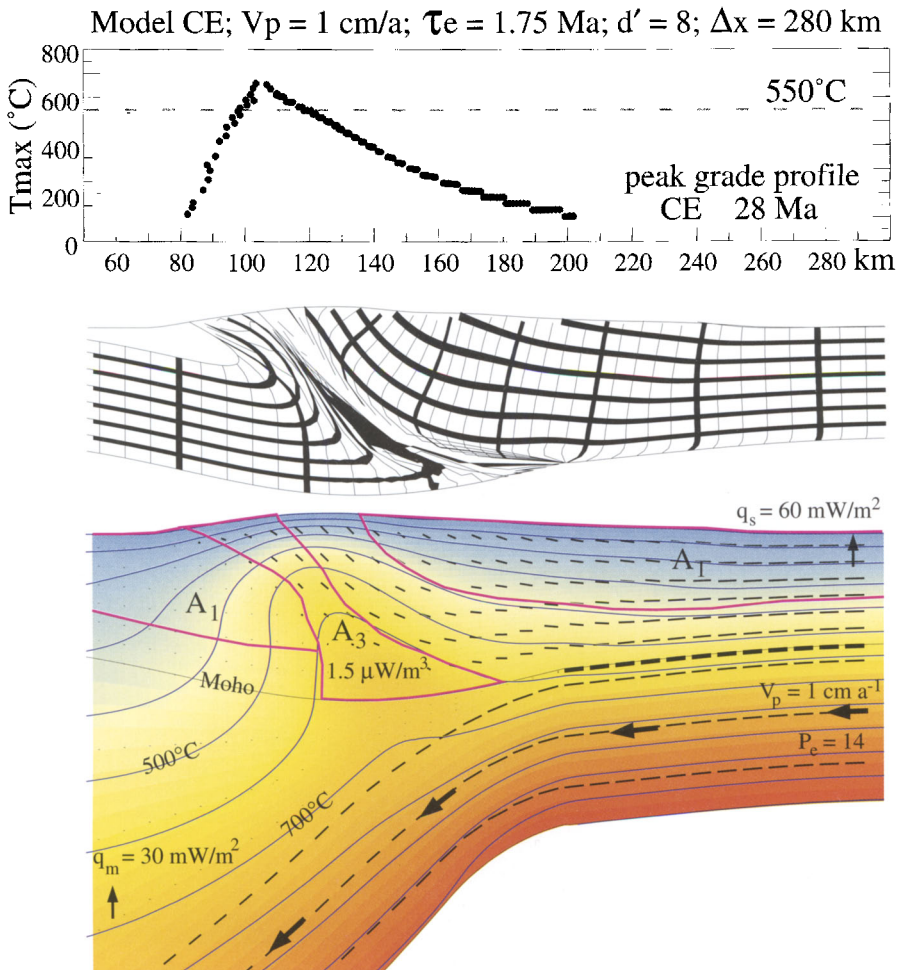


Fig. 18. Results from Model CE after 28 Ma of convergence; format as in Fig. 5. Note that the crustal tarm region (A_3) has been deformed and eroded so that it now forms a narrow zone lying along the retro-shear. Crustal isotherms are elevated in this region and heating from crustal tarm has compensated for the cooling effects of subduction. However, because the volume of tarm is being reduced, the orogen is now cooling. The deformation field (middle panel) shows that crustal tarm would be strongly deformed within the retro-shear zone. The peak grade profile is steep and asymmetric, with peak temperatures slightly above 650°C in the hanging wall of the retro-shear.

Fig. 17. Starting conditions, Models CE and CF. Model CE includes a broad region of crustal tarm (A_3), simulating the accretion of a crustal-scale zone of moderately radioactive sedimentary material during convergence. The model follows the thermal evolution and deformation of the crustal tarm zone during collision between two regions of standard continental crust (A_1). Model CE includes only crustal tarm; Model CF includes both crustal and mantle tarm with identical heat-producing properties (mantle tarm in CF has half the heat production of mantle tarm in CB, CC and CD). In these models, the initial temperature field corresponds to prolonged subduction of mantle lithosphere beneath the crustal tarm, A_3 , with $P_e = 14$. In Model CF, mantle tarm (A_2) is assumed to have accreted rapidly just prior to the start of the model. These initial conditions represent the opposite extreme from those in Models CA to CD, and serve to demonstrate the possible effect of precursor subduction on the coupled thermal-mechanics of the model.

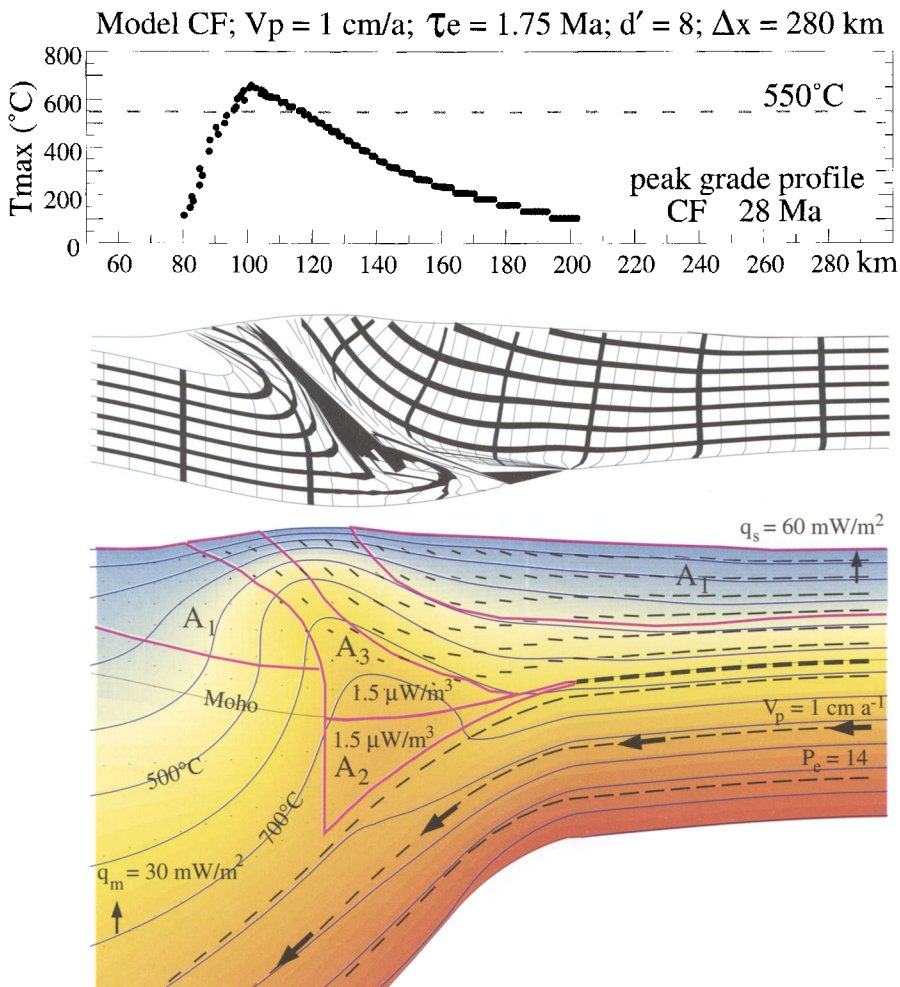


Fig. 19. Results from Model CF at 28 Ma; format as for Fig. 5. The model is very similar to CE, except that isotherms are drawn up into the mantle tarm wedge, so that the lower crust beneath the retro-shear exceeds 700°C. Deformation remains focused within the narrow, hot zone of crustal tarm. The peak grade profile is similar to CE, but slightly steeper.

lower crustal points could pass into the high-*P*-*T* part of the Barrovian field. The thermal structure of the middle to upper crust is relatively unaffected by the presence of mantle tarm, although some exhumation paths change substantially owing to the change in tectonic style. The points most likely to reach the surface in Models CB, CC and CD are therefore still too cold to resemble typical Barrovian sequences. However, buried mantle tarm reaches temperatures of 800–900°C (for $P > 12$ –15 kbar) within 20–30 Ma of the onset of convergence and stays hot long after convergence stops. This buried crustal material provides a potential source of

granitoid magma, which could be produced by high-pressure dehydration melting of hydrous phases at temperatures above c. 850°C (e.g. Thompson & Connolly 1995; Carrington & Harley 1995; Skjerlie & Johnson 1996).

Effects of crustal ‘tarm’

An alternative to accretion of tarm in the upper mantle is accretion of radioactive material within the orogenic crust. This could be accomplished by accumulation of sediments enriched in heat-producing elements in an accretionary

wedge or a tectonically thickened continental margin sequence. Under the model assumptions, crustal tarm differs from mantle tarm because it moves according to the dynamically determined crustal velocity field and is therefore transported through the model orogen, whereas mantle tarm, located in the non-deforming retro-mantle lithosphere, is assumed to be stationary ($v = 0$, Fig. 3). Three models (SA, CE, CF; Table 1) were run to investigate the thermal and tectonic effects of crustal tarm.

Model SA is a subduction model designed to investigate the thermal structure of an accretionary wedge formed from moderately radioactive sediments. A 10 km thick sedimentary layer ($A_4 = 1.5 \mu\text{W m}^{-3}$) is transported into a growing accretionary wedge (Fig. 14). The layer is both frontally accreted and tectonically underplated beneath the wedge (Fig. 15, middle panel); the accretionary wedge grows with time, ultimately producing a crustal-scale region of sedimentary material. After 28 Ma of convergence (Fig. 15), the 300°C isotherm is drawn up into the accretionary wedge by radioactive heating of A_4 , contrasting with the 400°C isotherm which is deflected downward by the subducting slab. There is thus a very broad region, encompassing the lower accretionary wedge and upper mantle, where temperatures lie between 300 and 400°C. $P-T-t$ paths for points entering the accretionary wedge from the pro-side of the system lie within the blueschist field (Model SA burial path, Fig. 16).

Model CE (Table 1) was designed to investigate the effects of collision following the accretion of a wide zone of crustal tarm with the same heat production as the accretionary wedge in Model SA (Figs 15 and 17). The rectangular zone A_3 (Fig. 17) represents in a simplified way the radioactive heat production of the accretionary wedge and/or similar sediments of a colliding rifted margin. Mantle tarm is not present in Model CE. The initial conditions also differ from earlier models in that the temperature field corresponds to thermal equilibrium with an assumed long-term precursor phase of mantle subduction with $\text{Pe} = 14$. It is only under these conditions that the Moho temperature and surface heat flux in the tarm region remain moderate (see Fig. 2, column 3, for corresponding values where $\text{Pe} = 0$). Clearly, very high temperature conditions would develop in Model CE if convergence ceases before the volume of crustal tarm is reduced by orogenic processes; conversely, unlike the earlier models, subduction is necessary for the model crust to retain some strength and to remain below its melting temperature.

After 28 Ma of convergence, the crustal tarm zone, initially 150 km wide, has been strongly deformed and eroded so that it forms a 10–20 km thick zone lying along the retro-shear zone (Fig. 18). Above the tarm zone lies an exhumed crustal section derived from the converging pro-crust; a thin wedge of crustal tarm is trapped beneath this overriding crust. Deformation and exhumation within the orogen are strongly focused along the tarm/retro-shear zone, which forms a relatively weak, hot zone caught between two cooler, stronger, converging continental blocks. Heating of the lower crust by the crustal tarm has resulted in some retro-ward migration of the orogen, although the effect is not as strong as seen in Model CB. In this case, heating by tarm is moderated by the cooler retro-mantle lithosphere (compare Figs 9 and 18), indicating that the thermal state of the lithosphere on the retro-side of the system may exert a significant control on the thermal and mechanical evolution of orogens involving mantle subduction. Crustal isotherms are drawn strongly up into the tarm zone, so that a significant volume of lower crust is at 600–650°C. The peak grade profile is strongly asymmetric, with maximum temperatures slightly above 650°C in the hanging wall of the retro-shear.

Particle trajectories from Model CE are shown in Fig. 7d. Points CE-2 and CE-6, which originate on the retro-side of the system, are deeply buried beneath the overriding orogen, resembling their equivalents in Model CA. Points CE-17 and CE-27 are transported from the pro- to the retro-side of the system, and reach the model surface near the middle and end of the model run, respectively. The particle trajectories for these points also resemble those for Model CA, but their transport through the orogen is faster owing to more focused and efficient exhumation in the retro-shear zone. Both CE-17 and CE-27 follow $P-T-t$ paths that pass through the Barrovian field (Fig. 16a). Point CE-17 reaches peak conditions within the Barrovian field, and passes through the sillimanite and andalusite fields during decompression. Point CE-27 reaches peak conditions on the high-pressure side of the Barrovian field, and its decompression path lies entirely within the stability field of kyanite. Points CE-2 and CE-6 reach maximum temperatures in the deep orogenic crust, and cool at high pressure because they are trapped in the weak crust beneath the retro-shear zone.

Model CF (Fig. 19) investigates the combined effects of crustal and mantle tarm. It has the same initial conditions as Model CE (Table 1, Fig. 17) with the addition of mantle tarm

wedge ($A_2 = 1.5 \mu\text{W m}^{-3}$) assumed to have been rapidly accreted shortly before the start of the model. Deformation fields and peak grade profiles for Models CE and CF are very similar (Figs 18 and 19). The main difference between the two models lies in the temperatures reached in and immediately above the mantle tarm, where temperatures exceeding 700°C are present in Model CF at 28 Ma (Fig. 19). Comparison of Model CB (Fig. 9) with Model CF (Fig. 19) demonstrates the thermal-mechanical pinning effect of the high lateral temperature gradient at the base of the retro-crust in Model CF, also seen in Models CB and CE. Both CB and CF have similar total heat production from tarm, although it is distributed differently (concentrated in mantle tarm in CB, distributed through crust and mantle tarm in CF). Both attain temperatures above 700°C at the base of the crust. However, the steeper lateral temperature gradient in Model CF leads to a feedback in the mechanics that results in more focused deformation and exhumation in the retro-shear. Consequently, isotherms are advected higher into the crust and exhumed particles follow an isothermal decompression path en route to the surface (compare CB-17, Fig. 8b, with CF-17, Fig. 16b). This contrasts with more diffuse deformation and velocity distributions in Model CB.

Particle trajectories for Model CF (Fig. 7e) closely resemble those for Model CE. Points CF-2 and CF-6 are also deeply buried, although point CF-2 does not show the limited exhumation shown by CE-2, and CF-6 shows an unusual pro-ward motion reflecting lower crustal shear during retro-ward migration of the overlying orogen. $P-T-t$ paths for all CF points are very similar to their equivalents in Model CE (Fig. 16), except that lower crustal points CF-6 and CF-27 reach substantially higher temperatures (743°C and 611°C respectively) owing to heating by underlying mantle tarm. Both CF-17 and CF-27 pass through the Barrovian $P-T$ field (Fig. 16b), but are not significantly hotter than their equivalents in Model CE because they pass above the high-temperature lower crustal region.

Particle paths and $P-T-t$ paths for three points (16, 17, 18) which initially form a vertical array near the pro-side of the crustal tarm zone (Fig. 7a) are shown in Fig. 20. Results from Models CE and CF are nearly identical and are therefore discussed together. Although the points 16, 17 and 18 originally formed a vertical column, they are dispersed during deformation; an initial vertical separation of about 7.5 km becomes a horizontal separation of 20–50 km, with lower crustal point 18 travelling substantially further towards the retro-side of

the system (Fig. 20c). Points 16 and 17 form $P-T-t$ loops resembling those from the low-grade and medium-grade parts of Barrovian sequences, respectively. In contrast, point 18, which spends about 20 Ma in the deep crust, reaches peak conditions at high pressure, forms a very tight $P-T$ loop with its exhumation path just slightly hotter than its burial path, and does not leave the kyanite stability field. Peak metamorphic conditions for this originally vertical array of points are reached in different places and at different times within the model orogen.

Although temperature-time histories have not been emphasized in this study, the model results serve to illustrate the important distinction between cooling and exhumation (Fig. 20b). Although cooling rates derived from thermo-chronological data are often converted into exhumation rates, the necessary assumption of a constant geotherm is clearly not appropriate for an actively deforming and eroding orogen (e.g. Stüwe *et al.* 1994; Whittington 1996; Batt & Braun 1997). In the models presented here, the tectonic velocity within the orogen advects hot material into the upper crust, strongly perturbing the geothermal gradient by drawing deep crustal isotherms toward the surface (Figs 18 and 19). Particles travelling through the region of elevated isotherms therefore undergo near-isothermal decompression, followed by very rapid near-surface cooling (Fig. 20a, b). Exhumation starts while these particles are still heating up, and the onset of rapid decompression significantly precedes the onset of rapid cooling (Fig. 20b). For the illustrated point CF-17, the cooling rate increases as the particle approaches the surface, whereas the amount of exhumation over the corresponding time intervals decreases. As clearly demonstrated by Batt & Braun (1997), this rapid cooling need not be related to increased tectonic convergence or uplift rates.

Tracking all 30 points through Models CE and CF shows that a broad region of the middle orogenic crust attains peak temperature conditions within the Barrovian $P-T$ field (Fig. 20d). Figure 21 shows $P-T-t$ paths and particle trajectories for five points that reach the surface of Model CF at 15 ± 2 Ma, the time at which combination of thermal and tectonic parameters is optimal for producing Barrovian $P-T$ conditions in models with crustal tarm. Mid-crustal points CF-8, 17 and 14, which were originally distributed over a lateral distance of 60 km, are tectonically juxtaposed during convergence so that they are separated at the surface by less than 15 km. Peak metamorphic conditions recorded by the five points increase structurally

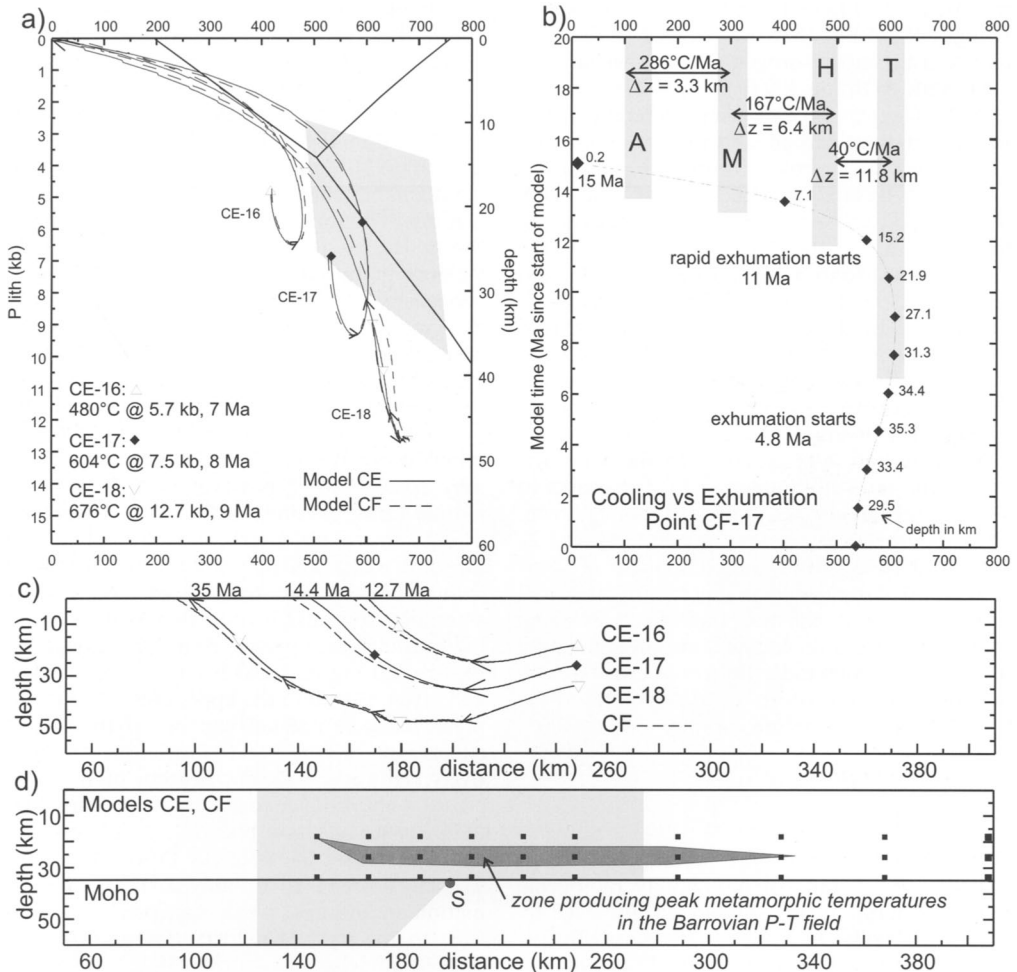


Fig. 20. Particle paths and P - T - t paths for three points forming a vertical array (c) near the pro-edge of the crustal tarm zone, Models CE and CF. Symbols in (a) and (c) as for Fig. 7, 8 and 16, with symbols shown at 10 Ma intervals and arrowheads at intervening 5 Ma intervals. Results from Model CE (solid lines with symbols) and CF (dashed lines, no symbols) are almost identical, except that CF-18 is slightly hotter during decompression than CE-18, reflecting the influence of mantle tarm on points in the deep crust. Note the separation of the points during deformation (c), and their different arrival times at the surface (times shown for CE; CF times are very similar). (b) Temperature–time history for point CF-17 (\approx CE-17) which reaches the surface at 15 Ma. Numbers on curve show burial depths in km at 1.5 Ma intervals indicated by the symbols. Note that exhumation (decrease in burial depth) starts at 4.8 Ma while the point is still heating up, and that rapid exhumation starts before rapid cooling. The vertical shaded bars indicate nominal closure temperature ranges for various thermochronometers: A = apatite fission track; M = mica $^{40}\text{Ar}/^{39}\text{Ar}$; H = hornblende $^{40}\text{Ar}/^{39}\text{Ar}$; T = U-Pb on titanite. Cooling rates ($^{\circ}\text{C Ma}^{-1}$) and amounts of exhumation (Δz) shown for 100–300°C, 300–500°C and 500–600°C intervals. (d) The model region containing points that reach peak temperatures within the Barrovian field. Points at shallower crustal levels reach maximum temperatures on the low-temperature side of the Barrovian field; points lying at deeper crustal levels reach peak temperatures on the high-pressure side of the Barrovian field.

upward across the retro-shear zone, then decrease again. The metamorphic field gradient that would be observed in a transect across the model orogen at this time corresponds approximately to the normal Barrovian progression

through the garnet, staurolite and kyanite zones back down to the garnet zone. However, this metamorphic field gradient does not correspond to any thermal gradient that existed in the model, since not only are the peak conditions

recorded at different times (e.g. Ruppel & Hodges 1994) but they are reached in different places in the model orogen (e.g. Jamieson *et al.* 1996; Batt & Braun 1997).

Although experiments using different values for convergence and erosion rates were not run for models with crustal tarm, the effects are predictable by analogy with Models CC and CD. Reducing the convergence rate allows the orogen to heat up; in the limit where $Pe = 0$, the equilibrium Moho temperature is 875°C and the surface heat flux is 82.5 mW m⁻² (Fig. 2, column 3). In these models, where the crustal tarm zone is progressively deformed, eroded and reduced in volume during convergence, the post-convergence heating effect will be much stronger if convergence ceases early in the orogenic evolution, e.g. before c. 15 Ma when the tarm zone is at its hottest, than if it ceases at 28 Ma when the orogen is already cooling down. Although the P - T - t paths for points 17 and 27 already show a substantial component of near-isothermal decompression, increasing the erosion rate would enhance this effect, bringing more points from the kyanite into the sillimanite field during exhumation. Enhanced erosion rates would also allow deep crustal points to be partially exhumed before cooling.

Discussion

Of the various model styles investigated, accretion of a wide zone of moderately radiogenic crustal material during subduction, followed by continental collision, is clearly the most effective way to generate Barrovian P - T conditions. In this respect, the present thermal-mechanical model results agree with those from thermal-kinematic models (e.g. Chamberlain & Sonder 1990; Ruppel & Hodges 1994; Huerta *et al.* 1996). However, our models show how thermal and mechanical effects interact during collision, and how material points are transported through the deforming orogen, so that their final positions at the model surface do not reflect their initial positions within the model orogen. In models with crustal tarm, a broad region of the middle orogenic crust (Fig. 20d) reaches Barrovian conditions within 15 Ma of the onset of collision. However, during convergence (at 1 cm a⁻¹) the crustal tarm is eroded and deformed into a narrow zone lying along the retro-shear, and becomes an ineffective mid-crustal heat source after about 20 Ma. Mantle tarm, bypassed by the orogenic crust during deformation, serves as an effective heat source for the deep crust over the 38.5 Ma time span

investigated in these models, but has only a minor effect on the middle and upper crust.

After 20–30 Ma of convergence, the mantle tarm wedge reaches temperatures greater than 800°C; temperatures in this zone would exceed 900°C within 10 Ma of the end of convergence (e.g. Fig. 11). Under these conditions, metasediment in this zone would undergo dehydration melting (Thompson & Connolly 1995; Carrington & Harley 1995; Skjerlie & Johnson 1996), yielding granitoid magma within 20 Ma of the orogenic peak. Heating is more rapid than that associated with lithospheric-scale diffusive thermal relaxation because the heat is radiogenic and generated within the buried crustal material itself. Some anatexis associated with dehydration of muscovite (e.g. Fig. 1) might be expected in the immediately overlying crust, where temperatures may exceed 700°C; however, in the absence of mantle tarm, melting within the orogenic crust is unlikely to yield large volumes of magma. Upward migration of granitoid magma would change the thermal structure of the crust substantially from that investigated here by advecting heat into the upper crust and by transferring heat-producing material from the upper mantle and lower crust into the upper crust. The models presented here are not capable of treating the effects of melting and plutonism quantitatively. However, efficient heating of the upper crust would produce regional low-pressure high-temperature metamorphism (e.g. Chamberlain & Sonder 1990; Sandiford & Powell 1991), and would also lead to broadly distributed deformation in the hot, weak upper crust, in contrast to the style of deformation shown in the present models.

Models using average initial values for crustal heat production produce orogenic crust that is too cold to attain Barrovian P - T conditions. However, the deep crust in these models reaches pressures in excess of 12 kbar at 600–750°C, making the formation of lower crustal eclogite a distinct possibility. In some models, cooling at high pressure (Fig. 16) suggests that eclogite assemblages would be preserved, although exhumation of the eclogites would be unlikely in the same orogenic phase. The subduction model yields P - T - t paths that lie within the blueschist field, with peak P - T conditions on the order of 300–400°C at 10–12 kbar (Fig. 16). These models thus provide a feasible way to form the high- P -low- T metamorphic assemblages normally associated with subduction.

An intriguing aspect of the models is the way in which the tectonic regime responds to heating of the lower orogenic crust to temperatures above c. 650°C. This reduces crust-mantle

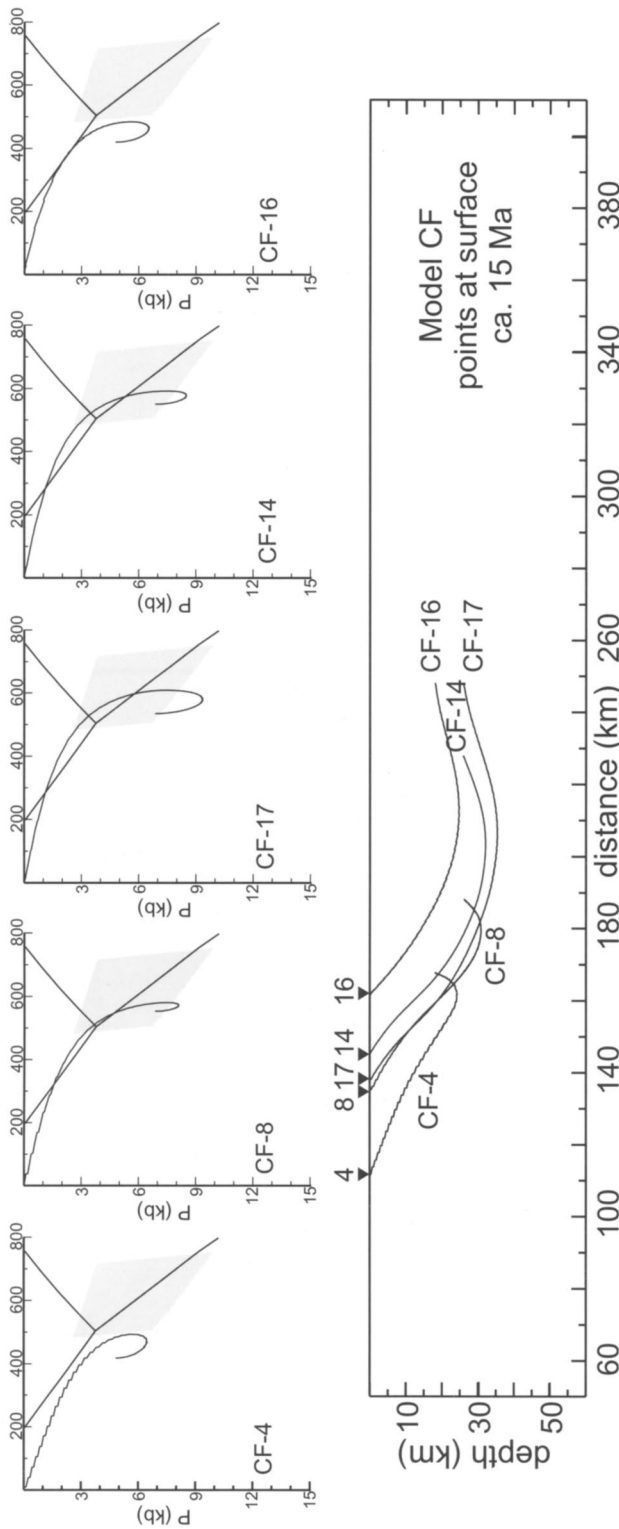


Fig. 21. Particle trajectories and P - T - t paths for five points from Model CF that reach the model surface at 15 ± 2 Ma, the optimum time for points attaining Barrovian P - T conditions within the crustal tarm zone to be examined to the model surface. Results from Model CF are very similar. The array of peak temperatures and P - T - t paths closely resembles a typical progressive Barrovian metamorphic sequence, with metamorphic grade first increasing, then decreasing up structural section. The maximum metamorphic grade at the surface at this time, shown by CF-17, corresponds roughly to staurolite-kyanite-zone conditions. Note that peak temperatures are achieved at somewhat different times, so that the model metamorphic field gradient does not correspond to a thermal gradient. Points defining the metamorphic field gradient originated over a lateral distance of 100 km; nowhere does their surface distribution at 1.5 Ma resemble their pre-collision distribution.

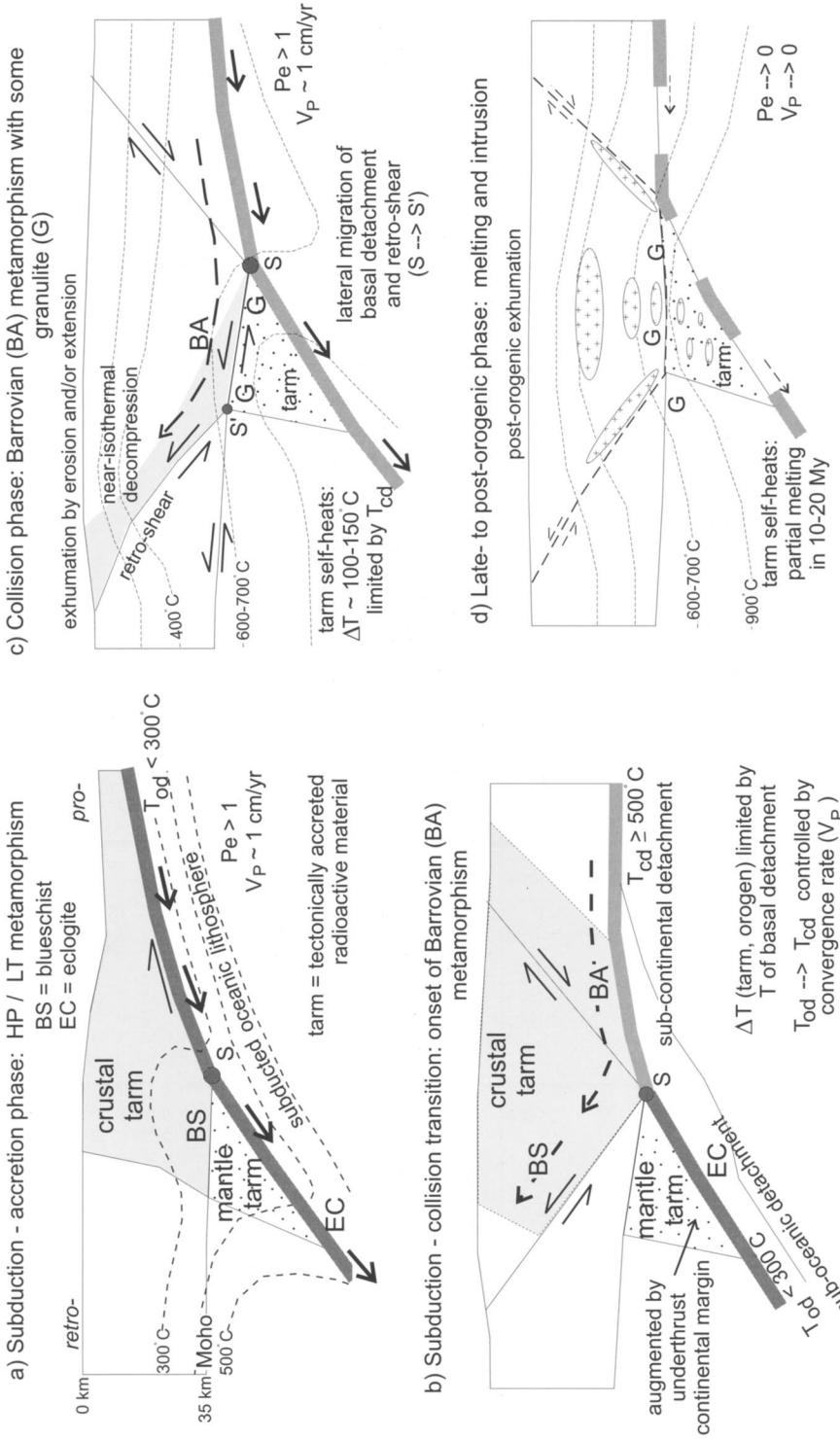


Fig. 22. Conceptual diagrams based on the numerical model results summarizing the metamorphic conditions accompanying a normal tectonic progression from subduction to continental collision, accompanied by tectonic accretion of radioactive material in the crust and mantle. Following the onset of collision, the volume of crustal tarm is reduced through deformation and erosion, but mantle tarm is assumed to be unaffected and continues to act as an effective heat source in the post-orogenic phase. The primary controls on thermal conditions are the Pelet number (Pe) and the temperature of the basal detachment (T_{cd} for oceanic lithosphere, T_{cd} for continental lithosphere), both associated with subduction, and the evolving redistribution of radioactive heat production in the overlying ocean. Further discussion in text.

coupling, allowing the orogenic crust to detach and migrate away from the S-point toward the retro-side of the system. The retro-shear zone is re-established where lateral strength contrasts focus deformation of the weak orogen against colder, stronger crust, for example, on the retro-side of the mantle tarm wedge in Models CB, CC and CD, or on the retro-side of the crustal tarm zone in models CE and CF. Decoupling of the middle and upper orogenic crust from the lower crust leads to the formation of a 5–10 km thick zone of hot, weak lower crust that is trapped beneath the actively deforming orogen. This zone, which would be characterized by relatively flat-lying synmetamorphic foliations, reaches temperatures of at least 700–750°C, hot enough to produce migmatites or granulites in rocks of suitable composition. These high-grade rocks are unlikely to be exhumed until a subsequent tectonic episode, if ever. Their prolonged residence at high temperature in the deep crust would initially lead to the formation of well-equilibrated peak metamorphic assemblages; however, these would be susceptible to retrograde zoning and exsolution during subsequent slow cooling. These are common features of many granulite terranes.

The models investigated here suggest that many first-order features of orogenic belts, including the array of metamorphic and structural styles, may be explained through a normal tectonic progression from subduction through accretion to collision (Fig. 22). The initial subduction phase is associated with the formation of blueschist in the accretionary wedge and eclogite in the deeper part of the subduction zone (Fig. 22a). Subduction that leads to the accumulation of a significant volume of radioactive sedimentary material in the crust or upper mantle provides the necessary precursor conditions for the development of Barrovian regional metamorphism during subsequent continental collision (Fig. 22b, c). With the onset of collision, the depth of the basal detachment changes from *c.* 10 to *c.* 35 km, with a corresponding increase in temperature from <300°C to >500°C (Fig. 22b) that decreases the cooling effect of the subducting slab. Because the volume of crustal tarm is progressively reduced during deformation and erosion accompanying collision (Fig. 22c), the optimal time scale for Barrovian metamorphism in the small orogens considered here is on the order of 15–20 Ma from the onset of collision. In orogens where crustal tarm is accreted during subduction, Barrovian assemblages would be expected to overprint blueschists or eclogites, a common pattern in metamorphic belts (e.g. Alps, Ring 1992; Fleur de Lys Super-

group, Jamieson 1990; Fig. 1). The progression of metamorphic zones predicted to appear at the surface in models with crustal tarm, with metamorphic grade increasing up structural section, approximates that seen in normal Barrovian sequences (Fig. 21). In orogens with mantle tarm, granulites should form, and remain buried, in the lower crust while Barrovian sequences are formed and exhumed at the same time in the middle and upper crust (Fig. 22c). Heating of mantle tarm to temperatures above 800°C, or greater than 900°C after convergence ceases, could yield late-orogenic to post-orogenic granitoid magma from partial melting of subducted crustal material (Fig. 22d) on time scales of 10–30 Ma. For models with crustal tarm, the presence of mantle tarm makes very little difference to the *P-T* conditions at mid-crustal levels and hence Barrovian metamorphism; however, in the models investigated here, only models with mantle tarm reach the high temperatures necessary to form lower crustal granulites or substantial volumes of granitoid magma.

Conclusions

The first-order predictions of the models presented in this paper are compatible with first-order observations from Barrovian regional metamorphic belts. However, some caution is required because the sensitivity of the model predictions to different thermal and tectonic parameters has not been tested, and the effects of gradual accretion of crustal and mantle tarm prior to collision have not been investigated. We concur with the conclusions of previous workers that tectonically accreted or thickened heat-producing crustal material is important for producing high-temperature metamorphism (e.g. Chamberlain & Sonder 1990; Ruppel & Hodges 1994; Huerta *et al.* 1996). However, this work shows that accumulation of tarm in the crust or upper mantle leads to complex feedbacks between thermal and tectonic processes which strongly influence orogenic evolution. These feedbacks would become even more important in models in which a more realistic distribution of material properties is likely to produce significantly lower effective viscosities and/or more pronounced lateral or vertical strength variations.

It is well known that particular metamorphic conditions and associated *P-T-t* paths can be reproduced by a range of model assumptions, including the unrealistic tectonic conditions

implicit in one-dimensional models; consequently, unique solutions will not be obtained from thermal modelling alone. Instead, we have addressed in simplified form the more complete and more complex problem of coupled thermal-tectonic evolution. The novelty lies not in the predicted $P-T-t$ paths themselves, but in linking the model metamorphic histories to the overall evolution of the model orogen in space and time. The models yield internally self-consistent sets of predictions, including metamorphic and thermal history and large-scale crustal structure, which can be compared with a diverse range of observations from orogens. As subduction progresses into collision, the model metamorphic and tectonic conditions correspond closely to those observed in small orogenic belts like the Alps. Model predictions concerning which types of metamorphic rocks will be buried, exhumed, or stored as pockets of weak material, only to be exhumed later, are also consistent with general observations. Lastly, the models indicate that special conditions, such as a long tectonically quiescent phase during which thermal relaxation occurs, are not necessary for model temperatures to correspond to those observed. Instead, Barrovian thermal conditions may be achieved while continental subduction continues during collisional orogenesis (e.g. as in the Alps), if heat production within the orogenic crust and upper mantle above the subduction zone is sufficient to offset cooling by subduction at $Pe \gg 1$. Since redistribution of heat-producing material within the deforming orogen means that this condition is likely to be transient, the orogenic phase associated with Barrovian metamorphism in small orogens is likely to be relatively short-lived, on the order of 20 Ma. It appears that the most promising direction for future research is the disequilibrium competition between the cooling effect of subduction and radioactive heat production within the deforming orogen.

This work was funded by NSERC Research Grants to R. A. J and C. B., an NSERC Collaborative Grant to C. B., R. A. J., and others, and an NSERC Lithoprobe Grant to C. B. C. B. acknowledges funding through the Inco Fellowship of the Canadian Institute for Advanced Research. Special thanks are extended to P. Treloar and P. O'Brien for organizing the conference at which a preliminary version of this work was presented, and to the many colleagues who provided spirited discussion at that meeting. The research has benefited from many helpful comments by colleagues including S. Willett, J. Braun and S. Ellis, and the manuscript was improved by constructive reviews from T. Dempster and C. Ruppel. Lithoprobe Publication No. 878.

References

BARROW, G. 1893. On an intrusion of muscovite biotite gneiss in the S. E. Highlands of Scotland and its accompanying metamorphism. *Quarterly Journal of the Geological Society, London*, **49**, 330–358.

— 1912. On the geology of lower Deeside and the southern highland border. *Proceedings of the Geologists' Association*, **23**, 268–284.

BATT, G. E. & BRAUN, J. 1997. On the thermo-mechanical evolution of compressional orogens. *Geophysical Journal International*, **128**, 364–382.

BEAUMONT, C., FULLSACK, P. & HAMILTON, J. 1994. Styles of crustal deformation caused by subduction of the underlying lithosphere. *Tectonophysics*, **232**, 119–132.

CARRINGTON, D. P. & HARLEY, S. L. 1995. Partial melting and phase relations in high-grade metapelites: an experimental petrogenetic grid in the KFMASH system. *Contributions to Mineralogy and Petrology*, **120**, 270–291.

CERMAK, V. & BODRI, L. 1996. Time-dependent crustal temperature modeling: Central Alps. *Tectonophysics*, **257**, 7–24.

CHAMBERLAIN, C. P. & SONDER, L. J. 1990. Heat-producing elements and the thermal and baric patterns of metamorphic belts. *Science*, **250**, 763–769.

ENGI, M., TODD, C. S. & SCHMATZ, D. R. 1995. Tertiary metamorphic conditions in the eastern Lepontine Alps. *Schweizerische Mineralogische und Petrographische Mitteilungen*, **75**, 347–369.

ENGLAND, P. C. & THOMPSON, A. B. 1984. Pressure-temperature-time paths of regional metamorphism I. Heat transfer during the evolution of regions of thickened continental crust. *Journal of Petrology*, **25**, 894–928.

FULLSACK, P. 1995. An arbitrary Lagrangian-Eulerian formulation for creeping flows and its application in tectonic models. *Geophysical Journal International*, **120**, 1–23.

HODGES, K. V., HUBBARD, M. S. & SILVERBERG, D. S. 1988. Metamorphic constraints on the thermal evolution of the central Himalayan orogen. *Philosophical Transactions, Royal Society of London, Series A*, **326**, 257–280.

HUERTA, A. D., ROYDEN, L. H., & HODGES, K. V. 1996. The interdependence of deformational and thermal processes in mountain belts. *Science*, **273**, 637–639.

JAMIESON, R. A. 1990. Metamorphism of an Early Paleozoic continental margin, western Baie Verte Peninsula, Newfoundland. *Journal of Metamorphic Geology*, **8**, 269–288.

—, BEAUMONT, C., HAMILTON, J. & FULLSACK, P. 1996. Tectonic assembly of inverted metamorphic sequences. *Geology*, **24**, 839–842.

MCLENNAN, S. M. & TAYLOR, S. R. 1996. Heat flow and the chemical composition of continental crust. *Journal of Geology*, **104**, 369–377.

RING, U. 1992 The Alpine geodynamic evolution of Penninic nappes in the eastern Central Alps: geothermobarometric and kinematic data. *Journal of Metamorphic Geology*, **10**, 33–54.

RUPPEL, C. & HODGES, K. V. 1994. Pressure-temperature-time paths from two-dimensional thermal models: Prograde, retrograde, and inverted metamorphism. *Tectonics*, **13**, 17–44.

SANDIFORD, M. & POWELL, R. 1991. Some remarks on high-temperature-low-pressure metamorphism in convergent orogens. *Journal of Metamorphic Geology*, **9**, 333–340.

SCHMID, S. M., PFIFFNER, O. A., FROITZHEIM, N., SCHONBORN, G. & KISSLING, E. 1996. Geophysical–geological transect and tectonic evolution of the Swiss Italian Alps. *Tectonics*, **15**, 1036–1064.

SKJERLIE, K. P. & JOINSON, A. D. 1996. Vapour-absent melting from 10 to 20 kbar of crustal rocks that contain multiple hydrous phases: Implications for anatexis in the deep to very deep continental crust and active continental margins. *Journal of Petrology*, **37**, 661–691.

ST. ONGE, M. R. 1987. Zoned poikiloblastic garnets: P-T paths and synmetamorphic uplift through 30 km of structural depth, Wopmay orogen, Canada. *Journal of Petrology*, **28**, 1–27.

STÜWE, K., WHITE, L. & BROWN, R. 1994. The influence of eroding topography on steady-state isotherms. Applications to fission track analysis. *Earth and Planetary Science Letters*, **124**, 63–74.

THOMPSON, A. B. & CONNOLLY, J. A. D. 1995. Melting of the continental crust: Some thermal and petrological constraints on anatexis in continental collision zones and other tectonic settings. *Journal of Geophysical Research*, **100**, 15565–15579.

TILLEY, C. E. 1925. Metamorphic zones in the southern Highlands of Scotland. *Quarterly Journal of the Geological Society, London*, **81**, 100–112.

VANCE, D. & HOLLAND, T. 1993. A detailed isotopic and petrological study of a single garnet from the Gassetts Schist, Vermont. *Contributions to Mineralogy and Petrology*, **114**, 101–118.

WHITTINGTON, A. G. 1996. Exhumation overrated at Nanga Parbat, northern Pakistan. *Tectonophysics*, **206**, 215–226.

WILLETT, S. D., BEAUMONT, C. & FULLSACK, P. 1993. Mechanical model for the tectonics of doubly vergent compressional orogens. *Geology*, **21**, 371–374.

Characterization and interpretation of P - T paths with multiple thermal peaks

DONNA L. WHITNEY¹ & YILDIRIM DILEK²

¹Department of Geology & Geophysics, University of Minnesota, Minneapolis, Minnesota 55455, USA

²Department of Geology, Miami University, Oxford, Ohio 45056, USA

Abstract: Using pressure-temperature (P - T) paths to decipher sequences of tectonic events in the evolution of contractional orogens is difficult because in most metamorphic terrains only a limited part of the path can be inferred from petrologic evidence. Perturbations such as thermal pulses may not be recorded if they occurred over very short geological time scales. Deviations from standard P - T path shapes (e.g. pressure and temperature increase followed by decompression and cooling) are seldom recognized although they may reflect major crustal processes that affect the thermal structure of continents during active tectonism. In particular, recognition of complex P - T trajectories with multiple thermal peaks is essential for understanding tectonic, metamorphic and magmatic processes that occur during unroofing of metamorphic terrains. Using the example of the Nigde metamorphic core complex (Turkey) and other similar terrains, we propose that P - T paths with initial Barrovian trajectories followed by one or more low-pressure-high-temperature thermal spikes (increase in temperature at nearly constant pressure) may be characteristic of metamorphic core complexes. These temperature spikes are commonly associated with granitic magmatism that results when metasedimentary rocks are buried and heated during regional metamorphism. Additional thermal contributions such as enhanced mantle heat flow or mafic magmatism are not required to explain the thermal spikes.

Pressure-temperature (P - T) paths can be reconstructed for rocks metamorphosed in the mid- to lower crust from petrologic information recorded in mineral compositions and textures. They are a primary means for linking petrologic and tectonic processes, and therefore for deducing and evaluating the driving forces of metamorphism in contractional orogens. P - T path shape, however, is not unique to any particular tectonic setting, as it is influenced by a range of factors such as radiogenic heat production in the crust, mantle heat flux, and timing/rates of deformation and decompression. Nevertheless, certain P - T paths (e.g. those with a component of nearly isothermal decompression) are interpreted by many geologists to describe characteristic sequences of tectonic events that occur during mountain building: burial, heating and unroofing by erosion and/or extension.

Most P - T paths reconstructed for contractional orogens comprise an initial increase in pressure and temperature, representing the crustal thickening phase; an increase in temperature during initial decompression, representing thermal relaxation to the peak of metamorphism; followed by a decrease in pressure and temperature during unroofing. In most cases, the simple shape of the reconstructed path reflects the difficulty in deciphering the complete history of

a metamorphic terrain from limited data. It is therefore generally not possible to use P - T paths to extract detailed information about the mechanisms responsible for or accompanying decompression (e.g. erosion, extension, magmatism), although documenting the exhumation process(es) is of great interest for understanding the evolution of mountain belts.

Syn- to post-contractional extension has been increasingly recognized as a major geodynamic process affecting the evolution of orogens (e.g. Glazner and Bartley 1985; Sonder *et al.* 1987; Liu 1996). A typical result of extension is the exhumation of medium- to high-grade metamorphic rocks and associated plutons, but the driving forces of extension are debated. If detailed P - T -time (t) paths can be determined for these rocks, the paths should provide useful information about the transition from crustal thickening to decompression, and may also help constrain unroofing mechanisms as a function of crustal depth and temperature.

In this paper, we describe the P - T evolution of a metamorphic core complex in central Anatolia, Turkey, that records two thermal peaks in its high-grade central region, and we compare its history to similar terrains. We discuss paths with multiple thermal peaks (MTP) in the context of the driving forces of regional metamorphism and associated magmatism.

Metamorphic geology of Turkey

The eastern Mediterranean region in Turkey consists of fragments of oceanic and continental crust that are exposed in east–west trending tectonic belts (Pontide, Anatolide, Tauride; Fig. 1) formed during closure of Tethyan seaways and subsequent collisional events in the Late Mesozoic–Early Cenozoic. Extension in the Aegean region followed convergence and resulted in widespread core complex development in the Cycladic Islands, Greek mainland, and Turkey (e.g. Lee & Lister 1992; Dinter & Royden 1993; Bozkurt & Park 1994).

The Anatolide tectonic belt in Turkey comprises several large crystalline massifs, including the Kırşehir, Akdağ and Niğde massifs – which together constitute the Central Anatolian crystalline complex (CACC) – and the Menderes massif in western Turkey (Fig. 1). Protoliths of the metamorphic rocks were platform sediments from the northern margin of Gondwana.

Burial and exhumation of crystalline rocks in the Anatolide tectonic belt occurred during an orogenic event in the Mesozoic and early Cenozoic. This paper focuses on the Niğde massif in south-central Anatolia because it contains well exposed metasedimentary rocks with

assemblages suitable for thermobarometry, and because it contains evidence for metamorphism and magmatism during both crustal thickening and extensional phases of the Alpine orogeny.

The Niğde massif

The Niğde massif is an isolated structural dome located at the southern margin of the CACC (Fig. 1), and has recently been interpreted as a metamorphic core complex that developed between Eocene and Miocene time (Whitney & Dilek 1996, 1997). It contains amphibolite- to granulite-facies metapelitic and metacarbonate gneiss in its core, with metamorphic grade decreasing structurally upward into lower-grade metaclastic schist and homogeneous marble. A detachment fault zone characterized by deformed marble in the footwall separates the metamorphic rocks in the footwall from unmetamorphosed, brittlely deformed sedimentary rocks of the hanging wall.

The pressure–temperature history of the Niğde massif has been deduced from reaction textures involving aluminosilicate polymorphs and garnet, and thermobarometric results from metapelitic rocks. Details of the petrology and *P*–*T*

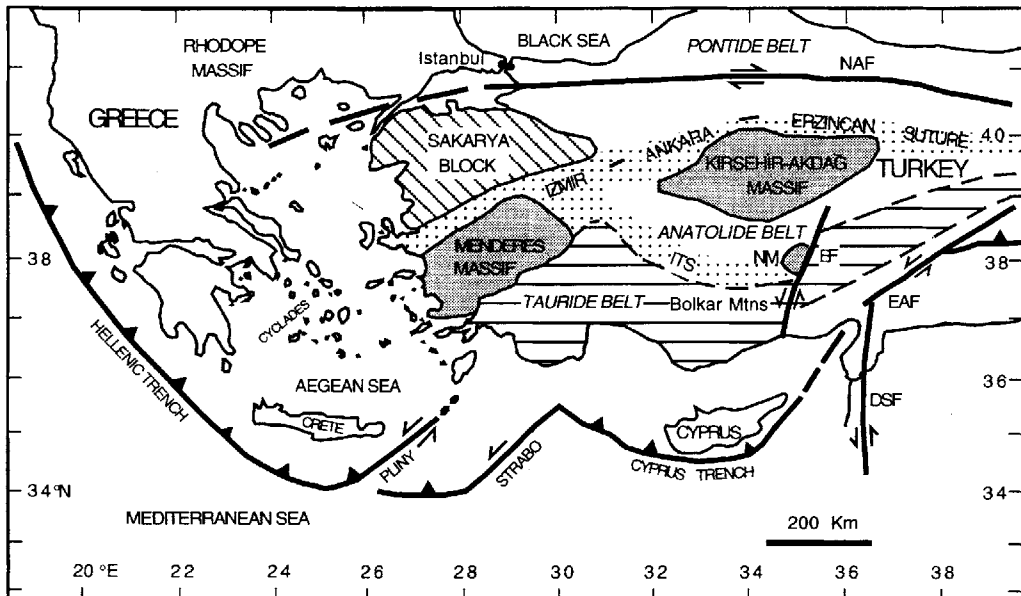


Fig. 1. Map of the Aegean region showing the location of crystalline massifs in the Anatolide tectonic belt, Turkey: the Menderes, and the Kırşehir, Akdağ and Niğde massifs (the latter three collectively constitute the Central Anatolian crystalline complex).

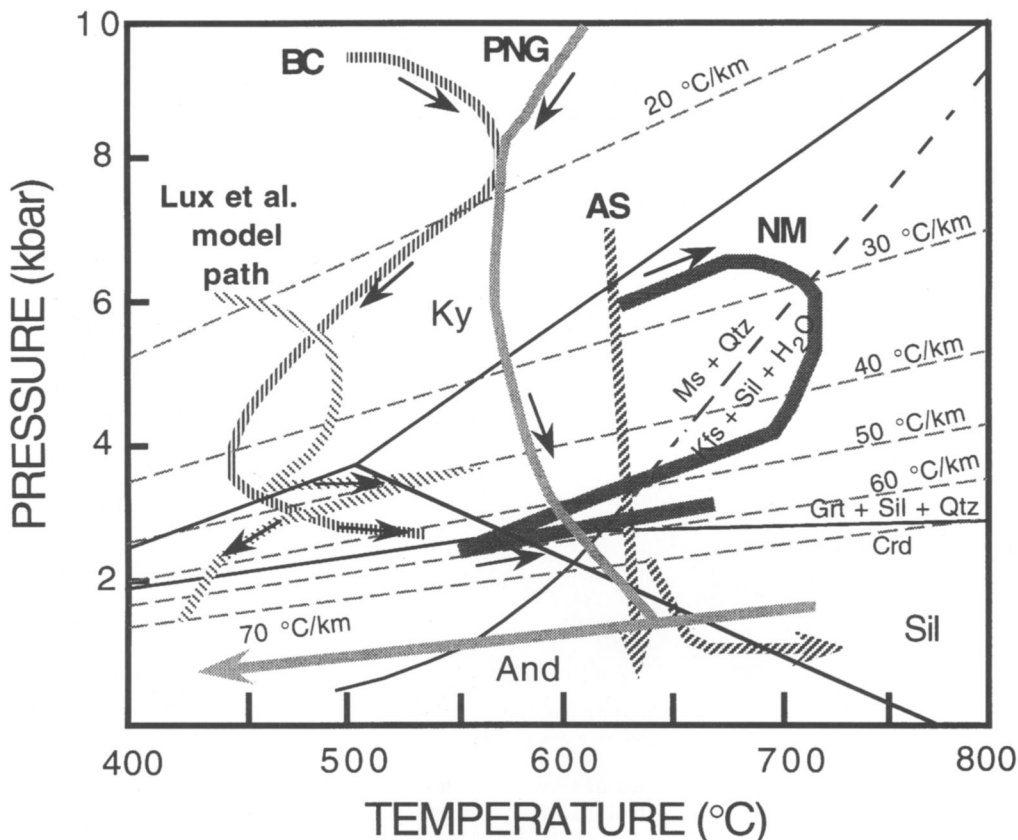


Fig. 2. Pressure–temperature diagram for the Niğde massif (Turkey) and other metamorphic terrains: AS = Alboran Sea (Platt *et al.* 1996); BC = Betic Cordillera (Bakker *et al.* 1989); NM = Niğde massif (Whitney & Dilek 1996); PNG = Papua New Guinea, D'Entrecasteaux Islands (Baldwin *et al.* 1995). The model path of Lux *et al.* (1986) describes the thermal effects of intrusion following thrusting for a hypothetical crustal section. Geotherms show the high gradients required for the prograde transformation of andalusite to sillimanite.

history of the Niğde massif are described by Whitney & Dilek (1997) (see also Göncüoğlu 1981, 1986), and are summarized here.

Sillimanite gneiss in the central part of the Niğde massif records an initial clockwise P - T path involving burial and heating to c. 730 °C at 5–6 kbar (Fig. 2), with formation of sillimanite + potassium feldspar and generation of peraluminous leucosomes (potassium feldspar + plagioclase + quartz + garnet + muscovite + tourmaline). This metamorphic peak was followed by decompression/cooling to much lower P - T conditions, as evidenced by growth of andalusite and cordierite in the contact aureole of a large Miocene granite (Göncüoğlu 1986). Intrusion of the granite caused a widespread increase in temperature in the core of the massif. This

second thermal peak occurred at low pressure and high temperature and resulted in the partial replacement of andalusite by sillimanite, i.e. the prograde transformation andalusite \rightarrow sillimanite (Fig. 3).

Although the main body of granite crops out in the central part of the massif, isolated exposures of petrologically identical two-mica (\pm garnet \pm tourmaline) granite occur elsewhere in the high-grade metasedimentary gneiss. These isolated exposures may be connected in the subsurface to the main body of the Üçkapılı granite, and the pluton may therefore have been emplaced as a large sill-like body. This interpretation could account for widespread, late thermal effects in the massif that appear to extend beyond the narrow contact aureole observed in the field around the Üçkapılı

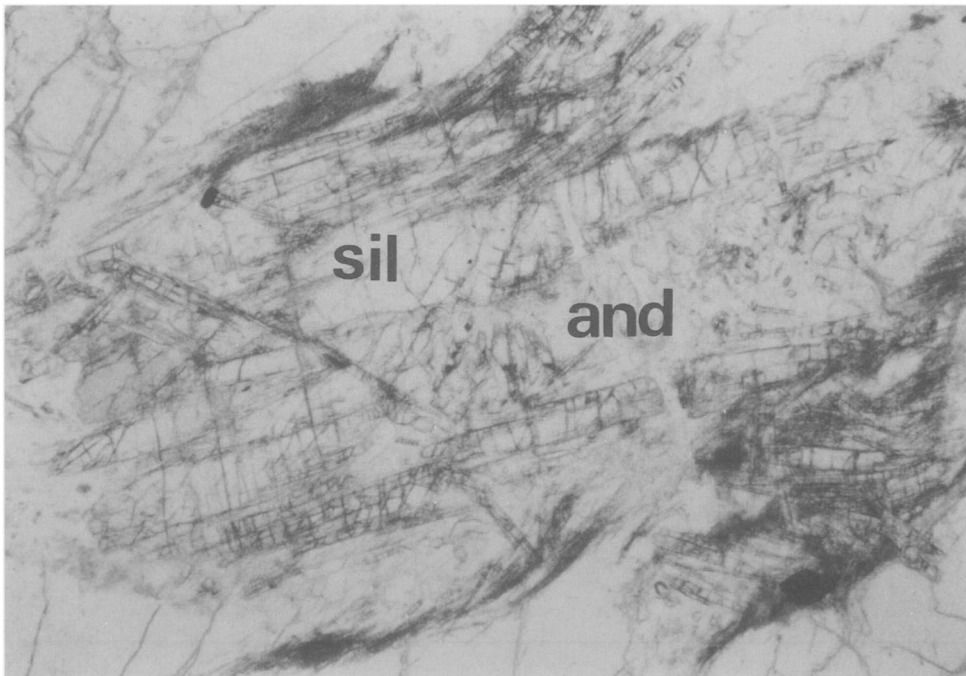


Fig. 3. Photomicrograph of andalusite (And) partially replaced by coarse-grained sillimanite (Sil) in the vicinity of a Miocene pluton, Niğde massif. Field of view = 1.75 mm.

granite. In addition, extensive exposures of gabbro (age unknown) that apparently intruded shallow levels of the crust are present in the northern part of the massif. Intrusion of mafic magma may also have contributed to the late temperature increase documented in the metamorphic rocks (see below for further discussion).

Estimates of the rate of exhumation of the Niğde massif are broadly constrained by the Miocene crystallization age of the Üçkapılı granite (Whitney & Dilek 1996), 12 Ma apatite fission track ages from the granite (Dilek *et al.* 1997), inferences from strata in adjacent sedimentary basins (i.e. sedimentary rocks in the hanging wall of the core complex), and comparison with age relations in the Menderes massif. Although there are significant uncertainties in estimates of the timing of the first thermal peak, calculated exhumation rates range from 1.9 to 5.7 mm a^{-1} .

Examples from other metamorphic terrains

P-T paths with multiple thermal peaks are recognized in other terrains that experienced synmetamorphic extension. In continental rocks underlying the Alboran Sea, isothermal decompression from relatively high pressure to the

andalusite stability field was followed by a late thermal spike at low pressure, as evidenced by the replacement of andalusite by sillimanite (Platt *et al.* 1996) (Fig. 2). Both the age of metamorphism (isothermal decompression) and the timing of extension in the region are inferred to be early Miocene (Platt & Vissers 1989; Platt *et al.* 1996), and the proposed *P-T* path is similar to those inferred for neighbouring regions of the Betic Cordillera (e.g. Bakker *et al.* 1989) (Fig. 2). The thermal spike has been attributed to the removal of lithospheric mantle and extensional thinning of the crust, processes which have been proposed for the region based on geophysical and other evidence (Vissers *et al.* 1995; Seber *et al.* 1996; but see also Lonergan and White 1997). Because the samples analysed from the Alboran Sea are drill-core rather than terrestrial exposures, it is difficult to rule out other possible explanations for the thermal spike (e.g. magmatism).

Although detailed *P-T* paths have yet to be described for the Menderes massif, a core complex in western Turkey, it has been suggested that other regions of the Aegean extensional province (e.g. metamorphic core complexes in the Cycladic Islands) may have experienced late thermal spikes following Barrovian metamorphism (Lister & Baldwin 1993). This proposal is

based on interpretation of $^{40}\text{Ar}/^{39}\text{Ar}$ data and inferred temperatures of deformation, rather than on observations of metamorphic mineral assemblages, but is consistent with the timing of intrusion of Miocene plutons relative to structural development of the core complexes as well as the spatial relation between plutons and shear zones (Lister & Baldwin 1993).

Metamorphic rocks exposed in active core complexes in the western Pacific (D'Entrecasteaux Islands, Papua New Guinea) record early high-pressure conditions (eclogite facies), followed by decompression and cooling through amphibolite facies (Baldwin *et al.* 1995; Hill *et al.* 1995) (Fig. 2). Late low- to moderate-pressure-high-temperature metamorphism (i.e. a second thermal peak; Fig. 2) is inferred from argon thermochronology and is attributed to the intrusion of a large sheet-like granodiorite during the final stages of exhumation. Although it is associated with contact metamorphism and retrogression of the host gneiss, the thermal spike was probably transient, as argon systematics of affected minerals were not reset (Baldwin *et al.* 1995). Rapid exhumation rates (10 mm a^{-1}) are required to account for the inferred P - T - t path (Baldwin *et al.* 1995).

Comparison with low-pressure-high-temperature (LP-HT) metamorphic terrains that are not exposed in core complexes is useful for understanding possible heat sources for thermal spikes. In a study of an Appalachian metamorphic terrain in central Maine, USA, De Yoreo *et al.* (1989) and Lux *et al.* (1986) proposed that intrusion of large granitic sills, the products of crustal thickening, drove regional-scale LP-HT metamorphism that is characterized by the prograde transformation of andalusite to sillimanite, with geothermal gradients of $80\text{--}100^\circ\text{C km}^{-1}$. The authors note that the plutons in the region do not have distinct contact aureoles, but that LP-HT metamorphic effects extend tens of kilometres from the nearest granite exposures. Similar late, high-temperature thermal spikes at low pressure, although transient, could be superimposed on an overall P - T path characteristic of crustal thickening (Fig. 2).

Discussion

The prograde transformation of andalusite to sillimanite requires a high geothermal gradient ($>40^\circ\text{C km}^{-1}$; Fig. 2), and can occur in regions with high values of radioactive heat production, thermal conductivity, mantle heat flux, or where extensive magmatism has affected the thermal structure of the crust. Where the andalusite to

sillimanite transformation has been preceded by Barrovian metamorphism, heat sources such as mantle heat flux and/or magmatism are implicated, as these parameters can change during the tectonic evolution of a mountain belt. In the following sections, we consider possible mechanisms for driving metamorphism and magmatism, with a focus on the relation between regional metamorphism and the generation of crustal melts during core complex development.

Role of magmatism

Numerous studies have documented a temporal and spatial relation between magmatism and metamorphic core complex development and have therefore inferred a genetic link between the two (e.g. Coney 1980; Gans *et al.* 1989; Armstrong & Ward 1991; Hill *et al.* 1995; Lister & Baldwin 1993). It is generally not known, however, whether emplacement of crustally derived magma can account for the thermal and structural features observed or whether an external source of heat is required (e.g. emplacement of mafic magma or enhanced mantle heat flow).

In the case of the Niğde massif, the first thermal peak was related to regional metamorphism accompanying Alpine contraction. Crustal thickening resulted in high-grade metamorphism and partial melting of metasedimentary rocks to produce migmatites in the middle crust. As described above, peraluminous magma (the Üçkapılı granite), which formed at greater depths, intruded the metamorphic rocks once they had been exhumed to relatively shallow crustal levels. Similar granitoids are common in other core complexes (e.g. in the Basin and Range province; Crittenden *et al.* 1980).

The late thermal spike recorded in the metasedimentary rocks is clearly related to the emplacement of the Üçkapılı granite. As the granite is peraluminous, it most likely formed by partial melting of metasedimentary protoliths. The burial and partial melting of the source region of the Üçkapılı magma may have been a deeper expression of the same tectonometamorphic event responsible for the regional (Barrovian) metamorphic event recorded in the metasedimentary rocks. Alternatively, the Üçkapılı granite may have been generated by additional thermal events such as influx of magma from the mantle or enhanced heat flow owing to lithospheric thinning. To explore these possibilities, we constructed a series of diagrams (Fig. 4) that illustrate possible P - T - t relations between the Niğde gneiss and a hypothetical, unexposed source rock for the peraluminous

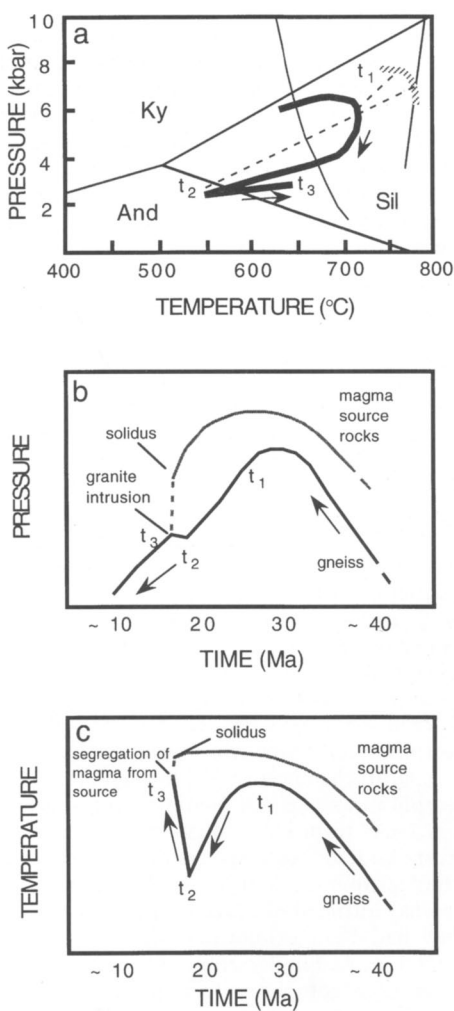


Fig. 4. Possible sequence of events to account for late low-pressure-high-temperature metamorphism as a result of intrusion of crustally derived granitic magma using the example of the Niğde massif. (a) Thick solid black line with arrows = P - T path for Niğde high-grade gneiss (see Fig. 2); thick striped line = possible path of magma source rocks, starting at greater depths than those recorded by exposed gneiss, with a decompression path that intersects the vapour-absent metapelite solidus (thin solid grey line). The water-saturated metapelite solidus (Le Breton & Thompson 1988) is also shown (curved solid grey line). Dashed lines are isochrons: t_1 = first thermal peak recorded in gneiss; t_2 = generation of magma at depth and arrival of magma in the upper crust; t_3 = second thermal peak ($\sim t_2$). (b) Change in depth with time of the gneiss and possible magma source rocks. Dashed line = magma path; t_1 , t_2 , t_3 as in (a). Ages are approximate. (c) Change in temperature with time showing the relation between the thermal history of the magma source rocks and the gneiss.

magma that intruded the gneiss. At the time of the first thermal peak (t_1) recorded in the gneiss, the magma source rock is at an arbitrary but greater depth than the gneiss (Figs 4a, b). The deeper rocks will reach their peak temperature slightly later and at a higher temperature than the shallower rocks (Figs 4a, c). According to this model, the gneiss follows the P - T path described above and the source rock follows a similar-shaped path until it reaches a solidus during decompression. If this model is correct, and the Üçkapılı magma largely formed by decompression melting rather than earlier during prograde (water-saturated or undersaturated) partial melting, then the timing of the emplacement of magma (t_2 , at an unknown time after generation and segregation of the magma) will occur after some amount of decompression of the country rock. As t_2 essentially coincides with the second thermal peak (t_3 ; transformation of andalusite to sillimanite), there is little discernible difference between t_2 and t_3 (Figs 4b, c). This scenario can account for the thermal spike being caused by crustally derived magma with no external source of heat if the hypothetical P - T path for the magma source rocks is valid and the magma formed during decompression.

As noted above, gabbro also intruded the Niğde massif. The age of the gabbro is unknown, so it is not possible to discuss its role, if any, in the thermal history of the metamorphic rocks. As the thermal contribution of mafic magma cannot be discounted in this particular case, the discussion above serves only to show that it is possible for crustally derived magma to generate thermal spikes without the help of external heat sources. Nevertheless, as the Niğde massif had already been largely exhumed at the time of intrusion of both felsic and mafic magmas, magmatism was probably the driving force for LP-HT metamorphism, but was not a cause of core complex formation. In addition, although the role of mantle-related processes (e.g. delamination, emplacement of basalt in the lower crust) also cannot be discounted, the geographically limited extent of core complex development in central Anatolia (Whitney and Dilek 1996, 1997) suggests that more local mechanisms, such as magmatism, were responsible for the late thermal spike.

Role of deformation

Tectonic mechanisms such as high-angle faulting can juxtapose hot rocks brought rapidly from depth with cooler rocks at higher crustal levels, driving an increase in temperature in the

originally cooler rocks. For example, two-dimensional heat-flow models for displacement rates of $1\text{--}5\text{ mm a}^{-1}$ on a high-angle fault (60°) predict a shift of isotherms at 6–10 km depth: $\sim 1\text{ km}$ upward on the footwall and a similar amount downward on the hanging wall (e.g. Ehlers & Chapman 1996).

Delivery of heat to shallow levels by fault-related uplift of solid rock will be less efficient than advection by magma because, in most cases, magma is hotter and because magma incorporates the latent heat of fusion. Thus, the temperatures reached will be lower and the duration of heating will be shorter for fault-related 'contact' heating than for conventional contact metamorphism. Although this general mechanism cannot be discounted, it is not the best explanation for many terrains that exhibit thermal spikes, as there is commonly a close spatial relation between plutonism and low-pressure–high-temperature metamorphism.

Exhumation rate and path preservation

Differences in peak pressure, temperature and dP/dT slopes among the paths shown for various metamorphic terrains in Fig. 2 reflect variation in the amount of burial, magmatic (or other) heating, and rates of tectonic processes affecting each terrain. Post-peak dP/dT slopes are to some extent controlled by the rate of decompression, which is accomplished by a combination of erosion and extensional unroofing. In the examples discussed above, exhumation rates as deduced from a variety of techniques were relatively rapid ($1\text{--}10\text{ mm a}^{-1}$), and therefore may have had a significant component of extension, consistent with the occurrence of MTP paths in core complexes. Rapid unroofing is also consistent with inferences made based on the preservation of metamorphic mineral assemblages recording multiple thermal peaks in these terrains, and, whatever the mechanism, is probably required to preserve evidence for transient thermal spikes.

Summary

Paths with multiple thermal peaks characterize terrains such as metamorphic core complexes that experienced crustal thickening followed by relatively rapid exhumation and in which synextensional magmatism resulted in late low-pressure–high-temperature metamorphism. Metamorphic reactions are initially driven by tectonic burial and associated heating and later

reactions by magmatic heating. Inferred $P-T-t$ paths suggest that late magmatism could have been generated by crustal melting associated with regional metamorphism and that external sources of heat are not required to account for the multiple thermal peaks.

This work was supported by National Science Foundation grant EAR-9317100 to Whitney and grant EAR-9219064 to Dilek. We thank E. Yazgan, Head of the Geological Research Department at the General Directorate of Mineral Research & Exploration of Turkey (MTA); the Adana Regional Office of MTA; and C. Demirkol of Çukurova University (Adana) for logistical support of the field work in the Niğde massif. Thorough and constructive reviews by P. J. O'Brien, J. Rötzler and J. Schumacher helped to improve the manuscript.

References

ARMSTRONG, R. L. & WARD, P. 1991. Evolving geographic patterns of Cenozoic magmatism in the North American Cordillera – the temporal and spatial association of magmatism and metamorphic core complexes. *Journal of Geophysical Research*, **96**, 13 201–13 224.

BAKKER, H., DE JONG, K., HELMERS, H. & BIERMANN, C. 1989. The geodynamic evolution of the internal zone of the Betic Cordilleras (Southeast Spain) – a model based on structural analysis and geothermobarometry. *Journal of Metamorphic Geology*, **7**, 359–381.

BALDWIN, S. L., LISTER, G. S., HILL, E. J., FOSTER, D. A. & McDougall, I. 1995. Thermochronologic constraints on the tectonic evolution of active metamorphic core complexes, D'Entrecasteaux Islands, Papua New Guinea. *Tectonics*, **12**, 611–628.

BOZKURT, E. & PARK, R. G. 1994. Southern Menderes Massif: an incipient metamorphic core complex in western Anatolia. *Journal of the Geological Society of London*, **151**, 213–216.

CONEY, P. J. 1980. Cordilleran metamorphic core complexes: An overview. In: CRITTENDEN, M. D. et al. (eds) *Cordilleran Metamorphic Core Complexes*. Geological Society of America Memoir, **153**.

CRITTENDEN, M. D. et al. (eds) *Cordilleran Metamorphic Core Complexes*. Geological Society of America Memoir, **153**.

DE YOREO, J. J., LUX, D. R. & GUIDOTTI, C. V. 1989. The role of crustal anatexis and magma migration in the thermal evolution of regions of thickened continental crust. In: DALY, J. S., CLIFF, R. A. & YARDLEY, B. W. D. (eds) *Evolution of Metamorphic Belts*. Geological Society, Special Publication, **43**, 187–202.

DILEK, Y., GARVER, J. I. & WHITNEY, D. L. 1997. Extension, uplift, and exhumation in a collision orogen and the geomorphic response, Central Anatolia (Turkey). *Geological Society of America Abstracts*, **29**.

DINTER, D. A. & ROYDEN, L. 1993. Late Cenozoic extension in northeastern Greece: Strymon Valley detachment system and Rhodope metamorphic core complex. *Geology*, **21**, 45–48.

EHLERS, T. A. & CHAPMAN, D. S. 1996. Thermal regime of the Wasatch normal fault, Utah: Model and observations. *EOS*, **77**, 665.

GANS, P. B., MAHOOD, G. A. & SCHERMER, E. R. 1989. *Syn-extensional magmatism in the Basin and Range province: a case study from the eastern Great Basin*. Geological Society of America, Special Paper, **233**.

GLAZNER, A. F. & BARTLEY, J. M. 1985. Evolution of lithospheric strength after thrusting: *Geology*, **13**, 42–45.

GÖNCÜOĞLU, M. C. 1981. Niğde Masifinde viridin-granatsin kökeni. *Türkiye Jeoloji Kurumu Bülteni*, **24**, 45–51.

— 1986. Geochronologic data from the southern part (Niğde area) of the Central Anatolian Massif. *Maden Tektik ve Arama Dergisi*, **105/106**, 83–96.

HILL, E. J., BALDWIN, S. L. & LISTER, G. S. 1995. Magmatism as an essential driving force for formation of active metamorphic core complexes in eastern Papua New Guinea. *Journal of Geophysical Research*, **100**, 10441–10451.

LE BRETON, N. & THOMPSON, A. B. 1988. Fluid-absent (dehydration) melting of biotite in pelitic rocks in the early stages of crustal anatexis. *Contributions to Mineralogy and Petrology*, **99**, 226–237.

LEE, J. & LISTER, G. S. 1992. Late Miocene ductile extension and detachment faulting, Mykonos, Greece. *Geology*, **20**, 121–124.

LISTER, G. S. & BALDWIN, S. L. 1993. Plutonism and the origin of metamorphic core complexes. *Geology*, **21**, 607–610.

LIU, M. 1996. Dynamic interactions between crustal shortening, extension, and magmatism in the North American Cordillera. *Pure and Applied Geophysics*, **146**, 447–467.

LONERGAN, L. & WHITE, N. 1997. Origin of the Betic-Rif mountain belt. *Tectonics*, **16**, 504–522.

LUX, D. R., DE YOREO, J. J., GUIDOTTI, C. V. & DECKER, E. R. 1986. Role of plutonism in low-pressure metamorphic belt formation. *Nature*, **323**, 794–797.

PLATT, J. P. & VISSERS, R. L. M. 1989. Extensional collapse of thickened continental lithosphere: A working hypothesis for the Alboran Sea and the Gibraltar arc. *Geology*, **17**, 540–543.

—, SOTO, J. I., COMAS, M. S. & LEG 161 SHIPBOARD SCIENTISTS 1996. Decompression and high-temperature-low-pressure metamorphism in the exhumed floor of an extensional basin, Alboran Sea, western Mediterranean. *Geology*, **24**, 447–450.

SEBER, D., BARAZANGI, M., IBENBRAHIM, A. & DEMNATI, A. 1996. Geophysical evidence for lithospheric delamination beneath the Alboran Sea and Rif-Betic Mountains. *Nature*, **379**, 785–790.

SONDER, L. J., ENGLAND, P. C., WERNICKE, B. & CHRISTIANSEN, R. L. 1987. A physical model for Cenozoic extension of western North America. In: COWARD, M. P., DEWEY, J. F. & HANCOCK, P. L. (eds) *Continental Extensional Tectonics*. Geological Society, London, Special Publication, **28**, 187–201.

VISSERS, R. L. M., PLATT, J. P. & VAN DER WAL, D. 1995. Late orogenic extension of the Betic Cordillera and the Alboran domain – a lithospheric view. *Tectonics*, **14**, 786–803.

WHITNEY, D. L. & DILEK, Y. 1996. Alpine crustal thickening and high-T exhumation in a metamorphic core complex, Central Anatolia. *Geological Society of America Abstracts*, **28**(7), 423.

— & — 1997. Core complex development in central Anatolia. *Geology*, **25**, 1023–1026.

Low- to medium-pressure Variscan metamorphism in Galicia (NW Spain): evolution of a kyanite-bearing synform and associated bounding antiformal domains

J. RECHE, F. J. MARTÍNEZ & M. L. ARBOLEYA

Dept de Geologia, Universitat Autònoma de Barcelona, 08193 Bellaterra, Spain

Abstract: Evidence for different substitution relationships between aluminosilicates in two domains east of the Ollo de Sapo gneiss antiform in Galicia (NW Spain) suggests a high dependence of metamorphic evolution on the local tectonic and granitoid intrusion history. The Vivero pelite belt constitutes a pinched synformal domain located between the Ollo de Sapo antiform to the west and the Lugo dome to the east. Within this synform, black, Al-rich Silurian pelites contain kyanite that, along with muscovite, formed pseudomorphically after early pre-D₂ andalusite. Syn-D₂ inversion of andalusite to kyanite indicates an evolution from early, low-*P* to medium-*P* regimes. Locally, near the Vivero transtensional fault, which constitutes the E boundary of the synform new, late post-D₂ pleochroic andalusite grew from staurolite and biotite indicating reinstallation of a new low-*P* regime during and after the D₃ deformation phase, which is related to movement along the fault zone. The Ollo de Sapo domain contains only a high *T*-low *P* series of metamorphic assemblages. The peak assemblage within this domain was cordierite-biotite-K-feldspar-andalusite/fibrolite related to emplacement of a pre- to syn-D₂ swarm of sheet-like peraluminous granitoids located mainly in the core of the antiform. Early pre- to syn-D₂ staurolite-biotite ± garnet, and late sillimanite-staurolite-biotite assemblages present on the west side of the Lugo dome testify to an early stage of nearly isothermal decompression followed by decompression with local heating. Stabilization of late andalusite in the Vivero pelite belt and of sillimanite west of the Lugo dome appear almost synchronous and clearly related to a syn-D₃ thermal peak induced by Upper Carboniferous granitoid intrusion along the Vivero transtensional fault separating both domains.

Low-pressure metamorphism with the prograde aluminium silicate sequence andalusite → sillimanite has been considered characteristic of the latest episode of thermal evolution of the Variscan Chain in the Pyrenees and the Iberian Peninsula (Zwart 1986; Julivert & Martínez 1987). Higher *P* events have been restricted to the very early stages of the Variscan orogeny. High *P*-high-*T* granulites and eclogites of Lower Devonian age (Santos Zalduegui *et al.* 1996) occur as allochthonous terranes (e.g. Cabo Ortegal) incorporated tectonically during the Variscan orogeny. The low-pressure metamorphism implies late high thermal gradients which appear related to granitoid intrusion (Capdevila 1968a, b; Oen 1970; Martínez & Rölet 1988; Reavy 1989; Hutton & Reavy 1992) that takes place after a first stage of isoclinal folding (D₁) with development of a pervasive slaty cleavage (S₁). Intrusions seem to be related to subsequent episodes of sub-vertical refolding and local normal faulting that occur during the latest deformation stages of the chain. However, a more careful study reveals this scheme to be too simplistic as diverse data (Ayora *et al.* 1993) seem to point towards the

existence of a medium-*P* event immediately predating the final high-*T*-low-*P* evolution.

In NW Spain (Fig. 1), medium-pressure, kyanite-bearing assemblages occur in Ordovician and Silurian pelite belts (Capdevila 1968a) which constitute pinched synforms situated between rimming low-*P*, high-*T*, antiforms cored by older materials of Precambrian and Cambrian age that sometimes constitute gneiss domes (Martínez *et al.* 1988). The western and eastern boundaries of these belts are constituted by ductile shear zones outlined by abundant granite intrusion; these zones are the Valdoviño sinistral strike-slip fault (Ponce de Leon & Choukroune 1980) and the Vivero normal dextral fault (Matte 1968; Ponce de Leon & Choukroune 1980; Martínez-Catalán 1985; Pérez-Estaún *et al.* 1991; Briggs 1995; Martínez *et al.* 1996). The most pronounced of these belts is the Vivero pelite belt (Fig. 1), occupying a syncline situated between two antiformal D₂ structures refolding D₁ folds: the Ollo de Sapo gneiss dome (Parga Ponal *et al.* 1964; González-Lodeiro 1983; Diez-Balda *et al.* 1990) and the Lugo dome (Matte 1968; Martínez-Catalán 1985; Bastida *et al.* 1986). The Vivero

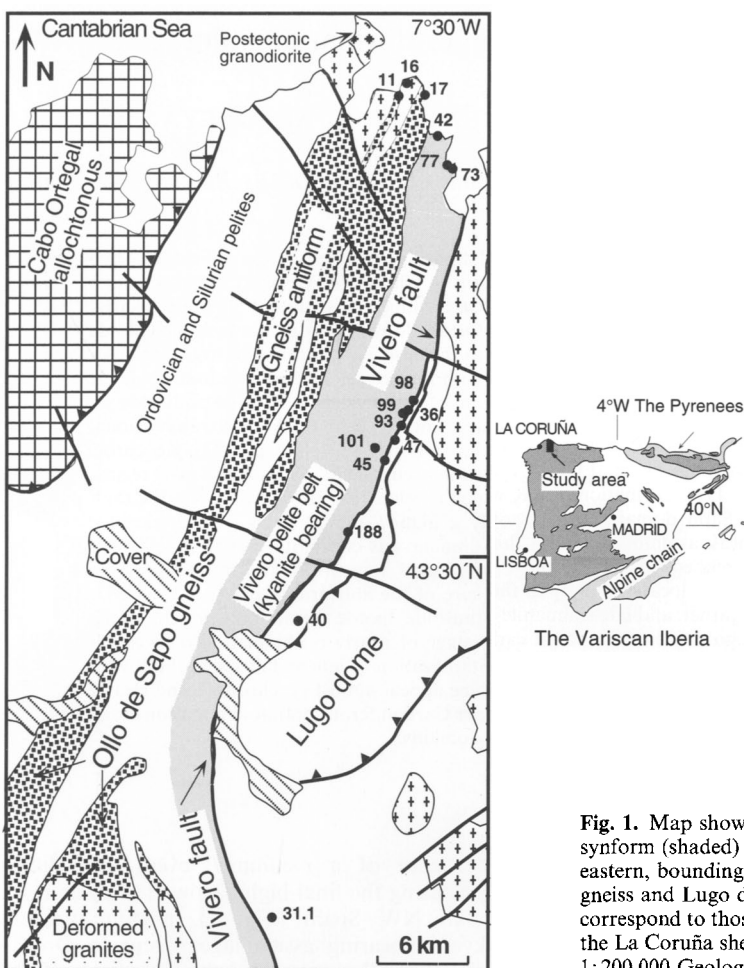


Fig. 1. Map showing the kyanite-bearing synform (shaded) and the two, western and eastern, bounding antiforms (Oollo de Sapo gneiss and Lugo dome). Sample numbers correspond to those in Table 1. Main units as in the La Coruña sheet (Bastida *et al.* 1984) of the 1:200,000 Geological Map of Spain.

fault is situated on the eastern flank of the above-mentioned syncline, and constitutes the eastern boundary of the kyanite-bearing Vivero pelite belt bringing it into contact with the Lugo dome, with respect to which the belt constitutes the hanging wall (Martínez *et al.* 1996).

Whereas the normal sequence of aluminium silicate polymorphs in the periphery of antiformal areas constituting thermal domes in NW Iberia (Den Tex 1966; Capdevila 1968b; Martínez *et al.* 1988; Pérez-Estaún *et al.* 1991), and in the Pyrenees (Guitard 1970; Autran *et al.* 1970; Vielzeuf 1984; Zwart 1986; Soula *et al.* 1986; Wickham & Oxburgh 1987; Gibson & Bickle 1994; Liesa 1994) is sillimanite following andalusite, kyanite occurs in the Vivero pelite belt replacing a subidioblastic, post-D₁ pre-D₂ andalusite. A later generation of post-D₂ andalusites normally includes staurolite plus biotite and

occasionally kyanite and chloritoid as well. These facts indicate that the kyanite-bearing medium-*P* event is located between two andalusite-bearing events of higher-*T* and lower-*P*. This detail in the progressive changes of thermal regime has not been described so far, and is shown in this paper to be controlled by deformation and by two granitoid emplacement events, one post-D₁ and pre- to syn-D₂ and another syn-D₂ lasting to post-D₃.

The aim of the present paper is to study the evolution of the metamorphism in the pelite belt and in the two bounding antiforms, west and east, in order to see the variation of the *P-T* conditions under which deformation has taken place. The occurrence of granitoid intrusions in the studied area causes local changes in the thermal gradient that substantially affect the metamorphic evolution. Since deformation takes

Table 1. Summary of localities, mineral assemblages, univariant reactions and relations with tectonic stages

Locality	Sample	Assemblage	Variance KFMASH or Mn-KFMASH (**)	Univariant reaction	Tectonic stage
Olla de Sapo					
Punta Anchousa	16	(Kfs)-Bt-Ms-Ptg	4		Syn-D ₂
Punta Anchousa	17	(Kfs)-Bt-Chl-Ms-Ptg	3		Syn-D ₂
Punta Anchousa		(And)-Crd-Sil-Bt-Kfs-Ptg	2	And = Sil Ms + Qtz = Als + Kfs + H ₂ O	Syn to post ?-D ₂
Pelite belt					
<i>Al-rich samples</i>					
Playa de San Roman	42	(And)-Ky-Chl-Chl	2		Pre to syn-D ₂
Playa de Abrela	73	(And)-Ky-Chl-Chl	2		Pre to syn-D ₂
Sixto	101	Ky-St-Chl	2		Pre-D ₃
Xuan Blanco	45	(Cld)-And-St-Bt	2		Syn to post-D ₃
Outol	98	(Ky,St,Cld)-And-Bt	3		Post-D ₃
<i>Al-poor, Mn-rich samples</i>					
Playa de Abrela	77	Cld-Chl	4**		Pre to syn-D ₂
Mosendo	93	Grt-St-Chl	3**		Pre-D ₃
Viso	47	Grt-St-And-Bt	2**		Syn-D ₃
Ourol	99	Grt-Bt	4**		Syn-D ₃
Ourol	36	(Grt)-And-Crd-Bt	2**		Post-D ₃
Lugo dome					
Villalba	31.1	(St)-Grt-Bt	2		Pre to syn ?-D ₂
Villalba	40	(Grt-Chl)-Sil-St-Bt	2		Syn ?- to post-D ₂
Murás	188	Sil-Bt	3		Syn ?- to post-D ₂

* Ionic reaction involving K⁺, H⁺ and Ms.

** Mn-KFMASH variance and univariant equilibria.

Phases enclosed within parentheses appear resorbed or as inclusions and are considered relicts.
All samples contain Ms and Qtz except 11 which contains Kfs and Qtz.

place contemporaneously with metamorphism, the mineral assemblage evolution is controlled by the structural history.

Since the pelite belt occurs in a synform rimmed by two antiforms, three areas have been chosen for study. One embraces the pelite belt itself, showing the variation in metamorphic assemblages across it from west to east. The other two areas are, respectively, the core of the Ollo de Sapo gneiss antiform situated to the west, and the western part of the Lugo dome antiform, situated to the east, whose contact with the pelite belt is constituted by the Vivero fault.

Pelitic and psammopelitic lithologies from these three areas have been selected for studying the evolution of their mineral assemblages in order to deduce, and compare, trajectories followed by rocks in the pelite belt and in the two rimming antiforms. Mineral assemblages found in a set of representative samples from the studied lithologies are listed in Table 1.

The lithology chosen from the Ollo de Sapo antiform (Fig. 1) corresponds to an augen gneiss with cordierite–K-feldspar–oligoclase–biotite–andalusite–fibrolite located near a pre- to syn- D_2 gneissic granite. The cordierite in this assemblage is pinnitized and includes remnants of resorbed andalusite (Fig. 2b); fibrolite occurs locally in contact with biotite (Fig. 2c) and seems later with respect to andalusite. Blastic secondary muscovite also occurs and part of the biotite is transformed into secondary chlorite. The main fabric in the augen gneiss is a composite foliation S_{1+2} , although D_2 folds containing an axial-planar S_2 crenulation can be locally observed; these D_2 folds are minor order folds of the larger D_2 structure that constitutes the Ollo de Sapo antiform (González-Lodeiro 1983; Dicz-Balda *et al.* 1990). Elongated cordierite aggregates that include resorbed andalusite and biotite seem to develop parallel to the conspicuous composite fabric (S_{1+2}) present in the rock defined by biotite, granoblastic elongated quartz and feldspars. Occasionally the cordierite aggregates are wrapped around feldspar augen. The bulk composition of this chosen lithology (sample 11, Fig. 8) plots below the garnet–chlorite AFM tie-line, and so do the other two samples (16 and 17) represented for comparison in the upper left inset of Fig. 8.

The lithologies chosen in the pelite belt correspond to Al-rich graphitic Caradocian and Silurian metapelites that plot well above the garnet–chlorite tie-line in an AFM projection (sample 42 of Fig. 9) and to less aluminous and Mn-richer samples that still plot above this tie-line but very close to it (sample 93 of Fig. 9). Metamorphic grade seems to stay constant

across the pelite belt from west to east, increasing rapidly and reaching the maximum grade some tens of metres from the Vivero fault, especially in places where syn- to post-tectonic fault-related granite intrusions occur, either in the pelite belt or in the Lugo dome. The most widespread assemblage in the pelite belt is chloritoid–chlorite–muscovite \pm kyanite in the selected Al-rich graphitic lithology. In this assemblage kyanite and muscovite are pseudomorphic after chiastolitic andalusite, whose shape and symmetric arrangement of inclusions can still be identified (Fig. 3c). As grade increases in the vicinity of the Vivero fault, the assemblages staurolite–chlorite–kyanite (Figs 4b and d), staurolite–andalusite–biotite (Figs 5a and b) and biotite–andalusite (Figs 6a, b and c) are progressively developed in the Al-rich metapelites, whereas Al-poorer Mn-richer rocks contain garnet–staurolite–chlorite, garnet–staurolite–andalusite–biotite and, finally, garnet–andalusite–cordierite–biotite (Fig. 6d).

A sub-vertical strong S_2 crenulation refolding the earlier S_1 fabric is developed in the pelite belt associated with metric D_2 fold hinges. The chiastolite pseudomorphosed by kyanite–muscovite aggregates overprints the S_1 slaty cleavage and appears either deformed by the S_2 sub-vertical crenulation, whenever this latter fabric is observed (Figs 3a, b) in fold hinges, or rotated in the composite S_{1+2} fabric in the D_2 fold limbs (Fig. 3c). Muscovite from the kyanite–muscovite aggregates that replace the pre-existing chiastolite appears stretched and incorporated into the external S_{1+2} fabric testifying for a pre- to syn- D_2 replacement. Kyanite and chloritoid are pre- to syntectonic with respect to S_2 (Fig. 3b).

Finally, a sub-aluminous pelite lithology was chosen from the western part of the Lugo Dome antiform (Fig. 1). This lithology contains the assemblages fibrolite–staurolite–biotite–(garnet)–muscovite (Fig. 7a), garnet–(staurolite)–biotite–muscovite–plagioclase (Fig. 7b) and fibrolite–staurolite–biotite (see Table 1). A strong sub-vertical recrystallized schistosity, which is an evolved S_2 crenulation, is observed in these rocks. Partially resorbed garnet and staurolite are wrapped around by this schistosity (Figs 7a and b).

KFMASH pseudosections have been constructed for the selected lithologies using versions 2.4 and 2.5 ppc of THERMOCALC (Powell & Holland 1988) with the most recent databases of August 95 and December 97 (Figs 8, 9 and 10). Values of bulk compositional parameters, corresponding to values in real samples (11 for the Ollo de Sapo antiform, 42 for the pelite belt and 31.1 for the Lugo dome) are used in THERMOCALC

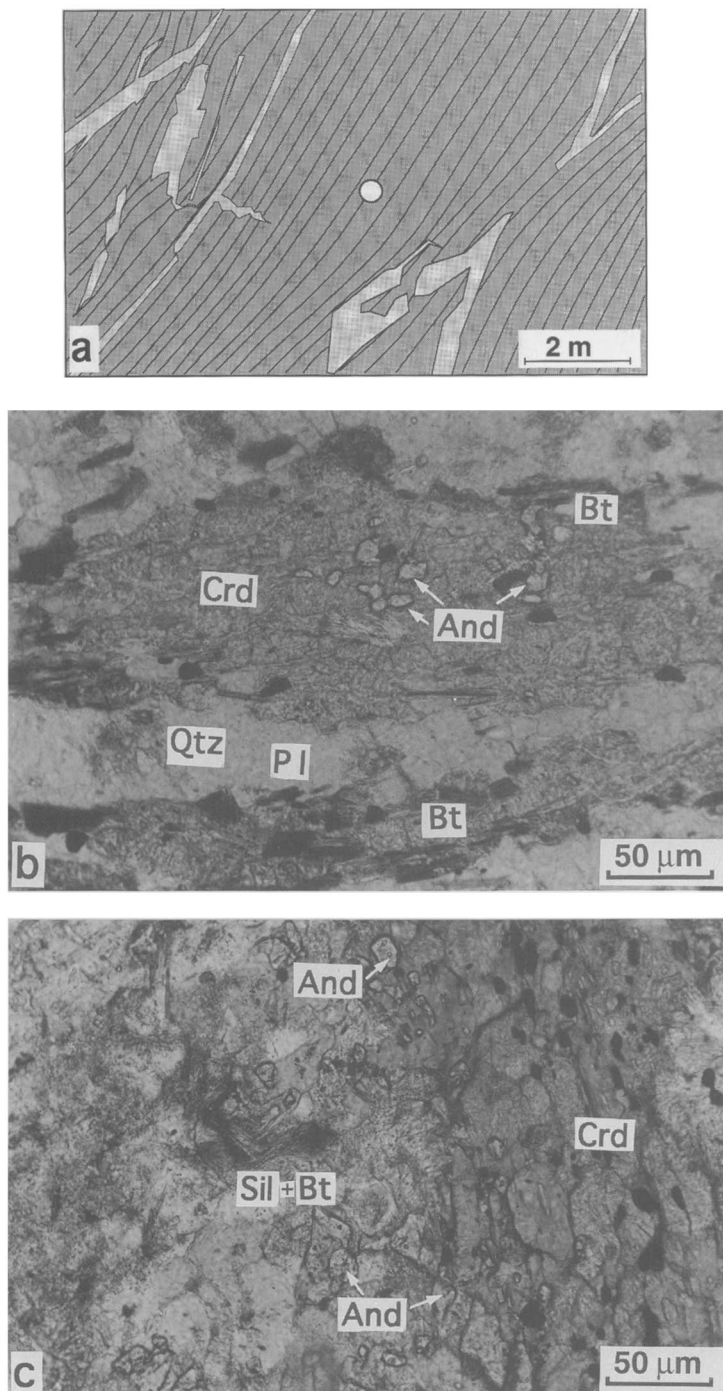


Fig. 2. (a) Mesoscale detail of pre- to syn-D₂ peraluminous granite veins in the Ollo de Sapo gneiss antiform. Main foliation is a composite S₁₊₂. White dot represents the location of sample 11 to which the photomicrographs correspond. (b) Elongated aggregates of pinnitized Crd including resorbed And. Light and dark bands define S₁₊₂ foliation. (c) Detail of a Crd aggregate with inclusion of relict And which also occurs in the proximity. Fibrolite nucleated on Bt occurs near resorbed And.

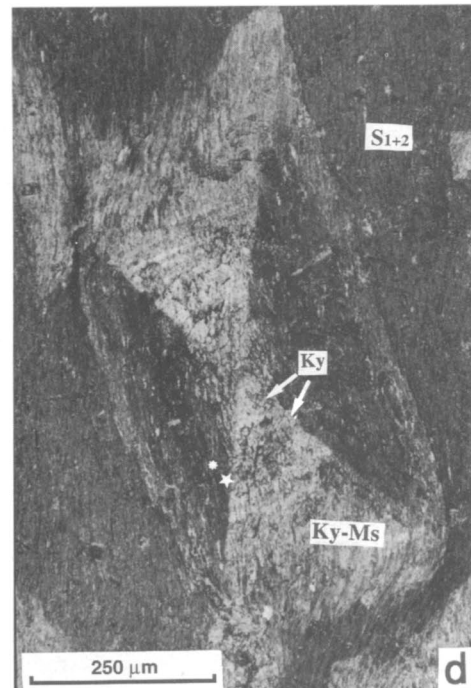
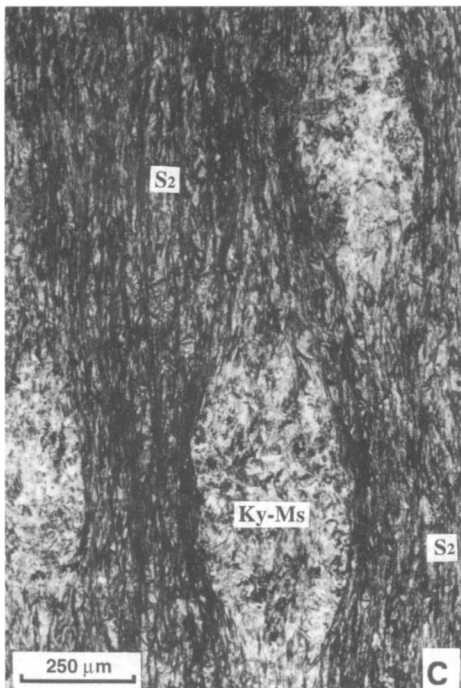
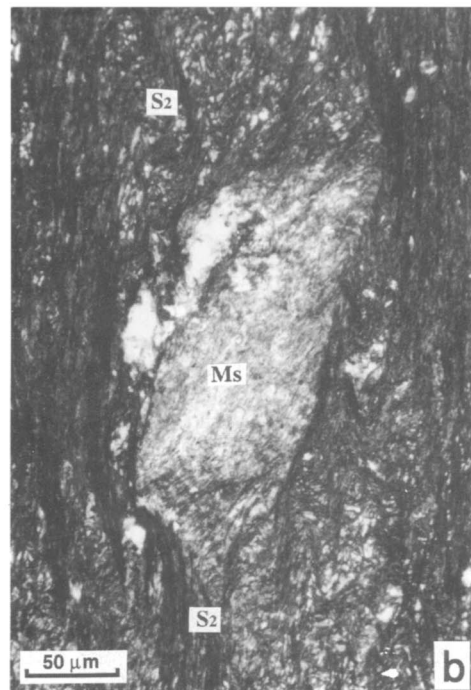
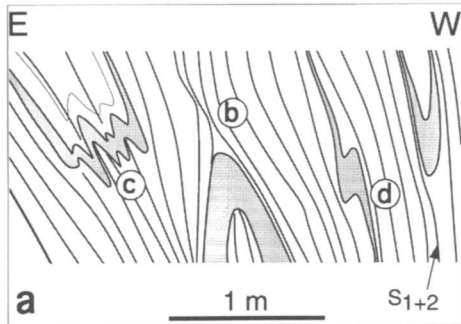


Fig. 3. Relations of meso- and microstructures in the western part of the pelite belt near the Ollo de Sapo gneiss antiform. (a) Detail of sub-vertical D_2 folds, defined by psammitic layers, showing location of photomicrographs. A strong S_2 crenulation is developed in fold hinges. (b) Ms pseudomorph after pre- D_2 chiastolite. S_2 crenulation wraps around the pseudomorph. (c) Ky-Ms aggregates after pre- D_2 chiastolite. S₂ flattens around them. Tiny needle-like crystals surrounded by S₂ in the matrix are Cld. Ky is also deformed by S₂. Other matrix minerals are Ms, Chl, Qtz and graphite. (d) Ky-Ms pseudomorph after chiastolite. External fabric is a composite S_{1+2} in which the pseudomorph appears slightly rotated in a D_2 fold limb.

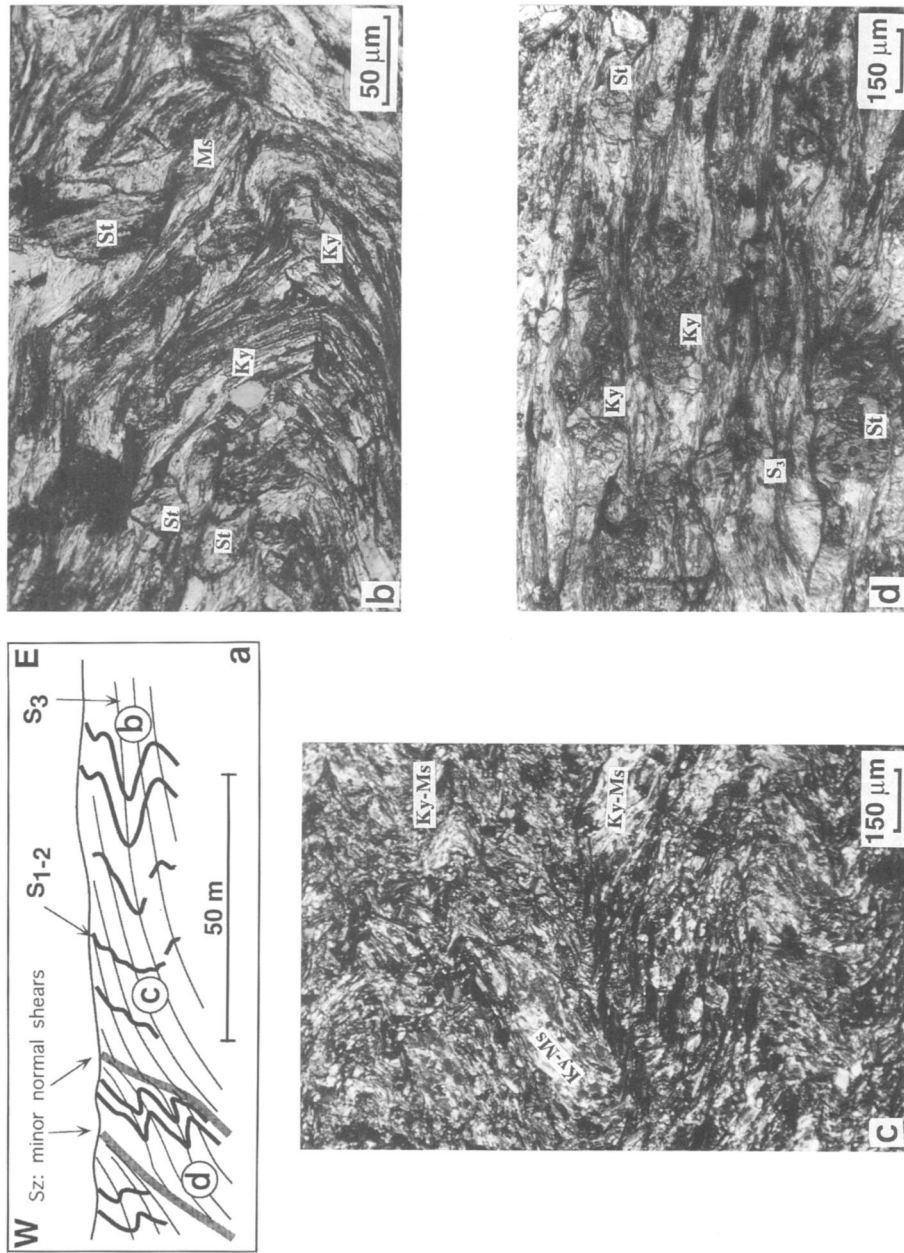


Fig. 4. (a) Relations between S_1 - S_2 and S_3 fabrics in the pelite belt near the Vivero fault zone. Encircled letters refer to photomicrographs. (b) Ky and St bent and broken in a sub-horizontal D_3 microfold hinge. The folded schistosity is a composite S_1 - S_2 . (c) Ky-Ms aggregates replacing former chiaxite porphyroblasts as those shown in Fig. 2. Elongated aggregates lie in a composite S_1 - S_2 schistosity that is folded by sub-horizontal S_3 related to the Vivero fault. (d) Ky and St affected by the sub-horizontal crenulation S_3 . Stable assemblage in the rock is Ky-St-Chl-Ms.

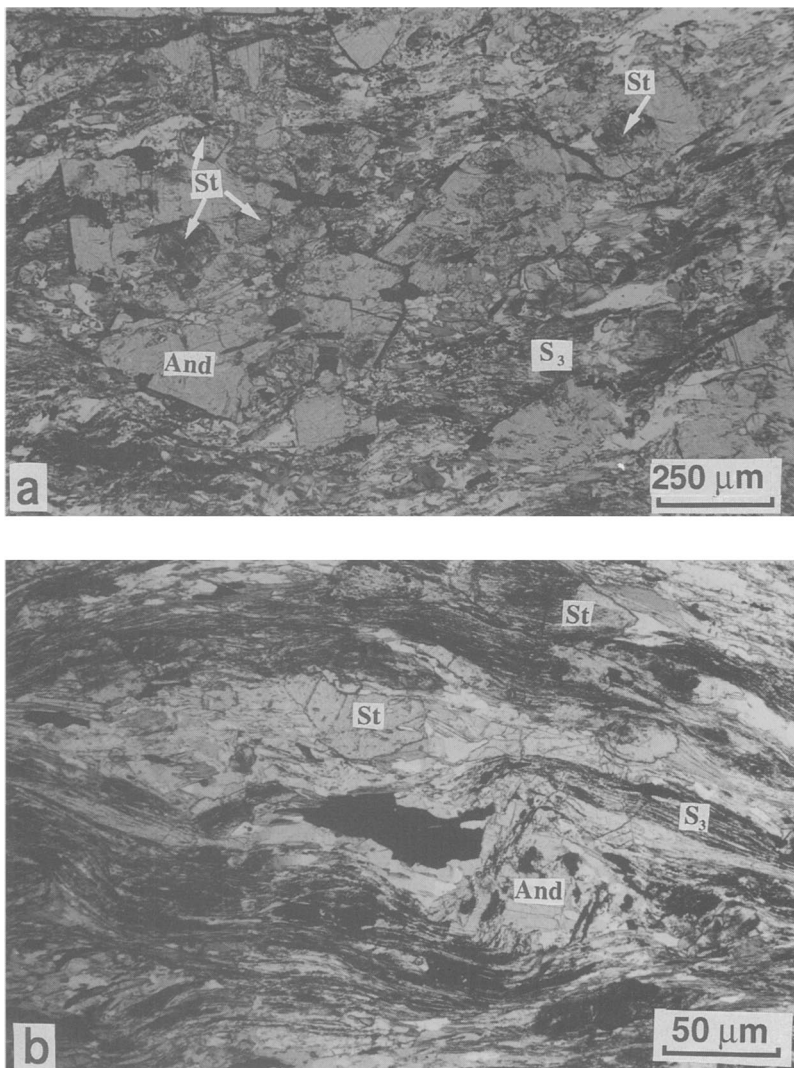


Fig. 5. (a) And-St Bt hornfelsic schist in the Vivero fault zone. St is stable in the matrix and partially resorbed inside late And. Ky relicts occur with Ms in the matrix. Qtz and blastic Plg are also present. (b) Rotated pleochroic late And and St in an And-St-Bt-Ms hornfelsic schist in the Vivero fault zone near the contact with the Lugo dome. S₃ lies at low angle with former S₁₊₂.

calculations and are indicated in each of the pseudosections. AFM diagrams depicting bulk composition for the rest of representative samples in each domain are presented in each. Additional pseudosections, drawn from bulk composition values of real samples, are also presented as insets in the figures so as to reflect the observed local variations in bulk composition within the Ollo de Sapo and the pelitic belt domains (samples 17 and 93, respectively). Other calculations have shown that minor bulk com-

position variations observed within Al-rich and Al-poor lithologies in each of the domains do not imply major displacements in the phase fields and hence seem not to have geological significance.

A value of 0.9 is used for the water activity due to the presence of graphite, and hence of a binary CO₂-H₂O fluid, in black metapelites (Ohmoto & Kerrick 1977; Connolly & Cesare 1993), whereas water activity was set at 1 in the Ollo de Sapo gneiss. Mineral solution models are

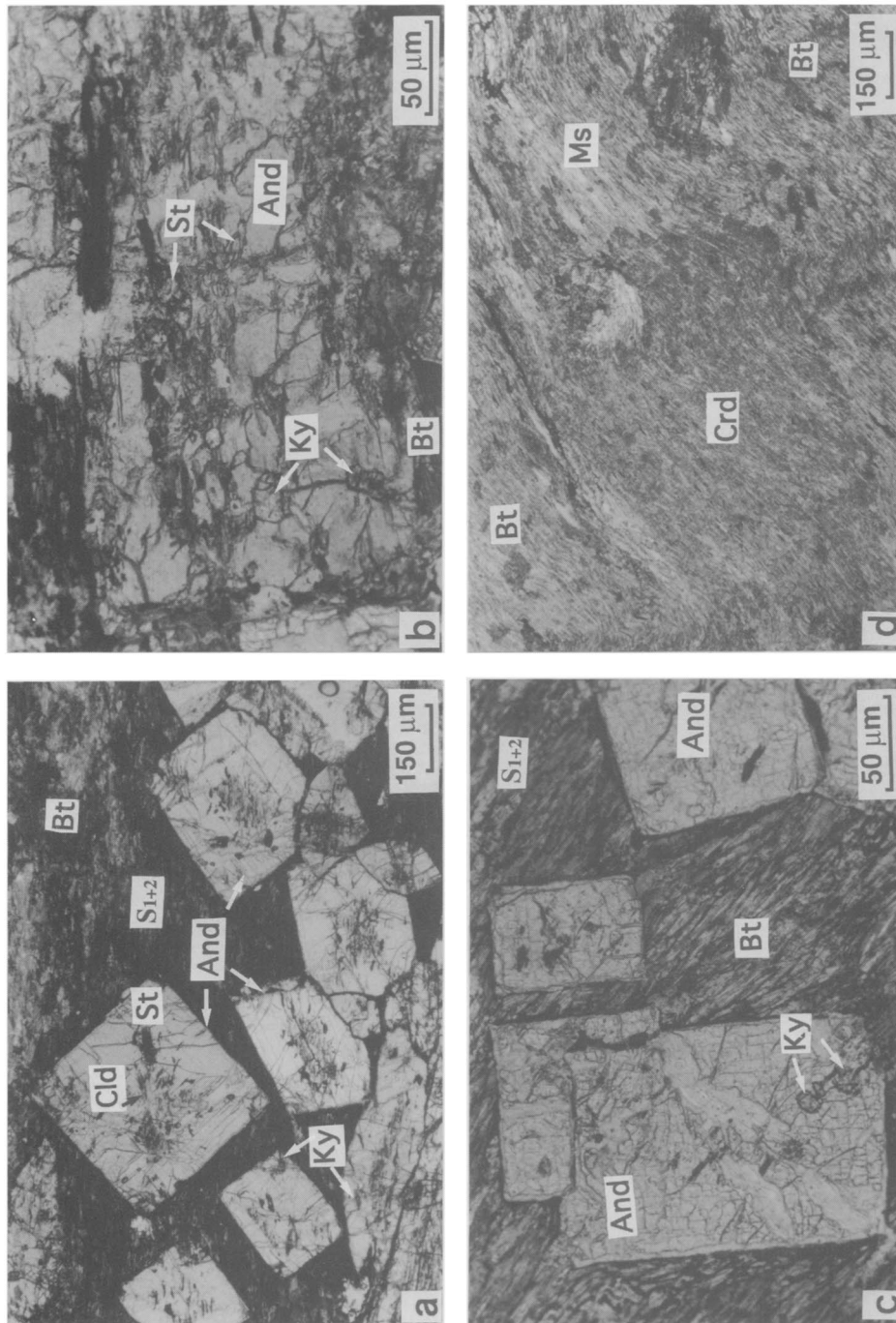


Fig. 6. (a) And–Bt hornfels schist near late-tectonic granite in the pelite belt, near the Vivero fault. Cld, St and Ky from former assemblages like those of Figs 3 and 4 occur as inclusions within post- D_3 idoblastic chiastolite. Included in the core of chiastolite is a relict S_{1+2} . Matrix is mainly formed by recrystallized Bt mimetic with the foliation. Ms, Qtz and Plg are also present. (b) Detail of an And crystal with inclusions of resorbed St and Ky aligned parallel to the relict S_{1+2} fabric. (c) Idoblastic And including remnants of Ky. Matrix is formed mainly by Bt mimetic with S_{1+2} . (d) Mn-richer, Al-poorer hornfelsic schist with (Grt)–Crd–Bt–And. White and dark large spots in the centre right are Ms–Bt aggregates replacing Grt which had pressure shadows. Photomicrographs (a), (b) and (c) correspond to sample 98; (d) is from sample 36.

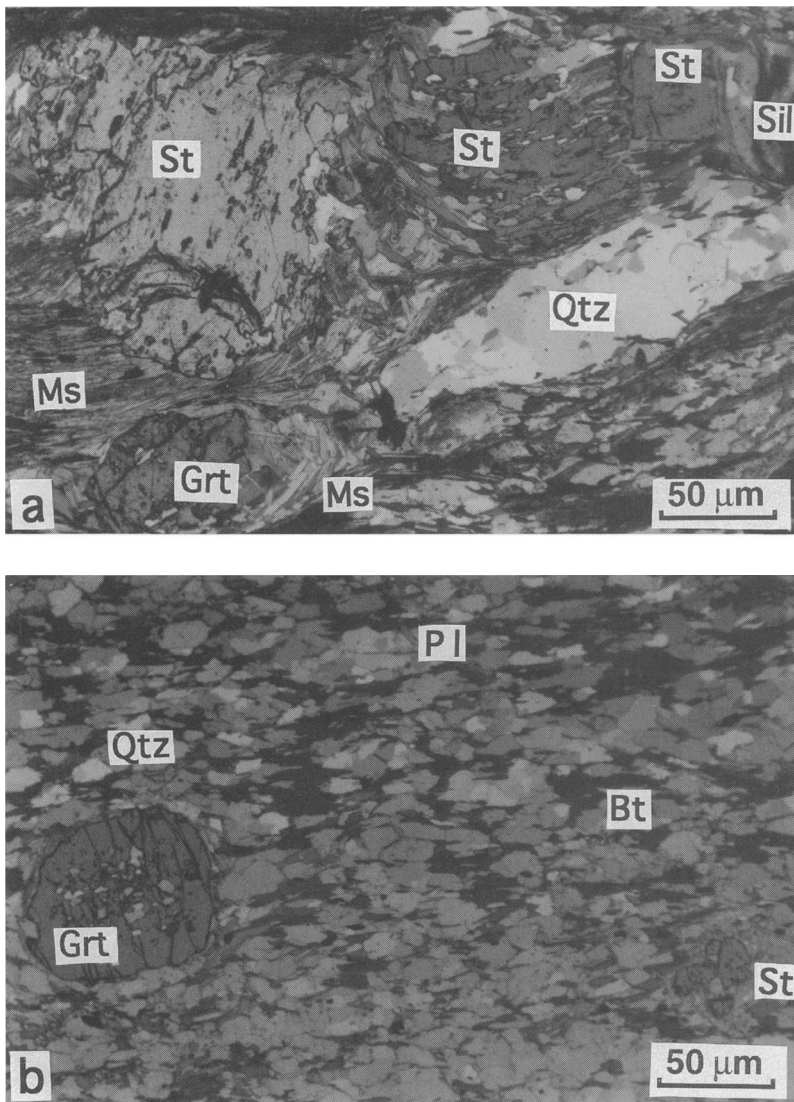


Fig. 7. (a) (Grt)-St-Bt-Sil-Ms schist from the Lugo dome. Grt is partially resorbed into Bt and Ms. Schistosity is a sub-vertical S₂. (b) (St)-Grt-Bt-Ms psammitic schist. Ms surrounds resorbed St. Both samples are from the Lugo dome and their matrix is coarser-grained than that in preceding figures.

used as in Xu *et al.* (1994) and Mahar *et al.* (1997). A corrected activity was used to account for the presence of additional components like Zn in staurolite (activity of ferro-staurolite is calculated as $0.95^4 x^4$ where $x = [\text{Fe}/(\text{Fe} + \text{Mg})]$) as in Pitra & Guiraud (1996).

Pressure-temperature evolution

A pseudosection for a fine-grained augen gneiss in the Ollo de Sapo antiform is presented in

Fig. 8, allowing deduction of the highest-T conditions reached by the western part of the antiform, where gneisses are high-grade rocks injected by a swarm of peraluminous granite veins deformed by D₂ (Fig. 2a). Conditions deduced for the gneisses are those of the cordierite-K-feldspar-biotite-andalusite fibrolite KFMASH divariant field, to the right side of the degenerated $\text{Ms} + \text{Qtz} = \text{Als} + \text{Kfs} + \text{H}_2\text{O}$ equilibrium since there are multiple contacts of pinnitized cordierite with K-feldspar, and the

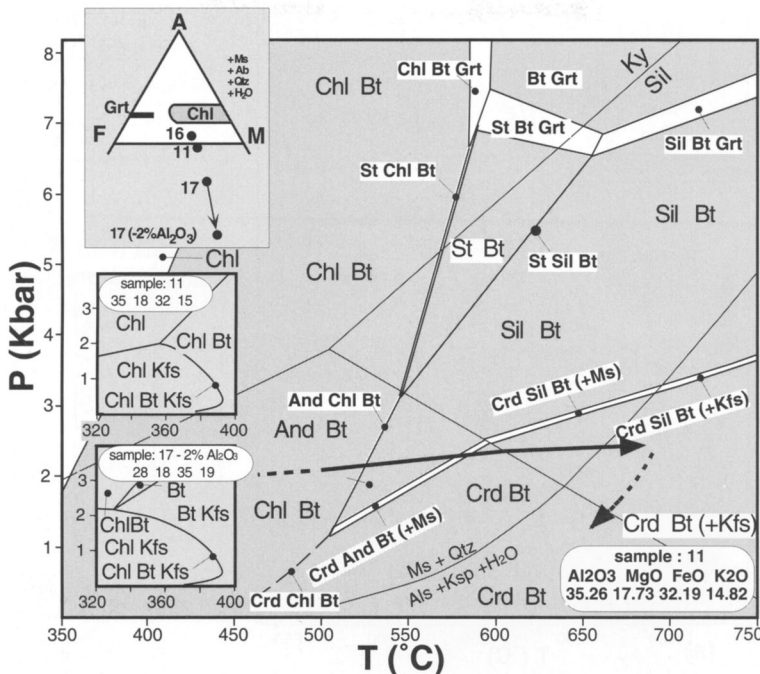


Fig. 8. KFMASH P - T pseudosection for sample 11 from the Ollo de Sapo gneiss, showing the three-, two- and one-phase fields. All assemblages include plagioclase, quartz, H_2O and either muscovite or K-feldspar. The two insets on the lower left represent the low- T assemblages developed in sample 11 and in a K-feldspar-rich, Al-poor lithology like samples 17 and 17 with 2% less Al_2O_3 . Inset on the upper left shows AFM projection for bulk compositions of the Ollo de Sapo gneiss. Univariant reactions separating the higher-variance fields are from left to right: $Chl + Ms + And + Qtz = Crd + Bt + H_2O$; $St + Chl + Ms = Bt + And + Qtz + H_2O$; $Grt + Chl + Ms = St + Bt + Qtz + H_2O$; $St + Bt + Qtz = Grt + Ms + Ky + H_2O$; $Bt + Als + \text{beta-Qtz} = Cd + Grt + Kfs + H_2O$. Mineral abbreviations are after Kretz (1983).

only existing muscovite is a blastic secondary one. However, given the narrowness of the divariant field, the occurrence of relict andalusite showing different degrees of resorption preserved inside the cordierite (Figs 2b and c) might reflect overstepping of the divariant field bringing the rock into the trivariant cordierite-K-feldspar-biotite field, at P conditions below the intersection of the andalusite-sillimanite boundary with the cordierite-andalusite-biotite-muscovite divariant band at c. 2.4 kbar (Fig. 8).

Fibrolite surrounds corroded andalusite relicts and is also nucleated on biotite in the proximity of the andalusite (Fig. 2c), which suggests that the path has crossed the andalusite-sillimanite boundary. The absence of primary muscovite, which together with biotite defined the lower-grade rock foliation S_{1+2} , in the cordierite-biotite gneiss suggests that the univariant breakdown of muscovite + quartz was also crossed. The peraluminous granite veins intruded in the cordierite-biotite-bearing gneiss contain aggre-

gates of pinnitized cordierite and corroded relicts of andalusite and sillimanite which resemble those observed in the host rock. The presence of these aggregates, that most likely constitute microxenoliths, means that the granite was in equilibrium with the host rock. On the other hand, the absence of either staurolite or garnet in the Ollo de Sapo seems to imply that the prograde trajectory should have passed below the fields containing these minerals and so at pressures below 3.2 kbar at 545°C, which represents the lowest pressure conditions of stability for the staurolite-bearing divariant bands (Fig. 8).

Away from the granites, lower-grade augen gneisses containing chlorite-biotite-muscovite-oligoclase \pm K-feldspar constitute the more abundant lithology within the Ollo de Sapo gneiss. Plagioclase (oligoclase) forms the majority of the augen and is more abundant than K-feldspar which appears relict inside plagioclase. Biotite-muscovite or biotite-K-feldspar-muscovite assemblages, lacking chlorite, have

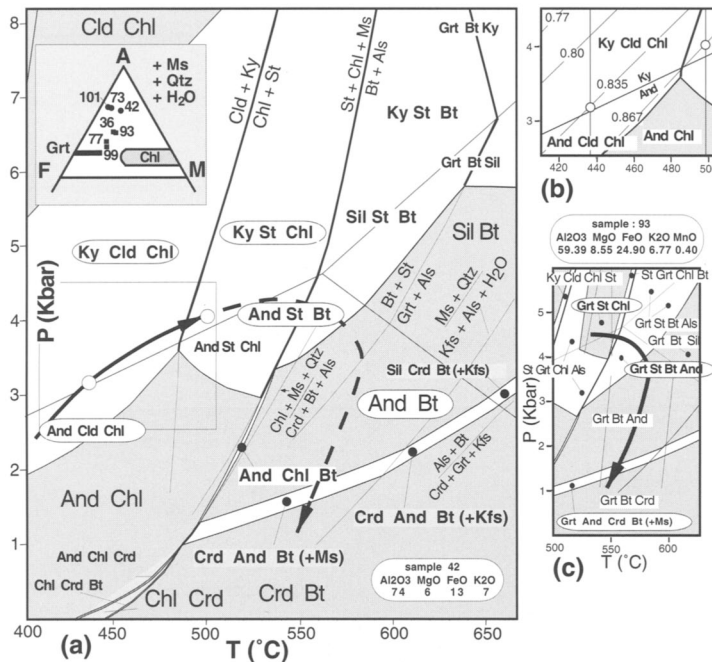


Fig. 9. Pseudosections for the pelite belt synform. (a) KFMASH pseudosection for Al-rich sample 42. The dashed part of the path is deduced from assemblages observed in Al-rich samples similar to 42 as well as by assemblages in and thermometry done for Mn-richer lithologies represented by the lower right inset (c). (b) Outlined area in (a) showing chloritoid isopleths for studied samples (lines labelled with XFe in Cld) and Chl–Cld exchange thermometry (vertical lines). Open dots represent intersections for chloritoid core (left) and rim (right). (c) Mn–KFMASH pseudosection for Al-poorer, Mn-richer lithologies as sample 93. Sub-vertical lines in fields Grt–St–Chl and Grt–Bt–And represent, respectively, rim Grt–Chl and Grt–Bt exchange thermometry. Assemblages enclosed within ovals correspond to those observed in samples. Inset in the upper left corner shows AFM projection for bulk compositions of the Vivero pelite belt. All assemblages contain Ms, Qtz and H₂O.

been observed in practically all low-grade samples, although restricted to feldspar-rich, felsic microdomains. Sample 11 also contains biotite and biotite–K-feldspar assemblages although the corresponding pseudosection of Fig. 8 does not show any of them. The two insets in Fig. 8 show the progressive expansion of different low-grade assemblages as bulk composition becomes K-richer and less aluminous than sample 11, as happens in a hypothetical Al-poorer sample 17 with 2% less Al₂O₃. The presence of biotite and biotite–K-feldspar assemblages in thin-section sub-domains of samples 17 and 11, probably represents local equilibrium in K-rich and Al-poor parts of the rock, such as those within the feldspar augen. It is interesting to observe that the coexistence of chlorite–K-feldspar is restricted to the least aluminous compositions of all. Reactions responsible for K-feldspar resorption, observed in these samples, could have been related to

prograde crossing of the divariant band chlorite–biotite–K-feldspar 2%.

Taking into account all these constraints, an almost isobaric prograde path would result, the initial conditions being those of a chlorite–biotite–muscovite–oligoclase rock (Fig. 8). The pressure starting conditions for the path would be around 2.5 kbar, similar to those of the western part of the pelite belt which is in contact with the gneiss, as will be explained below. It should be pointed out that this trajectory only reflects local conditions close to the peraluminous granite intrusions (De Yoreo *et al.* 1991), and means that during D₂ antiform formation rocks were in the andalusite stability field, at conditions around 2.5 kbar (Fig. 8). Peak temperatures must definitely have remained in the sillimanite field, at temperatures above the muscovite + quartz equilibrium and pressures below the divariant band cordierite–sillimanite–biotite–K-feldspar (Fig. 8).

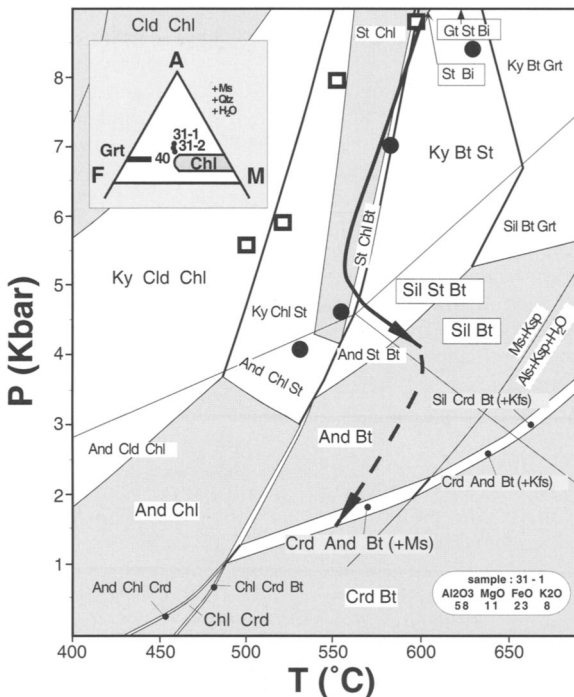


Fig. 10. KFMASH P - T pseudosection for sample 31.1 from the Lugo dome. Assemblages enclosed within rectangles correspond to those that have been recorded in this and other similar samples. Black dots are determinations using garnet-biotite-plagioclase barometry (Höisch 1990) plus garnet-biotite thermometry (Hodges & Spear 1982). Open squares are average P , T determinations with Thermocalc 2.5, using the same mineral compositions.

Figure 9 represents conditions for graphitic, black slates from the Vivero pelite belt. These lithologies occur all across the belt from its contact with the Ollo de Sapo augen gneiss, in the west, to its eastern contact with the Lugo dome. The lowest grade recorded in these lithologies is represented by the divariant KFMASH assemblage kyanite-chloritoid-chlorite-muscovite. In these rocks kyanite and muscovite aggregates pseudomorphically replace subidioblastic chiastolitic andalusite, whose shape and inclusions can still be identified. As explained before, microstructural relations indicate that the former andalusite crystallized post- D_1 but before D_2 (Figs 3b, c and d).

The muscovite-kyanite aggregates can be recognized in appropriate lithologies all across the pelite belt up to the higher-grade rocks, near the contact between the belt and the easterly Lugo dome-rimming antiform. Textural observations indicate that lower-grade black slates, containing aluminosilicate plus chloritoid and chlorite, underwent the andalusite to kyanite replacement. The prograde attitude of the

trajectory (Fig. 9a) has been deduced from chlorite-chloritoid thermometry plus the attitude of chloritoid isopleths in the kyanite-chloritoid-chlorite divariant field, which indicates higher T conditions of equilibration for the rims than for the cores of chloritoid, precluding any retrograde crossing of the andalusite-kyanite boundary and hence any anticlockwise P - T path. Perchuk's (1991) calibration was used for chlorite-chloritoid thermometry. Temperatures were obtained using matrix chlorite ($X_{\text{Fe}} = 0.655$, $X_{\text{Mg}} = 0.340$, $X_{\text{Mn}} = 0.005$, $X_{\text{Al-M2}} = 0.810$) from sample 77, containing the chloritoid-chlorite trivariant assemblage, together with chloritoid cores ($X_{\text{Fe}} = 0.874$, $X_{\text{Mg}} = 0.106$, $X_{\text{Mn}} = 0.020$) and rims ($X_{\text{Fe}} = 0.866$, $X_{\text{Mg}} = 0.115$, $X_{\text{Mn}} = 0.019$) of the same sample, and give values of 440 and 500°C respectively. The intersections of these core and rim temperatures with calculated isopleths representing composition of chloritoid cores ($X_{\text{Fe}} = 0.835$, $X_{\text{Mg}} = 0.165$) and rims ($X_{\text{Fe}} = 0.867$, $X_{\text{Mg}} = 0.133$) from sample 73, containing the divariant assemblage kyanite-chloritoid-

chorite, are represented in Fig. 9b. Mn in this sample ($X_{\text{Mn}} = 0.01$) is not taken into account to calculate X values of the isopleths.

Higher-grade rocks, which are chemically equivalent to the lower-grade Al-rich black slates previously mentioned, contain the assemblages staurolite–chlorite–kyanite and staurolite–andalusite–biotite. Kyanite–muscovite aggregates are still recognized in the first of these two assemblages where they occur folded by a newly developed S_3 sub-horizontal fabric that affects the earlier fabrics S_1 and S_2 (Fig. 4c) and which is only observed in the proximity of the fault. The latter of the two assemblages, the first containing biotite, occurs restricted to a narrow band in the eastern part of the pelite belt, near the Vivero fault, just at the contact between the pelite belt and the Lugo dome. Andalusite from this assemblage (Figs 5a and b) is late with respect to the earlier chiastolite pseudomorphed by kyanite–muscovite; it is subidioblastic and pleochroic and occurs syn- to post-tectonic with respect to the S_3 sub-horizontal fabric. In addition, relicts of kyanite within muscovite aggregates, recalling those that originated after earlier andalusite, are still found in the rock matrix. Staurolite from the assemblage staurolite–andalusite–biotite is found partially resorbed, included in late andalusite and also stable in the matrix (Figs 5a and b), indicating that rocks with this assemblage crossed the relatively restricted divariant field staurolite–andalusite–biotite following a staurolite-consuming trajectory (Fig. 9a). Eventually, andalusite–biotite hornfelsic rocks are found representing the final prograde stage in Al-rich metapelites (sample 36 in Table 1) in contact with late tectonic granite. In these rocks, remnants of kyanite, staurolite and chloritoid occur enclosed in post- D_3 idioblastic andalusite (Figs 6a, b and c).

More psammitic, hornfelsic rocks with Al-poorer and Mn-richer compositions found in the same location, close to the Vivero fault, as those with andalusite–biotite, contain the assemblages: garnet–staurolite–chlorite, garnet–staurolite–andalusite–biotite and garnet–cordierite–andalusite–biotite (Fig. 6d). A decompression trajectory can be deduced for these assemblages from the Mn–KFMASH pseudosection of Fig. 9c. Temperatures for the peak pressure stage of the P – T path followed by these rocks were obtained from garnet–chlorite pairs in sample 93 containing garnet–staurolite–chlorite (see Table 1). Calibrations used for garnet rims were those of Dickenson & Hewitt (1986) and Perchuk (1991). Temperatures using matrix chorite ($X_{\text{Fe}} = 0.591$, $X_{\text{Mg}} = 0.409$, $X_{\text{Al-M2}} = 0.800$) plus garnet rim

($X_{\text{Alm}} = 0.744$, $X_{\text{Prp}} = 0.051$, $X_{\text{Sps}} = 0.121$, $X_{\text{Grs}} = 0.084$) are 532 and 544°C for 4.6 kbar and 6.3 kbar, respectively, for the P -dependent calibration of Dickenson & Hewitt (1986) and 552°C for the P -independent calibration of Perchuk (1991). Temperatures obtained using Fe-richer garnet cores ($X_{\text{Fe}} = 0.931$ –0.964) are in the range 390–486°C, which are lower than those obtained using garnet rims and well outside the stability field of garnet–staurolite–chlorite in Fig. 9c. Peak temperatures were obtained using sample 99 (see Table 1) garnet–biotite pairs. Matrix biotite composition ($X_{\text{Fe}} = 0.591$, $X_{\text{Mg}} = 0.409$, $X_{\text{Al-M2}} = 0.52$) was taken as an average of 17 analyses. Hedges & Spear's (1982) calibration gives around 546–556°C at 2.3–5 kbar using garnet rim ($X_{\text{Alm}} = 0.819$, $X_{\text{Prp}} = 0.053$, $X_{\text{Sps}} = 0.026$, $X_{\text{Grs}} = 0.102$) and matrix biotite pairs, whereas Williams & Grambling's (1990) calibration gives 600–608°C at 2.4–4.6 kbar using the same garnet (rim)–biotite pairs. Garnet cores ($X_{\text{Alm}} = 0.707$, $X_{\text{Prp}} = 0.034$, $X_{\text{Sps}} = 0.165$, $X_{\text{Grs}} = 0.094$) give much lower T than any of the previously cited calibrations when using the same average matrix biotite composition. The earlier segments of the trajectory followed by these Al-poor rocks is assumed to be equivalent to that deduced for the Al-richer ones within which they are intercalated.

A pseudosection valid for the Lugo dome psammitic schist is shown in Fig. 10. Simultaneous solution using the GPT Excel™ spreadsheet (Reche & Martínez 1996), the garnet–biotite (Hedges & Spear 1982) thermometer and the garnet–biotite–plagioclase–quartz barometer (Höisch 1990) (Fig. 10) was performed in sample 31.1 (see Table 1). Using matrix biotite ($X_{\text{Fe}} = 0.456$, $X_{\text{Mg}} = 0.544$, $X_{\text{Al-M2}} = 0.198$) and matrix plagioclase ($X_{\text{An}} = 0.286$), gives pressures between 7.1 and 8.4 kbar and temperatures between 582 and 628°C for garnet cores ($X_{\text{Alm}} = 0.70$ –0.68, $X_{\text{Prp}} = 0.13$ –0.15, $X_{\text{Sps}} = 0.07$ –0.07, $X_{\text{Grs}} = 0.09$ –0.10), whereas garnet rims ($X_{\text{Alm}} = 0.75$ –0.75, $X_{\text{Prp}} = 0.14$ –0.13, $X_{\text{Sps}} = 0.06$ –0.07, $X_{\text{Grs}} = 0.06$ –0.06) give pressures between 4.6 and 4.1 kbar for temperatures between 554 and 530°C. These results agree with conditions within the garnet-absent fields in the pseudosection drawn in Fig. 10 for sample 31.1. Average P – T calculations using THERMOCALC (Powell & Holland 1988) 2.5 with recent database of Spring 97 gives a set of P – T points displaced towards lower T and slightly higher P than those obtained with conventional thermobarometry. Activities of the end-members used in the average P – T calculations were calculated with the program AX of T. J. B.

Holland, according to a two-site mixing model plus Newton & Haselton's (1981) activity coefficients for garnets, Holland & Powell's (1990) mixing model with Eugster *et al.*'s (1972) gammas for biotite, and Holland & Powell's (1992) mixing model 1 for plagioclase. Results range from 7.9 to 8.8 kbar and from 551 to 596°C if garnet cores are used, and from 5.9 to 5.6 kbar and from 522 to 499°C using garnet rims. Re-equilibration and compositional resetting of the core of the resorbing garnets and of matrix phases during decompression and cooling could be responsible for the discrepancy between the results from core thermobarometry and the location of garnet–staurolite–biotite divariant and staurolite–biotite trivariant fields in the pseudosection of Fig. 10.

Major decompression in the Lugo dome, deduced from thermobarometry, is confirmed by the sequence of progressively lower-pressure assemblages going from staurolite–biotite ± garnet through fibrolite–staurolite–biotite to, finally, fibrolite–biotite. Garnet and staurolite are found showing different degrees of resorption to biotite, muscovite (Figs 7a and b) and occasionally to fibrolite as well. Chlorite is present inside staurolite in sample 40 and is considered to be a relict phase as staurolite or garnet. The occurrence of chlorite together with the absence of kyanite reinforces the simultaneous cooling during decompression (Fig. 10), as outlined by thermobarometric results, as opposed to a merely isothermal P – T path.

The higher-pressure assemblages containing garnet and staurolite in the Lugo dome seem to

be pre- D_2 , since S_2 schistosity defined by micas and fibrolite wraps around the resorbed garnet and staurolite porphyroblasts. The last part of the Lugo dome evolution is given by the progressive consumption of staurolite within the divariant assemblage fibrolite–staurolite–biotite, leading to a final fibrolite–biotite trivariant assemblage. This evolution would be coherent with decompression and heating, assuming a previous earlier part of the trajectory characterized by cooling and decompression as shown in Fig. 10. Presence of assemblages with fibrolite implies conditions of only slightly higher P and T than those recorded by the andalusite–staurolite–biotite assemblage in the Vivero pelite belt, which developed partially

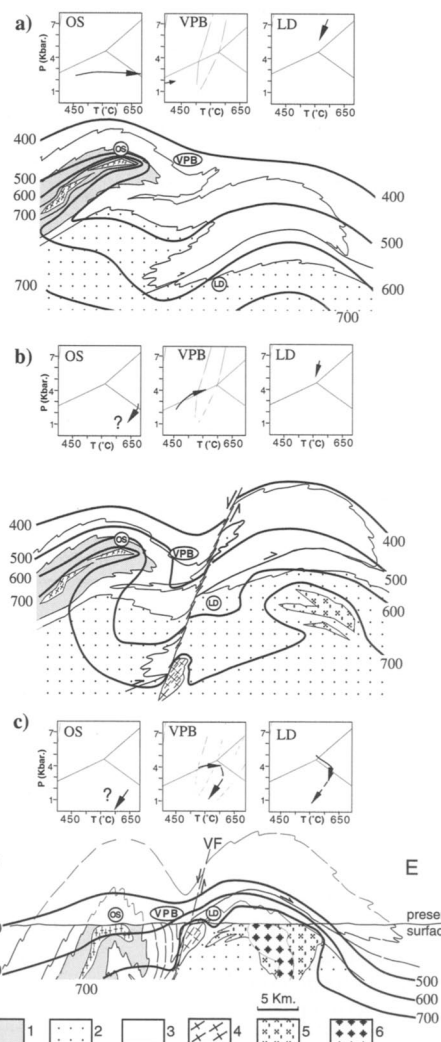


Fig. 11. Schematic cross-section including the Ollo de Sapo antiform, the Vivero pelite belt synform and the Lugo dome antiform, showing a qualitative interpretation for the related tectono-thermal evolution within all three domains during the Variscan orogeny. (a) Tectono-thermal picture at the onset of D_2 deformation phase, which refolds previous D_1 overturned folds and nappes. Above each locality the corresponding progression of the interpreted P – T path is depicted in a simplified P – T diagram. (b) Advanced stage of D_2 deformation phase showing an evolved synform, nucleation of the Vivero fault and further granitoid intrusions. (c) Cross-section showing present level of erosion. Position of isotherm as during D_3 deformation phase. P – T paths show evolution during and after this phase of deformation. VF, Vivero fault; OS, Ollo de Sapo antiform; VPB, Vivero pelite belt; LD, Lugo Dome. 1, Ollo de Sapo gneiss; 2, Cambrian and Precambrian of the Lugo dome; 3, Ordovician and Silurian of the Vivero pelite belt; 4, syntectonic granitoids (syn- D_2 within OS and syn- D_3 along VF); 5, Syn- D_2 to syn- D_3 Vivero granite; 6, Post-tectonic granitoids.

syntectonically with fault-related sub-horizontal cleavage S_3 . This suggests that the location of Lugo dome and Vivero pelite belt referenced samples did not differ much at this stage of evolution, the two staurolite-consuming reactions being approximately synchronous in both domains, also suggesting a common heating episode, which is interpreted to be related to granite intrusion during syn- D_3 fault movement.

The similar P - T conditions and metamorphic evolution recorded in the pelite belt and Lugo dome samples would mean that they were about to become levelled during the syn-fault-movement heating episode, and finally became coupled and followed a common decompressional evolution after motion ceased along the Vivero fault. Whereas during the early stages, when the two samples were nearly level, heating due to granite emplacement along the Vivero fault dominated the thermal regime, later on both areas cooled down. During this late stage of general cooling, post-tectonic granites induced local heating that was recorded by hornfelsic samples containing the andalusite-biotite and cordierite-biotite-bearing assemblages which have been found in the eastern part of the pelite belt.

Summary of metamorphic and tectonic evolution

The P - T paths deduced indicate that it would be too simplistic to ascribe the low- P Variscan metamorphism in the studied areas to an almost isobaric T increase in a local extensional regime. Actually, the close relationship between the location of kyanite belts resulting from andalusite to kyanite replacement in D_2 synforms indicates that sub-vertical refolding played a major role in the metamorphic evolution, down-dragging the pre- D_2 chiastolite-bearing materials, and bringing them into the kyanite stability field. Then, although the overall attitude of the P - T paths deduced reflects a temperature increase, dP/dT did not remain constant since, locally, previous low- P gradients of $c. 45^\circ\text{C km}^{-1}$ (Fig. 8), possibly related to intrusion of earlier peraluminous granitoids, as deduced from the presence of chiastolite previous to kyanite in the pelite belt, evolved to intermediate- P ones ($c. 34^\circ\text{C km}^{-1}$). The localized change in dP/dT is related to the D_2 sub-vertical planar, coaxial, synformal refolding of D_1 fabric, since the replacement of chiastolite by kyanite is confined to the synform constituted by the pelite belt located between the Ollo de Sapo and Lugo dome antiforms.

It is assumed that after the first deformation phase (D_1), which caused isoclinal folding and thrusting in the area, isotherms should have been sub-horizontal. D_2 caused subvertical folding of the isotherms. In the Ollo de Sapo antiform, granitoid intrusion substantially modified the attitude of isotherms (Fig. 11a) generating locally high thermal gradients. Rock bodies within the Ollo de Sapo domain, located close to lens-shaped injections of peraluminous granitoids, would attain their thermal peak immediately after granite intrusion, undergoing the andalusite to sillimanite replacement. Nucleation of fibrolitic sillimanite was probably not only due to changing P and T conditions but also driven by 'Carmichael-type' ionic reactions that imply fluid flow in an open system with exchange of K^+ and H^+ ions (Carmichael 1969; Vernon 1987; Yardley 1989). Rocks in the Ollo de Sapo would probably have undergone decompression as a result of antiform evolution during D_2 , but this is not recorded by the observed staurolite or garnet-free assemblages. Alternative hypotheses explaining why decompression is not recorded are either that the heating event was short-lived and hence substantial decompression did not take place during it, or that the decompression really existed (the P - T path thus having transected staurolite-bearing stability fields), although remains of these higher- P assemblages have not been found yet, due in part to the existence of strong gradients implying extremely condensed zoning and to complete final re-equilibration of rocks near the granites at very high T , near 700°C .

During D_2 the Vivero belt pelites underwent an increase in P due to their down-dragging into a synform (Fig. 11b). Simultaneously, temperature increased due to progressive relaxation of isotherms caused by heat transfer from the Ollo de Sapo antiform; an additional effect of early granite intrusions in the nearby Ollo de Sapo domain may have enhanced the increase in temperature. The scarce penetration of the kyanite stability field by the prograde P - T path (Fig. 9a) is coherent with the fact that transformation from andalusite to kyanite is not related to a polymorphic inversion but to ionic reactions involving phyllosilicates. Those reactions would be kinetically more favourable, not requiring a large overstep into the kyanite stability field and probably would be enhanced by D_2 deformation as proved by the fact that the nearly completely replaced chiastolites are those surrounded by the strongest D_2 fabrics (crenulations or reworked composite S_{1+2}).

Progressive decompression and cooling was taking place in the Lugo dome simultaneously

with sinking of the pelite belt. The onset of slip on the Vivero fault zone increased the raising of the Lugo dome and locally modified the isotherms, inducing higher gradients near the fault. Granite intrusion along the fault zone also caused modification of the thermal structure in the proximity of the fault, and the same happened in the Lugo dome core where granites were intruded contemporaneously with the movement of the fault. As a result, the area near the Vivero fault became a region characterized by a strong thermal gradient in its deeper parts (Fig. 11b). At the present erosion level (Fig. 11c), granite intrusions caused a temperature increase in the materials situated on both sides of the Vivero fault, in such a way that the Vivero pelite belt and the Lugo dome underwent contemporaneous heating. When the thermal effect of synfault granites vanished, both areas cooled down during continuous uplift. Probably the Ollo de Sapo domain was also undergoing decompression during this late stage as no major fault is present between this domain and the Vivero pelite belt but, since no late intrusions were emplaced in the eastern Ollo de Sapo domain, this decompression event is not recorded. Therefore the later part of the path designed for the Ollo de Sapo in Figs 11b and 11c is hypothetical and has been designed with the same slope as that in the pelite belt. Post-tectonic granites, emplaced in the Lugo dome antiform and locally along the Vivero fault, may have induced local thermal effects at some points along this later segment of the decompressional P - T path being responsible for the post- D_3 andalusite–biotite or cordierite–biotite assemblages in hornfelsic samples close to the Vivero fault in the pelite belt.

Absolute time constraints for the proposed tectonometamorphic evolution are difficult to set precisely as scarce data are at present available for granitoid intrusives within the studied areas. The thermal peak in the Ollo de Sapo gneiss near Sanabria, 200 km south of the studied area, was dated as intra-Namurian (325 ± 2 Ma) by Lancelot *et al.* 1985. This is in good agreement with ages measured for metaluminous and peraluminous early granitoids, whose ages cluster around 320 to 335 Ma (Pinto & Gil Ibarguchi 1987; Priem & Den Tex 1984; Galán *et al.* 1996). As, in our model, compression related to D_2 in the Vivero pelite belt nearly coincides with the thermal peak in the Ollo de Sapo, it follows that the establishment of the Barrovian gradients in the syncline involving replacement of early chiastolite by kyanite–muscovite aggregates should also be intra-Namurian. The Rb–Sr age of a post-tectonic

pluton in the Lugo dome, south of the studied area, is 287 ± 10 Ma (Cocherie 1978), and a K/Ar age for a post-tectonic granodiorite in the northwesternmost tip of Ollo de Sapo antiform (see Fig. 1) is 280 Ma (Ries 1979). These Stephano-Permian ages are probably those of the decompressional part of the path shared by the three domains. K–Ar dating of biotite from the mylonitic foliation present in the Vivero fault zone syntectonic granitoid also gives a late Carboniferous age of 269 Ma (Ries 1979). As this is a cooling age, it only places a minimum age constraint on the intrusion of synfault granites and hence on the episode of heating under which the rocks near the fault on the Vivero pelite belt and Lugo dome areas attained their thermal peak.

A similar kyanite-bearing belt has been described south of Oporto in northern Portugal in the Oliveira de Azemeis–Albergaria a Velha metamorphic belt (Atherton *et al.* 1974; Oen 1974) although the age of the metasediments in which this belt develops is not known (unlike the case in NW Spain). However, the similar position of this belt, occurring in the hanging wall of a late normal fault separating the kyanite belt from the Oporto–Viseu low-pressure metamorphic belt, strongly suggests that its meaning might well be very similar to the one presented in this study.

J. R. and F. J. M. gratefully acknowledge support by DGICYT Research Project PB94-0684-CO2. M. L. A. was funded by DGICYT Research Project PB94-0685. J. Reinhardt and M. Guiraud are acknowledged for their reviews of an earlier version of the manuscript.

References

- AERTHERTON, M. P., ATKIN, B. P., & NAGGAR, M. H. 1974. Kyanite in the Hercynian metamorphic rocks of the Oporto–Viseu belt, North Portugal. *Geologie en Mijnbouw*, **53**, 189–192.
- AUTRAN, A., FONTEILLES, M. & GUITARD, G. 1970. Relations entre les intrusions de granitoïdes, l'anatexie et le métamorphisme régional considérées principalement du point de vue du rôle de l'eau: cas de la chaîne hercynienne des Pyrénées orientales. *Bulletin de la Société Géologique de France*, **12**, 673–731.
- AYORA, C., LIESA, M. & DELGADO, J. 1993. Low-thermal-gradient Hercynian metamorphism in the eastern Pyrenees. *Journal of Metamorphic Geology*, **11**, 49–58.
- BASTIDA, F., MARCOS, A., MARQUÍNEZ, J., MARTÍNEZ CATALÁN, J. R., PÉREZ-ESTAÚN, A. & PULGAR, J. A. 1984. *Geological Map of Spain, scale 1:200,000, Sheet No. 1, La Coruña*. Instituto Geológico y Minero de España, Madrid, Spain.

—, MARTÍNEZ CATALÁN, J. R. & PULGAR, J. A. 1986. Structural, metamorphic and magmatic history of the Mondoñedo nappe (Hercynian belt, NW Spain). *Journal of Structural Geology*, **8**, 415–430.

BRIGGS, W. D. 1995. *Pressure-temperature deformation history of the Ollo de Sapo antiform, Variscan orogen, northwest Spain*. PhD dissertation, University of Cincinnati.

CAPDEVILA, R. 1968a. Les types de métamorphisme intermédiaires de basse pression dans le segment Hercynien de Galice Nord Orientale (Espagne). *Comptes Rendues Académie Sciences Paris*, **266**, 1924–1927.

— 1968b. Zones de métamorphisme régional progressif, dans le segment hercynien de Galice Nord Orientale (Espagne). *Comptes Rendues Académie Sciences Paris*, **266**, 309–312.

CARMICHAEL, D. M. 1969. On the mechanisms of prograde metamorphic reactions in quartz bearing pelitic rocks. *Contributions to Mineralogy and Petrology*, **20**, 244–267.

COCHERIE, A. 1978. *Géochimie des terres rares dans les granitoïdes*. PhD dissertation, Université de Rennes.

CONNOLLY, J. A. D. & CESARE, B. 1993. C-O-H-S fluid composition and oxygen fugacity in graphitic metapelites. *Journal of Metamorphic Geology*, **11**, 379–388.

DE YOREO, J. J., LUX, D. R. & GUIDOTTI, C. V. 1991. Thermal modelling in low-pressure/high-temperature metamorphic belts. *Tectonophysics*, **188**, 209–238.

DEN TEX, E. 1966. Aperçu pétrologique et structural de la Galice cristalline. *Leidse Geologische Mededelingen*, **36**, 211–222.

DICKENSON, M. P. & HEWITT, D. 1986. A garnet–chlorite geothermometer: *Geological Society of America Abstracts with Programs*, **18**, 584.

DIEZ BALDA, M. A., VEGAS, R. & GONZÁLEZ LODEIRO, F. 1990. Structure of the Central Iberian zone. In: DALLMEYER, R. D. & MARTÍNEZ GARCÍA, E. (eds) *Pre-Mesozoic Geology of Iberia*. Terranes in the Circum-Atlantic Paleozoic Orogen, Springer-Verlag, Berlin, 172–188.

EUGSTER, H. P., ALBEE, A. L., BENCE, A. E., THOMPSON, J. B. JR & WALDBAUM, D. R. 1972. The two phase region and excess mixing properties of paragonite–muscovite crystalline solutions. *Journal of Petrology*, **13**, 147–179.

GALAN, G., PIN, C. & DUTHOU, J-L. 1996. Sr-Nd isotopic record of multi-stage interactions between mantle-derived magmas and crustal components in a collision context. The ultramafic-granitoid association from Vivero (Hercynian belt, NW Spain). *Chemical Geology*, **131**, 67–91.

GIBSON, R. L. & BICKLE, M. J. 1994. Thermobarometric constraints on the conditions of metamorphism in the Canigou massif, Pyrenees: implications for Hercynian geothermal gradients. *Journal of the Geological Society, London*, **151**, 987–997.

GUITARD, G. 1970. Le métamorphisme Hercynien mesozonal et les gneiss oeillets du massif du Canigou (Pyrenees Orientales). *Bureau de Recherches Géologiques et Minières Memoire*, **63**.

GONZÁLEZ-LODEIRO, F. 1983. La estructura del anticlinal del Ollo de Sapo. In: COMBA, J. A. (ed.) *Geología de España, Libro Jubilar de J.M. Ríos*. I. Instituto Geológico y Minero de España, Madrid, Spain.

HODGES, K. V. & SPEAR, F. S. 1982. Geothermometry, geobarometry and the Al_2SiO_5 triple point at Mt. Moosilauke, New Hampshire. *American Mineralogist*, **67**, 1118–1134.

HOISCH, T. D. 1990. Empirical calibration of six geobarometers for the mineral assemblage quartz + muscovite + biotite + plagioclase + garnet. *Contributions to Mineralogy and Petrology*, **104**, 225–234.

HOLLAND, T. J. B. & POWELL, R. 1990. An enlarged and updated internally consistent thermodynamic dataset with uncertainties and correlations: the system $\text{K}_2\text{O}-\text{Na}_2\text{O}-\text{CaO}-\text{MgO}-\text{MnO}-\text{FeO}-\text{Fe}_2\text{O}_3-\text{Al}_2\text{O}_3-\text{TiO}_2-\text{SiO}_2-\text{C}-\text{H}_2\text{O}_2$. *Journal of Metamorphic Geology*, **8**, 89–124.

— & POWELL, R. 1992. Plagioclase feldspars: Activity–composition relations based upon Darfen's quadratic formalism and Landau theory. *American Mineralogist*, **77**, 53–61.

HUTTON, D. H. W. & REAVY, R. J. 1992. Strike-slip tectonics and granite petrogenesis. *Tectonics*, **11**, 960–967.

JULIVERT, M. & MARTÍNEZ, F. J. 1987. The structure and evolution of the Hercynian foldbelt in the Iberian Peninsula. In: SCHAER, J. P. & RODGERS, J. (eds). *Comparative Anatomy of Mountain Ranges*. Princeton University Press, 65–103.

KRETZ, R. 1983. Symbols for rock-forming minerals. *American Mineralogist*, **68**, 277–279.

LANCELOT, J. R., ALLEGRET, A. & IGLESIAS PONCE DE LEÓN, M. 1985. Outline of Upper Precambrian and Lower Paleozoic evolution of the Iberian Peninsula according to U-Pb dating of zircons. *Earth and Planetary Science Letters*, **74**, 325–337.

LIESA, M. 1994. Relations of Hercynian metamorphism with magmatism and deformation in the Eastern Pyrenees. Implications for the Hercynian evolution. *Geologie en Mijnbouw*, **72**, 295–304.

MAHAR, E. M., BAKER, J. M., POWELL, R., HOLLAND, T. J. B. & HOWELL, N. 1997. The effect of Mn on mineral stability in metapelites. *Journal of Metamorphic Geology*, **15**, 223–238.

MARTÍNEZ, F. J. & RÖLET, J. 1988. Late Palaeozoic metamorphism in the northwestern Iberian Peninsula, Brittany and related areas in SW Europe. In: HARRIS, A. L. & FETTES, D. J. (eds) *The Caledonian–Appalachian Orogen*. Geological Society, Special Publication, **38**, 611–620.

—, CARRERAS, J., ARBOLEYA, M. L. & DIETSCH, C. 1996. Structural and metamorphic evidence of local extension along the Vivero fault coeval with bulk crustal shortening in the Variscan chain (NW Spain). *Journal of Structural Geology*, **18**, 61–73.

—, JULIVERT, M., SEBASTIÁN, A., ARBOLEYA, M. L. & GIL IBARGUCHI, J. I. 1988. Structural and thermal evolution of high-grade areas in the Northwestern parts of the Iberian massif. *American Journal of Science*, **288**, 969–996.

MARTÍNEZ-CATALÁN, J. R. 1985. Estratigrafía y estructura del Domo de Lugo (Sector Oeste de la zona Asturoccidental-Leonesa). *Corpus Geologicum Gallaeciae*, 2nd serie. La Coruña, Spain, 1-191.

MATTE, PH. 1968. La estructure de la virgation hercynienne de Galice (Espagne). *Geologie Alpine*, **44**, 155-280.

NEWTON, R. C. & HASELTON, H. T. 1981. Thermodynamics of the garnet-plagioclase- Al_2SiO_5 -quartz geobarometer. In: NEWTON, R. C., NAVROTSKY, A. & WOOD, B. J. (eds) *Thermodynamics of Minerals and Melts*, Vol. 1. Springer-Verlag, New York, 131-145.

OEN, I. S. 1970. Granite intrusion, folding and metamorphism in central northern Portugal. *Boletín Geológico y Minero, Spain*, **81**, 157-184.

— 1974. A note on lower pressure and higher pressure metamorphic belts in North Portugal. *Geologie en Mijnbouw*, **53**, 193-194.

OHMOTO, H. & KERRICK, D. 1977. Devolatilization equilibria in graphitic systems. *American Journal of Science*, **277**, 1013-1044.

PARGA PONDAL, I., MATTE, PH. & CAPDEVILA, R. 1964. Introduction à géologie de "l'Ollo de Sapo" formation porphyroïde anteesilurienne du nordouest de l'Espagne. *Notas y Comunicaciones Instituto Geológico Minero España*, **76**, 119-154.

PERCHUK, L. L. 1991. Derivation of a thermodynamically consistent set of geothermometers and geobarometers for metamorphic and magmatic rocks. In: PERCHUK, L. L. (ed.) *Progress in Metamorphic and Magmatic Petrology, A memorial volume in honor of D. S. Korzhinskiy*. Cambridge University Press, 93-112.

PÉREZ-ESTAÚN, A., MARTÍNEZ CATALÁN, J. R. & BASTIDA, F. 1991. Crustal thickening and deformation sequence in the footwall to the suture of the Variscan belt of northwest Spain. *Tectonophysics*, **191**, 243-253.

PINTO, M. S. & GIL IBARGUCHI, J. I. 1987. Revisión de datos geocronológicos e isotópicos de granitoides Hercínicos y ante-Hercínicos de la región Galaico-Castellana. *Memorias Museo Laboratorio mineralogía e geología Facultade de Ciencias do Porto*, 1. Oporto, Portugal, 171-186.

PITRA, P. & GUIRAUD, M. 1996. Probable anticlockwise P-T evolution in extending crust: Hlinsko region, Bohemian Massif. *Journal of Metamorphic Geology*, **14**, 49-60.

ponce de LEON, M. I. & CHOUKROUNE, P. 1980. Shear zones in the Iberian Arc. *Journal of Structural Geology*, **2**, 63-68.

POWELL, R. & HOLLAND, T. J. B. 1988. An internally consistent dataset with uncertainties and correlations: 3. Applications to geobarometry, worked examples and a computer program. *Journal of Metamorphic Geology*, **6**, 173-204.

PRIEM, H. N. A. & DEN TEX, E. 1984. Tracing crustal evolution in the NW Iberian Peninsula through the Rb-Sr and U-Pb systematics of Palaeozoic granitoids: a review. *Physics of the Earth and Planetary Interiors*, **35**, 121-130.

REAVY, R. J. 1989. Structural controls on metamorphism and syn-tectonic magmatism: The Portuguese Hercynian collision belt. *Journal of the Geological Society, London*, **146**, 649-657.

RECHE, J. & MARTÍNEZ, F. J. 1996. GPT: An Excel spreadsheet for thermobarometric calculations in metapelitic rocks. *Computers and Geosciences*, **22**, 775-784.

RIES, A. C. 1979. Variscan metamorphism and K-Ar dates in the Variscan fold belt of S Brittany and NW Spain. *Journal of the Geological Society of London*, **136**, 89-103.

SANTOS-ZALDUEGUI, J. F., SCHÄRER, U., GIL IBARGUCHI, J. I. & GIRARDEAU, J. 1996. Origin and evolution of the Paleozoic Cabo Ortegal ultra-mafic-mafic complex (NW Spain): U-Pb, Rb-Sr and Pb-Pb isotope data. *Chemical Geology*, **129**, 281-304.

SOULA, J. C., DEBAT, P., DERAMOND, J. & POUGET, P. 1986. A dynamic model of the Hercynian Pyrenees. *Tectonophysics*, **129**, 29-51.

VERNON, R. 1987. Growth and concentration of fibrous sillimanite related to heterogeneous deformation in K-feldspar-sillimanite metapelites. *Journal of Metamorphic Geology*, **5**, 51-68.

VIELZEUF, D. 1984. *Relations de phases dans le facies granulite et implications géodynamiques. L'exemple des granulites des Pyrénées*. PhD Thesis, Clermont University.

WICKHAM, S. M. & OXBURGH, E. R. 1987. Low-pressure regional metamorphism in the Pyrenees and its implications for the thermal evolution of rifted continental crust. *Philosophical Transactions of the Royal Society of London, A* **321**, 219-248.

WILLIAMS, M. L. & GRAMBLING, J. A. 1990. Manganese, ferric iron and the equilibrium between garnet and biotite. *American Mineralogist*, **75**, 886-908.

XU, G., WILL, T. M. & POWELL, R. 1994. A calculated petrogenetic grid for the system $K_2O-FeO-MgO-Al_2O_3-SiO_2-H_2O$, with particular reference to contact-metamorphosed pelites. *Journal of Metamorphic Geology*, **12**, 99-119.

YARDLEY, B. W. D. 1989. *An Introduction to Metamorphic Petrology*. Longman Scientific & Technical, Singapore.

ZWART, H. J. 1986. The Variscan geology of the Pyrenees. *Tectonophysics*, **129**, 9-27.

On the occurrence and characterization of ultrahigh-temperature crustal metamorphism

SIMON L. HARLEY

Department of Geology and Geophysics, University of Edinburgh, Kings Buildings, West Mains Road, Edinburgh, EH9 3JW, UK

Abstract: Ultrahigh-temperature (UHT) crustal metamorphism is a division of medium-pressure granulite facies metamorphism where peak temperatures of 900–1100°C have been attained at pressures in the range 7–13 kbar. The key indicators of UHT conditions are mineral assemblages involving combinations of sapphirine, garnet, aluminous orthopyroxene, cordierite, sillimanite, spinel and quartz in pelites and quartzites. Experimentally constrained and calculated FMAS and KFMASH petrogenetic grids involving these phases and additional osumilite and melt indicate that sapphirine + quartz is stable only at >1040°C in reduced rocks, that osumilite is restricted to >900°C for pressures greater than 6 kbar and has an ultimate stability limit of 9 kbar in FMAS, and that the orthopyroxene + sillimanite + quartz assemblage is restricted to pressures greater than 8 kbar in KFMASH. These criteria, coupled with the grids isoplethed for the $Mg/(Mg + Fe)$ of garnet and Al-content of orthopyroxene allow the peak pressure–temperature (P – T) conditions of several UHT occurrences to be defined and the post-peak P – T paths delineated.

UHT conditions are seldom determined from slowly cooled granulites using conventional geothermometry principally because of the propensity of Fe–Mg exchange thermometry to only record closure temperatures of 700–850°C. However, pressure-convergence calculations for several granulites with UHT mineral assemblages yield back-calculated mineral compositions that are consistent with temperatures of 950–1000°C prior to post-peak Fe–Mg re-equilibration. The best compositional indicator of UHT conditions remains the preservation of high Al_2O_3 contents (8–12 wt%) in orthopyroxene coexisting with garnet, sillimanite or sapphirine.

The P – T conditions and records preserved in the currently documented UHT localities and terranes are varied. Both types of post-peak P – T path isobaric cooling and isothermal decompression (ITD) are recorded from reaction textures in different UHT terranes, and several preserve very similar ITD histories that may reflect the final stage of collisional orogenesis. Although counter-clockwise and clockwise P – T paths have been proposed on the basis of textural observation for some terranes, the prograde P – T histories of most UHT areas are not known. Such information, and further experimental constraints on quartz-absent assemblages at UHT conditions, are of prime importance to interpret further this extreme form of crustal metamorphism.

In recent years the realm of metamorphic petrology has undergone a radical reappraisal, and what we now regard as being the pressure–temperature domain of metamorphism has been vastly expanded as its extremes have become increasingly recognized in the geological record. In terms of pressures and depths of metamorphism, the discovery of metamorphic coesite and, more recently, of metamorphic diamonds has led to the recognition of ultrahigh-pressure (UHP) metamorphism, with its major implications for how continental crust may behave during subduction, collision and thickening in convergent

plate regimes. Likewise, at the extremes of temperature, the reality of ultrahigh-temperature (UHT) regional metamorphism in which crustal rocks are subjected to temperatures of 900–1050°C at only moderate pressures (7–13 kbar) is now generally accepted by the metamorphic community. This too has important implications for the rheological and chemical behaviour of the continental crust during orogeny, its resilience to mantle-derived thermal pulses, and the tectonic situations in which such extreme thermal conditions can arise. Determination of the pressure–temperature (P – T) conditions and P – T histories of such granulites remains fundamental to evaluation of the tectonomagmatic models applied to high-grade gneiss terranes (e.g. Bohlen 1987, 1991; Ellis 1987; Sandiford 1989; Harley 1989, 1992; Loosveld & Etheridge 1990; Sandiford & Powell 1990, 1991).

Mineral abbreviations: Bt, biotite; Crd, cordierite; Crn, corundum; Grt, garnet; Kfs, K-feldspar; Ky, kyanite; L, liquid (granitic melt); Opx, orthopyroxene; Os, osumilite; Plag, plagioclase; Qz, quartz; Sil, sillimanite; SpL, spinel; Spr, sapphirine.

Table 1. *Garnet-orthopyroxene-sillimanite and sapphirine-spinel-quartz granulites*

Numbered reactions seen from textures: (1) $\text{Grt} = \text{Opx} + \text{Spr} + \text{Sil}$; (2) $\text{Grt} = \text{Opx} + \text{Spr} + \text{Crd}$; (3) $\text{Opx} + \text{Sil} = \text{Spr} + \text{Crd}$; (4) $\text{Grt} + \text{Sil} + \text{Qz} = \text{Spr} + \text{Crd}$; (5) $\text{Grt} + \text{Sil} = \text{Spr} + \text{Qz}$; (6) $\text{Grt} = \text{Opx} + \text{Spr} + \text{Crd}$; (7) $\text{Grt} + \text{Qz} = \text{Opx} + \text{Spr} + \text{Sil}$; (8) $\text{Grt} + \text{Qz} = \text{Spr} + \text{Qz}$; (10) $\text{Opx} + \text{Sil} = \text{Spr} + \text{Qz}$; (11) $\text{Opx} + \text{Sil} + \text{Qz} = \text{Spr} + \text{Qz}$; (12) $\text{Grt} + \text{Sil} (+ \text{Crd}) = \text{Spr} + \text{Qz}$; (13) $\text{Opx} (\text{or Crd}) + \text{Sil} = \text{Crd} + \text{Spr}$; (14) $\text{Grt} + \text{Sil} (+ \text{Crd}) = \text{Spr} + \text{Qz}$. Direction of reaction indicated by R (to the right) or L (to the left) Key to sources: 1a, Ellis *et al.* (1980); 1b, Motoyoshi & Matsueda (1984); 1c, Harley (1985); 2, Sandiford *et al.* (1987); 3, Morse & Talley (1971), Arima *et al.* (1986), Currie & Gittins (1988); 4, Arima & Smith (1987), Dawson *et al.* (1997); 5, Dawson & Smith (1984); 5, Dawson *et al.* (1997); 6a, Lal *et al.* (1987); 6b, Dasgupta *et al.* (1994); 6c, Dasgupta *et al.* (1995); 6d, Sengupta *et al.* (1995); 7a, Mohan *et al.* (1986); 7b, Raith *et al.* (1997); 8a, Kienast & Ouzegane (1987); 8b, Ouzegane & Bouzama (1996); 9a, Marakushev & Kudryavisev (1991); 10, Harley *et al.* (1985); 10, Harley *et al.* (1990); 11, Harley & Fitzsimons (1991); 12, Motoyoshi & Ishikawa, (1997); 13, Herd *et al.* (1986); 14, Kriegsman, (1991); 15, Droop & Bucher-Nurminen (1984); 16a, Droop (1989), Harris & Holland (1984); 16b, Hisada & Miyano (1996); 17, Lutts & Konanayeva (1968); 18, Kihle & Bucher-Nurminen (1992).

In this paper I will present a brief overview of UHT crustal metamorphism, including a description of some examples of UHT metamorphism on both regional and more local scales. I will also describe and evaluate the available mineral assemblage and thermobarometric constraints that allow the characterization of UHT metamorphism, and introduce some new constraints and approaches derived from recent experimental studies and models of reaction behaviour under UHT conditions. Although a number of UHT terranes and localities have now been documented, an undue reliance on cation partitioning geothermometers has in many cases led workers to report erroneously low peak temperature conditions for these examples. As a consequence, the peak temperature remains the key parameter to constrain when dealing with UHT metamorphism. This work outlines two approaches to temperature estimation and demonstrates how the P - T histories of UHT terranes can be determined through the judicious combination of reaction texture interpretations with improved petrogenetic grids developed from recent experiments. Of course, any such P - T history or 'path' only provides part of the information necessary to infer past tectonic settings and crustal evolution, and the question of whether the P - T record documents a continuous thermal and baric evolution or is instead the result of episodic overprinting in a punctuated history requires complementary and multi-technique geochronology. The latter aspect of the characterization of high-grade and UHT metamorphism is both broad and also specific to any given terrane, and will not be dealt with in general terms here.

Definition of UHT: The P - T field of interest

UHT metamorphism can be considered as a subdivision of the granulite facies, which itself is generally regarded as embracing metamorphic conditions of 3–15 kbar and 700–1000°C (Harley 1989, 1992). For the purposes of this work, but not entirely as a matter of convenience as will be seen later, UHT metamorphism is defined as crustal metamorphism that has occurred at peak conditions of greater than 900°C and at mid- to deep-crustal levels. The effective field of UHT metamorphism involves temperatures of 900–1100°C and pressures in the range 7–13 kbar.

Granulites have traditionally been divided into three baric types, largely based on the appearance of garnet in quartz-deficient and quartz-bearing metabasites. Hence, we can consider low-, medium- and high-pressure granulites

as an initial division of the facies (Green & Ringwood 1967). UHT granulites are generally medium-pressure granulites in the sense of Green & Ringwood (1967). Low-pressure granulites, such as those in Namaqualand and numerous other areas worldwide (e.g. Waters 1986, 1991; Clarke *et al.* 1989) are often referred to as high- T /low- P granulites and are the ultimate products of low-pressure regional metamorphism. Such granulite terranes certainly imply high transient geotherms (e.g. Loosveld & Etheridge 1990; Sandiford & Powell 1990) as characterized by their high field geothermal gradients of 45–55°C km⁻¹. However, the maximum temperatures attained in these terranes seldom exceed 850°C, even at depths equivalent to 5–6 kbar, and so these high- T /low- P granulite terranes are not examples of UHT metamorphism as defined herein. The mineral assemblage and reaction features of high- T /low- P terranes will only be discussed here where they bear upon problems of defining P - T conditions from spinel + quartz assemblages, which may also appear in definitive UHT terranes (Nixon *et al.* 1973; Lal *et al.* 1987; Sandiford *et al.* 1987; Sengupta *et al.* 1991), and in relation to osumilite stability relations.

Occurrence and distribution of UHT terranes and localities

Several examples of terranes that have experienced UHT regional metamorphism are now recognized. These are the Napier Complex of Antarctica (Dallwitz 1968; Sheraton *et al.* 1980, 1987; Ellis *et al.* 1980; Grew 1980; Harley 1985; Sandiford 1985); Wilson Lake, Labrador (Morse & Talley 1971; Arima *et al.* 1986; Currie & Gittins 1988); the Eastern Ghats of India (Grew 1982b; Lal *et al.* 1984, 1987; Dasgupta 1995); the In Ouzzal complex of Algeria (Kienast & Ouzegane 1987; Bertrand *et al.* 1992; Ouzegane & Boumaza 1996); the Labwor Hills of Uganda (Nixon *et al.* 1973; Sandiford *et al.* 1987); and the Sutam Block of the Aldan Shield, Siberia (Marakushev & Kudryavtsev 1965; Perchuk *et al.* 1985). These terranes are listed and key mineral composition, assemblage and textural features summarized in Table 1. A greater number of relatively isolated UHT localites or areas of restricted proven extent are also known (e.g. Karsakov 1973; Lutts & Kopaneva 1968; Harley *et al.* 1990; Motoyoshi & Ishikawa 1998), and will be considered here as these often preserve excellent evidence for assemblage and P - T evolutions. These localites or 'sub-areas' are also summarized in Table 1.

It should be noted that the age distribution of these terranes and localities demonstrates that UHT crustal metamorphism does not reflect the secular thermal evolution of the Earth in any simple way. Whilst the Napier Complex, Sipiwesk Lake, Sutam Block and possibly the Labwor Hills are Archaean in age, Proterozoic ages for UHT metamorphism are documented or inferred for many of the other terranes and localities listed in Table 1, and Phanerozoic UHT metamorphism has been documented at Rundvågshetta, Antarctica (Motoyoshi & Ishikawa 1998) and the Gruf Complex, Italy (Droop & Bucher-Nurminen 1984). It is not possible here to detail all the UHT occurrences, or to describe any one in full. The aim instead is to outline those key features that individually and collectively bear on the characterization and documentation of UHT crustal metamorphism, following an analysis of the principal constraints now available and being developed.

Pelite grids: key indicators of UHT metamorphism

The FMAS system

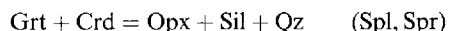
Mineral assemblages and reaction textures in sapphirine-, spinel- and orthopyroxene-sillimanite granulites have been instrumental in defining and demonstrating UHT metamorphism. In particular, petrogenetic grids involving mineral equilibria in the $\text{FeO}-\text{MgO}-\text{Al}_2\text{O}_3-\text{SiO}_2$ (FMAS) (Hensen 1971, 1986, 1987; Hensen & Green 1973; Grew 1980; Bertrand *et al.* 1991) and KFMAS(H) systems (Hensen 1977; Ellis *et al.* 1980; Grew 1982a; Hensen & Harley 1990; Audibert *et al.* 1995; Carrington & Harley 1995a, b; Holland *et al.* 1996) enable qualitative analysis of the changes in pressure or temperature implied by arrested symplectite and corona textures in these aluminous granulites.

Pioneering studies of the stability of $\text{Grt} + \text{Crd}$ assemblages and their limiting reactions (Hensen 1971; Hensen & Green 1971, 1972, 1973) identified a $\text{Spr} + \text{Qz}$ stability field at temperatures in excess of 1050°C and defined $\text{Opx} + \text{Sil} + \text{Qz}$ to occur at pressures beyond maximum cordierite stability conditions of $10-11$ kbar. However, these results conflicted with experiments in simpler systems which define a significantly lower-pressure maximum stability for anhydrous Mg-cordierite (Newton 1972). Furthermore, Annersten & Seifert (1981) produced $\text{Spl} + \text{Qz}$ as breakdown products of $\text{Opx} + \text{Sil}$ under the $P-T$ conditions where $\text{Spr} + \text{Qz}$ would be predicted from the Hensen

& Green (1973) experiments. As a consequence, the UHT conditions implied by $\text{Spr} + \text{Qz}$ and $\text{Opx} + \text{Sil} + \text{Qz}$ have been treated with some scepticism by many petrologists.

Recent experimental data and theoretical considerations now provide support for the general applicability of the Hensen & Green (1973) grid and its derivatives. Firstly, Hensen (1986) and Powell & Sandiford (1988) have shown that the grid and the experiments of Annersten & Seifert (1981) can be reconciled when the relative effects of f_{O_2} on spinel and sapphirine stability are taken into account. Experiments on the stability relations of sapphirine and H_2O - or CO_2 -bearing cordierite in FMAS and at low f_{O_2} (Bertrand *et al.* 1991) confirm that $\text{Grt} + \text{Crd} + \text{Sil} + \text{Qz}$ stability can extend to pressures as high as 11 kbar, consistent with calculations by Aranovich & Podlesskii (1989), and that $\text{Spr} + \text{Qz}$ is encountered only at temperatures above 1050°C .

The key to the FMAS grid, presented here in Fig. 1, is the location of the Spl -absent invariant point (hereafter referred to as $[\text{Spl}]$) that involves the phases Grt , Crd , Opx , Sil , Spr and Qz . The pressure position is largely controlled by the stability of $\text{Grt} + \text{Crd}$ relative to the higher pressure assemblage $\text{Opx} + \text{Sil} + \text{Qz}$. Hensen & Green (1973) placed the invariant points $[\text{Spl}]$ and $[\text{Opx}]$ at $P-T$ conditions of 9.5 ± 1 kbar, 1030°C and 8.1 ± 1 kbar, 1040°C respectively, in an approximate FMAS system in which cordierite was probably stabilized by H_2O and CO_2 , and garnet by minor Ca. Bertrand *et al.* (1991) determined similar pressure stability limits for cordierite under both H_2O - and CO_2 -bearing conditions, and placed the equivalent FMAS invariant points at 10.8 ± 1 kbar, 1040°C and 9.6 ± 1 kbar, 1060°C (Fig. 1). Recent calculations of the $P-T$ location of the reaction:



in the FMASH system with fully hydrated cordierite and using an internally consistent dataset (Berman & Aranovich 1996; Aranovich & Berman 1996; see curve AB96 in Fig. 2) place the reaction at $10.2-10.5$ kbar at temperatures appropriate to the incoming of $\text{Spr} + \text{Qz}$ at the $[\text{Spl}]$ point ($1000-1050^\circ\text{C}$). This vindicates the experimental work, and also predicts mineral compositions near $[\text{Spl}]$ (X_{Mg} of $\text{Grt} = 60$, c. 9% Al_2O_3 in Opx) that are in reasonable agreement with predictions from natural assemblages (Harley 1985; Hensen & Harley 1990).

Hensen (1987) placed the FMAS $[\text{Qz}]$ point at c. $920-950^\circ\text{C}$ and $8-9$ kbar from topological and natural assemblage constraints. Reactions

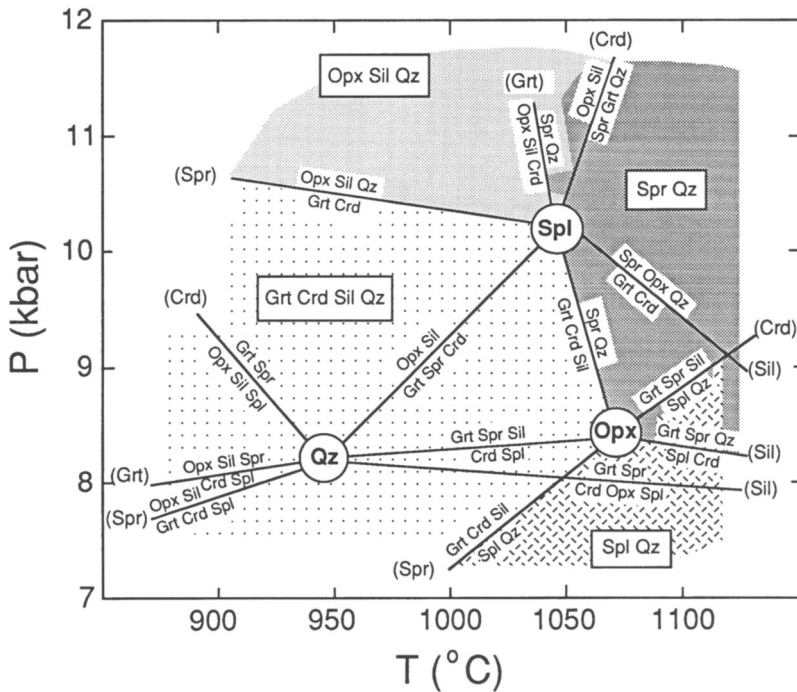


Fig. 1. P - T diagram of the model FMAS system grid for low f_{O_2} pelites, modified after Hensen & Green (1973), Hensen & Harley (1990) and Bertrand *et al.* (1991). See text for discussion of positioning of invariant points [Spl], [Opx] and [Qz] and uncertainties on the pressure location of the equilibria. Fields of key FMAS assemblages ($\text{Spr} + \text{Qz}$, $\text{Opx} + \text{Sil} + \text{Qz}$, $\text{Spl} + \text{Qz}$ and $\text{Grt} + \text{Crd} + \text{Sil} + \text{Qz}$) are distinguished by shading. Note that Crd involved in those equilibria that form the experimental basis for this grid is likely to have contained variable H_2O and CO_2 .

extending from this point to the other, higher P or T points in FMAS are critical for the interpretation of mineral assemblages and reaction textures involving Grt, Opx, Sil, Spr, Crd and Spl in many examples of quartz-deficient but nevertheless UHT gneisses. The precise locations of this point and the related Qz-absent univariant lines are, however, not yet experimentally determined.

The KFMASH system: osumilite stability

The FMAS results summarized above are for experiments in systems where a free fluid phase was probably present and the Crd was either fully hydrated or had maximum channel occupancy of H_2O and CO_2 . In hydrous systems with additional K_2O (KFMASH) the presence of melt is inescapable, and the phase relations will be largely determined by melt-bearing equilibria. Recent KFMASH experimental studies of biotite dehydration melting (Carrington & Harley 1995a) and the determination of osumilite

stability relations in KMAS (Motoyoshi *et al.* 1993) and KFMASH (Audibert *et al.* 1995; Carrington & Harley 1995b) now provide a useful framework for characterizing UHT assemblages formed at temperatures between 900 and 1050°C (e.g. Ellis *et al.* 1980; Arima & Gower 1991).

The KFMASH grid of Carrington & Harley (1995a) for equilibria involving Bt, Grt, Crd, Opx, Sil, Os, Qz, Kfs and L is presented in simplified form in Fig. 2, and will be used as a basis for evaluating mineral compositional variations in later sections (Fig. 4). A KFMAS(H) grid produced from combining this work with the higher-temperature Spr-bearing but Bt-absent experiments of Audibert *et al.* (1995), modified from Carrington & Harley (1995b) in the light of calculations by Holland *et al.* (1996), is presented in Fig. 3. An important feature of these grids is the constraints they place on the stability of osumilite. For pressures of greater than 6 kbar, the Os + Grt assemblage is restricted to temperatures of $>900^\circ\text{C}$ in KFMASH (Fig. 3a). The ultimate

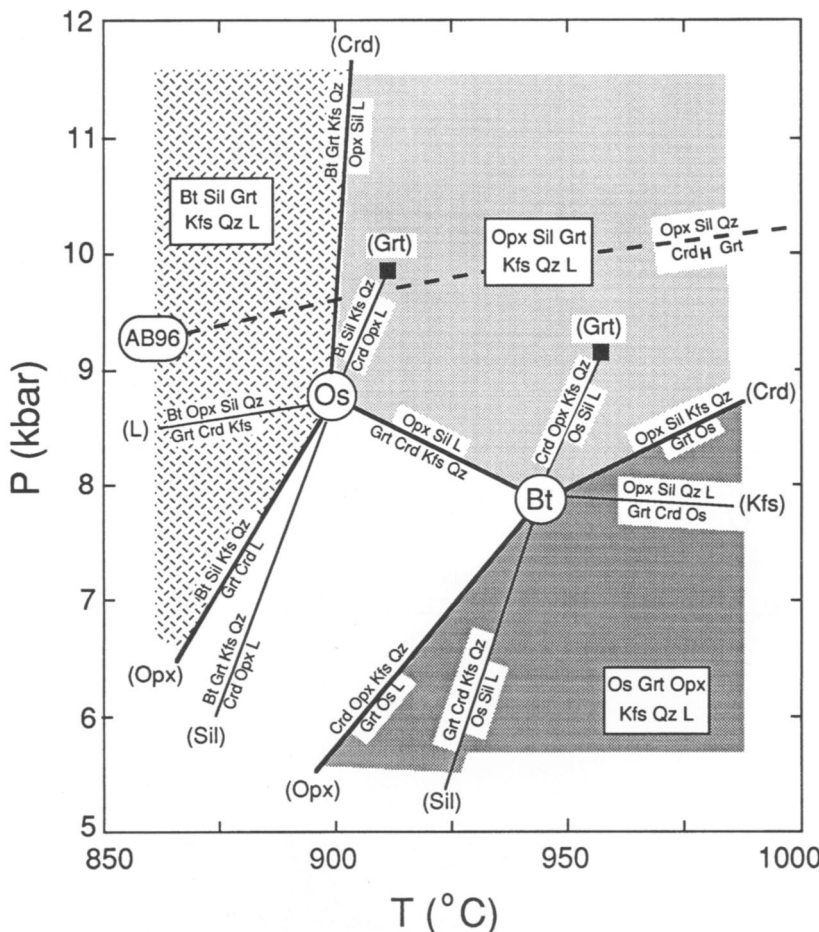
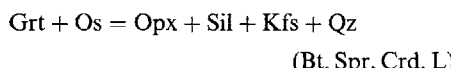
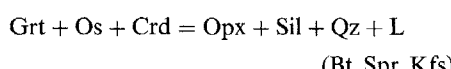


Fig. 2. P - T diagram of the KFMASH system grid involving reactions between Bt, Grt, Sil, Crd, Opx, Os, Qz, Kfs and L. This is modified slightly from Carrington & Harley (1995a) in light of the calculations of Holland *et al.* (1996). The dashed curve AB96 is the calculated position if the breakdown of fully hydrated Crd in FMASH according to Aranovich & Berman (1996). Important assemblage fields are distinguished by shading. Note the restriction of Os + Grt KFMASH assemblages to the low- P /high- T part of the grid, and of Opx + Sil + Qz to pressures greater than c. 8 kbar.

pressure stability of Os + Grt in KFMAS is limited to less than c. 9 kbar at 950–1050°C by the reaction (Fig. 3a):

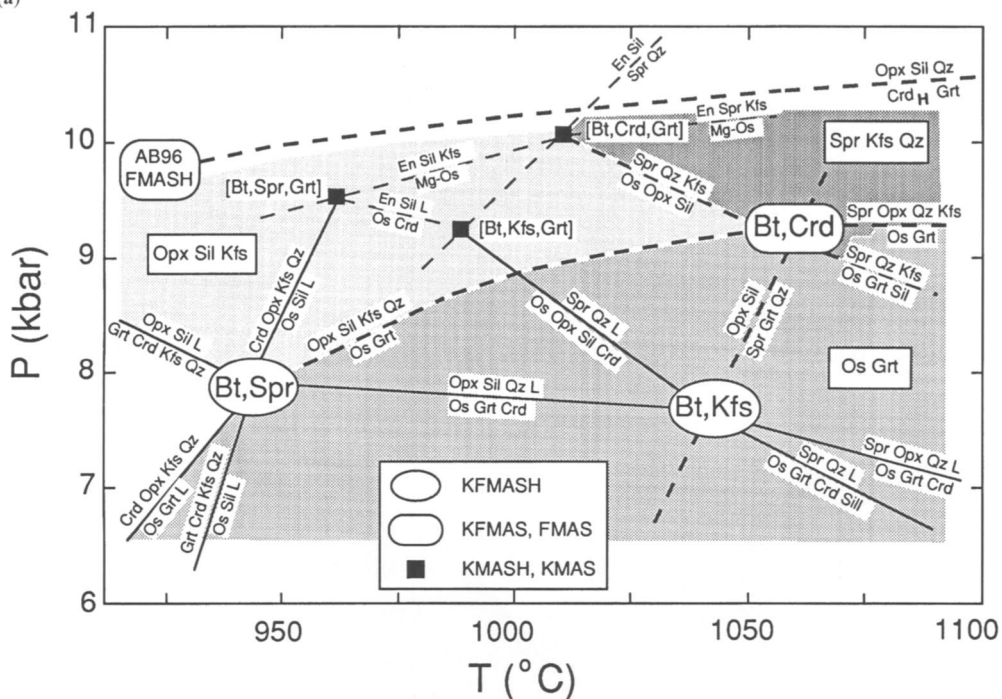


and in the presence of melt (in KFMASH) Os + Grt + Crd assemblages are restricted to less than c. 7.5–8 kbar by the non-degenerate reaction (Fig. 3a):

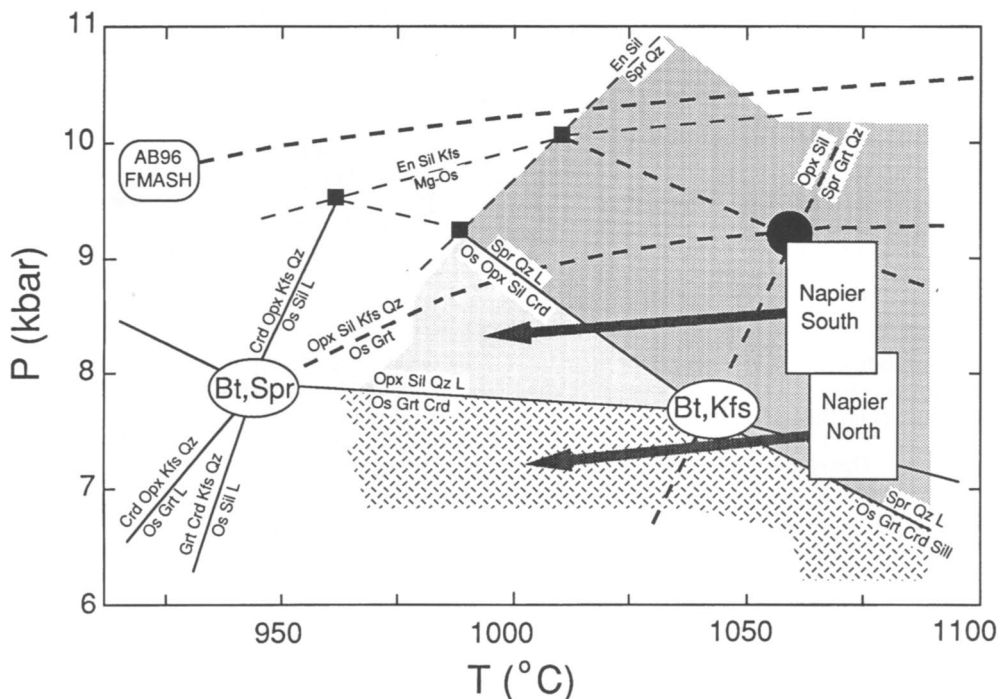


These pressure-sensitive equilibria have been successfully used to elucidate the pressures of post-peak near-isobaric cooling (IBC) in the Napier Complex (Audibert *et al.* 1995; Carrington & Harley 1995b), and verify the NNE to SSW pressure gradient inferred in earlier work (Sheraton *et al.* 1980; Harley 1985; Hensen & Harley 1990). IBC at less than 8 kbar is inferred for those parts of the Napier Complex where Grt + Crd coronas form on Spr + Qz and where Os + Grt is stable, whereas higher pressures (8–10 kbar) can be deduced for areas where Opx + Sil coronas form on Spr + Qz and where the assemblage Opx + Sil + Kfs + Qz occurs in preference to

(a)



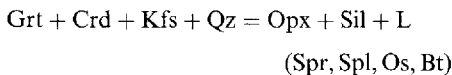
(b)



Os + Grt, as shown in Fig. 3b. The grids can also constrain the *P-T* conditions and histories of other UHT terranes from which Os or its breakdown products have been reported. For example, the former stability of Os with Opx + Sil + Qz and Spr at various localities in the northern domain of the Eastern Ghats (Lal *et al.* 1987; Lal 1997) indicates peak pressures of >8–10 kbar.

The KFMASH system: biotite dehydration melting and garnet–cordierite stability

The grid of Fig. 2, based on the experimental results of Carrington & Harley (1995a) and the calculations of Holland *et al.* (1996), also forms a useful framework for interpreting quartz-bearing mineral assemblages in the hitherto elusive temperature range 875 to 975°C. Firstly, in this simple system in which Bt is not stabilized by additional components such as Ti and F (e.g. Mouri *et al.* 1996), Opx + Sil + Qz assemblages will be restricted to pressures greater than 7.5 kbar, and to temperatures greater than 900°C if melting has taken place (e.g. Long Point (Harley & Fitzsimons 1991); Forefinger Point (Harley *et al.* 1990); Palni Hills (Raith *et al.* 1997)). Melting at lower pressures results in Grt + Crd assemblages that may be stable to significantly lower temperatures (800–850°C) and hence do not necessarily imply UHT. Secondly, Carrington & Harley (1995a) and Carrington (1995) deduced that the (Spl, Spr) reaction controlling the upper stability limit of Grt + Crd in the KFMASH system is of the form:



rather than being as written for (Spl, Spr) in the FMAS system described above. The Crd in this reaction is hydrous but H_2O -undersaturated, buffered by the presence of granitic melt down to a minimum H_2O content dictated by the partitioning behaviour of H_2O between Crd–L ($D_w = 4$; Carrington & Harley 1996). This melt-bearing KFMASH reaction has a negative slope

and occurs at 8.9 to 7.8 kbar (each ± 0.5 kbar) in the temperature range 900–950°C (Fig. 2). Crd H_2O contents along this reaction calculated using Crd–L volatile partitioning data (Carrington & Harley 1996), vary from 1.1 to 0.5 wt% with increasing temperature. Comparison of the experimental data obtained by Carrington & Harley (1995a) with the higher-temperature KFMASH experiments of Audibert *et al.* (1995) led Carrington & Harley (1995b) to perform cross-calibration experiments to test the pressures reported in the latter study. Compatibility between the experimental datasets is achieved if the pressures of the high-*T* osumilite grid of Audibert *et al.* (1995) are corrected downwards by c. 2 kbar, as presented here in Fig. 3. Holland *et al.* (1996) have extracted thermodynamic data on osumilite and developed a calculated grid broadly consistent with the KFMASH experiments and grid of Carrington & Harley (1995a, b). The internally consistent dataset produced by Holland *et al.* (1996) also indicates that the pressure positions of reactions determined by Audibert *et al.* (1995), and by Motoyoshi *et al.* (1994) in KMAS, are 1.5–2 kbar too high.

As shown in Fig. 2, the pressures at which volatile-undersaturated cordierite and garnet react to form Opx + Sil-bearing assemblages (with melt) in the KFMASH system are lower than those defined by Hensen & Green (1973) for FMAS(H) but are still near or above 8 ± 0.5 kbar, in a CO_2 -free system. These pressures are also 0.7–2 kbar lower than the position of the FMASH (Spl, Spr) reaction as calculated by Aranovich & Berman (1996) using fully hydrated Crd (Fig. 2). The KFMASH results imply that the analogue of the [Spl] point in this system, involving Grt, Opx, Sil, Qz, Spr and CO_2 -free Crd coexisting with a KFMASH silicate melt, will occur at pressures lower than those in the FMAS(H) system but still at ultrahigh temperature (1050°C; Audibert *et al.* 1995). By the same reasoning, the position of any equivalent to the [Qz] point (Fig. 1) in KFMASH (i.e. [Bt, Qz]) is likely to be shifted to lower pressures than those preferred by Hensen (1987) for this point in FMAS(H). Experiments

Fig. 3. (a) KFMASH *P-T* diagram showing the relation of the lower-*T*, Spr-absent equilibria focused on invariant point [Bt, Spr] (labelled [Bt] in Fig. 2) to the higher-*T* equilibria involving Spr with Os determined by Audibert *et al.* (1995). This grid is modified from Carrington & Harley (1995b) in light of revised estimates of Mg-osumilite (Mg–Os) stability by Holland *et al.* (1996). Note the presence of different sub-systems, denoted by distinctive invariant point symbols and line styles. Some key assemblages are distinguished by shading. Original experimental data are from Chatterjee & Schreyer (1972), Motoyoshi *et al.* (1993), Audibert *et al.* (1995) and Carrington & Harley (1995b). (b) The same grid as in (a) but simplified to illustrate the stability range of Spr + Qz in the presence of melt (L) and the effect of IBC at higher pressures (greater than the pressure of (Bt, Spr, Kfs) reaction) in the southern part of the Napier Complex compared with the northern part of the Complex.

are currently in progress to define the key reactions involving biotite dehydration and sapphirine stability in the silica-undersaturated portion of KFMASH, but the stability of the [Bt, Qz] invariant point is not yet established.

Improvements on pelite grids: isoplethed diagrams and their applications

The utility of the FMAS and KFMASH pelite grids described above is vastly improved if they can be contoured for variations in mineral compositions along the univariant reactions and in the intervening divariant fields. Such isopleth diagrams, and the related pseudosections developed by Hensen (1971) to depict the incoming and outgoing of assemblages for specific rock compositions, are powerful tools for the definition of P - T conditions and interpretation of reaction histories (Hensen & Green 1973; Hensen 1986, 1987; Powell & Sandiford 1988; Aranovich & Podlesskii 1989; Hensen & Harley 1990; Aranovich & Berman 1996). For example, as noted in the preceding section, Aranovich & Berman (1996) have recently calculated the X_{Mg} of garnet in the Grt + Opx + Crd + Qz divariant field in FMASH and found that it has an X_{Mg} of 60–62 at the UHT conditions of the (Spl, Spr) reaction.

The P - T diagrams of Fig. 4 are isoplethed with the X_{Mg} of Grt (Figs 4a and b) and Opx (Fig. 4b), and the X_{Al} of Opx (Fig. 4c) in key assemblages defined from the experiments of Carrington & Harley (1995a). These diagrams have been constructed using the Opx and Crd X_{Mg} compositional data reported by Carrington & Harley (1995a) for various P - T conditions and in the KFMASH assemblages (all with excess Kfs and L) Grt + Opx + Sil + Qz, Grt + Opx + Crd + Qz and Grt + Crd + Sil + Qz. These data have been combined with existing Fe–Mg partitioning thermometers to calculate the X_{Mg} of coexisting garnet at these P - T points, a procedure adopted because Carrington & Harley (1995a) were unable to obtain consistent and reproducible garnet X_{Mg} data in their experiments. The Fe–Mg partitioning relations used were Harley (1984a) for Grt–Opx and Perchuk *et al.* (1985) for Grt–Crd. A total of 35 Grt X_{Mg} values extending over the P - T ranges 5–12.8 kbar and 875–1000°C were calculated using this approach, and in 12 of these cases the results were cross-checked using both Fe–Mg partitioning relations and found to be mutually consistent. Contours for X_{Mg} were then fitted to the calculated Grt data and extrapolated to be internally consistent along the relevant bounding

univariant reactions (Fig. 4a and Grt isopleths in Fig. 4b). For example, the Grt isopleths in the Bt + Sil + Grt field of Fig. 4a were inserted to be consistent with the strongly pressure-sensitive variations in X_{Mg} along the Bt melting curves (Os, Opx) and (Os, Crd). In a second calculation cycle, Opx X_{Mg} values were interpolated between the starting compositional data using the calculated Grt isopleths to produce the Opx isopleths of Fig. 4b. The Al isopleths for Opx in Grt + Qz assemblages with Crd or Sil (Fig. 4c) were then calculated using the starting and interpolated Opx X_{Mg} values obtained at various P - T conditions coupled with the P - T dependent Al-solubility relationship inherent in the thermobarometer of Harley & Green (1982).

The resultant X_{Mg} isopleths are precise to ± 2 units, equivalent to pressure uncertainties of ± 0.5 –0.7 kbar. The actual values at a given P - T depend on the Fe–Mg partitioning relationship chosen. If the thermometer of Lee & Ganguly (1988) is used instead of Harley (1984a) the calculated Grt X_{Mg} values are lower by approximately 2 units at any given P - T condition, and any Opx X_{Mg} values then calculated using the Grt compositions will be lower by *c.* 2 units. In effect, the isopleths would be shifted up-pressure by *c.* 0.5–0.7 kbar. The Al isopleths for Opx (Fig. 4c) are precise to 15 Al units (or 0.015 in terms of X_{Al}), equivalent to 15–20°C, but are dependent upon the positions of the Opx X_{Mg} isopleths and will be displaced to higher T if the Opx X_{Mg} is actually lower than the values used in the calculations at a given P - T . Slightly lower Al contents (by 10 units or 0.01 in terms of X_{Al}) are also calculated at the higher- T conditions if the Harley (1984b) thermobarometer is used rather than that of Harley & Green (1982).

As would be expected, Fe-richer Bt + Grt + Sil + Qz assemblages begin melting at lower temperatures than Mg-richer ones (Fig. 4a). Grt isopleths in the lower-pressure Crd-bearing assemblages have positive dP/dT slopes, consistent with recent calculations (e.g. Aranovich & Berman 1996). Isopleths in the Grt + Opx + Sil field are negative at $T < 975^\circ\text{C}$ (Fig. 4a), and as a consequence isobaric increases in T at $P > 8$ kbar will produce garnet at the expense of Opx + Sil in the melt-bearing assemblage. The X_{Mg} of Grt at the [Os] invariant point is 60 ± 2 , and that at the incoming of Os (the [Bt] point) is near 55. Along the key reaction (Os, Bt) that joins these points and across which Grt + Crd breaks down to Opx + Sil in KFMASH, Grt decreases in X_{Mg} with increasing temperature, and the coexisting Opx would have X_{Mg} decreasing from 75 to 69 and Al_2O_3 increasing from 7.5 to 9 wt%. The steep dP/dT slopes of the Al

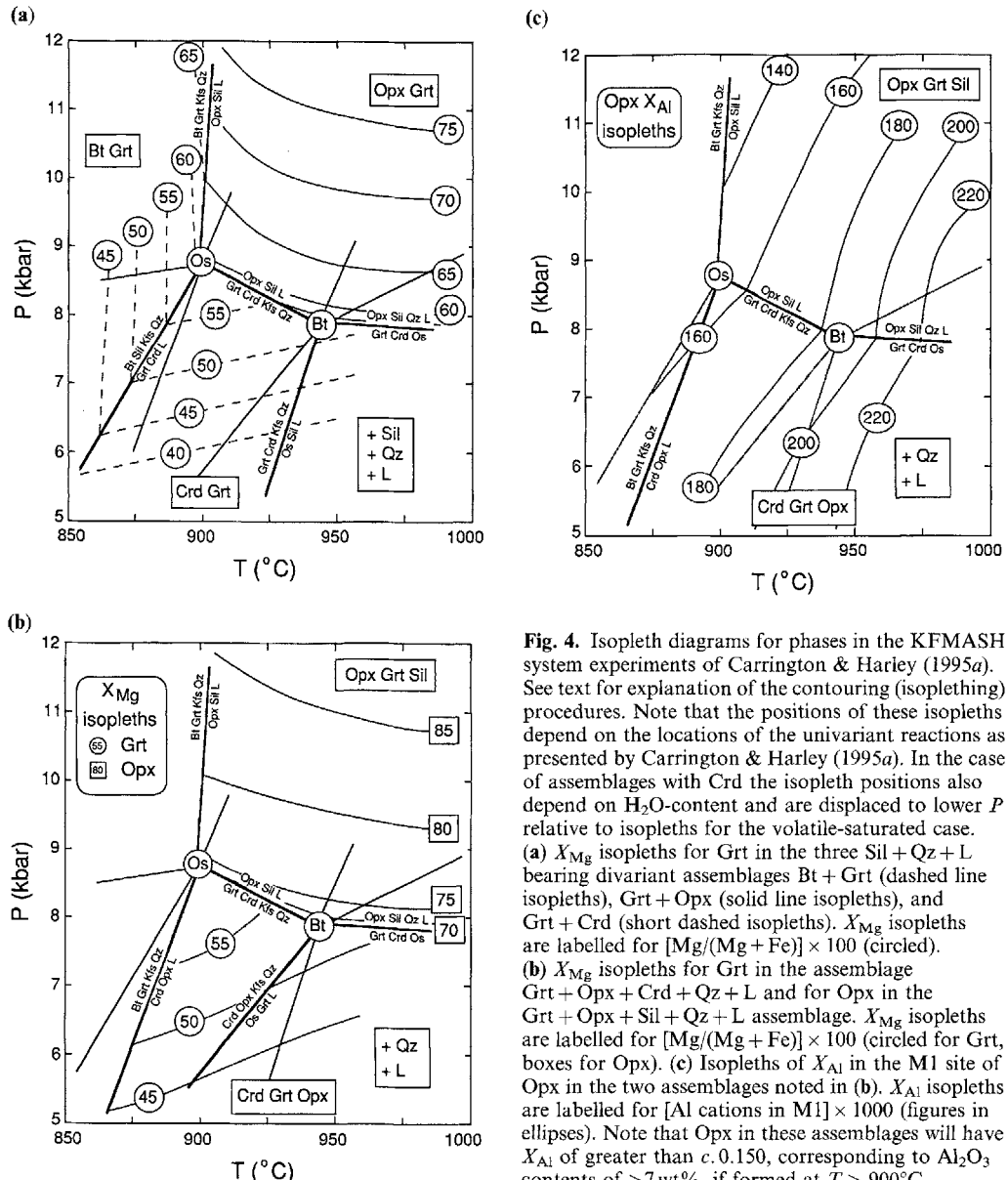


Fig. 4. Isopleth diagrams for phases in the KFMASH system experiments of Carrington & Harley (1995a). See text for explanation of the contouring (isoplething) procedures. Note that the positions of these isopleths depend on the locations of the univariant reactions as presented by Carrington & Harley (1995a). In the case of assemblages with Crd the isopleth positions also depend on H_2O -content and are displaced to lower P relative to isopleths for the volatile-saturated case.

(a) X_{Mg} isopleths for Grt in the three $\text{Sil} + \text{Qz} + \text{L}$ bearing divariant assemblages $\text{Bt} + \text{Grt}$ (dashed line isopleths), $\text{Grt} + \text{Opx}$ (solid line isopleths), and $\text{Grt} + \text{Crd}$ (short dashed isopleths). X_{Mg} isopleths are labelled for $[\text{Mg}/(\text{Mg} + \text{Fe})] \times 100$ (circled).

(b) X_{Mg} isopleths for Grt in the assemblage $\text{Grt} + \text{Opx} + \text{Crd} + \text{Qz} + \text{L}$ and for Opx in the $\text{Grt} + \text{Opx} + \text{Sil} + \text{Qz} + \text{L}$ assemblage. X_{Mg} isopleths are labelled for $[\text{Mg}/(\text{Mg} + \text{Fe})] \times 100$ (circled for Grt, boxes for Opx).

(c) Isopleths of X_{Al} in the M1 site of Opx in the two assemblages noted in (b). X_{Al} isopleths are labelled for $[\text{Al cations in M1}] \times 1000$ (figures in ellipses). Note that Opx in these assemblages will have X_{Al} of greater than c. 0.150, corresponding to Al_2O_3 contents of >7 wt%, if formed at $T > 900^{\circ}\text{C}$.

isopleths in Fig. 4c confirm that high equilibrium Al_2O_3 contents in Opx (e.g. >7–8 wt%) are excellent indicators of UHT conditions, notwithstanding the discrepancies between the various datasets and approaches to calculating these isopleths.

The isopleths in Fig. 4 can be compared with calculations recently presented by Holland *et al.* (1996) and Aranovich & Berman (1996). Holland *et al.* (1996), using an updated Thermocalc dataset, calculate Grt and Opx X_{Mg} values near

the two invariant points that are in good accord with, though slightly more magnesian than, the X_{Mg} values indicated here. For example, Grt at [Os] and [Bt] has X_{Mg} of c. 63 and 61 respectively (Holland *et al.* 1996). Aranovich & Berman (1996) calculate a high-pressure stability limit for Grt + fully hydrated Crd that lies 0.7 kbar higher at 900°C and 1.9 kbar higher at 940°C than the limits given here. This discrepancy is attributable to the H_2O -undersaturated character of Crd in the KFMASH melt-bearing

system, a factor that also affects the comparative positions of the X_{Mg} isopleths for Crd and hence Grt and Opx. As fully hydrated Crd of any given X_{Mg} will also be stabilized to higher pressure relative to the fluid-undersaturated case, it follows that X_{Mg} isopleths calculated by Aranovich & Berman (1996) for Crd-bearing assemblages will be displaced to higher pressures by between 0.7 and 1.5 kbar relative to those in Fig. 4. Hence, the Grt X_{Mg} at the P - T conditions used here for the [Os] point would be *c.* 54, and that at the [Bt] point only *c.* 43, if the FMASH calibration of Aranovich & Berman (1996) is applied. Like Holland *et al.* (1996), Aranovich & Berman (1996) calculate Opx Al_2O_3 contents of between 6 and 7 wt% at these points, lower than the contents given in Fig. 4c but consistent with the conclusion that highly aluminous Opx (with 8–12 wt% Al_2O_3) in pelitic gneisses is indicative of UHT metamorphism.

The contoured KFMASH grid can be used to estimate P - T conditions for garnet-bearing UHT assemblages reported in the literature. Qz-bearing and Qz-deficient Grt + Opx + Sil assemblages from several areas summarized in Table 1 contain garnets with uncorrected X_{Mg} values of 60 or greater, and also preserve high initial Al_2O_3 contents (8–12 wt%) in early orthopyroxene. These compositional features are consistent with UHT metamorphic conditions of 8–9 kbar and $>950^{\circ}\text{C}$ (Figs 4a, c). Grt ($X_{\text{Mg}} = 70$) + Opx + Sil assemblages from Long Point (Harley & Fitzsimons 1991; see below) would imply P - T conditions of >10 kbar and 1000°C on the basis of Fig. 4, and 11 kbar/ 1060°C using the calculations of Aranovich & Berman (1996) and assuming unit water activity.

Pitfalls and problems with pelitic grids: spinel and f_{O_2} considerations

A key feature of a number of UHT terranes noted in Table 1, including Labwor Hills (Nixon *et al.* 1973; Sandiford *et al.* 1987), Wilson Lake (Morse & Talley 1971; Arima *et al.* 1986; Currie & Gittins 1988) and the Eastern Ghats northern region (e.g. Lal *et al.* 1987; Sengupta *et al.* 1991; Dasgupta *et al.* 1995) is the stability of spinel in quartz-bearing assemblages. These assemblages generally contain Fe–Ti oxide phases (magnetite, hemoilmenite, hematite) rather than rutile, may coexist with sapphirine, cordierite and orthopyroxene, but almost invariably lack garnet. In particular, the assemblage Opx + Sil + Spl + Qz, recognized at Labwor Hills and in the Eastern Ghats (here also denoted (Spr, Grt, Crd)) is not allowable in the 'low f_{O_2} ' grid

of Hensen (1971, 1986) but is stabilized in the inverse topologies presented for 'high f_{O_2} ' conditions (Hensen 1986; Powell & Sandiford 1988), consistent with experimental data at high f_{O_2} (Annersten & Seifert 1981). This arises principally because the additional components in spinel, particularly Zn and Fe^{3+} , stabilize Spl + Qz to higher pressures relative to Grt + Crd and other FMAS and FAS assemblages (Hensen 1986; Harley 1986; Shulters & Bohlen 1989). Ultimately this will lead to a topological inversion, where the formerly metastable invariant points become stable, when the stability field of an intervening assemblage collapses. In the case of oxidation the stability fields of Opx + Sil + Qz and Spl + Qz converge and overlap at the expense of the intervening Grt + Crd + Sil + Qz field, and Spr + Qz also migrates to lower temperatures.

The precise nature of these inversions and their importance depends on the partitioning of the minor components (Zn, Cr and Fe^{3+}) between spinel and the other ostensibly FMAS phases. In the case of Fe^{3+} the situation is not straightforward, as emphasized by Hensen (1986) and Powell & Sandiford (1988), because appreciable Fe^{3+} can enter sapphirine, sillimanite and orthopyroxene as well as stabilizing hematite as f_{O_2} increases. In addition, spinel is often observed to have undergone decomposition (granular exsolution) into polyphase domains of $\text{spinel}_{\text{ss}} + \text{magnetite}_{\text{ss}} + \text{hemoilmenite} + \text{corundum}$. In these circumstances it is extremely difficult to reconstruct the initial, UHT, spinel composition and hence determine the correct partitioning behaviour of Fe^{3+} between spinel and the other phases (e.g. sapphirine). Integration of former spinel compositions using image analysis usually shows that its composition was far removed from the FMAS system and hence not amenable to treatment either using simple-system grids or thermodynamic databases. For example, Dasgupta *et al.* (1995) reconstructed an initial spinel composition of $\text{Mt}_{50}(\text{Spl} + \text{Hc} + \text{Gh})_{50}$ for spinel in a Spl + Opx + Qz granulite from the Eastern Ghats for which P - T conditions of approximately 950°C and >9 kbar have been deduced.

As a consequence of these effects and uncertainties it is not reasonable to infer UHT metamorphic conditions solely on the basis of Spl + Qz and even Spl + Spr + Qz assemblages in oxidized rock types, a point discussed elegantly by several workers (Hensen 1986; Powell & Sandiford 1988; Waters 1991) and recently emphasized for the sole to the Semail ophiolite (Gnos & Kurz 1994). Nevertheless, the oxidized Opx + Sil + Spl + Qz assemblage has proven to

be a UHT one when considered along with all the other mineral assemblage evidence in Labwör Hills and the Eastern Ghats.

Constraints from other rock types

When searching for other unequivocal evidence for UHT mid- to deep-crustal metamorphism it is important to restrict the evidence to that which is derived from rocks that are not of igneous parentage. Such orthogneisses may preserve partially recrystallized but inherited high-*T* igneous phases (e.g. hypersolvus feldspars, sub-calcic ferroaugites and pigeonite) that have no direct relation to the grade of metamorphism. Two distinctive rock types that have potential to record UHT signatures are meta-ironstones and calc-silicates.

Metamorphic pigeonite and sub-calcic pyroxene have been reported in quartz–magnetite ironstones from the Napier Complex (Grew 1982a; Sandiford & Powell 1986; Harley 1987), where their high X_{Mg} values of 38–44, obtained after reintegration of exsolved phases, imply temperatures (980–1030°C) that are entirely consistent with those deduced from pelite phase relations and from thermobarometric retrieval calculations (see below). Likewise, relatively magnesian ($X_{\text{Mg}} = 30$) but Mn-bearing metamorphic pigeonite from Scourie (Barnicoat & O'Hara 1979) provides some of the best evidence for peak temperatures in excess of 900°C in the mainland Lewisian of NW Scotland.

The assemblage wollastonite + scapolite, occurring along with other phases such as Plag, grossular-rich Grt, Qz and calcite in calc-silicate granulites, also has some potential as a UHT indicator (Harley & Buick 1992). This is only the case, however, if the scapolite is highly calcic ($\text{EqAn} > 88$) and if the pressures of metamorphism can be independently determined to be greater than 8 kbar. Even with these additional constraints, few granulite terranes have yet been shown to preserve the buffering assemblages that are required in order to fully define T – X_{CO_2} conditions from wollastonite–scapolite calc-silicates. Buffering assemblages of wollastonite–scapolite–calcite–grossular–quartz in calc-silicates of the Rauer Group (Harley & Buick 1992) only require temperatures of c. 870°C at 7–8 kbar and hence fall short of the UHT field for the preferred pressures. However, Dasgupta (1993) deduced peak temperatures in excess of 900°C (and hence UHT conditions) from similar calc-silicate assemblages in the Eastern Ghats on the assumption that they equilibrated at 9 kbar, a

pressure obtained from nearby pelites. Clearly there is much scope for further investigation of calc-silicate equilibria under UHT conditions.

Thermobarometry and retrieval calculations

As noted in the Introduction, the reliable calculation of the P – T conditions is a prerequisite for any further understanding of the processes involved in metamorphism. Fe–Mg exchange thermometers have been extensively applied to granulites and many workers have used them with varying success to infer peak, or near-peak, temperatures in upper-amphibolite to lower-granulite terranes that have, from independent mineral assemblage criteria, experienced temperatures of 700–850°C. The applicability of Fe–Mg thermometers to UHT granulite terranes is, however, fraught with problems. Reliance on this approach has led to the popular notion that most granulites formed at 750–850°C (Bohlen 1987, 1991), and many workers may still be of the view that UHT metamorphism is an incidental oddity. Mineral thermobarometry is inherently unreliable for UHT metamorphism because of post-peak diffusional exchange and closure effects (Harley 1984b; Frost & Chacko 1989; Perkins 1990) that lead to both mismatch and feedback (Harley 1989) between temperature and pressure estimates. This can, however, be used to advantage to estimate peak temperature through retrieval, or convergence, calculations.

The principle underlying retrieval calculations as applied to thermobarometers is explained by Fitzsimons & Harley (1994) and Pattison & Begin (1994). If Fe–Mg exchange between two phases continues subsequent to the cessation of effective Al exchange or net-transfer, then the pressures calculated using an Al barometer in which the activities of the components also depend on Mg/Fe will diverge from pressures calculated using independent equilibria that are not affected by such feedback. The independent pressure estimator, which may be a geobarometer or an appropriate grid constraint, is termed the reference pressure. An important feature seen in coherent sets of data from single terranes is that the difference between the reference pressure and that estimated by Grt–Opx Al barometry increases as the temperature calculated using the Grt–Opx Fe–Mg exchange thermometer decreases: the Grt–Opx Al barometer pressure estimates are closure pressures resulting from the feedback effect (Fitzsimons & Harley 1994).

Retrieval and convergence tests then involve back-calculating the Fe–Mg compositions of the

participating phases until the pressure estimate (e.g. Grt–Opx Al barometry) overlaps with the reference pressure for that sample or group of samples. The ‘retrieved’ or ‘back-exchanged’ mineral compositions may then be used to calculate the temperature at which Al transfer ceased, which may be a reasonable estimate of the peak metamorphic temperature. Mineral compositional data are required from several

samples with differing mineral modes and grain sizes and it is very important to use such a suite of samples to enable the internal consistency of the method to be tested and realistic uncertainties placed on the retrieved peak temperature estimates. Application of such retrieval calculations to several UHT terranes, and to other granulites, confirms that a high content of Al_2O_3 in orthopyroxene (8–12 wt%) is one of the most reliable indicators of high metamorphic temperatures, a point emphasized by Hensen (1987) and Harley (1989) and noted above in relation to the contoured phase diagrams.

Retrieval calculations have been performed on 26 Grt + Opx granulites from the UHT region of the Napier Complex (Fig. 5). This uses the data of Harley (1985) but includes only those samples in which the garnets have low grossular contents (<5 mol%) and both garnet and orthopyroxene are magnesian ($\text{Grt } X_{\text{Mg}} > 45$) in order to minimize the uncertainty in estimated pressure arising from analytical uncertainties in X_{Al} (i.e. dP/dX_{Al}). The extent of pressure underestimation obtained using the Fe–Mg sensitive Grt–Opx Al barometer (Harley 1984b) ranges from 8 to -1 kbar and correlates very well with the apparent temperatures calculated using the Grt–Opx Fe–Mg exchange thermometer of Harley (1984a) (Fig. 5a). The latter range from 800 to 960°C , but only three Grt + Opx pairs yield Fe–Mg temperatures within 50–100°C of the peak of metamorphism. Back-calculation of Grt or Opx X_{Mg} values following the approach of Fitzsimons & Harley (1994) yields an internally consistent peak temperature estimate of $980 \pm 40^{\circ}\text{C}$ for the range of peak pressures (8–11 kbar) defined by independent barometry and petrogenetic grids. In this case the reference pressures are provided by the thermobarometer of Harley & Green (1982) [$P(\text{HG})$] supported by Grt + Opx + Qz + Plag barometry (Moecher *et al.* 1988), Grt + Sil + Qz + Plag barometry based on THERMOCALC (Holland & Powell 1990), and the experimentally constrained KFMASH petrogenetic grids described above. The correlation between the reference pressure across the Napier Complex and the pressures calculated using the Harley (1984b) barometer following correction for Fe–Mg exchange is shown for 1000°C in Fig. 5b.

Grt–Opx data on suitably magnesian samples from other UHT terranes are limited, and checks for internal consistency of the retrieved temperatures in any one terrane cannot be applied rigorously. However, the retrieval procedure has been applied collectively to ten sapphirine granulites from UHT terranes (Eastern Ghats, 5; Wilson Lake, 1; Sipiwers Lake, 1; In Ouzzal, 1;

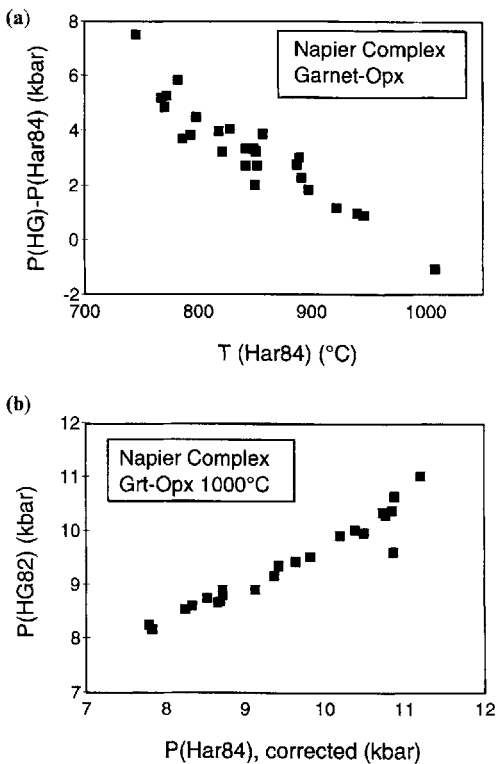


Fig. 5. Results of retrieval calculations for 26 magnesian Grt–Opx granulites from the Napier Complex (see Harley (1985) for summary of analytical data). (a) Correlation of the extent of pressure underestimation [$P(\text{HG}) - P(\text{Har84})$ where $P(\text{HG})$ is a reference pressure and $P(\text{Har84})$ is the pressure recorded using Harley (1984b)] with the Fe–Mg exchange temperature as recorded using the thermometer of Harley (1984a) (horizontal axis). The reference pressure, $P(\text{HG})$, is based on Harley & Green (1982) and a range of other grid and barometer estimates as noted in the text. The range of pressures recorded in the Napier Complex. Reference barometry indicates a range from 8 to 11 kbar (north to south; see earlier discussion) that correlates well with corrected pressures obtained using Harley (1984b) when the Grt and Opx compositions are back-exchanged so that the Fe–Mg exchange thermometer records 1000°C, a reasonable estimate of the peak of metamorphism.

Labwor Hills, 1; Forefinger Point, 1) and the results are illustrated for assumed peak temperatures of 1000 and 950°C in Fig. 6. These plots again show that the extent of pressure underestimation using Grt–Opx Al barometry correlates well with the temperature underestimate obtained using Grt–Opx Fe–Mg exchange thermometry. Five samples from the Eastern Ghats define a best-fit peak temperature of 950°C and underestimate that temperature by between 40 and 105°C. Further reliable reference pressure data, including the grid constraints, are required to confirm these peak temperature estimates.

The calculations outlined above indicate that Fe–Mg exchange, as monitored by the Harley

(1984a) thermometer, in general continues to temperatures some 100–200°C (average 141°C) lower than the retrieved peak temperatures relevant to UHT metamorphism. Even if more recent calibrations of this Fe–Mg exchange thermometer are used (Lee & Ganguly 1988; Aranovich & Berman 1996) the extent of temperature underestimation for most UHT samples is still 40–150°C, and the average underestimate is 81–51°C. If the change in mineral X_{Mg} , or tie-line rotation, is partitioned equally between the phases then the shift in X_{Mg} of garnet for most Grt + Opx + Sil granulites is 3–4 units, and takes the Grt X_{Mg} to values in the range 67–63 for all areas apart from Long Point, where X_{Mg} is as high as 71, and Wilson Lake, where oxidized Grt + Opx + Spr + Sil gneisses contain Grt with X_{Mg} of only 50. In the latter area the compositional adjustment would be to 54. These Grt–Opx compositional shifts would be less if the Lee & Ganguly (1988) thermometer is applied to the data, but are still of the order of $2X_{\text{Mg}}$ units in each phase.

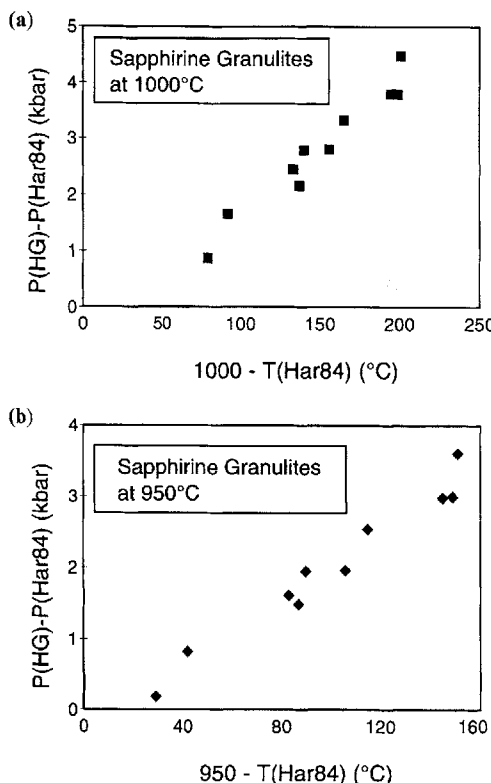


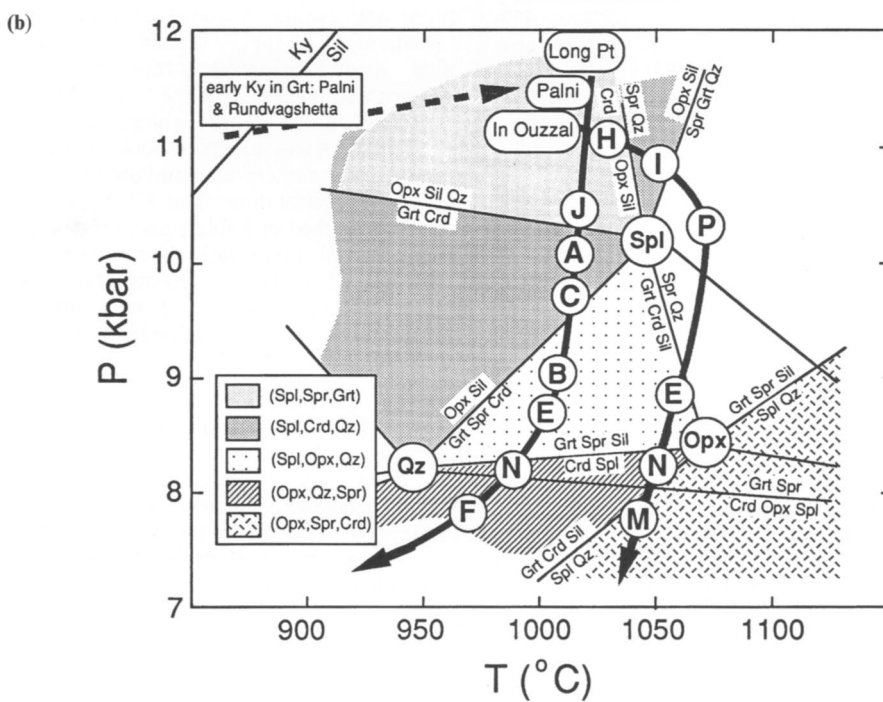
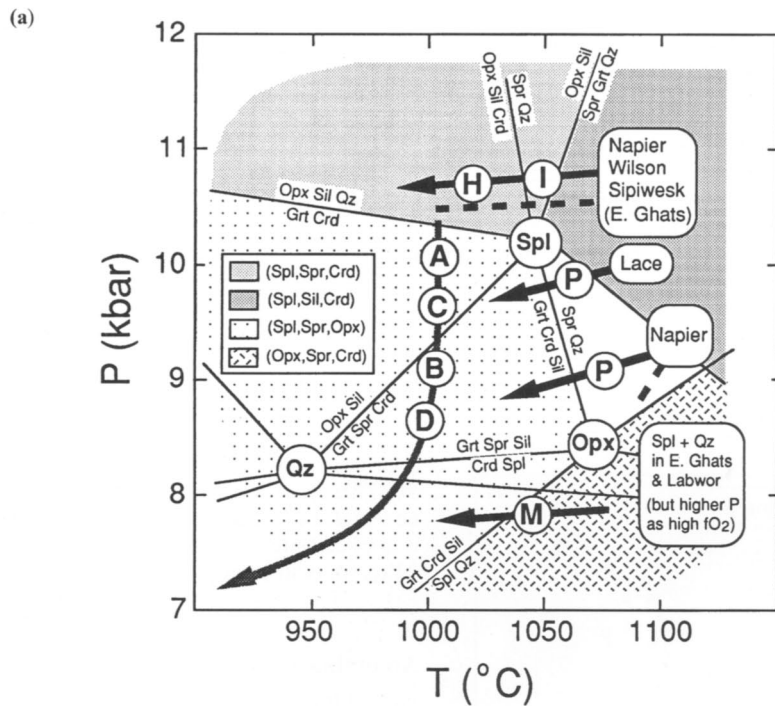
Fig. 6. Results of retrieval calculations for ten examples of magnesian Grt–Opx sapphirine granulites from some UHT terranes summarized in Table 1. Both (a) and (b) show a good correlation of the extent of pressure underestimation [$P(\text{HG}) - P(\text{Har84})$] with the amount of temperature underestimation recorded using the Fe–Mg exchange thermometer of Harley (1984a) (horizontal axis). In (a) the assumed peak temperature is 1000°C whereas in (b) it is 950°C. Most of these UHT samples fit a line through the origin (i.e. no P or T underestimation) for case (b).

An outline of key UHT areas and their P – T path interpretation

The constraints, approaches and caveats introduced and evaluated above allow for detailed consideration of the P – T conditions and paths of most of the presently documented UHT terranes and localities. In the following sections I selectively describe and highlight some of these UHT occurrences to illustrate both how their features can be interpreted and the present limits on our understanding. The UHT occurrences are distinguished in Table 1 and are depicted on Figs 7 and 8 along with their post-peak P – T ‘path’ – IBC or ITD. The Eastern Ghats, where a spectrum of possible P – T paths have been proposed, is considered individually.

The Napier Complex and other areas with IBC histories

Napier Complex, Enderby Land, Antarctica. In the 3000–2500 Ma Archaean Napier Complex, the best preserved example of UHT regional metamorphism, the extreme metamorphic conditions are best defined from the occurrence of Spr + Opx + Qz, Grt + Opx + Sil + Qz, Spr + Qz and Os + Grt (Sheraton *et al.* 1980, 1987; Ellis, 1980; Ellis *et al.* 1980; Grew 1980, 1982a; Harley 1985; Sandiford 1985). Spr + Grt assemblages, with Opx + Sil and occasionally Qz also occur



(Harley & Hensen 1990). The stability of relatively calcic mesoperthite in pelites (Sheraton *et al.* 1980; Ellis *et al.* 1980; Harley 1986), and the presence of Mg-rich inverted pigeonite and sub-calcic pyroxenes already noted above for meta-ironstones from this Complex, confirm the UHT conditions of $>1000^{\circ}\text{C}$. High alumina contents in orthopyroxene (8–11 wt% Al_2O_3) coexisting with garnet yield high calculated temperatures (950 – 1000°C) consistent with the basic FMAS and KFMAS assemblage constraints. In addition, the FMAS and new KFMASH grids discussed in previous sections support previous interpretations that post-peak near-isobaric cooling occurred at less than 8 kbar in the northern parts of the UHT region and at 9–10 kbar in areas further south (Sheraton *et al.* 1980; Harley 1985; Harley & Hensen 1990). A peak- T pressure gradient (Figs 3b, 7a; areas 1a, 1b and 1c in Fig. 8) is strongly supported by the following features.

1. Lower core Al_2O_3 and higher X_{Mg} in Opx equilibrated with Grt + Sil and either Spr or Qz in the southerly part of the complex (Harley 1985, and unpublished data);
2. Spr + Qz is rimmed by coronas involving combinations of Crd, Sil and Grt in the northerly areas whereas it is rimmed by Opx + Sil in the areas south of Amundsen Bay (Sheraton *et al.* 1980; Motoyoshi & Matsueda 1984; Harley 1985; Sandiford 1985). This implies cooling at $P < P[\text{Spl}]$ in the north compared with $P > P[\text{Spl}]$ in the south (Sheraton *et al.* 1980, 1987).
3. Os + Grt, stable in the areas to the north of Amundsen Bay, gives way to the compositionally equivalent assemblage Opx + Sil + Kfs + Qz southwards and eastwards, implying pressure conditions either side of the (Bt, Spr) reaction shown in Fig. 3b (Audibert *et al.* 1995; Carrington & Harley 1995b).
4. The consistency of the reference barometry in the retrieval calculations described in the previous sections.

IBC is well documented in the Napier Complex not only on the basis of the pelite corona textures noted in point 2 above but also from Grt and Grt + Qz coronas developed on Opx in pelites, Opx + Plag in intermediate and semi-pelitic rocks, and Opx + Cpx in mafic granulites and pyroxenites (Sheraton *et al.* 1980, 1987; Ellis 1980; Harley 1985; Sandiford 1985). Whether the IBC is real, in the sense of being a continuous path, or apparent, resulting from episodic overprinting in discrete deformation events, is not fully established. Harley (1985) interpreted a high- T phase of IBC but also pointed out that lower- T coronas formed at 7–8 kbar and 650 – 750°C may reflect an overprinting event (see also Harley & Black 1987).

The prograde path of the UHT granulites in the Napier Complex has received considerable attention, with both clockwise (Ellis 1987; Harley 1989) and counter-clockwise (Motoyoshi & Hensen 1989; Hensen & Motoyoshi 1992) trajectories being proposed. Whilst there is little clear evidence for the clockwise model, and it is very likely that polymetamorphism has obscured the prograde paths, the counter-clockwise path model is consistent with the following observations.

1. Only Sil (never Ky) is observed as inclusions in Grt porphyroblasts.
2. Motoyoshi & Matsueda (1984) and Motoyoshi & Hensen (1989) have described classic Spr + Qz (+minor Opx) graphic and lamellar intergrowths (see also Ellis *et al.* 1980; Sheraton *et al.* 1987) and interpreted them as pseudomorphs after earlier Crd on the basis of their morphology and point-counted average compositions. If this critical interpretation is correct it provides not only a key to the prograde path of the Napier Complex but also those of other UHT areas where Spr + Qz intergrowths have been observed. This textural interpretation warrants further evaluation from a larger range of samples.

Fig. 7. Slightly simplified versions of the FMAS(H) grid of Fig. 1 annotated with some examples of (a) apparent IBC and (b) apparent ITD post-peak P – T paths and key reaction textures. The divariant reactions interpreted from textures at various localities are labelled with alphabetic letters as in Table 1, and some P – T fields of relevant divariant reactions are shown with ornaments as given in the key. (a) Examples of IBC paths from the Napier Complex, Lace xenoliths and other areas given in Table 1. Note the counter-clockwise prograde path suggested for the Napier Complex on the basis of early Spr + Qz and potential Spr + Qz pseudomorphs after Crd. The paths for Labwor Hills and some northern Eastern Ghats localities are placed at low P on this diagram but will be displaced to higher pressures because of their oxidized character (see text for discussion). Also shown is a summary ITD path for the northern Eastern Ghats area. This may post-date the IBC features also seen in these granulites (dashed IBC path at P near $P[\text{Spl}]$). (b) Examples of ITD paths. Long Point is used to represent and illustrate the progression of reactions seen in several areas (see Table 1 and text for details). In Ouzzal preserves a distinctive ITD path involving heating to beyond the $P[\text{Spl}]$ point. Note the clockwise prograde paths inferred for some areas from the presence of early kyanite.

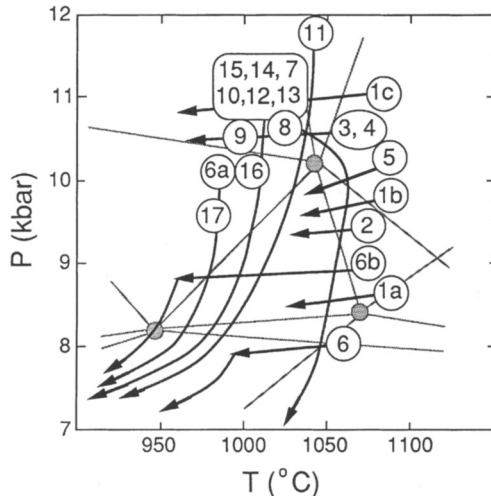


Fig. 8. Summary of the peak P – T conditions of the various UHT terranes and localities listed in Table 1 and identified by the numeral given to them in that table. Apparent post-peak P – T paths IBC, IBC/ITD and ITD are shown by arrowed heavy lines and the FMAS(H) grid is positioned in light lines behind the P – T circles. Peak P – T conditions have been obtained by combining the assemblage–temperature constraints from the grids of Figs 1, 2 and 3 with pressures calculated using Grt–Opx thermobarometry (Harley 1984b; Fitzsimons & Harley 1994) following back-exchange of Fe–Mg to be consistent with these temperatures, pressures obtained from Harley & Green (1982), or pressures quoted from other barometers in the original sources, corrected back to UHT peak temperatures. Using this approach most UHT terranes and localities cluster near 10 ± 1 kbar at 1000°C , and all are in the 8–12 kbar range.

3. Spl is present as an early phase mantled by Spr in some Sil -bearing pelites (Ellis *et al.* 1980; Harley 1986). This Spl usually contains Zn and Fe^{3+} , but in some cases these contents are low and hence an approach to UHT conditions from lower P may be argued.

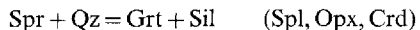
New evidence in favour of either cooling or compression at UHT conditions beyond the (Spl , Sil) univariant of Fig. 1 (i.e. at >1050 – 1100°C) is seen in $\text{Spr} + \text{Opx} + \text{Qz}$ gneisses from Mt Riiser Larsen, where pressures of 8 kbar have been estimated (Figs 7a, 8). Layers containing coarse (0.3–0.6 mm), oriented subhedral Opx and Spr trace out isoclinal folds, but the phases are recrystallized to granoblastic fabrics with a higher $\text{Spr} : \text{Opx}$ ratio after this folding. The coarse Opx contains 11–12.5 wt% Al_2O_3 whereas the Opx in $\text{Opx} + \text{Spr} + \text{Qtz}$ granoblastic mosaics

contains only 8.5–10 wt% Al_2O_3 . These features suggest the following continuous reaction:



which would progress from left to right with increasing pressure or cooling within the $\text{Spr} + \text{Opx} + \text{Qz}$ field and hence would be consistent with a counter-clockwise P – T path at these elevated temperatures.

Other IBC Areas. Near-isobaric P – T trajectories have also been deduced from reaction textures in a number of other UHT granulites (Fig. 8). Of those apparently equilibrated under low f_{O_2} conditions, with rutile–ilmenite (and graphite) stable rather than magnetite–hematite, Sipiwek Lake and the Lace granulite xenoliths provide some of the best examples of high- T coronas. The Archaean (*c.* 2550 Ma) $\text{Spr} + \text{Qz}$ xenoliths in the Lace Kimberlite pipe, South Africa, imply peak P – T conditions of 9–11 kbar and $>1040^\circ\text{C}$ (locality 5, Fig. 8), and may be representative of a significant part of the surrounding Kaapvaal Craton. Coronas of $\text{Grt} + \text{Sil}$ between $\text{Spr} + \text{Qz}$ in initial $\text{Grt} + \text{Spr} + \text{Sil} + \text{Qz}$ xenolith assemblages, reflect progress of the FMAS divariant reaction:



from left to right with either cooling or compression. Rarer coronas involving $\text{Grt} + \text{Crd}$, formed through the related divariant reaction:



also imply cooling, and a post-peak P – T path with dP/dT of between 9 ± 6 bars $^\circ\text{C}^{-1}$ is consistent with the two divariant reactions (Dawson *et al.* 1997). This cooling occurred at pressures between the [Spr] and [Opx] FMAS invariant points of Fig. 7a. A similar IBC trajectory can be deduced for Sipiwek Lake where similar textures related to (Spl, Opx, Crd) are observed (Arima & Barnett 1984; Hensen 1987). The Archaean $\text{Spr} + \text{Sil} + \text{Qz}$ granulites at the latter locality equilibrated at 9.4–10.3 kbar (Arima & Barnett 1984) if the peak temperature was 1000°C , a minimum suggested here from the grid constraints and retrieval calculations (locality 4, Fig. 8). This peak temperature is significantly greater than that originally estimated by Arima & Barnett (1984) on the basis of Grt–Bt Fe–Mg thermometry ($830 \pm 50^\circ\text{C}$). Although the evidence is sparse, a counter-clockwise prograde P – T path for the Sipiwek Lake was proposed by Hensen (1987), who interpreted the presence of Spl and Crn relicts in $\text{Opx} + \text{Spr} + \text{Crd}$

granulites in terms of the former stability of $\text{Opx} + \text{Crn}$, replaced up-temperature by successive Spl - and Spr -bearing assemblages. The stability of $\text{Opx} + \text{Crn}$ in silica-undersaturated granulites remains an important question to be resolved.

IBC under higher f_{O_2} conditions has been described in detail for the c. 8–10 kbar $\text{Spl} + \text{Sil} + \text{Qz}$ granulites of Labwor Hills (Sandiford *et al.* 1987; locality 2, Fig. 8) and considered here in relation to the problem of grid inversions. At Wilson Lake, Labrador, both highly oxidized $\text{Spr} + \text{Sil} + \text{oxide}$ rocks and less-oxidized (but still relatively high f_{O_2}) quartzofeldspathic gneisses with Sil and minor $\text{Spr} + \text{Opx}$ occur (Arima *et al.* 1986; Currie & Gittins 1988). Initial $\text{Spr} + \text{Opx} + \text{Sil} + \text{Qz}$ (+ hematite) suggests peak P – T conditions near $[\text{Spl}]$, which in this case will be displaced to lower P – T conditions than given in Figs 1 and 7 due to the presence of substantial Fe^{3+} in Spr , Sil and Opx . Initial post-peak IBC here is suggested by the presence of $\text{Opx} + \text{Sil}$ coronas on $\text{Spr} + \text{Qz}$ (Morse & Talley 1971; Currie & Gittins 1988) and by Grt coronas on $\text{Opx} + \text{Plag}$ in other rocks. Currie & Gittins (1988) have also demonstrated a later phase of isothermal decompression (ITD) at c. 800–700°C that resulted in the breakdown of gedrite assemblages formed late in the IBC stage.

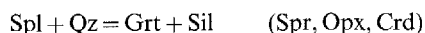
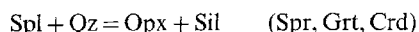
The Eastern Ghats, India: complexity in IBC and ITD histories

Spr -, Opx – Sil and Spl -bearing quartz-saturated and undersaturated granulites have been recognized from the Eastern Ghats of India for some time (Grew 1982b). These have now been described in some detail and their extensive reaction textures interpreted based on FMAS and KFMASH system grids (Mohan *et al.* 1986; Lal *et al.* 1987; Hensen 1987, 1988; Kamineni & Rao 1988; Sengupta *et al.* 1990, 1991; Dasgupta 1995; Dasgupta *et al.* 1994, 1995; Raith *et al.* 1997). Although the Eastern Ghats is often referred to as one ‘terrane’, the UHT assemblages have been recognized from localities in two principal regions: a northerly area some 10 000 km² in size centred on Paderu–Anantigiri in Andhra Pradesh; and a southern region west of Madras and further south near Kodiakanal (Ganguvarpatti, the Palni Hills, and Kiranur). Geochronology in the Eastern Ghats has not yet clarified which of the early Proterozoic, 1000 Ma or 500–600 Ma, tectonothermal events correlates with the UHT assemblages and post-peak P – T paths in each region (e.g. Dasgupta 1995;

Raith *et al.* 1997), and it is probable that the P – T conditions and evolutions in each reflect tectonic events of differing age.

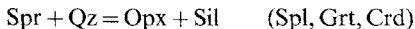
Peak metamorphism in the northern UHT region, where the former stability of $\text{Spr} + \text{Qz}$ and of osumilite is inferred, occurred at 8–10 kbar and >950–1000°C (Dasgupta 1995; Dasgupta *et al.* 1994, 1995; see Fig. 8), although Fe–Mg exchange geothermometers record lower temperatures (see retrieval section). $\text{Opx} + \text{Sil} + \text{Spl} + \text{Qz}$ forms a peak assemblage (e.g. Lal *et al.* 1987; Sengupta *et al.* 1991; Dasgupta *et al.* 1995), stabilized by the presence of Zn , Cr and Fe^{3+} in spinel. The most magnesian Grt in the UHT assemblages is reported from Anakapalle ($X_{\text{Mg}} = 59$: Dasgupta *et al.* 1995). UHT conditions are indicated in the southern Eastern Ghats region by the presence of $\text{Opx} + \text{Sil} + \text{Qtz}$ (Grew 1982b), but the best evidence is described from Qz -deficient assemblages at Ganguvarpatti and nearby localities in the Palni Hill Ranges (Mohan *et al.* 1986; Hensen 1987, 1988; Raith *et al.* 1997). At these localities early Mg-rich Grt ($X_{\text{Mg}} = 52$ –60 and up to ?70) + Opx (8–9 wt% Al_2O_3) assemblages also may involve Sil , but the field of $\text{Spr} + \text{Qz}$ was not reached. From the available evidence it appears likely that the southern region experienced UHT metamorphism at marginally higher pressures (up to 11 kbar cf. 8–10 kbar) and slightly lower temperatures than the northern region (Fig. 8).

Dasgupta (1995) has noted that evidence for both IBC and ITD is present in the northern domain of the Eastern Ghats. Post-peak decompression (ITD; Fig. 7a; localities 6a, 6b in Fig. 8) is strongly suggested by reaction textures including the breakdown of Mg-rich Grt to $\text{Opx} + \text{Spr} + \text{Sil}$ and $\text{Opx} + \text{Spr} + \text{Crd}$ symplectites, Fe-richer $\text{Grt} + \text{Qz}$ replaced by $\text{Opx} + \text{Plag}$ (Dasgupta *et al.* 1994) and $\text{Spr} + \text{Crd}$ replacing $\text{Opx} + \text{Sil}$ (Lal 1997). However, coronas of $\text{Grt} + \text{Sil}$ and $\text{Opx} + \text{Sil}$ on early $\text{Spr} + \text{Qz}$ or $\text{Spr} + \text{Qz}$ (Lal *et al.* 1987; Sengupta *et al.* 1991; Dasgupta *et al.* 1995; Lal 1997) are not consistent with this. In this case the interpretation of these textures is complicated by the presence of Zn and Cr in spinel in the high f_{O_2} conditions relevant to some assemblages (Fe^{3+} in the spinel, coexisting magnetite–hematite). Nevertheless, the reactions involving a complex ZnFMASO system Spl :



are comparable to those reported from the Labwor Hills (Nixon *et al.* 1973; Sandiford

et al. 1987) and most likely reflect IBC. This is supported by the reactions involving Spr + Qz:



which are consistent with cooling at pressures near an analogue of the [Spl] point of Fig. 7a, which again will be displaced to lower pressures (and temperatures) than those shown in the figure because of the extensive Fe^{3+} incorporated into Spr, Opx and Sil (Lal *et al.* 1987: 0.7–1.5 % Fe_2O_3 in Sil). These corona textures on Spr + Qz are essentially the same as those observed in the Napier Complex (Ellis *et al.* 1980; Sheraton *et al.* 1987) and the other UHT localities where IBC has been inferred.

The relative timing of these IBC and ITD P – T segments from the northern region is not clear. Certainly, the Opx + Sil coronas cannot have formed following decompression to 5–6 kbar as at such pressures Grt + Crd would form instead. IBC at c. 9 kbar is consistent with the Opx + Sil textures and it is suggested that IBC was followed by ITD that may be related to exhumation in a separate tectonic event. However, Dasgupta *et al.* (1994) deduce from textural relations that cooling post-dated the high- T decompression seen in granulites at Anakapalle. Possible evidence in support of this interpretation, not considered by Dasgupta *et al.* (1994), can be seen in the textures portrayed in their fig. 11 (p. 441). This back-scattered electron image (BEI) shows Grt partially replaced by a rib-like intergrowth of Spr + Opx and another phase (dark in BEI; Crd?); Sil is reported to be in the symplectite but cannot be seen in the photograph (it too should be dark in BEI). On closer inspection this texture also has more localized domains of what could be interpreted to be new Grt growing outwards from the resorbed Grt/symplectite interface along and around the Opx + Spr ribs, reflecting a Grt-forming reaction:



This would be indicative of either cooling or compression/burial following the decompression phase, and would progress at pressures of 7–8 kbar (Figs 1, 7a).

In contrast to the northern UHT domain of the Eastern Ghats, single- or multistage ITD paths appear to characterize the southern UHT region (Fig. 7b; locality 7, Fig. 8). At Ganguvarpatti, Hensen (1987) has demonstrated how the different symplectites formed during garnet breakdown related to the initial garnet X_{Mg} composition, with Opx + Spr + Crd forming on the less-magnesian garnets at lower pressures

than Opx + Spr + Crd symplectites on garnets with higher X_{Mg} . Raith *et al.* (1997) also describe textures in which Opx + Sil, Grt and Grt + Sil break down to assemblages involving sub-sets of the phases Opx, Spr, Crd and Spl. These assemblages are then partially replaced by Bt prior to a final stage of Opx + Crd corona formation. These textures, and their relative timing, are very similar to those reported from Forefinger Point, Antarctica (Harley *et al.* 1990) and are attributed to decompression from 11 to c. 8 kbar at 950–1000°C (i.e. $T < T[\text{Spl}]$), followed by another stage of decompression at 850–900°C in both examples (Harley *et al.* 1990; Raith *et al.* 1997). Oriented sillimanite aggregates are interpreted by Raith *et al.* (1997) to be pseudomorphs after coarse twinned kyanite formed in the prograde stage of a clockwise P – T evolution. This interpretation invokes a similar P – T history to that determined for 520 Ma (Pan African) Grt + Opx + Sil UHT assemblages from Rundvågshetta, Lützow-holm Bay, Antarctica, where Ky has actually been observed as inclusions in highly magnesian Grt ($X_{\text{Mg}} = 57$; Motoyoshi & Ishikawa 1998; Fig. 7b).

Occurrences with ITD histories: the In Ouzzal terrane and other localities

In Ouzzal. Metamorphic assemblages and reaction relationships in the In Ouzzal UHT terrane of the Hoggar, Algeria, have been superbly documented in a series of papers over the past decade (Kienast & Ouzegane 1987; Bertrand *et al.* 1992; Mouri *et al.* 1996; Ouzegane & Boumaza 1996). Peak conditions of 1050°C and 10 kbar are deduced from assemblages in pelitic or aluminous rock compositions, and a clockwise P – T trajectory terminated by near-isothermal decompression inferred from textures (Fig. 7b; locality 8, Fig. 8). This P – T history is widely considered to be continuous and related to the Eburnean tectonic cycle at c. 2000 Ma (Ouzegane & Boumaza 1996).

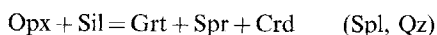
UHT in this terrane is well defined from quartz-present assemblages including Opx + Sil + Qz, Grt₆₀ + Qz, former osumilite, and Spr + Qz (+ Opx). Quartz-deficient assemblages including Opx + Sil + Spr and Grt + Opx + Sil are consistent with the quartz-bearing ones and imply peak conditions located near or above the FMAS [Spl] point (Fig. 7b). Three further features noted for this terrane distinguish it from several others.

1. The rare and elusive assemblage Opx + Crn is inferred to have been stable prior to

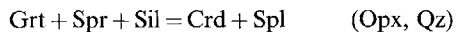
Spr + Sil on the prograde P - T evolution (Bertrand *et al.* 1991). This, together with the occurrence of texturally early Mg-rich garnet breaking down to coarse fabrics involving Opx + Sil and even Spr + Qz, has been used to suggest a clockwise prograde path.

2. Ouzegane & Boumaza (1996) report Spr + Qz replacing Opx + Sil assemblages. This is consistent with decompression (and heating?) initially at temperatures greater than those of the [Spl] point. This feature is unique among the presently recognized UHT terranes with ITD paths, as all the other examples appear to have experienced ITD at $T < T[\text{Spl}]$ (e.g. Harley *et al.* 1990; Raith *et al.* 1997; see Table 1 and Fig. 7b).
3. Despite the very high peak temperatures, biotite (phlogopite) remained stable throughout the P - T history because of its high F contents (up to 4.2 wt% F: Mouri *et al.* 1996). Mouri *et al.* (1996) provide a detailed analysis of how the presence of F in biotite affects KFMASH phase relations. These workers also show how the [Qz] point in the grid of Hensen & Harley (1990) will be rendered metastable with respect to dehydration melting reactions involving F-biotite, ultimately causing a grid inversion and stabilization of the unique assemblage Bt + Spr + Qz. The continued stability of biotite to the highest UHT conditions contrasts with the situation seen in other areas (e.g. Herd *et al.* 1986; Harley *et al.* 1990; Harley & Fitzsimons 1991; Motoyoshi & Ishikawa 1998; Raith *et al.* 1997) where early biotites with low F (and Ti) contents are only found included in garnet, and biotite disappeared through melting reactions at temperatures lower than the peak conditions but then reappeared on the post-peak P - T path as late platy grains overprinting Spr + Opx symplectites.

Other ITD case studies. As demonstrated for the Eastern Ghats and In Ouzzal areas, the textural and assemblage evolutions of Qz-deficient Grt + Opx + Sil granulites can be nicely interpreted with reference to the FMAS P - T grid modified from Hensen (1986) and Hensen & Harley (1990) (Figs 1, 7b). The reactions controlling texture formation are usually at least divariant in FMAS and define P - T fields or bands focused either on the univariant (Spl, Qz) point which lies at P - T conditions between the [Spl] and [Qz] points:



or on the (Opx, Qz) and (Sil, Qz) reactions that occur at lower pressures (Fig. 7b):



As discussed by Hensen (1987, 1988), these univariant reactions are themselves rarely 'seen' by the reacting rock compositions.

Examples from Forefinger Point (Harley *et al.* 1990), St Maurice (Herd *et al.* 1986), Long Point (Harley & Fitzsimons 1991), Rundvågshetta (Motoyoshi & Ishikawa 1998), Sri Lanka (Kriegsman 1991), the Sutam and Tokskii blocks of Siberia (Perchuk *et al.* 1985), the central zone of the Limpopo Belt (Harris & Holland 1984; Droop 1989; Hisada & Miyano 1996) and the Gruf Complex (Droop & Bucher-Nurminen 1984) are all consistent with high- T evolutions from pressures near or greater than the [Spl] point through to lower pressures near or below [Qz], with Spr + Opx + Crd and Spl + Crd symplectites being produced through divariant breakdown of garnets with X_{Mg} varying from 65 to 48. As the features from several of these localities are very similar to those described above from the southern UHT domain of the Eastern Ghats, they need not be considered further. However, the unique features of two important localities, Rundvågshetta and Long Point, should be emphasized.

As noted with reference to the textural interpretations of Raith *et al.* (1997), the UHT locality Rundvågshetta in Lützow Holm Bay, Antarctica (Fig. 7b; locality 12, Fig. 8), preserves kyanite as inclusions in magnesian Grt (Motoyoshi & Ishikawa 1998). As in the Gruf Complex (Droop & Bucher-Nurminen 1984), this implies a clockwise prograde P - T path at high pressure. Moreover, the presence of early kyanite is totally consistent with inclusion assemblages reported in the lower-grade (amphibolite to granulite) gneisses within the Lützow Holm Bay complex as a whole.

Magnesian pelites from Long Point in the Rauer Group, Antarctica (Fig. 7b; locality 11, Fig. 8), contain Grt + Opx + Sil, Opx + Sil + Qz and Grt + Sil + Qz assemblages but lack Os and Spr + Qz. This locality preserves the most pyropic Grt yet recorded in equilibrium with Sil ($X_{\text{Mg}} = 68\text{--}71$ in Qz-absent domains). Unusually, peak metamorphic conditions of 12 kbar and 1050°C are in this instance indicated by petrogenetic grids and by geothermobarometry (Harley & Fitzsimons 1991). Indeed, Fe–Mg partitioning between Grt and included Opx (8–11 wt% Al_2O_3) records temperatures of over 1030°C. ITD at >950°C (symplectite Opx with

8 wt% Al_2O_3) is well defined as Grt with different X_{Mg} (70, 68–65, 58 and 50) and Opx + Sil are replaced by domain- and reactant-specific lower-pressure symplectites similar to those from other ITD areas. The experimental petrogenetic grid of Carrington & Harley (1995a) contoured for the X_{Mg} ratios of Grt and Opx (Figs 4a, b) demonstrates that partial melting to produce Grt ($X_{\text{Mg}} > 58$) + Opx + Sil migmatites in this case proceeded at minimum P – T conditions of 8.6 kbar and 910°C along a prograde heating path, and implies a clockwise P – T trajectory.

Summary comments on UHT occurrences

The features of various UHT terranes outlined above and in Table 1 demonstrate that there is real diversity in both their peak P – T conditions, their post-peak P – T paths, and potentially (though less confidently) in their prograde evolutions. However, like the many granulites that have not been to such extreme conditions (Harley 1989, 1992), the UHT areas group into those characterized by real or apparent IBC post-peak paths, those with ITD paths, and some in which both paths are seen probably as a result of polymetamorphism (Fig. 8). Hence, the same problems of tectonic interpretation and synthesis that are recognized in granulites in general apply to UHT metamorphism, only more so. The positive aspect that emerges from consideration of all the occurrences examined here is that in general we now have a reasonable framework in which to make first-order inferences (e.g. P – T conditions, textural evolutions) that provide a sound basis for further interpretation and modelling.

Concluding remarks

Tectonic scenarios: cautionary comments

The precise tectonic settings necessary for the development of UHT metamorphism remain problematic, and it is not within the scope of this paper to develop or present a holistic model for the formation and evolution of UHT metamorphic terranes. The extreme temperatures attained, however, suggest that convective thinning or detachment of the lithospheric thermal boundary layer during or after crustal thickening may play a major role in the formation of UHT metamorphic belts and hence the evolution of the deep continental crust (e.g. Harley

1989; Sandiford 1989; Sandiford & Powell 1990). Whilst this concept may be appropriate at least as a starting model for the larger UHT terranes such as the IBC-dominated Napier Complex, its applicability to the small or isolated UHT localities that preserve high-temperature ITD in otherwise 'lower-grade' areas is not obvious. The tectonic and relative structural significance of many of the latter occurrences are in general not well defined or understood, and a major goal of further work with UHT localities must be to elucidate their local structural evolution in more detail and then place this in regional contexts using precise dating methods. For example, Forefinger Point in Enderby Land was interpreted by Harley *et al.* (1990) as a margin of the Archaean Napier Complex reworked in the Proterozoic. However, recent isotopic dating suggests a Pan-African age and would be consistent with a collisional setting comparable to that inferred for the 520 Ma Rundvågshetta locality on the basis of integrated structural and metamorphic studies (Motoyoshi & Ishikawa 1998).

This problem of context and the age relationship between the UHT event and the preserved post-peak history, central to any tectonic interpretation, is also manifest in other localities and terranes. The uncertainty surrounding the relative significance of 500 Ma, 1000 Ma and earlier events in the Eastern Ghats has already been alluded to. The St Maurice UHT occurrence in Quebec has been interpreted as part of a polycyclic allochthonous terrane caught up in later collisional Grenvillian events (Herd *et al.* 1986), though its age and the timing of its ITD path are not known. The In Ouzzal granulites, and their textures indicative of ITD, have been attributed to a 2000 Ma metamorphism associated with collision, though it is possible that final uplift and exposure may have been caused by an unrelated and considerably younger Pan-African event (Bertrand *et al.* 1991). It is clear that a unified model for the origin of UHT metamorphism is not yet warranted in view of the present gaps in our knowledge of these and other areas.

Further issues to be addressed

I have demonstrated that there is significant and consistent evidence for UHT crustal metamorphism, and that many of its key features can be constrained using present quantitative and semi-quantitative methods. However, to further refine the characterization of UHT

crustal metamorphism, more experimental and petrological data and observations are required, some of which are noted below:

1. Qz-absent equilibria need to be experimentally located and defined both in FMAS and KFMASH so that the existing grids can be developed further and quantified in the 900–1000°C region.
2. Reliable experimental data on FMAS-system Spr are urgently needed to enable the upgrading of internally consistent thermodynamic datasets and their application to UHT assemblages.
3. An intensive study of textural and compositional variations in Spr from UHT localities needs to be undertaken using the latest imaging methods to place better limits on its reintegrated peak composition under both relatively reduced and oxidized conditions.
4. Evidence of pre-peak evolutions – the prograde paths – have to be searched for intensively, with a focus on inclusions in porphyroblasts (e.g. Ky, Fe-rich Crd). Related to this, the scarce and little-known Opx + Crn assemblage requires detailed documentation and potential pseudomorph textures after Grt and Crd require further textural and bulk analysis.
5. Lastly, Crd remains a key phase that controls the positions and stoichiometry of many reactions both in and bounding the UHT field. New data in KFMASH are only consistent with FMASH calculations if we take the volatile undersaturation of Crd into account. Quantitative data on Crd–L volatile partitioning and the Crd volatile saturation state in the presence of L and CO₂-bearing vapour will be essential to define the reactions most relevant to natural cordierites, as those formed under or near UHT conditions contain appreciable CO₂ (0.5 to 1.05 wt% in the Napier Complex: Harley, unpublished SIMS data) and hence are stabilized to higher pressures than would be predicted from KFMASH data alone.

I thank the organizers of the 'What Controls Metamorphism?' meeting at Kingston for their excellent efforts and for the invitation to present this work. I especially thank P. Treloar for his extra efforts to prompt an otherwise tardy contributor. This work has benefited from discussions over the years with many people, but most notably B. Hensen, I. Fitzsimons, M. Brown, Y. Motoyoshi, L. Y. Aranovich, M. Sandiford and L. Kriegsman. M. Sandiford and C. Friend are thanked for their positive reviews. Fieldwork at Long Point was funded by NERC grant GR9/271 and ASAC projects DV/05/88 and 497. This work was

supported by NERC grant GR3/9099 and is a contribution to the granulites theme of IGCP project 368 'Proterozoic Events in East Gondwana'.

References

ANNERSTEN, H. & SEIFFERT, F. 1981. Stability of the assemblage orthopyroxene–sillimanite–quartz in the system MgO–FeO–Fe₂O₃–Al₂O₃–SiO₂–H₂O. *Contributions to Mineralogy and Petrology*, **77**, 158–165.

ARANOVICH, L. Y. & BERMAN, R. G. 1996. Optimized standard state and solution properties of minerals II. Comparisons, predictions, and applications. *Contributions to Mineralogy and Petrology*, **126**, 25–37.

— & PODLESSKII, K. K. 1989. Geothermometry of high-grade metapelites: simultaneously operating reactions. In: DALY, J. S., CLIFF, R. A. & YARDLEY, B. W. D. (eds) *Evolution of Metamorphic Belts*. Geological Society, London, Special Publication, **43**, 45–62.

ARIMA, M. & BARNETT, R. L. 1984. Sapphirine bearing granulites from the Sipiwek Lake area of the late Archaean Pikwitonei granulite terrain, Manitoba, Canada. *Contributions to Mineralogy and Petrology*, **88**, 102–112.

— & GOWER, C. F. 1991. Osumilite-bearing granulites in the eastern Grenville Province, eastern Labrador, Canada: mineral parageneses and metamorphic conditions. *Journal of Petrology*, **32**, 29–62.

—, KERRICH, R. & THOMAS, A. 1986. Sapphirine-bearing paragneiss from the northern Grenville province in Labrador, Canada: protolith composition and metamorphic *P*–*T* conditions. *Geology*, **14**, 844–847.

AUDIBERT, N., HENSEN, B. J. & BERTRAND, P. 1995. Experimental study of phase relations involving osumilite in the system K₂O–FeO–MgO–Al₂O₃–SiO₂–H₂O at high pressure and temperature. *Journal of Metamorphic Geology*, **13**, 331–344.

BARNICOAT, A. C. & O'HARA, M. J. 1979. High-temperature pyroxenes from an ironstone at Scourie, Sutherland. *Mineralogical Magazine*, **43**, 371–75.

BERMAN, R. G. & ARANOVICH, L. Y. 1996. Optimized standard state and solution properties of minerals I. Model calibration for olivine, orthopyroxene, cordierite, garnet, and ilmenite in the system system MgO–FeO–MgO–CaO–Al₂O₃–TiO₂–SiO₂. *Contributions to Mineralogy and Petrology*, **126**, 1–24.

BERTRAND, P. H., ELLIS, D. J., & GREEN, D. H. 1991. The stability of sapphirine-quartz and hypersthene–sillimanite–quartz assemblages: an experimental investigation in the system system FeO–MgO–Al₂O₃–SiO₂ under H₂O and CO₂ conditions. *Contributions to Mineralogy and Petrology*, **108**, 55–71.

—, OUZEGANE, K. H. & KIENAST, J.-R. 1992. P–T–X relationships in the Precambrian Al–Mg-rich granulites from In Ouzzal, Hoggar, Algeria. *Journal of Metamorphic Geology*, **10**, 17–31.

BOHLEN, S. R. 1987. Pressure-temperature-time paths and a tectonic model for the evolution of granulites. *Journal of Geology*, **95**, 617–632.

— 1991. On the formation of granulites. *Journal of Metamorphic Geology*, **9**, 223–229.

CARRINGTON, D. P. 1995. The relative stability of garnet–cordierite and orthopyroxene–sillimanite–quartz assemblages in metapelitic granulites: experimental data. *European Journal of Mineralogy*, **7**, 949–960.

— & HARLEY, S. L. 1995a. Partial melting and phase relations in high-grade metapelites: an experimental petrogenetic grid in the KFMASH system. *Contributions to Mineralogy and Petrology*, **120**, 270–291.

— & — 1995b. The stability of osumilite in metapelitic granulites. *Journal of Metamorphic Geology*, **13**, 613–625.

— & — 1996. Cordierite as a monitor of fluid and melt water contents in the lower crust: an experimental calibration. *Geology*, **24**, 647–650.

CHATTERJEE, N. D. & SCHREYER, W. 1972. The reaction $\text{enstatites} + \text{sillimanite} = \text{sapphires} + \text{quartz}$ in the system $\text{MgO}-\text{Al}_2\text{O}_3-\text{SiO}_2$. *Contributions to Mineralogy and Petrology*, **36**, 49–62.

CLARKE, G. L., POWELL, R. & GUIRAUD, M. 1989. Low-pressure granulite facies metapelitic assemblages and corona textures from MacRobertson Land, east Antarctica: the importance of Fe_2O_3 and TiO_2 in accounting for spinel-bearing assemblages. *Journal of Metamorphic Geology*, **7**, 323–335.

CURRIE, K. L. & GITTINS, J. 1988. Contrasting sapphirine parageneses from Wilson Lake, Labrador and their tectonic implications. *Journal of Metamorphic Geology*, **6**, 603–622.

DALLWITZ, W. B. 1968. Coexisting sapphirine and quartz in granulites from Enderby Land, Antarctica. *Nature*, **219**, 476–477.

DASGUPTA, S. 1993. Contrasting mineral parageneses in high-temperature calc-silicate granulites: examples from the Eastern Ghats, India. *Journal of Metamorphic Geology*, **11**, 193–202.

— 1995. Pressure-temperature evolutionary history of the Eastern Ghats granulite province: recent advances and some thoughts. *India and Antarctica During the Precambrian. Memoir of the Geological Society of India*, **34**, 101–110.

—, SANYAL, S., SENGUPTA, P. & FUKUOKA, M. 1994. Petrology of granulites from Anakapalle – evidence for Proterozoic decompression in the Eastern Ghats, India. *Journal of Petrology*, **35**, 433–459.

—, SENGUPTA, P., EHL, J., RAITH, M. & BARDHAN, S. 1995. Reaction textures in a suite of spinel granulites from the Eastern Ghats Belt, India: evidence for polymetamorphism, a partial petrogenetic grid in the system KFMASH and the roles of ZnO and Fe_2O_3 . *Journal of Petrology*, **36**, 435–461.

DAWSON, J. B. & SMITH, J. V. 1987. Reduced sapphirine granulite xenoliths from the Lace Kimberlite, South Africa: implications for the deep structure of the Kaapvaal Craton. *Contributions to Mineralogy and Petrology*, **95**, 376–383.

—, HARLEY, S. L., RUDNICK, R. L. & IRELAND, T. 1997. Equilibration and reaction in Archaean sapphirine granulite xenoliths from the Lace kimberlite pipe, South Africa. *Journal of Metamorphic Geology*, **15**, 253–266.

DROOP, G. T. R. 1989. Reaction history of garnet–sapphirine granulites and conditions of Archaean high-pressure granulite facies metamorphism in the Central Limpopo Mobile Belt, Zimbabwe. *Journal of Metamorphic Geology*, **7**, 383–403.

— & BUCHER-NURMINEN, K. 1984. Reaction textures and metamorphic evolution of sapphirine-bearing granulites from the Gruf Complex, Italian Central Alps. *Journal of Petrology*, **25**, 766–803.

ELLIS, D. J. 1980. Osumilite–sapphirine–quartz granulites from Enderby Land, Antarctica: $P-T$ conditions of metamorphism, implications for garnet–cordierite equilibria and the evolution of the deep crust. *Contributions to Mineralogy and Petrology*, **74**, 201–210.

— 1987. Origin and evolution of granulites in normal and thickened crust. *Geology*, **15**, 167–170.

—, SHERATON, J. W., ENGLAND, R. N. & DALLWITZ, W. B. 1980. Osumilite–sapphirine–quartz granulites from Enderby Land, Antarctica – mineral assemblages and reactions. *Contributions to Mineralogy and Petrology*, **72**, 123–143.

FITZSIMONS, I. C. W. & HARLEY, S. L. 1994. The influence of retrograde cation exchange on granulite $P-T$ estimates and a convergence technique for the recovery of peak metamorphic conditions. *Journal of Petrology*, **35**, 543–576.

FROST, B. R. & CHACKO, T. 1989. The granulite uncertainty principle: limitations on thermobarometry in granulites. *Journal of Geology*, **97**, 435–450.

GNOS, E. & KURZ, D. 1994. Sapphirine–quartz and sapphirine–corundum assemblages in metamorphic rocks associated with the Semail Ophiolite (United Arab Emirates). *Contributions to Mineralogy and Petrology*, **116**, 398–410.

GREEN, D. H. & RINGWOOD, A. E. 1967. An experimental investigation of the gabbro to eclogite transformation and its petrological applications. *Geochimica et Cosmochimica Acta*, **31**, 767–833.

GREW, E. S. 1980. Sapphirine + quartz association from Archaean rocks in Enderby Land, Antarctica. *American Mineralogist*, **65**, 821–836.

— 1982a. Osumilite in the sapphirine–quartz terrane of Enderby Land, Antarctica: implications for osumilite petrogenesis in the granulite facies. *American Mineralogist*, **67**, 762–787.

— 1982b. Sapphirine, kornerupine and sillimanite orthopyroxene in the charnockitic region of south India. *Journal of the Geological Society of India*, **23**, 469–505.

HARLEY, S. L. 1984a. An experimental study of the partitioning of Fe and Mg between garnet and orthopyroxene. *Contributions to Mineralogy and Petrology*, **86**, 359–373.

— 1984b. The solubility of alumina in orthopyroxene coexisting with garnet in $\text{FeO}-\text{MgO}-\text{Al}_2\text{O}_3-\text{SiO}_2$ and $\text{CaO}-\text{FeO}-\text{MgO}-\text{Al}_2\text{O}_3-\text{SiO}_2$. *Journal of Petrology*, **25**, 665–696.

— 1985. Garnet-orthopyroxene bearing granulites from Enderby Land, Antarctica: metamorphic pressure-temperature-time evolution of the Archaean Napier Complex. *Journal of Petrology*, **26**, 819–856.

— 1986. A sapphirine-cordierite-garnet-sillimanite granulite from Enderby Land, Antarctica: implications for FMAS petrogenetic grids in the granulite facies. *Contributions to Mineralogy and Petrology*, **94**, 452–460.

— 1987. A pyroxene-bearing metaironstone and other pyroxene-granulites from Tonagh Island, Enderby Land, Antarctica: further evidence for very high temperature ($>980^{\circ}\text{C}$) Archaean regional metamorphism in the Napier Complex. *Journal of Metamorphic Geology*, **5**, 341–356.

— 1989. The origins of granulites: a metamorphic perspective. *Geological Magazine*, **126**, 215–247.

— 1992. Proterozoic granulite terranes. In: CONDIE, K. (ed.) *Proterozoic Crustal Evolution*. Elsevier, Amsterdam, 301–359.

— & BLACK, L. P. 1987. The Archaean geological evolution of Enderby Land, Antarctica. In: PARK, R. G. & TARNEY, J. (eds) *Evolution of the Lewisian and Comparable High-grade Terranes*. Geological Society, London, Special Publication, **27**, 285–296.

— & BUICK, I. S. 1992. Wollastonite-scapolite assemblages as indicators of granulite pressure-temperature-fluid histories: the Rauer Group, East Antarctica. *Journal of Petrology*, **33**, 693–728.

— & FITZSIMONS, I. C. W. 1991. Pressure-temperature evolution of metapelitic granulites in a polymetamorphic terrane: the Rauer Group, East Antarctica. *Journal of Metamorphic Geology*, **9**, 231–243.

— & GREEN, D. H. 1982. Garnet-orthopyroxene barometry for granulites and peridotites. *Nature*, **300**, 697–701.

— & HENSEN, B. J. 1990. Archaean and Proterozoic high-grade terranes of East Antarctica (40° – 80°E): a case study of diversity in granulite facies metamorphism. In: ASHWORTH, J. R. & BROWN, M. (eds) *High-temperature Metamorphism and Crustal Anatexis*. Unwin Hyman, London, 320–370.

—, — & SHERATON, J. W. 1990. Two-stage decompression in orthopyroxene-sillimanite granulites from Forefinger Point, Enderby Land, Antarctica: implications for the evolution of the Archaean Napier Complex. *Journal of Metamorphic Geology*, **8**, 591–613.

HARRIS, N. B. W. & HOLLAND, T. J. B. 1984. The significance of cordierite-hypersthene assemblages from the Beitbridge region of the Central Limpopo Belt: evidence for rapid decompression in the Archaean? *American Mineralogist*, **69**, 1036–1049.

HENSEN, B. J. 1971. Theoretical phase relations involving cordierite and garnet in the system $\text{MgO-FeO-Al}_2\text{O}_3-\text{SiO}_2$. *Contributions to Mineralogy and Petrology*, **33**, 191–214.

— 1977. The stability of osumilite in high grade metamorphic rocks. *Contributions to Mineralogy and Petrology*, **64**, 197–204.

— 1986. Theoretical phase relations involving garnet and cordierite revisited: the influence of oxygen fugacity on the stability of sapphirine and spinel in the system Mg-Fe-Al-Si-O . *Contributions to Mineralogy and Petrology*, **92**, 191–214.

— 1987. $P-T$ grids for silica-undersaturated granulites in the systems MAS ($n+4$) and FMAS ($n+3$) – tools for the derivation of $P-T$ paths of metamorphism. *Journal of Metamorphic Geology*, **5**, 255–271.

— 1988. Chemical potential diagrams and chemo-graphic projections: application to sapphirine-granulites from Kiranur and Gangavarapatti, Tamil Nadu. Evidence for rapid uplift in part of the South Indian Shield? *Neues Jahrbuch für Mineralogie Abhandlungen*, **158**, 193–210.

— & GREEN, D. H. 1971. Experimental study of the stability of cordierite and garnet in pelitic compositions at high pressures and temperatures. I. Compositions with excess alumino-silicate. *Contributions to Mineralogy and Petrology*, **33**, 309–330.

— & — 1972. Experimental study of the stability of cordierite and garnet in pelitic compositions at high pressures and temperatures. II. Compositions without excess alumino-silicate. *Contributions to Mineralogy and Petrology*, **35**, 331–354.

— & — 1973. Experimental study of the stability of cordierite and garnet in pelitic compositions at high pressures and temperatures. III. Synthesis of experimental data and geological applications. *Contributions to Mineralogy and Petrology*, **38**, 151–166.

— & HARLEY, S. L. 1990. Graphical analysis of $P-T-X$ relations in granulite facies metapelites. In: ASHWORTH, J. R. & BROWN, M. (eds) *High Temperature Metamorphism and Crustal Anatexis*. Unwin Hyman, London, 19–56.

— & MOROYOSHI, Y. 1992. Osumilite-producing reactions in high-temperature granulites from the Napier Complex, East Antarctica: tectonic implications. In: YOSHIDA, Y., KAMINUMA, K. & SHIRAISHI, K. (eds) *Recent Progress in Antarctic Earth Science*. Terrapub, Tokyo, 87–92.

HERD, R. K., ACKERMAN, D., WINDLEY, B. F. & RONDOT, J. 1986. Sapphirine-garnet rocks, St. Maurice area, Quebec: petrology and implications for tectonics and metamorphism. In: MOORE, J. M., DAVIDSON, A. & BAER, A. J. (eds) *The Grenville Province*. Geological Association of Canada, Special Paper, **31**, 241–253.

HISADA, K. & MIYANO, T. 1996. Petrology and microthermometry of aluminous rocks in the Botswanan Limpopo Central Zone: evidence for isothermal decompression and isobaric cooling. *Journal of Metamorphic Geology*, **14**, 183–197.

HOLLAND, T. J. B. & POWELL, R. 1990. An enlarged and updated internally consistent data-set with uncertainties and correlations: the system $\text{K}_2\text{O-Na}_2\text{O-CaO-MgO-MnO-FeO-Fe}_2\text{O}_3-\text{Al}_2\text{O}_3-\text{TiO}_2-\text{SiO}_2-\text{C-H}_2\text{-O}_2$. *Journal of Metamorphic Geology*, **8**, 89–124.

—, BABU, E. V. S. S. K. & WATERS, D. J. 1996. Phase relations of osumilite and dehydration melting in pelitic rocks: a simple thermodynamic model for the KFMASH system. *Contributions to Mineralogy and Petrology*, **124**, 383–394.

KAMINENI, D. C. & RAO, A. T. 1988. Sapphirine-bearing quartzite from the Eastern Ghats granulite terrain, Visianagaram, India. *Journal of Geology*, **96**, 517–533.

KARSAKOV, L. P. 1973. Pyrope–bronzite–sillimanite schist of Eastern Stanovik and the pressure–temperature conditions during its metamorphism. *Doklady Akademii Nauk SSSR*, **210**, 187–190 (translated in *Doklady of the Academy of Sciences of the USSR, Earth Science Sections*, **210**, 171–173, 1973).

KIENAST, J. R. & OUZEGANE, K. 1987. Polymetamorphic Al–Mg rich parageneses in Archaean rocks from Hoggar, Algeria. *Geological Journal*, **22**, 57–79.

KIHLE, J. & BUCHER-NURMINEN, K. 1992. Orthopyroxene–sillimanite–sapphirine granulites from the Bamble granulite terrane, southern Norway. *Journal of Metamorphic Geology*, **10**, 671–683.

KRIEGSMAN, L. 1991. Sapphirine-bearing granulites from central Sri Lanka: outcrop description and mineral chemistry. In: KRONER, A. (ed.) *The crystalline crust of Sri Lanka. Part 1. Summary of research of the German–Sri Lankan Consortium*. Geological Survey Department of Sri Lanka, Professional Paper, **5**, 178–187.

LAL, R. K. 1997. Internally consistent calibrations for geothermobarometry of high-grade Mg–Al rich rocks in the system MgO–Al₂O₃–SiO₂ and their application to sapphirine–spinel granulites of Eastern Ghats, India and Enderby Land, Antarctica. *Proceedings of the Indian Academy of Sciences (Earth and Planetary Sciences)*, **106**, 91–113.

—, ACKERMUND, D., RAITH, M., RAASE, P. & SEFIERT, F. 1984. Sapphirine-bearing assemblages from Kiranur, Southern India – a study of chemographic relationships in the Na₂O–FeO–MgO–Al₂O₃–SiO₂–H₂O system. *Neues Jahrbuch für Mineralogie Abhandlungen*, **150**, 121–152.

—, —, — & UPADHYAY, H. 1987. P–T–X relationships deduced from corona textures in sapphirine–spinel–quartz assemblages from Paderu, southern India. *Journal of Petrology*, **28**, 1139–1168.

LEE, H. Y. & GANGULY, J. 1988. Equilibrium compositions of coexisting garnet and orthopyroxene: experimental determinations in the system FeO–MgO–Al₂O₃–SiO₂, and applications. *Journal of Petrology*, **29**, 1, 93–114.

LOOSVELD, R. J. H. & ETHERIDGE, M. A. 1990. A model for low-pressure facies metamorphism during crustal thickening. *Journal of Metamorphic Geology*, **8**, 257–267.

LUTTS, B. G. & KOPANEVA, L. N. 1968. A pyrope–sapphirine rock from the Anabar Massif and its conditions of metamorphism. *Doklady Akademii Nauk SSSR*, **179**, 1200–1202 (translated in *Doklady of the Academy of Sciences of the USSR, Earth Science Sections*, **179**, 161–163, 1968).

MARAKUSHEV, A. A. & KUDRYAVTSEV, V. A. 1965. Hypersthene–sillimanite paragenesis and its implication. *Doklady Akademii Nauk SSSR*, **164**, 179–182 (translated in *Doklady of the Academy of Sciences of the USSR, Earth Science Sections*, **164**, 145–148, 1966).

MOECHER, D. P., ESSENE, E. J. & ANOVITZ, L. M. 1988. Calculation and application of clinopyroxene–garnet–plagioclase–quartz geobarometers. *Contributions to Mineralogy and Petrology*, **100**, 92–106.

MOHAN, A., ACKERMUND, D. & LAL, R. K. 1986. Reaction textures and P–T–X trajectory in the sapphirine–spinel bearing granulites from Ganguvapatti, Southern India. *Neues Jahrbuch für Mineralogie Abhandlungen*, **154**, 1–19.

MORSE, S. A. & TALLEY, J. H. 1971. Sapphirine reactions in deep seated granulites near Wilson Lake, Central Labrador, Canada. *Earth and Planetary Science Letters*, **10**, 325–328.

MOTOYOSHI, Y. & HENSEN, B. J. 1989. Sapphirine–quartz–orthopyroxene symplectites after cordierite in the Archaean Napier Complex, Antarctica: evidence for a counterclockwise P–T path. *European Journal of Mineralogy*, **1**, 467–471.

— & ISHIKAWA, M. 1998. Metamorphic and structural evolution of granulites from Rundvågshetta, Lützow-Holm Bay, East Antarctica. In: RICCI, C. A. (ed.) *The Antarctic Region: Geological Evolution and Processes*. Terra Antarctica Publications, Siena.

— & MATSUEDA, H. 1984. Archaean granulites from Mt. Riiser-Larsen in Enderby Land, East Antarctica. *Memoirs of National Institute of Polar Research (Tokyo): Special Issue*, **33**, 103–125.

—, HENSEN, B. J. & ARIMA, M. 1993. Experimental study of the high-pressure stability limit of osumilite in the system K₂O–MgO–Al₂O₃–SiO₂: implications for high-temperature granulites. *European Journal of Mineralogy*, **5**, 439–445.

—, ISHIKAWA, M. & FRASER, G. L. 1994. Reaction textures in granulites from Forefinger Point, Enderby Land, East Antarctica: an alternative interpretation on the metamorphic evolution of the Rayner Complex. *Proceedings of the NIPR Symposium on Antarctic Geosciences*. National Institute of Polar Research, Tokyo, **7**, 101–114.

MOURI, H., GUIRAUD, M. & HENSEN, B. J. 1996. Petrology of biotite–sapphirine-bearing Al–Mg granulites from Ihouhaouene, In Ouzzal, Hoggar, Algeria: an example of phlogopite stability at high temperature. *Journal of Metamorphic Geology*, **14**, 725–738.

NEWTON, R. C. 1972. An experimental determination of the high-pressure stability limits of magnesian cordierite under wet and dry conditions. *Journal of Geophysical Research*, **80**, 398–420.

NIXON, P. H., REEDMAN, A. J. & BURNS, L. K. 1973. Sapphirine-bearing granulites from Labwor, Uganda. *Mineralogical Magazine*, **39**, 420–428.

OUZEGANE, K. & BOUMAZA, S. 1996. An example of ultrahigh-temperature metamorphism: orthopyroxene–sillimanite–garnet, sapphirine–quartz and spinel–quartz parageneses in Al–Mg granulites from In Hiaou, In Ouzzal, Hoggar. *Journal of Metamorphic Geology*, **14**, 693–708.

PATTISON, D. R. M. & BEGIN, N. J. 1994. Compositional maps of metamorphic orthopyroxene and garnet: evidence for a hierarchy of closure temperatures and implications for geothermometry of granulites. *Journal of Geology*, **12**, 387–410.

PERCHUK, L. L., ARANOVICH, L. YA., PODLESSKII, K. K., LAVRENT'EEVA, I. V., GERASIMOV, V. Y., KITSUL, V. I., KORSAKOV, L. P. & BERDNIKOV, N. V. 1985. Precambrian granulites of the Aldan Shield, eastern Siberia, the USSR. *Journal of Metamorphic Geology*, **3**, 265–310.

PERKINS, D. 1990. Thermometry and barometry of mafic granulites based on garnet–clinopyroxene–plagioclase–quartz assemblages. In: VIELZEU, D. & VIDAL, PH. (eds) *Granulites and Crustal Evolution*. Kluwer Academic, Dordrecht, 435–450.

POWELL, R. & SANDIFORD, M. 1988. Sapphirine and spinel phase relationships in the system $\text{FeO}-\text{MgO}-\text{Al}_2\text{O}_3-\text{SiO}_2-\text{TiO}_2-\text{O}_2$ in the presence of quartz and hypersthene. *Contributions to Mineralogy and Petrology*, **98**, 64–71.

RAITH, M., KARMAKAR, S. & BROWN, M. 1997. Ultra-high temperature metamorphism and multistage decompressional evolution of sapphirine granulites from the Palni Hill Ranges, southern India. *Journal of Metamorphic Geology*, **15**, 379–400.

SANDIFORD, M. 1985. The metamorphic evolution of granulites at Fyfe Hills: implications for Archaean crustal thickness in Enderby Land, Antarctica. *Journal of Metamorphic Geology*, **3**, 155–178.

— 1989. Horizontal structures in granulite terrains: a record of mountain building or mountain collapse? *Geology*, **7**, 449–452.

— & POWELL, R. 1986. Pyroxene exsolution in granulites from Fyfe Hills, Enderby Land, Antarctica: evidence for 1000°C metamorphic temperatures in Archaean continental crust. *American Mineralogist*, **71**, 946–954.

— & — 1990. Some isostatic and thermal consequences of the vertical strain geometry in convergent orogens. *Earth and Planetary Science Letters*, **98**, 154–165.

— & — 1991. Some remarks on high-temperature–low pressure metamorphism in convergent orogens. *Journal of Metamorphic Geology*, **9**, 333–340.

—, NEALL, F. B. & POWELL, R. 1987. Metamorphic evolution of aluminous granulites from Labwor Hills, Uganda. *Contributions to Mineralogy and Petrology*, **95**, 217–225.

SENGUPTA, P., DASGUPTA, S., BHATTACHARYA, P. K., FUKUOKA, M., CHAKRABORTI, S. & BHOWMICK, S. 1990. Petro-tectonic imprints in the sapphirine granulites from Anantagiri, Eastern Ghats mobile belt, India. *Journal of Petrology*, **31**, 971–996.

—, KARMAKAR, S., DASGUPTA, S. & FUKUOKA, M. 1991. Petrology of spinel granulites from Araku, Eastern Ghats, India, and a petrogenetic grid for sapphirine-free rocks in the system FMAS. *Journal of Metamorphic Geology*, **9**, 451–459.

SHERATON, J. W., OFFE, L. A., TINGEY, R. J. & ELLIS, D. J. 1980. Enderby Land, Antarctica; an unusual Precambrian high-grade metamorphic terrain. *Journal of the Geological Society of Australia*, **27**, 1–18.

—, TINGEY, R. J., BLACK, L. P., OFFE, L. A. & ELLIS, D. J. 1987. Geology of Enderby Land and Western Kemp Land, Antarctica. *Australian Bureau of Mineral Resources, Bulletin*, **223**.

SHULTERS, J. C. & BOHLEN, S. R. 1989. The stability of hercynite and hercynite–gahnite spinel in corundum- or quartz-bearing assemblages. *Journal of Petrology*, **30**, 1017–1031.

WATERS, D. J. 1986. Metamorphic history of sapphirine-bearing and related magnesian gneisses from Namaqualand, South Africa. *Journal of Petrology*, **27**, 541–565.

— 1991. Hercynite–quartz granulites: phase relations, and implications for crustal processes. *European Journal of Mineralogy*, **3**, 367–386.

Australian Proterozoic high-temperature, low-pressure metamorphism in the conductive limit

MIKE SANDIFORD & MARTIN HAND

*Department of Geology and Geophysics, University of Adelaide,
South Australia 5005, Australia*

Abstract: High-temperature, low-pressure (HTLP) metamorphism often reflects transient advection of heat due to magma ascent. However, the origin of HTLP metamorphism in a number of Australian Proterozoic terranes remains contentious either because of the deficiency of magmatic bodies in the terranes, or because the long time delay (>100 Ma) between magmatism and metamorphism precludes heating by existing magmatic bodies. Furthermore, a number of Australian Proterozoic HTLP terranes (such as the Reynolds Range in central Australia) show evidence of an extended history ($c. 30$ Ma) of HTLP mineral growth suggesting metamorphism during a thermal regime dominated by conduction at lithospheric length scales. Australian Proterozoic metamorphic terranes are characterized by both elevated modern-day heat flows (averaging $c. 85 \text{ mW m}^{-2}$) and granitic gneisses with anomalously high heat production rates (commonly $>5-10 \mu\text{W m}^{-3}$). We show that the conditions required for HTLP metamorphism may result from conduction if the crustal heat production responsible for modern-day heat flows is concentrated at mid-crustal levels (15–20 km). Importantly, for low-intermediate mantle heat fluxes ($10-20 \text{ mW m}^{-2}$) and moderate synmetamorphic crustal thicknesses ($c. 45$ km), the conductive geotherms attendant with such HTLP metamorphism do not necessarily lead to significant melting of a refractory lower crust. Importantly, the thermal regimes are very sensitive to the depths at which crustal heat production is localized. The strong dependence of the resulting geotherms on the depth of the heat-producing layer has the important consequence that only minor burial may be required to induce HTLP metamorphism, while only minor erosion ($c. 5$ km) is necessary to terminate the event.

High-temperature, low-intermediate-pressure (HTLP) metamorphism at temperatures in excess of about 600°C and pressures of less than about 5 kbar has been widely interpreted as resulting from transient thermal events associated with the ascent of magmas through the crust (Lux *et al.* 1978; DeYoreo *et al.* 1991; Collins & Vernon 1991; Sandiford *et al.* 1991). In many HTLP terranes the close spatial and temporal association between metamorphism and magma emplacement clearly supports this interpretation (Holdaway *et al.* 1988; Sisson *et al.* 1989; Sisson & Hollister 1988) which remains the governing paradigm for such metamorphism (Barton & Hanson 1989). Metamorphism governed by advective heat transfer should be characterized by dramatic lateral variations of grade and temporal transience (Sandiford *et al.* 1991, 1995b). As shown by Sandiford *et al.* (1991), the inverse exponential temperature dependence of crustal strength provides a logical reason for the coupling of deformation and heating in such terranes (e.g. Karlstrom & Williams 1995). In convergent orogens, such a thermomechanical coupling may be expected to be evidenced by ‘anticlockwise’ pressure–temperature–time paths.

In HTLP terranes that lack compelling field evidence or geochronological data supporting a

close genetic association of magmatism and metamorphism, the necessity for magmatic heat advection has been advanced largely on the basis of thermal arguments. For example, Sandiford & Powell (1991) argued ‘...high-T-low-P metamorphic terranes cannot simply reflect the conductive response to crustal thickening since the resulting Moho temperatures would greatly exceed the crustal solidus.’ With regard to this kind of thermal argument, it is important to realize that the uncertainty in the basic properties governing the thermal regime within the mid- to deep continental crust (such as thermal conductivities at elevated temperature and the distribution of heat-producing elements) implies a corresponding uncertainty in the deep crustal thermal structure. For example, available measurements would (conservatively) allow an uncertainty of at least 30% in the thermal conductivity structure of the mid- to deep crust, leading to equivalent uncertainties in deep crustal temperatures (that is, an uncertainty in Moho temperature of around 200°C due to conductivity uncertainties alone).

Recent studies in a number of Australian Proterozoic HTLP terranes (e.g. Mt Isa and northern Arunta Inliers) that contain abundant granitic bodies have shown that the main HTLP metamorphism post-dates the major granite

emplacement events by as much as 150 Ma (Jaques *et al.* 1982; Reinhardt 1992; Connors & Page 1995; Williams *et al.* 1996; Hand *et al.* 1995; Vry *et al.* 1996). Furthermore, thermo-chronological data in the Reynolds Range (Williams *et al.* 1995) indicate that elevated temperatures during the HTLP event were sustained for as much as 30 Ma, with little change in pressure, suggesting that synmetamorphic thermal regimes approached steady state.

A notable feature of many Australian Proterozoic HTLP terranes is the unusually high present-day surface heat production (Fig. 1). For example, in the Mesoproterozoic Mt Painter Inlier in South Australia, heat production in granitic gneisses typically exceeds $10 \mu\text{W m}^{-3}$ (Fig. 1a). The mean and median heat produc-

tions (recalculated at 1500 Ma) of 227 samples (granitic gneisses and metasediments) for which analyses are available are 16 and $8 \mu\text{W m}^{-3}$, respectively. In the Reynolds and Anmatjira Ranges in central Australia, 89 analyses of granitic gneisses (which constitute more than 60% of the terrane) indicate a mean heat production of $c. 8 \mu\text{W m}^{-3}$ at the time of metamorphism some 1600 Ma ago (Fig. 1b). Similarly, high heat production values are known from regionally extensive granites in the Mt Isa region, such as the Sybella and Wonga granites (Loosveld 1989). Modern-day heat flows averaging around 85 mW m^{-2} , and locally in excess of 100 mW m^{-2} , through this Australian Proterozoic metamorphic province (Sass & Lachenbruch 1979; Cull 1982; Fig. 2) confirm the regional influence of these high heat production values but also imply that any near-surface, high heat production layer is of only moderate thickness. For example, considering that this province now forms part of a tectonically quiescent craton with a lithosphere estimated to be about 250 km thick (Zielhuis & van der Hilst 1996), we might expect reduced heat flows of around $10-15 \text{ mW m}^{-2}$, with the remaining $70-75 \text{ mW m}^{-2}$ of the observed surface heat flow due to crustal sources. For the observed surface heat productions of between 5 and $10 \mu\text{W m}^{-3}$

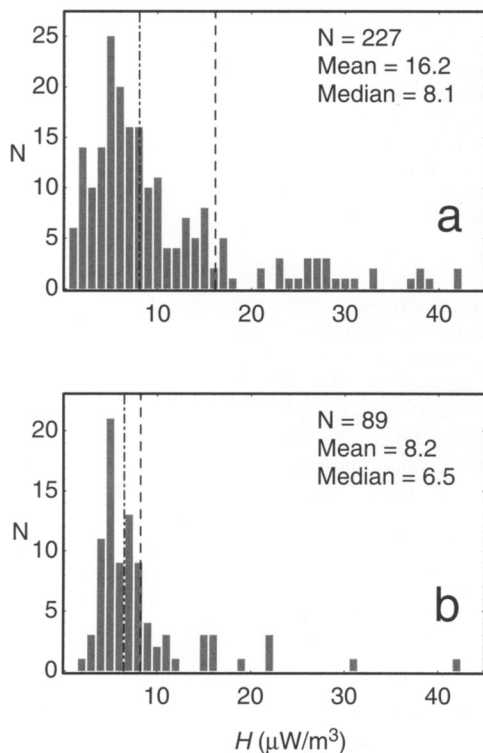


Fig. 1. Heat production values for some Australian metamorphic HTLP terranes. (a) Mesoproterozoic Mt Painter Inlier, South Australia. Data were compiled by N. Wall mostly from Minerals and Energy South Australia unpublished reports (227 analyses). (b) Anmatjira and Reynolds Ranges (total number of analyses is 89, and includes data from Australian Geological Survey Organisation). For clarity, extreme heat production values (in excess of 45 W m^{-3}) are not shown but have been incorporated in calculation of the mean and median of the distributions.

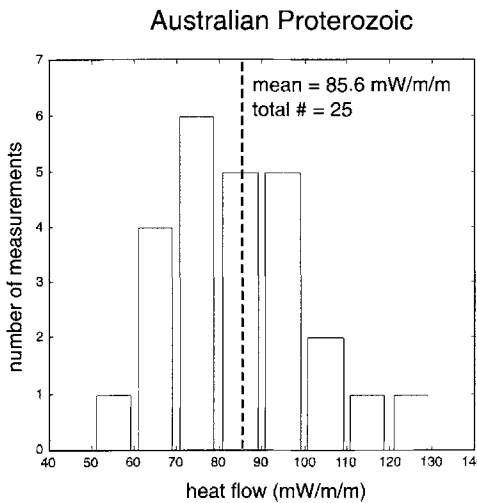


Fig. 2. Heat flow data from Australian Proterozoic terranes, illustrating the generally anomalous nature of this heat flow province (the data are taken from the tabulation of Cull 1982). Two outlying measurements from Warrego (160 mW m^{-2}) and Cattle Creek (48 mW m^{-2}) have been excluded from the analysis. The mean of 25 remaining measurements is 85 mW m^{-2} .

such a contribution would be provided by a layer of total thickness 7–15 km.

The notion that anomalous heat production associated with granites and/or metasediments within the metamorphic pile (as opposed to advective heating) provides a primary control on metamorphic grade in high-grade terranes has been suggested by Chamberlain & Sonder (1990), who were able to correlate variations in the metamorphic grade in New England with current heat flow and surface heat production. Similarly, unconformity-related HTLP metamorphism in the Mt Painter region of the northern Flinders Ranges, South Australia, has been attributed to the anomalous heat production in the basement (Mildren & Sandiford 1995). One obvious question raised by this discussion is *whether it is feasible to generate the conditions associated with HTLP metamorphism without generating significant quantities of melt in the deeper crust*. Motivated by this question, we seek to evaluate the plausibility of HTLP metamorphism in the steady-state

thermal limit. Our approach is essentially parametric in that we are primarily concerned with evaluating the thermal parameter space that may allow steady-state HTLP at mid- to upper crustal levels without appreciably melting the deep crust. In the discussion we return to the question of applicability of our calculations to the metamorphic and geochemical character of select Australian HTLP terranes.

A model for heat production distributions in Australian Proterozoic HTLP terranes

The way in which heat production is distributed with depth in the continental crust has been a long-standing source of interest (e.g. Lachenbruch 1968). The upper crust has long been recognized as having significantly greater heat production than the lower crust, both from the analysis of surface heat flow–heat production data (Lachenbruch 1968) and from geochemical studies of the distribution of heat-producing

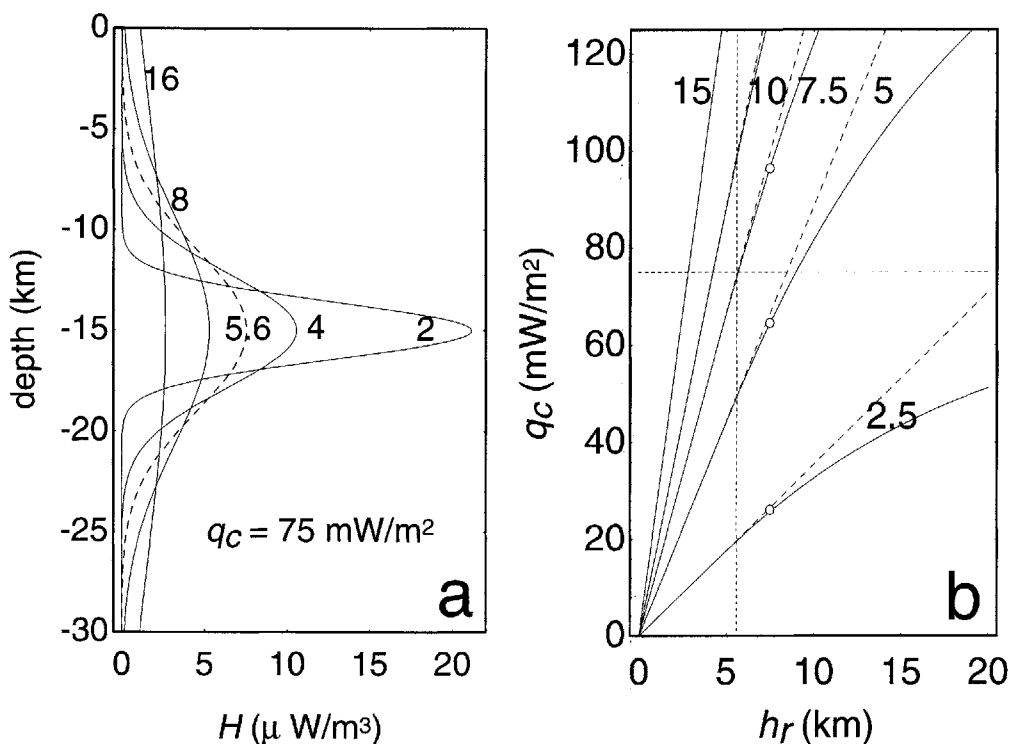


Fig. 3. (a) Heat production distribution specified by equation (2) for a range of values of h_r (2 km, 4 km, 5.6 km (dashed), 8 km and 16 km), with H_i set so the total crustal heat production $q_c = 75 \text{ mW m}^{-2}$. (b) Total crustal heat production values for a range in H_i ($2.5 \mu\text{W m}^{-3}$, $5 \mu\text{W m}^{-3}$, $7.5 \mu\text{W m}^{-3}$, $10 \mu\text{W m}^{-3}$ and $16 \mu\text{W m}^{-3}$) and h_r . Note that providing h_r is less than about 7.5 km ($< z_i/2$) then q_c is linear in H_i and h_r (equation (3) reduces to $q_c \approx H_i h_r \pi^{0.5}$, as shown by the dashed lines).

elements. Such studies have led to the notion that heat production ($H(z)$) varies approximately with an inverse exponential dependence on depth (z), with a form:

$$H(z) = H_i \exp\left(\frac{-z}{h_r}\right) \quad (1)$$

with a characteristic length scale (h_r) of about 10 km. At the time of metamorphism of many Australian Proterozoic HTLP terranes (when current surface exposures were at 15–20 km depth) this relation would imply implausibly high surface heat production rates ($>30 \mu\text{W/m}^3$), and thus is unlikely to be appropriate. Rather, the high heat production at the current surface exposures is likely to have been anomalous not only in terms of the deeper crust but also the shallower crust during metamorphism. The implication of an anomalous heat production at the crustal levels appropriate to these HTLP terranes suggests that the attendant thermal regimes may be approximated by a heat production distribution that is concentrated at a discrete horizon within the crust (we leave the question of the origin of such heat production distributions until the discussion). In order to investigate the thermal consequences of heat production distributions that are concentrated at a discrete level within the crust we propose a variation of equation (1):

$$H(z) = H_i \exp\left(\frac{-(z - z_i)^2}{h_r^2}\right) \quad (2)$$

In this distribution $H(z)$ varies exponentially with depth but rather than reaching its maximum value H_i at the surface, the maximum heat production occurs at depth z_i (Fig. 3a). As for equation (1), the parameter h_r provides a measure of the spread of the heat production distribution (Fig. 3a), with the heat production falling to $H_i e^{-1}$ at depths $z_i \pm h_r$.

In the steady state, the integrated crustal heat production (q_c) represents the crustal contribution to the surface heat flow:

$$q_c = \int_0^{z_c} H(z) dz$$

For the heat production distribution given by equation (2), the integrated crustal heat production is given by:

$$q_c = \frac{H_i h_r \sqrt{\pi}}{2} \left(\text{Erf}\left(\frac{z_c - z_i}{h_r}\right) + \text{Erf}\left(\frac{z_i}{h_r}\right) \right) \quad (3)$$

and the steady-state temperature distribution in the crust of thickness z_c subject to a basal heat

flux q_m with a depth-independent thermal conductivity k is:

$$\begin{aligned} T(z) = & -\frac{q_m z}{k} + \frac{H_i h_r^2}{2k} \\ & \times \left(\exp\left(-\frac{z_i^2}{h_r^2}\right) - \exp\left(-\frac{(z_i - z)^2}{h_r^2}\right) \right) \\ & + \frac{h_r H_i \sqrt{\pi}}{2k} \left(z \text{Erf}\left(\frac{z_c - z_i}{h_r}\right) \right. \\ & \left. + (z_i - z) \text{Erf}\left(\frac{z - z_i}{h_r}\right) \right. \\ & \left. + z_i \text{Erf}\left(\frac{z_i}{h_r}\right) \right) \end{aligned} \quad (4)$$

In the following sections we use equation (4) to evaluate the steady-state limit to HTLP metamorphism. One useful attribute of the distribution specified by equation (2) is that it allows evaluation of the effect of variably concentrating a given total heat production (as highlighted by Fig. 3a). Providing $z_i > 2h_r$ then the integrated crustal heat production is linear in H_i and h_r (see Fig. 3b) and consequently the effect of lumping up (or spreading out) the heat production for a given total crustal heat production is obtained by varying h_r as $1/H_i$.

Parameter ranges and solutions to equation (4)

We are interested in seeking solutions to equation (4) that allow HTLP metamorphism without violating (our) imposed Moho melting condition (see below). Such solutions must comply with known constraints on the independent parameters and boundary conditions that govern the behaviour of equation (4), notably thermal conductivity (k) and mantle heat flow (q_m). We also require a definition of the *Moho melting criterion* and realistic bounds on the magnitude of q_c and z_c during metamorphism. In the following discussion we consider explicitly thermal conductivity in the range 1.5 – $3.5 \text{ W m}^{-1} \text{ K}^{-1}$ and mantle (or reduced) heat flows in the range 10 – 40 mW m^{-2} .

The thermal regimes required for large-scale melting of the lower crust are likely to depend on the lithological makeup of the deep crust which in turn will depend greatly on its prior tectonothermal history. Fertile crust may undergo significant melt extraction at temperatures as low as 700 – 750°C . However, in the HTLP terranes we are concerned with here, metamorphism typically post-dates (by up to

150 Ma) very significant granite melt extraction events, that are likely to have produced a refractory lower crust (as well as enriching the mid-crustal levels in heat production; see Discussion). Such a lower crust is probably able to withstand very high temperatures (up to 1000°C) without significant melting. An example of a lower crustal fragment that withstood temperatures of at least 1000°C without significant melting is provided by the Napier Complex in Enderby Land, Antarctica (Harley 1991; Sandiford 1985). In the following discussion we set, somewhat arbitrarily, an upper limit of 1000°C on the maximum sustainable temperatures $T(Moho)$ in the deep crust without significant melting.

A lower limit on total crustal heat production q_c relevant to the Australian Proterozoic terranes is provided by the measured heat flows (averaging 85 mW m⁻²) which, together with evidence for a 250 km thick lithosphere (Zielhuis & van der Hilst 1996), suggests that presently the integrated crustal heat production contributes, on average, at least 70 mW m⁻² to the surface heat flow. At the time of metamorphism, total crustal heat productions are likely to have been considerably higher, due to the contribution from the upper 10–20 km that has subsequently been removed from the metamorphic pile, and the secular decline in radiogenic heat production (resulting in a decline in heat production of about 20% over the last 1500–1600 Ma for the analyses shown in Fig. 1). We consider the likely range for synmetamorphic q_c to be 75–100 mW m⁻². Note that this is a factor of 2–3 higher than is typically used in modelling metamorphic conditions in the crust (e.g. England & Thomson 1984).

As discussed by Sandiford & Powell (1991), total crustal thicknesses (z_c) during metamorphism of HTLP terranes are unlikely to exceed about 45–50 km, because greater crustal thicknesses are likely to have induced deeper levels of denudation. Note that estimating z_c simply by summing the total denudation and current crustal thicknesses is compounded by significant post-metamorphic deformation in many of the Australian Proterozoic terranes relevant to our discussion.

Main results

A summary of the principal results is provided in Figs 4–9. Figures 4a, 5a, 6a and 7a show geotherms for a range of k , q_m , z_i and h_r values. Note that, in these figures, the heat production parameters have been set such that total crustal

heat production $q_c = 75 \text{ mW m}^{-2}$. In Figs 4–6 this has been achieved by using a fixed parameter set ($H_i = 7.5 \mu\text{W m}^{-3}$ and $h_r = 5.6 \text{ km}$) while Fig. 7 shows the effect of varying H_i as $1/h_r$ for a constant $q_c = 75 \text{ mW m}^{-2}$. Figures 4b, 5b, 6b

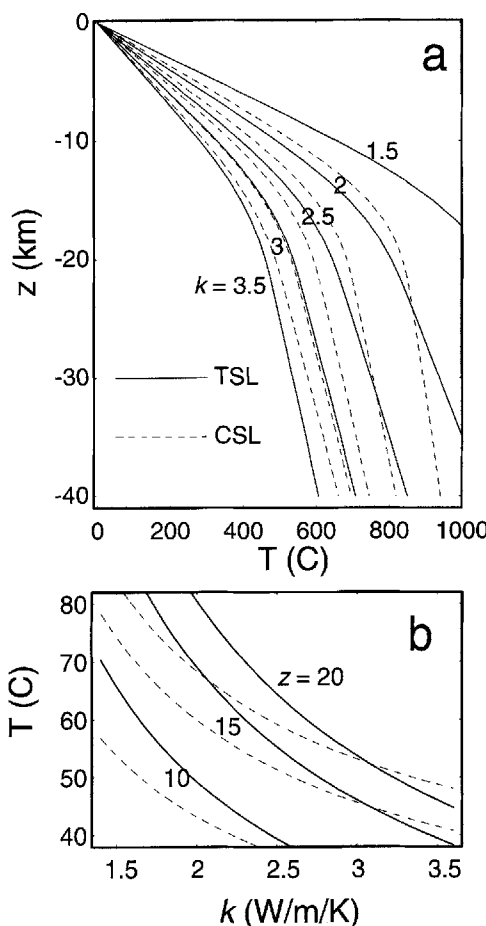


Fig. 4. (a) Geotherms for a range of thermal conductivities with total crustal heat production $q_c = 75 \text{ mW m}^{-2}$. In this figure (and Figs 5–7) solid lines represent solutions to equation (4) and are appropriate to a thermally stabilized lithosphere (TSL) while dashed lines are appropriate to a chemically stabilized lithosphere (CSL). (b) Variation of temperatures T_z at depths of 10, 15 and 20 km with thermal conductivity. Note that variations of thermal conductivity within the experimentally plausible range (1.5–3 W m⁻¹ K⁻¹) have a dramatic effect on the geotherm, allowing a range in temperatures at 15 km in excess of 300°C for both the TSL and CSL (note that not all solutions shown are viable since some lead to unrealistically high Moho temperatures). Default parameter ranges for Figs 4–7 are $z_c = 40 \text{ km}$, $z_i = 15 \text{ km}$, $h_r = 5.6 \text{ km}$, $H_i = 7.5 \mu\text{W m}^{-3}$, $q_m = 25 \text{ mW m}^{-2}$ and $k = 2.25 \text{ W m}^{-1} \text{ K}^{-1}$.

and 7b show the temperatures attained at depths of 10, 15 and 20 km as a function of the variable parameters. Default parameter ranges for Figs 4-7 are: $z_c = 40$ km, $z_i = 15$ km, $h_r = 5.6$ km, $H_i = 7.5 \mu\text{W m}^{-3}$, $q_m = 25 \text{ mW m}^{-2}$ and $k = 2.25 \text{ W m}^{-1} \text{ K}^{-1}$.

Figures 4-7 indicate that the thermal structure of the crust is very sensitive to the thermal conductivity (Fig. 4), and to the depth of the heat-producing layer z_i (Fig. 6). In comparison, the variations in the reduced heat flow q_m and the spread of the heat production distribution h_r (for a given total crustal heat production) provide only second-order controls. The important results illustrated in these figures are that lowering the conductivity and increasing the depth of the heat-producing layer both effect a

dramatic rise in mid-crustal temperatures. More details relating to the individual diagrams can be found in the figure captions.

A problem with the representation in Figs 4-7 is that it is not obvious how mid-crustal and

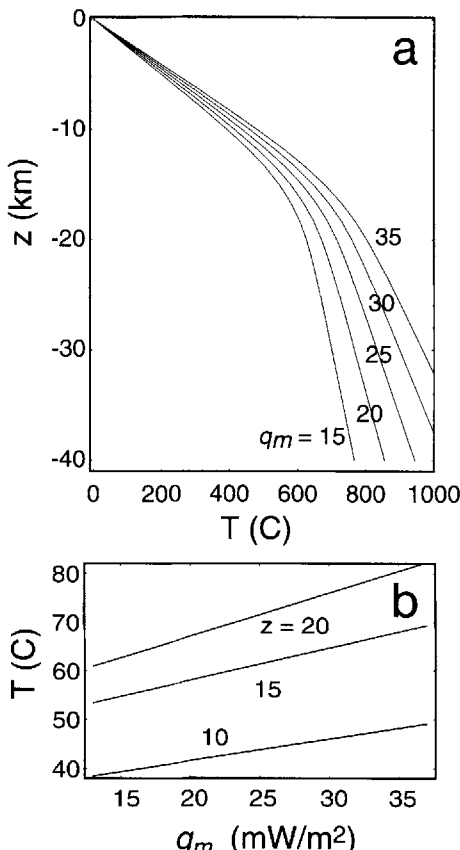


Fig. 5. As for Fig. 4 but with variable reduced heat flow q_m . Varying q_m within the defined range ($20-30 \text{ mW m}^{-2}$) results in a 70°C range in temperature at 15 km depth (b) and thus in comparison with the effect of conductivity (Fig. 4b) and depth of the radiogenic layer (Fig. 7b), provides only a second-order control.

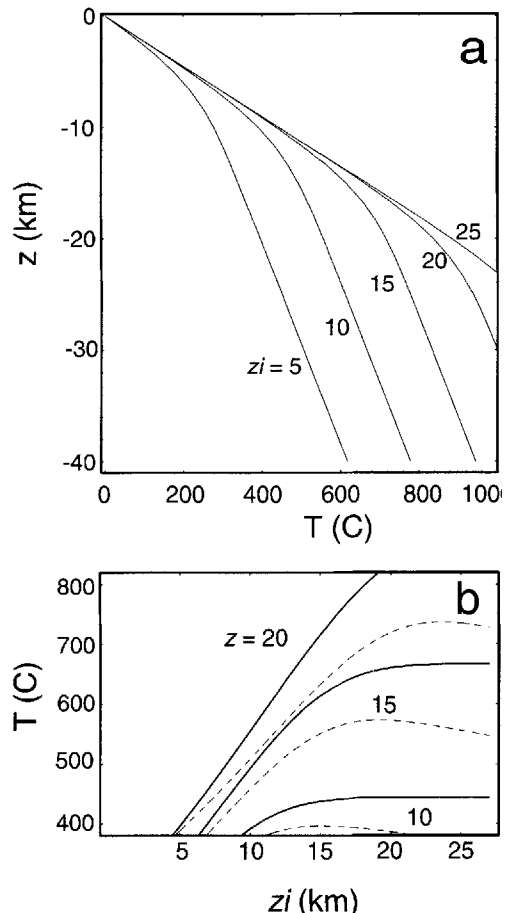


Fig. 6. As for Fig. 4 but with variable depth (z_i) of the radiogenic layer. The figure shows that the parameter z_i has a first-order effect on the temperatures at mid-crustal levels (of the same order as variations in conductivity). The effect is somewhat diminished in the CSL model (dashed lines in Fig. 4b), but remains profound. Note that once the heat-producing layer is significantly below the depth of the observation, then temperatures cease to change with further increases in z_i (and for the CSL model even decline a little with further burial of the heat-producing layer). This figure has profound implications when we consider that changes in z_i will reflect the processes of burial and excavation essential to orogenesis. For example, the burial of radiogenic granitic basement beneath a sedimentary succession provides an excellent model for the heat production distribution specified by equation (2).

Moho temperatures correlate for a given thermal parameter range. Furthermore, these diagrams do not show the effects of varying the total crustal heat production q_c with the other independent parameters. Figure 8a is an attempt to show these effects by plotting solutions to equations (3) and (4) in a parameter space defined by the Moho temperature $T(\text{Moho})$ that results from a particular thermal configuration and either k (Figs 8a and 8b) or z_i (Figs 8c and 8d). Note that we have specifically chosen k and z_i as the independently variable parameters because, as shown in Figs 4–7, they provide

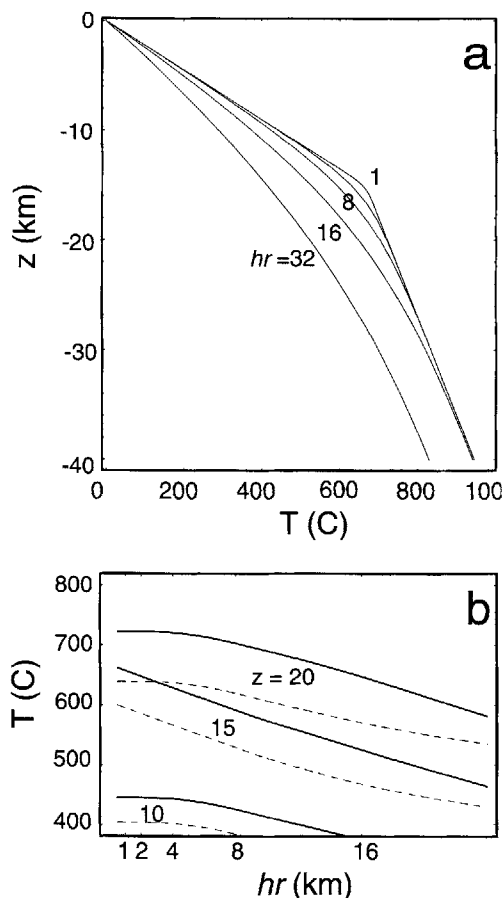


Fig. 7. As for Fig. 4 but with variable heat production parameters h_r and H_i . Note that the total heat production H_i is varied inversely with h_r such that the product $H_i h_r \pi^{0.5}$ remains fixed at 75 mW m^{-2} . For $h_r < 7.5 \text{ km}$ ($0.5z_i$) the total crustal heat production q_c is given by $H_i h_r \pi^{0.5}$ (Fig. 3b). (b) shows that variations in h_r for a given q_c provide only a small (second-order) variation in temperatures $T(z)$ at depths near z_i and very limited variation in temperatures at any significant depths above or below z_i .

the first-order controls on the thermal structure of the middle crust. In Fig. 8, shaded areas indicate regions where parameter ranges produce the approximate conditions of HTLP metamorphism without violating our *Moho melting criterion* or requiring excessive total crustal heat production.

The darker shaded areas in Fig. 8 indicate that thermal conductivities in the range $2.0\text{--}2.5 \text{ W m}^{-1} \text{ K}^{-1}$ combined with an anomalous heat-producing layer buried to depths of around $15\text{--}20 \text{ km}$ may allow steady-state conditions appropriate to HTLP metamorphism without excessively high Moho temperatures (i.e. $T(\text{Moho}) < 1000^\circ\text{C}$), or requiring excessive total crustal heat production (i.e. $q_c < 75 \text{ mW m}^{-2}$). For higher total heat productions (up to 100 mW m^{-2}) the solution space pertinent to low HTLP metamorphism spans the much larger range in thermal conductivities $2.0\text{--}3.0 \text{ W m}^{-1} \text{ K}^{-1}$. At $q_c = 75 \text{ mW m}^{-2}$ and $T(\text{Moho}) = 1000^\circ\text{C}$, the maximum attainable temperatures at 15 km $T(15 \text{ km}) = 620^\circ\text{C}$, and $T(20 \text{ km}) = 715^\circ\text{C}$; for $q_c = 100 \text{ mW m}^{-2}$ the corresponding temperature maxima are $T(15 \text{ km}) = 660^\circ\text{C}$, and $T(20 \text{ km}) = 755^\circ\text{C}$.

The role of conductivity highlighted by Fig. 8, which suggests that intermediate to high thermal conductivities favour the prospect of HTLP metamorphism, may seem at odds with Fig. 4, in which low thermal conductivities clearly result in steeper geotherms. This apparent contradiction reflects the role of conductivity in mediating the geothermal gradient not only in the middle to upper crust but also in the deep crust. Since decreasing k results in steeper lower crustal geotherms (for a given mantle heat flux) it will reduce the maximum sustainable mid-crustal temperature for a given Moho temperature. Conversely, a higher k will, by reducing lower crustal thermal gradients, allow higher mid-crustal temperatures for a given Moho temperature. For very high k , steep geotherms in the upper crust can only be maintained by unrealistically high heat production levels. Thus the apparent contradiction between Figs 4 and 8 simply reflects the important balance resulting from the requirement to minimize lower crustal temperatures whilst maximizing mid-crustal temperatures.

Alternative boundary conditions

In deriving equation (4) we have assumed a thermally stabilized lithosphere (TSL) effecting a constant heat flow through the mantle part of

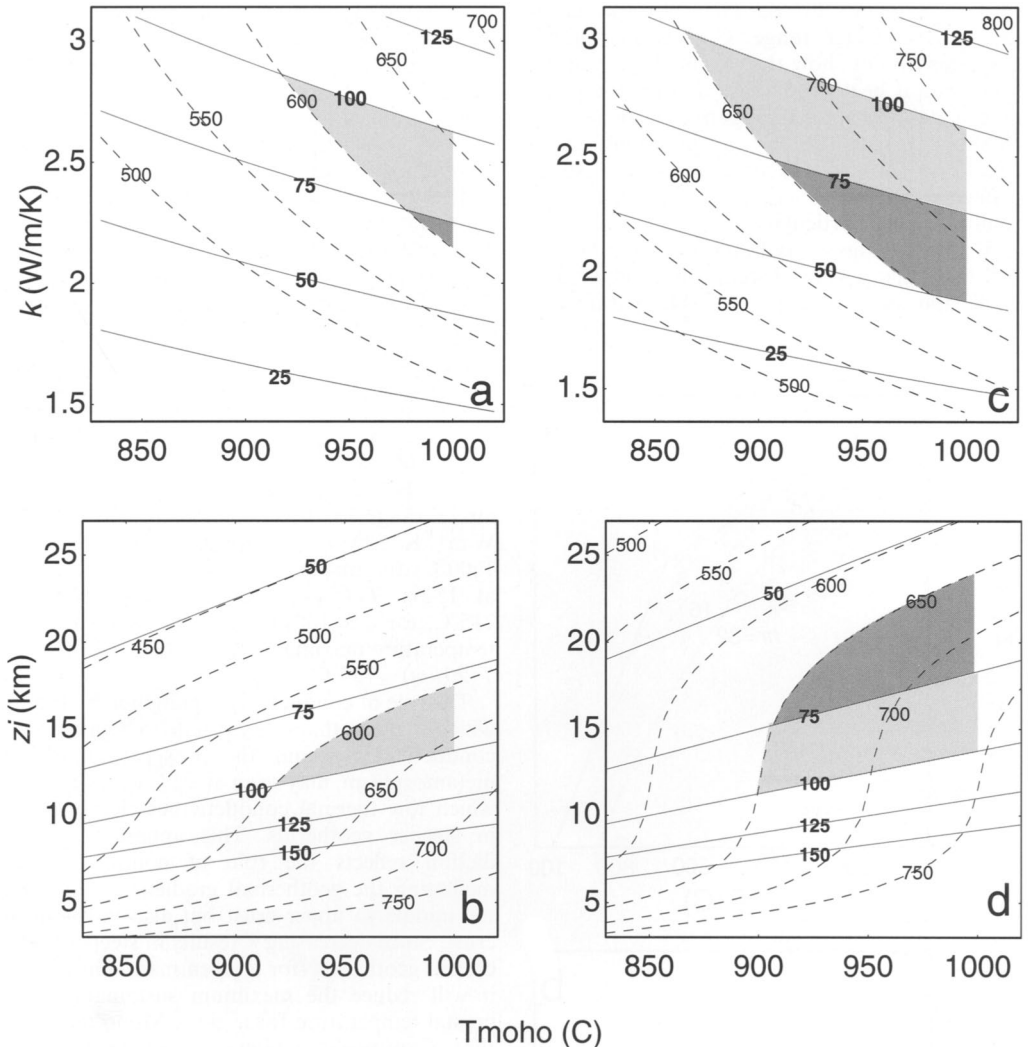


Fig. 8. Solutions to equations (2) and (4) plotted in a parameter space defined by the Moho temperature T_{moho} for $z_c = 45$ km and either k (a and c) or z_i (b and d). Solid contours indicate the total crustal heat production needed to achieve the limiting Moho temperature, while dashed contours indicate the resulting temperatures $T(z)$ at depths of 15 km (a and b) and 20 km (c and d). Shaded areas indicate regions where parameter ranges produce conditions acceptable for HTLP metamorphism without violating our Moho melting criterion or requiring excessive total crustal heat production (heavy shade $q_c < 75 \text{ mW m}^{-2}$, light shade $75 \text{ mW m}^{-2} < q_c < 100 \text{ mW m}^{-2}$ and $T(z = 15 \text{ km}) > 600^\circ\text{C}$ or $T(z = 20 \text{ km}) > 650^\circ\text{C}$). Note that we have used a fixed value for h_r ($= 5.6 \text{ km}$) and thus contours for total crustal heat production can be equated with contours for H_i ($q_c = 50 \text{ mW m}^{-2}$ equates to $H_i \approx 5 \mu\text{W m}^{-3}$, $q_c = 100 \text{ mW m}^{-2}$ equates to $H_i \approx 10 \mu\text{W m}^{-3}$). In a and c, $z_i = 15 \text{ km}$, while in b and d, $k = 2.25 \text{ W m}^{-1} \text{ K}^{-1}$.

the lithosphere. An alternative model that may be equally applicable is that of a chemically stabilized lithosphere (CSL) in which the basal boundary condition is specified as a constant temperature condition at the base of the lithosphere, z_i . The important difference is that in the

CSL model the thermal properties of the crust will modulate the effective heat flow from the mantle, whereas for the TSL model the heat flow through the mantle lithosphere is independent of the overlying crust. There is a good deal of uncertainty in just how thick the continental

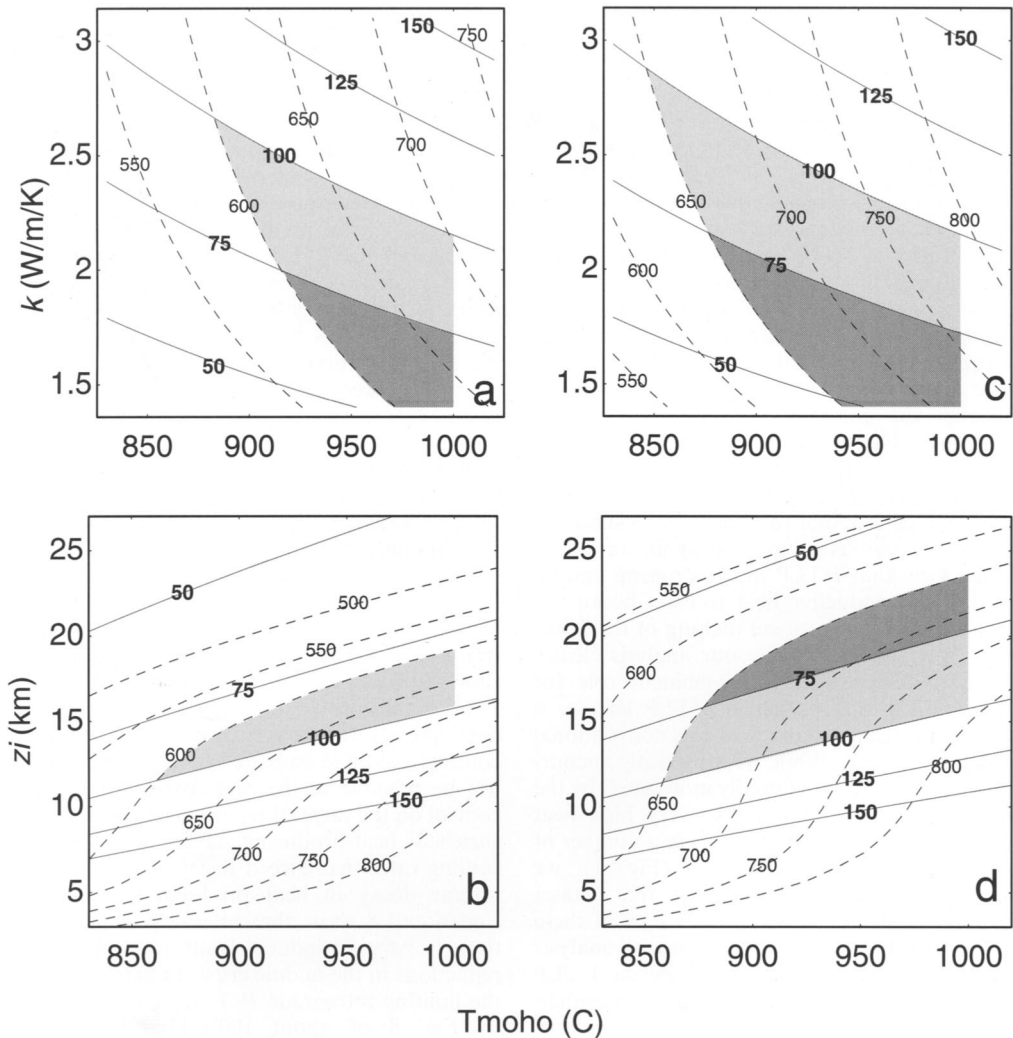


Fig. 9. As for Fig. 8 but with $T(z)$ contours (dashed) based on the CSL model with total lithospheric thickness z_i set at 100 km. The assumed temperature at the base of the lithosphere $T(z_i)$ is 1300°C.

lithosphere may be, and thus specifying the boundary condition for the CSL model is subject to the same kind of uncertainty as specifying q_m for the TSL model.

Figures 4a, 4b, 6b, 7b and 9 show the main results for the CSL model. Note that, for high Moho temperatures, a lower boundary condition of fixed temperature at fixed depth appropriate to the CSL effectively limits the heat flow into the lower crust and thus is equivalent to reducing q_m in the TSL model. For the CSL, this effective heat flow parameter is inversely coupled

to the thermal state of the overlying lithosphere (and thus reduces with decreasing conductivity k , as shown by the dashed lines in Fig. 4a, or increasing the depth of the radiogenic layer z_i). Consequently, the thermal effects of changing k and z_i are somewhat diminished for the CSL, compared to the TSL. An important implication of this is that the effective range of parameters allowing HTLP metamorphism is significantly larger for the CSL than the TSL, as shown by the comparative sizes of the shaded regions in Figs 8 and 9.

Discussion

As illustrated in Figs 4–9, solutions to equation (4) clearly indicate that burial of an anomalously radiogenic layer *c.* 5 km thick, to depths appropriate to HTLP metamorphism, allows the possibility of generating HTLP metamorphism in conductive thermal regimes for a plausible range in thermal parameters. Importantly, at Moho depths of 40–50 km the temperatures may remain lower than 1000°C and thus could preclude widespread melting of a refractory lower crust during the HTLP metamorphism in the middle crust. Of course, for more fertile lower crust, such thermal regimes engender the possibility of extensive melting, with any consequent advection of the melt serving to boost the already elevated geotherms in the middle crust (e.g. Chamberlain & Sonder 1990). We believe that the calculations summarized in the previous section cast significant doubt on the view that HTLP metamorphism cannot result from conductive heat transfer because it would result in widespread melting of the lower crust. We note that, while our analysis clearly does not demonstrate a pre-eminent role for conduction in any particular HTLP terrain, it does demonstrate a fallacy in this conventional thermal argument. While we are greatly encouraged (and indeed were initially motivated) by the existing datasets that point to very high heat production levels ($5\text{--}10 \mu\text{W m}^{-3}$) in a number of Australian Proterozoic terranes (Fig. 1), we must stress that the quality of the dataset pertinent to the thermal energy budget of these terranes is still very poor. Any thorough analysis of the thermal energy budget of specific HTLP terranes will require much more detailed evaluation of heat production parameters, and we urge workers interested in assessing the thermal energy budgets of metamorphic terranes to undertake such evaluations.

A principal finding of our analysis concerns the influence of the depth of an anomalous heat-producing layer z_i on the thermal structure of the crust. As shown in Fig. 6, a change in depth of the radiogenic layer by *c.* 5 km may induce a change in $T(z=15 \text{ km})$ of *c.* 150°C. This finding has a number of potentially important ramifications. For example, it implies that only minor tectonic burial may be required to induce such HTLP metamorphism, while only minor erosion (*c.* 5 km) is necessary to terminate the event. Of great relevance here is the fact that the resulting Moho temperature is also strongly coupled to the depth of the heat-producing layer particularly for the thermally stabilized lithosphere (Figs 8 and 9). In view of the very strong

dependence of lithosphere strength on Moho temperature (e.g. England 1987; Zhou & Sandiford 1992), changes in the depth of burial of a radiogenic layer may have dramatic implications for the mechanical response of the lithosphere. We note that many of the Australian Mesoproterozoic provinces of relevance to this discussion, show extensive reactivation during the Phanerozoic, where they have been deformed in 'thick-skinned' fashion along with a thick cover succession. The implication is that the burial of these high-heat-production Mesoproterozoic provinces beneath Neoproterozoic and Phanerozoic sedimentary basins effected a local thermal weakening of the lithosphere (Sandiford *et al.* 1995a).

A second implication of the sensitivity of conductive temperatures to the depth of an anomalous heat-producing layer is the relationship between the rates of cooling and the shapes of retrograde P – T paths. The notion that HTLP events result from advective thermal processes (Lux *et al.* 1978; DeYoreo *et al.* 1991; Collins & Vernon 1991; Sandiford *et al.* 1991) provides a framework for understanding P – T paths that show isobaric cooling (England & Thomson 1984; Sandiford *et al.* 1991), which should consequently reflect very fast cooling rates. In contrast, genuine isobaric cooling paths would not be possible in the case where the primary control on the thermal regime is an anomalously enriched heat-producing layer (at least, for cooling rates that exceed the time constants for secular decay in heat production). However, Figs 6 and 8 show that relatively small reductions in z_i could induce significant temperature reductions in the middle crust. In many systems, the limiting retrograde P – T trajectories implied by Fig. 8 of about $100^\circ\text{C kbar}^{-1}$, may be petrologically indistinguishable from truly isobaric paths.

As we have noted in the Introduction, Australian Proterozoic HTLP terranes typically form in crustal provinces that have experienced very significant differentiation events associated with voluminous granite magmatism up to 150 Ma prior to metamorphism. This early differentiation presumably has had the twofold effect of developing a very refractory lower crust depleted in heat-producing elements and a complementary middle to upper crust enriched in heat-producing elements, thus providing an ideal setting for the style of HTLP metamorphism advocated here. Of course, in order to generate the heat production distributions appropriate to HTLP metamorphism, it is not enough to differentiate the crust. Equally important is the requirement for the

total crustal heat production to be anomalous ($c. 75-100 \text{ mW m}^{-2}$), and we suggest that the absolute heat production levels in the Australian Proterozoic provinces are likely to be intimately related to the style of granite magmatism that is characterized by very high temperature, strongly fractionated granites, with a strong mantle signature. Of course, while such high-heat-production granite provinces abound in the Proterozoic record, they are clearly not unique to the era. The Cornubian batholith, which is associated with total crustal heat productions of around $90-100 \text{ mW m}^{-2}$, provides a younger example. The analysis presented here suggests that anywhere such enriched granites (or other rocks types) occur there is the potential for developing HTLP metamorphism as a conductive response to the burial of the granitic layer.

We thank N. Wall who collated the data shown in Fig. 1a as part of her BSc Honours research programme, and A. Bingemer whose research around the Mount Painter Inlier has helped clarify many of our views on how geology works in this astonishing region. I. Cartwright, J. Clemens and S. Harley are thanked for their reviews of an earlier version of this manuscript.

References

BARTON, M. D. & HANSON, R. B. 1989. Magmatism and the development of low pressure metamorphic belts: implications from the western United States and thermal modelling. *Geological Society of America Bulletin*, **101**, 1051, 1065.

CHAMBERLAIN, C. P. & SONDER, L. J. 1990. Heat-production elements and the thermal and baric patterns of metamorphic belts. *Science*, **250**, 763-769.

COLLINS, W. J. & VERNON, R. H. 1991. Orogeny associated with anticlockwise P-T-t paths: Evidence from low-P, high-T metamorphic terranes in the Arunta Inlier, central Australia. *Geology*, **19**, 835-838.

CONNERS, K. A. & PAGE, R. W. 1995. Relationships between magmatism, metamorphism and deformation in the western Mount Isa Inlier, Australia. *Precambrian Research*, **71**, 131-154.

CULL, J. P. 1982. An appraisal of Australian heat-flow data. *BMR Journal of Australian Geology and Geophysics*, **7**, 11-21.

DEYOREO, J. J., LUX, D. R., & GUIDOTTI, C. V. 1991. Thermal modelling in low-pressure/high-temperature metamorphic belts. *Tectonophysics*, **188**, 209, 238.

ENGLAND, P. C. 1987. Diffuse continental deformation: length scales, rates and metamorphic evolution. *Philosophical Transactions of the Royal Society, A321*, 17561-17579.

— & THOMSON, A. B. 1984. Pressure-temperature-time paths during metamorphism 1. Heat transfer during the evolution of regions of thickened continental crust. *Journal of Petrology*, **25**, 894-928.

HAND, M., FANNING, M. & SANDIFORD, M. 1995. Low-P high-T metamorphism and the role of high-heat producing granites in the northern Arunta Inlier. *Geological Society of Australia, Abstracts*, **40**, 60-61.

HARLEY, S. L. 1991. The origins of granulites: a metamorphic perspective. *Geological Magazine*, **126**, 215-247.

HOLDAWAY, M. J., DUTROW, B. L. & HINTON, R. W. 1988. Devonian and Carboniferous metamorphism in west-central Maine: the muscovite-almandine geobarometer and the staurolite problem revisited. *American Mineralogist*, **73**, 20-47.

JACQUES, A. L., BLAKE, D. H. & DONCHAK, P. J. T. 1982. Regional metamorphism in the Selwyn area, northwest Queensland. *BMR Journal of Australian Geology and Geophysics*, **7**, 181-196.

KARLSTROM, K. E. & WILLIAMS, M. L. 1995. The case for simultaneous deformation, metamorphism and plutonism: an example from Proterozoic rocks in central Arizona. *Journal of Structural Geology*, **17**, 59-81.

LACHENBRUCH, A. H. 1968. Preliminary geothermal model of the Sierra Nevada. *Journal of Geophysical Research*, **73**, 6977-6989.

LOOSVELD, R. 1989. The synchronism of crustal thickening and low-pressure facies metamorphism in the Mount Isa Inlier, Australia 2. Fast convective thinning of mantle lithosphere during thickening. *Tectonophysics*, **165**, 191-218.

LUX, D. R., DEYOREO, J. J., GUIDOTTI, C. V. & DECKER, E. R. 1978. Role of plutonism in low-pressure metamorphic belt formation. *Nature*, **323**, 795-797.

MILDREN, S. & SANDIFORD, M. 1995. A heat refraction mechanism for low-P metamorphism in the northern Flinders Ranges, South Australia. *Australian Journal of Earth Sciences*, **42**, 241-247.

REINHARDT, J. 1992. The Corella Formation of the Rose-bud Syncline (central Mount Isa Inlier): deposition, deformation, and metamorphism. In: STEWART, A. J. & BLAKE, D. H. (eds) *Detailed Studies of the Mount Isa Inlier*. AGSO Report, **243**, 229-256.

SANDIFORD, M. 1985. The metamorphic evolution of granulites from Fyse Hills, implications for Archaean crustal thickness in Enderby Land, Antarctica. *Journal of Metamorphic Geology*, **3**, 155-178.

— & POWELL, R. 1991. Some remarks on high temperature-low pressure metamorphism in convergent orogens. *Journal of Metamorphic Geology*, **9**, 333-340.

—, BINGEMER, A. & HAND, M. 1995a. Basement involved deformation, heat production and low-pressure metamorphism in the Adelaide fold belt and some wider implications. *Geological Society of Australia, Abstracts*, **40**, 146.

—, FRASER, G., ARNOLD, J., FODEN, J. & FARROW, T. 1995b. Some causes and consequences of high-T, low-P metamorphism, Mount Lofty Ranges. *Australian Journal of Earth Sciences*, **42**, 233–240.

—, MARTIN, N., ZHOU, S. & FRASER, G. 1991. Mechanical consequences of granite emplacement during high-T, low-P metamorphism and the origin of “anticlockwise” PT paths. *Earth and Planetary Science Letters*, **107**, 164–172.

SASS, J. H. & LACHENBRUCH, A. H. 1979. Thermal regimes of the Australian continental crust. In: McELHINNY, M. (ed.) *The Earth: its Origin, Structure and Evolution*. Academic Press, New York, 301–351.

SISSON, V. B. & HOLLISTER, L. S. 1988. Low pressure facies series metamorphism in an accretionary sedimentary prism, southern Alaska. *Geology*, **16**, 358–361.

—, — & ONSTOTT, T. C. 1989. Petrologic and age constraints on the origin of a low pressure/high temperature metamorphic complex southern Alaska. *Journal of Geophysical Research*, **94**, 4392–4410.

VRY, J., COMPSTON, W. & CARTWRIGHT, I. 1996. SHRIMP II dating of zircons and monazites: reassessing the timing of high-grade metamorphism and fluid flow in the Reynolds Range, northern Arunta Block, Australia. *Journal of Metamorphic Geology*, **14**, 566–587.

WILLIAMS, I. S., BUICK, I. S. & CARTWRIGHT, I. 1996. An extended episode of early Mesoproterozoic metamorphic fluid flow in the Reynolds Range, central Australia. *Journal of Metamorphic Geology*, **14**, 29–47.

ZHOU, S. & SANDIFORD, M. 1992. On the stability of isostatically compensated mountain belts. *Journal of Geophysical Research*, **97**, 14 207–14 221.

ZIELHUIS, A. & VAN DER HILST, R. D. 1996. Upper-mantle shear velocity beneath eastern Australia from inversion of waveforms from Skippy portable arrays. *Geophysical Journal International*, **127**, 1–16.

Regional metamorphism due to anorogenic intracratonic magmatism

ROGER L. GIBSON¹ & GARY STEVENS²

¹ Department of Geology and ² Economic Geology Research Unit, University of the Witwatersrand, Private Bag 3, PO WITS, Johannesburg 2050, South Africa

Abstract: The Vredefort Dome, the central uplifted portion of the c. 300 km diameter, 2.02 Ga Vredefort Impact Structure, exposes a c. 20 km deep profile through the crust of the Kaapvaal Craton of southern Africa which displays evidence of greenschist- to granulite-facies low-pressure metamorphism. Reaction textures in the medium- to high-grade metamorphic rocks indicate an anticlockwise isobaric cooling P - T evolution, and peak metamorphic temperatures consistent with a mid- to upper-crustal geotherm of 40–50°C km⁻¹. The metamorphism is attributed to craton-wide intraplating of mantle-derived magmas into the deep crust during the 2.05–2.06 Ga Bushveld Event. Felsic volcanic rocks and high-level intrusions in the Bushveld Complex represent anatetic derivatives from the deeper, high-grade parts of the metamorphic terrane. The intracratonic setting, the absence of evidence of concomitant orogenic deformation, and the preservation of the pre-existing diamondiferous lithospheric root beneath the craton, suggest that the thermal event was triggered by the transient positioning of the Kaapvaal Craton over a mantle plume.

Mantle-derived magmas are widely regarded as playing a major role in advecting heat into the crust in order to effect regional high-temperature low-pressure metamorphism (e.g. Wells 1980; Harley 1989; De Yoreo *et al.* 1991). In most cases of low- P metamorphism documented in the literature, the root is inferred to be a disturbance in the structure of the lithosphere, and immediately underlying asthenosphere, brought about by plate tectonic processes such as subduction (Bohlen 1987), tectonic thinning of the lithosphere (Sandiford & Powell 1986) or removal of the mantle lithosphere from the crust due to tectonic overthickening (Loosveld 1989; Sandiford & Powell 1991). In this paper we document an early Proterozoic regional, greenschist- to granulite-facies, low- P metamorphic terrane in the Kaapvaal Craton (South Africa) which occurs in an intracratonic setting, spatially and temporally unrelated to orogenic activity. We attribute this event to intraplating of mafic-ultramafic magmas generated by mantle plume activity. The preservation of some of the magmatic rocks and voluminous felsic extrusive and intrusive rocks in proximity to the metamorphic rocks provides a rare example where the link between mantle magmatism, regional low- P metamorphism and crustal anatexis can be studied.

Regional setting

The Kaapvaal Craton of southern Africa (Fig. 1) is one of the oldest known fragments of Archaean continental crust, comprising a nucleus of subsidiary arc-like oceanic terranes (greenstones)

and tonalite-trondjhemite-granodiorite basement ranging in age from 3.7 to 3.1 Ga (De Wit *et al.* 1992). Following consolidation of the cratonic nucleus at 3.1 Ga, four major unconformity-bounded supracrustal sequences (the Dominion Group and the Witwatersrand, Ventersdorp and Transvaal Supergroups) were deposited on the craton in Late Archaean to Early Proterozoic times (Table 1). Between 2.7 and 2.65 Ga, the craton was docked with the Zimbabwe Craton to the north along the Limpopo Belt (Fig. 1).

Following the formation of the Archaean to Proterozoic basins, the Kaapvaal Craton experienced a major magmatic episode, the Bushveld Event, at c. 2.05–2.06 Ga (Table 1). The most voluminous component of this magmatism comprises ultramafic to mafic intrusive rocks in the Bushveld (Rustenburg Layered Suite) and Molopo Farms Complexes (Fig. 1) which are located within the upper levels of the Transvaal Supergroup, as well as abundant sills in the immediately underlying supracrustal succession. Geochronological data (Table 2) indicate an age of 2061 ± 27 Ma for the Rustenburg Layered Suite (Walraven *et al.* 1990). Coetzee & Kruger (1989) obtained a similar age (2041 ± 41 Ma) for the Losberg Complex, a small outlier of mafic and ultramafic rocks located 100 km south of the main outcrops of the Bushveld Complex (Fig. 1).

The Rustenburg Layered Suite is intruded and overlain by rocks of the Lebowa Granite Suite (Fig. 1), dated at 2054 ± 2 Ma (Walraven & Hattingh 1993). Both Suites intrude a sequence of heterogeneous, predominantly felsic, volcanics and minor intercalated sedimentary rocks (Rooiberg Group) and granophyre sills (Rashoop

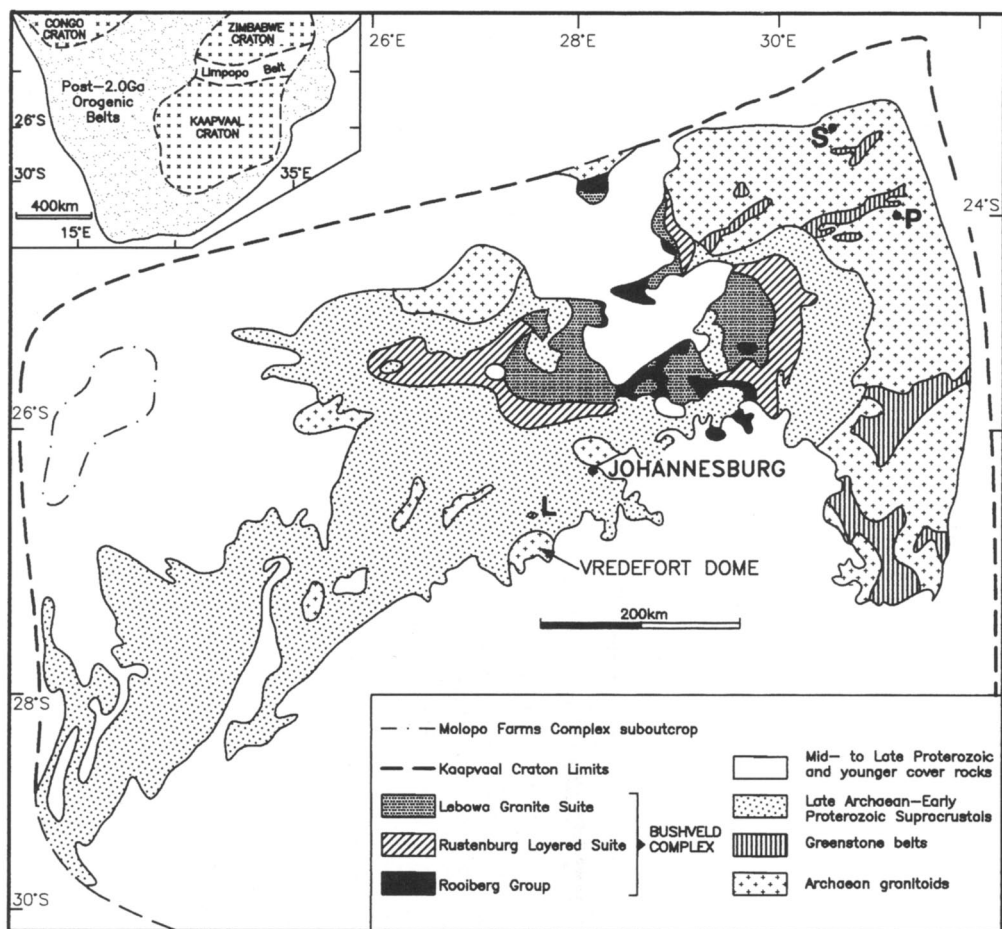


Fig. 1. Regional geology of the Kaapvaal Craton showing the locations of the Bushveld Complex and related intrusions (S, Schiel Alkaline Complex; P, Phalaborwa Alkaline Complex; L, Losberg Complex), and the Vredefort Dome. The sub-outcrop limits of the Molopo Farms Complex, which is not exposed at surface, are shown in the west of the craton.

Granophyre Suite) (Fig. 1) which were originally regarded as being over 100 Ma older than the Bushveld intrusions (Coertze *et al.* 1978). However, recent field and geochemical studies (Hatton & Schweitzer 1995; Schweitzer *et al.* 1995) suggest that the eruption of the Rooiberg Group was penecontemporaneous with the intrusion of the Rustenburg Layered Suite. This is supported by a U-Pb zircon age of 2061 ± 2 Ma for a Rooiberg Group lava (Table 2; Walraven 1997).

In addition to the mafic-ultramafic and felsic magmatism in the central and western portions of the craton, two alkaline complexes of similar age (Table 2), Phalaborwa (2060.6 ± 0.5 Ma;

Reischmann 1995) and Schiel (2059 ± 35 Ma; Walraven *et al.* 1992), intrude the Archaean basement in the northeast of the craton (Fig. 1).

The Bushveld Event was closely followed by the formation of the Vredefort Dome in the south-central parts of the craton (Fig. 1) at *c.* 2.02 Ga (Table 1). Apart from limited tectonic reactivation of cratonic lineaments, and localized magmatic activity and intracratonic basin sedimentation in some parts of the craton, most subsequent tectonomagmatic activity in the region was confined to the craton boundaries where lateral accretion of material onto the craton occurred towards the end of the early Proterozoic Ubendian Event (*c.* 1.8 Ga; Master

Table 1. Generalized Archaean to Early Proterozoic evolutionary scheme for the Kaapvaal Craton

Age (Ga)	Event	Interpretation
2.02	Vredefort	large meteorite impact
2.05–2.06	Bushveld	voluminous mafic-ultramafic intrusions, felsic volcanics and intrusions
2.2–1.8	Ubendian	SE-directed subduction beneath Kaapvaal Craton along NW margin, culminating in orogenesis at 1.8 Ga
2.43–2.22	Upper Transvaal	c. 3–4 km arenaceous–argillaceous foreland basin sedimentation
2.58–2.43	Lower Transvaal	c. 1–2 km dolomite epicontinental shelf sedimentation
2.70–2.65	Limpopo	Alpine convergence and amalgamation of Kaapvaal and Zimbabwe Cratons
2.71	Ventersdorp	c. 4 km tholeiitic flood basalts and subsidiary rift sedimentation
2.84–2.71	Upper Witwatersrand	c. 3 km arenaceous–rudaceous fluvio-deltaic foreland basin sedimentation
2.98–2.91	Lower Witwatersrand	c. 4 km argillaceous–arenaceous sub-tidal passive margin sedimentation
3.09–3.07	Dominion	c. 2.5 km bimodal volcanics and subsidiary rift sedimentation
3.7–3.1	Archaean craton	mafic-ultramafic volcanic arcs and sediments + tonalite–trondjhemite–granodiorite–granite intrusions

After Stanistreet & McCarthy (1991), De Wit *et al.* (1992), Robb & Meyer (1995), Cheney 1996.

Table 2. Detailed geochronology of the Bushveld Complex

Unit	Age (Ma)	Technique	Source
Lebowa Granite Suite	2054 ± 2	single-zircon Pb-evaporation	Walraven & Hattingh (1993)
Rustenburg Layered Suite	2061 ± 27	Rb-Sr whole-rock	Walraven <i>et al.</i> (1990)
Rashoop Granophyre Suite	2060 ± 2	single-zircon Pb-evaporation	Walraven (1997)
Rooiberg Group	2061 ± 2	single-zircon Pb-evaporation	Walraven (1997)

1991) and during the 1.2–1.0 Ga Namaqua, and c. 500 Ma Pan-African Events (Thomas *et al.* 1994). As a result, much of the Archaean and Early Proterozoic structure of the craton has been preserved largely intact.

General geology of the Vredefort Dome

The Vredefort Dome is an 80-km-wide structure located 120 km southwest of Johannesburg, partially covered by Phanerozoic sediments and dolerites of the Karoo Supergroup (Figs 1 and 2). Its core is composed of heterogeneous pre-3.1 Ga granitoid gneisses and subsidiary metamorphosed supracrustal rocks and mafic intrusions. Stepto (1990) divided this core into an inner domain, dominated by leucogneisses (Inlandsee Leucogranofels Terrane), and an outer domain dominated by heterogeneous granodioritic, trondjhemitic and granitic gneisses and granites (Outer Granite Gneiss Terrane) (Fig. 2). The core is surrounded by a collar of generally sub-vertical to overturned supracrustal rocks of the post-3.1 Ga late Archaean to early Proterozoic sedimentary–volcanic sequences of the Dominion Group and the Witwatersrand, Ventersdorp and

Transvaal Supergroups (Fig. 2). The steep dip of the supracrustal strata in the collar shallows outward into a rim synclinorium that surrounds the dome. The stratigraphically highest unit exposed in the core of this syncline is the mafic to ultramafic Losberg Complex (Fig. 1). Other intrusive rocks in the supracrustal succession include Bushveld-related mafic sills in the Transvaal Supergroup beneath the Losberg Complex, Ventersdorp-age mafic sills in the Witwatersrand Supergroup (Pybus *et al.* 1995), and several small peralkaline and dioritic complexes (Fig. 2). Walraven & Elsenbroek (1991) estimated a c. 2.2 Ga age for these complexes, but recently Moser (1997) obtained a U/Pb single-zircon age of 2078 ± 12 Ma.

A variety of unusual features in the rocks of the Vredefort Dome (shatter cones, planar microdeformation lamellae in quartz, coesite and stishovite) indicates that they have been exposed to shock pressures in excess of 20 kbar, consistent with an origin by meteoritic impact (see review in Reimold & Gibson 1996). The Vredefort Dome is thus interpreted as the rebound-induced central uplift of a large, c. 250–300 km diameter impact structure that encompasses most of the Witwatersrand Basin

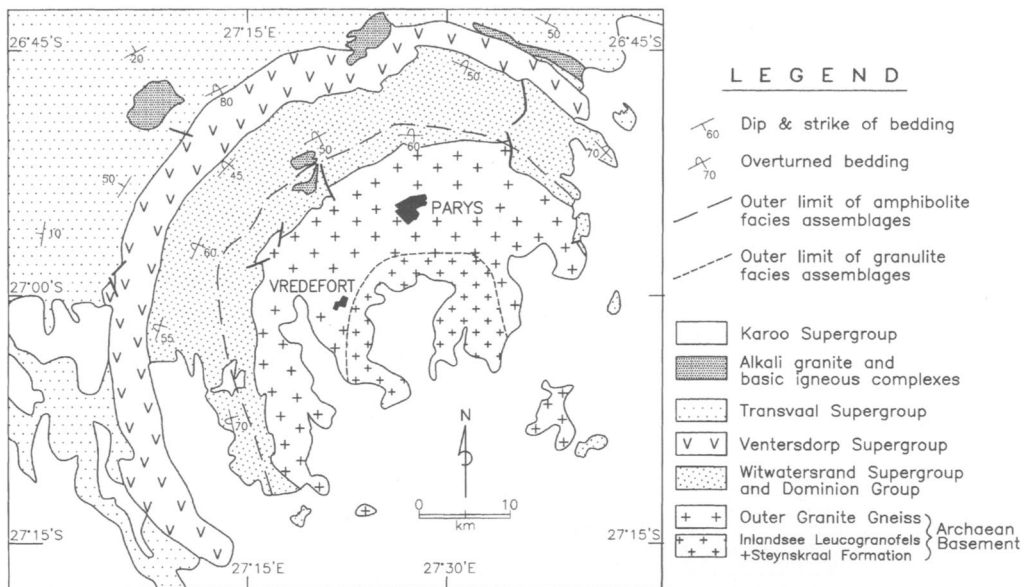


Fig. 2 Simplified geological map of the Vredefort Dome showing the distribution of the amphibolite- and granulite-facies metamorphic zones.

(Henkel & Reimold 1995; Reimold & Gibson 1996, and references therein). One of the effects of the impact-related deformation was the generation of abundant, extremely voluminous pseudotachylitic breccias (Reimold & Colliston 1994; Gibson *et al.* 1997a, b) similar to those observed in the Sudbury impact structure in Canada (Thompson & Spray 1996). U-Pb dating of shock-metamorphosed zircons from the basement rocks, and zircons from these pseudotachylitic breccias, indicates an age of 2023 ± 4 Ma for the impact event (Kamo *et al.* 1996), corroborating earlier Ar-Ar results of *c.* 2.02 Ga from other pseudotachylitic and impact breccias (Walraven *et al.* 1990; Allsopp *et al.* 1991; Trieloff *et al.* 1994; Spray *et al.* 1995).

The geometry of the dome indicates that it exposes a cross-section through a large part of the crust of the Kaapvaal Craton. Based on geochemical studies in the core of the dome, Slawson (1976) proposed that the exposures represent an almost complete crustal section, a view shared by Hart *et al.* (1990) who suggested that ultramafic rocks situated close to the surface in the centre of the dome represented upper mantle. Recent geophysical modelling of the impact structure (Henkel & Reimold 1995) and quantitative thermobarometry (see below) suggest, however, that only upper- and mid-crustal levels are exposed. In the remainder of this paper we describe the metamorphic features

observed in these rocks and relate these to a model for their formation.

Greenschist- to granulite-facies rocks exposed in the Vredefort Dome

In the goldfields at the margins of the Witwatersrand Basin, which surrounds the Vredefort Dome, the regional grade of metamorphism has been established as lower greenschist facies ($350 \pm 50^\circ\text{C}$, 2–3 kbar; Phillips & Law 1994). In the dome itself, metamorphic facies are distributed broadly concentrically, with grade increasing radially inwards (Fig. 2). The peak metamorphic assemblages are affected by the shock deformation phenomena and pseudotachylitic breccias (Gibson & Wallmach 1995; Gibson *et al.* 1997b; Stevens *et al.* 1997b), indicating that this metamorphism predated the shock event (Fig. 3a, b).

Greenschist-facies zone

The greenschist-facies zone in the outer collar of the dome is located in dolomites (lower Transvaal Supergroup), mafic lavas and sills (Ventersdorp Supergroup) and orthoquartzites with minor pelites (upper Witwatersrand Supergroup). The pelites contain chloritoid and aluminosilicate minerals (Nel 1927; Bisschop 1982)

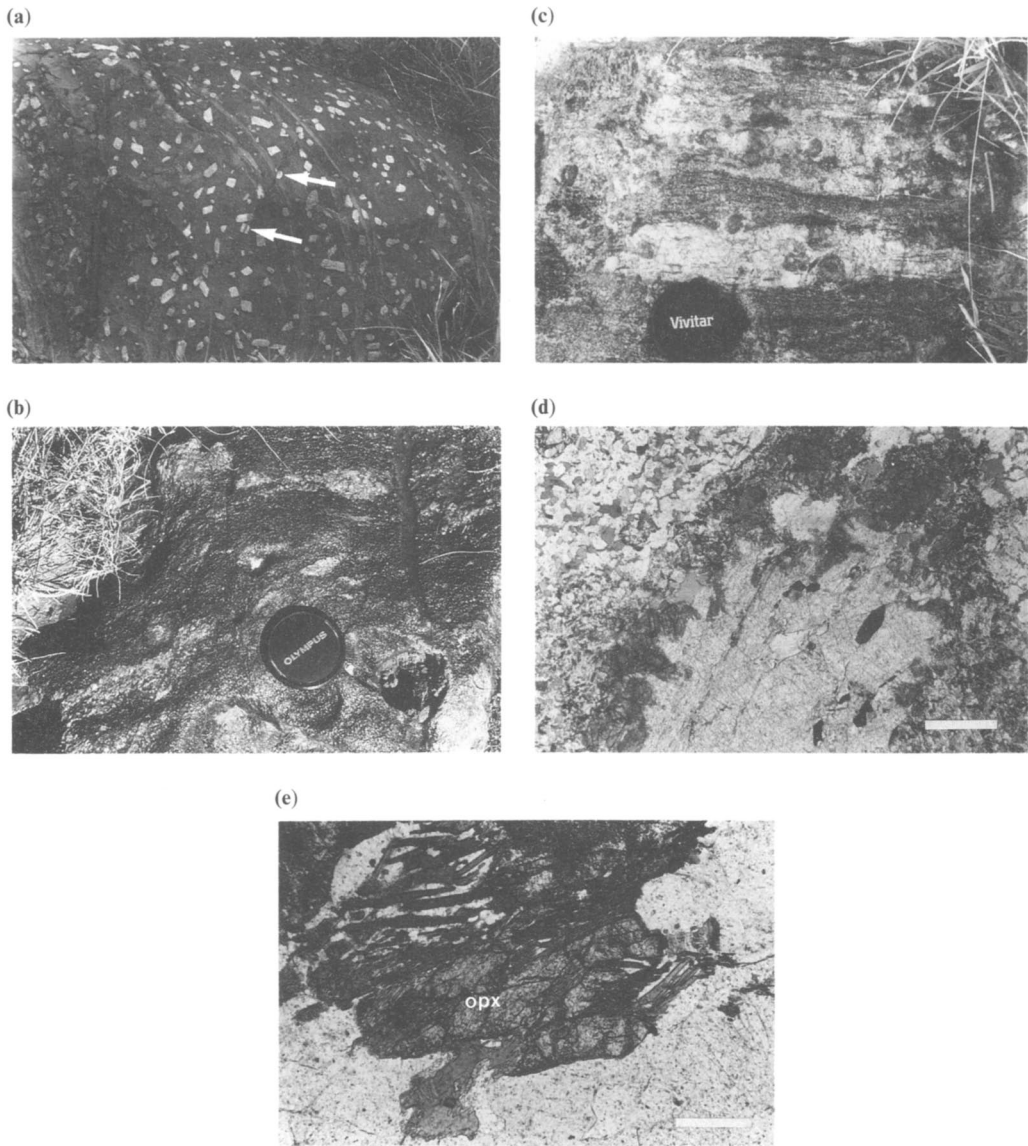


Fig. 3. Metamorphic features of metapelites from the Vredefort Dome. (a) Andalusite metapelite from the lower Witwatersrand Supergroup (amphibolite-facies zone). Note the well preserved sedimentary bedding defined by the light grey quartz-rich layers and the thin pseudotachylite veinlet cutting andalusite porphyroblasts (arrowed). (b) Pelitic migmatite (granulite-facies zone) showing pseudotachylitic breccia veins cutting and displacing thin leucosomes. (c) Pelitic stromatic migmatite from the granulite facies zone showing large garnet crystals produced by fluid-absent biotite melting. (d) Staurolite-muscovite-quartz aggregates replacing andalusite porphyroblast (centre); lower Witwatersrand Supergroup, amphibolite-facies zone. Scale bar 500 μm . (e) Retrogressive replacement of peak metamorphic orthopyroxene (opx) by vermicular biotite-quartz intergrowths related to leucosome recrystallization in granulite-facies migmatite. Scale bar 150 μm .

and $\text{Bt} + \text{Chl} +$ white mica (mineral abbreviations after Kretz 1983), indicative of lower- to mid-greenschist-facies conditions. This is confirmed by assemblages in the mafic lavas of the

Ventersdorp Supergroup and the Ventersdorp-age mafic sills within the upper Witwatersrand Supergroup ($\text{Chl} + \text{Act} + \text{Pl}$ (relict) + Ep ; Bisschop 1982).

Amphibolite-facies zone

The amphibolite-facies zone straddles the boundary between the supracrustal rocks in the collar of the dome and the Archaean basement in the core (Fig. 2). In the collar, this zone includes pelites, orthoquartzites and banded ironstones of the lower Witwatersrand Supergroup, the mafic lavas of the Dominion Group and intercalated Ventersdorp mafic sills. The boundary between the greenschist- and amphibolite-facies zones is defined by the appearance of fibrous hornblende, with clinozoisite partially replacing calcic plagioclase in the mafic sills (hornblende-zoisite zone; Bisschoff 1982). In the lowermost parts of the Witwatersrand Supergroup, the sills contain a $Hbl + Pl$ (andesine) + $Qtz + Spn \pm Zo$ paragenesis (hornblende-andesine zone; Bisschoff 1982), indicative of mid-amphibolite-facies metamorphic grades. A similar assemblage occurs in the mafic Dominion Group lavas (Jackson 1994). The most informative assemblages are those in the metapelites, which involve biotite, chlorite, muscovite, cordierite, andalusite, garnet and/or staurolite, and which occur in various combinations depending on bulk rock composition (Bisschoff 1982; Gibson & Wallmach 1995). The rocks contain two poorly defined, synmetamorphic foliations oriented oblique to bedding (Gibson 1993), but no evidence has been found of related outcrop- or larger-scale folding and the preservation of delicate sedimentary structures indicates only low ductile strain in these rocks (Fig. 3a). Kyanite and fibrolitic sillimanite occur as rare phases, always in association with andalusite. Minerals show no evidence of compositional zoning (Gibson & Wallmach 1995).

In the Archaean basement in the outer parts of the core of the dome (Outer Granite Gneiss; Stepto 1990; Fig. 2), amphibolitic xenoliths contain $Hbl + Bt + Pl + Qtz$ assemblages, consistent with upper amphibolite facies conditions. There are no other rock types containing diagnostic assemblages.

Granulite-facies zone

The amphibolite- to granulite-facies transition coincides with the gradational transition between the Outer Granite Gneiss and the Inlandsee Leucogranofels Terranes (Fig. 2). Outcrop within the granulite-facies zone is poor and field relationships are complicated by extensive structural disruption caused by the impact event. Within the leucogneiss are found xenoliths of a dismembered supracrustal succession comprising pelitic, ironstone and mafic

granulites. Peak metamorphic assemblages are coarse-grained and texturally well equilibrated and, in the pelites, are associated with anatetic features (Fig. 3b, c). The peak assemblage in the ironstones is $Grt + Opx + Qtz + Mag \pm Cpx$ whereas the mafic granulite assemblages comprise $Cpx + Hbl + Pl + Mag \pm Opx$ (Stepto 1979). In the metapelites, coarse-grained garnet, cordierite and orthopyroxene crystals occur in association with stromatic leucosomes (Fig. 3c) or in anhydrous, aluminous restitic assemblages. The garnet commonly contains inclusions of relict sillimanite and biotite and, more rarely, hercynitic spinel. The evidence points to the attainment of conditions consistent with incongruent biotite melting such as: $Bt + Sil + Qtz + Pl = Grt + Crd \pm Opx \pm Kfs + M$. The restitic assemblages, e.g. $Grt + Qtz$, $Grt + Opx$, $Crd + Kfs + Rt$, indicate that temperatures in some parts of the terrane exceeded the upper limit of biotite stability.

Peak P-T conditions, P-T paths and geothermal gradients

The calculation of peak $P-T$ conditions in the amphibolite-facies metapelites in the collar of the dome is hampered by a pervasive retrograde event that post-dates the impact shock event. This led to overgrowth of the peak metamorphic assemblages by a secondary paragenesis, and to chemical re-equilibration of garnet and biotite (Gibson & Wallmach 1995; Gibson *et al.* 1997b). However, two critical prograde to peak reaction textures are preserved, and allow constraints to be placed on the $P-T$ conditions and $P-T$ path:

1. in magnesian bulk rock compositions ($X_{Mg} \approx 0.5-0.6$), andalusite occurs as a rim around cordierite porphyroblasts, suggesting the reaction: $Crd + Ms = And + Bt + Qtz$; and
2. in intermediate X_{Mg} bulk compositions ($X_{Mg} \approx 0.3-0.45$), staurolite replaces andalusite by the reaction: $And + Bt = St + Ms + Qtz$ (Fig. 3d). Staurolite also pseudomorphs cordierite porphyroblasts in these rocks.

Both of the above reactions have shallow positive dP/dT slopes, with the products occurring on the high- P side (Holland & Powell 1990) (Fig. 4). The textures thus indicate an anti-clockwise $P-T$ path for the rocks and peak $P-T$ conditions of 570–600°C at 4.0–4.5 kbar (Fig. 4). Similar $P-T$ conditions were estimated by Jackson (1994), from assemblages in the mafic Dominion Group lavas. A broadly isobaric cooling (IBC) path is inferred for these

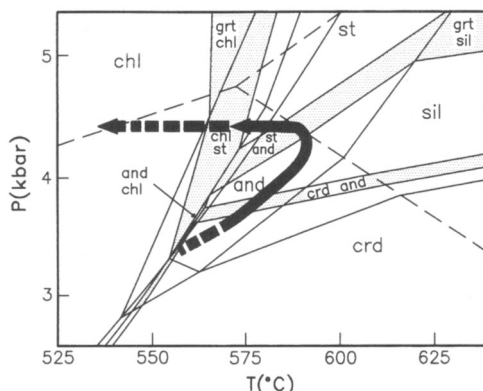


Fig. 4. P - T path for amphibolite facies metapelites from the lower Witwatersrand Supergroup in the Vredefort Dome, based on reaction textures. P - T pseudosection for $X_{\text{Mg}} = 0.3$ for the assemblage $\text{Grt} + \text{St} + \text{Als} + \text{Crd} + \text{Chl} + \text{Bt}$ (excess $\text{Ms} + \text{Qtz} + \text{H}_2\text{O}$) from Dymoke & Sandiford (1992).

rocks as estimates of the depth of overburden at the time of the meteorite impact (estimated to be 14 km from reconstructions using shatter-cone orientations; Manton 1965) are similar to the maximum burial depths of the rocks during the metamorphic peak (Fig. 4).

In the metapelitic granulites, the restitic, biotite-free nature of some of the assemblages indicates that they experienced peak temperatures in excess of the upper limit of biotite stability. Experimental studies suggest that this limit is reached at $c. 920^{\circ}\text{C}$ in pelites containing biotite with normal Ti and F contents (Vielzeuf & Hollaway 1988; Stevens *et al.* 1997a). The presence of peak metamorphic biotite in some of the migmatites indicates that not all of the granulites experienced these temperatures. However, minimum temperatures of $c. 850^{\circ}\text{C}$ are necessary to produce significant melt proportions in pelitic protoliths by biotite breakdown (Stevens *et al.* 1997c). Schreyer (1983) estimated similar peak temperatures of $>875^{\circ}\text{C}$ for the mafic granulite assemblages and Schreyer *et al.* (1978) estimated peak temperatures of $>800^{\circ}\text{C}$ in the ironstone granulites, based on clinoeulite–ferroaugite exsolution textures after ferropigeonite.

Mineral compositional data for the pressure estimates (Table 3) were obtained from the JEOL JSM 6400 SEM in the Geology Department at the University of Manchester (for operating conditions, see Stevens *et al.* 1997b). Using the program Thermocalc (Powell & Holland 1988) with the updated dataset of Holland & Powell

(1990), the assemblage Grt–Crd–Opx–Qtz in samples VT596 and VGS3 yields peak metamorphic pressures of 5.1 ± 1.6 kbar and 4.8 ± 1.3 kbar respectively at 900°C . The Grt + Sil = Spl + Qtz geobarometer of Nichols *et al.* (1992) yielded similar pressures of 4.9 ± 0.9 kbar at 800°C and 6.3 ± 0.8 kbar at 900°C respectively, for sample VT600.

The near-peak prograde P - T path for the granulites can be constrained from the textural relations between spinel and garnet. Spinel occurs only as inclusions within garnet, indicating that the reaction $\text{Grt} + \text{Sil} = \text{Spl} + \text{Qtz}$ was crossed from the spinel to the garnet side. As this reaction has a positive dP/dT slope, and as the spinel occurs as inclusions in the peak-metamorphic garnet (indicating that the reaction occurred prior to or during the attainment of peak metamorphic temperatures), the rocks must have evolved along an anticlockwise P - T path (Fig. 5).

Post-peak, retrograde cooling in the migmatitic metapelites involved partial rehydration of cordierite from the peak assemblage to produce $Bt + Sil + Qtz$, and orthopyroxene to produce $Bt + Qtz$ (Fig. 3e). The absence of similar retrograde effects in the melt-depleted restitic granulites suggests that this reaction was related to crystallization of the leucosomes. No evidence has been found of concurrent garnet breakdown through pressure-sensitive equilibria, suggesting that cooling was approximately isobaric.

Both the peak and the retrograde granulite assemblages are overprinted by a post-impact, lower- P , lower-granulite-facies event which produced fine-grained symplectic partial replacement textures involving Opx + Crd \pm Spl (Stevens *et al.* 1997b).

The peak P - T estimates obtained from the amphibolite- and granulite-facies metapelitic assemblages indicate that the synmetamorphic geothermal gradient in the upper and middle crust must have reached values of 40 – $50^{\circ}\text{C km}^{-1}$, at least locally. This is similar to the estimate for the greenschist-facies metamorphism observed in the Witwatersrand gold-fields (Phillips & Law 1994) and implies extremely high heat flux through the craton at this time.

Discussion

Timing of the metamorphism

The textural evidence from the metapelites in the Vredefort Dome (Fig. 3a, b) indicates that the metamorphic peak occurred prior to the impact

Table 3. Mineral compositions for geobarometry

	Garnet			Cordierite		Orthopyroxene		Spinel	
	VT596	VGS3	VT600	VT596	VGS3	VT596	VGS3	VT600	VT600
SiO ₂	37.82	37.57	38.88	49.81	50.41	50.77	51.12	—	—
Al ₂ O ₃	20.68	20.39	20.64	34.12	33.97	3.12	3.11	56.99	57.63
Cr ₂ O ₃	0.41	0.32	0.41	—	—	—	—	2.31	2.37
Fe ₂ O ₃	1.90	1.51	2.07	—	—	—	—	1.96	1.55
FeO	32.77	31.98	28.41	4.48	4.33	28.75	28.53	24.62	25.33
V ₂ O ₅	—	—	—	—	—	—	—	1.42	0.82
MnO	0.93	1.04	0.84	—	—	—	—	0.11	0.11
MgO	5.72	5.66	8.62	10.84	10.94	16.92	17.24	7.99	7.75
ZnO	—	—	—	—	—	—	—	4.61	4.24
CaO	1.05	1.53	1.33	—	—	0.16	—	—	—
Na ₂ O	—	—	—	0.31	0.36	—	—	—	—
Total	101.28	100.00	101.19	99.56	99.38	99.72	100.00	100.01	99.80
Si	5.94	5.97	6.00	4.98	3.98	1.96	1.95	—	—
Al	3.83	3.82	3.74	4.01	3.98	0.15	0.14	15.01	15.17
Cr	0.05	0.04	0.05	—	—	—	—	0.41	0.42
Fe ³⁺	0.22	0.18	0.24	—	—	—	—	4.60	4.73
Fe ²⁺	4.31	4.25	3.66	0.37	0.36	0.93	0.91	0.33	0.26
V	—	—	—	—	—	—	—	0.21	0.12
Mn	0.12	0.14	0.11	—	—	—	—	0.02	0.02
Mg	1.35	1.34	1.98	1.62	1.62	0.97	0.98	2.66	2.58
Zn	—	—	—	—	—	—	—	0.76	0.70
Ca	0.18	0.26	0.22	—	—	0.01	—	—	—
Na	—	—	—	0.06	0.07	—	—	—	—
Total	16.00	16.00	16.00	11.04	11.04	4.02	3.98	24.00	24.00
O	24.00	24.00	24.00	18.00	18.00	6.00	6.00	32.00	32.00
Mg#	23.85	23.97	35.11	81.41	81.81	51.05	51.85	36.64	35.29

event. The available geochronological data from the amphibolite- and granulite-facies rocks, however, suggests a temporal overlap between the metamorphism and the impact event:

1. Ar-Ar mineral (Allsopp *et al.* 1991; Gibson, unpublished data) and Rb-Sr whole-rock data (Hart *et al.* 1981; Walraven *et al.* 1990; Allsopp *et al.* 1991) display a spread between *c.* 2070 Ma and *c.* 1950 Ma, with the main cluster between *c.* 2060 Ma and *c.* 2010 Ma (Reimold *et al.* 1995); and
2. a SHRIMP U-Pb zircon age of 2017 ± 5 Ma obtained from a small leucogranite body in the granulite facies gneisses (Gibson *et al.* 1997a) is indistinguishable from the age obtained for the impact event (2023 ± 4 Ma; Kamo *et al.* 1996).

Additional, circumstantial evidence supporting a close temporal relationship between the metamorphism and the impact event is provided by textural studies of the impact-related shock deformation features (e.g. Grieve *et al.* 1990; Martini 1992) and quantitative and semi-quantitative geothermometry from metamorphic assemblages that post-date the impact event

(Schreyer 1983; Fricke *et al.* 1990; Gibson & Wallmach 1995; Gibson *et al.* 1997a, b; Stevens *et al.* 1997b). These indicate unusually high post-impact temperatures in the rocks of the dome, compared with the rocks exposed in the comparably sized Sudbury impact structure in Canada (e.g. Dressler 1984). Such elevated post-impact temperatures are best explained if the crustal geotherm at the time of impact exceeded that expected in stable cratonic crust. Gibson *et al.* (1997b) estimated a minimum value for the pre-impact geotherm in the Vredefort region of *c.* $25^{\circ}\text{C km}^{-1}$, in contrast to a value of $15\text{--}16^{\circ}\text{C km}^{-1}$ predicted from heat-flow studies (Grieve *et al.* 1990; Jones (1988) in Martini 1992). Such an elevated pre-impact geotherm suggests the occurrence of a transient thermal event on the craton shortly before the 2.02 Ga impact.

Further evidence is provided by the persistence, until after the impact event, of anatetic melts derived during the metamorphic peak in the granulites (Gibson *et al.* 1997a; Stevens *et al.* 1997b). This indicates that parts of the granulite-facies terrane were still at temperatures above the granite solidus at the time of impact.

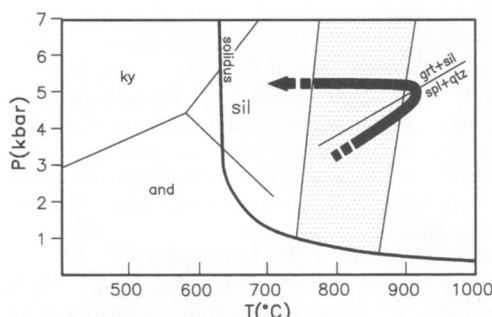


Fig. 5. P - T path for metapelitic granulites in the Vredefort Dome. Stippled field represents the experimentally determined field of biotite-melt coexistence (after Stevens *et al.* 1997a). Slope of $\text{Grt} + \text{Sil} = \text{Spl} + \text{Qtz}$ reaction from Nichols *et al.* (1992).

From this, we conclude that the metamorphic and impact events must have occurred within a period of no more than a few tens of millions of years. As the Bushveld Complex predates the impact by only some 30 Ma (2.05–2.06 Ga; Table 1), the most plausible explanation is that the metamorphism was linked to the Bushveld magmatic event.

The Bushveld magmatothermal event

Given the temporal link between the greenschist- to granulite-facies metamorphism and the Bushveld magmatism indicated by the geochronological studies, the anticlockwise P - T paths documented for the medium- and high-grade rocks are inferred to reflect magmatic thickening of the upper crust due to shallow-level intrusions and/or volcanism (the lateral equivalents of the Bushveld Complex and the underlying mafic sills). The thermobarometric data for the rocks in the Vredefort Dome indicate, however, that the heat source for the mid-crustal metamorphism was located at depth. Thus, the Bushveld event must have also included voluminous lower- to sub-crustal mantle-derived intrusions.

Mid- to lower-crustal harzburgitic intrusions which display a chemical affinity with the Rustenburg Layered Suite have been described from borehole core from the central granulite terrane in the Vredefort Dome (Merkle & Wallmach 1997). In addition, deep-crustal reflection seismic data from the vicinity of the Vredefort Dome indicate several major, laterally extensive, sub-horizontal lower crustal reflectors

that could represent mafic to ultramafic sills (Durrheim *et al.* 1991). The main evidence in support of voluminous lower crustal intraplating of mantle magmas during the Bushveld Event comes, however, from bulk and mineral chemical studies of the Rustenburg Layered Suite. Cawthorn & Davies (1983) and Kruger (1994) noted that the parental magmas for the Rustenburg Layered Suite are enriched in Si, K, Rb and $^{87}\text{Sr}/^{86}\text{Sr}$, indicating contamination by a siliceous source. The mineral chemistry and crystallization sequence observed in the Rustenburg Layered Suite also suggests that the parental magmas underwent varying degrees of crystal fractionation in deeper-level magma chambers prior to their final emplacement (Cawthorn & Walraven 1997). The remarkably uniform chemistry of individual magma pulses across the Bushveld Complex indicates that the magmas spent sufficient time at these deeper levels to achieve thorough mixing with the crustal contaminants.

Cawthorn & Walraven (1997) conservatively estimated the volume of mafic to ultramafic rock preserved within the present outcrop limits of the Bushveld Complex to be 384 000 km³. This figure does not include eroded material, the Molopo Farms Complex (Fig. 1) which has an estimated volume of 200 000 km³ (Reichardt 1994), or the sills in the underlying Transvaal Supergroup which attain a cumulative thickness of 2.5 km in places (Sharpe 1984). Modelling of the crystallization history of the Rustenburg Layered Suite also indicates that a volume of magma at least equivalent to that comprising the presently preserved Rustenburg Layered Suite must have escaped from the Bushveld Complex magma chamber before it could crystallize (Cawthorn & Walraven 1997). In addition to this, the crystallized residuum left in the deeper-level magma chambers must be included. Thus, the evidence suggests a cumulative volume of mantle-derived magma in excess of 1×10^6 to 1.5×10^6 km³. This volume is comparable to the volumes of mafic volcanic rocks found in major flood basalt provinces such as the Deccan and North Atlantic Tertiary Province, although the estimates for the latter do not include the intrusive rocks inferred to underlie these provinces (White & McKenzie 1995). The most recent geochronological data available for the Bushveld Complex (Table 2), although not as precise as those obtained for some flood basalt provinces, suggest that rates of magma production during the Bushveld Event were of the same order of magnitude (i.e. cubic kilometres per year) (White & McKenzie 1995; Cawthorn & Walraven 1997).

Experimental studies by Cawthorn & Biggar (1993) suggest that the parental magmas of the Rustenburg Layered Suite intruded at temperatures in excess of 1300°C. Given that the magmas underwent fractional crystallization at lower crustal levels prior to their final emplacement, this implies that their initial temperatures were even higher. Experimental and theoretical work by Huppert & Sparks (1988) has shown that, in the case of intraplating at such temperatures and in such volumes, the lower crust in contact with the intraplated magmas would have undergone widespread partial melting on a time scale of the order of 10^2 to 10^3 years. This is in marked contrast to terranes dominated by conductive heat transfer where prograde heating through the fluid-absent melting interval is either extremely unlikely or, in the case of crust with a prior elevated heat flux, will take tens of millions of years (e.g. England & Thompson 1984). Geochemical studies of the felsic volcanic rocks and granophyres (Schweitzer *et al.* 1995) and the Lebowa Granite Suite (Kleeman & Twist 1989) in the Bushveld Complex have established both that they were derived from crustal sources, and that they were emplaced at the same time as the Rustenburg Layered Suite. This, together with their exceptional volumes ($>110\,000\text{ km}^3$ to $300\,000\text{ km}^3$ for the lavas of the Rooiberg Group (Twist & French 1983; J. Schweitzer, pers. comm. 1997)), and a minimum of approximately $90\,000\text{ km}^3$ for the Lebowa Granite Suite (Kleeman & Twist 1989) supports the existence of a regionally extensive, intraplating-driven heating event in the lower crust of the Kaapvaal Craton. The emplacement temperature of the granites (in excess of 900 °C; Kleeman & Twist 1989) suggests that they were derived from levels similar to those exposed in the central granulite-facies terrane in the core of the Vredefort Dome.

To summarize, the greenschist-to granulite-facies metamorphic terrane exposed in the Vredefort Dome represents part of a much more extensive, craton-wide, low-*P* metamorphic terrane that developed in response to the intrusion of voluminous mantle-derived magmas at *c.* 2.05–2.06 Ga. In the next section we discuss the constraints on the origin of the mantle magmatism which gave rise to this event.

Constraints on the origin of the Bushveld magmatic event

Voluminous mafic magmatism is generally attributed to decompression melting of the upper mantle asthenosphere (e.g. McKenzie &

Bickle 1988) associated with thinning of the overlying lithosphere or convection within the asthenosphere itself. In recent years, a variety of mechanisms for lithospheric thinning have been proposed to explain how such decompression might also account for regional low-*P* metamorphism in which magmatic intraplating or underplating was involved (e.g. Bird 1979; Houseman *et al.* 1981; Sandiford & Powell 1986, 1991; Loosveld 1989). Most of these studies invoke lithospheric plate tectonic processes (subduction, tectonic overthickening or tectonic thinning) as the cause of the decompression.

In the case of the Bushveld event, it is apparent from regional studies in the Kaapvaal Craton that the magmatism and metamorphism could not have been associated with orogenic activity, as (a) the rocks of the Transvaal Supergroup show no evidence of significant pre-Bushveld deformation, and (b) their preservation over large parts of the craton indicates a lack of significant erosional exhumation which is a normal consequence of crustal thickening. At 2 Ga, the craton formed part of a larger continental mass incorporating, *inter alia*, the Zimbabwe Craton and several other smaller cratons to the north, the Grunehogna Block of Antarctica to the east and, possibly, the Pilbara Craton to the south (Master 1991; Cheney 1996). According to Master (1991), between 2.2 Ga and 1.8 Ga this continental mass formed the overriding plate above a SE-dipping subduction zone whose trench was located some 1200 km to the NW of the central parts of the Kaapvaal Craton. Subduction was finally terminated at *c.* 1.8 Ga (Ubendian Orogeny; Master 1991). During the Bushveld Event the Kaapvaal Craton experienced extensional and strike-slip reactivation of Archaean structures, consistent with NE–SW directed extension which A. Friese (pers. comm. 1997) attributes to plate boundary forces related to this subduction event. The preservation of the volcanic rock and shallow-level intrusive rocks of the Bushveld Complex indicates, furthermore, that the significant magmatic thickening related to the Bushveld event must have been compensated by concomitant crustal thinning.

The volume of magma estimated to have been involved in the Bushveld event is similar to that of a small- to medium-sized flood basalt event (White & McKenzie 1995). White & McKenzie (1995) suggest that the optimum conditions for such an event involve the interaction of a mantle plume with lithosphere that has been thinned to between 110 and 50 km. However, some authors (e.g. Richards *et al.* 1989) maintain that such

volumes of melting might be achieved within abnormally hot plumes without the need for lithospheric thinning. It is unfortunate that fractionation of the magmas that produced the Rustenburg Layered Suite, and their contamination by crustal material (Cawthorn & Davies 1983; Kruger 1994; Cawthorn & Walraven 1997), preclude direct estimation of the depth of formation of the parent magmas, which might resolve this issue. Homogeneous thinning of the Kaapvaal lithosphere to the values proposed by White & McKenzie (1995) can, however, be ruled out as the craton contains abundant Late Proterozoic to Cretaceous diamondiferous kimberlites which contain a predominantly *c.* 3.1 Ga diamond population (Richardson *et al.* 1984). This indicates that a lithospheric root in excess of 140 km must have existed beneath the craton in the Archaean and that it must have survived the Bushveld event. One way to reconcile this with the White & McKenzie (1995) model is if lithospheric thinning was heterogeneous and the arrival of a plume beneath the lithosphere led to localized decompression melting in 'thinspots' (Thompson & Gibson 1991). Limited published geophysical data indicate that the crustal thicknesses in the central parts of the craton vary by up to 30%, from 32 km to 45 km (Green *et al.* 1995). If similar amounts of thinning also affected the underlying mantle lithosphere, it could indicate regions where the Kaapvaal lithosphere was only 100 km thick. However, this value is at the lower limit of the range required for major melting proposed by White & McKenzie (1995). To compensate for this, the plume head would have to have been exceptionally hot and voluminous, conditions which are most likely to be achieved in juvenile plumes (Richards *et al.* 1989; Griffiths & Campbell 1990; White & McKenzie 1995). Either the transient nature of such young plumes, which rapidly degenerate into cooler, smaller, steady-state plumes (Richards *et al.* 1989; Griffiths & Campbell 1990; White & McKenzie 1995), or migration of the craton away from the plume source, might explain why the Bushveld event never proceeded to the development of oceanic crust.

Figure 6 shows the envisaged model for the Bushveld magmatothermal event, in which a hot juvenile plume reached the base of the Kaapvaal lithosphere at *c.* 2.06 Ga, leading to partial melting within the plume head and in asthenosphere beneath thinned regions of the lithosphere (Fig. 6a). These 'thinspots' may already have existed in the Kaapvaal lithosphere prior to the Bushveld event. However, the tectonic reconstructions (A. Friese, pers. comm. 1997)

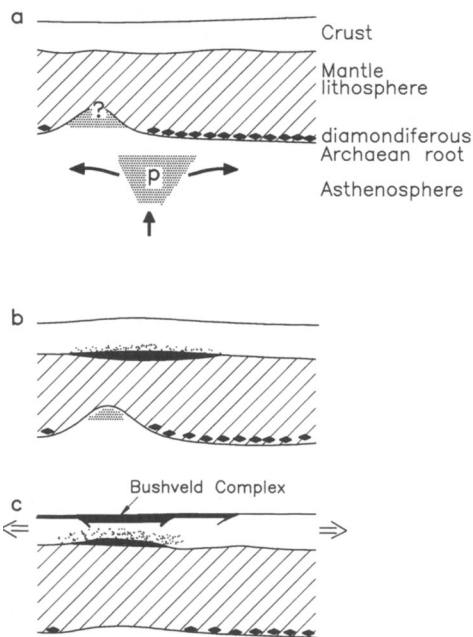


Fig. 6. Proposed model for the Bushveld magmatic and metamorphic event. (a) Rising plume beneath the thick Kaapvaal lithosphere results in decompression melting (dark stipple) in the plume head (p) and, possibly, in thinspots. (b) Mantle magmas (black) underplate and intraplate the deep Kaapvaal crust and undergo partial fractional crystallization, leading to medium- to high-grade metamorphism, with widespread anatexis at the highest grades (stipple). (c) Felsic anatectic melts and remaining mafic to ultramafic melts from the deep crustal magma chambers rise and are emplaced as the Bushveld Complex. Thermal weakening of the crust leads to thinning, assisted by rifting due to extensional boundary forces, to accommodate the magmatic overthickening.

allow for syn-Bushveld extensional thinning. Once these mantle melts had formed, they rose to levels immediately below, or within, the crust where partial fractional crystallization occurred (Fig. 6b). The heat released from these magmas resulted in an elevated crustal geotherm, to values approaching $40-50^{\circ}\text{C km}^{-1}$, and regional metamorphism of the adjacent crust. Crustal anatectic magmas generated by this event rose to form the felsic volcanic rocks of the Rooiberg Group and the shallow-level intrusions of the Raschoop Granophyre and Lebowa Granite Suites. At the same time, the partially fractionated and contaminated mafic magmas were remobilized and rose to intrude shallow crustal levels as the Rustenburg Layered Suite and its

extensions in the Molopo Farms and Losberg Complexes (Fig. 6c). These rocks were preserved as a result of concomitant crustal thinning to compensate for the magmatic overthickening. This thinning prevented exhumation of the deeper levels of the metamorphic terrane until the Vredefort impact event at 2.02 Ga in the south-central parts of the craton, explaining the IBC paths observed in the metamorphic rocks. The absence of evidence of the formation of oceanic crust suggests that the magmatic event was transient, either due to degeneration of the mantle plume from its initial state to a steady state, or due to migration of the craton away from the plume source.

*Implications for regional low-*P* metamorphism*

It is clear from studies of recent and present-day plume activity (e.g. Hawaii, Kerguelen, Réunion) that mantle plumes can exist independently both of the movement of lithospheric plates and of lithospheric plate boundaries. Starting plumes, in particular, appear capable of inducing voluminous, transient, mantle-derived intraplating events in the crust which, under the right conditions, could generate regional low-*P* metamorphism and extensive crustal anatexis in intraplate settings unrelated to orogenic or other tectonic activity. This does not preclude such magmatothermal events being associated with large-scale crustal deformation; magmatic intraplating may trigger deformation in the thermally weakened crust, due to plate boundary forces. Given that starting plumes may produce thermal anomalies over regions 1500–2000 km or more across (White & McKenzie 1995), such deformation could be of regional extent.

Conclusions

1. A greenschist- to granulite-facies low-*P* metamorphic terrane exposed in the central parts of the Kaapvaal Craton, in the Vredefort Dome, is linked to intracratonic, anorogenic mantle-derived magmatism at 2.05–2.06 Ga. The highest-grade rocks in the dome correspond to the upper levels of the anatexic lower crust that generated the felsic magmas, preserved as volcanic rocks and shallow-level granites in the Bushveld Complex.
2. The anticlockwise *P-T* paths deduced for the medium- and high-grade zones in the metamorphic terrane are consistent with

3. magmatic loading by mantle-derived magmas and felsic melts derived from the lower crust.
4. The volumes of mafic and felsic magma are consistent with the metamorphic event being regionally extensive.
5. The lack of erosion of the Bushveld volcanics and high-level intrusions, and the IBC paths for the metamorphic rocks, indicate crustal extension and thinning concomitant with magmatic thickening.
6. Evidence that diamondiferous, lower lithospheric levels (beneath large parts of the craton) survived the Bushveld event indicates that extensive mantle lithospheric thinning may not be a prerequisite for low-*P* metamorphism.
7. The intracratonic setting of the metamorphic rocks, and the lack of evidence of temporally related orogenic activity and lithospheric thinning, suggest a mantle plume as the ultimate cause of the Bushveld magmatothermal event. The coincidence of felsic and mafic magmatism indicates that prograde heating of the lower and middle crust is likely to have been extremely fast (<10 Ma).
7. Exhumation of the amphibolite- to granulite-facies mid-crustal levels of the terrane was unrelated to the magmatothermal event itself and required the highly unusual mechanism of meteorite impact.

R. Gibson acknowledges financial support from the Foundation for Research Development (Grant Number GUN2034547). G. Stevens is grateful to the Foundation for Research Development for comprehensive research support. This paper has benefited from discussions with P. Buchanan, G. Cawthorn, A. Friese and S. Webb. The manuscript was greatly improved by reviews by J. Clemens, N. Harris, N. Petford and P. Treloar. L. Whitfield and D. du Toit drafted the diagrams.

References

ALLSOOPP, H. L., FITCH, F. J., MILLER, J. A. & REIMOLD, W. U. 1991. $^{40}\text{Ar}/^{39}\text{Ar}$ stepheating age determinations relevant to the formation of the Vredefort Dome, South Africa. *South African Journal of Science*, **87**, 431–442.

BIRD, P. 1979. Continental delamination and the Colorado Plateau. *Journal of Geophysical Research*, **83**, 4975–4987.

BISSCHOFF, A. A. 1982. Thermal metamorphism in the Vredefort Dome. *Transactions of the Geological Society of South Africa*, **85**, 43–57.

BOHLEN, S. R. 1987. Pressure-temperature-time paths and a tectonic model for the evolution of granulites. *Journal of Geology*, **95**, 617–632.

CAWTHORN, R. G. & BIGGAR, G. M. 1993. Crystallization of titaniferous chromite, magnesian ilmenite and armalcolite in tholeiitic suites in the Karoo Igneous Province. *Contributions to Mineralogy and Petrology*, **114**, 221–235.

— & DAVIES, G. 1983. Experimental data at 3 Kbars pressure on parental magma to the Bushveld Complex. *Contributions to Mineralogy and Petrology*, **83**, 128–135.

— & WALRAVEN, F. 1997. *The Bushveld Complex: A time to fill and a time to cool*. Information Circular, Economic Geology Research Unit, University of the Witwatersrand, **307**.

CHENEY, E. S. 1996. Sequence stratigraphy and plate tectonic significance of the Transvaal succession of southern Africa and its equivalent in western Australia. *Precambrian Research*, **79**, 3–24.

COERTZ, F. J., BURGER, A. J., WALRAVEN, F., MARLOW, A. G. & MACCASKIE, D. R. 1978. Field relations and age determinations in the Bushveld Complex. *Transactions of the Geological Society of South Africa*, **81**, 1–11.

COETZEE, H. & KRUGER, F. J. 1989. The geochronology and Sr- and Pb-isotope geochemistry of the Losberg Complex, and the southern limit of Bushveld Complex magmatism. *South African Journal of Geology*, **92**, 37–41.

DE WIT, M. J., ROERING, R., HART, R. J., ARMSTRONG, R. A., DE RONDE, C. E. J., GREEN, R. W. E., TREDOUX, M., PEBENDY, E. & HART, R. A. 1992. Formation of an Archaean continent. *Nature*, **357**, 553–562.

DE YOREO, J. J., LUX, D. R. & GUIDOTTI, C. V. 1991. Thermal modelling in low-pressure/high-temperature metamorphic belts. *Tectonophysics*, **188**, 209–238.

DRESSLER, B. O. 1984. General geology of the Sudbury area. In: PYE, E. G., NALDRETT, A. J. & GIBLIN, P. E. (eds) *The Geology and Ore Deposits of the Sudbury Structure*. Ontario Geological Survey Special Volume 1, 57–82.

DURRHEIM, R. J., NICOLAYSEN, L. O. & CORNER, B. 1991. A deep seismic reflection profile across the Archean-Proterozoic Witwatersrand Basin, South Africa. *American Geophysical Union, Geodynamics Series*, **22**, 213–224.

DYMOKE, P. & SANDIFORD, M. 1992. Phase relationships in Buchan facies series pelitic assemblages: calculations with application to andalusite–staurolite paragenesis in the Mount Lofty Ranges, South Australia. *Contributions to Mineralogy and Petrology*, **110**, 121–132.

ENGLAND, P. C. & THOMPSON, A. B. 1984. Pressure–temperature–time paths of regional metamorphism I. Heat transfer during the evolution of regions of thickened continental crust. *Journal of Petrology*, **25**, 894–928.

FRICKE, A., MEDENBACH, O. & SCHREYER, W. 1990. Fluid inclusions, planar elements and pseudotachylites in the basement rocks of the Vredefort structure, South Africa. *Tectonophysics*, **171**, 169–183.

GIBSON, R. L. 1993. When is a hornfels not a hornfels? Metapelitic rocks from the lower Witwatersrand Supergroup, Vredefort Dome, South Africa. *South African Journal of Geology*, **96**, 42–48.

— & WALLMACH, T. 1995. Low pressure–high temperature metamorphism in the Vredefort Dome, South Africa – anticlockwise pressure–temperature path followed by rapid decompression. *Geological Journal*, **30**, 319–331.

—, ARMSTRONG, R. A. & REIMOLD, W. U. 1997a. The age and thermal evolution of the Vredefort impact structure: A single-grain U-Pb zircon study. *Geochimica et Cosmochimica Acta*, **61**, 1531–1540.

—, REIMOLD, W. U. & WALLMACH, T. 1997b. Origin of pseudotachylite in the lower Witwatersrand Supergroup, Vredefort Dome (South Africa): constraints from metamorphic studies. *Tectonophysics*, **283**, 241–262.

GREEN, R. W. E., WEBB, S. J. & WRIGHT, C. 1995. Broad-band seismic studies in southern Africa. *South African Journal of Science*, **91**, 234–239.

GRIEVE, R. A. F., CODERRE, J. M., ROBERTSON, P. B. & ALEXOPOULOS, J. 1990. Microscopic planar deformation features in quartz of the Vredefort structure: Anomalous but still suggestive of an impact origin. *Tectonophysics*, **171**, 185–200.

GRIFFITHS, R. W. & CAMPBELL, I. H. 1990. Interaction of mantle plume heads with the Earth's surface and the onset of small-scale convection. *Journal of Geophysical Research*, **96**, 18 295–18 310.

HARLEY, S. L. 1989. The origins of granulites: a metamorphic perspective. *Geological Magazine*, **126**, 215–247.

HART, R. J., ANDREOLI, M. A. G., SMITH, C. B., OTTER, M. L. & DURRHEIM, R. 1990. Ultramafic rocks in the centre of the Vredefort structure: possible exposure of the upper mantle. *Chemical Geology*, **83**, 233–248.

—, NICOLAYSEN, L. O. & GALE, N. H. 1981. Radioelement concentrations in the deep profile through Precambrian basement of the Vredefort structure. *Journal of Geophysical Research*, **86**, 10 639–10 652.

HATTON, C. J. & SCHWEITZER, J. K. 1995. Evidence for synchronous extrusive and intrusive Bushveld magmatism. *Journal of African Earth Sciences*, **21**, 579–594.

HENKEL, H. & REIMOLD, W. U. 1995. *Integrated gravity and magnetic modelling of the Vredefort impact structure – reinterpretation of the Witwatersrand Basin as the erosional remnant of an impact basin*. Information Circular, Economic Geology Research Unit, University of the Witwatersrand, **299**.

HOLLAND, T. J. B. & POWELL, R. 1990. An enlarged and updated internally consistent thermodynamic dataset with uncertainties and correlations: the system $K_2O-Na_2O-CaO-MgO-MnO-FeO-Al_2O_3-TiO_2-SiO_2-C-H_2O_2$. *Journal of Metamorphic Geology*, **8**, 89–124.

HOUSEMAN, G. A., MCKENZIE, D. & MOLNAR, P. 1981. Convective instability of a thickened boundary layer and its relevance for the thermal evolution of continental convergence belts. *Journal of Geophysical Research*, **86**, 6115–6132.

HUPPERT, H. E. & SPARKS, R. S. J. 1988. The generation of granitic magmas by intrusion of basalt into continental crust. *Journal of Petrology*, **29**, 599–624.

JACKSON, M. C. 1994. Geochemistry and metamorphic petrology of Dominion Group metavolcanics in the Vredefort area, South Africa. *South African Journal of Geology*, **97**, 62–77.

JONES, M. Q. W. 1988. Heat flow in the Witwatersrand basin and its environs and its significance for the South African shield geotherm and lithosphere thickness. *Journal of Geophysical Research*, **93**, 3243–3260.

KAMO, S. L., REIMOLD, W. U., KROGH, T. E., & COLLISTON, W. P. 1996. A 2.023 Ga age for the Vredefort impact event and a first report of shock metamorphosed zircons in pseudotachylitic breccias and granophyre. *Earth and Planetary Science Letters*, **144**, 369–388.

KLEEMAN, G. J. & TWIST, D. 1989. The compositionally zoned sheet-like granite pluton of the Bushveld Complex: Evidence bearing on the nature of A-type magmatism. *Journal of Petrology*, **30**, 1381–1414.

KRETZ, R. 1983. Symbols for rock-forming minerals. *American Mineralogist*, **68**, 277–279.

KRUGER, F. J. 1994. The Sr-isotope stratigraphy of the western Bushveld Complex. *South African Journal of Geology*, **97**, 393–398.

LOOSVELD, R. J. H. 1989. The synchronism of crustal thickening and low-pressure facies metamorphism in the Mount Isa Inlier, Australia. 2. Fast convective thinning of mantle lithosphere during crustal thickening. *Tectonophysics*, **165**, 191–218.

MANTON, W. I. 1965. The orientation and origin of shatter cones in the Vredefort Ring. In: *Geological Problems in Lunar Research*. New York Academy of Sciences Annals **123**, 1017–1049.

MARTINI, J. J. 1992. The metamorphic history of the Vredefort dome at approximately 2 Ga as revealed by coesite-stishovite-bearing pseudotachylites. *Journal of Metamorphic Geology*, **10**, 517–527.

MASTER, S. 1991. *The origin and controls on the distribution of copper and precious metal mineralization at the Mangula and Norah Mines, Mhangura, Zimbabwe*. PhD Thesis, University of the Witwatersrand.

MCKENZIE, D. & BICKLE, M. J. 1988. The volume and composition of melt generated by extension of the lithosphere. *Journal of Petrology*, **29**, 625–679.

MERKLE, R. K. W. & WALLMACH, T. 1997. Ultramafic rocks in the centre of the Vredefort Structure (South Africa): geochemical affinity to Bushveld rocks. *Chemical Geology*, **143**, 43–64.

MOSER, D. E. 1997. Dating the shock wave and thermal imprint of the giant Vredefort impact, South Africa. *Geology*, **25**, 7–10.

NEL, L. T. 1927. *The Geology of the Country Around Vredefort*. Geological Survey of South Africa, Special Publication, **6**.

NICHOLS, G. T., BERRY, R. F. & GREEN, D. H. 1992. Internally-consistent garnite–spinel–cordierite–garnet equilibria in the FMASHZn system: geothermobarometry and applications. *Contributions to Mineralogy and Petrology*, **111**, 362–377.

PHILLIPS, G. N. & LAW, J. D. M. 1994. Metamorphism of the Witwatersrand gold fields: A review. *Ore Geology Reviews*, **9**, 1–31.

POWELL, R. & HOLLAND, T. J. B. 1988. An internally consistent dataset with uncertainties and correlations: 3. Applications to geobarometry, worked examples and a computer program. *Journal of Metamorphic Geology*, **6**, 173–204.

PYBUS, G. Q. J., REIMOLD, W. U., COLLISTON, W. P. & SMITH, C. B. 1995. Mineralogical and chemical classification of mafic intrusives in the central region of the Witwatersrand Basin. *Extended Abstract, Centennial Geocongress of the Geological Society of South Africa, Johannesburg*, 581–584.

REICHARDT, F. J. 1994. The Molopo Farms Complex, Botswana: history, stratigraphy, petrography, petrochemistry and Ni–Cu–PGE mineralization. *Exploration and Mining Geology*, **3**, 263–284.

REIMOLD, W. U. & COLLISTON, W. P. 1994. Pseudotachylites of the Vredefort Dome and the surrounding Witwatersrand Basin, South Africa. In: DRESSLER, B. O., GRIEVE, R. A. F., & SHARPTON, V. L. (eds) *Large Meteorite Impacts and Planetary Evolution*. Geological Society of America Special Paper, **293**, 177–196.

— & GIBSON, R. L. 1996. Geology and evolution of the Vredefort Impact Structure, South Africa. *Journal of African Earth Sciences*, **23**, 125–162.

—, —, FRIESE, A. & LAYER, P. W. 1995. A chronological framework for the Witwatersrand Basin – with emphasis on metamorphic/hydrothermal events. In: *Proceedings of the Symposium on the Economic Significance of Metamorphism and Fluid Movement within the Witwatersrand Basin*. Information Circular, Economic Geology Research Unit, University of the Witwatersrand, **296**, 30–37.

REISCHMANN, T. 1995. Precise U/Pb age determination with baddeleyite (ZrO_2), a case study from the Phalaborwa Igneous Complex, South Africa. *South African Journal of Geology*, **98**, 1–4.

RICHARDS, M. A., DUNCAN, R. A. & COURTILOT, V. E. 1989. Flood basalts and hotspot tracks: Plume heads and tails. *Science*, **246**, 103–107.

RICHARDSON, S. H., GURNEY, J. J., ERLANK, A. J. & HARRIS, J. W. 1984. Origin of diamonds in old enriched mantle. *Nature*, **310**, 198–202.

ROBB, L. J. & MEYER, F. M. 1995. The Witwatersrand Basin, South Africa: Geological framework and mineralization processes. *Ore Geology Reviews*, **10**, 67–94.

SANDIFORD, M. & POWELL, R. 1986. Deep crustal metamorphism during continental extension: modern and ancient examples. *Earth and Planetary Science Letters*, **79**, 151–158.

— & — 1991. Some remarks on high-temperature–low-pressure metamorphism in convergent orogens. *Journal of Metamorphic Geology*, **9**, 223–236.

SCHREYER, W. 1983. Metamorphism and fluid inclusions in the basement of the Vredefort Dome, South Africa: guidelines to the origin of the structure. *Journal of Petrology*, **24**, 26–47.

—, STEPTO, D., ABRAHAM, K. & MUELLER, W. F. 1978. Clinoeulite (magnesian clinoferrosillite) in a eulysite of a metamorphosed iron formation in the Vredefort structure, South Africa. *Contributions to Mineralogy and Petrology*, **65**, 351–361.

SCHWEITZER, J. K., HATTON, C. J. & DE WAAL, S. A. 1995. Regional lithochemical stratigraphy of the Rooiberg Group, upper Transvaal Supergroup: A proposed new subdivision. *South African Journal of Geology*, **98**, 245–255.

SHARPE, M. R. 1984. Petrography, classification and chronology of mafic sill intrusions beneath the eastern Bushveld Complex. *Geological Survey of South Africa Bulletin*, **77**.

SLAWSOHN, W. F. 1976. Vredefort core: a cross-section of the upper crust? *Geochimica et Cosmochimica Acta*, **40**, 117–121.

SPRAY, J. G., KELLEY, S. P. & REIMOLD, W. U. 1995. Laser-probe ^{40}Ar – ^{39}Ar dating of pseudotachylites and the age of the Vredefort impact event. *Meteoritics*, **30**, 335–343.

STANISTREET, I. S. & MCCARTHY, T. S. 1991. Changing tectono-sedimentary scenarios relevant to the development of the late-Archaean Witwatersrand basin. *Journal of African Earth Sciences*, **13**, 65–81.

STEPTO, D. 1979. *A geological and geophysical study of the central portion of the Vredefort Dome Structure*. PhD Thesis, University of the Witwatersrand, Johannesburg.

— 1990. The geology and gravity field in the central core of the Vredefort structure. *Tectonophysics*, **171**, 75–103.

STEVENS, G., CLEMENS, J. D. & DROOP, G. T. R. 1997a. Melt production during granulite-facies anatexis: The data from experiments on “primitive” metasedimentary protoliths. *Contributions to Mineralogy and Petrology*, **128**, 352–370.

—, GIBSON, R. L. & DROOP, G. T. R. 1997b. Mid-crustal granulite facies metamorphism in the Central Kaapvaal Craton: The Bushveld Complex connection. *Precambrian Research*, **82**, 113–132.

THOMAS, R. J., CORNELL, D. H., MOORE, J. M. & JACOBS, J. 1994. Crustal evolution of the Namaqua-Natal Metamorphic Province, southern Africa. *South African Journal of Geology*, **97**, 8–14.

THOMPSON, L. M. & SPRAY, J. G. 1996. Pseudotachylite petrogenesis: constraints from the Sudbury impact structure. *Contributions to Mineralogy and Petrology*, **125**, 359–374.

THOMPSON, R. N. & GIBSON, S. A. 1991. Subcontinental mantle plumes, hotspots and pre-existing thinspots. *Journal of the Geological Society, London*, **148**, 973–977.

TRIELOFF, M., REIMOLD, W. U., KUNZ, J., BOER, R. H. & JESSBERGER, E. K. 1994. ^{40}Ar – ^{39}Ar thermochronology of pseudotachylites at the Ventersdorp Contact Reef, Witwatersrand Basin. *South African Journal of Geology*, **97**, 365–384.

TWIST, D. & FRENCH, B. M. 1983. Voluminous acid volcanism in the Bushveld Complex: a review of the Rooiberg Felsite. *Bulletin of Volcanology*, **46**, 225–242.

VIELZEUT, D. & HOLLOWAY, J. R. 1988. Experimental determination of the fluid-absent melting relations in the pelitic system. *Contributions to Mineralogy and Petrology*, **98**, 257–276.

WALRAVEN, F. 1997. *Geochronology of the Rooiberg Group, Transvaal Supergroup, South Africa*, Information Circular, Economic Geology Research Unit, University of the Witwatersrand, **316**.

— & ELSENBROEK, J. H. 1991. Geochronology of the Schurweddraai Alkali Granite and associated nepheline syenite and implications for the origin of the Vredefort Structure. *South African Journal of Geology*, **94**, 228–235.

— & HATTINGH, E. 1993. Geochronology of the Nebo Granite, Bushveld Complex. *South African Journal of Geology*, **96**, 31–42.

—, ARMSTRONG, R. A. & KRUGER, F. J. 1990. A chronostratigraphic framework for the north-central Kaapvaal Craton, the Bushveld Complex and the Vredefort structure. *Tectonophysics*, **171**, 23–48.

—, FRICK, C. & LUBALA, R. T. 1992. Pb-isotope geochronology of the Schiel Complex, Northern Transvaal, South Africa. *Journal of African Earth Sciences*, **15**, 103–110.

WELLS, P. R. A. 1980. Thermal models for the magmatic accretion and subsequent metamorphism of continental crust. *Earth and Planetary Science Letters*, **46**, 253–265.

WHITE, R. S. & MCKENZIE, D. 1995. Mantle plumes and flood basalts. *Journal of Geophysical Research*, **100**, 17 543–17 585.

Ridge–trench interactions and high-*T*–low-*P* metamorphism, with particular reference to the Cretaceous evolution of the Japanese Islands

MICHAEL BROWN

Laboratory for Crustal Petrology, Department of Geology, University of Maryland, College Park, MD 20742, USA

Abstract: A corollary of plate tectonics is that spreading ridges ultimately interact with trenches; this is a consequence of the closure phase of the Wilson cycle that eliminates ocean basins. Ridge–trench interactions generate distinctive igneous, metamorphic, structural and sedimentation effects, which commonly are diachronous parallel to the trench; effects vary with plate boundary geometry and rate of migration is controlled by relative motion vectors. Identification of such interactions in the geological record is uncommon, which suggests that geological events triggered by ridge–trench interactions are attributed to other phenomena, such as changes in plate motion or a singularity at the trench. The estimated greater length of plate boundaries in the past means that subduction of a spreading ridge system could have been more common earlier in Earth history.

High-*T*–low-*P* metamorphism requires a tectonic setting that allows enhanced heat flux, transient advection of heat due to magma ascent, unusually large internally generated heat, or some combination of these features. Subduction of a spreading ridge system produces anomalously high temperatures at shallow crustal depth through the development of a slab window, which allows transfer of sub-slab asthenospheric mantle across the slab to create an enhanced heat flux beneath the overriding plate. This process is important along convergent margins that develop a subduction–accretion complex, and drives low *P/T* ratio metamorphism and anatexis of the complex. Heat transport occurs by rising magma near the trench, which leads to formation of plutons with characteristic contaminated MORB geochemistry. Near-trench igneous activity and low *P/T* ratio metamorphism are the most striking features attributable to spreading ridge subduction and slab window formation, and together are likely to be diagnostic of ridge–trench interactions. Geological features of the Cretaceous Ryoke and Abukuma high-*T*–low-*P* metamorphic belts in Japan are consistent with the expectations of ridge subduction and slab window formation. Based on modelled plate interactions in the North Pacific Ocean basin during the Cretaceous, a tectonic scenario is presented for the evolution of the Japanese Islands that involves interactions between the Farallon–Izanagi ridge and a trench along the Asian continental margin. Other low *P/T* ratio metamorphic belts that owe their high-*T* lineage to interactions between spreading ridges and trenches are the Shimanto and Hidaka belts of Japan, and the Chugach belt of Alaska, USA. The complex tectonic evolution of Palaeozoic orogenic belts such as the Appalachian orogen of eastern Canada and USA, implies that ridge–trench interactions were involved in their evolution, although terminal continental collision makes the effects of these interactions difficult to identify in the geological record. There are many older belts for which ridge subduction and slab window formation should be evaluated, including the Palaeoproterozoic evolution of the Arunta Inlier, Australia, and the late Archean evolution of the Slave Province, northern Canada.

Regional metamorphism is a dynamic process intimately linked with orogenesis (Brown 1993), and orogenesis generally is related to plate tectonics, particularly along convergent margins (Şengör 1991). Convergent margin processes may be separated into two groups: subduction-related processes and collision-related processes. Orogenic belts cannot be formed by convergent margin collision-related processes alone, as such processes are always superimposed on subduction-related processes (e.g. the Appalachian, Variscan and Alpine–Himalayan orogenic systems), but orogenic belts can be formed by subduction-related processes alone (e.g. the Andean orogenic system). In the 30 years since

the introduction of plate tectonics, our understanding of processes that occur along convergent margins has increased dramatically. Examples include development of the terrane idea (e.g. Jones *et al.* 1983; Schermer *et al.* 1984), the recognition of orogen-parallel stretching (e.g. Toriumi 1985; Ellis & Watkinson 1987), that probably reflects major displacements (e.g. Beck 1991), and the realization that bathymetric highs of sufficient size within ocean basins eventually collide with overriding plates in trenches, where their ultimate fate is decided by their relative buoyancy (e.g. Nur & Ben-Avraham 1983; Cloos 1993). Plate convergence typically is oblique, leading to the formation of transpressive

orogenic belts by basal forcing (Ellis *et al.* 1995). Thus, regional metamorphism is most commonly the manifestation of thermomechanical perturbations due to convergent margin processes. These include depression of the geotherm in trenches and elevation of the geotherm in arcs, crustal thickening and orogen collapse, and advection of heat by the rise of magma through the crust in both extensional and contractional environments. However, the burial and exhumation history of rocks during an orogenic cycle involves a complex four-dimensional evolution in which modification of the geotherm occurs synchronously with orogen-normal and orogen-parallel displacements that lead to non-plane strain progressive deformation (Thompson *et al.* 1997; Brown & Solar 1998).

Plates meet at spreading ridge (R), transform fault (F) and subducting trench (T) boundaries, so that interactions among three plates must generate a triple junction defined by some combination of these boundaries. Migration along trenches of triple junctions that involve transform faults or spreading ridges is common in Mesozoic–Cenozoic plate tectonic history (Sisson *et al.* 1994). Accordingly, past plate interactions can be expected to leave their imprint in orogenic belts exposed at the surface of the Earth. A corollary of plate tectonics is that spreading ridge systems ultimately interact with trenches during the subduction process (DeLong & Fox 1977; DeLong *et al.* 1979). Orogenic belts formed by collision-related processes involve the elimination of ocean basins by subduction (the Wilson cycle). An implication of ocean basin closure is that a minimum of one spreading ridge system must have been subducted during the closure process, unless subduction stops before the ridge intersects the trench, which may end sea-floor spreading. In spite of this implication, the identification of ridge–trench interactions in the geological record is uncommon (Pavlis *et al.* 1995), which indicates that geological events triggered by ridge subduction are attributed to other phenomena at the trench. For example, such events are typically interpreted to have been driven by changes in plate motion, and are less commonly interpreted to have been caused by some singularity at the trench, such as the impingement of an aseismic ridge (e.g. Brown 1995a) or seamount chain (Cloos 1993).

A minority of orogenic belts appear not to have involved ocean basin closure, such as the Neoproterozoic evolution of the Dalradian and Moine blocks of the Scottish Highlands (Dempster & Bluck 1995); for these belts the description ‘ensialic’ remains useful. In the model

proposed by Dempster & Bluck (1995), narrow orogenic belts characterized by Barrovian-type regional metamorphism are interpreted to develop in long-lived transform zones. These zones represent a tectonic setting in which extension and sedimentation may be followed by contraction and orogenesis. Metamorphic belts of this type are not considered further in this paper.

Types of metamorphism and ‘paired’ metamorphic belts

Miyashiro’s (1959, 1961) classification of regional metamorphic belts into five types, based on P/T ratio, placed high- T -low- P (low P/T ratio) and low- T -high- P (high P/T ratio) metamorphism as end-members of a diverse field of $P-T$ conditions recorded by metamorphic belts exhumed to the surface. The occurrence in adjacent parallel belts of contrasting types of metamorphism in the circum-Pacific regions led him to develop the model of ‘paired’ metamorphic belts. In this model, the low P/T ratio belt was formed on the foreland side of a subduction-related orogenic belt in a magmatic arc setting, whereas an associated high P/T ratio belt was formed in the depth of the adjacent trench zone on the hinterland side of the orogenic belt. Although there is agreement concerning the tectonic setting in which low- T -high- P metamorphism occurs, the nature of the $P-T$ history and tectonic setting that lead to high- T -low- P metamorphism have remained debatable. There are two principal issues: (1) the question of distinguishing between clockwise and anticlockwise $P-T$ paths (e.g. Williams & Karlstrom 1996); and (2) the question of explaining the overall high thermal gradient during low P/T ratio metamorphism.

The idea that ridge–trench interactions are the cause of high- T -low- P metamorphism raises a question about the validity of the classic idea that ‘paired’ metamorphic belts formed *in situ* by Pacific-type orogenesis. In an alternative view, ‘paired’ metamorphic belts are formed by juxtaposition of tectonostratigraphic terranes with contrasting metamorphic histories because of trench-parallel displacements during oblique subduction. Allochthonous terranes (e.g. Nelson *et al.* 1994) and microplates (e.g. Stock & Lee 1994) are features that form along active continental margins during ridge–trench interactions. Ridge subduction and slab window formation imply that any outboard high P/T ratio metamorphic belt must have been accreted after interaction between the spreading centre

and the trench, otherwise thermal overprinting and erasure of the high P/T ratio metamorphic history would have occurred. Thus, the *in situ* development of 'paired' metamorphic belts may be incorrect, and belts with these different $P-T$ histories are likely to be contemporaneous lateral equivalents subsequently juxtaposed (Brown 1998).

High- T -low- P metamorphism

It follows from the discussion above that a key issue in petrology is to explain the cause of high- T -low- P metamorphism. Although debate has focused on the roles of granite magmatism to advect heat versus thermal relaxation during exhumation in producing anomalously hot rocks in the shallow crust, most high- T -low- P metamorphism probably requires a tectonic scenario that allows an enhanced heat flux and heat transport by sub-crustal magmas. In this section, the possible causes of high- T -low- P metamorphism and $P-T$ paths inferred from low P/T ratio metamorphic belts are reviewed.

Possible causes of high- T -low- P metamorphism

At first sight, low P/T ratio metamorphism in fore-arc sedimentary sequences appears to conflict with plate tectonics, since the metamorphism typically expected in trench environments is of the high P/T ratio type. However, anomalous near-trench igneous activity in a setting where low heat flow is the rule has often been regarded as the most striking geological effect of ridge subduction and slab window formation (e.g. Marshak & Karig 1977), and such magmatism is often associated with low P/T ratio metamorphism. Many mechanisms for the development of high temperatures in fore arcs have been proposed, including subduction beneath a hot hanging wall (e.g. Platt 1975), relaxation of isotherms following the cessation of subduction (Hudson & Plafker 1982; James *et al.* 1989; Dirks *et al.* 1992), shear heating (Graham & England 1976; England & Molnar 1993; Molnar & England 1995) and subduction of an active oceanic spreading ridge (e.g. Uyeda & Miyashiro 1974; Marshak & Karig 1977; DeLong & Fox 1977; DeLong *et al.* 1979; Kinoshita & Ito 1986; Kinoshita 1995; Sisson & Hollister 1988; Sisson & Pavlis 1993; Nakajima *et al.* 1990; Nakajima 1994; Brown & Nakajima 1994; Brown 1995b, 1998).

Other processes proposed for high- T -low- P metamorphism include the following. (1) Thermal re-equilibration after orogenic thickening of anoxic basins next to continental margins; because the sediments in such basins have high contents of heat-producing elements, thermal relaxation following thickening generates higher than normal heat in the shallow crust that may produce large areas of high-grade metamorphic rocks and granites (e.g. Chamberlain & Sonder 1990). (2) Thickening of tectonically thinned continental crust (lithosphere) and overlying sedimentary basins (e.g. Soula *et al.* 1986; Thompson 1989; Brown & Treloar 1992), in which the blanketing effect of cold low-conductivity sediments retards decay of the enhanced geotherm consequent upon extension so that subsequent basin inversion generates clockwise hairpin-like or looping $P-T$ paths. (3) Continental rifting (e.g. Wickham & Oxburgh 1985, 1987) or extension (e.g. Sandiford & Powell 1986; Zen 1995), involving enhanced heat flow and/or advection of heat through influx of sub-crustal magma (see also the rift-drift-delamination model for regional low- P metamorphism of Collins & Vernon (1994)). (4) Regional contact (overlapping temporally separate and spatially localized thermal events) or pluton-enhanced metamorphism, in which advection of heat occurred by upward transfer of magma typically of granodioritic or granitic composition (e.g. Lux *et al.* 1986; Barton & Hanson 1989; De Yoreo *et al.* 1989a, b, 1991; Droop & Al-Filali 1989; Collins & Vernon 1991; Stüwe *et al.* 1993; Sandiford *et al.* 1995; Amato *et al.* 1994; Warren & Ellis 1996; Williams & Karlstrom 1996), or fluids (e.g. Chamberlain & Rumble 1988; Sisson & Hollister 1988), mainly in transpressional belts that exhibit limited overthickening. (5) Crustal thickening and synchronous erosion (thinning) of the mantle lithosphere (Loosveld & Etheridge 1990) or delamination of the mantle lithosphere (Midgley & Blundell 1997). (6) Heat refraction due to lateral variations in the thermal conductivity of rocks, such as might be consequent on the emplacement of mantled gneiss domes or folding of basement-cover unconformities (e.g. Jaupart & Provost 1985; Allen & Chamberlain 1989; Mildren & Sandiford 1995). (7) Transition from low- T -high- P to high- T -low- P conditions coincident with the cessation of subduction (e.g. Hudson & Plafker 1982, James *et al.* 1989; Hand *et al.* 1994), or with a transition from subduction to a transform plate boundary (Wakabayashi 1996). (8) Transition from high- T -high- P to high- T -low- P metamorphism during catastrophic collapse of thickened

crust, extensive high-temperature crustal anatexis and advection of heat to shallow crustal depths through ascent and emplacement of hot granite melts (Brown & O'Brien 1997). Additionally, the mechanical consequences of granite emplacement during high-*T*-low-*P* metamorphism have been considered by Sandiford *et al.* (1991), Stüwe *et al.* (1993) and Stüwe & Sandiford (1994, 1995).

P-T paths in low P/T ratio metamorphic belts

P-T paths found in low *P/T* ratio metamorphic belts vary from clockwise to anticlockwise, even from the same region (e.g. the southwestern United States (Grambling 1986; Grambling *et al.* 1989; Grambling & Dallmeyer 1993); the Arunta Inlier in central Australia (Collins & Vernon 1991, 1993; Hand *et al.* 1992, 1993; Vernon 1996)), although sometimes with good reason, such as paths that are clockwise in the hanging wall and anticlockwise in the footwall of an overthrust complex (e.g. southern Alaska (Sisson & Hollister 1988)). Williams & Karlstrom (1996) have argued that apparent *P-T* paths composed of a prograde thickening segment with moderate dP/dT and an isobaric cooling segment with shallow dP/dT may be connected by a tight clockwise loop in *P-T* space. They propose that some *P-T* paths previously inferred to be anticlockwise are better interpreted as clockwise, once the two segments are connected by a loop rather than a simple 'corner'. Such looping *P-T* paths may be typical of high-*T*-low-*P* metamorphism imprinted during long-term middle crustal residence, and Williams & Karlstrom (1996) argue that this may provide a general explanation for apparent clockwise and anticlockwise *P-T* histories in regions of high-*T*-low-*P* metamorphism, such as the southwestern United States. In contrast, Stüwe & Sandiford (1994, 1995) have related conflicting clockwise and anticlockwise *P-T* paths derived from high-*T*-low-*P* metamorphic terrains to the interplay of rapid changes of the deviatoric and lithostatic components of the pressure field. They recommend that caution should be taken in the tectonic interpretation of *P-T* paths from high-*T* low-*P* metamorphic belts that involve decompression of <1 kbar, and suggest that the widespread record of clockwise paths in many high-*T*-low-*P* metamorphic belts may be an artefact of the time scale of deformation rather than reflecting the exhumation history of the belt.

Summary

High-*T*-low-*P* metamorphism remains topical for two principal reasons. First, an unambiguous evaluation of the changing depth with evolving *T* is difficult in circumstances where lithostatic *P* is low and variations in deviatoric *P* may be significant. Second, there is no general solution to the requirement to attain anomalously high temperatures at shallow crustal depths; this has led to multiple proposed solutions but little consensus. Although there may be more than one origin for high-*T*-low-*P* metamorphism, subduction of young oceanic lithosphere, and ultimately a spreading ridge system, must be common to many collisional orogens, and should be evaluated as part of the driving force for this type of metamorphism.

Triple junction interactions at convergent plate margins

Plate tectonics requires triple junction interactions, so it is important to identify the effects of triple junction interactions at convergent margins during the evolution of recent tectonic systems, to interpret orogenic belts and infer ancient tectonic systems (Cronin 1992). There are 18 possible types of triple junction interactions that involve trenches at convergent plate margins (one RRT junction, two types of TTT junction, three types of TTR junction, four types of RTF, TTF and FTT junctions, where R = spreading ridge, T = subducting trench, F = transform fault; after Cronin 1992). Modelling the finite time evolution of triple junctions that include one or more subduction zones has enabled us to understand better the motion of magmatic, metamorphic and deformation fronts that pass through an overriding plate during subduction of spreading ridge systems (McKenzie & Morgan 1969; Cronin 1992).

What are the effects of triple junction interactions at convergent plate margins?

The effects described briefly below are possible characteristics of a triple junction 'event'. The greater the number of these effects identified in any orogenic belt, the more certain is the attribution of part of the evolution of that belt to triple junction interactions at a convergent plate margin.

1. Diachroneity. It has been argued that a distinctive feature of triple junction interactions

in general, and ridge subduction in particular, is that the resultant geological 'event' migrates in time (Pavlis *et al.* 1995). For ridge-trench interactions, however, this will be decided by the relative orientation between the trench and the ridge segment being subducted. At a larger scale, the space-time relation is likely to be a step function as subduction of individual segments of the spreading ridge system alternates with TTF triple junction evolution. Although diachroneity of a geological 'event' is not an exclusive characteristic of the effects of triple junction interactions, Pavlis *et al.* (1995) concluded that evidence for a rapidly migrating event is the most clear manifestation of a triple junction system.

2. Kinematics. Triple junction interactions are associated with abrupt changes in the kinematics of deformation at regional scale (e.g. Sisson & Pavlis 1993), commonly recorded as superimposed deformation events (e.g. Byrne & DiTullio 1992; Onishi & Kimura 1995; Pavlis & Sisson 1995), and by juxtaposition of contrasting tectonostratigraphic terranes (e.g. Pavlis & Sisson 1995; Brown 1998). Changes in plate motion or collision-related processes, such as large-scale block rotations, however, may produce similar effects, and arc-parallel strike-slip systems can dismember and obscure the geological record, whatever its origin.

3. Magmatism. Magmatic signatures caused by ridge-trench interactions can include a gap in volcanic stratigraphy and/or location of volcanoes, a change from arc-like volcanism to MORB/OIB volcanism as a slab window opens (e.g. Hole & Larter 1993), parautochthonous MORB or contaminated MORB magmas in the fore arc (e.g. Harris *et al.* 1996; Lytwin *et al.* 1997), volcanic products with characteristics of slab melting, such as high Sr, Zr and La/Yb, and isotope signatures indicative of MORB, and alkaline magmatism in the back-arc region. The magmatic products of triple junction systems are a complex function of the thermal structures of the mantle wedge and the subducted slab (e.g. Tsuchiya & Kanisawa 1994), and the evolution of the slab window (Thorkelson 1996). Furthermore, the presence of a subduction-accretion complex may be important, and the occurrence of contaminated MORB magmas suggests that the presence of a subduction-accretion complex prevents basalt rising to the surface, so that ponded basalt may cause low P/T ratio metamorphism and granite magmatism. It is unclear, however, whether the

petrogenetic processes that occur consequent upon ridge-trench interactions are unique to these systems, and the potential to misinterpret an ancient fore-arc system as a magmatic arc assemblage, particularly in systems overprinted by collision-related processes, is clear.

4. Fluid circulation. High- T regional-scale hydrothermal overprinting of palaeothermal structure in an accretionary prism may be common in ridge-trench systems, and in southern Alaska such an interaction was responsible for the widespread gold mineralization (Haeussler *et al.* 1995). Fluid activity is common, however, in other tectonic situations and is unlikely to be diagnostic.

5. Metamorphism. Low P/T ratio metamorphism in the fore arc closely associated with plutonism is a typical effect of subduction of a spreading ridge (e.g. Sisson & Hollister 1988; Nakajima 1994; Barnett *et al.* 1994; Brown 1998), although the magmatism may extend normal to the trench with time as the slab window is subducted deeper under the overriding plate (Nakajima 1996). Such metamorphism is likely to involve rapid heating and cooling, which may be reflected in distinctive hornfelsic textures and unusually fine grain size in high-grade metamorphic rocks (Brown 1998), and freezing-in of igneous microstructures in migmatites (Vernon & Collins 1989). Although low P/T ratio metamorphism may be a unique manifestation of ridge subduction and slab window formation, the potential for misinterpretation as a magmatic arc system is obvious.

6. Basin evolution. Ridge-trench interactions typically lead to dynamic fore-arc sedimentation that records rapid lateral migration of sedimentary sources and basins, and vertical responses to thermal perturbations, i.e. uplift followed by subsidence (e.g. Taira *et al.* 1983). Trench-parallel strike-slip fault systems may disrupt or destroy these basins, however, and similar basin evolution may be generated by other interactions at the trench, such as the impingement of an aseismic ridge or seamount chain.

7. Accretionary prism evolution and ophiolite emplacement. Ridge-trench interactions may lead to punctuated periods of tectonic erosion of the accretionary prism, systematic younging in the age of accreted sediments that may culminate in accretion of zero-age pelagic sediments associated with near-trench MORB volcanic rocks (Osozawa 1992, 1994), and accretion of

fore-arc ophiolite complexes characterized by an overall MORB chemistry but showing contamination by sedimentary components (e.g. Kaeding *et al.* 1990; Lytwyn *et al.* 1997). Unfortunately, there are other potential causes of tectonic erosion at trenches, many ancient accretionary prisms preserve an incomplete record of accretion events, and there may be difficulty in distinguishing between stratigraphic associations in ophiolite complexes formed by ridge-trench interactions and those formed in back-arc basins.

Ridge-trench interactions and slab window formation

Ridge-trench interactions affect the overriding plate in three ways: (1) tectonic erosion of the fore arc; (2) change from arc-type to MORB-type volcanism; and (3) broad, thermally supported uplift, high heat flow, and extension. The kinematic effects of ridge-trench interactions and the fate of the subducted slab depend on plate boundary geometry and the relative motion vectors between the plates (Farrar & Dixon 1993; Thorkelson 1996). Additional variables that must be considered include the presence and size of a subduction-accretion complex, the type of overriding plate (continental or oceanic), and at depth the style and vigour of corner flow in the asthenospheric mantle below the overriding plate. At the extremes, either welding of the trailing oceanic plate to the overriding plate or transform motion between the trailing oceanic and overriding plates may result, and development of microplates and ophiolite emplacement might be expected to occur. In most other cases, a spreading ridge ceases to exist upon subduction. In its place, an ever-widening slab window may open down-dip; the slab may steepen with depth, it may be removed by lateral displacement or it may decay thermally.

Before a spreading ridge is subducted at a trench, it is an axial zone of plate growth where basalt generated by decompression melting of upwelling asthenosphere is added to the trailing edges of the diverging plates. As the ridge interacts with the trench, one or both of the plates descends and the plates continue to diverge. However, progressive thermal equilibration of the plate edges inhibits and stops plate growth, while continued divergence results in a 'window' (Dickinson & Snyder 1979). Maximum slab window development may be approximated by assuming that magmatic accre-

tion ceases when a ridge has fully entered a trench, while plate separation continues.

The geometrical pattern and kinematics of the triple junction that forms when the spreading ridge system collides with the trench control whether a slab window develops and its evolution. The simple case of a spreading ridge system oriented parallel to the trench (Fig. 1a) illustrates the basic principle of slab window formation (DeLong & Fox 1977). Although there are 18 types of triple junctions that involve trenches (Cronin 1992), from a generic viewpoint there are two important combinations of triple junctions that evolve slab windows for all ridge orientations, TTF-TTR and FFT-RTF systems. Normally, for a spreading ridge system oriented obliquely to a trench, there is an alternation at the trench between TTF and TTR triple junctions, so that a slab window forms (Fig. 1b). Slab windows generally form in FFT-RTF systems, although the geometry will differ in detail between leading and trailing transform segments in the overriding plate (Fig. 1c).

The slab window is an anomalously hot interface between the base of the overriding plate and upwelling asthenosphere from beneath the slab (e.g. DeLong & Fox 1977; Thorkelson & Taylor 1989; Thorkelson 1994, 1996; Goes *et al.* 1997); it is this upwelling asthenosphere that provides the enhanced heat flux from the sub-slab asthenospheric mantle into the overriding plate, either by fluid advection or conduction. According to Liu & Furlong (1992), surface volcanism associated with slab window formation lags behind a migrating triple junction because of the time lag in upwelling processes; modelling suggests that complete thermal decay by conduction may take up to 10 Ma. The role of heat transport by magmas remains unclear, in particular since adiabatic decompression melting in a subducting spreading ridge system is likely to be inhibited and then stopped with increasing depth of subduction. As a result, the importance of basaltic underplating compared with conductive heating is still debated. Geophysical (e.g. Murdie *et al.* 1993; Daniel *et al.* 1995) and geochemical (see summary by Thorkelson 1996) data support the development of slab windows during continued subduction of a spreading centre after its entry into the trench.

The age, thickness and density of oceanic lithosphere decrease towards a spreading ridge, so that as a ridge approaches a trench the negative buoyancy of the subducting slab decreases and subduction becomes more difficult (Luyendyk 1995; Thorkelson 1996). According to Cloos (1993), oceanic lithosphere older than c. 10 Ma is negatively buoyant and inherently subductable,

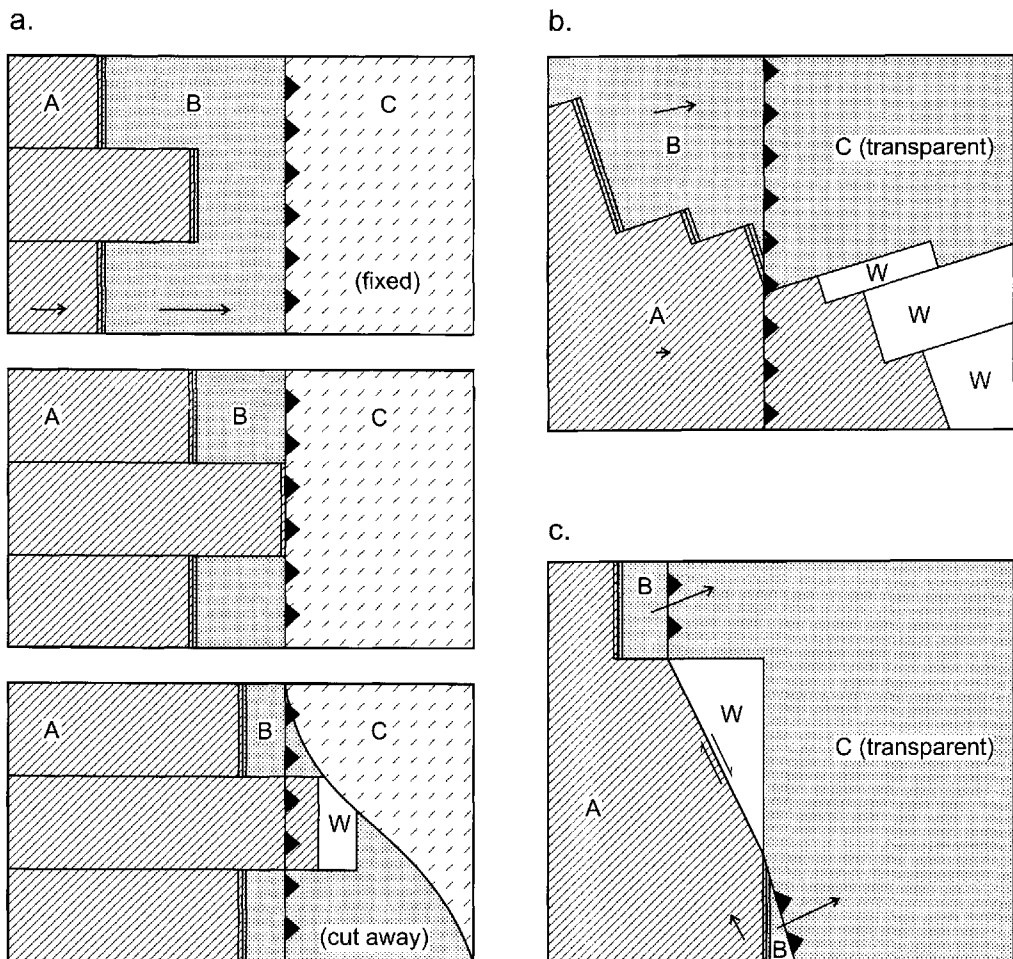


Fig. 1. Schematic examples of ridge-trench interactions between three plates (A, B and C) and slab window formation (W). (a) Subduction of a spreading ridge system parallel to the trench, with velocities as defined in the upper frame, evolves so that the central ridge segment arrives at the trench (middle frame) and is subducted under the overriding plate to create a slab window (bottom frame) (after DeLong & Fox 1997). (b) General case of ridge-trench interaction that involves oblique subduction of the spreading ridge system (TTF-TTR triple junction system), based on the southern Chile triple junction (after Murdie *et al.* 1993). (c) Special case of ridge-trench interaction in which a transcurrent arm is developed on the trench hanging wall (FFT-RTF triple junction system). The triple junction in the north is of Mendocino type and the triple junction in the south is of the Rivera type (after Farrar & Dixon 1993).

whereas oceanic lithosphere younger than this is positively buoyant. The width of the zone of positively buoyant oceanic lithosphere at a ridge depends on spreading rate. However, since ridge systems are composed of alternating ridge and transform segments, during subduction of any ridge segment the effect of the zone of positively buoyant lithosphere on the balance of forces that drive subduction may be insufficient to prevent subduction of the ridge system. Alternatively, the approach of a spreading ridge to

the trench may stop subduction, and the spreading ridge may stall outboard of the subduction zone. In these circumstances, Luyendyk (1995) has argued that the subducted plate welds to the outboard plate across the dormant spreading centre and is captured by it. If subduction is not stopped, all but the youngest parts of the positively buoyant lithosphere will become negatively buoyant during subduction because of progressive metamorphism to amphibolite and eclogite (Cloos 1993).

Potential indicators of ridge-trench interactions

Investigations of modern systems such as the southern Chile triple junction (Forsythe & Nelson 1985; Forsythe & Prior 1992; Murdie *et al.* 1993; Behrmann *et al.* 1994; Daniel *et al.* 1995), in which the subducting ridge segments are sub-parallel to the trench and at a high angle to convergence vectors (e.g. the schema in Fig. 1b, which is based upon this example), imply that (1) oceanic kinematics continue as a spreading ridge system enters a trench, and (2) the continuing oceanic kinematics within the downgoing slab profoundly influence the tectonics of the overriding plate. There are several unique geological features associated with the southern Chile triple junction. These include the Taitao ophiolite, the Liquine-Ofqui fault system, the Golfo de Penas basin and associated gap in arc volcanic activity, and associated thermal effects that have increased hydrothermal activity. The site of ridge subduction can be traced onshore by several means, including a large east-west gravity anomaly, a gap in seismicity, a lack of back-arc basins, a time-transgressive structural history in the back-arc region, different mean elevations, ages of arc volcanic rocks, style of deformation, and the presence of igneous rocks thought to represent slab melts in the back-arc region (Forsythe & Prior 1992; Ramos & Kay 1992; Kay *et al.* 1993; Murdie *et al.* 1993; Behrmann *et al.* 1994; Daniel *et al.* 1995).

In contrast to the evolution of the southern Chile triple junction, when part of the Pacific-Farallon spreading ridge system interacted with the trench along the western North American continental margin, subduction was replaced by translational movement of the type observed along the San Andreas Fault system today (e.g. the schema in Fig. 1c, which is based upon this example), and the Mendocino and Rivera triple junctions were formed (see summary in Atwater 1989). As the Mendocino triple junction moved to the north, a slab window filled with upwelling, hot, asthenospheric material was left in its wake (Dickinson & Snyder 1979). The asthenospheric material gradually cools and accretes to the Pacific and North American plates. The change in mechanical behaviour of the material in the slab window in space and time controls the evolution of the plate boundary at depth and is responsible for the complex patterns of crustal deformation and volcanism associated with the San Andreas Fault system (e.g. Atwater 1989). Evidence of shallow emplacement of hot material has been found in surface

heat flow, gravity anomalies, tomographic models of P-wave velocities, and variations in the depth of seismicity, and the thermal effects have been explored in the three-dimensional modelling of Goes *et al.* (1997).

Based on these two recent examples, we expect the consequences of ridge-trench interactions to produce distinctive igneous, metamorphic, structural and sedimentation effects in orogenic belts exhumed to the surface (Pavlis *et al.* 1995). However, there is no consensus on what these effects are, particularly in respect of the crust below the brittle-plastic transition, and it remains an important challenge to identify these effects to help in the correct interpretation of ancient systems.

Questions that remain

From the perspective of low P/T ratio metamorphism, there are several questions that relate to the thermal manifestation and evolution of ridge-trench interactions that cannot be answered without more quantitative data on the time-temperature history of both ancient and modern systems. These questions include: (1) What are the controlling parameters in the thermal system and the relative roles of advective versus conductive heat transport? (2) What are the interactions between the upwelling asthenospheric mantle beneath, and the corner flow in the asthenospheric mantle wedge above, the subducting spreading ridge system during slab window formation? (3) Can we simulate the thermal systems using numerical models and test the models with empirical data from modern systems and ancient systems? An example that addresses these questions is the work of Goes *et al.* (1997), who present a three-dimensional thermal model for the area around the Mendocino triple junction that is based on its kinematic evolution, incorporating the effects of a slab window, changes in relative plate motions and the trenchward migration of the spreading ridge system.

Purpose of this review

The primary objective of the present paper is to characterize features of Mesozoic-Cenozoic metamorphic belts likely to have involved ridge-trench interaction in their evolution. Examples of ridge-trench interactions in the younger part of the geological record include Cenozoic interactions between the Kula-Pacific spreading centre and the trench along the Asian

continental margin (e.g. Shimanto and Hidaka belts in Japan) and the Kula–Farallon (or Pacific–Farallon) spreading centre and the southern Alaska fore arc, and Cretaceous interactions between the trench along the Asian continental margin and the Farallon–Izanagi spreading centre (Kitakami batholith, and Abukuma and Ryoke belts in Japan).

An important key to understanding Mesozoic–Cenozoic orogenic belts is the record of sea-floor spreading present in the ocean basins. During Pre-Mesozoic Earth history, however, no record of the sea-floor spreading history of the ocean basins is available, and tectonic systems must be inferred from the geological record preserved in the continents. This record may be incomplete and partially to completely obscured through overprinting by younger orogenic events. For example, during the Palaeozoic, the complex succession of events recorded in the Appalachian orogen of eastern USA and Canada reflects an evolution that involved multiple episodes of subduction and terrane accretion during oblique plate convergence. Although the main features of the development and destruction of the Iapetus and Rheic Ocean basins, and the subsequent collision of the adjacent continents, are generally understood (e.g. Pickering & Smith 1995; Dalziel 1997; Mac Niocaill *et al.* 1997; and references therein), details of the timing and kinematics of terrane accretion are not completely resolved. Each terrane accretion event was probably preceded by ridge–trench interactions during the subduction phase of orogenic evolution, but identification of the effects in the geological record caused by these interactions is difficult due to overprinting by the terminal continental collision and associated transcurrent displacements.

A second objective is to identify and briefly review examples of older metamorphic belts for which ridge–trench interaction should be investigated as a possible cause of high-*T*–low-*P* metamorphism. In the Precambrian, if estimates of the length of plate boundary at 2.4 Ga of approximately twice the present length are correct, then we would expect many more triple junctions than there are today and we would expect subduction of spreading ridge systems and slab window formation to be a common source of thermal anomalies in the crust during the Archean (Nelson & Forsythe 1989; Abbott & Menke 1990). Precambrian belts for which ridge–trench interactions might be an appropriate part of the evolutionary history include the Palaeoproterozoic Arunta Inlier, central Australia, and the late Archean Slave Province, northern Canada.

The Cretaceous evolution of the Japanese Islands

Miyashiro's (1959, 1961) perspicacious idea of 'paired' metamorphic belts was based on an inferred coeval relationship between the Ryoke and Abukuma belts before wide application of geochronology, and synchronicity of development with the spatially adjacent Sambagawa belt before the development of the terrane idea. Re-examination of the geology and relations between the Mesozoic metamorphic belts of Japan reveals that metamorphism in the Abukuma belt occurred c. 10 Ma before that in the Ryoke belt (see summaries in Hiroi *et al.* 1998 (Abukuma belt) and Brown 1998 (Ryoke belt)), and although exhumation of the Ryoke and Sambagawa belts essentially was coeval, this probably occurred during sinistral transcurrent displacement and terrane accretion (Dallmeyer & Takasu 1991; Brown 1998). In this section the Cretaceous development of the Japanese Islands is summarized with particular reference to the Ryoke and Abukuma belts, and a new plate tectonic model for their evolution is presented.

The Ryoke belt

In southwest Japan, the Ryoke belt extends for c. 700 km in length but has a width of only 30–50 km (Fig. 2); it is superimposed on part of the Jurassic accretionary complex, the Mino–Tanba belt. Metamorphic rocks occupy only 20–30% of the total area of the Ryoke belt, because of the large number of granites that are characteristic of the belt; the metamorphism has been considered typical of Miyashiro's (1961) low-pressure facies series or andalusite–sillimanite type, with metamorphic grade increasing towards the Median Tectonic Line. The Median Tectonic Line is a major plastic-to-brittle, predominantly strike-slip fault with a complex displacement history (Takagi 1986, 1992), although the dominant sense of plastic displacement is inferred to have been left-lateral. Next to the Median Tectonic Line, on the Ryoke belt side, is the Izumi belt (Fig. 2), a series of synclinally folded Late Cretaceous fore-arc sedimentary basins that young successively eastward. Southward from the Median Tectonic Line are the Sambagawa (high *P/T* ratio metamorphic belt), Chichibu and Shimanto belts (Fig. 2).

Deformation. In the Ryoke belt, early deformation produced a bedding-parallel schistosity overprinted by peak metamorphic porphyroblasts. Fabriès defined by mineral inclusions

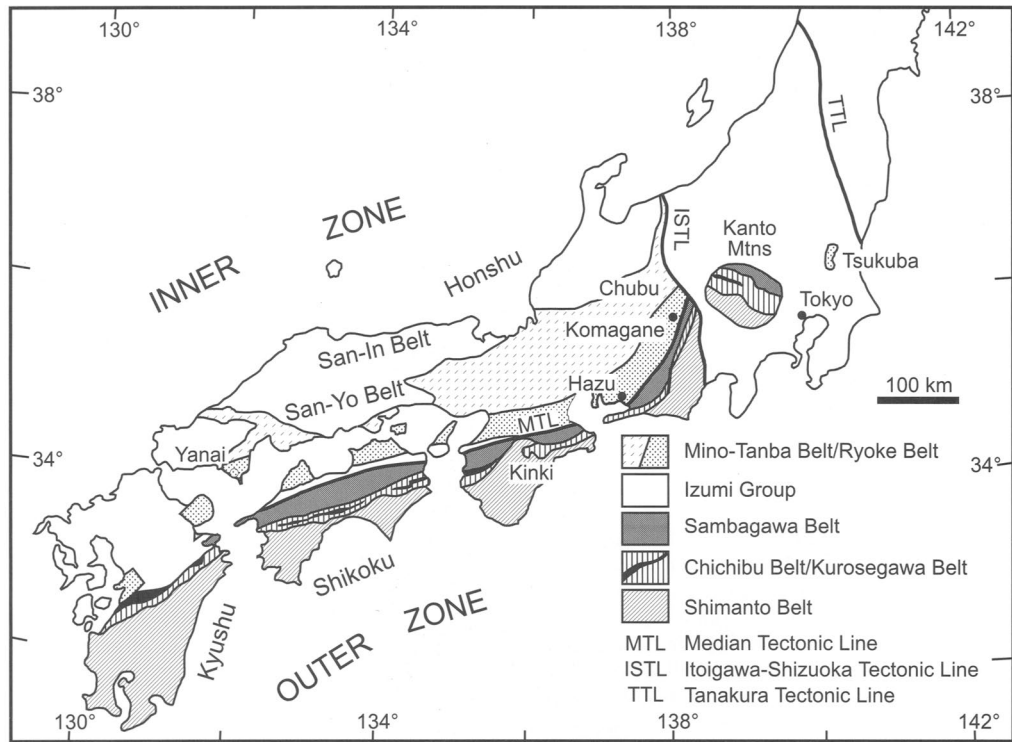


Fig. 2. Geological map of southwest Japan, particularly to show the spatial arrangement of the Ryoke and Sambagawa belts.

within porphyroblasts may be straight and continuous with the external foliation, they may curve through the rims of porphyroblasts into the matrix fabric, or the matrix fabric may wrap the porphyroblasts and be discordant to the internal fabric (e.g. Seo *et al.* 1981; Okudaira *et al.* 1995). At the scale of the belt, deformation and metamorphism were broadly synchronous. In the west, migmatites exhibit small leucosome-filled shear zones oriented N60°E, parallel with the strike of the belt, developed during progressive deformation synchronous with anatexis; they show a sinistral component of displacement. At map scale, the trend of the metamorphic isograds conforms with the orientation of the dominant tectonic structures, such as the axes of intrafolial folds of schistosity and a mineral elongation lineation defined by the parallel alignment of the main metamorphic phases, which trend parallel to the belt (e.g. N80°E in the western part) with shallow plunges, and to contours of strain magnitude (Nureki 1960; Toriumi 1985; Toriumi & Masui 1986). The strain is prolate with a positive correlation between increasing metamorphic grade and increasing strain magnitude (Toriumi

1985; Toriumi & Masui 1986). Generally, the maximum principal finite elongation is parallel to the thermal structure, and both are parallel to the belt, consistent with synmetamorphic belt-parallel plastic stretching (Toriumi 1985; Toriumi & Masui 1986). In both the west (Okudaira *et al.* 1995) and the east (M. Brown, unpubl. data), leucosome-filled extensional shears and an extensional crenulation cleavage have been developed; these show a component of top-to-the-north (*sensu lato*) extension. On the eastern side of the Komagane-Kashio District, rock units rotate sinistrally into the Median Tectonic Line and become mylonitic (e.g. Takagi 1986; Yamamoto 1994).

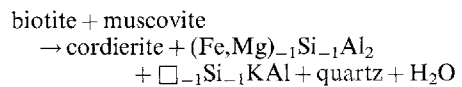
Granites. Although granitic rocks are abundant within the Ryoke belt, the regional metamorphic isograds generally are independent of the outline of these intrusive rocks (e.g. Ikeda 1991, 1993; Morikiyo 1984). Ryoke belt granites comprise strongly gneissose to massive varieties. The gneissose granites exhibit concordant relationships with the high-grade metamorphic rocks, and they have been interpreted as synmetamorphic (Hayama 1964; Ryoke

Research Group 1972; Okudaira *et al.* 1993). Thus, a component of the heat necessary to achieve the high temperatures at shallow crustal depths may have been advected internally within the Ryoke belt by ascent of granitic melt from lower to upper crustal levels (Okudaira *et al.* 1995; Okudaira 1996a, b). In contrast, massive granites of the Ryoke belt clearly crosscut the gneissose granites (Higashimoto *et al.* 1983; Ryoke Research Group 1972). The Late Cretaceous-Early Paleogene granite province of southwest Japan extends north from the Ryoke belt into the San-Yo and San-In belts. According to Terakado & Nakamura (1984), initial Sr isotope ratios increase to the E, while εNd_t values decrease eastward in a stepwise fashion. Kagami *et al.* (1992) report variations in initial Sr isotope ratios and initial εNd_t values in granites across the Ryoke, San-Yo and San-In belts (in the south: high Sr_i of 0.7070 to 0.7088 and low εNd_t of -3.0 to -8.0; in the north: low Sr_i of 0.7048 to 0.7068 and high of εNd_t +3.0 to -2.2). These data are consistent with a decreasing crustal component and an increasing mantle component both eastward along strike and northward across strike of the belts, although the relative roles of partial melting of juvenile basaltic crust and mantle wedge magmas cannot be resolved with these data.

Age data. Radiolarians suggest a pre-Early Cretaceous stratigraphic age for the protolith accretionary complex sediments (Wakita 1987). Very low-grade protolith rocks have yielded a Rb-Sr isochron age of 128 ± 14 Ma and whole-rock K-Ar ages of *c.* 133–125 Ma (Shibata & Mizutani 1980), and K-Ar mica ages of *c.* 134–122 Ma (Takami *et al.* 1993; Takami & Itaya 1996), interpreted to record the age of low-grade subduction-related metamorphism. The age of the superimposed Ryoke belt metamorphism is suggested to have been *c.* 100 Ma, in both the west and east of the Ryoke belt, based on recently published Th-U-total Pb ages on monazite from samples of high-grade parts of the belt (Suzuki *et al.* 1994, 1996; Suzuki & Adachi 1998), interpreted to date peak metamorphism. In the west of the Ryoke belt, the age span of the granites is *c.* 99 Ma to *c.* 83 Ma, whereas in the east the granites were emplaced over a longer period, from *c.* 100 Ma to *c.* 64 Ma (Suzuki *et al.* 1995, 1996; Suzuki & Adachi 1998; Nakai & Suzuki 1996), based on Th-U-total Pb ages on monazite interpreted to date crystallization. Nakajima (1996) has reported U-Pb zircon ages from two granites in the Komagane-Kashio District, a Ryoke granite that yielded a crystallization age of 86.1 ± 1.4 Ma and a San-Yo

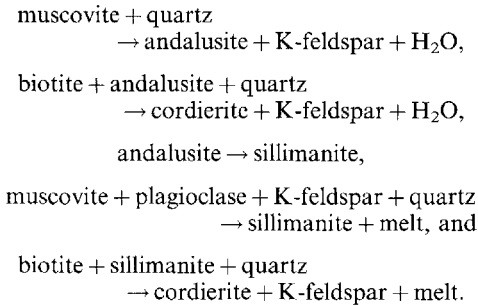
granite that yielded a crystallization age of 71.3 ± 1.6 Ma; these data were interpreted by Nakajima to imply an across-strike younging in the age of plutonism. An along-belt variation of systematic eastward younging in mineral ages (K-Ar hornblende, Rb-Sr/K-Ar biotite and K-Ar K-feldspar ages) from Ryoke metamorphic rocks and Ryoke/San-Yo type granites has been established (Kinoshita & Ito 1986; Kinoshita 1995; Nakajima *et al.* 1990). For example, the K-Ar biotite age data compiled by Kinoshita (1995) indicate cooling through *c.* 300°C (Harrison *et al.* 1985) at *c.* 90 Ma in the W and *c.* 70 Ma *c.* 700 km to the E. Fission-track ages on zircon in the western part of the belt, in Kyushu, yield 90–74 Ma (Kamp & Takemura 1993), whereas in the eastern part of the belt, east of the Izumi Group basins, fission-track ages on zircon/apatite are *c.* 64/52 Ma in the Kinki region in the SW and *c.* 54/49 Ma in the Chubu region in the NE (Tagami *et al.* 1988). The age data yield smooth cooling curves, which suggest fast rates of cooling of *c.* 40–10°C Ma⁻¹, declining with decreasing *T* and faster in the west than in the east (Nakajima *et al.* 1990; Suzuki & Adachi 1998). Synchronous peak metamorphism but diachronous exhumation at a decreasing rate from west to east are implied by these data.

Metamorphism. In the west of the belt, at medium and high metamorphic grades, up to five metamorphic zones may be distinguished in the Yanai District (Ikeda 1991, 1993, 1998; Okudaira *et al.* 1993, 1995; Nakajima 1994), after the disappearance of chlorite. The transition from the biotite zone to the muscovite-cordierite zone can be represented by:

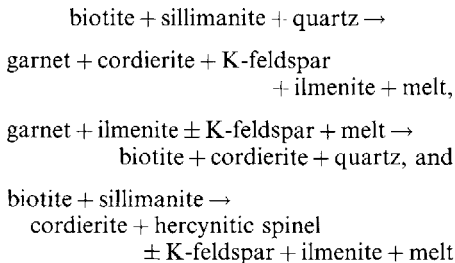


based on textures and mineral chemical data (Brown 1998; Ikeda 1998). Andalusite occurs in the lower-grade part of the K-feldspar-cordierite zone, but sillimanite is typical of the higher-grade part, and cordierite is abundant. At metamorphic grades above the muscovite-cordierite zone, pelites are variably migmatized; locally, schlieric diatexites (*sensu* Brown 1973) occur. Ikeda (1998) has discussed the progressive sequence of reactions, with particular reference to the formation of cordierite. Brown (1998) has catalogued petrographic features that he has used to define the *P-T* paths of the higher-grade metamorphic zones. Based on information documented in Ikeda (1998) and

Brown (1998), the sequence of metamorphic reactions inferred from samples that record segments of *P-T* paths successively along the metamorphic field gradient is:

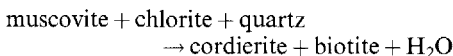


Garnet coexisting with cordierite, and hercynitic spinel coexisting with cordierite, in migmatites record reactions such as:



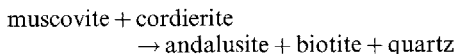
and record the prograde to retrograde part of the *P-T* path at high *T*. More siliceous and less aluminous rock types are characterized by $\text{biotite} + \text{plagioclase} + \text{K-feldspar} + \text{quartz}$ assemblages (sillimanite-absent) throughout the three highest-grade metamorphic zones (Ikeda 1998). Thus, an upper limit to temperature may be derived from the absence of hypersthene-bearing assemblages, which shows that the stability of $\text{biotite} + \text{quartz}$ is not exceeded.

In the east of the Ryoke belt, Morikiyo (1984, 1986) has used index minerals in metasedimentary rocks to distinguish nine metamorphic zones in the Komagane area, building on the earlier work of Hayama & Yamada (1977) and Ono (1969), and Brown (1998) has discussed pertinent petrographic information to constrain the *P-T* paths of the higher-grade metamorphic zones. In highly aluminous pelite, cordierite coexists with muscovite, biotite and chlorite (no K-feldspar) to suggest the reaction:

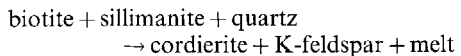


At progressively higher grade, in highly aluminous pelite, the assemblage $\text{biotite} + \text{muscovite} + \text{andalusite}$ (no K-feldspar) is stable, which

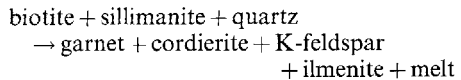
suggests the following reaction has been crossed:



This is succeeded, in 'normal' pelite, by the stable coexistence of andalusite and K-feldspar with residual muscovite and quartz and by the polymorphic inversion of andalusite to sillimanite. In the mesosome of fine-grained, finely migmatitic rocks, abundant cordierite (c. 0.5 mm) occurs with biotite and sillimanite inclusions, whereas in and next to the leucosome, cordierite is larger (c. 1.0 mm) and has fewer inclusions, especially in the rims of the crystals, which are also more euhedral, consistent with the reaction:



At the highest grades of metamorphism, garnet (up to c. 1 mm), cordierite and K-feldspar (up to c. 2 mm) coexist in fine-grained rocks that are distinctly migmatitic. In these rocks, cordierite commonly is found against garnet but a clear reaction relationship is not apparent; sillimanite occurs as inclusions in cordierite. These features are consistent with the reaction:



An upper limit on temperature is inferred from the absence of hypersthene-bearing assemblages, which shows that the stability of $\text{biotite} + \text{quartz}$ was not exceeded.

P-T path. Mineral assemblages show that high temperatures were achieved at middle crustal depths. Peak metamorphic conditions in the highest-grade zones of the Ryoke belt metamorphism probably correspond to c. 5 kbar and c. 850°C, based upon the mineral assemblages and an appropriate petrogenetic grid (Brown 1998). The succession of mineral assemblages developed in pelites along the metamorphic field gradient suggests a nested series of hairpin-like 'clockwise' *P-T* paths, with limited prograde thickening, only minor decompression at peak-*T*, and near isobaric cooling (Fig. 3). This *P-T* evolution contrasts dramatically with the *P-T* evolution of the Sambagawa belt (Takasu 1989), which is shown for comparison in Fig. 3.

The Abukuma belt

The Mesozoic geology of northeast Japan (Fig. 4) comprises accretionary prism sedimentary rocks and an accreted terrane element of

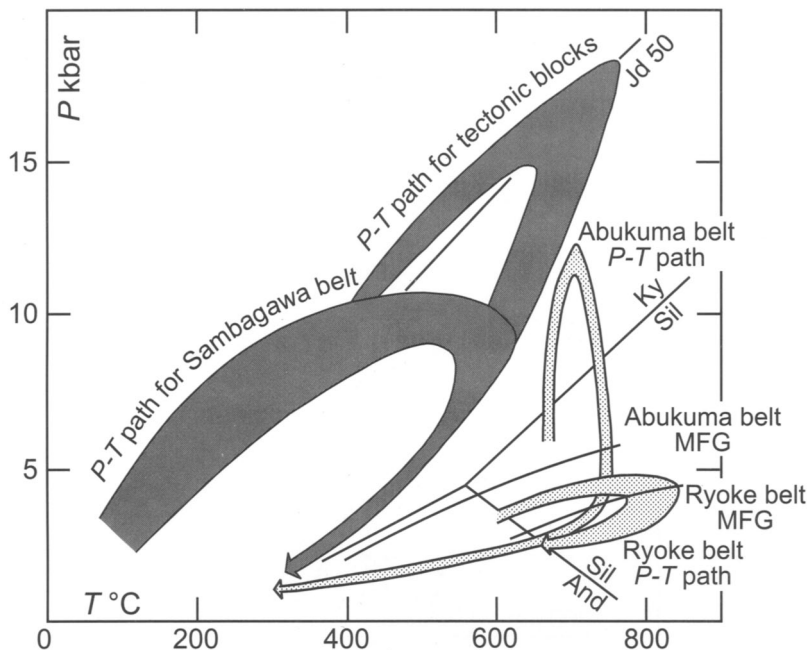


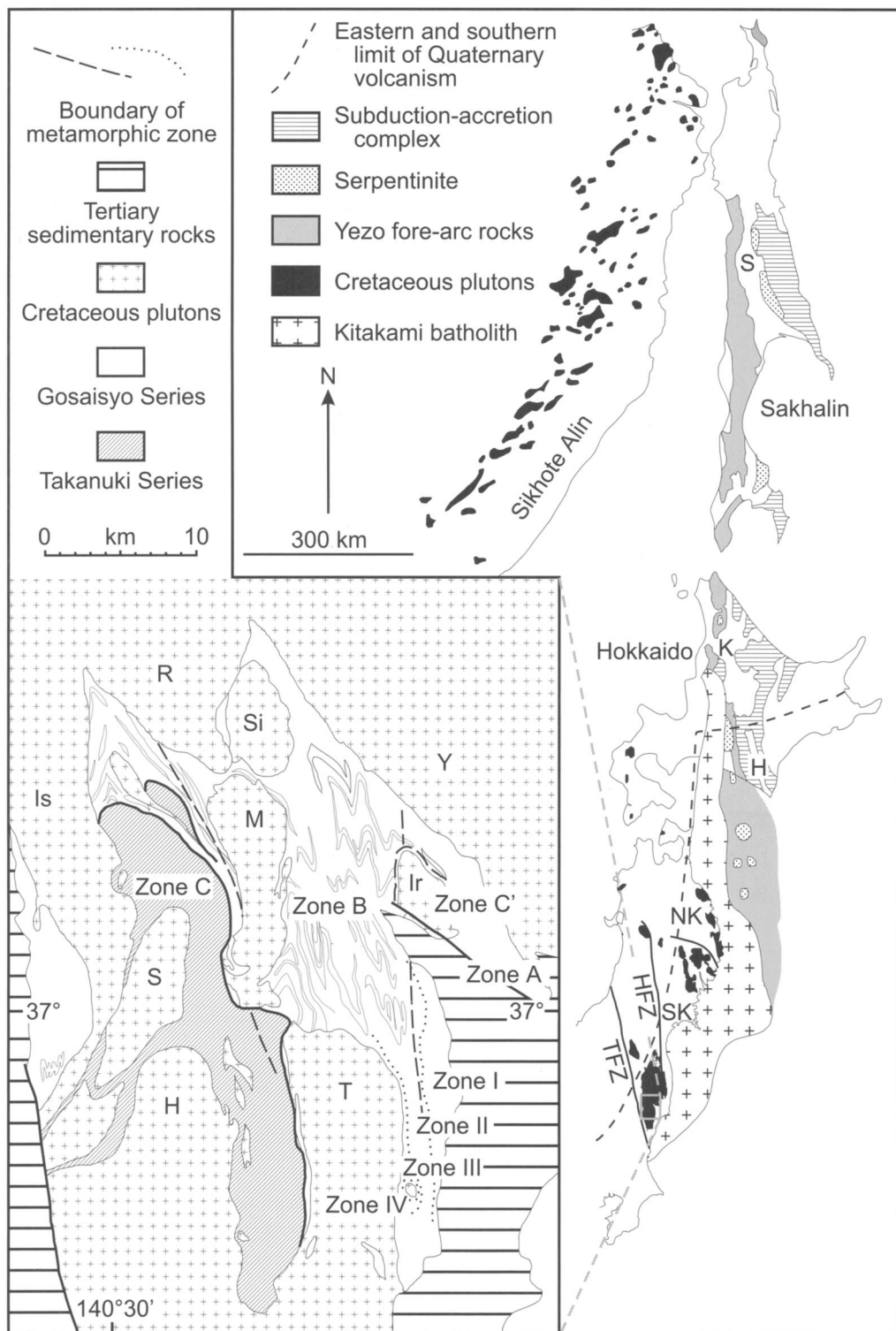
Fig. 3. P - T diagram to show metamorphic field gradients (MFG) and P - T paths for high-grade metamorphic rocks of the Ryoke and Abukuma belts (after Brown 1998; Hiroi *et al.* 1998). Also shown for comparison are the P - T trajectories of the Sambagawa progressive metamorphism and included tectonic blocks (after Takasu 1989).

continental affinity (the Kitakami allochthonous terrane; see Saito & Hashimoto 1982), into which was emplaced a linear belt of Early Cretaceous plutons, the Kitakami batholith (part of the Kitakami magmatic arc), the full extent of which has been delineated using aeromagnetic mapping (Finn 1994; Finn *et al.* 1994). Magmatic activity in the Kitakami arc ceased by c. 110 Ma (Shibata 1968), but probably shifted westward as evidenced by Late-Cretaceous plutons in Sikhote Alin (Fig. 4). Three of the exposed plutons of the Kitakami batholith exhibit distinctive geochemical characteristics, particularly high Sr, that suggest derivation by melting of young oceanic lithosphere, probably the Izanagi plate (Tsuchiya & Kanisawa 1994). East of the Kitakami batholith are a Cretaceous fore-arc basin and high P/T ratio metamorphic rocks of the Kamuikotan (Hokkaido) and Susunai (Sakhalin) belts (Fig. 4).

At the western margin of the Kitakami allochthonous terrane, and separated from it by the Hatagawa fracture zone, is the Abukuma belt (Fig. 4). Across the Hatagawa fracture zone there are differences in the geophysical signature, expressed on both aeromagnetic and residual gravity maps, between intrusive rocks

of the Abukuma belt and those of the Kitakami batholith (Kubo & Yamamoto 1990). Major transcurrent displacement is associated with the Hatagawa fracture zone and its extension to the north (Sasada 1988), and mylonites within the zone exhibit S-C fabrics and shear band structures that record left-lateral motion (Koshiya 1988). On its western side, the Abukuma belt is bounded by the Tanakura fault zone, a major sinistral plastic shear zone system (Koshiya 1986) that separates the low P/T ratio metamorphic belt to the E from metamorphosed Jurassic accretionary complex rocks of the Ashio belt to the W (equivalent to the Mino-Tanba belt west of the Itoigawa-Shizuoka Tectonic Line). Isotopic age data obtained from the mylonites (Shibata & Takagi 1989) suggest that plastic deformation and accumulation of plastic strain had started by c. 107 Ma and continued until c. 82 Ma, with sporadic rejuvenation after that (Otsuki 1992).

The Abukuma Plateau in the southern part of the belt represents a classic andalusite-sillimanite metamorphic terrain (Miyashiro 1958; Shidô 1958), originally correlated with the Ryoke belt (Miyashiro 1959, 1961). Unfortunately, subsequent work has shown that the



sequence of aluminosilicate minerals developed during the *P-T* evolution of the metasedimentary rocks in the western part of the Plateau was sillimanite → kyanite → sillimanite → andalusite (Hiroi *et al.* 1998), and isotopic dating methods have shown that metamorphism in the Abukuma belt occurred earlier than that in the Ryoke belt (Kimbrough *et al.* 1994; Hiroi *et al.* 1998). Supracrustal rocks of the Abukuma Plateau are divided into the terrigenous Takanuki series and the structurally overlying oceanic Gosaisho series (Fig. 4), with the metamorphic grade generally increasing westward (Miyashiro 1958; see Fig. 4).

The Takanuki series crops out in the western part of the Abukuma Plateau; it is mainly composed of medium-grained pelitic-psammitic gneisses with subordinate calc-silicate rock and amphibolite (Hiroi *et al.* 1998). The metasedimentary gneisses are commonly migmatitic, indicating that partial melting took place during high-grade metamorphism. The Gosaisho series crops out in the eastern part of the Abukuma Plateau; it consists principally of fine-grained mafic schists intercalated with pelitic schists and metacherts. Within the mafic schists, original textures of volcanic rocks have been recognized (Tagiri *et al.* 1993), and pillow-structured basaltic protoliths have chemical characteristics of MORB (Nohara & Hiroi 1989); Jurassic radiolarians have been recovered from finely bedded metacherts (Hiroi *et al.* 1987).

Plutonic complexes dominate the map pattern (Fig. 4) and form a significant component of the Abukuma Plateau; contact metamorphism associated with the 'older' plutonic complexes is superimposed on the westward increase in regional metamorphic grade (Shidō 1958; Tagiri *et al.* 1993; see Fig. 4). In the west, the Ishikawa and Samegawa ('older'), and Hanawa ('younger') plutonic complexes (Fig. 4) are predominantly composed of diorite/tonalite and granodiorite/granite; a wide zone of migmatites was developed in host Takanuki series rocks around the Samegawa plutonic complex and migmatites were developed to a lesser degree around the Ishikawa plutonic complex, but the contact metamorphism associated with the Hanawa plutonic complex was slight, consistent

with the interpretation that it is a 'younger' plutonic complex (Maruyama 1970; Faure *et al.* 1986; Tanaka & Ochiai 1988). Further east, the Miyamoto and Tabito plutonic complexes (Fig. 4) exhibit a wider range of compositions, from hornblende gabbro/diorite to granodiorite/granite; they were emplaced across the contact between the Gosaisho series and the Takanuki series, and in contact aureoles mafic schists have recrystallized to pyroxene hornfelses whereas metasedimentary protoliths have developed migmatites (Shidō 1958; Tanaka 1974; Kishi 1987; Tagiri *et al.* 1993).

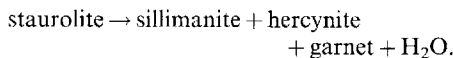
Deformation. Tectonic structures within the Gosaisho series comprise bedding-parallel schistosity associated with small-scale isoclinal folds refolded during progressive deformation by tight upright folds; there is a sub-horizontal mineral elongation lineation (Faure *et al.* 1986; Ishikawa & Otsuki 1990). Mesoscopic and microscopic asymmetric structures such as S-C fabrics, pressure shadows, rotated crystals, fold asymmetry and boudinage are superimposed on the earlier structures during sinistral plastic shearing (Ishikawa & Otsuki 1990). The observations suggest oblique transpressional deformation that became highly oblique with time. The oceanic Gosaisho series is inferred to have been thrust onto the terrigenous Takanuki series (Umemura 1979; Faure *et al.* 1986; Goto 1990). Hiroi & Kishi (1989b) postulated that this was related to obduction during oblique ridge collision. In the Takanuki series, east-plunging lineations to the northeast of the Samegawa plutonic complex and associated asymmetric boudins show top-to-the-east extension along this lineation (Faure *et al.* 1986) that suggests tectonic exhumation of the Takanuki series metamorphic rocks during transtension.

Age data. An extensive dataset of whole-rock and mineral isotopic ages using the Rb-Sr, K-Ar and Sm-Nd isotope systems has been accumulated from granites and metamorphic rocks in the Abukuma Plateau. K-Ar and Rb-Sr mica ages from metamorphic rocks are in the range 115–100 Ma (Ueno 1977), and K-Ar ages on

Fig. 4. Simplified geology of northeast Japan, Sikhote Alin and Sakhalin (after Hiroi *et al.* 1998; Finn 1994; Finn *et al.* 1994). S = Susunai belt; K = Kamuikotan belt; H = Hidaka belt; NK = North Kitakami block; SK = South Kitakami block; together these make up the Kitakami allochthonous terrane. HFZ = Hatagawa fracture zone; TFZ = Tanakura fault zone. Inset shows geology of the southern part of the Abukuma Plateau. Is = Ishikawa plutonic complex; S = Samegawa plutonic complex; H = Hanawa plutonic complex; R = Ronden plutonic complex; Si = Shibayama plutonic complex; M = Miyamoto plutonic complex; T = Tabito plutonic complex; Y = Yoshimawara plutonic complex; Ir = Iritono plutonic complex; metamorphic zones A, B and C after Miyashiro (1958), and C' after Shidō (1958); metamorphic zones I–IV after Tagiri *et al.* (1993).

hornblades from granitic rocks are in the range 119–96 Ma (Shibata & Uchiumi 1983). In the west, the Ishikawa plutonic complex has yielded a Rb-Sr whole-rock isochron age of 106 ± 16 Ma ($Sr_i 0.70518 \pm 15$, MSWD 0.74), which is consistent with a less precise Sm-Nd whole-rock and mineral isochron age of 111 ± 42 Ma ($Nd_i 0.51251 \pm 3$, MSWD 0.18) (Shibata & Tanaka 1987). The Miyamoto plutonic complex has yielded Rb-Sr whole-rock isochron ages of 120 ± 17 Ma on tonalites ($Sr_i 0.70518 \pm 11$, MSWD 0.32) and 119 ± 18 Ma on granites ($Sr_i 0.70489 \pm 26$, MSWD 0.13), consistent with the observed sequence of emplacement (Fujimaki *et al.* 1991). Kimbrough *et al.* (1994) have reported a near concordant U-Pb age of 113 ± 2 Ma on monazite separated from amphibolite-facies sillimanite gneiss of the Takanuki series, interpreted to date the metamorphic peak. Additionally, Hiroi *et al.* (1998) have reported a weighted mean $^{206}\text{Pb}/^{238}\text{U}$ age of 111.9 ± 2.3 Ma on zircon separated from amphibolite of the Takanuki series, and a concordant U-Pb age of $c. 110$ Ma from rims of structured zircon grains separated from Takanuki series metapelitic. The consistency among these U-Pb ages suggests that peak metamorphism in the Takanuki series occurred at $c. 110$ Ma, and consistency with K-Ar and Rb-Sr mineral ages suggests rapid cooling to temperatures below $c. 500^\circ\text{C}$.

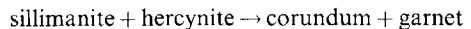
Metamorphism. Metapelitic rocks of the Takanuki series typically have an assemblage composed of sillimanite + cordierite + garnet + biotite + plagioclase + K-feldspar + quartz + ilmenite + pyrrhotite + graphite without primary muscovite, to suggest that the stability of muscovite + quartz had been exceeded (Miyashiro 1958). Urano & Kanisawa (1965) described staurolite-bearing rocks derived from silica-deficient Al-Ferich protoliths; staurolite occurs with sillimanite, hercynite, garnet, corundum, plagioclase, biotite and ilmenite. Staurolite is extensively replaced by sillimanite, hercynite and garnet to suggest the following reaction:



Relict kyanite was discovered as inclusions in plagioclase in sillimanite-K-feldspar-grade metapelites of the Takanuki series (Kano & Kuroda 1968; Urano *et al.* 1974; Hiroi & Kishi 1989a), and Kano & Kuroda (1973) showed that garnet in metapelites of the Takanuki series has Mn-enriched rims consistent with garnet consumption during the P - T evolution. Hiroi & Kishi (1989a, b) and Hiroi (1990) have argued for

rapid loading and unloading during a single Cretaceous orogenic event based on a temporally short excursion to high pressure before decompression to peak metamorphic temperatures during the P - T evolution of rocks of the Abukuma Plateau.

Hiroi *et al.* (1998) provide a summary of recent data concerning the clockwise P - T evolution of the Takanuki series. Texturally sector-zoned garnet includes sillimanite (\pm kyanite), plagioclase and quartz and exhibits dramatic chemical zoning from low Ca ($c. 3$ mol% grs) in cores, through high Ca ($c. 30$ mol% grs) interiors to low Ca ($c. 3$ mol% grs) rims, interpreted to record an early low- P stage, a high- P stage and the peak- T stage of the P - T evolution. Additionally, garnet preserves rutile inclusions whereas ilmenite characteristically is the matrix Fe-Ti mineral. Textural relationships between garnet and cordierite suggest replacement during decompression, while andalusite-biotite-quartz \pm muscovite assemblages that replace garnet reflect close to isobaric cooling to the stable geotherm. In the silica-deficient Al-Ferich rocks, Hiroi (1990) reported textures that he interpreted to reflect crossing the reaction:



during the transition from the early low- P stage to the high- P stage and in reverse during decompression to the peak- T stage. In the same paper, Hiroi reported widespread occurrence of anorthite-wollastonite-quartz assemblages in calc-silicate rocks of the Takanuki series that support low- P at the peak- T stage.

Emplacement depth of the plutonic complexes can be evaluated with the Al-in-hornblende barometer (Hammarstrom & Zen 1986), which relates total aluminum (Al_t) in hornblende to pressure. This has been calibrated empirically and experimentally (Schmidt 1992, and references therein). Schmidt (1992) suggested that his experimental calibration is accurate to ± 0.6 kbar, although there are additional uncertainties that reflect the variability of the analytical data. When these factors are combined, the calculated pressures are accurate to ± 1 kbar. Close agreement between the empirical calibration of Hammarstrom & Zen (1986) and the experimental calibration of Schmidt (1992) confirms a linear relation between Al_t in hornblende and pressure. This suggests that relative differences in calculated pressures may be significant. Samples collected from the Ishikawa, Samegawa and Hanawa plutonic complexes along the west side of the southern Abukuma Plateau have the complete buffering-phase assemblage for application of this barometer.

Rim compositions of late-crystallized hornblende (small euhedral hornblende crystals enclosed in interstitial quartz or alkali feldspar) were analysed by electron microprobe WDS (Center for Microanalysis, UMCP). For the Ishikawa plutonic complex sample, six hornblende analyses yield a mean Al_i of 1.974 ± 0.023 , which suggests a pressure of 6.4 ± 0.1 kbar. Six hornblende analyses from a sample of the Samegawa plutonic complex sample yield a mean Al_i of 1.933 ± 0.100 , which suggests a pressure of 6.2 ± 0.5 kbar. For the Hanawa plutonic complex sample, three hornblende analyses yield a mean Al_i of 1.699 ± 0.075 , which suggests a pressure of 5.1 ± 0.4 kbar. Although total uncertainties of at least 1 kbar limit interpretation of differences between the Ishikawa and Samegawa plutonic complexes and the Hanawa plutonic complex, the relative difference is consistent with younger emplacement of the Hanawa plutonic complex during decompression. Perhaps more importantly, the results suggest that the plutonic complexes were emplaced at crustal depths shallower than peak- P conditions and probably at depths close to the peak- T part of the metamorphic evolution.

$P-T$ path. Based on the mineral assemblages, textural interpretations and mineral chemistry, Hiroi & Kishi (1989b) and Hiroi *et al.* (1998) have proposed an early low- P stage of metamorphism in the sillimanite stability field, a high- P stage in the kyanite stability field with maximum P of c. 12 kbar, decompression to peak- T conditions of c. 750°C at c. 6 kbar and near-isobaric cooling from the sillimanite to the andalusite stability field, as recorded by the late growth of andalusite in metapelites (Fig. 3). The preservation of both textural sector zoning and growth zoning in garnet suggests rapid growth and short duration of high-grade metamorphic conditions.

Relationship to plate interactions in the North Pacific Ocean basin

Linking plate tectonic models to convergent margin processes, particularly with respect to triple junction interactions and their effects, remains an important but elusive challenge in geology. The definitive model for plate interactions along the continental margins in the North Pacific Ocean basin is that of Engebretson *et al.* (1985; see also Hilde *et al.* 1977; Cox *et al.* 1989). Unfortunately, the timing of magmatic activity in the Kitakami arc and the timing of metamorphism and plutonism in the Abukuma and

Ryoke belts lie within the Cretaceous normal polarity superchron (119–83 Ma), so no isochrons are available in the ocean floor to mark plate boundaries. Cox *et al.* (1989) suggested that comparison of their results with the geologic record along the margin of the North Pacific Ocean basin would provide a test of the models proposed by them. This is an important point since models of plate interactions along continental margins before the Mesozoic can only be based on the geological record of the continents. In this section, a plate tectonic scenario is proposed for the Cretaceous evolution of the Japanese Islands that involves ridge-trench interactions along the Asian continental margin (Fig. 5).

Plate interactions. During the Cretaceous–Paleogene, the plate geometry next to the Asian continental margin was a complex system of ridges and transforms (Cox *et al.* 1989). In Japan, the identity of the oceanic plate under-thrust at the trench along the Asian continental margin before c. 74 Ma is ambiguous, but was probably either the Farallon or the Izanagi plate. Before c. 110 Ma, the boundary between these plates is thought to have been a spreading ridge system. This spreading ridge system could have interacted with the trench along the Asian continental margin during the Early Cretaceous. Although the motion of the Farallon and Izanagi plates compared with Asia is known, the orientation of the system of ridges and transforms that formed the boundary between them and the ridge segment/transform segment lengths along the boundary are not well constrained.

Cox *et al.* (1989) have resolved convergence velocities into components normal and tangential to the continental margin (orientation taken to be N15°E), to allow comparison with geological evidence for contractional or transcurrent tectonics along continental margins of the North Pacific Ocean basin. For Japan, two pulses of rapid convergence normal to the margin are suggested, one from 135 to 115 Ma and another from 100 to 56 Ma. The magnitude of these pulses depends upon whether the subducting plate was Farallon (moderate to high rate) or Izanagi (high to very high rate). Between these two periods, rates of convergence were moderate or low and during the first half of the normal polarity superchron the rate of convergence of the Farallon plate was negligible. For the tangential component of convergence velocity, a model with the Farallon plate at the trench gives a component of left-lateral motion before 119 Ma and essentially no tangential motion after that. With the Izanagi plate at the

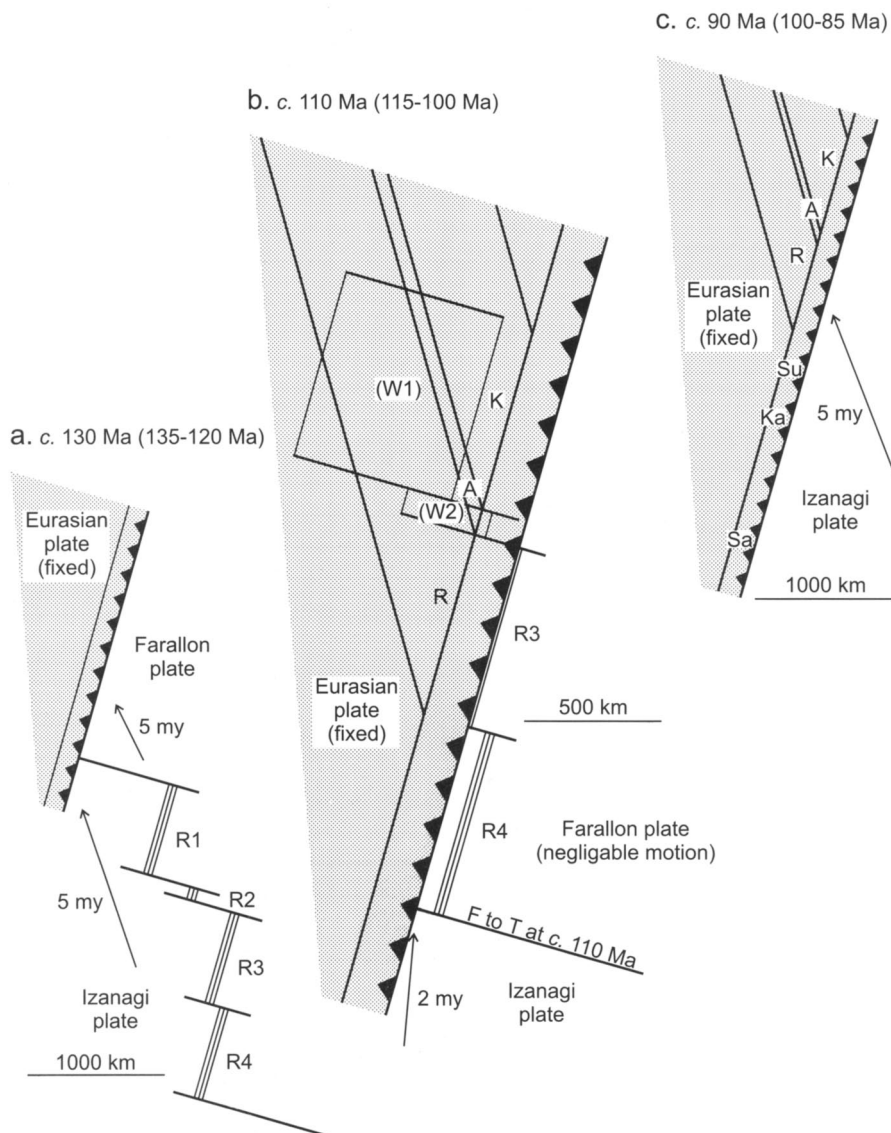


Fig. 5. Schematic plate boundary relations along the Asian continental margin at *c.* 130 Ma (135–120 Ma), *c.* 110 Ma (115–100 Ma) and *c.* 90 Ma (100–85 Ma), based on the analysis of plate interactions by Cox *et al.* (1989). Sometime before 120 Ma, a segment of the ridge boundary between the Farallon and Izanagi plates subducted under the Kitakami batholith (K). A short segment of the ridge boundary further to the south subducted under the Abukuma belt (A) prior to *c.* 110 Ma. (W1) and (W2) are the projected positions of slab windows formed during ongoing ridge subduction. At *c.* 110 Ma, further segments of the ridge boundary between the Farallon and Izanagi plates subducted under the Ryoke belt (R). By *c.* 90 Ma, a TTT triple junction had migrated northeast along the Eurasian trench and the Izanagi plate was subducting under the Eurasian plate. As a consequence, the Susunai (Su), Kamuikotan (Ka) and Sambagawa (Sa) belts were translated from the southwest to dock against the Sikhote Alin, Kitakami batholith and Ryoke belt, respectively, during the late Cretaceous and Paleogene.

trench, left-lateral motion at very high tangential velocities of more than 200 mm a^{-1} occurred from 135 to 85 Ma.

An analysis of velocity fields in a fixed hot-spot reference frame for both plates (Engebretson *et al.* 1985) suggests that sometime during the normal polarity superchron, the boundary between the Farallon and Izanagi plates became dominantly convergent. Cox *et al.* (1989) postulate subduction of the Izanagi plate under the Farallon plate, with the subduction zone originating along the locus of an earlier transform at *c.* 110 Ma. After 74 Ma, Cox *et al.* (1989) suggest that the Pacific plate was at the trench, although it is more likely to have been successively the Izanagi plate followed by the Kula plate (Byrne & DiTullio 1992; Onishi & Kimura 1995).

Geological constraints: Ryoke belt. In recent years, ridge subduction has become a popular model for the origin of the thermal anomaly recorded by the Ryoke belt low-*P/T* type metamorphism (Kinoshita & Ito 1986; Nakajima *et al.* 1990; Brown & Nakajima 1994; Kinoshita 1995; Brown 1998). Although not individually diagnostic, the following features are consistent with the ridge subduction hypothesis: (1) the long length and narrow width of the Ryoke belt, which suggest a linear thermal anomaly; (2) the very high temperatures at shallow crustal depths of *c.* 15 km, which require an enhanced heat flux from the mantle; (3) the fine-grained nature of even the highest-grade metamorphic rocks, which implies rapid heating and cooling on a regional scale; (4) the lack of evidence of significant crustal thickening, which is consistent with the absence of evidence of collision-related processes; (5) the hairpin-like 'clockwise' *P-T* paths, which require a thermal spike at shallow crustal depths; and (6) the fast rates of cooling implied by the geochronological data, which are in agreement with rapid passage of a sub-crustal thermal anomaly and subsequent exhumation.

The west-to-east pattern of younging in cooling ages has led to interpretations that the thermal anomaly responsible for the metamorphism and the granite magmatism migrated with time (Kinoshita & Ito 1986; Nakajima *et al.* 1990; Kinoshita 1995). However, the similarity of Th-U-total Pb ages on monazite from high-grade metamorphic rocks in the west and east of the Ryoke belt shows that peak metamorphism occurred synchronously along the length of the belt (Suzuki *et al.* 1994, 1996). Furthermore, granite plutonism began at a similar time as the peak of metamorphism, as discussed above and summarized by Suzuki & Adachi (1998). Thus,

neither the thermal anomaly nor the granite magmatism migrated along the length of the belt with time, and another explanation for the west-to-east decrease in cooling ages is required. Additionally, the granites may become younger from south to north, from the Ryoke to the San-Yo belt, as discussed by Nakajima (1996), and the isotopic compositions show a decreasing crustal component from south to north (Kagami *et al.* 1992), which may reflect deeper sources, consistent with increasing depth to a slab window with distance from the trench in a ridge subduction model.

Geological constraints: Kitakami batholith and Abukuma belt. After formation of the Early Cretaceous Kitakami batholith, which was finished by *c.* 110 Ma, arc magmatism probably shifted westward, as suggested by Late Cretaceous plutons in Sikhote Alin. The presence of three plutons within the Kitakami batholith that have geochemical characteristics implying slab melting requires subduction of young oceanic lithosphere, consistent with a spreading ridge system approaching the trench during active magmatism along the Kitakami arc. In the Abukuma belt, peak metamorphism in the southern Abukuma Plateau occurred at *c.* 110 Ma. The Abukuma belt is characterized by a distinctive tectonic history that involved obduction and rapid thickening during highly oblique sinistral transpression, followed by rapid tectonic exhumation of high-temperature rocks from deeper to shallower crustal levels during transtension. It is likely that the evolution of the Abukuma belt is the result of triple junction interaction at the convergent plate margin.

A Tectonic scenario. Figure 5 illustrates plausible plate tectonic geometries at three points in time, *c.* 130 Ma, *c.* 110 Ma and *c.* 90 Ma. The consistent age of peak metamorphism from W to E in the Ryoke Belt suggests that the thermal anomaly developed simultaneously along *c.* 700 km of the overlying accretionary complex sediments of the facing plate. This thermal anomaly responsible for the Ryoke belt low-*P/T* ratio metamorphism is inferred to reflect subduction of a spreading ridge system. An implication of the synchronicity in metamorphism along the length of the Ryoke belt is that the spreading ridge system was approximately parallel to the trench. Given the age of peak metamorphism in the Ryoke belt of *c.* 100 Ma, and assuming *c.* 10 Ma time lag between initial subduction of the spreading ridge system and its thermal manifestation in

the overlying subduction-accretion complex, I postulate subduction of the spreading ridge system at c. 110 Ma (Fig. 5b). The obliquity of the Izanagi plate convergence vector with the trench created a circumstance in which the force due to slab pull probably exceeded the positively buoyant force associated with the ridge-proximal part of the subducting plate (Larter & Baker 1991). Also, the strength of the plate must have been sufficient for the slab to subduct without breaking up (van den Beukel 1990). The principal kinematic change consequent upon ridge subduction, which brought the Farallon plate into the trench, was to decrease displacement between the continental and oceanic plates (Cox *et al.* 1989). Ongoing divergence at the spreading ridge system during subduction is assumed, which would have created a slab window and thermal anomaly (cf. Murdie *et al.* 1993; Thorkelson 1996).

Subduction of a ridge segment or several closely spaced ridge segments of the Farallon-Izanagi spreading centre under northeast Japan before the ridge-trench interaction in southwest Japan is consistent with the orientation, age and petrogenesis of the Kitakami batholith (Tsuchiya & Kanisawa 1994) and the age of metamorphism in the Abukuma belt (Hiroi *et al.* 1998; Brown 1998). The change in plate convergence vectors from c. N (Izanagi plate, present coordinates) to c. NE (Farallon plate, present coordinates) after subduction of a ridge segment under the Kitakami arc, implies sinistral displacement along the Hatagawa fracture zone and the Tanakura fault zone and sinistral transpression between. In the Abukuma belt, obduction of oceanic materials during sinistral transpressional deformation occurred as a short ridge segment between two RTF triple junctions approached the trench. Thus, the high temperature loading recorded in the metamorphic history is enabled by the underthrusting of progressively younger oceanic lithosphere during obduction and sinistral transpressional deformation. Subsequent subduction of this short ridge segment under the Abukuma belt brought the Farallon plate into the trench and changed the kinematics so that transtension occurred between the Hatagawa fracture zone and the Tanakura fault zone. This enabled rapid decompression during high temperature maintained by an opening slab window.

Around 110 Ma, a transform between the Farallon and Izanagi plates was converted to a subduction zone, and the TTF triple junction between the Farallon, Izanagi and Asian plates became a TTT triple junction. The N-directed convergence vector of the Izanagi plate implies

that these triple junctions migrated NE along the trench at the Asian continental margin. Thus, the Sambagawa belt was probably translated from the SW, and juxtaposition of the high-*P/T* type metamorphic rocks against the Ryoke belt was a result of strike-slip displacement following ridge subduction (Fig. 5c). Removal of part of the fore arc by lateral displacement may have been initiated during ridge subduction (c.f. Forsythe & Nelson 1985; Murdie *et al.* 1993). Such an interpretation of the tectonic relationship between the Ryoke belt and the Sambagawa belt raises questions about the validity of the classic idea of 'paired' metamorphic belts formed by Pacific-type orogenesis. Although $^{40}\text{Ar}/^{39}\text{Ar}$ mineral age data from the Sambagawa belt suggest exhumation and cooling during the Late Cretaceous, no detritus from that belt occurs in the Late Cretaceous Izumi belt sedimentary rocks that overlie unconformably the Ryoke belt (Itaya & Takasugi 1988; Isozaki & Itaya 1990; Dallmeyer & Takasu 1991; Takasu & Dallmeyer 1990, 1992; Takasu *et al.* 1994). Late Cretaceous exhumation of the Sambagawa belt probably reflects the significant decrease in tangential component of convergence velocity after c. 85 Ma during a period of moderate to high normal component of convergence velocity (Cox *et al.* 1989). The dominant regional tectonic fabric within rocks of the Sambagawa belt was formed during exhumation and plastic extension that involved c. 50% thinning during orogen-parallel shear, which requires a changing strike-slip component of displacement along-strike (Wallis 1995). The diachronous nature and decreasing rate of cooling of rocks within the Ryoke belt from W to E is consistent with progressive docking at a decreasing rate of a Sambagawa belt terrane against the Ryoke belt, and the sequential younging from W to E of sedimentation within the Izumi belt.

On Hokkaido and in Sakhalin to the north, the Kamuikotan and Susunai metamorphic belts lie outboard of the Early Cretaceous Kitakami Batholith of northeast Japan and the Cretaceous plutonic province of Sikhote Alin on the Asian mainland, respectively (Kimura 1994). It is likely that these high-pressure metamorphic belts have also been translated sinistrally along the Asian continental margin (Fig. 5c). Arc-parallel strain in fore arcs is sufficient to produce geologically significant effects, such as exhumation of high-grade metamorphic rocks during arc-parallel extension and disruption of transported fore-arc terranes (McCaffrey 1996). Furthermore, there is little evidence for wholesale arc-parallel translation of rigid fore arcs (Jarrard 1986;

Beck 1991), and they are probably not transported great distances without breaking up. The time between ridge subduction and peak metamorphism in the Ryoke Belt (*c.* 110–100 Ma) and cooling below *c.* 260°C (T_c zircon fission tracks), interpreted to record exhumation, is *c.* 25 Ma in the west of the belt and *c.* 50 Ma in the east of the belt, consistent with several thousand kilometres of sinistral displacement during this time. Thus, the Susunai, Kamuikotan and Sambagawa Belts have probably been displaced from a position SW of Japan (present coordinates) along the Median Tectonic Line to their present locations by the Early Paleocene.

Other high-T-low-P metamorphic belts

Cretaceous–Neogene examples

The Chugach metamorphic complex. Many investigators have recognized Paleogene subduction of the Kula–Farallon spreading ridge beneath North America as a fundamental feature of plate reconstructions in the North Pacific Ocean basin (e.g. Engebretson *et al.* 1985; Atwater 1989). The geology of southern Alaska has been interpreted to record passage of the Kula–Farallon ridge beneath the Chugach–Prince William composite terrane, a subduction–accretion complex formed along the North American continental margin (Marshak & Karig 1977; DeLong *et al.* 1978; Bradley *et al.* 1993). The most compelling evidence of ridge–trench interaction occurs within the Chugach terrane, which is the Mesozoic part of the accretionary wedge. Here, plutons and related dykes were emplaced into the accretionary prism anomalously close to the palaeotrench and far seaward of the coeval volcanic arc (Hudson 1979; Bradley *et al.* 1993, and references therein). From *c.* 66 Ma in the west to *c.* 47 Ma in the east, the near-trench magmatism migrated *c.* 2200 km along the continental margin (e.g. Wallace & Engebretson 1984; Bradley *et al.* 1993). Evidence that Paleogene near-trench magmatism was related to subduction of the Kula–Farallon spreading centre consists of: (1) the diachronous nature of the magmatism; (2) the near-trench position of the magmatism; and (3) the geochemistry of the igneous rocks that suggests a mixture of MORB source material and more local anatetic melts of the accretionary complex sedimentary rocks (Hudson *et al.* 1979), with the proportion of mantle-derived components increasing through time (Harris *et al.* 1996). The accretionary prism includes several dismembered ophiolites with

ages that agree closely with those of the fore-arc plutons to suggest that the ophiolites are also relicts of ridge–trench interaction (Bradley *et al.* 1993). Haeussler *et al.* (1995, and references therein) relate gold mineralization to fluid circulation consequent upon ridge–trench interaction.

A high-*T*–low-*P* metamorphic belt, the Chugach metamorphic complex, was developed within the Mesozoic part of the accretionary prism; the metamorphic grade increases from greenschist to upper amphibolite facies, with the development of anatetic migmatites (Hudson & Plafker 1982; Sisson & Hollister 1988; Sisson *et al.* 1989; Barnett *et al.* 1994). Pervasive andalusite occurs with staurolite in the lower amphibolite facies; the polymorphic inversion of andalusite to sillimanite and the elimination of staurolite both occur before the onset of anatexis, to suggest *P* of *<4* kbar at *T* probably *>650*°C (Sisson & Hollister 1988). The *P*–*T* path is inferred to have been essentially isobaric at the highest grades, and the heating is inferred to have been through advection in fluids and associated melts, now represented by abundant plutons (Sisson & Hollister 1988; Barnett *et al.* 1994).

The belt has a complex structural evolution (Sisson & Pavlis 1993; Pavlis & Sisson 1995) with an early history of dextral orogen-parallel motions along a low-angle ductile shear zone followed by dramatic telescoping during oblique dextral transpression coincident with peak metamorphism. These events have been interpreted as the products of ridge subduction and a plate reorganization at *c.* 56–52 Ma; the change in kinematics involved clockwise rotation of the relative motion vector as the triple junction passed, with a consequent increase in the contractional component of deformation. It is not clear to what extent these events are unique to the Chugach metamorphic complex and the complexities of the particular triple junction interactions there, and to what extent orogen-parallel extension followed by contraction might be a characteristic structural imprint associated with passage of a subducting ridge segment.

The Shimanto belt, Japan. The Shimanto belt is one of the most studied subduction–accretion complexes in the world. The age of the subducted oceanic plate, the nature of the oceanic and infilled-trench sedimentary sequences, the style of deformation and the thermal history are well constrained by the large amount of data. The Shimanto belt is composed of a coherent turbidite sequence and a highly deformed mélange belt, thought to have been brought together

during subduction of juvenile oceanic lithosphere from c. 70 Ma (Taira & Ogawa 1991). A major phase of accretion in the Shimanto belt occurred during the Paleocene as recorded by K-Ar ages determined on cleavage-forming potassium-bearing phyllosilicates of c. 55 Ma in sediments with a Maastrichtian stratigraphic age (Agar *et al.* 1989). Evidence presented by Osozawa (1992) and Sakaguchi (1996) suggests Paleocene subduction of the ridge between the Kula plate and either the Pacific or the North New Guinea plate, according to the particular reconstruction used. A second ridge subduction event was related to subduction of the Shikoku basin and its actively spreading ridge from c. 15 Ma (Hibbard & Karig 1990; Underwood *et al.* 1992). The thermal history of the Shimanto belt suggests two episodes of cooling at ≤ 70 Ma and c. 15 Ma, respectively (Tagami *et al.* 1995), consistent with uplift following each of the ridge subduction events.

The Hidaka belt, Japan. In northeast Japan, the Hidaka belt crops out in central Hokkaido. Upthrusting of the belt along the western foothills of the Hidaka Mountains since the late Miocene has exposed a section of upper mantle to upper crust that shallows eastward (Komatsu *et al.* 1994). Metamorphic grade increases westward from greenschist to granulite facies to maximum conditions of c. 800°C and c. 5 kbar (Osanai *et al.* 1991; Komatsu *et al.* 1994) at c. 55 Ma (Owada *et al.* 1992). Large gabbro plutons probably enhance the thermal perturbation through advection of heat; they represent primitive basaltic rocks typical of MORB (Maeda & Kagami 1996). The $P-T$ path of the granulite facies unit of Hidaka metamorphic belt has the form of a clockwise-hairpin loop (Komatsu *et al.* 1994), similar to that within the highest-grade part of the Ryoke belt. Geochemical data from plutonic rocks, synchronicity of magmatism and metamorphism, and the likely location of the Kula-Pacific ridge along the northeast Japan part of the Asian continental margin in the Early Eocene suggest that the magmatism and metamorphism are related to ridge subduction and slab window formation.

Precambrian examples

Palaeoproterozoic evolution of the Arunta Inlier, central Australia. The Arunta Inlier is one of the largest Proterozoic terrains in Australia; it has been subjected to a protracted tectono-thermal history, the details of which have

become clear because of structural, metamorphic and isotopic studies during the last decade (e.g. Collins & Shaw 1995; Collins *et al.* 1991; Warren & Hensen 1989). During the Palaeoproterozoic, the Arunta Inlier was formed by repeated terrane accretion and orogenic activity along the southern margin of a North Australian Craton. This evolution involved four main orogenic events at c. 1880–1850 Ma, 1780–1730 Ma, 1680–1650 Ma and c. 1620–1580 Ma, respectively (Collins & Shaw 1995; Myers *et al.* 1996). In the northern part of the Arunta Inlier, two separate episodes of high- T –low- P metamorphism were partly superimposed during the first two orogenic events, but in the central part of the Arunta Inlier, high- T metamorphism was associated with the middle two orogenic events. These events represent short-lived thermal pulses of c. 10 Ma duration (Collins & Williams 1995) during which emplacement of granites was an integral part of the driving force for granulite facies metamorphism through advection of heat into the shallow crust. However, the kind of mantle perturbation that might generate such short-lived, spatially restricted thermal pulses was not specified. The recent proposal by Myers *et al.* (1996), that the Palaeoproterozoic tectonic evolution of the southern margin of the North Australian Craton can be interpreted to result from terrane accretion during convergent margin processes, implies loss of ocean basins and subduction of ridge systems. Thus, the short-lived, spatially restricted low P/T ratio metamorphism may relate to ridge subduction during accretion of crustal fragments.

Late Archean evolution of the Slave Province, Northern Canada. Tectonic models for the Slave Province are of two types: (1) those in which crustal thinning or rifting to form extensional basins generate a higher than normal geotherm so that sedimentation followed by basin inversion will drive high- T –low- P metamorphism and granite magmatism (e.g. Thompson 1989); and (2) variations of plate tectonic models in which convergent margin processes of subduction, accretion and collision drive high- T –low- P metamorphism and granite magmatism (e.g. Hoffman 1986; Fyson & Helmstaedt 1988; Kusky 1989; King *et al.* 1992; Davis *et al.* 1994). In the plate tectonic models, the western part of the Slave Province (Fig. 6) represents a microcontinent with its imbricated leading edge (Anton and Sleepy Dragon terranes) exhumed along a suture zone, and the central and eastern parts of the Slave Province represent a west-verging fold-and-thrust belt

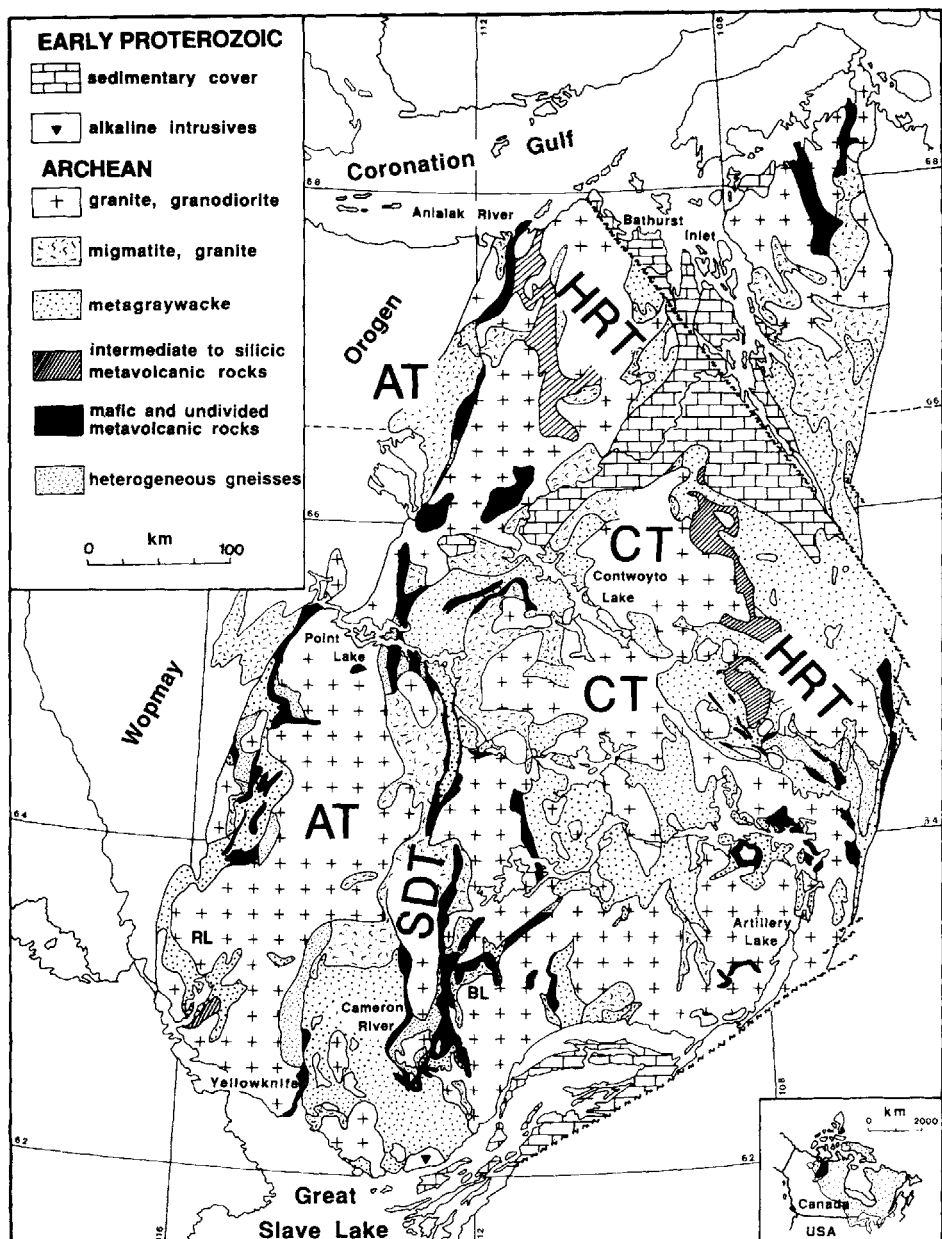


Fig. 6. Geological map of the Slave Province. AT = Anton terrane; SDT = Sleepy Dragon terrane; CT = Contwoyto terrane; HRT = Hackett River terrane. From Kusky, T.M., 1989, Accretion of the Archean Slave province, *Geology*, 17, p. 64. Modified and reproduced with permission of the publisher, The Geological Society of America, Boulder, Colorado, USA. Copyright © 1989 Geological Society of America.

(Contwoyto terrane), equivalent to an accretionary prism, and an associated magmatic arc (Hackett River terrane) formed above an east-dipping subduction zone (Kusky 1989). Three

groups of plutons emplaced at 2689–2650 Ma (both high Al_2O_3 and low Al_2O_3 trondhjemite and diorite), 2610–2600 Ma (hornblende-biotite monzodiorite to granodiorite, and

trondhjemite) and 2599–1580 Ma (muscovite-biotite granite and biotite granite) are linked to subduction-related processes before 2610 Ma and collision-related processes, including lithosphere delamination, after that (Kusky 1990; King *et al.* 1992; Davis *et al.* 1994). Qualitative P - T paths interpreted for the Contwoyto terrane in the central Superior Province are clockwise and achieve temperatures sufficient to generate anatectic migmatites at pressures not much above the aluminosilicate triple point. As King *et al.* (1992) have pointed out, traditional mechanisms for tectonic perturbations of the geotherm, such as thermal relaxation following crustal thickening and advection of heat through magma transfer and pluton construction, were probably contributing to the driving force for metamorphism. However, ridge subduction has been proposed as a component of the driving force by Kusky (1990) and inevitably must have occurred during the ocean-closure phase before collision.

The northeastern extension of the Slave Province across the Bathurst fault zone (Fig. 6) is enigmatic, in that it is composed of metasedimentary rocks that record a prograde andalusite–sillimanite-type metamorphism, leading to extensive migmatization by anatexis and massive crustally derived plutonism (Thompson 1989; Culshaw & van Breeman 1990), but its relationship to the remainder of the province is not clear. Thompson (1989) has established clockwise hairpin and looping P - T paths with increasing depth within the metasedimentary rocks, and he has related the high- T -low- P metamorphism to overthickening of a sedimentary basin and underlying thinned sialic crust. Essentially, Thompson (1989) regards the tectonic evolution of the northeastern extension of the Slave Province to be one of ensialic orogenesis. The sillimanite zone schists formed a ductile envelope into which were emplaced bodies of two-mica granite derived from an underlying anatectic migmatite level (Culshaw & van Breeman 1990). Based on U-Pb zircon dating of early tonalite–diorite plutonic complexes (*c.* 2592 Ma) and U-Pb monazite dating of late two-mica granites (*c.* 2597–2585 Ma), the evolution of the complex was rapid and took *c.* 10–15 Ma (Culshaw & van Breeman 1990). The distinctive style of metamorphic–plutonic–structural zoning recorded in this part of the Slave Province is similar to that reported by Brown & Solar (1998) for part of the Acadian belt in west-central Maine. Furthermore, the short length of the evolutionary cycle is consistent with data from other high- T -low- P metamorphic belts, such as those of the Arunta

Inlier of central Australia, the Acadian belt of eastern Canada and USA, the Abukuma and Ryoke belts of Japan and the Chugach belt of Alaska, USA. Although the tectonic setting of this displaced part of the Slave belt is uncertain, an origin in common with other low P/T ratio metamorphic belts that probably involved ridge subduction and slab window formation cannot be ruled out.

Discussion and conclusions

The impact of ridge–trench and other triple junction interactions on the development of orogenic belts is largely unappreciated. Perhaps this is not surprising, since a glance at the present pattern of plate boundaries along the western margin of the Pacific Ocean shows a complexity that will be difficult to unravel once the Pacific Ocean basin is closed and the recent history of its margins has been overprinted by collision-related processes. Ridge–trench interactions occur at the present day, as exemplified by the southern Chile triple junction and the Mendocino triple junction, and occur commonly along Pacific-type ocean margins. These interactions are required by plate tectonics and are an inevitable component of the Wilson cycle. The process of subduction of a spreading ridge system may be a major overlooked mechanism in the formation and modification of the continents.

The geological evolution of Mesozoic–Cenozoic metamorphic belts in Japan is consistent with convergent margin processes that include triple junction interactions, both ridge–trench and trench–trench interactions. Ridge–trench interactions are also identified within the Chugach–Prince William composite terrane in southern Alaska. However, the Mesozoic–Cenozoic evolution of the continental margins in the North Pacific Ocean basin has proved difficult to unravel, in part because the history of convergence along a continental margin depends critically upon knowing which oceanic plate lay adjacent to the margin, yet this is frequently the least well constrained element of any plate tectonic model. Complexity similar to the present-day Western Pacific Ocean basin appears to have been common in Earth history, well illustrated by the evolutionary history of the Appalachian orogen, but interpretation is very difficult without information from the contemporaneous ocean basins. Thus, extrapolation of plate tectonics to pre-Mesozoic Earth history is more difficult because the only evidence for interactions between oceanic plates in the

geological record is the effects of those interactions recorded in the history of the overriding continental plates. These effects may be difficult to identify if masked by overprinting collisional orogenesis. Nonetheless, this should not be used as an excuse to ignore triple junction interactions, although it may explain why such interactions are difficult to establish unambiguously.

In conclusion, ridge-trench interactions must have occurred and their effects must be recorded in pre-Mesozoic orogenic belts. Thus, identification of these interactions remains an important goal of geology. The most distinctive characteristic of triple junction interactions is an event that migrates in time, but diachroneity is not a requirement of all triple junction interactions. Ridge-trench interactions are likely to be characterized also by one or more of the following: (1) accreted units exhibit juxtaposition of rocks with a progressive decrease in the age gap between sediments and underlying basalt, reflecting the approach of zero-age lithosphere; (2) migration of magmatic provinces and their thermal manifestations; (3) systematic changes in geochemical signatures of igneous rocks, including products with slab melt components and contaminated MORB compositions; (4) low P/T ratio metamorphism; (5) abrupt changes in the kinematics of deformation at regional scales; and (6) dynamic fore-arc sedimentation that records rapid lateral migration of sedimentary sources and basins, plus vertical responses to thermal perturbations. Although diachroneity of an 'event', near-trench magmatism and low P/T ratio metamorphism together may be diagnostic of ridge-trench interactions, not all high- T -low- P metamorphic belts need be formed by these interactions. Thus, the assignment of ridge-trench interactions as the primary driving force for low P/T ratio metamorphism can normally only be made with support from other characteristic features of ridge-trench interactions. Unfortunately, such characteristic features are difficult to identify unambiguously in pre-Mesozoic orogenic belts.

M. Tagiri and T. Nakajima (Abukuma belt) and Y. Hiroi, T. Ikeda, T. Morikiyo and T. Nakajima (Ryoke belt) generously guided me to key outcrops in Japan, for which I thank them. Visits to Japan were supported by the Geological Survey of Japan and by several universities. G. Droop and P. Treloar provided constructive reviews, for which I thank them; of course, remaining infelicities are my responsibility alone. Also, I thank J. Martin for her word processing skills and patience, G. Solar for assistance in drafting Figs 1-5, and the Geological Society of America for permission to reproduce Fig. 6.

References

ABBOTT, D. & MENKE, W. 1990. Length of the global plate boundary at 2.4 Ga. *Geology*, **18**, 58-61.

AGAR, S. M., CLIFF, R. A., DUDDY, I. R. & REX, D. C. 1989. Accretion and uplift in the Shimanto belt, SW Japan. *Journal of the Geological Society, London*, **146**, 893-896.

ALLEN, T. & CHAMBERLAIN, C. P. 1989. Thermal consequences of mantled gneiss dome emplacement. *Earth and Planetary Sciences Letters*, **93**, 392-404.

AMATO, J. M., WRIGHT, J. E., GANS, P. B. & MILLER, E. L. 1994. Magmatically induced metamorphism and deformation in the Kigluaik gneiss dome, Seaward Peninsula, Alaska. *Tectonics*, **13**, 515-527.

ATWATER, T. 1989. Plate tectonic history of the northeast Pacific and western North America. In: WINTERER, E. L., HUSSONG, D. M. & DECKER, R. W. (eds) *The Geology of North America*, Vol. N, *The Eastern Pacific Ocean and Hawaii*. Geological Society of America, Boulder, Colorado, 21-72.

BARNETT, D. E., BOWMAN, J. R., PAVLIS, T. L., RUBENSTONE, J. R., SNEE, L. W. & ONSTOTT, T. C. 1994. Metamorphism and near-trench plutonism during initial accretion of the Cretaceous Alaskan forearc. *Journal of Geophysical Research*, **99**, 24007-24024.

BARTON, M. D. & HANSON, R. B. 1989. Magmatism and development of low-pressure metamorphic belts: Implications from the western United States and thermal modeling. *Geological Society of America Bulletin*, **101**, 1051-1065.

BECK, M. E. 1991. Coastwise transport reconsidered: Lateral displacements in oblique subduction zones, and tectonic consequences. *Physics of the Earth and Planetary Interiors*, **68**, 1-8.

BEHRMANN, J. H., LEWIS, S. D., CANDE, S. C. & ODP LEG 141 SCIENTIFIC PARTY 1994. Tectonics and geology of spreading ridge subduction at the Chile Triple Junction: A synthesis of results from Leg 141 of the Ocean Drilling Program. *Geologische Rundschau*, **83**, 832-852.

BRADLEY, D. C., HAEUSSLER, P. J. & KUSKY, T. M. 1993. Timing of early Tertiary ridge subduction in southern Alaska. *US Geological Survey Bulletin*, **2068**, 163-177.

BROWN, M. 1973. The definition of metatexis, diatexis and migmatite. *Proceedings of the Geologists' Association*, **84**, 371-382.

— 1993. $P-T-t$ evolution of orogenic belts and the causes of regional metamorphism. *Journal of the Geological Society, London*, **150**, 227-241.

— 1995a. Late-Precambrian geodynamic evolution of the Armorican Segment of the Cadomian Belt (France): Distortion of an active continental margin during south-west directed convergence and subduction of a bathymetric high. *Géologie de la France*, **3**, 3-22.

— 1995b. Ridge-trench interactions as the cause of low- P metamorphism: Evidence from the Ryoke Belt, Japan and comparison with other belts.

Geological Society of America Annual Meeting, New Orleans, Louisiana, Abstracts with Programs, 27, A-316.

— 1998. Unpairing metamorphic belts: $P-T$ paths and a tectonic model for the Ryoke Belt, southwest Japan. *Journal of Metamorphic Geology*, **15**, 3–22.

— & NAKAJIMA, T. 1994. High T –low- P metamorphism in the Ryoke belt of Japan: Consequence of ridge subduction. *Geological Society of America Annual Meeting, Seattle, Washington, Abstract with programs, 26(6)*, A-214.

— & O'BRIEN, P. J. 1997. Evolution of metamorphic belts: A changing view. *Proceedings of the 30th International Geological Congress, 17*, 217–231.

— & SOLAR, G. S. 1998. Shear zone systems and melts: feedback relations and self-organization in orogenic belts. *Journal of Structural Geology*, **20**, 211–227.

— & TRELOAR, P. J. 1992. Radiogenic heating of overthickened basins and magmatic advection: Modelling high- T metamorphism and origin of low- P metamorphic belts. *GAC-MAC Joint Annual Meeting, Wolfville, Canada, 17*, A12-A13.

BYRNE, T. & DiTULLIO, L. 1992. Evidence for changing plate motions in southwest Japan and reconstructions of the Philippine Sea plate. *The Island Arc*, **1**, 148–165.

CHAMBERLAIN, C. P. & RUMBLE, D. 1988. Thermal anomalies in a regional metamorphic terrain: An isotopic study of the role of fluids. *Journal of Petrology*, **29**, 1215–1232.

— & SONDER, L. J. 1990. Heat-producing elements and the thermal and baric patterns of metamorphic belts. *Science*, **250**, 763–769.

CLOOS, M. 1993. Lithospheric buoyancy and collisional orogenesis: Subduction of oceanic plateaus, continental margins, island arcs, spreading ridges, and seamounts. *Geological Society of America Bulletin*, **105**, 715–737.

COLLINS, W. J. & SHAW, R. D. 1995. Geochronological constraints on orogenic events in the Arunta Inlier: A review. *Precambrian Research*, **71**, 315–346.

— & VERNON, R. H. 1991. Orogeny associated with anticlockwise $P-T-t$ paths: Evidence from low- P , high- T metamorphic terranes in the Arunta Inlier, central Australia. *Geology*, **19**, 835–838.

— & — 1993. How well established is isobaric cooling in Proterozoic orogenic belts? An example from the Arunta Inlier, central Australia – comment. *Geology*, **21**, 953–954.

— & — 1994. A rift–drift–delamination model of continental evolution: Palaeozoic tectonic development of eastern Australia. *Tectonophysics*, **235**, 249–275.

— & WILLIAMS, I. S. 1995. SHRIMP ion probe dating of short-lived Proterozoic tectonic cycles in the Northern Arunta Inlier, Central Australia. *Precambrian Research*, **71**, 69–89.

—, VERNON, R. H. & CLARK, G. L. 1991. Discrete Proterozoic structural terranes associated with low- P , high- T metamorphism, Anmatjira Range, Arunta Inlier, central Australia: Tectonic implications. *Journal of Structural Geology*, **13**, 1157–1171.

COX, A., DEBICHE, M. G. & ENGBRETSON, D. C. 1989. Terrane trajectories and plate interactions along continental margins in the north Pacific basin. In: BEN-AVRAHAM, Z. (ed.) *The Evolution of the Pacific Ocean Margins*. Oxford University Press, New York, 20–35.

CRONIN, V. S. 1992. Types and kinematic stability of triple junctions. *Tectonophysics*, **207**, 287–301.

CULSHAW, N. & VAN BREEMAN, O. 1990. A zoned low P –high T complex at the level of anatexis – structural and plutonic patterns in metasediments of the Archean Yellowknife Super Group, near Bathurst Inlet, N.W.T., Canada. *Precambrian Research*, **48**, 1–20.

DALLMEYER, R. D. & TAKASU, A. 1991. Middle Paleocene terrane juxtaposition along the Median Tectonic Line, southwest Japan: Evidence from ^{40}Ar – ^{39}Ar mineral ages. *Tectonophysics*, **200**, 281–297.

DALZIEL, I. W. D. 1997. Neoproterozoic-Paleozoic geography and tectonics: review, hypothesis, environmental speculation. *Geological Society of America Bulletin*, **109**, 16–42.

DANIEL, A. J., KUSZNIR, N. J. & STYLES, P. 1995. A temperature and gravity model of spreading-centre subduction, with application to southern Chile. In: GROCOTT, J., PETFORD, N. & TRELOAR, P. J. (eds) *Current Geosciences Research in the Andes: Abstracts*. Kingston University, UK, 8.

DAVIS, W. J., FRYER, B. J. & KING, J. E. 1994. Geochemistry and evolution of late Archean plutonism and its significance to the tectonic development of the Slave Craton. *Precambrian Research*, **67**, 207–241.

DELONG, S. E. & FOX, P. J. 1977. Geological consequences of ridge subduction. In: TALWANI, M. & PITMAN, W. C. (eds) *Island Arcs, Deep Sea Trenches, and Back-arc Basins*. American Geophysical Union, Morris Ewing Series, **1**, 221–228.

—, — & McDOWELL, F. W. 1978. Subduction of the Kula Ridge at the Aleutian Trench. *Geological Society of America Bulletin*, **89**, 83–95.

—, SCHWARZ, W. M. & ANDERSON, R. N. 1979. Thermal effects of ridge subduction. *Earth and Planetary Science Letters*, **44**, 239–246.

DEMPSTER, T. J. & BLUCK, B. J. 1995. Regional metamorphism in transform zones during supercontinent breakup: Late Proterozoic events of the Scottish Highlands. *Geology*, **23**, 991–994.

DE YOREO, J. J., LUX, D. R. & GUIDOTTI, C. V. 1989a. The role of crustal anatexis and magma migration in regions of thickened continental crust. In: DALY, J. S., CLIFF, R. A. & YARDLEY, B. W. D. (eds) *Evolution of Metamorphic Belts*. Geological Society Special Publication, **43**, 187–202.

—, —, —, DECKER, E. R. & OSBERG, P. H. 1989b. The Acadian thermal history of western Maine. *Journal of Metamorphic Geology*, **7**, 169–190.

—, — & — 1991. Thermal modelling in low-pressure/high-temperature metamorphic belts. *Tectonophysics*, **188**, 209–238.

DICKINSON, W. R. & SNYDER, W. S. 1979. Geometry of subducted slabs related to San Andreas transform. *Journal of Geology*, **87**, 609–627.

DIRKS, P. H. G. M., HAND, M., COLLINS, W. J. & OFFLER, R. 1992. Structural–metamorphic evolution of the Tia Complex, New England fold belt; thermal overprint of an accretion subduction complex in a compressional back-arc setting. *Journal of Structural Geology*, **14**, 669–688.

DROOP, G. T. R. & AL-FILALI, I. Y. 1989. Magmatism, deformation and high-*T*, low-*P* regional metamorphism in the Nabihah mobile belt, southern Arabian Shield. In: DALY, J. S., CLIFF, R. A. & YARDLEY, B. W. D. (eds) *Evolution of Metamorphic Belts*. Geological Society Special Publication, **43**, 469–480.

ELLIS, M. & WATKINSON, A. J. 1987. Orogen-parallel extension and oblique tectonics, the relation between stretching lineations and relative plate motions. *Geology*, **15**, 1022–1026.

ELLIS, S., FULLSACK, P. & BEAUMONT, C. 1995. Oblique convergence of the crust driven by basal forcing: Implications for length-scales of deformation and strain partitioning in orogens. *Geophysical Journal International*, **120**, 24–44.

ENGEBRETSON, D. C., COX, A. & GORDON, R. G. 1985. *Relative motions between oceanic and continental plates in the Pacific Basin*. Geological Society of America Special Paper, **206**.

ENGLAND, P. & MOLNAR, P. 1993. The interpretation of inverted metamorphic isograds using simple physical calculations. *Tectonics*, **12**, 145–157.

FARRAR, E. & DIXON, J. M. 1993. Ridge subduction: Kinematics and implications for the nature of mantle upwelling. *Canadian Journal of Earth Sciences*, **30**, 893–907.

FAURE, M., LALEVÉE, F., GUSOKUJIMA, Y., ITAYAMA, J. T. & CADET, J.-P. 1986. The pre-Cretaceous deep-seated tectonics of the Abukuma massif and its place in the structural framework of Japan. *Earth and Planetary Science Letters*, **77**, 384–398.

FINN, C. 1994. Aeromagnetic evidence for a buried Early Cretaceous magmatic arc, northeast Japan. *Journal of Geophysical Research*, **99**, 22 165–22 185.

—, KIMURA, G. & SUYEHIRO, K. 1994. Introduction to the Special Section Northeast Japan: A case history of subduction. *Journal of Geophysical Research*, **99**, 22 137–22 145.

FORSYTHE, R. D. & NELSON, E. P. 1985. Geological manifestations of ridge collision: Evidence from the Golfo de Peñas–Taitao Basin, southern Chile. *Tectonics*, **4**, 477–495.

— & PRIOR, D. J. 1992. Cenozoic continental geology of South America and its relations to the evolution of the Chile Triple Junction. In: BEHRMANN, J. H. et al. (eds) *Proceedings of the Ocean Drilling Program, Initial Results*. College Station Texas Ocean Drilling Program, **141**, 23–31.

FUJIMAKI, H., MIYAJIMA, S. & AOKI, K. 1991. Rb-Sr chronological study of the Miyamoto composite mass, southern Abukuma, Fukushima prefecture, northeast Japan. *Journal of Mineralogy, Petrology and Economic Geology*, **86**, 216–225.

FYSON, W. K. & HELMSTAEDT, H. 1988. Structural patterns and tectonic evolution of supracrustal domains in the Archean Slave Province, Canada. *Canadian Journal of Earth Science*, **25**, 301–315.

GOES, S., GOVERS, R., SCHWARTZ, S. & FURLONG, K. 1997. 3-Dimensional thermal modeling for the Mendocino triple junction area. *Earth and Planetary Science Letters*, **148**, 45–57.

GOTO, J. 1990. On the relationship between the Gosaisyo and Takanuki metamorphic rocks in the Abukuma terrane, with special reference to the textural and compositional characteristic of garnet in pelitic rocks. *Journal of Mineralogy, Petrology and Economic Geology*, **85**, 193.

GRAHAM, C. M. & ENGLAND, P. C. 1976. Thermal regimes and regional metamorphism in the vicinity of overthrust faults: An example of shear heating and inverted metamorphic zonation from southern California. *Earth and Planetary Science Letters*, **31**, 142–152.

GRAMBLING, J. A. 1986. Crustal thickening during Proterozoic metamorphism and deformation in New Mexico. *Geology*, **14**, 149–152.

— & DALLMEYER, R. D. 1993. Tectonic evolution of Proterozoic rocks in the Cimarron Mountains, northern New Mexico, USA. *Journal of Metamorphic Geology*, **11**, 739–755.

—, WILLIAMS, M. L., SMITH, R. F. & MAWER, C. K. 1989. The role of crustal extension in the metamorphism of Proterozoic rocks in northern New Mexico. In: GRAMBLING, J. A. & TEWKSBURY, B. J. (eds) *Proterozoic Geology of the Southern Rocky Mountains*. Geological Society of America Special Paper **235**, 87–110.

HAEUSLER, P. J., BRADLEY, D., GOLDFARB, R., SNEE, L. & TAYLOR, C. 1995. Link between ridge subduction and gold mineralization in southern Alaska. *Geology*, **23**, 995–998.

HAMMARSTROM, J. E. & ZEN, E-AN 1986. Aluminum in hornblende: An empirical igneous geobarometer. *American Mineralogist*, **71**, 1297–1313.

HAND, M., DIRKS, P. H. G. M., POWELL, R. & BUICK, I. S. 1992. How well established is isobaric cooling in Proterozoic orogenic belts? An example from the Arunta Inlier, central Australia. *Geology*, **20**, 649–652.

—, —, — & — 1993. How well established is isobaric cooling in Proterozoic orogenic belts? An example from the Arunta Inlier, central Australia – reply. *Geology*, **21**, 954–955.

HARRIS, N. R., SISSON, V. B., WRIGHT, J. E. & PAVLIS, T. L. 1996. Evidence for Eocene mafic underplating during fore-arc intrusive activity, eastern Chugach Mountains, Alaska. *Geology*, **24**, 263–266.

HARRISON, T. M., DUNCAN, I. & McDougall, I. 1985. Diffusion of ^{40}Ar in biotite: Temperature, pressure and composition effects. *Geochimica et Cosmochimica Acta*, **49**, 2461–2468.

HAYAMA, Y. 1964. Progressive metamorphism of pelitic and psammitic rocks in the Komagane district, central Japan. *Journal of the Faculty of Science, University of Tokyo, Section II*, **15**, 321–369.

-- & YAMADA, T. 1977. II. Ryoke metamorphic belt in the Komagane-Kashio district. In: Geological Survey of Japan, *Mesozoic felsic activity and related metamorphism in central Japan from Nagoya to Toyama*, 7–32.

HIBBARD, J. P. & KARIG, D. E. 1990. Structural and magmatic responses to spreading ridge subduction: An example from southwest Japan. *Tectonics*, **9**, 207–230.

HIGASHIMOTO, S., NUREKI, T., HARA, I., TSUKUDA, E. & NAKAJIMA, T. 1983. *Geology of the Iwakuni District*. Quadrangle Series, Scale 1:50,000, Geological Survey of Japan.

HILDE, T. W. C., UYEDA, S. & KROENKE, L. 1977. Evolution of the western Pacific and its margin. *Tectonophysics*, **38**, 145–165.

HIROI, Y. 1990. High-pressure and low-pressure mineral assemblages at the same outcrop near Yokokawa, Abukuma metamorphic terrane, Japan – evidence for unique metamorphic evolution. *Journal of Mineralogy, Petrology and Economic Geology*, **85**, 207–222.

-- & KISHI, S. 1989a. Staurolite and kyanite in the Takanuki pelitic gneisses of the Abukuma metamorphic terrane, northeast Japan. *Journal of Mineralogy, Petrology and Economic Geology*, **84**, 141–151.

-- & -- 1989b. P-T evolution of Abukuma metamorphic rocks in north-east Japan: Metamorphic evidence for oceanic crust obduction. In: DALY, J. S., CLIFF, R. A. & YARDLEY, B. W. D. (eds) *Evolution of Metamorphic Belts*. Geological Society Special Publication, **43**, 481–486.

--, NOHARA, T., SATO, K. & GOTO, J. 1998. Cretaceous high-temperature quick loading and unloading in the Abukuma metamorphic terrane, Japan. *Journal of Metamorphic Geology*, **16**, 67–81.

--, YOKOSE, M., OBA, T., KISHI, S., NOHARA, T. & YAO, A. 1987. Discovery of Jurassic radiolaria from ackmite-rhodonite-bearing metachert of the Gosaisyo metamorphic rocks in the Abukuma terrane, northeastern Japan. *Journal of the Geological Society of Japan*, **93**, 445–448.

HOFFMAN, P. F. 1986. Crustal accretion in a 2.7–2.5 Ga “granite-greenstone” terrane, Slave Province, N.W.T.: A prograde in arc-trench system? In: DE WITT, M. J. & ASHWALL, L. D. (eds) *Tectonic Evolution of Greenstone Belts*. Lunar and Planetary Institute Report, **86-10**, 120.

HOLE, M. J. & LARTER, R. D. 1993. Trench-proximal volcanism following ridge crest-trench collision along the Antarctic Peninsular. *Tectonics*, **12**, 897–910.

HUDSON, T. 1979. Mesozoic plutonic belts of southern Alaska. *Geology*, **7**, 230–234.

-- & PLAFKER, G. 1982. Paleogene metamorphism of an accretionary flysch terrane, eastern Gulf of Alaska. *Geological Society of America Bulletin*, **93**, 128–1290.

--, -- & PETERMAN, Z. E. 1979. Paleogene anatexis along the Gulf of Alaska margin. *Geology*, **7**, 573–577.

IKEDA, T. 1991. Heterogeneous biotite from Ryoke metamorphic rocks in the Yanai District, southwest Japan. *Journal of the Geological Society of Japan*, **97**, 537–547.

-- 1993. Compositional zoning patterns of garnet during prograde metamorphism from the Yanai District, Ryoke metamorphic belt, southwest Japan. *Lithos*, **30**, 109–121.

-- 1998. Progressive sequence of reactions of the Ryoke metamorphism in the Yanai District, southwest Japan: The formation of cordierite. *Journal of Metamorphic Geology*, **16**, 39–52.

ISHIKAWA, M. & OTSUKI, K. 1990. Fold structures and left-lateral ductile shear in the Gosaisho metamorphic belt, northeast Japan. *Journal of the Geological Society of Japan*, **96**, 719–730.

ISOZAKI, Y. & ITAYA, T. 1990. Chronology of Sambagawa metamorphism. *Journal of Metamorphic Geology*, **8**, 401–411.

ITAYA, T. & TAKASUGI, H. 1988. Muscovite K-Ar ages of the Sambagawa schists, Japan and argon depletion during cooling and deformation. *Contributions to Mineralogy and Petrology*, **100**, 281–290.

JAMES, T. S., HOLLISTER, L. S. & MORGAN, W. J. 1989. Thermal modelling of the Chugach metamorphic complex. *Journal of Geophysical Research*, **94**, 4411–4423.

JARRARD, R. D. 1986. Terrane motion by strike-slip faulting of forearc slivers. *Geology*, **14**, 780–783.

JAUPART, C. & PROVOST, A. 1985. Heat focusing, granite genesis and inverted metamorphic gradients in continental collision zones. *Earth and Planetary Science Letters*, **73**, 385–397.

JONES, D. L., HOWELL, D. G., CONEY, P. J. & MONGER, J. W. H. 1983. Recognition, character, and analysis of tectonostratigraphic terranes in western North America. In: HASHIMOTO, M. & UYEDA, S. (eds) *Accretion Tectonics in the Circum-Pacific Regions*. Terra Scientific Publishing, Tokyo, 21–35.

KAEDING, M., FORSYTHE, R. D. & NELSON, E. P. 1990. Geochemistry of the Taitao ophiolite and near-trench intrusions from the Chile margin triple junction. *Journal of South American Earth Sciences*, **3**, 161–177.

KAGAMI, H., IZUMI, S., TAINOSHIO, Y. & OWADA, M. 1992. Spatial variations of Sr and Nd isotope ratios of Cretaceous–Paleogene granitoid rocks, southwest Japan arc. *Contributions to Mineralogy and Petrology*, **112**, 165–177.

KAMP, P. J. J. & TAKEMURA, K. 1993. Thermo-tectonic history of Ryoke basement in Hohi volcanic zone, northeast Kyushu, Japan: Constraints from fission track thermochronology. *The Island Arc*, **2**, 213–227.

KANO, H. & KURODA, Y. 1968. On the occurrence of staurolite and kyanite from the Abukuma Plateau, northeastern Japan. *Proceedings of the Japan Academy*, **44**, 77–82.

-- & -- 1973. On the chemistry of coexisting garnet and biotite in pelitic-psammitic metamorphic rocks, central Abukuma, Japan. *Journal of the Geological Society of Japan*, **79**, 621–641.

KAY, S. M., RAMOS, V. A. & MARQUEZ, M. 1993. Evidence in Cerro Pampa volcanic rocks for slab-melting prior to ridge-trench collision in southern South America. *Journal of Geology*, **101**, 703–714.

KIMBROUGH, D. L., HERZIG, C. T., WATANABE, T., ARITA, K., KURIYA, M., KAGAMI, H., HAYASAKA, Y. & TAINOSHIO, Y. 1994. Uranium-lead dating of ophiolite, granitoid and high-grade metamorphic rocks, Japan. In: *From Paleoasian Ocean to Paleo-Pacific Ocean, Hokkaido University*, 48–51.

KIMURA, G. 1994. The latest Cretaceous–early Paleogene rapid growth of accretionary complex and exhumation of high pressure series metamorphic rocks in Northwestern Pacific Margin. *Journal of Geophysical Research*, **99**, 22 147–22 164.

KING, J. E., DAVIS, W. J. & RELF, C. 1992. Late Archean tectono-magmatic evolution of the central Slave Province, Northwest Territories. *Canadian Journal of Earth Science*, **29**, 2156–2170.

KINOSHITA, O. 1995. Migration of igneous activities related to ridge subduction in Southwest Japan and the east Asian continental margin from the Mesozoic to the Paleogene. *Tectonophysics*, **245**, 25–35.

— & ITO, H. 1986. Migration of Cretaceous igneous activity in southwest Japan. *Journal of the Geological Society of Japan*, **92**, 732–735 (in Japanese with English abstract).

KISHI, S. 1987. On the metamorphism of granulite facies rocks of the Kaidomari-Hanazono District, southern Abukuma Mountains. *Journal of the Japanese Association of Mineralogists, Petrologists and Economic Geologists*, **82**, 156.

KOMATSU, M., TOYOSHIMA, T., OSANAI, Y. & ARAI, M. 1994. Prograde and anatetic reactions in the deep arc crust exposed in the Hidaka metamorphic belt, Hokkaido, Japan. *Lithos*, **33**, 31–49.

KOSHIYA, S. 1986. Tanakura shear zone: The deformation process of fault rocks and its kinematics. *Journal of the Geological Society of Japan*, **92**, 15–29.

— 1988. C-axis fabrics of quartz and microstructures in mylonite: Application to the Hatakawa shear zone, northeast Japan. *Structural Geology*, **33**, 13–32.

KUBO, K. & YAMAMOTO, T. 1990. Cretaceous intrusive rocks of the Haramachi District, eastern margin of the Abukuma Mountains. *Journal of the Geological Society of Japan*, **96**, 731–734.

KUSKY, T. M. 1989. Accretion of the Archean Slave Province. *Geology*, **17**, 63–67.

— 1990. Evidence for Archean ocean opening and closing in the southern Slave Province. *Tectonics*, **9**, 1533–1563.

LARTER, R. D. & BAKER, P. S. 1991. Effects of ridge crest-trench interaction on Antarctic–Phoenix spreading: Forces on a young subducting plate. *Journal of Geophysical Research*, **96**, 19 583–19 607.

LIU, M. & FURLONG, K. P. 1992. Cenozoic volcanism in the California Coast Ranges: Numerical solutions. *Journal of Geophysical Research*, **97**, 4941–4951.

LOOSVELD, R. J. H. & ETHERIDGE, M. A. 1990. A model for low-pressure facies metamorphism during crustal thickening. *Journal of Metamorphic Geology*, **8**, 257–267.

LUX, D. R., DE YOREO, J. J., GUIDOTTI, C. V. & DECKER, E. R. 1986. Role of plutonism in low-pressure metamorphic belt formation. *Nature*, **323**, 794–797.

LUYENDYK, B. P. 1995. Hypothesis for Cretaceous rifting of east Gondwana caused by subducted slab capture. *Geology*, **23**, 373–376.

LYTWIN, J., CASEY, J., GILBERT, S. & KUSKY, T. 1997. Arc-like mid-ocean ridge basalt formed seaward of a trench-forearc system just prior to ridge subduction: An example from subaccreted ophiolites in southern Alaska. *Journal of Geophysical Research*, **102**, 10 225–10 243.

MCCAFFREY, R. 1996. Estimates of modern arc-parallel strain rates in fore arcs. *Geology*, **24**, 27–30.

MCKENZIE, D. P. & MORGAN, W. J. 1969. The evolution of triple junctions. *Nature*, **224**, 125–133.

MAC NIOMAID, C., VAN DER PLUIJM, B. A. & VAN DER VOOR, R. 1997. Ordovician paleogeography and the evolution of the Iapetus ocean. *Geology*, **25**, 159–162.

MAEDA, J. & KAGAMI, H. 1996. Interaction of a spreading ridge and an accretionary prism: Implications from MORB magmatism in the Hidaka magmatic zone, Hokkaido, Japan. *Geology*, **24**, 31–34.

MARSHAK, R. S. & KARIG, D. E. 1977. Triple junctions as a cause for anomalously near-trench igneous activity between the trench and volcanic arc. *Geology*, **5**, 233–236.

MARUYAMA, T. 1970. Geology and structure of the Samegawa-Ishikawa District, Abukuma Plateau with special reference to the structure of the older-type granitic rocks, part 1. *Journal of the Geological Society of Japan*, **76**, 355–366.

MIDGLEY, J. P. & BLUNDELL, D. J. 1997. Deep seismic structure and thermo-mechanical modelling of continental collision zones. *Tectonophysics*, **273**, 155–167.

MILDREN, S. D. & SANDIFORD, M. 1995. Heat refraction and low-pressure metamorphism in the northern Flinders Ranges, South Australia. *Australian Journal of Earth Sciences*, **42**, 241–247.

MIYASHIRO, A. 1958. Regional metamorphism of the Gosaisyo-Takanuki District in the Central Abukuma Plateau. *Journal of the Faculty of Science, University of Tokyo, Section II*, **11**, 219–272.

— 1959. Abukuma, Ryoke and Sambagawa metamorphic belts. *Journal of the Geological Society of Japan*, **65**, 624–637.

— 1961. Evolution of metamorphic belts. *Journal of Petrology*, **2**, 277–311.

MOLNAR, P. & ENGLAND, P. 1995. Temperatures in zones of steady-state underthrusting of young oceanic lithosphere. *Earth and Planetary Science Letters*, **131**, 57–70.

MORIKIYO, T. 1984. Carbon isotopic study on coexisting calcite and graphite in the Ryoke metamorphic rocks, northern Kiso District, central Japan. *Contributions to Mineralogy and Petrology*, **87**, 251–259.

— 1986. Hydrogen and carbon isotope studies on the graphite-bearing metapelites in the northern Kiso District of central Japan. *Contributions to Mineralogy and Petrology*, **94**, 165–177.

MURDIE, R. E., PRIOR, D. J., STYLES, P., FLINT, S. S., PEARCE, R. G. & AGAR, S. M. 1993. Seismic responses to ridge-transform subduction: Chile Triple Junction. *Geology*, **21**, 1095–1098.

MYERS, J. S., SHAW, R. D. & TYLER, I. M. 1996. Tectonic evolution of Proterozoic Australia. *Tectonics*, **15**, 1431–1446.

NAKAI, Y. & SUZUKI, K. 1996. CHIME monazite ages of the Kamihara Tonalite and the Tenryukyo granodiorite in the eastern Ryoke Belt of central Japan. *Journal of the Geological Society of Japan*, **102**, 431–439.

NAKAJIMA, T. 1994. The Ryoke plutonometamorphic belt: Crustal section of the Cretaceous Eurasian continental margin. *Lithos*, **33**, 51–66.

— 1996. Cretaceous granitoids in SW Japan and their bearing on the crust-forming process in the eastern Eurasian margin. *Transactions of the Royal Society of Edinburgh: Earth Sciences*, **87**, 183–191.

—, SHIRAHASE, T. & SHIBATA, K. 1990. Along-arc variation of Rb-Sr ages of Cretaceous granitic rocks in southwest Japan. *Contributions to Mineralogy and Petrology*, **104**, 381–389.

NELSON, E. P. & FORSYTHE, R. D. 1989. Ridge collision at convergent margins: Implications for Archean and post-Archean crustal growth. *Tectonophysics*, **161**, 307–315.

—, — & ARIT, I. 1994. Ridge collision tectonics in terrane development. *Journal of South American Earth Sciences*, **7**, 271–278.

NOHARA, T. & HIROI, Y. 1989. On the original rocks of the Gosaisyo metabasites, Abukuma terrane – with special reference to their major, trace and rare earth element chemistry. *Journal of Mineralogy, Petrology and Economic Geology*, **84**, 118.

NUR, A. & BEN-AVRAHAM, Z. 1983. Break-up and accretion tectonics. In: HASHIMOTO, M. & UYEDA, S. (eds) *Accretion Tectonics in the Circum-Pacific Regions*. Terra Scientific Publishing, Tokyo, 3–18.

NUREKI, T. 1960. Structural investigation of the Ryoke metamorphic rocks of the area between Iwakuni and Yanai, southern Japan. *Journal of Science of the Hiroshima University, Series 3*, **1**, 69–141.

OKUDAIRA, T. 1996a. Temperature-time path for the low-pressure Ryoke metamorphism, Japan, based on chemical zoning and garnet. *Journal of Metamorphic Geology*, **14**, 427–440.

— 1996b. A thermal model for the Ryoke Belt, southwest Japan. *The Island Arc*, **5**, 373–385.

—, HARA, I., SAKURAI, Y. & HAYASAKA, Y. 1993. Tectono-metamorphic processes of the Ryoke belt in the Iwakuni-Yanai District, southwest Japan. *Memoirs of the Geological Society of Japan*, **42**, 91–120.

—, — & TAKESHITA, T. 1995. Emplacement mechanism of the Older Ryoke Granites in the Yanai District, southwest Japan, with special reference to extensional deformation in the Ryoke metamorphic belt. *Journal of Science of the Hiroshima University, C*, **10**, 357–366.

ONISHI, C. T. & KIMURA, G. 1995. Change in fabric of melange in the Shimanto Belt, Japan: Change in relative convergence? *Tectonics*, **14**, 1273–1289.

ONO, A. 1969. Zoning of the metamorphic rocks in the Takato-Sioziri Area, Nagano Prefecture. *Journal of the Geological Society of Japan*, **75**, 521–536.

OSANAI, Y., KOMATSU, M. & OWADA, M. 1991. Metamorphism and granite genesis in the Hidaka metamorphic belt, Hokkaido, Japan. *Journal of Metamorphic Geology*, **9**, 111–124.

OSOZAWA, S. 1992. Double ridge subduction recorded in the Shimanto accretionary complex, Japan, and plate reconstruction. *Geology*, **20**, 939–942.

— 1994. Plate reconstruction based upon age data of Japanese accretionary complexes. *Geology*, **22**, 1135–1138.

OTSUKI, K. 1992. Oblique subduction, collision of microcontinents and subduction of oceanic ridge: Their implications on the Cretaceous tectonics of Japan. *The Island Arc*, **1**, 51–63.

OWADA, M., OSANAI, Y. & KAGAMI, H. 1992. Generation of granitic magma in the deeper crust and its timing: An example in the Hidaka metamorphic belt. *Chikyu Monthly*, **14**, 291–296.

PAVLIS, T. L. & SISSON, V. B. 1995. Structural history of the Chugach metamorphic complex in the Tana River region, eastern Alaska: A record of Eocene ridge subduction. *Geological Society of America Bulletin*, **107**, 1333–1355.

—, UNDERWOOD, M., SISSON, V. B., SERPA, L. A., PRIOR, D., MARSAGLIA, K. M., LEWIS, S. D. & BYRNE, T. 1995. The effects of triple junction interactions at convergent plate margins. *Report on the Results of the Joint JOI/USSAC and GSA Penrose Conference*.

PICKERING, K. T. & SMITH, A. G. 1995. Arcs and backarc basins in the Early Paleozoic Iapetus Ocean. *The Island Arc*, **4**, 1–67.

PLATT, J. P. 1975. Metamorphic and deformational processes in the Franciscan complex, California: Some insights from the Catalina schist terrane. *Geological Society of America Bulletin*, **86**, 1337–1347.

RAMOS, V. A. & KAY, S. M. 1992. Southern Patagonian plateau basalts and deformation: Back arc testimony of ridge collisions. *Tectonophysics*, **205**, 261–282.

RYOKE RESEARCH GROUP 1972. The mutual relations of the granitic rocks of the Ryoke Metamorphic Belt in central Japan. *Earth Science (Chikyu Kagaku)*, **26**, 205–216.

SAITO, Y. & HASHIMOTO, M. 1982. South Kitakami region: An allochthonous terrane in Japan. *Journal of Geophysical Research*, **87**, 3691–3696.

SAKAGUCHI, A. 1996. High paleogeothermal gradient with ridge subduction beneath the Cretaceous Shimanto accretionary prism, southwest Japan. *Geology*, **24**, 795–798.

SANDIFORD, M. & POWELL, R. 1986. Deep crustal metamorphism during continental extension;

modern and ancient examples. *Earth and Planetary Science Letters*, **79**, 151–158.

—, MARTIN, N., ZHOU, S. & FRASER, G. 1991. Mechanical consequences of granite emplacement during high-T, low-P metamorphism and the origin of "anticlockwise" PT paths. *Earth and Planetary Science Letters*, **107**, 164–172.

—, FRAZIER, G., ARNOLD, J., FODEN, J. & FARROW, T. 1995. Some causes and consequences of high-temperature, low-pressure metamorphism in the eastern Mt Lofty Ranges, South Australia. *Australian Journal of Earth Sciences*, **42**, 233–240.

SASADA, M. 1988. Onikobe-Yuzawa mylonite zone. *Earth Science (Chikyu Kagaku)*, **42**, 346–353.

SCHERMER, E. R., HOWELL, D. G. & JONES, D. L. 1984. The origin of allochthonous terranes: Perspectives on the growth and shaping of continents. *Annual Reviews of Earth and Planetary Science*, **12**, 107–131.

SCHMIDT, M. W. 1992. Amphibole composition in tonalite as a function of pressure: An experimental calibration of the Al-in-hornblende barometer. *Contributions to Mineralogy and Petrology*, **110**, 304–310.

SENGÖR, A. M. C. 1991. Plate tectonics and orogenic research after 25 years: Synopsis of a Tethyan perspective. *Tectonophysics*, **187**, 315–344.

SEO, T., YOKOYAMA, S. & HARA, I. 1981. Metamorphism and tectonism of the Ryoke metamorphic belt. In: HARA, I. (ed.) *Tectonics of Paired Metamorphic Belts*. Hiroshima University Press, 65–72.

SHIBATA, K. 1968. K-Ar determinations on granitic and metamorphic rocks in Japan. *Bulletin of the Geological Survey of Japan*, **227**, 1–73.

—, — & MIZUTANI, S. 1980. Isotopic ages of siliceous shale from Hida-Kanayama, central Japan. *Geochimical Journal*, **14**, 235–241.

—, — & TAKAGI, H. 1989. Tectonic relationship between the Median Tectonic Line and the Tanakura Tectonic Line view from isotopic ages and Sr isotopes of granitic rocks. *Journal of the Geological Society of Japan*, **95**, 687–700.

—, — & TANAKA, T. 1987. Age of formation for the Ishikawa composite mass, Abukuma Mountains, inferred from Nd and Sr isotopic systematics. *Journal of the Japanese Association of Mineralogists, Petrologists and Economic Geologists*, **82**, 433–440.

—, — & UCHIUMI, S. 1983. K-Ar ages on hornblendes from granitic rocks in the southern Abukuma Plateau. *Journal of the Japanese Association of Mineralogists, Petrologists and Economic Geologists*, **78**, 405–410.

SHIDŌ, F. 1958. Plutonic and metamorphic rocks of the Nakoso and Iritono Districts in the Central Abukuma Plateau. *Journal of the Faculty of Science, University of Tokyo, Section II*, **11**, 131–217.

SISSON, V. B. & HOLLISTER, L. S. 1988. Low-pressure facies metamorphism in an accretionary sedimentary prism, southern Alaska. *Geology*, **16**, 358–361.

—, — & PAVLIS, T. L. 1993. Geologic consequences of plate reorganization: A example from the Eocene southern Alaska forearc. *Geology*, **21**, 913–916.

—, —, HOLLISTER, L. S. & ONSTOTT, T. C. 1989. Petrologic and age constraints on the origin of a low-pressure/high-temperature metamorphic complex, southern Alaska. *Journal of Geophysical Research*, **94**, 4392–4410.

—, —, PAVLIS, T. L. & PRIOR, D. J. 1994. Effects of triple junction interactions at convergent plate margins. *GSA Today*, **4**, 248–249.

SOULA, J. C., DEBAT, P., DERAMOND, J. & POUGET, P. 1986. A dynamic model of the structural evolution of the Hercynian Pyrenees. *Tectonophysics*, **129**, 29–51.

STOCK, J. N. & LEE, J. 1994. Do microplates in subduction zones leave a geological record? *Tectonics*, **13**, 1472–1487.

STÜWE, K. & SANDIFORD, M. 1994. Contribution of deviatoric stresses to metamorphic P-T paths: An example appropriate to low-P, high-T metamorphism. *Journal of Metamorphic Geology*, **12**, 445–454.

—, — & — 1995. A description of metamorphic P-T paths with implications for low-P high-T metamorphism. *Physics of the Earth and Planetary Interiors*, **88**, 211–221.

—, — & POWELL, R. 1993. Episodic metamorphism and deformation in low-pressure, high-temperature terranes. *Geology*, **21**, 829–832.

SUZUKI, K. & ADACHI, M. 1998. Uplift history of the high T/P Ryoke metamorphic belt, southwest Japan: Constraints from CHIME monazite ages of gneisses and granitoids. *Journal of Metamorphic Geology*, **16**, 22–37.

—, — & KAJIZUKA, I. 1994. Electron microprobe observations of Pb diffusion in metamorphosed detrital monazites. *Earth and Planetary Science Letters*, **128**, 391–405.

—, — & NUREKI, T. 1996. CHIME age dating of monazite from metamorphic rocks and granitic rocks of the Ryoke Belt in the Iwakuni area, southwest Japan. *The Island Arc*, **5**, 43–55.

—, —, NASU, T. & SHIBATA, K. 1995. CHIME monazite ages of the Otagiri and Ichida granites in the Komagane area, Nagano Prefecture. *Journal of Earth and Planetary Sciences*, **42**, 17–30.

TAGAMI, T., HASEBE, N. & SHIMADA, D. 1995. Episodic exhumation of accretionary complex: Fission-track thermochronologic evidence from the Shimanto belt and its vicinities, southwest Japan. *The Island Arc*, **4**, 209–230.

—, —, LAL, L., SORKHABI, R. B. & NISHIMURA, S. 1988. Fission-track thermochronologic analysis of the Ryoke belt and the Median Tectonic Line, southwest Japan. *Journal of Geophysical Research*, **93**, 13 705–13 715.

TAGIRI, M., SATO, H., MATSUMURA, E. & NEMOTO, H. 1993. Late Mesozoic low-P/high-T metamorphism preceding emplacement of Cretaceous granitic rocks in the Gosaisho-Takanuki District, Abukuma metamorphic belt. *The Island Arc*, **3**, 152–156.

TAIRA, A. & OGAWA, Y. 1991. Cretaceous to Holocene forearc evolution in Japan and its implication to crustal dynamics. *Episodes*, **14**, 205–212.

—, SAITO, Y. & HASHIMOTO, M. 1983. The role of oblique subduction and strike-slip tectonics in the evolution of Japan. In: HILDE, T. W. C. & Uyeda, S. (eds) *Geodynamics of the Western Pacific-Indonesian Region*. American Geophysical Union, Geodynamic Series **11**, 303–316.

TAKAGI, H. 1986. Implications of mylonitic microstructures for the geotectonic evolution of the Median Tectonic Line, central Japan. *Journal of Structural Geology*, **8**, 3–14.

— 1992. Mylonites along the Median Tectonic Line in central Japan. In: *Metamorphic Belts and Related Photonism in the Japanese Islands*. 29th IGC Field Trip Guidebook, Geological Survey of Japan, Tsukuba, 327–335.

TAKAMI, M. & ITAYA, T. 1996. Episodic accretion and metamorphism of Jurassic accretionary complex based on biostratigraphy and K-Ar geochronology in the western part of the Mino-Tanba belt, southwest Japan. *The Island Arc*, **5**, 321–336.

—, ISOZAKI, Y., NISHIMURA, Y. & ITAYA, T. 1993. Effect of detrital white mica and contact metamorphism on K-Ar dating of a weakly metamorphosed accretionary complex – an example of Jurassic accretionary complex in eastern Yamaguchi Prefecture southwest Japan. *Journal of the Geological Society of Japan*, **99**, 545–563.

TAKASU, A. 1989. *P-T* histories of peridotite and amphibolite tectonic blocks in the Sanbagawa metamorphic belt, Japan. In: DALY, J. S., CLIFF, R. A. & YARDLEY, B. W. D. (eds) *Evolution of Metamorphic Belts*. Geological Society Special Publication, **43**, 533–538.

— & DALLMEYER, R. D. 1990. $^{40}\text{Ar}/^{39}\text{Ar}$ age constraints for the tectonothermal evolution of the Sambagawa metamorphic belt, central Shikoku, Japan: A Cretaceous accretionary prism. *Tectonophysics*, **185**, 111–139.

— & — 1992. $^{40}\text{Ar}/^{39}\text{Ar}$ mineral ages within metamorphic clasts from the Kuma Group (Eocene), central Shikoku, Japan: implications for tectonic development of the Sambagawa accretionary prism. *Lithos*, **28**, 69–84.

—, WALLIS, S. R., BANNO, S. & DALLMEYER, R. D. 1994. Evolution of the Sambagawa metamorphic belt, Japan. *Lithos*, **33**, 119–133.

TANAKA, H. 1974. On the Tabito composite mass in the Abukuma Plateau. *Journal of the Japanese Association of Mineralogists, Petrologists and Economic Geologists*, **69**, 18–31.

— & OCHIAI, K. 1988. On the Hanawa pluton and surrounding metamorphic rocks in the southern Abukuma Mountains. *Journal of Mineralogy, Petrology and Economic Geology*, **83**, 318–331.

TERAKADO, Y. & NAKAMURA, N. 1984. Nd and Sr isotopic variations in acidic rocks from Japan: Significance of upper-mantle heterogeneity. *Contributions to Mineralogy and Petrology*, **87**, 407–417.

THOMPSON, A. B., SCHULMANN, K. & JEZEK, J. 1997. Thermal evolution and exhumation in obliquely convergent (transpressive) orogens. *Tectonophysics*, **280**, 171–184.

THOMPSON, P. H. 1989. Moderate overthickening of thinned sialic crust and the origin of granitic magmatism and regional metamorphism in low-*P*–high-*T* terrains. *Geology*, **17**, 520–523.

THORKELSON, D. J. 1994. Ridge subduction: Kinematics and implication for the nature of mantle upwelling: Discussion. *Canadian Journal of Earth Sciences*, **31**, 1486–1489.

— 1996. Subduction of diverging plates and the principles of slab window formation. *Tectonophysics*, **255**, 47–63.

— & TAYLOR, R. P. 1989. Cordilleran slab windows. *Geology*, **17**, 833–836.

TORIUMI, M. 1985. Two types of ductile deformation/ regional metamorphic belt. *Tectonophysics*, **113**, 307–326.

— & MASUI, M. 1986. Strain patterns in the Sanbagawa and Ryoke paired metamorphic belts, Japan. *Geological Society of America Memoir*, **164**, 387–394.

TSUCHIYA, N. & KANISAWA, S. 1994. Early Cretaceous Sr-rich silicic magmatism by slab melting in the Kitakami Mountains, northeast Japan. *Journal of Geophysical Research*, **99**, 22 205–22 220.

UENO, N. 1977. Rb-Sr and K-Ar isotopic investigations of granodiorites and the associated metamorphic rocks in the Abukuma Plateau, Japan. *Earth Science (Chikyu Kagaku)*, **31**, 49–54.

UMEMURA, H. 1979. Tectonic movement in the Gosaisyo-Takanuki District, with special reference to tectonic junction of the Gosaisyo and Takanuki metamorphic rocks. In: *The basement of the Japanese Islands*. Toko Printing, Sendai, 491–512.

UNDERWOOD, M. B., LAUGHLAND, M. M., BYRN, E. T., HIBBARD, J. P. & DI TULLIO, L. 1992. Thermal evolution of the Tertiary Shimanto belt, Muroto Peninsular, Shikoku, Japan. *The Island Arc*, **1**, 116–132.

URUNO, K. & KANISAWA, S. 1965. Staurolite-bearing rocks in the Abukuma metamorphic belt, Japan. *Earth Science (Chikyu Kagaku)*, **81**, 1–12.

—, KANO, H. & MARUYAMA, T. 1974. An additional find of relic kyanite from the Gosaisyo-Takanuki metamorphic rocks of the Abukuma Plateau. *Journal of the Japanese Association of Mineralogists, Petrologists and Economic Geologists*, **69**, 81–88.

UYEDA, S. & MIYASHIRO, A. 1974. Plate tectonics and the Japanese Islands: A synthesis. *Geological Society of America Bulletin*, **85**, 1159–1170.

VAN DEN BEUKEL, J. 1990. Breakup of young oceanic lithosphere in the upper part of a subduction zone: Implications for the emplacement of ophiolites. *Tectonics*, **9**, 828–844.

VERNON, R. H. 1996. Problems with inferring *P-T-t* paths in low-*P* granulite facies rocks. *Journal of Metamorphic Geology*, **14**, 143–153.

— & COLLINS, W. J. 1989. Igneous microstructures in migmatites. *Geology*, **16**, 1126–1129.

WAKABAYASHI, J. 1996. Tectono-metamorphic impact of a subduction-transform transition and implications for interpretation of orogenic belts. *International Geology Review*, **38**, 979–994.

WAKITA, K. 1987. The occurrence of Latest Jurassic – Earliest Cretaceous radiolarians at the Hida-Kanayama area in the Mino terrane, central Japan. *Journal of the Geological Society of Japan*, **93**, 441–443.

WALLACE, W. K. & ENGBRETSON, D. C. 1984. Relationships between plate motions and Late Cretaceous to Paleogene magmatism in southwestern Alaska. *Tectonics*, **3**, 295–315.

WALLIS, S. 1995. Vorticity analysis and recognition of ductile extension in the Sambagawa belt, SW Japan. *Journal of Structural Geology*, **17**, 1077–1093.

WARREN, R. G. & ELLIS, D. J. 1996. Mantle underplating, granites tectonics, and metamorphic P - T - t paths. *Geology*, **24**, 663–666.

— & HENSEN, B. J. 1989. The P - T evolution of the Proterozoic Arunta Block, central Australia, and implications for tectonic evolution. In: DALY, J. S., CLIFF, R. A. & YARDLEY, B. W. D. (eds) *Evolution of Metamorphic Belts*. Geological Society Special Publication, **43**, 349–355.

WICKHAM, S. M. & OXBURGH, E. R. 1985. Continental rifts as a setting for regional metamorphism. *Nature*, **318**, 330–333.

— & — 1987. Low-pressure regional metamorphism in the Pyrenees and its implications for the thermal evolution of rifted continental crust. *Philosophical Transactions of the Royal Society, London*, **A321**, 219–242.

WILLIAMS, M. L. & KARLSTROM, K. E. 1996. Looping P - T paths and high- T , low- P middle crustal meta-morphism: Proterozoic evolution of the southwestern United States. *Geology*, **24**, 1119–1122.

YAMAMOTO, H. 1994. Kinematics of mylonitic rocks along the Median Tectonic Line, Akaishi Range, central Japan. *Journal of Structural Geology*, **16**, 61–70.

ZEN, E-AN 1995. Crustal magma generation and low-pressure high-temperature regional metamorphism in an extensional environment; possible application to the Lachlan Belt, Australia. *American Journal of Science*, **295**, 851–874.

The implications of Sr-isotope disequilibrium for rates of prograde metamorphism and melt extraction in anatetic terrains

NIGEL HARRIS & MICHAEL AYRES

Department of Earth Sciences, The Open University, Milton Keynes, MK7 6AA, UK

Abstract: The preservation of chemical disequilibrium during anatexis can provide constraints on the rates of high-temperature processes provided that, firstly, the appropriate diffusion coefficients are known, and secondly, isotopes in the protolith have not been reset by dynamic recrystallization. In one example of an anatetic migmatite from the western Himalaya, isotopic homogenization has been approached between the leucosome, mesosome and melanosome at c. 20 Ma, although apatite, with a low Sr diffusivity, remained in strong disequilibrium at that time. Intrusive granites are more likely to preserve evidence of isotopic disequilibrium provided a rapid rate of prograde metamorphism culminates in a rapid rate of melt extraction. Evaluation of the available Sr-isotope database from the Miocene Himalayan granites and their metasedimentary protoliths suggests that any increase of $^{87}\text{Sr}/^{86}\text{Sr}$ in the melt relative to its source is less than 0.002. Mass-balance calculations indicate that isotopic exchange between plagioclase and mica in the protolith, and plagioclase and melt prior to extraction, must have occurred over a period in excess of 100–200 ka. Since rapid melt extraction (within <50 ka) is indicated by accessory phase dissolution rates, a comparatively slow rate of prograde metamorphism is indicated by the lack of Sr-isotope disequilibrium. This supports heating from internal heat production in thickened crust rather than from thermal advection or dissipative heating.

The measurement of rates of geological processes is a key objective for many recent geochemical studies. The rates of melt formation in volcanic systems over time scales of 10–100 ka have been constrained by the application of short-lived radiogenic isotopes (Ivanovich & Harmon 1992) whereas longer timescales required for orogenic processes (1–10 Ma) have been obtained from interpretation and forward modelling of trace-element diffusion profiles in garnets (Vance 1995). Chemical disequilibrium may be preserved for a range of chemical tracers during crustal anatexis due to the low temperatures involved (<800°C) relative to temperatures required for mantle-derived melts. In general, disequilibrium is most likely to be observed during crustal melting from the incongruent melting of mica, particularly muscovite, since such reactions provide the lowest temperature conditions for melt formation in continental crust.

In this study we explore the potential use of disequilibrium chemistry of Sr-isotopes for constraining the rates of metamorphic and magmatic processes, and more specifically discuss the implications of apparent equilibrium between melt and protolith for the formation of Himalayan crustal melts. These results are reviewed in the context of possible mechanisms for thermal heating during prograde metamorphism and for subsequent melt extraction.

Sr-isotope disequilibrium during crustal melting

The $^{87}\text{Sr}/^{86}\text{Sr}$ ratios of igneous rocks are frequently used to fingerprint their source region, an approach underpinned by the assumption that melts inherit the same isotopic ratio as their bulk sources at the time of their formation. If isotopic disequilibrium prevails during melt extraction, this assumption is clearly invalid. In general, disequilibrium during prograde metamorphism and melting will occur when the time required for equilibrium to be attained by volume diffusion is greater than the time during which the system is open to diffusion between coexisting phases.

For a migmatite, provided equilibration is determined by volume diffusion, the equilibration period is the time during which the temperature of the rock exceeds the closure temperature for the phase with the slowest diffusion rate (Dodson 1973). For a protolith with two Sr-bearing phases, muscovite and plagioclase, the Sr-isotope ratio of each phase will increase through time at a rate dependent on its Rb/Sr ratios from the time of initial homogenization of Sr isotopes in the bulk rock, which in many cases will be an early metamorphic event. During subsequent prograde metamorphism, diffusive re-equilibration will be initiated at t_p (Fig. 1),

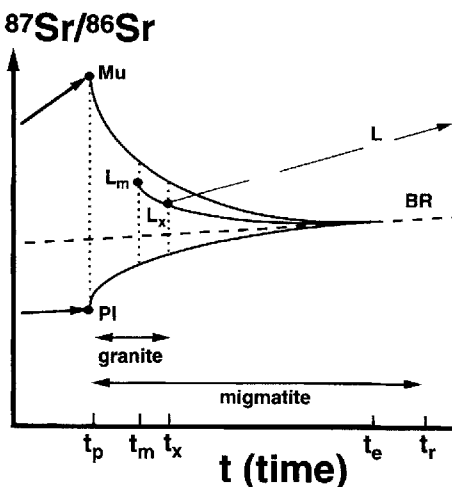


Fig. 1. Schematic evolution of $^{87}\text{Sr}/^{86}\text{Sr}$ in a muscovite-plagioclase protolith. Prograde temperatures exceed closure temperature in plagioclase at t_p and retrograde temperatures decrease below this closure temperature at t_r ; melting is initiated at t_m ; melt is extracted at t_x ; isotopic equilibrium is reached in the protolith at t_e . $L_m = {^{87}\text{Sr}}/{^{86}\text{Sr}}$ of initial melt, $L_x = {^{87}\text{Sr}}/{^{86}\text{Sr}}$ of melt when extracted from source; $L = {^{87}\text{Sr}}/{^{86}\text{Sr}}$ evolution of granite extracted at t_x . BR = bulk-rock evolution for protolith. Double-headed arrows indicate overall equilibration periods available for granite and migmatite.

the time at which the closure temperature for exchange between muscovite and plagioclase is exceeded. Melt formation at t_m (Fig. 1) introduces a third Sr-bearing phase. The precise $^{87}\text{Sr}/^{86}\text{Sr}$ of the melt L_m (and incidentally of any Sr-bearing peritectic phases that may form by an incongruent melt reaction) will be determined by the Sr-isotope ratios and elemental abundances for plagioclase and muscovite at this time and by the stoichiometric coefficients of the melt reaction. The system continues to re-equilibrate until melt, muscovite and plagioclase reach equilibrium at t_e . The available equilibration period for the migmatite is therefore $t_p - t_r$, where t_r is the time at which retrograde temperatures drop below the relevant closure temperature for Sr. This period is a function of the rate of prograde heating, the duration of peak metamorphism, and the rate of retrograde cooling subsequent to peak metamorphism. If $t_p - t_r > t_p - t_e$, as shown in Fig. 1, then equilibration will be attained. Although heating may be rapid,

depending on the mechanism of heat transfer, cooling of a migmatite will invariably result from conduction, a relatively slow process for both metamorphic and plutonic rocks. For such a T-t path, homogenization times calculated using Sr-diffusion coefficients for plagioclase suggest that the preservation of isotopic disequilibrium between melt (leucosome) and resite in a migmatite is unlikely. Moreover, isotopic equilibration can also be achieved by pervasive dynamic recrystallization at temperatures well below the closure temperatures of component phases (Inger & Cliff 1994).

For a granite melt that has segregated from its source, the period available for equilibration may be shortened by rapid melt extraction from its protolith. As with a migmatite, diffusional exchange during prograde metamorphism is initiated at t_p and melt formation occurs at t_m (Fig. 1). Instantaneous extraction of this melt would result in a Sr-isotope ratio in the melt equivalent to L_m . For a melt extracted after a finite period, at t_x , the Sr-isotope ratio of the melt would be equivalent to L_x at the time of extraction, clearly distinct from the equilibrium value of the bulk rock. Diffusional exchange between protolith phases and the melt is effectively terminated at t_x , hence the equilibration period for an intrusive granite is $t_p - t_x$. In other words, the period during which isotopic exchange can occur (the equilibration period) is the sum of two components: the time the solid phase assemblage in the protolith experiences prograde metamorphism above the closure temperature for diffusive exchange prior to melt formation, and the time the melt resides at its source prior to extraction.

This analysis assumes that isotopic equilibration is controlled by volume diffusion rates. During anatexis in a texturally static environment, isotopic readjustment may not be driven by volume diffusion but by textural reorganization, as determined by changes in dihedral angles and grain coarsening, in which case isotopic equilibration will be reached more rapidly. Although during mantle melting high temperatures allow textural equilibrium to be maintained, for the much lower temperatures at which crustal melting can occur textural equilibrium may not be established, in which case volume diffusion will provide the rate-determining step. This is supported by abundant evidence of chemical disequilibrium in both natural and experimental studies of crustal anatexis. For example, studies of rhyolites and dacites indicate the prevalence of Sr-isotope disequilibrium between phenocrysts and liquid in anatexic magma systems (Munksgaard

1984; Ferrara *et al.* 1989; Feldstein *et al.* 1994), reflecting magma-chamber processes. Anatetic granites generated by biotite breakdown during the Hercynian event in Spain have lower initial $^{87}\text{Sr}/^{86}\text{Sr}$ ratios (by about 0.005) than their pelitic protoliths (Barbero & Villaseca 1995). In contrast, experimental studies suggest that partial melting of a plagioclase–mica protolith can result in elevated $^{87}\text{Sr}/^{86}\text{Sr}$ ratios in the melt due to the faster melting kinetics of mica (Hammouda *et al.* 1996; Knesel & Davidson 1996; Pichavent *et al.* 1996). It is probably true to say that virtually all detailed isotopic studies of crustal anatexis have revealed some degree of isotopic disequilibrium, either between coexisting phases in the melt, or between melts and their source regions.

The rate of Sr-isotope equilibration between melt and restite will be determined largely by the diffusivity of Sr isotopes in plagioclase, both because plagioclase is the major Sr reservoir in metasedimentary assemblages and because the Sr diffusivity for plagioclase is lower than for micas (Giletti 1991). Diffusion parameters have been obtained for diffusion of an isotopic tracer (^{86}Sr) in plagioclase (Giletti & Casserly 1994). The rate of tracer diffusion of Sr through plagioclase is strongly dependent not only on temperature but also on the composition of plagioclase. At a temperature of 700°C, and over 1 Ma time interval, the diffusion length scale in albite ($X_{\text{ab}} = 0.9$) is 1.3 mm compared to a value of 0.3 mm for andesine ($X_{\text{ab}} = 0.6$). Disequilibrium is clearly favoured by plagioclase of calcic composition metasediments.

Under some circumstances, isotopic and elemental equilibration may be decoupled. Certainly for major elements where element substitutions affect the melt framework structure, isotopes will equilibrate by replacing isotopes of the same atomic species whilst retaining elemental disequilibrium between melt and mineral (van der Laan *et al.* 1994). Hence isotopic ratios can equilibrate more rapidly than elemental concentrations. Sr-isotope diffusivities are reported to be up to ten times faster than elemental Sr diffusivities (Baker 1989). A study of Sr diffusion in plagioclase from Rutherford backscatter spectroscopy (Cherniak & Watson 1994) confirms the dependence of diffusivities on plagioclase composition and indicates slower Sr diffusion rates than obtained for tracer diffusion (Giletti & Casserly 1994). For example, Sr diffusion length scales are 40–80% of tracer diffusion length scales at 700°C for oligoclase–andesine compositions. In the present study we are concerned primarily with isotopic homogenization of Sr and so have adopted the tracer

diffusion parameters of Giletti & Casserly (1994) unless otherwise indicated.

Anatexis during Himalayan metamorphism

The High Himalayan Crystalline Series forms a belt of metasedimentary rocks and anatetic granites that extends along the strike of the Himalaya. It comprises a sequence of metapelites, metagreywackes and metacarbonates metamorphosed during the Himalayan orogeny (Hodges *et al.* 1993). Small plutons and sheet complexes of peraluminous leucogranites were intruded into the northernmost exposures of these metasediments about 20 Ma ago (Le Fort *et al.* 1987; Harris & Massey 1994). Major-element abundances and modal mineralogy indicate minimum-melt compositions formed at pressures of 500–1000 MPa, and at temperatures of 700–750°C (Harris *et al.* 1995). Their isotope geochemistry (Sr, Nd and Pb) is strongly indicative of a mature crustal source (Deniel *et al.* 1987; Gariépy *et al.* 1985). Two-mica and tourmaline-bearing varieties are seen to form distinct intrusive phases (Reddy *et al.* 1993) with slightly differing initial Sr-isotope ratios due to the nature of their respective protoliths (Guillot & Le Fort 1995).

Modal mineral abundances from metapelitic schists from the High Himalayan Crystalline Series are not only strongly micaceous (up to 20% muscovite) but also include a high plagioclase component, of oligoclase composition, similar to the 'optimum mode' composition for the generation of granitic melts (Patiño Douce & Johnston 1991). Trace-element and isotope systematics of the leucogranites and the metapelitic lithologies of the High Himalayan Crystalline Series indicate that these metasediments provide a likely source for the leucogranite magmas (Deniel *et al.* 1987; Inger & Harris 1993).

The age of melt formation has been well constrained at *c.* 20 Ma by a range of isotopic studies for a number of leucogranite intrusions (see Harris & Massey (1994) for review). However, the age and duration of metamorphism in the High Himalayan Crystalline Series is more equivocal. Two periods of metamorphism are recognized: an earlier Barrovian event, rising to kyanite grade, has been locally overprinted by a sillimanite-grade event associated with anatexis (Hodges & Silverburg 1988; Inger & Harris 1992). The earlier metamorphism appears to be Oligocene (37–25 Ma) in age (Vannay & Hodges 1996; Vance *et al.* 1997). The sillimanite overprint has been dated as early Miocene (22–19 Ma) by several studies of accessory

phases (Noble & Searle 1995; Parrish & Hodges 1996) coeval with the formation of the leuco-granite intrusions. In this study we examine the anatetic event that led to granite formation during the early Miocene.

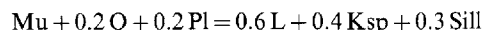
Sr-isotope behaviour during anatexis of Himalayan metasediments

Crustal anatexis results from the melting of protolith assemblages that incorporate some combination of mica, feldspar and quartz. Strontium in such protoliths is almost entirely sited in plagioclase and micas, although a small proportion (<0.5%) may be incorporated in apatite. In general, Sr-isotope ratios in micas are much more radiogenic than in feldspars due to their higher Rb/Sr ratios. Incongruent melting of micas could therefore result in a melt with a high $^{87}\text{Sr}/^{86}\text{Sr}$ ratio which, depending on diffusion rates, might re-equilibrate with feldspar prior to melt/restite segregation. However, over 75% of the Sr budget for Himalayan mica-schists and gneisses resides in plagioclase (Harris *et al.* 1995). The precise isotopic composition of the melt is therefore a balance between a small proportion of highly radiogenic Sr derived from mica, and a relatively large proportion of Sr with isotopic ratios from plagioclase that are only slightly below whole-rock values.

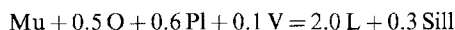
Detailed Sr, Nd and O isotope studies of the leucogranites of northern Nepal indicate that their source lies in kyanite-grade metapelitic schists, or a geochemically similar lithology (Inger & Harris 1993; Harris & Massey 1994). Melt generation occurred through the breakdown of muscovite in biotite-muscovite-kyanite-plagioclase-quartz schists (Harris *et al.*

1995). The precise melt reaction and available melt fraction are determined by the activity of H_2O during anatexis. We consider here two kyanite schists under both fluid-absent and fluid-present conditions. These represent end-members of feasible melt conditions. Stoichiometric coefficients (given in mass units) for the two assemblages obtained from mineral compositions and from average melt compositions are virtually identical for each reaction (Harris *et al.* 1995).

For fluid-absent conditions:



For fluid-present melting:



Melt fractions (in mass ratios) obtained are 0.10–0.17 and 0.44–0.55 respectively. In this study we have calculated the $^{87}\text{Sr}/^{86}\text{Sr}$ ratio of the melt that results from these reactions by assuming that mass balance is preserved. The required input parameters from two meta-sedimentary rocks from the High Himalayan Crystalline Series are given in Table 1.

The disequilibrium of isotope ratios between melt and protolith during melt formation is dependent on the difference between the isotopic compositions of component phases in the protolith (i.e. the displacement between muscovite and plagioclase isotopic ratios at t_p , Fig. 1). This is a function of contrasting Rb/Sr ratios in coexisting phases and of the time elapsed since the previous whole-rock homogenization event. Melt formation and high-grade metamorphism occurred in the High Himalayan Crystalline Series at 20 Ma. An earlier 500 Ma event is indicated by whole-rock Rb-Sr errorchrons of that age (Inger &

Table 1. Critical modal and geochemical data for two Himalayan metapelites

	Bulk-rock	Biotite	Muscovite	Plagioclase	
SSM6					$X_{\text{Ab}}=0.78$
Modal (wt%)		14	23	11	
Rb (ppm)	197	801	431	276	
Sr (ppm)	111	7	106	776	
$^{87}\text{Sr}/^{86}\text{Sr}$	0.76231				
$(^{87}\text{Sr}/^{86}\text{Sr})_{20}^*$	0.76083	3.02838	0.80612	0.72841	
PAN3					$X_{\text{Ab}}=0.84$
Modal (wt%)		13	29	11	
Rb (ppm)	173	560	271	118	
Sr (ppm)	113	4.2	128	321	
$^{87}\text{Sr}/^{86}\text{Sr}$	0.76207				
$(^{87}\text{Sr}/^{86}\text{Sr})_{20}^*$	0.76081	3.37862	0.77245	0.74043	

Data for SSM6 from Harris *et al.* (1992); for PAN3 from Ayres (1997).

* $(^{87}\text{Sr}/^{86}\text{Sr})_{20}$ calculated at 20 Ma assuming bulk-rock homogenization at 500 Ma.

Table 2. Change in $^{87}\text{Sr}/^{86}\text{Sr}$ ratio* of melt relative to source for two Himalayan metapelitic schists

		(i)	(ii)
Vapour-absent melting	SSM6	+0.029	+0.005
	PAN3	+0.016	+0.004
Vapour-present melting	SSM6	-0.007	-0.001
	PAN3	-0.004	-0.001

* The change in ratio is calculated assuming (i) no isotopic exchange between mica and feldspar; (ii) 50% of Sr in plagioclase has exchanged with mica.

Harris 1993), by Cambro-Ordovician granitoid intrusions exposed across the orogen (Pognante 1992) and by inherited zircon ages from high-grade metapelites from the High Himalayan Crystalline Series (Noble & Searle 1995). For this study, we assume mineral homogenization occurred at 500 Ma, but that subsequent radioactive decay proceeded in a closed system for the component minerals until prograde heating of the metasedimentary rocks during Himalayan metamorphism.

The rate of heating during this prograde event is a critical factor in preserving disequilibrium between coexisting phases, since a gradual increase in grade during the prograde history will cause partial or complete equilibration between reactants, thus reducing the effects of disequilibrium melting. Tracer diffusivities for Sr in micas are at least two to three orders of magnitude faster than those of feldspars (Giletti 1991). Since crustal anatexis cannot occur at temperatures $<650^\circ\text{C}$, even in the presence of a fluid phase, it is highly improbable that two-mica metapelites will reach solidus temperatures before Sr-isotope equilibration between the two micas has occurred. Such exchange will have the effect of increasing the $^{87}\text{Sr}/^{86}\text{Sr}$ ratio of muscovite whilst decreasing that of biotite. Thus strontium diffusivities in micas are too rapid to affect the degree of isotopic equilibration preserved between melt and restite, which must then largely be a function of the rate of isotopic exchange between plagioclase and contiguous phases. The role of Sr exchange between mica and plagioclase is apparent from Table 2; for either vapour-absent or vapour-present conditions, the consequence of partial equilibration between mica and plagioclase is to reduce significantly the isotopic disequilibrium between melt and protolith. We therefore assume that inter-mica equilibration has been reached and calculate the proportion of Sr residing in plagioclase that can equilibrate with the radiogenic Sr of coexisting mica over a given exchange period

in order to estimate the difference in $^{87}\text{Sr}/^{86}\text{Sr}$ ratio between protolith and melt.

Precise calculations of the proportion of feldspar in a protolith lithology that reaches isotopic equilibrium in a given time are complicated by a number of factors, including the shape of the feldspar crystals and the fact that neither crystal nor melt represent an infinite reservoir. However, to a first-order approximation we have calculated the diffusion length scale (x) from the relationship $x^2 = Dt$ (where D is the diffusivity and t the available time). We have also assumed that feldspars are spherical, and that homogenization is approached by tracer diffusion (i.e. no concentration gradient is implied) within an outer annulus of thickness $a - x$, where a is the radius of the sphere. For $x > a$, complete homogenization has occurred.

The modelled relationships between exchange period and isotopic disequilibrium during anatexis of two Himalayan schists are illustrated in Fig. 2. For all melt reactions, Sr-isotope ratios in melt and source are virtually indistinguishable for an exchange period greater than c. 1 Ma, assuming a temperature of 700°C , the mean melt temperature obtained from accessory phase dissolution in leucogranite magmas from the Himalayas (Ayres *et al.* 1997). In practice, the modelled times will be a function of the dT/dt path of the protolith, but since thermal buffering is likely to prevent the temperature of the protolith significantly exceeding the solidus temperature (Hodges *et al.* 1988) this approximation provides a realistic estimate of the degree of disequilibrium expected over a given time scale.

During vapour-absent melting, the $^{87}\text{Sr}/^{86}\text{Sr}$ ratio of the melt is dominated by radiogenic Sr released by muscovite breakdown; this effect is enhanced by Sr exchange of muscovite with coexisting biotite prior to melting. Consequently the melt will inherit a higher $^{87}\text{Sr}/^{86}\text{Sr}$ ratio than the source. However, vapour-present melting leads to larger melt fractions and requires a

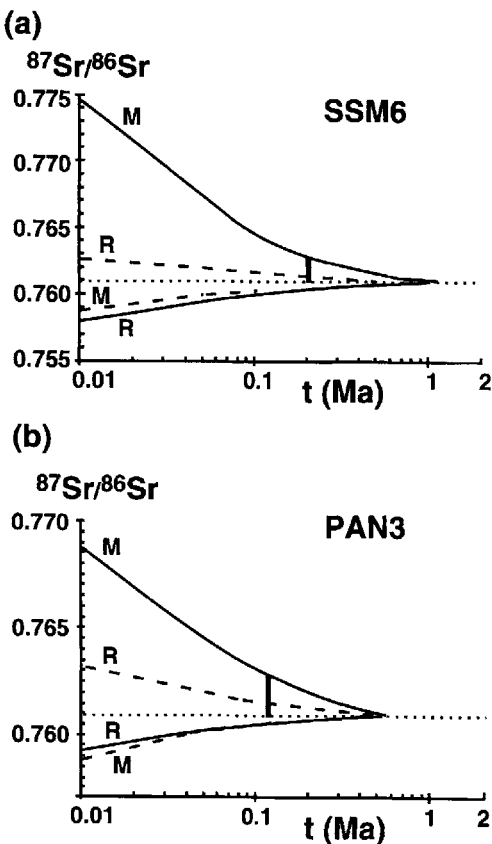


Fig. 2. Modelled disequilibrium for $^{87}\text{Sr}/^{86}\text{Sr}$ between restite (R) and melt (M) during incongruent melting of muscovite under fluid-absent conditions (heavy line) and fluid-present conditions (dashed lines); dotted line indicates $^{87}\text{Sr}/^{86}\text{Sr}$ ratio for protolith; t = time elapsed since system was open for Sr exchange between mica and feldspar. Tracer diffusion coefficients from Giletti & Casserly (1994). Assumed grain size = 2 mm and temperature = 700°C. (a) Langtang metapelite SSM6. (b) Zanskar metapelite PAN3 calculated from data in Table 1. Vertical bar indicates disequilibrium of 0.002 between melt and protolith.

greater contribution from plagioclase, resulting in little disequilibrium between Sr isotopes in melt and source. The sense of this small disequilibrium shift depends on the modal composition of the source and the composition of plagioclase.

Is isotopic disequilibrium preserved between Himalayan melts and their protoliths?

Anatectic migmatites provide the simplest case for investigating isotopic disequilibrium since

the isotopic characteristics of melt and protolith are clearly identified. Sr-isotope analyses of bulk rock and three separated components (leucosome, melanosome, mesosome) from a stromatic migmatite from the Western Himalaya do not define an isochron but form a sub-linear array (errorchron) that lies close to a reference line of 20 Ma (Fig. 3, Table 3), suggesting that isotopic homogenization over a scale of centimetres was approached during the early Miocene Himalayan event. Interestingly, whole-rock Rb-Sr systematics for high-grade migmatites separated by distances of kilometres define a c. 500 Ma errorchron (Inger & Harris 1993), placing a maximum constraint on the length scale of isotopic re-equilibration during the early Miocene. However, for phases with low Sr diffusivities, such as apatite, disequilibrium appears to be preserved even over short length scales (Fig. 3). A bulk-rock apatite age of 346 Ma is unlikely to date a tectonic event of that age as there is no record of Carboniferous metamorphism in the Himalayas. However, it may indicate that partial equilibration occurred during Himalayan (Miocene) prograde metamorphism. If a grain size of 200 μm and a peak temperature of 700°C are assumed then a period of 200 ka is required for complete equilibration, applying the Sr-isotope diffusion coefficients of Cherniak and Ryerson (1993). Although this value is subject to considerable uncertainty in the diffusion data, and will decrease by almost an order of magnitude if actual temperatures rose to 750°C, it illustrates how accessory phases from polymetamorphic assemblages can retain evidence of early events and potentially provide quantitative information on heating rates during the younger event.

In contrast to migmatites, intrusive granites are more likely to preserve isotopic disequilibrium, since after extraction from their source region they are unable to equilibrate further with protolith phases. Detailed studies of the geochemistry of Himalayan leucogranites and their possible source regions have documented over 200 Sr-isotope analyses (see caption to Fig. 4 for references). Average $^{87}\text{Sr}/^{86}\text{Sr}$ ratios (calculated at 20 Ma) for coeval granite sheets are 0.755 ± 0.011 , compared with average ratios of 0.763 ± 0.035 for the metapelitic schists. The large variability of Sr-isotope ratios in the metasediments reflects lithological variations.

However, comparing average Sr-isotope ratios is unlikely to yield actual isotopic shifts from disequilibrium melting since (i) sampling of the metasediments across the Himalayan orogen may not be representative of the precise protolith lithologies for the leucogranites, and (ii) the

Table 3. Rb-Sr isotopic data for a stromatic migmatite (BR) and leucosome (lc), melanosome (ml), mesosome (ms) and apatite (ap) separates from sample 56.1a (Zanskar)

	Rb (ppm)	Sr (ppm)	$^{87}\text{Rb}/^{86}\text{Sr}$	$^{87}\text{Sr}/^{86}\text{Sr}$	$\pm (1\sigma)$
BR	209.0	108.0	5.60	0.76540	0.00001
ms	221.4	78.9	8.12	0.76598	0.00001
ml	245.0	120.0	5.91	0.76535	0.00001
lc	219.9	193.4	3.29	0.76472	0.00001
ap	<1	115.0	0.00	0.73783	0.00003

Analyst MA on Finigan MAT261 at the Open University. Apatite separated from bulk rock crushate using heavy liquids. Rb and Sr concentrations in apatite determined by ion-microprobe at the University of Edinburgh (Ayres 1997).

leucogranites may not all be derived from the same protolith composition. A comparison of data from three detailed studies of Himalayan leucogranites and their associated protoliths (Fig. 4) suggests that in each case the minimum value of the $^{87}\text{Sr}/^{86}\text{Sr}$ ratio observed from the leucogranites exceeds that from metasediments from the same region of the orogen. In each case the offset lies in the range 0.005–0.01. The significance of this observation is equivocal.

It may be that the leucogranites are derived from a range of metasedimentary sources, and thus each isotope analysis determined from a leucogranite represents a weighted average of contributing sources. This would explain why neither the lowest, nor the highest, initial ratios in the protoliths is reflected in the derived melts. Equally it could be argued that only protoliths with the appropriate combination of mica and feldspar (the 'optimum mode' composition) have melted, and these are characterized by a fairly narrow isotopic range. It could also be argued that if disequilibrium melting has occurred, the $^{87}\text{Sr}/^{86}\text{Sr}$ ratio in the melt has increased by up to c. 0.01 relative to its source. Whichever of these explanations is correct, it appears that changes in $^{87}\text{Sr}/^{86}\text{Sr}$ ratio between melt and source due to isotopic disequilibrium must be less than c. 0.01.

This estimate can be further constrained from the detailed isotopic study of the Manaslu leucogranite (Guillot & Le Fort 1995). This work documents a bimodal peak in the $^{87}\text{Sr}/^{86}\text{Sr}$ ratios (calculated at 20 Ma) of both metasedimentary protoliths and leucogranites (Fig. 4a). More specifically, metagreywackes ($^{87}\text{Sr}/^{86}\text{Sr} \approx 0.746$) provide an appropriate protolith for two-mica leucogranites ($^{87}\text{Sr}/^{86}\text{Sr} = 0.7475 \pm 0.0055$) whereas metapelites ($^{87}\text{Sr}/^{86}\text{Sr} \approx 0.758$) provide a protolith for tourmaline leucogranites ($^{87}\text{Sr}/^{86}\text{Sr} = 0.7591 \pm 0.0069$). These data suggest that any increase in the $^{87}\text{Sr}/^{86}\text{Sr}$ ratio of the melt relative to its source is less than 0.002.

The minimum time for isotopic equilibration can be inferred using the theoretical prediction of equilibration time scales. Since any disequilibrium results in a variation in $^{87}\text{Sr}/^{86}\text{Sr}$ ratio between melt and source of less than c. 0.002, it can be seen from modelled disequilibrium for two Himalayan metapelites (Fig. 2) that isotopic exchange between plagioclase and mica in the protolith, and plagioclase and melt prior to

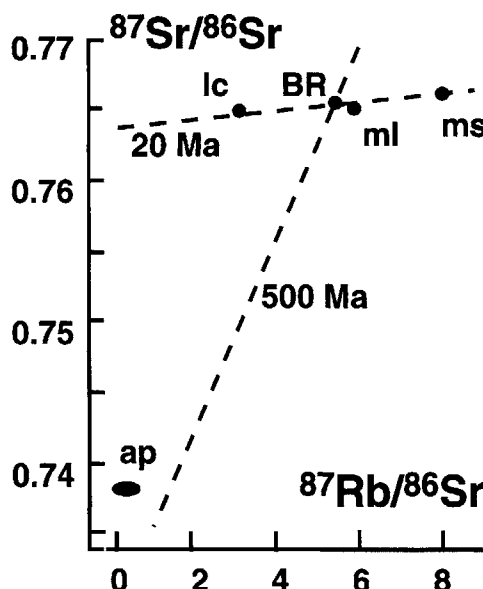


Fig. 3. Rb-Sr errorchron for a stromatic migmatite (BR) and leucosome (lc), melanosome (ml), mesosome (ms) and apatite (ap) separates from sample 56.1a from the Zanskar Himalaya. Reference lines plotted through BR for 20 Ma and 500 Ma. Errors less than symbol size for all data given in Table 3.

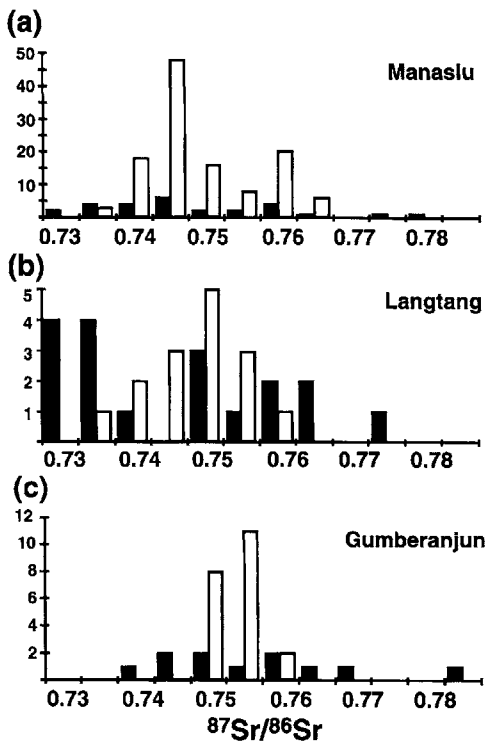


Fig. 4. Compilation of $^{87}\text{Sr}/^{86}\text{Sr}$ data (calculated at 20 Ma) for leucogranites (open bars) and metasedimentary schists (black bars) from three Himalayan leucogranite localities. (a) Manaslu (data from Guillot & Le Fort 1995); (b) Langtang (data from Inger & Harris 1993); (c) Gumberanjun (data from Searle & Fryer 1986; Ferrara *et al.* 1991; Ayres 1997).

extraction, must have occurred over a period of at least 100–200 ka. More rapid rates of prograde metamorphism and melt extraction would result in a demonstrable increase in $^{87}\text{Sr}/^{86}\text{Sr}$ ratios of melts relative to their source, unless the protolith had undergone dynamic recrystallization.

For plagioclase-rich metasediments, the exchange period extends from the time the temperature of the protolith rose above the approximate closure temperature of Sr in plagioclase. This has been estimated at 600°C assuming an infinite reservoir for Sr (Dodson 1973), but if it is assumed that equilibrium is reached locally along grain boundaries the effective closure temperature may be a function of the modal composition, particularly the mica/plagioclase ratio (Jenkin *et al.* 1995). Under these circumstances the closure temperature of plagioclase–biotite mineral pairs may drop to 550°C. If melting occurred at temperatures of c. 700°C,

and if it is assumed that temperatures did not exceed c. 600°C until the Early Miocene, this suggests that Sr-isotope disequilibrium can only be preserved if (i) prograde heating rates from c. 600°C to the solidus temperature occurred at an average rate in excess of $0.5^\circ\text{C ka}^{-1}$, and (ii) extraction of the melt was extremely rapid ($\ll 200$ ka).

Clearly it would be valuable to distinguish the rate of prograde metamorphism from the rate of melt extraction. It is theoretically possible to use the elemental partitioning of Sr between melt and source to provide a minimum constraint on the melt extraction rate. Unfortunately, the variability of Sr concentrations in metapelitic schists, coupled with large uncertainties in appropriate crystal/melt partition coefficients, means that the proportion of elemental Sr in the Himalayan metasediments that has equilibrated cannot be realistically constrained.

It might be argued that disequilibrium of Nd isotopes would provide a more useful indicator of rates of metamorphic processes since in general REE diffusivities are lower than those of Sr for major phases such as garnet (Coghlan 1990). A very high proportion of the bulk-rock LREE budget for granites lies in accessory phases such as monazite and apatite (Harris *et al.* 1995), and although disequilibrium can be detected for $^{143}\text{Nd}/^{144}\text{Nd}$ between Himalayan melts and their protoliths (Ayres & Harris 1997), this does not provide quantitative constraints on prograde heating or melt extraction rates because of the paucity of experimental data on isotopic diffusivities for monazite and apatite.

Implications for physical processes during Himalayan metamorphism and anatexis

Prograde heating models

Alternative mechanisms for crustal melting imply differing rates of prograde heating. For example, advective heating from intrusion of basic magmas (Huppert & Sparks 1988) will lead to rapid heating rates (depending on the size of and distance from the intrusive body) and consequently to disequilibrium of Sr-isotopes between melt and restite (Knesel & Davidson; 1996, Pichavent *et al.* 1996). Obduction of hot oceanic lithosphere onto continental crust is a particular form of advective heating which has been associated with rapid melt formation and the preservation of $^{87}\text{Sr}/^{86}\text{Sr}$ disequilibrium (Tommasini & Davies 1995). However, advective heating is unlikely to be relevant for the

Himalayan orogen since there is no evidence for basic and/or intermediate magmatism of appropriate age nor for obduction of hot lithosphere.

For convergent orogens, the most frequently invoked mechanism for thermal transfer is conductive heating by internal heat sources following crustal thickening (England & Thompson 1984; Thompson & Connolly 1995). Heating by this mechanism will be of the order of $10-50^{\circ}\text{C Ma}^{-1}$, up to two orders of magnitude too slow for Sr-isotope disequilibrium to be preserved. Dissipative or frictional heating during active thrusting is also suggested as a mechanism for generating some Himalayan granites (England *et al.* 1992). This process could result in virtually instantaneous heating, depending on the proximity to the thrust. It would also subject the shear zone to dynamic recrystallization thus favouring isotopic equilibration, even at temperatures below the appropriate closure temperature. Finally, decompression melting (under fluid-absent conditions) resulting from rapid exhumation has been invoked as the cause of melting of Himalayan metasediments (Harris & Massey 1994). This mechanism requires that the temperature of the protolith is sufficiently hot for the fluid-absent solidus to be crossed during exhumation. The preservation of isotopic disequilibrium would depend on whether the protolith was initially heated slowly, as by thermal relaxation, or rapidly, as by frictional heating. Overall we conclude that the apparent lack of significant isotopic disequilibrium in Himalayan leucogranites is consistent with heating by internal heat sources, although it could be argued that it reflects frictional heating associated with dynamic recrystallization. However, the lack of textural evidence from migmatitic assemblages for dynamic recrystallization and indeed, the preservation of accessory phase disequilibrium in these assemblages (Fig. 3), do not support this interpretation.

Melt extraction models

There are several processes that control how rapidly a melt is extracted. Firstly, the grain-boundary melts must be driven into a vein network, and secondly, magma that has collected in the veins must migrate through the network. Several recent studies have established that gravity-driven models cannot adequately account for the extraction of viscous granitic melts over realistic time scales (Clemens & Mawer 1992; Brown *et al.* 1995). For a melt fraction of less than 0.2, as suggested for

Himalayan granites (Harris & Massey 1994), melt segregation is initially controlled by diffusion, usually resulting in migmatites (Vigneresse *et al.* 1996). Such melts can only escape in response to non-coaxial forces. Experimental studies have highlighted the importance of deviatoric stress in aiding melt extraction (Rutter & Neumann 1995), suggesting that shear-enhanced compaction can reduce the extraction rates of granitic melts from many millions of years to less than 1 Ma. Once a melt has entered a vein network it can be rapidly extracted by porous flow through a high-permeability vein network. This process can be accelerated by fracture propagation that transports magma large distances over a time scale of $<1\text{ ka}$ (Petford *et al.* 1993). Fracture propagation is particularly likely where fluid-absent melting occurs due to an increase in molar volume resulting from the melt reaction.

The rate-determining step for melt extraction is critically dependent on the viscosity of the magma, which in turn depends on its water content and temperature. Applying equation 23 of Rutter & Neumann (1995) to Himalayan leucogranite melts formed under fluid-absent conditions at temperatures of $700-750^{\circ}\text{C}$, a viscosity in the range 10^7-10^9 Pa s is obtained, consistent with estimates for viscosities of melts formed in migmatites (Brown *et al.* 1995). Under these conditions the rate-determining step is more likely to be flow through the vein network (Rutter & Neumann 1995, fig. 16); extraction of a 10% melt fraction by this process will occur over a period of 1–50 ka.

For Himalayan leucogranites, evidence for rapid melt extraction rates comes from the undersaturation of LREE relative to Zr found in some leucogranites (Ayres *et al.* 1997). The relative dissolution rates of monazite and zircon suggest that the melt was extracted from its source over a period $<50\text{ ka}$. This observation confirms that the lack of Sr-isotope disequilibrium observed between granite and protolith results from slow prograde heating rates rather than from a protracted melt residence time.

Conclusions

The direct controls on the extent of possible isotopic disequilibrium during crustal anatexis are: (i) the rate of prograde heating and melt extraction; (ii) the time elapsed since isotopic homogenization of the protolith prior to the prograde event leading to anatexis; (iii) the relative masses of mica and feldspar consumed by

the melt reaction; (iv) the composition of plagioclase in the protolith; (v) the grain size of the source rock; (vi) the degree of strain and resulting dynamic recrystallization experienced by the protolith.

In general, tracer diffusivities for plagioclase require that in order for significant isotopic disequilibrium to be preserved between melt and source, the protolith must be heated above 600°C and melts extracted from their source over very short time scales (<200 ka). Sluggish heating rates will favour isotopic homogenization during prograde metamorphism. In contrast, frictional or advective heat sources will favour isotopic disequilibrium. Melt extraction through a combination of shear-enhanced compaction and vein-network flow is likely to be sufficiently rapid that disequilibrium between protolith phases at the solidus will result in disequilibrium between melt and the restite assemblage.

During prograde metamorphism in the Himalaya, Sr-isotopes in micas and feldspars have approached equilibrium (on the scale of a hand specimen) in anatectic migmatites, although disequilibrium is preserved by apatite due to its low diffusivity. The extent of melt–restite disequilibrium in the intrusive leucogranites is more difficult to determine but the change in $^{87}\text{Sr}/^{86}\text{Sr}$ ratio is probably negligible and certainly less than 0.002. This suggests that at least 200 ka elapsed between the onset of prograde metamorphism in the protolith (>600°C) and final melt extraction. Given that trace-element data indicate rapid extraction of melt from its source, such a conclusion suggests that heat transfer during prograde heating resulted from internal heat production in thickened crust. A frictional heat source is only possible if isotopic equilibration has been achieved by dynamic recrystallization of the protolith.

We thank D. Vance, C. Hawkesworth, G. Jenkin and M. Holness for comments on aspects of this manuscript, and F. McDermott and J. Wheeler for helpful suggestions and corrections. N. Harris gratefully acknowledges research grants from the Royal Society that supported field work in Langtang, Zanskar and Garhwal Himalaya. M. Ayres was supported by a NERC studentship.

References

AYRES, M. 1997. *Trace element behaviour during high-grade metamorphism and anatexis of the Himalaya*. PhD thesis, Open University, UK.

— & HARRIS, N. 1997. REE fractionation and Nd-isotope disequilibrium during crustal anatexis: constraints from Himalayan leucogranites. *Chemical Geology*, **139**, 249–269.

—, — & VANCE, D. 1997. Possible constraints on anatectic melt residence times from accessory mineral dissolution rates: an example from Himalayan leucogranites. *Mineralogical Magazine*, **61**, 29–36.

BAKER, D. R. 1989. Tracer versus trace element diffusion: diffusional decoupling of Sr concentration from Sr isotope composition. *Geochimica et Cosmochimica Acta*, **53**, 3015–3023.

BARBERO, L. & VILLASECA, C. 1995. Geochemical and isotopic disequilibrium in crustal melting: an insight from the anatectic granitoids from Toledo, Spain. *Journal of Geophysical Research*, **100**, 15 745–15 765.

BROWN, M., AVERKIN, Y. A., MCCLELLAN, E. L. & SAWYER, E. W. 1995. Melt segregation in migmatites. *Journal of Geophysical Research*, **100**, 15 655–15 679.

CHERNIAK, D. J. & RYERSON, F. J. 1993. A study of strontium diffusion in apatite using Rutherford backscattering spectroscopy and ion implantation. *Geochimica et Cosmochimica Acta*, **57**, 4653–4662.

— & WATSON, E. B. 1994. A study of diffusion in plagioclase using Rutherford backscattering spectroscopy. *Geochimica et Cosmochimica Acta*, **58**, 5179–5190.

CLEMENS, J. D. & MAWER, C. K. 1992. Granitic magma transport by fracture propagation. *Tectonophysics*, **204**, 339–360.

COGHLAN, R. A. N. 1990. *Studies in diffusional transport: grain-boundary transport of oxygen and feldspars, diffusion of oxygen, strontium and REEs in garnet and thermal histories of granitic intrusions in south-central Maine using oxygen isotopes*. PhD thesis, Brown University Rhode Island, USA.

DENIEL, C., VIDAL, P., FERNANDEZ, A., LE FORT, P. & PEUCAT, J. 1987. Isotopic study of the Manaslu granite (Himalaya, Nepal): inferences of the age and source of Himalayan leucogranites. *Contributions to Mineralogy and Petrology*, **96**, 78–92.

DODSON, M. H. 1973. Closure temperatures in cooling geochronological and petrological systems. *Contributions to Mineralogy and Petrology*, **40**, 259–274.

ENGLAND, P. & THOMPSON, A. B. 1984. Pressure–temperature–time paths of regional metamorphism. I. Heat transfer during the evolution of regions of thickened crust. *Journal of Petrology*, **25**, 894–928.

—, LE FORT, P., MOLNAR, P. & PECHER, A. 1992. Heat sources for Tertiary magmatism and anatexis in the Annapurna–Manaslu region of Central Nepal. *Journal of Geophysical Research*, **97**, 2107–2128.

FELDSTEIN, S. N., HALLIDAY, A. N., DAVIES, G. R. & HALL, C. M. 1994. Isotope and chemical micro-sampling: constraints on the history of an S-type rhyolite, San Vicenzo, Tuscany, Italy. *Geochimica et Cosmochimica Acta*, **58**, 943–958.

FERRARA, G., LOMBARDO, B., TONARINI, S. & TURI, B. 1991. Sr, Nd and O isotopic characterisation of the Gopha La and Gumberanjun leucogranites (High Himalaya). *Schweizerische Mineralogische und Petrographische Mitterungen*, **71**, 31–51.

—, PETRINI, R., SERRI, G. & TONARINI, S. 1989. Petrology and isotope geochemistry of San Vincenzo thyolites (Tuscany, Italy). *Bulletin Volcanologique*, **51**, 379–388.

GARIÉPY, C., ALLÉGRE, C. J. & RONGHUAU, XU 1985. The Pb-isotope geochemistry of granitoids from the Himalaya–Tibet collision zone: implications for crustal evolution. *Earth and Planetary Science Letters*, **74**, 220–234.

GILETTI, B. J. 1991. Rb and Sr diffusion in alkali feldspars, with implications for cooling histories of rocks. *Geochimica et Cosmochimica Acta*, **55**, 1331–1343.

— & CASSERLY, J. E. D. 1994. Strontium diffusion kinetics in plagioclase feldspars. *Geochimica et Cosmochimica Acta*, **58**, 3785–3793.

GUILLOT, S. & LE FORT, P. 1995. Geochemical constraints on the bimodal origin of High Himalayan leucogranites. *Lithos*, **35**, 221–234.

HAMMOUDA, T., PICHAVENT, M. & CHAUSSIDON, M. 1996. Isotopic equilibration during partial melting: an experimental study of the behaviour of strontium. *Earth and Planetary Science Letters*, **144**, 109–121.

HARRIS, N. B. W. & MASSEY, J. A. 1994. Decompression and anatexis of Himalayan metapelites. *Tectonics*, **13**, 1537–1546.

—, AYRES, M. & MASSEY, J. A. 1995. Geochemistry of granitic melts produced during the incongruent melting of muscovite: Implications for the extraction of Himalayan leucogranite magmas. *Journal of Geophysical Research*, **100**, 15 767–15 777.

HODGES, K. V. & SILVERBERG, D. S. 1988. Thermal evolution of the Greater Himalaya, Garhwal, India. *Tectonics*, **7**, 583–600.

—, BURCHFIELD, B. C., ROYDEN, L. H., CHEN, Z. & LIEU, Y. 1993. The metamorphic signature of contemporaneous extension and shortening in the central Himalayan orogen: data from the Nyamal transect, southern Tibet. *Journal of Metamorphic Geology*, **11**, 721–737.

—, LE FORT, P. & PECHER, A. 1988. Possible thermal buffering by crustal anatexis in collisional orogens: thermobarometric evidence from the Nepalese Himalaya. *Geology*, **16**, 707–710.

HUPPERT, H. E. & SPARKS, R. J. 1988. The generation of granitic magmas by intrusion of basalt into continental crust. *Journal of Petrology*, **29**, 599–624.

INGER, S. & CLIFF, R. A. 1994. Timing of metamorphism in the Tauern window, Eastern Alps: Rb-Sr ages and fabric formation. *Journal of Metamorphic Geology*, **12**, 695–707.

— & HARRIS, N. B. W. 1992. Tectonothermal evolution of the High Himalayan Crystalline Sequence, Langtang Valley, northern Nepal. *Journal of Metamorphic Geology*, **10**, 439–452.

— & — 1993. Geochemical constraints on leucogranite magmatism in the Langtang Valley, Nepal Himalaya. *Journal of Petrology*, **34**, 345–368.

IVANOVICH, M. & HARMON, R. S. 1992. *Uranium Series Disequilibrium: Applications to Earth, Marine and Environmental Sciences*, University Press, Oxford.

JENKIN, G. R. T., ROGERS, G., FALICK, A. E. & FARROW, C. M. 1995. Rb-Sr closure temperatures in bi-mineralic rocks: a mode effect and test for different diffusion models. *Chemical Geology*, **122**, 227–240.

KNESEL, K. M. & DAVIDSON, J. P. 1996. Isotopic disequilibrium during melting of granite and implications for crustal contamination of magmas. *Geology*, **24**, 243–246.

LE FORT, P., CUNFY, M., DENIEL, C., FRANCELON, C., SHEPPARD, S. M. F., UPRETTI, B. N. & VIDAL, PH. 1987. Crustal generation of the Himalayan leucogranites. *Tectonophysics*, **134**, 39–57.

MUNKSGAARD, N. C. 1984. High $\delta^{18}\text{O}$ and possible pre-eruptive Rb-Sr isochrons in cordierite-bearing Neogene volcanics from South-East Spain. *Contributions to Mineralogy and Petrology*, **87**, 351–358.

NOBLE, S. R. & SEARLE, M. P. 1995. Age of crustal melting and leucogranite formation from U-Pb zircon and monazite dating in the western Himalaya, Zanskar, India. *Geology*, **23**, 1135–1138.

PARRISH, R. R. & HODGES, K. V. 1996. Isotopic constraints on the age and provenance of the Lesser and Greater Himalayan sequences. *Geological Society of America, Bulletin*, **108**, 904–911.

PATIÑO DOUCE, A. E. & JOHNSTON, A. D. 1991. Phase equilibria and melt productivity in the pelitic system: implications for the origin of peraluminous granitoids and aluminous granites. *Contributions to Mineralogy and Petrology*, **107**, 202–218.

PETFORD, N., KERR, R. C. & LISTER, J. R. 1993. Dike transport of granitoid magmas. *Geology*, **21**, 845–848.

PICHAVENT, M., HAMMOUDA, T. & SCAILLET, B. 1996. Control of redox state and Sr isotopic composition of granitic magmas: a critical evaluation of the role of source rocks. *Transactions of the Royal Society of Edinburgh*, **88**, 321–329.

POGNANTE, U. 1992. Migmatites and leucogranites of Tertiary age from the High Himalayan Crystallines of Zanskar (NW India): a case history of anatexis of Palaeozoic orthogneisses. *Mineralogy and Petrology*, **46**, 291–313.

REDDY, S. M., SEARLE, M. P. & MASSEY, J. M. 1993. Structural evolution of the High Himalayan Gneiss sequence, Langtang Valley, Nepal. In: TRELOAR, P. J. & SEARLE, M. P. (eds) *Himalayan Tectonics*. Geological Society, London, Special Publications, **74**, 375–389.

RUTTER, E. H. & NEUMANN, D. H. K. 1995. Experimental deformation of partially molten Westerly granite under fluid-absent conditions with implications for the extraction of granitic magmas. *Journal of Geophysical Research*, **100**, 15 697–15 715.

SEARLE, M. P. & FRYER, B. J. 1986. Garnet, tourmaline and muscovite-bearing leucogranites, gneisses and migmatites of the Higher Himalayas from Zanskar, Kulu, Lahoul and Kashmir. In: COWARD, M. P. & RIES, A. C. (eds) *Collision Tectonics*. Geological Society, London, Special Publication, **19**, 185–201.

THOMPSON, A. B. & CONNOLLY, A. D. 1995. Melting the continental crust: some thermal and petrological constraints on anatexis in continental collision zones. *Journal of Geophysical Research*, **100**, 565–579.

TOMMASINI, S. & DAVIES, G. R. 1995. Isotopic disequilibrium during anatexis; consequences for radiogenic isotope systematics. *Terra Abstracts*, **7**, 154.

VAN DER LAAN, S., ZHANG, Y., KENNEDY, A. K. & WYLLIE, P. J. 1994. Comparison of element and isotope diffusion of K and Ca in multi-component silicate melts. *Earth and Planetary Science Letters*, **123**, 155–166.

VANCE, D. 1995. Rate and time controls on metamorphic processes. *Geological Journal*, **30**, 241–259.

—, PRINCE, C. I., ANCZKIEWICZ, R. & HARRIS, N. 1997. The timing and rate of prograde metamorphism in the Himalayan orogen. *Terra Nova*, **9**, 64.

VANNAY, J-C. & HODGES, K. V. 1996. Tectonometamorphic evolution of the Himalayan metamorphic core between the Annapurna and Dhaulagiri, central Nepal. *Journal of Metamorphic Geology*, **14**, 635–656.

VIGNERESSE, J. L., BARBEY, P. & CUNNEY, M. 1996. Rheological transitions during partial melting and crystallisation with application to felsic magma segregation. *Journal of Petrology*, **37**, 1579–1600.

Low-pressure crustal anatexis: the significance of spinel and cordierite from metapelitic assemblages at Nanga Parbat, northern Pakistan

ALAN WHITTINGTON¹, NIGEL HARRIS¹ & JUDY BAKER²

¹ Department of Earth Sciences, Open University, Walton Hall,
Milton Keynes MK7 6AA, UK

² Department of Earth Sciences, University of Cambridge,
Downing Street, Cambridge CB2 3EQ, UK

Abstract: Spinel-bearing domains in high-grade metapelitic rocks from Nanga Parbat represent zones of partial melting during biotite breakdown under vapour-undersaturated conditions. Spinel is essentially of the $MgAl_2O_4$ – $FeAl_2O_4$ solid solution, and is therefore not stabilized by the presence of trace elements such as zinc, but is restricted to a quartz-absent petrogenesis. A new petrogenetic grid for metapelites has been constructed to allow for both vapour-undersaturated and quartz-undersaturated conditions. This grid contains a quartz-absent invariant point in KFASH that predicts quartz-absent melting will occur in biotite–sillimanite assemblages at low pressures.

A P – T pseudosection drawn for bulk compositions with intermediate Fe/Mg ratios shows that at low pressures biotite will break down initially in the presence of quartz, to produce cordierite and K-feldspar and melt. At higher temperatures the quartz-absent reaction will be crossed, and biotite will break down to produce spinel in addition to cordierite, K-feldspar and melt. The sequence of assemblages is biotite–cordierite, biotite–cordierite–spinel, and finally cordierite–spinel. This biotite-absent assemblage is not observed, indicating that the quartz-absent reaction did not go to completion. Limits can be placed on the pressures and temperatures at which the biotite breakdown reaction is crossed, from the coexistence of solid phases and granite melt over a range of water activities. For the Nanga Parbat assemblages, pressures and temperatures lay at about 720°C and 5 kbar at water activity, $a_{H_2O} \geq 0.6$. These conditions are consistent with a rapidly exhuming terrane, as suggested by isotopic constraints and thermal modelling of the region.

Crustal anatexis of metapelitic assemblages in the absence of a free fluid phase usually involves the breakdown of biotite and/or muscovite leading to the coexistence of a melt and anhydrous peritectic phases (Gardien *et al.* 1995; Le Breton & Thompson 1988; Patiño Douce & Johnston 1991; Vielzeuf & Holloway 1988). In Himalayan lithologies, Miocene leucogranites have been associated with sillimanite formation during the dehydration melting of muscovite (Harris *et al.* 1995), but temperatures were insufficient for biotite breakdown to occur. Cordierite–spinel metapelitic assemblages are reported here for the first time from the Himalayas. The significance of spinel formation and its possible relationship with melt formation are investigated, using standard thermobarometric techniques combined with theoretical calculations in the K_2O – FeO – MgO – Al_2O_3 – SiO_2 – H_2O (KFMASH) system.

The rocks we have used in this study are from the Nanga Parbat–Haramosh Massif in northern Pakistan (Fig. 1). The massif, which marks the western extremity of the High Himalayas, is a polymetamorphic terrain comprising granitic orthogneisses and psammitic, pelitic and

calcareous paragneisses which have experienced metamorphism both as part of the Indian craton, and more recently during the Himalayan orogeny. The most recent metamorphic episode is associated with rapid exhumation of the massif over the last 10 Ma (Zeitler *et al.* 1982; Zeitler 1985), which has led to leucogranite generation through fluid-absent muscovite breakdown (Zeitler & Chamberlain 1991; Butler *et al.* 1997; Whittington *et al.* 1998) and high- T low- P metamorphic assemblages containing cordierite, sillimanite and K-feldspar. These assemblages fall into two categories: cordierite–K-feldspar leucosomes localized in shear zones, and biotite–sillimanite–K-feldspar \pm spinel domains within migmatitic pelitic \pm gneisses. The leucosomes have been attributed to fluid infiltration and localized fluid-present melting in shear zones (Whittington *et al.* 1998). This paper investigates the origins of spinel-bearing domains in the pelitic gneisses.

Petrography

Metapelitic gneisses from the core of the Nanga Parbat Massif typically contain biotite, garnet,

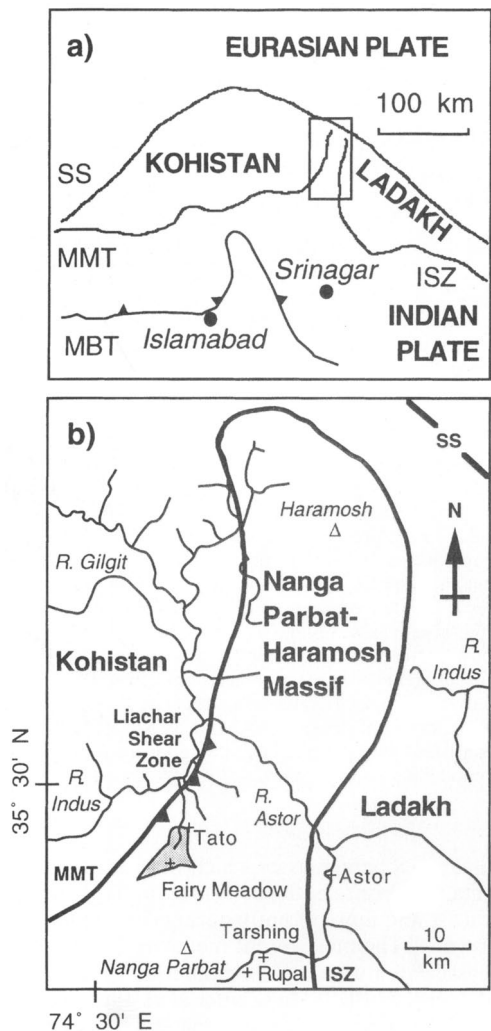
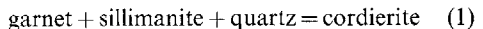


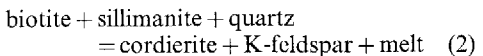
Fig. 1. Location maps for the sampled area. SS, Shyok Suture; MMT, Main Mantle Thrust; ISZ, Indus suture zone; MBT, Main Boundary Thrust. The rocks used in this study come from the Tato Valley, on the western margin of the massif (shaded area). At this point the western margin of the massif is marked by the Liachar Shear zone, still active.

sillimanite, quartz, K-feldspar and plagioclase, with cordierite commonly occurring, and more rarely green hercynitic spinel. Ilmenite, pyrite and apatite are common accessory phases, with rutile, magnetite, chalcopyrite, zircon and monazite occurring more rarely. Small (centimetre scale) granitic leucosomes are common in these gneisses and some melting is inferred to have occurred.

The most recent fabrics are defined by sheaves of biotite and sillimanite, wrapping around garnets which show inclusion trails at steep angles to foliation (Fig. 2a). This suggests that garnet was present before the most recent metamorphism. Garnet is often mantled by cordierite (Fig. 2b), which is not apparently associated with leucosome formation, and which is readily explained by the solid-state decompression reaction:



In many thin sections, biotite is observed to be breaking down in the presence of sillimanite. Microprobe investigation shows that cordierite-K-feldspar intergrowths are common. These textures may be explained by the reaction:



Carrington & Watt (1995) found that for the KFMASH system, reaction (2) was close to K-feldspar-absent degeneracy, and that K-feldspar was a reactant in experiments where the $\text{H}_2\text{O}/\text{K}_2\text{O}$ ratio in the melt was less than the $\text{H}_2\text{O}/\text{K}_2\text{O}$ ratio in reacting biotite. In previous experiments on reaction (2), where cordierite is a product, LeBreton & Thompson (1988) found K-feldspar was a product phase, but Vielzeuf & Holloway (1988) and Patiño Douce & Johnston (1991) found no K-feldspar generated by the reaction. While K-feldspar is common throughout Nanga Parbat metapelites, its occurrence as an intergrowth with cordierite suggests that in this case it is a reaction product.

In some sections, thin zones of cordierite-spinel intergrowths are seen intimately associated with decomposing biotite (Fig. 2c). Where spinel is found in these zones, quartz is absent or present only as inclusions within other phases, for example plagioclase, and hence is texturally isolated from reaction (2). All available quartz has been consumed within these domains, although quartz coexists with biotite elsewhere in the same thin section, indicating chemical disequilibrium on a very small (sub-centimetre) scale. Spinel can be clearly seen overgrowing biotite, and spinel-cordierite intergrowths also occur (Fig. 2d), hence both these phases are reaction products.

Mineral chemistry

In this paper we have studied several spinel-bearing assemblages through microprobe analyses of coexisting biotite, cordierite and spinel.

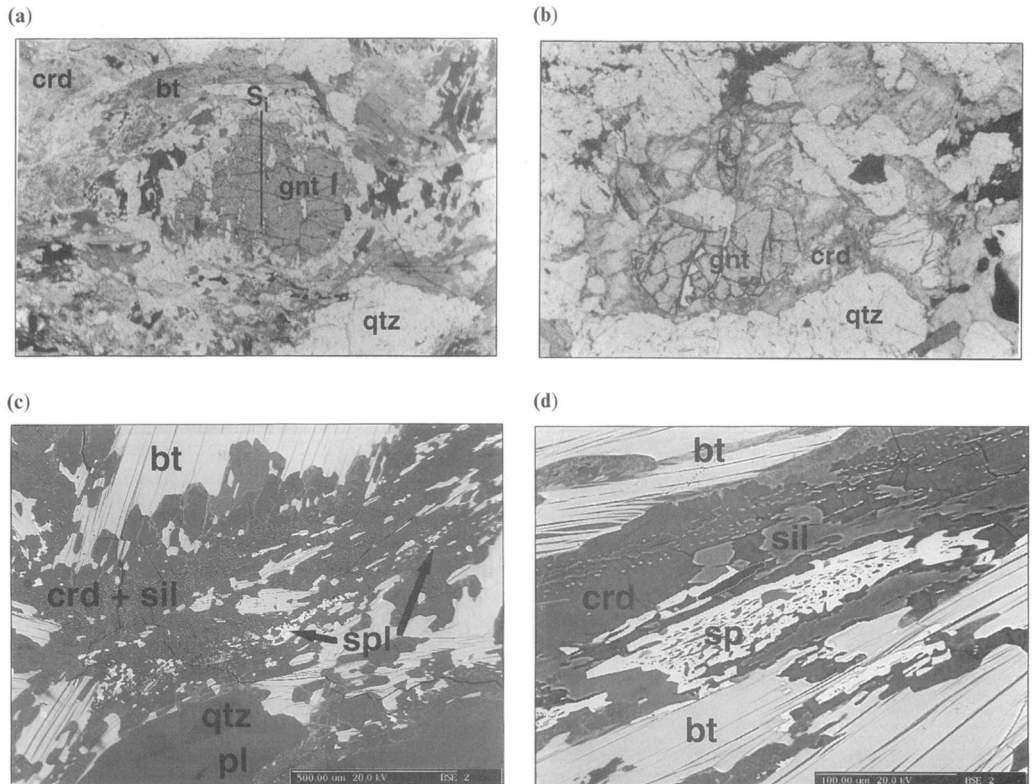


Fig. 2. Photomicrographs of thin sections, mineral abbreviations follow Kretz (1983). (a) Garnet showing inclusion trail (S_1) oriented at a steep angle to external foliation defined by biotite and sillimanite in the presence of quartz and cordierite. (b) Cordierite rimming garnet and biotite, which are breaking down. Plain polarized light; long dimensions of photographs are 3 mm. (c) Backscattered electron image of spinel-bearing zone, showing biotite and sillimanite breaking down, with intimately associated cordierite and spinel. Scale bar is 500 μ m. (d) Spinel-cordierite intergrowth, and spinel rimming decomposing biotite and sillimanite. Scale bar is 100 μ m.

Spinel data are given in Table 1, and representative analyses of all phases used in thermo-barometry are given in Table 2, including a silica-saturated biotite-cordierite-garnet metapelite (N1) for comparison. Of particular interest is the variation in mineral chemistry within a single thin section, depending on textural relations.

As an example, X8 is a spinel-bearing metapelite which also contains a garnet porphyroblast, rimmed by stable fabric-forming biotite and plagioclase. Biotite and plagioclase are also found as inclusions within the garnet, and biotite is observed breaking down in the presence of spinel elsewhere in the thin section. Garnet cores are of composition $alm_{76}prp_{15}grs_{5}sps_{4}$. Rims are less Mg-rich, but more Fe- and Mn-rich, with composition $alm_{79}prp_{11}grs_{4}sps_{6}$ where in contact with biotite. $Fe\#$ varies from 84 in the core to 89 in the rim, where $Fe\# = (\text{mol\% } Fe^{2+}) / (\text{mol\% } Fe^{2+} + \text{mol\% } Mg) \times 100$.

Biotite from X8 shows systematic variations in Fe number with its petrographic location (Table 2). Biotite inclusions in garnet have an average $Fe\#$ of 60, while biotite rimming garnet has an average $Fe\#$ of 65. Biotite analyses from the spinel zone show even higher $Fe\#$ of 67. Matrix plagioclase shows zoning, from about An_{28} in cores to An_{35} in rims. Plagioclase inclusions in garnet contain An_{30} , approximately the core composition of matrix plagioclase.

In spinel zones, cordierite has a fairly uniform composition within a single thin section, and even between different thin sections. Spinel has a limited range of Fe/Mg ratio, with $Fe\#$ varying only between 86 and 89, with only zinc abundances varying significantly. In contrast, biotite varies in composition across a single decomposing grain; for example X2 analyses 28 and 30 shows variation of $Fe\#$ between 59 and 64 in a

Table 1. Microprobe analyses of spinel from metapelitic assemblages at Nanga Parbat

	Z135r4 ave.	Z135r4 st dev.	Z147r1 ave.	Z147r1 st dev.	X8 ave.	X8 st dev.	X7 ave.	X7 st dev.	X2 ave.	X2 st dev.	004A ave.	004Cr1 ave.	004Cr2 ave.
Oxides													
SiO ₂	0.42	0.35	0.26	0.27	0.35	0.40	0.29	0.30	0.25	0.26	0.11	0.21	0.50
TiO ₂	0.09	0.02	0.12	0.03	0.11	0.04	0.11	0.03	0.12	0.03	0.04	0.07	0.03
Al ₂ O ₃	56.80	0.68	56.52	0.49	56.14	0.96	57.02	0.83	55.72	0.63	56.49	57.16	57.16
Cr ₂ O ₃	0.19	0.07	0.18	0.14	0.13	0.06	0.32	0.21	0.23	0.23	0.01	0.00	0.02
Fe ₂ O ₃	2.71	0.96	2.36	0.78	4.27	1.08	3.01	0.97	3.23	0.72	5.75	3.01	5.57
FeO	34.47	0.77	35.91	0.46	34.93	0.89	34.50	0.78	33.76	0.89	29.80	33.11	24.68
MnO	0.31	0.01	0.18	0.01	0.35	0.02	0.32	0.02	0.37	0.02	0.21	0.22	0.22
MgO	2.88	0.06	2.50	0.10	2.72	0.11	3.37	0.11	3.04	0.13	1.55	2.18	2.17
CaO	0.00	0.00	0.00	0.01	0.01	0.01	0.01	0.01	0.01	0.01	0.00	0.00	0.04
Na ₂ O	0.07	0.02	0.02	0.01	0.05	0.02	0.03	0.02	0.05	0.02	0.48	0.28	0.89
K ₂ O	0.00	0.00	0.05	0.05	0.09	0.09	0.04	0.02	0.05	0.05	0.04	0.02	0.00
ZnO	2.25	0.05	0.87	0.11	1.48	0.29	1.28	0.29	1.40	0.47	6.75	3.43	10.20
Total	100.11 (n = 17)		98.96 (n = 47)		100.61 (n = 34)		100.28 (n = 22)		98.20 (n = 63)		101.13 (n = 3)	99.65 (n = 3)	100.91 (n = 2)
Cations													
Si	0.012	0.010	0.008	0.008	0.010	0.011	0.008	0.008	0.007	0.007	0.003	0.006	0.014
Ti	0.002	0.000	0.002	0.001	0.002	0.001	0.002	0.001	0.002	0.001	0.000	0.001	0.001
Al	1.916	0.008	1.930	0.010	1.893	0.017	1.914	0.013	1.914	0.011	1.907	1.940	1.913
Cr	0.004	0.002	0.004	0.003	0.003	0.001	0.007	0.007	0.005	0.005	0.000	0.000	0.001
Fe ³⁺	0.059	0.021	0.051	0.017	0.092	0.024	0.065	0.021	0.071	0.016	0.132	0.065	0.119
Fe ²⁺	0.825	0.014	0.870	0.010	0.835	0.018	0.823	0.017	0.823	0.019	0.711	0.798	0.586
Mn	0.008	0.000	0.004	0.001	0.009	0.001	0.008	0.000	0.009	0.001	0.004	0.005	0.005
Mg	0.123	0.002	0.108	0.004	0.116	0.004	0.143	0.004	0.132	0.005	0.065	0.094	0.092
Ca	0.000	0.000	0.000	0.000	0.000	0.000	0.000	0.000	0.000	0.000	0.000	0.000	0.002
Na	0.004	0.001	0.001	0.001	0.003	0.001	0.002	0.001	0.003	0.001	0.031	0.015	0.049
K	0.000	0.000	0.002	0.002	0.003	0.003	0.001	0.001	0.002	0.002	0.000	0.001	0.000
Zn	0.048	0.001	0.019	0.002	0.031	0.006	0.027	0.008	0.030	0.010	0.141	0.073	0.214
Total	2.999	0.001	2.999	0.001	2.997	0.001	2.998	0.001	2.998	0.001	2.993	2.999	2.995
End-member activities ²													
Spinel	0.115	0.002	0.102	0.004	0.106	0.004	0.133	0.005	0.123	0.006	0.062	0.079	0.090
Hercynite	0.771	0.018	0.821	0.016	0.764	0.024	0.764	0.020	0.766	0.019	0.675	0.732	0.579
Gahnite	0.044	0.001	0.018	0.002	0.029	0.006	0.025	0.008	0.028	0.010	0.134	0.098	0.211
Galaxite	0.007	0.000	0.004	0.000	0.008	0.000	0.007	0.000	0.008	0.000	0.000	0.000	0.000
Fe# ³	87.0	0.3	89.0	0.4	87.8	0.5	85.2	0.6	86.2	0.6	91.6	89.1	87.5

¹ Fe³⁺ calculated by site allocation.² End-member activities assume ideal mixing.³ Fe# = (Fe²⁺)/(Fe²⁺ + Mg) cations.Analyses were carried out on a Cameca SX-100 at the Open University, and a Cameca SX-50 at Cambridge University (004A, 004C) using 1 μm beam size and 20 nA beam current.

Table 2. Representative mineral analyses used in thermobarometric calculations

Z135 spinel zone ¹				Z147 garnet rim ²				Z147 spinel zone ¹			
crd #42	spol #31	bt #135	ksp #119	gnt #136	plag #141	bt #144	ksp #166	bt #108	bt #108	bt #108	spol #47
SiO ₂	48.03	0.25	33.99	64.13	37.24	60.51	34.28	63.82	34.26	0.08	
TiO ₂	0.00	0.06	3.40	0.18	0.00	0.06	1.81	0.00	5.63	0.09	
Al ₂ O ₃	32.44	57.19	17.37	18.48	20.79	24.46	18.67	18.16	18.80	57.77	
Cr ₂ O ₃	0.00	0.18	0.07	0.00	0.05	0.03	0.07	0.04	0.05	0.18	
Fe ₂ O ₃	1.62	2.73	0.00	0.26	1.73	0.03	0.00	0.13	0.00	1.60	
FeO	9.57	34.30	23.54	0.00	32.65	0.00	20.21	0.00	22.29	36.29	
MnO	0.29	0.31	0.26	0.00	2.06	0.00	0.21	0.00	0.06	0.18	
MgO	6.58	2.83	6.92	0.00	4.21	0.00	9.07	0.00	6.38	2.42	
CaO	0.01	0.00	0.00	0.08	1.73	6.29	0.00	0.10	0.00	0.00	
Na ₂ O	0.26	0.07	0.13	2.76	0.00	7.74	0.42	1.95	0.17	0.02	
K ₂ O	0.00	0.00	9.33	12.93	0.02	0.47	9.37	14.02	9.23	0.03	
ZnO	n/a	2.28	n/a	n/a	n/a	n/a	n/a	n/a	n/a	0.90	
Totals	98.80	100.20	95.01	98.83	100.48	99.58	94.11	98.24	96.87	99.55	
Si	4.980	0.007	2.667	2.974	2.705	2.667	2.987	2.607	2.607	0.002	
Ti	0.000	0.001	0.201	0.006	0.000	0.002	0.106	0.000	0.322	0.002	
Al	3.966	1.927	1.607	1.010	1.955	1.289	1.712	1.002	1.687	1.956	
Cr	0.000	0.004	0.004	0.000	0.003	0.001	0.004	0.001	0.003	0.004	
Fe ²⁺	0.126	0.059	0.000	0.009	0.104	0.001	0.004	0.000	0.000	0.034	
Fe ²⁺	0.830	0.820	1.545	0.000	2.178	0.000	1.315	0.000	1.419	0.872	
Mn	0.026	0.008	0.017	0.000	0.139	0.000	0.014	0.000	0.004	0.004	
Mg	1.017	0.121	0.809	0.000	0.500	0.000	1.052	0.000	0.724	1.044	
Ca	0.002	0.000	0.000	0.004	0.148	0.301	0.000	0.005	0.000	0.000	
Na	0.053	0.004	0.020	0.248	0.000	0.670	0.064	0.177	0.024	0.001	
K	0.000	0.000	0.935	0.766	0.002	0.027	0.931	0.838	0.897	0.001	
Zn	n/a	0.048	n/a	n/a	n/a	n/a	n/a	n/a	n/a	0.019	
Sum	11.000	2.999	7.804	5.017	4.996	8.000	5.016	7.687	3.000	66.2	
Fe#	44.9	87.2	65.2	81.3	65.2	81.3	65.2	81.3	65.2	81.3	89.3

Table 2 (continued)

crd #53	X2 spinel zone ¹				X2 garnet rim ³				X7 garnet rim ³				X7 spinel zone ¹			
	bt #28	bt #30	spl #36	ksp #6	bt #7	gnt #9	bt #7	ksp 4rl	plag #23	plag 4rl	gnt 2.2	bt 2.1	spl #198	fsp #222	bt #175	
SiO ₂	47.24	34.17	38.29	0.88	65.37	37.11	34.14	60.15	65.10	61.08	37.01	33.97	0.07	52.31	34.09	
TiO ₂	0.00	3.16	3.06	0.12	0.00	0.07	2.98	0.00	0.00	0.00	2.06	0.09	0.07	5.38		
Al ₂ O ₃	32.25	20.12	21.82	56.57	18.34	20.98	17.75	24.48	18.75	24.25	20.74	17.50	56.95	35.16	18.77	
Cr ₂ O ₃	0.00	0.12	0.12	0.10	0.00	0.02	0.00	0.00	0.00	0.00	0.11	0.00	0.13	0.00	0.27	
Fe ₂ O ₃	2.10	3.17	0.00	2.00	0.00	0.49	0.00	0.19	0.07	0.00	0.41	2.85	3.72	1.81	0.00	
FeO	8.59	19.77	20.08	35.75	0.00	33.97	23.71	0.00	0.00	0.00	33.60	22.17	34.54	0.00	22.37	
MnO	0.32	0.22	0.12	0.36	0.00	3.64	0.18	0.04	0.03	0.02	4.21	0.31	0.30	0.01	0.09	
MgO	6.98	7.75	6.21	3.17	0.00	3.16	7.52	0.00	0.00	0.00	2.63	7.75	3.49	0.72	6.78	
CaO	0.04	0.06	0.10	0.10	0.10	0.10	1.17	0.00	6.98	0.11	6.02	1.46	0.03	0.00	0.00	
K ₂ O	0.17	0.19	0.22	0.03	1.81	0.00	0.20	7.66	1.77	0.00	0.23	0.23	0.01	0.31	0.18	
K ₂ O	0.01	6.56	8.24	0.01	14.53	0.00	9.47	0.51	13.77	0.63	0.00	8.64	0.01	8.79	9.23	
ZnO	n/a	n/a	n/a	1.17	n/a	n/a	n/a	n/a	n/a	n/a	n/a	n/a	n/a	n/a	n/a	
Totals	97.70	95.30	98.26	100.16	100.16	100.61	95.96	100.01	99.61	99.71	100.17	95.51	100.02	99.22	97.17	
Si	4.945	2.591	2.778	0.025	3.000	2.980	2.652	2.687	2.992	2.724	2.992	2.644	0.002	2.378	2.591	
Ti	0.000	0.180	0.167	0.003	0.000	0.004	0.174	0.000	0.000	0.000	0.000	0.121	0.002	0.002	0.307	
Al	3.980	1.798	1.866	1.903	0.992	1.986	1.626	1.289	1.016	1.275	1.977	1.606	1.915	1.884	1.682	
Cr	0.000	0.007	0.007	0.002	0.000	0.001	0.000	0.000	0.000	0.000	0.007	0.000	0.003	0.000	0.016	
Fe ³⁺	0.165	0.181	0.000	0.043	0.000	0.030	0.000	0.006	0.002	0.000	0.025	0.167	0.080	0.062	0.000	
Fe ²⁺	0.752	1.254	1.218	0.853	0.000	2.281	1.541	0.000	0.000	0.000	2.272	1.443	0.824	0.000	1.422	
Mn	0.028	0.014	0.007	0.009	0.000	0.248	0.012	0.002	0.001	0.001	0.288	0.020	0.007	0.000	0.006	
Mg	1.090	0.876	0.671	0.135	0.000	0.378	0.871	0.000	0.000	0.000	0.317	0.899	0.148	0.049	0.768	
Ca	0.005	0.008	0.000	0.005	0.101	0.000	0.334	0.005	0.288	0.127	0.003	0.000	0.001	0.000	0.000	
Na	0.035	0.027	0.031	0.002	0.161	0.000	0.030	0.664	0.158	0.667	0.000	0.035	0.001	0.027	0.027	
K	0.001	0.635	0.763	0.000	0.852	0.000	0.940	0.029	0.808	0.036	0.000	0.859	0.000	0.510	0.896	
Zn	n/a	n/a	n/a	0.025	n/a	n/a	n/a	n/a	n/a	n/a	n/a	n/a	0.015	n/a	n/a	
Sum	11.000	7.568	7.516	2.999	5.010	8.008	7.846	5.011	4.982	8.004	7.796	84.8	2.998	4.915	7.715	
Fe#	40.8	58.9	64.5	86.4	—	85.8	63.9	—	—	87.8	61.6	84.8	—	64.9	—	

Table 2 (continued)

	X8 spinel zone ¹			X8 garnet core ³			X8 garnet rim ³			N1 garnet rim ³		
	spl #53	bt #4/1	bt #6/3	bt 5c3	gnt #2/2	plag #8/3	bt #3r4	plag #1/2	crd crd.2/3	gnt gnt.2/2	ksp ksp.1r2	bt bt.1/1
SiO ₂	0.40	33.59	34.80	37.81	60.99	34.77	37.38	60.39	47.56	36.20	64.86	33.97
TiO ₂	0.10	4.45	4.27	0.00	0.96	0.06	0.00	0.00	0.03	0.03	0.00	4.13
Al ₂ O ₃	55.43	18.54	18.73	21.42	23.99	18.69	20.99	25.18	31.88	20.80	18.61	18.58
Cr ₂ O ₃	0.26	0.00	0.00	0.00	0.00	0.00	0.09	0.00	0.02	0.02	0.00	0.00
Fe ₂ O ₃	4.24	0.00	0.00	0.00	0.29	0.00	0.54	0.17	0.00	0.61	0.40	0.00
FeO	35.00	23.43	21.21	34.02	0.00	25.31	35.22	0.00	11.07	36.93	0.00	22.54
MnO	0.37	0.13	0.05	2.44	0.06	0.12	1.91	0.00	0.06	1.85	0.06	0.10
MgO	2.58	6.49	7.92	3.69	0.00	7.11	3.20	0.00	6.43	2.02	0.00	6.64
CaO	0.01	0.00	0.05	1.69	6.28	0.00	1.69	7.36	0.00	1.39	0.08	0.00
Na ₂ O	0.04	0.20	0.26	n/a	7.93	0.26	0.00	7.35	0.22	0.00	2.95	0.28
K ₂ O	0.05	9.37	8.87	n/a	0.66	8.92	0.00	0.54	0.00	0.00	12.38	9.28
ZnO	1.50	n/a	n/a	n/a	n/a	n/a	n/a	n/a	n/a	n/a	n/a	n/a
Totals	99.96	96.20	96.16	101.09	100.21	96.14	101.08	101.01	97.22	99.83	99.34	95.52
Si	0.012	2.599	2.646	2.999	2.717	2.696	2.984	2.671	5.018	2.958	2.983	5.262
Ti	0.002	0.259	0.244	0.000	0.000	0.057	0.003	n/a	0.000	0.002	0.000	0.481
Al	1.885	1.690	1.679	2.002	1.259	1.708	1.975	1.313	0.977	2.003	1.009	3.393
Cr	0.006	0.000	0.000	0.000	0.000	0.000	0.006	n/a	0.000	0.001	0.000	0.000
Fe ³⁺	0.092	0.000	0.000	0.000	0.010	0.000	0.033	0.006	0.000	0.038	0.014	0.000
Fe ²⁺	0.844	1.516	1.349	2.256	0.000	1.642	2.351	0.000	0.977	2.524	0.000	2.921
Mn	0.009	0.004	0.004	0.164	0.002	0.008	0.129	0.000	0.006	0.128	0.002	0.013
Mg	0.111	0.749	0.898	0.436	0.000	0.822	0.381	0.000	1.012	0.246	0.000	1.533
Ca	0.000	0.000	0.004	0.144	0.300	0.000	0.144	0.349	0.000	0.122	0.004	0.000
Na	0.002	0.030	0.038	n/a	0.685	0.040	n/a	0.630	0.045	0.000	0.263	0.083
K	0.002	0.926	0.861	n/a	0.038	0.883	n/a	0.030	0.000	0.000	0.727	1.835
Zn	0.032	n/a	n/a	n/a	n/a	n/a	n/a	n/a	n/a	n/a	n/a	n/a
Sum	2.997	7.775	7.721	8.001	5.010	7.855	8.006	5.000	11.022	8.020	5.001	19.520
Fe#	88.4	67.1	60.1	84.7	—	66.8	86.8	—	49.1	91.1	—	65.6

Analyses were carried out on: ¹a Cameca SX-100 at the Open University using a 1 μm beam size and 20 nA beam current; ²a Cameca SX-50 at Cambridge University using a 20 μm beam size and 20 nA beam current; ³a Cameca SX-50 at Leeds University using a 20 μm beam size and 20 nA beam current. n/a, not analysed Fe³⁺ by site allocation

single grain. Holtz & Johannes (1991), and Patiño Douce & Johnston (1991) reported that biotite compositions in equilibrium with a melt become more Mg-rich as biotite melting progresses. Since unmelted matrix biotite from this same thin section has an $Fe\#$ of 64, this was probably the original biotite composition, and the more Mg-rich composition from the spinel zone reflects the coexistence of a melt. Furthermore, Patiño Douce & Johnston (1991) noted an increase in TiO_2 content of biotite with increasing temperature, and biotites from spinel-bearing zones at Nanga Parbat are also more Ti-rich than biotites from garnet-bearing zones (e.g. Z147 and X7, Table 2).

Spinel stability

The presence of spinel in metapelitic assemblages has been accredited to a number of factors. At temperatures greater than $900^\circ C$ and pressures less than 8 kbar, spinel is stable in the presence of quartz and cordierite following garnet breakdown (Hensen & Green 1973). The stability field of spinel may be extended to lower temperatures by the presence of additional components such as ferric iron (Dasgupta *et al.* 1995) and chromium, which substitute for aluminium, or zinc (Dasgupta *et al.* 1995; Nichols *et al.* 1992; Waters 1991), which substitutes for iron and magnesium. In such cases, spinel cannot be used as a guide to metamorphic grade in petrogenetic grids constructed in the KFMASH system, which can strictly only account for the hercynite ($FeAl_2O_4$) and spinel *sensu stricto* ($MgAl_2O_4$) end-members.

Microprobe analyses in Table 1 have been recalculated by site allocation to estimate the ferrous/ferric iron ratios in spinel. Ferric iron averages between 3 and 5 wt% of spinel, comprising less than 10% of trivalent cations. Zinc, chromium and titanium occur in concentrations of up to 10.3, 1.2 and 0.3 wt% respectively. Zinc is clearly the most significant component outside the KFMASH system.

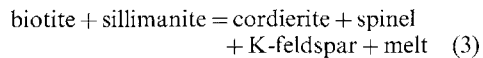
The gahnite end-member ($ZnAl_2O_4$) may have an activity of up to 0.214 in spinel from these rocks, while coexisting phases contain no detectable zinc. Within a single domain, on the scale of a few millimetres, zinc concentrations are relatively constant, although zinc concentrations vary considerably between different samples and even between different domains in the same thin section (e.g. sample 004 rings 1 and 2, Table 1), suggesting a local bulk compositional control. However, since in some sections spinel contains an average of less than 1 wt% of zinc (e.g. sample Z147, Table 1), it appears unlikely

that spinel is stabilized primarily by the zinc content of the rock. Rather, it has scavenged available zinc during its formation (Stoddard 1979). This view is supported by the lack of correlation between zinc content and modal abundance of spinel.

Thus spinel does not appear to be stabilized primarily by significant components outside the hercynite–spinel solid-solution series, and its stability can be investigated within the KFMASH system.

Phase equilibria

For the AFM diagram (Fig. 3a), the coexistence of cordierite–sillimanite biotite is illustrated in the presence of K-feldspar, quartz and granitic liquid (Fig. 3b). However, the coexistence of spinel and cordierite in the absence of quartz suggests a new spinel–cordierite tie-line. The relative Fe/Mg ratios of the ferromagnesian phases can be seen to be $Fe\#_{spl} > Fe\#_{bt} > Fe\#_{crd}$ (Table 2). This implies that biotite and sillimanite coexist with cordierite and spinel in the absence of quartz through the reaction:



Alternatively, it could be argued that spinel is not a product of a quartz-absent melting reaction, but is a reactant in the production of cordierite from the solid-state reaction:



Whilst this accounts for the incompatibility between spinel and quartz, it does not explain the complex intergrowths between spinel and cordierite as apparent reaction products of biotite breakdown (Fig. 2d). Reaction (4) should lead to cordierite rims separating spinel from quartz-rich domains which are not observed.

We can further explore quartz-absent stability through the HS(FM) diagram (Fig. 3c) which can illustrate the effect of changing bulk silica and water content on phase compatibilities. On this diagram it is clear that as H_2O and/or SiO_2 contents decrease, the stable assemblage for the given bulk composition will change from biotite–cordierite–quartz to biotite–cordierite–spinel. The local stability of spinel may then be explained if melting occurs and melt is removed, which will reduce the H_2O content of the rock since melts are significantly more hydrous than the bulk rock, leading to the assemblage biotite–cordierite–spinel. Some compositional variation within Nanga Parbat metapelites has been observed on a sub-centimetre scale as banding

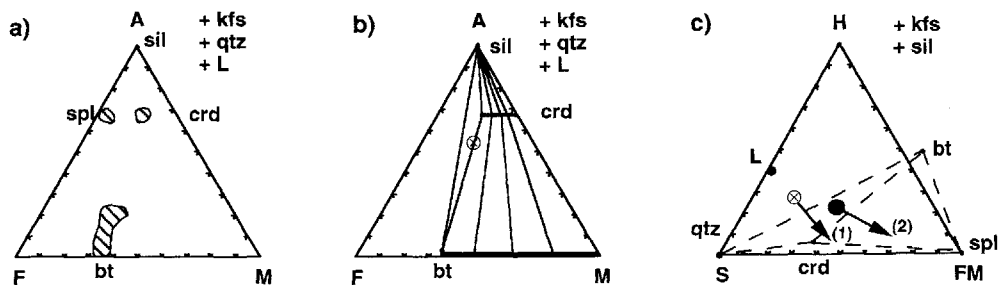


Fig. 3. $\text{AlO}_{1.5}$ – FeO – MgO and $\text{HO}_{1.5}$ – SiO_2 –($\text{FeO} + \text{MgO}$) diagrams for Z135. Phase compositions in Table 2. The crossed circle indicates the bulk composition of Z147, a typical spinel-bearing metapelite, measured by XRF analysis. (a) AFM diagram projected from quartz, liquid and K-feldspar, showing composition fields (striped) of all phases analysed in spinel-bearing zones. The average leucogranite of Whittington *et al.* (1998) was used for the liquid composition in all diagrams, assuming a water content of 7 wt%. (b) AFM diagram showing phases analysed in a spinel-bearing zone of Z135. Tie-lines drawn for coexistence of biotite–cordierite–sillimanite, as observed outside spinel-bearing zones. (c) HS(FM) composition diagram showing phase analyses from Z135. In order to achieve the assemblage biotite–cordierite–spinel, the bulk composition of Z147 requires reduction of the water content, which may be achieved by removal of melt. This process is illustrated by arrow (1). More mafic compositions (solid circle) will have both silica and water contents reduced by melt removal, shown by arrow (2). Note that because FeO and MgO should be considered as separate components, the three-phase triangles shown (dashed lines) are actually four-phase tetrahedra with L as the fourth phase.

visible in hand specimen, and removal of melt from a silica-poor band will result in movement away from both H and S apices (Fig. 3c).

Unfortunately it is not possible to show separate FeO and MgO components (in addition to SiO_2 and water) rigorously on a two-dimensional ternary plot. The extra degree of freedom generated by separate consideration of FeO and MgO components is accounted for by the coexistence of a liquid phase (L) with each of the three-phase assemblages shown in Fig. 3c.

We conclude that anatexis and melt removal will favour the formation of spinel in the restite, as has been invoked by Srogi *et al.* (1993) for similar anatexic assemblages from the Wilmington complex, although Fig. 3 suggests the role of melt in removing silica may be less significant than its effect in depleting H_2O content. In the Wilmington example silica depletion was more marked, and corundum was stabilized locally within restitic melanosomes.

KFMASH petrogenetic grid

The K_2O – FeO – MgO – Al_2O_3 – SiO_2 – H_2O (KFMASH) system incorporates the major chemical components in pelitic rocks. It is, however, a simplification of the natural system: omission of TiO_2 and Fe_2O_3 from KFMASH precludes consideration of the Fe-Ti oxides, and omission of CaO and Na_2O precludes consideration of plagioclase and natural granitoid melts.

The KFMASH grid for dehydration melting of biotite at moderate pressures (>5 kbar) has been established by Powell & Downes (1990) and Hensen & Harley (1990), and developed at higher temperatures by Carrington & Harley (1995). In this study we have extended this grid to lower pressures, where cordierite rather than garnet is the stable peritectic phase under vapour-absent conditions in normal pelitic bulk compositions. We have also investigated equilibria under quartz-absent conditions.

A low-pressure KFMASH grid is shown in Fig. 4, assuming excess orthoclase and sillimanite. The grid was constructed for $\text{Fe}^\#$ (Spl) $>$ $\text{Fe}^\#$ (Gnt) $>$ $\text{Fe}^\#$ (L) $>$ $\text{Fe}^\#$ (Bt) $>$ $\text{Fe}^\#$ (Crd), in accordance with analysed minerals from Nanga Parbat (Table 2). The average leucogranite of Whittington *et al.* (1998) was used for the liquid composition. Invariant points in the KFMASH system and in the KMASH system are linked by a univariant line in the KFMASH system, so that for example f2 and m2, which are both garnet-, muscovite-, orthopyroxene- and spinel-absent, are linked by the KFMASH univariant reaction (2). The single KFMASH invariant point (marked 1), is vapour-, muscovite-, and spinel-absent, and has been fixed in P – T space at about 890–910°C and 9 kbar (Carrington & Harley 1995).

The shaded low-temperature field between the KFMASH and KMASH end-member reactions represents the water-saturated solidus for bulk compositions of intermediate Fe/Mg ratio.

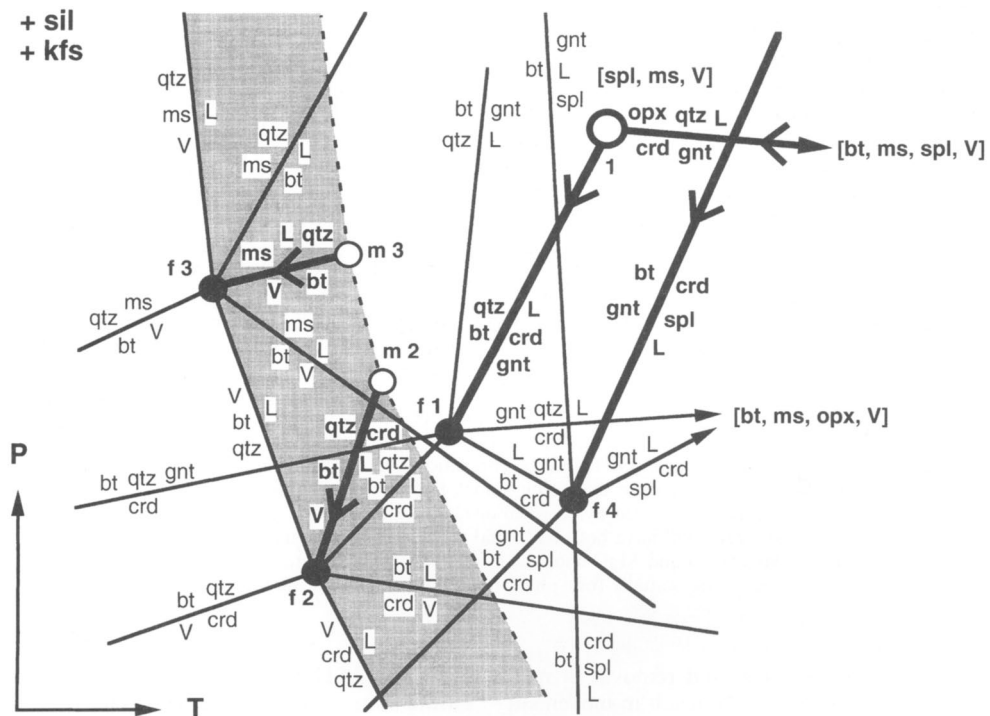
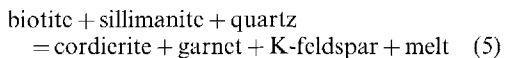


Fig. 4. Low-pressure petrogenetic grid for metapelites in the KFMASH system, assuming excess orthoclase and sillimanite, adapted from Powell & Downes (1990) to allow for silica-undersaturation. Other mineral abbreviations follow Kretz (1983), with melt phase (L) and vapour phase (V). Solid lines are univariant reactions in KFASH, and thick solid lines are univariant reactions in KFMASH. Large arrows indicate direction of increasing Fe. Filled circles are invariant points in KFASH (f1, etc.), open circles are invariant points in KMASH (m1, etc.), and the bold open circle is invariant point 1 in KFMASH. The shaded field is the zone of water-saturated melting for compositions between pure Fe- and Mg-end-members. Invariant points are: f1, m1 [ms, opx, spl, V]; f2, m2 [gnt, ms, opx, spl]; f3, m3 [crd, gnt, opx, spl] and f4 [qtz, ms, opx, V].

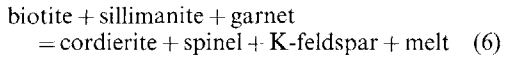
The reaction linking f2 and f3 is annite + sillimanite + quartz + V = melt, and occurs at higher temperatures for phlogopite + sillimanite + quartz + V = melt, which links m2 and m3. At higher pressures than f3-m3, muscovite is a reactant during vapour-present melting, and at lower pressures than f2-m2, cordierite is a reactant during vapour-present melting. None of these reactions leads to cordierite or spinel as product phases, suggesting that if spinel is a peritectic phase, melting must have been vapour-undersaturated (i.e. at higher temperatures, and to the right of, the shaded field). The KFASH invariant point f2 has been fixed in $P-T$ space at around 725°C and 2.5 kbar (Vielzeuf & Holloway 1988, fig. 5). This is a considerably higher temperature than the water-saturated haplogranite solidus, because f2 was determined for the Na-absent KFASH system. A quartz-absent invariant point (f4) occurs at the intersection

between the quartz-absent reactions from f1, and from a higher temperature KFASH invariance [bt, ms, opx] which stabilizes the coexistence of spinel and quartz.

In the full KFMASH system, there are two vapour-absent univariant reactions relevant to the Nanga Parbat assemblages:



linking f1 and l, and:



This reaction is terminated at low pressures by the KFASH invariant point f4, which is both vapour-absent and quartz-absent. With increasing temperature, crossing reaction (5) consumes quartz and produces peritectic cordierite, consistent with assemblages at Nanga Parbat.

Reaction (6) consumes both biotite and garnet, and results in cordierite and spinel forming as peritectic phases with a melt.

The absence of garnet in the Nanga Parbat assemblages results from low pressures during prograde metamorphism, as can be illustrated by a *P-T* pseudosection constructed for a fixed bulk composition of intermediate Fe# (Hensen 1971), between pure KFASH and pure KMASH end-member reactions (Fig. 5), after Powell and Downes (1990). A qualitative *P-T* path for Nanga Parbat rocks in the pseudosection has been drawn (X-Y on Fig. 5), illustrating the change in mineralogy consistent with petrographic observation. This path does not extend into the orthopyroxene field, because we have found no evidence for orthopyroxene in these assemblages.

For assemblages at 'X', a melt will be present only if fluid-present conditions prevail. Under fluid-absent conditions, with either an increase in temperature or decompression, fluid-absent melting results in the formation of cordierite as the cordierite-biotite-quartz-melt field is entered, from reaction (2). Note that for higher Fe/Mg ratios or pressures, both garnet and cordierite would be formed. For compositions of low to moderate bulk SiO₂ content, melting will exhaust quartz, and spinel is formed as the cordierite-biotite-spinel-melt field is entered from reaction (3). Further increase in temperature and/or decompression results in biotite-absent cordierite-spinel assemblages, which are

not observed. The presence of minor non-KFMASH components in biotite, such as Ti and F, will contribute to the broadening of this reaction interval in natural systems.

Thermobarometry

Petrogenetic grid topologies of potential reactions provide essential constraints on qualitative *P-T* paths. However, with only two points on the KFMASH grid of Fig. 4 fixed experimentally, quantitative *P-T* information on the Nanga Parbat assemblages requires thermobarometry based on analysed activities from coexisting phases. To calculate pressure and temperature conditions, we have used version 2.4 of the Thermocalc program (Powell & Holland 1988) and the extended internally consistent thermodynamic dataset of Holland & Powell (1990).

The early metamorphic history of the Nanga Parbat assemblages may be constrained by garnet-bearing assemblages. X8 is a spinel-bearing metapelite which also contains garnet with inclusions of biotite, plagioclase and quartz. The garnet is rimmed by stable fabric-forming biotite apparently in textural equilibrium with garnet, in contrast to biotite found in spinel-bearing zones in the same thin section, which is breaking down. Biotite rimming garnet has a low Ti content of less than 1 wt%, in contrast to biotite in the spinel zone which has a Ti content of over 4 wt%, and hence may have grown via retrograde garnet breakdown.

Average (*P-T*) conditions for the core and rim were computed by Thermocalc using the end-members almandine, pyrope, grossular, anorthite, orthoclase, annite, phlogopite, sillimanite and quartz, and a range of water activities under fluid-absent conditions. Analyses of phase compositions used in calculations are provided in Table 2. These calculations suggest conditions of $720 \pm 50^\circ\text{C}$ at $7.6 \pm 1.5 \text{ kbar}$ for the core, and $670 \pm 40^\circ\text{C}$ at $6.3 \pm 0.4 \text{ kbar}$ for the rim, assuming a water activity of 0.9. For a water activity of 0.5, the results are $655 \pm 50^\circ\text{C}$ at $6.7 \pm 1.7 \text{ kbar}$ for the core, and $610 \pm 40^\circ\text{C}$ at $5.5 \pm 1.3 \text{ kbar}$ for the rim. The differences in *P-T* conditions between core and rim are within error, but probably represent some decompression and cooling.

For determining conditions during melt formation, thermobarometry on the cordierite-spinel assemblages is required. From petrographic observation, we infer that some degree of partial melting during fluid-absent biotite breakdown has occurred. The presence of a melt phase makes thermobarometric calculations on

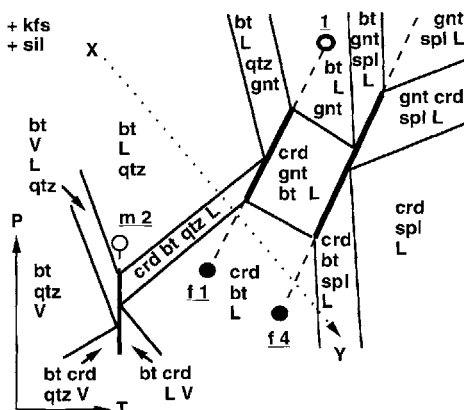


Fig. 5. *P-T* pseudosection constructed for a fixed intermediate bulk composition, adapted from Powell & Downes (1990) to allow for silica-undersaturation. Mineral abbreviations and invariant point symbols as for Fig. 4. Dotted line X-Y is a qualitative *P-T* path for Nanga Parbat rocks consistent with petrographic observation.

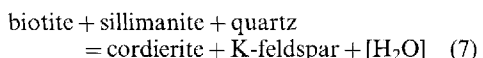
these assemblages more problematic, as it is not currently possible to introduce a melt phase to Thermocalc without further experimental constraints (Holland *et al.* 1996). However, both solid-phase equilibria and melt must coexist under conditions of identical water activities. Hence if P - T fields from solid phases are calculated for a range of water activities, $a_{\text{H}_2\text{O}}$, and overlain on the granite solidi determined at varying $a_{\text{H}_2\text{O}}$, both solids and melt will coexist where water activities for the melt and for the mineral assemblage are equal (Fig. 6; cf. Waters 1991, fig. 4).

Calculations were conducted on a spinel-cordierite metapelite (Z135) using the analyses listed in Table 2. Calculated end-member activities and P - T results are listed in Table 3, using a silica activity of 0.95 to represent the quartz-absent nature of the assemblage. For this rock, the minimum water activity required for the biotite-cordierite-spinel assemblage to coexist with a melt is 0.5 at conditions of $687 \pm 58^\circ\text{C}$ at 4.6 ± 1.0 kbar, although if the 2 sigma uncertainties on the P - T results are considered, $a_{\text{H}_2\text{O}}$ could be as low as 0.4 (Fig. 6). The actual intersection is at a water activity of 0.6, suggesting conditions of $710 \pm 60^\circ\text{C}$ at 5.0 ± 1.1 kbar.

Although such a water activity could be achieved from the hydroxyl component of biotite that is released as water on biotite breakdown,

these temperatures are significantly below those obtained from experimental studies of biotite breakdown under fluid-absent conditions (Gardien *et al.* 1995; Patiño Douce & Johnston 1991; Vielzeuf & Holloway 1988). Low pressures and Fe-rich bulk compositions will enable melting to occur at lower temperatures, but there is no evidence to suggest that dehydration melting of biotite at 5 kbar can occur below 800°C . We infer that some fluid ingress is required to allow limited melting. In other words, while final equilibration of the analysed assemblage probably took place at a water activity of about 0.6 (Fig. 6), a higher water activity was probably required to initiate melting at the P - T conditions encountered by rocks from Nanga Parbat, followed by buffering of the water activity by the melt phase at about 0.6. Similar calculations for a cordierite-bearing leucosome indicate that $a_{\text{H}_2\text{O}}$ must have been at least 0.7 and probably greater than 0.9 for melting to occur, consistent with fluid-present melting localized in shear zones (sample Z130; Whittington *et al.* 1998).

Quantitative P - T constraints for the petrogenetic grid (Fig. 4) can now be obtained by considering biotite breakdown reaction (2). If it is assumed that water activity is buffered by the melt, rather than being externally controlled, the reaction can be constrained in P - T space (Fig. 7), following the approach of Waters (1991). This will be valid even with limited influx of external fluid, provided the water activity remains buffered by the melt. Such an approach can only be applied to reaction (2), since the granitic solidi are for a silica-saturated melt. Some uncertainty is introduced in this case since the granitic solidi are for the sodium-bearing NaKASH system, whereas the reaction is calculated in KFMASH. K-feldspar will be the only phase sensitive to Na content, and an orthoclase activity of 0.752 was used in the calculation, from analysis #119 (Table 2). The addition of components FeO and MgO to NaKASH would reduce the temperatures of the granitic solidi by only a few degrees, within the error of thermobarometric calculations. The melt-free equivalent of reaction (2) is:



When calculated for coexisting phases from Z135, this reaction occurs at 720°C at 5 kbar for a melt-buffered water activity of 0.6, in excellent agreement with average $(P$ - T) calculations (Fig. 7).

Hence P - T conditions during partial melting are constrained between about 650 and 770°C , at between 3.9 and 6.1 kbar. It is not possible to

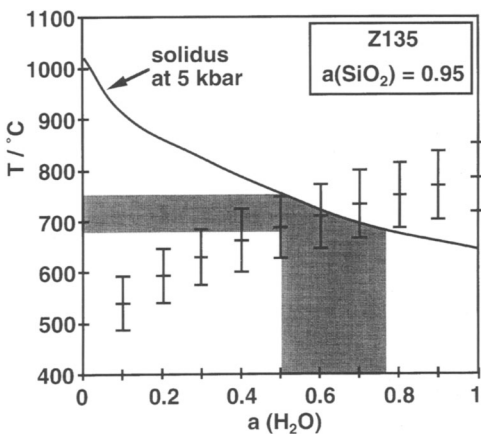


Fig. 6. Average $(P$ - T) calculations for a spinel-bearing assemblage (Z135) for $a_{\text{SiO}_2} = 0.95$ and variable $a_{\text{H}_2\text{O}}$, compared with the 5 kbar haplogranite solidi of Johannes & Holtz (1990). End-member activities and results of calculations are listed in Table 3, and error bars shown are ± 1 sigma. This indicates that $a_{\text{H}_2\text{O}}$ must have been greater than 0.4 for melting to have occurred (allowing 2 sigma errors), and probably lay within the range 0.5 to 0.7, at temperatures between 700 and 760°C (shaded bands).

Table 3. End-member activities and Thermocalc P-T results

Endmember activities

Mineral	End-member	Formula	Activity ¹
Biotite	phlogopite	KMg ₃ Si ₃ AlO ₁₀ (OH) ₂	0.0162
	annite	KFe ₃ Si ₃ AlO ₁₀ (OH) ₂	0.113
Cordierite	Fe-cordierite	Fe ₂ Si ₅ Al ₄ O ₁₈	0.196
	Mg-cordierite	Mg ₂ Si ₅ Al ₄ O ₁₈	0.295
Spinel ²	hercynite	FeAl ₂ O ₄	0.772
	spinel	MgAl ₂ O ₄	0.113
K-feldspar	orthoclase	KAlSi ₃ O ₈	0.752
Sillimanite		Al ₂ SiO ₅	1
Quartz		SiO ₂	variable
Fluid	water	H ₂ O	variable

Thermocalc P-T calculations³

a(H ₂ O)	T (°C)	sd	P (kbar)	sd	cor ⁴	f ⁵
1.0	785	66	6.3	1.2	0.87	1.18
0.9	768	64	6.0	1.2	0.86	1.18
0.8	750	63	5.7	1.1	0.86	1.19
0.7	731	61	5.3	1.1	0.85	1.20
0.6	710	59	5.0	1.1	0.84	1.22
0.5	687	58	4.6	1.0	0.84	1.24
0.4	661	56	4.3	1.0	0.83	1.26
0.3	631	54	3.8	1.0	0.82	1.29
0.2	593	52	3.4	0.9	0.81	1.34
0.1	539	49	2.9	0.9	0.79	1.44

¹ Activities were calculated using the 'ax' program written by T. Holland, using mixing models from Holland and Powell (1990) and references therein.

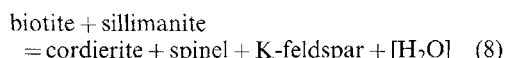
² Spinel activities assume ideal mixing, ferric iron calculated by site allocation.

³ Calculations assume fluid-absent conditions, and include all end-members listed above, with fixed a(SiO₂) = 0.95 and variable a(H₂O).

⁴ Correlation between P and T. These values indicate significant correlation, and hence an elongate error ellipse.

⁵ Statistical fit parameter. All results are statistically acceptable.

calculate reaction (3) until a silica-undersaturated liquid phase can be introduced to Thermocalc, but it is expected to occur at higher temperatures and/or lower pressures than reaction (2), from the petrogenetic grid (Fig. 4). The melt-absent equivalent reaction is:



This reaction was calculated for Z135, and occurs at temperatures a few tens of degrees higher than reaction (7) for pressures less than 6 kbar, as predicted.

Discussion

The P-T-a_{H2O} constraints obtained from thermodynamic considerations can be related to the tectonothermal history of the Nanga Parbat-Haramosh Massif. Thermal modelling of Nanga

Parbat suggests a very steep decompression path, attributed to rapid erosion in the absence of extensional structures (Whittington 1996). P-T estimates from Thermocalc do not appear to record higher pressure stages of this path in many pelitic rocks, probably due to peak temperatures being maintained throughout most of the decompression history.

Thermobarometry on biotite and plagioclase inclusions records early garnet growth at about 720°C and 7.6 kbar (A, Fig. 8) with final garnet-rim equilibration at 670°C and 6.3 kbar (B, Fig. 8). Water activities are likely to have been close to unity prior to melting, due to sub-solidus dehydration reactions, hence calculations assuming a_{H2O} of 0.9 are shown. If a_{H2O} is assumed to be 0.5 then calculated pressures and temperatures are reduced by 0.8 kbar and 60°C respectively for both sets of calculations. Independent of assumed a_{H2O}, the difference between core and rim conditions is about

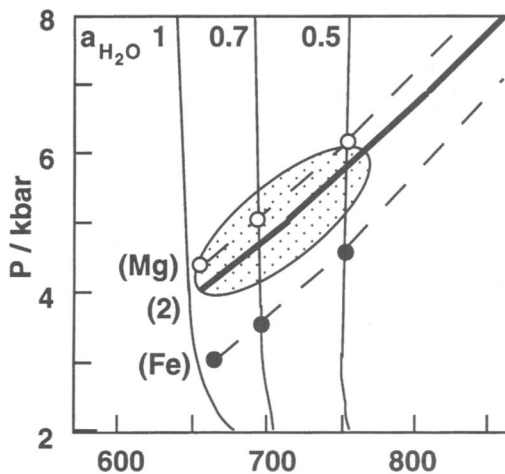
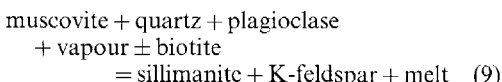


Fig. 7. Biotite breakdown reaction (2) (thick solid line) calculated using mineral compositions from the spinel-bearing zone of Z135, and assuming that water activity is buffered by the melt, using water activities in granitic melts for $a_{\text{H}_2\text{O}} = 1.0, 0.7$ and 0.5, from Johannes & Holtz (1990). Dashed lines indicate Fe and Mg endmember curves for reaction (2), intersections of reaction curves with solidi at $a_{\text{H}_2\text{O}} = 0.9, 0.7$ and 0.5 shown as filled circles (Fe) and open circles (Mg). Note the significant effect of bulk composition on $P-T$ conditions of the reaction. Shaded field is the average (PT) estimate for $a_{\text{H}_2\text{O}} = 0.6$, with 1 sigma errors, from Table 3.

1.3 kbar and 500°C, the equivalent of decompression through 4 or 5 km.

Although in many studies it is assumed that the garnet core preserves the 'peak' $P-T$ conditions, for these assemblages the spinel-bearing assemblages clearly post-date garnet growth. Vapour-absent melting reactions have positive slopes in $P-T$ space, and hence 'prograde' reactions can occur during decompression even if accompanied by slight cooling.

Initial melting in the massif is likely to be controlled by local fluid distribution; where a local grain-boundary fluid is present, small melt fractions may be generated at higher pressures (greater than about 6 kbar), but no peritectic phases will result. The first melt reaction to occur during decompression is the vapour-absent muscovite breakdown reaction:



which is associated with leucogranite formation (Whittington *et al.* 1998). This reaction will terminate once muscovite is exhausted (C, Fig. 8).

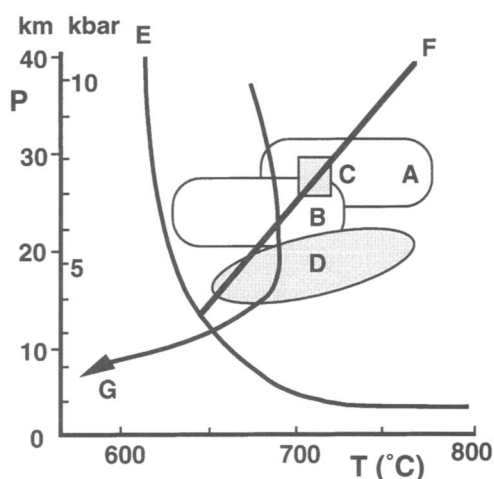


Fig. 8. Summary diagram of $P-T$ information from the Tato Valley of the Nanga Parbat Haramosh Massif. A: Garnet inclusion thermobarometry from this study. B: Garnet rim thermobarometry from this study. C (shaded): $P-T$ conditions of leucogranite formation by vapour-absent muscovite breakdown (Butler *et al.* 1997). D (shaded): Thermobarometry from a spinel-bearing zone in metapelite Z135, from this study. E: Water-saturated granitic solidus from Johannes & Holtz (1990). F: Vapour-absent muscovite melting reaction, from Petö (1976). G: Modelled exhumation path for rocks currently exposed in the Tato Valley from Whittington (1996).

With further decompression, reaction (5) allows a liquid to form from fluid-absent biotite melting with peritectic cordierite and/or garnet. At low pressures, a bulk composition with intermediate Fe/Mg ratio will not necessarily produce garnet. These assemblages have equilibrated between 650 and 770°C, and between 3.9 and 6.1 kbar (D, Fig. 8). Reaction (5) will continue until quartz or biotite are entirely consumed. In the absence of quartz, the ensuing melt reaction (6), or the divariant reaction (3), generates both cordierite and spinel with melt at higher temperatures and/or lower pressures. At Nanga Parbat neither reaction (6) nor (3) has gone to completion, since biotite and sillimanite have not been exhausted in spinel-bearing zones. A similar interpretation has also been made for silica-poor metapelitic migmatites from Antarctica (Fitzsimons 1996).

For the Nanga Parbat assemblages it seems probable that some fluid ingress occurred initially to allow biotite melting reactions to progress at temperatures less than 800°C. However, any such fluid infiltration was insufficient to saturate the melt, and $a_{\text{H}_2\text{O}}$ was buffered at about 0.6.

While this approach constrains conditions of melting, it does not constrain the slope of the $P-T$ path, which requires only that the melting reaction is crossed in the prograde direction (Vernon 1996). Such a path is possible by either heating or cooling during decompression, or even by isobaric heating. For the assemblages at Nanga Parbat, however, rapid exhumation has been documented by several geochronological techniques (Zeitler *et al.* 1982, 1993; Zeitler 1985; Smith *et al.* 1992; Winslow *et al.* 1994; Whittington 1996). The modelled $P-T$ path for this scenario (Whittington 1996) suggests a near-isothermal decompression path for this latest metamorphic episode (G, Fig. 8), followed by rapid cooling as rocks approached the surface and isotherms are telescoped.

We thank D. Carrington and D. Waters for careful reviews, M. Ali and A. Khwaja for hospitality in Islamabad, and P. Treloar and P. O'Brien for organizing the meeting in Kingston. A.W. thanks E. Condiffe, D. Newling, P. Potts, S. Reed and A. Tindle for assistance with microprobe analyses. J. Davis is praised for stoicism in the face of giardia, and we are grateful to G. Nabi for providing traditional remedies. A.W. was funded by a NERC studentship.

References

BUTLER, R. W. H., HARRIS, N. B. W. & WHITTINGTON, A. G. 1997. Interactions between deformation, magmatism and hydrothermal activity during active crustal thickening: a field example from Nanga Parbat, Pakistan Himalayas. *Mineralogical Magazine*, **61**, 37–51.

CARRINGTON, D. P. & HARLEY, S. H. 1995. Partial melting and phase relations in metapelites: an experimental petrogenetic grid in the KFMASH system. *Contributions to Mineralogy and Petrology*, **120**, 270–291.

— & WATT, G. R. 1995. A geochemical and experimental study of the role of K-feldspar during water-undersaturated melting of metapelites. *Chemical Geology*, **122**, 59–76.

DASGUPTA, S., SENGUPTA, P., EHL, J., RAITH, M. & BARDHAN, S. 1995. Reaction textures in a suite of spinel granulites from the Eastern Ghats Belt, India: Evidence for polymetamorphism, a partial petrogenetic grid in the system KFMASH and the roles of ZnO and Fe_2O_3 . *Journal of Petrology*, **36**, 435–461.

FITZSIMONS, I. C. W. 1996. Metapelitic migmatites from Brattstrand Bluffs, East Antarctica – metamorphism, melting and exhumation of the mid crust. *Journal of Petrology*, **37**, 395–414.

GARDIEN, V., THOMPSON, A. B., GRUJIC, D. & ULMER, P. 1995. Experimental melting of biotite + plagioclase + quartz \pm muscovite assemblages and implications for crustal melting. *Journal of Geophysical Research*, **100 B8**, 15 581–15 591.

HARRIS, N. B. W., AYRES, M. W. & MASSEY, J. 1995. Geochemistry of granitic melts produced during the incongruent melting of muscovite; implications for the extraction of Himalayan leucogranite magmas. *Journal of Geophysical Research*, **100 B8**, 15 767–15 777.

HENSEN, B. J. 1971. Theoretical phase relations involving cordierite and garnet in the system $MgO-FeO-Al_2O_3-SiO_2$. *Contributions to Mineralogy and Petrology*, **33**, 191–214.

— & GREEN, D. H. 1973. Experimental study of the stability of cordierite and garnet in pelitic compositions at high pressures and temperatures, III: synthesis of available experimental data and geological applications. *Contributions to Mineralogy and Petrology*, **38**, 151–166.

— & HARLEY, S. L. 1990. Graphical analysis of $P-T-X$ relations in granulite facies metapelites. In: ASHWORTH, J. R. & BROWN, M. (eds) *High Temperature Metamorphism and Crustal Anatexis*. Unwin Hyman, New York, 19–56.

HOLLAND, T. J. B. & POWELL, R. 1990. An enlarged and updated internally consistent thermodynamic dataset with uncertainties and correlations: the system $K_2O-Na_2O-CaO-MgO-MnO-FeO-Fe_2O_3-Al_2O_3-TiO_2-SiO_2-C-H_2O$. *Journal of Metamorphic Geology*, **8**, 89–124.

—, BABU, E. V. S. S. K. & WATERS, D. J. 1996. Phase-relations of osumilite and dehydration melting in pelitic rocks – a simple thermodynamic model for the KFMASH system. *Contributions to Mineralogy and Petrology*, **124**, 383–394.

HOLTZ, F. & JOHANNES, W. 1991. Genesis of peraluminous granites 1. Experimental investigation of melt compositions at 3 and 5 kb and various H_2O activities. *Journal of Petrology*, **32**, 935–958.

JOHANNES, W. & HOLTZ, F. 1990. Formation and composition of H_2O -undersaturated granitic melts. In: ASHWORTH, J. R. & BROWN, M. (eds) *High-temperature Metamorphism and Crustal Anatexis*. Unwin Hyman, London, 87–101.

KRETZ, R. 1983. Symbols for rock-forming minerals. *American Mineralogist*, **68**, 277–279.

LE BRETON, N. & THOMPSON, A. B. 1988. Fluid-absent (dehydration) melting of biotite in metapelites in the early stages of crustal anatexis. *Contributions to Mineralogy and Petrology*, **99**, 226–237.

NICHOLS, G. T., BERRY, R. F. & GREEN, D. H. 1992. Internally consistent gahnitic spinel-cordierite-garnet equilibria in the FMASHZn system: geothermobarometry and applications. *Contributions to Mineralogy and Petrology*, **111**, 362–377.

PATIÑO DOUCE, A. E. & JOHNSTON, A. D. 1991. Phase equilibria and melt productivity in the pelitic system: implications for the origin of peraluminous granitoids and aluminous granulites. *Contributions to Mineralogy and Petrology*, **107**, 202–218.

PETÖ, P. 1976. An experimental investigation of melting relations involving muscovite and paragonite in the silica-saturated portion of the system $K_2O-Na_2O-Al_2O_3-SiO_2-H_2O$ to 15 kbar total pressure. In: *Progress in Experimental Petrology*, NERC, London, 3rd Report, 41–45.

POWELL, R. & DOWNES, J. 1990. Garnet porphyroblast-bearing leucosomes in metapelites: mechanisms, phase diagrams, and an example from Broken Hill, Australia. In: ASHWORTH, J. R. & BROWN, M. (eds) *High Temperature Metamorphism and Crustal Anatexis*. Unwin Hyman, New York, 105–123.

— & HOLLAND, T. J. B. 1988. An internally consistent dataset with uncertainties and correlations: 3. Applications to geobarometry, worked examples and a computer program. *Journal of Metamorphic Geology*, **6**, 173–204.

SMITH, H. A., CHAMBERLAIN, C. P. & ZEITLER, P. K. 1992. Documentation of Neogene regional metamorphism in the Himalayas of Pakistan using U-Pb in monazite. *Earth and Planetary Science Letters*, **113**, 93–105.

SROGI, L., WAGNER, M. E. & LUTZ, T. M. 1993. Dehydration partial melting and disequilibrium in the granulite-facies Wilmington complex, Pennsylvania-Delaware piedmont. *American Journal of Science*, **293**, 405–462.

STODDARD, E. F. 1979. Zinc-rich hercynite in high-grade metamorphic rocks: a product of the dehydration of staurolite. *American Mineralogist*, **64**, 736–741.

VERNON, R. H. 1996. Problems with inferring P-T-t paths in low-P granulite facies rocks. *Journal of Metamorphic Geology*, **14**, 143–153.

VIELZEUF, D. & HOLLOWAY, J. R. 1988. Experimental determination of the fluid-absent melting relations in the pelitic system. Consequences for crustal differentiation. *Contributions to Mineralogy and Petrology*, **98**, 257–276.

WATERS, D. J. 1991. Hercynite-quartz granulites: phase relations, and implications for crustal processes. *European Journal of Mineralogy*, **3**, 367–386.

WHITTINGTON, A. G. 1996. Exhumation overprinted at Nanga Parbat, northern Pakistan. *Tectonophysics*, **260**, 215–226.

—, HARRIS, N. B. W. & BUTLER, R. W. H. 1998. Contrasting anatexis styles at Nanga Parbat, northern Pakistan. In: MACFARLANE, A., SORKHIABI, R. & QUADE, J. (eds) *Geological Society of America Special Publication*, **328**, in press.

WINSLOW, D. M., ZEITLER, P. K., CHAMBERLAIN, C. P. & HOLLISTER, L. S. 1994. Direct evidence for a steep geotherm under conditions of rapid denudation, Western Himalaya, Pakistan. *Geology*, **22**, 1075–1078.

ZEITLER, P. K. 1985. Cooling history of the NW Himalaya, Pakistan. *Tectonics*, **4**, 127–151.

— & CHAMBERLAIN, C. P. 1991. Petrogenetic and tectonic significance of young leucogranites from the northwestern Himalaya, Pakistan. *Tectonics*, **10**, 729–741.

—, —, & SMITH, H. A. 1993. Synchronous anatexis, metamorphism, and rapid denudation at Nanga Parbat (Pakistan Himalaya). *Geology*, **21**, 347–350.

—, JOHNSON, N. M., NAESEN, C. M. & TAIIRKHELI, R. A. K. 1982. Fission-track evidence for Quaternary uplift of the Nanga Parbat region, Pakistan. *Nature*, **298**, 255–257.

Disequilibrium during metamorphism: the role of nucleation kinetics

DAVID C. RUBIE

Bayerisches Geoinstitut, Universität Bayreuth, D-95440 Bayreuth, Germany

Abstract: The sluggishness of nucleation, one of the most poorly understood and least-discussed processes involved in mineral reactions, is an important cause of disequilibrium during metamorphism. Both field-based and experimental petrological studies show that metastable phases can persist far from equilibrium on long time scales because the stable phases are unable to nucleate. This behaviour applies not only to solid–solid reactions but also to some dehydration and melting reactions. Although the degree of overstepping required for nucleation during polymorphic phase transformations is relatively small (2–4 kbar on an experimental time scale), nucleation can be much more sluggish for reactions involving two or more product phases. When reactions occur at conditions of large overstepping due to delayed nucleation, reaction rates can be very fast because of the effect of the large free energy change on growth kinetics. Under these circumstances, new metastable phases may form instead of the stable mineral assemblage, as predicted by the Ostwald step rule. Such metastable phases can persist during metamorphism, even during high-strain ductile deformation and fluid influx, but without any obvious texture evidence to indicate that they are metastable.

A commonly held view amongst many petrologists is that metamorphic reactions occur at conditions close to equilibrium. On the basis of this assumption, observed mineral assemblages can be interpreted as recording discrete pressure–temperature (P – T) conditions which are determined using phase equilibria, with the aim of reconstructing the P – T paths followed during metamorphism. This equilibrium model clearly has significant limitations because otherwise mineral assemblages recording high pressures and temperatures within thickened continental crust would never survive during uplift to the Earth's surface.

An alternative and less common view is that metamorphic reactions can be kinetically hindered and can consequently occur under disequilibrium conditions. In this case two distinct end-member models can be considered. (1) Reactions occur progressively and continuously along the pressure–temperature–time (PTt) path, at a rate which is dependent mainly on temperature. This model has been applied to the polymorphic aragonite to calcite transformation in order to constrain PTt paths during uplift of blueschist terrains, as discussed below. (2) Mineral assemblages persist metastably outside of their stability fields on long time scales in the absence of deformation. Reaction to a lower-energy mineral assemblage (possibly also metastable), if it occurs, takes place rapidly under pronounced disequilibrium conditions due to a 'triggering' event. In the case of hydration reactions, triggering can be caused by the influx of H_2O into a previously fluid-absent mineral

assemblage. However, reaction of metastable assemblages under disequilibrium conditions can also be initiated by the *delayed nucleation* of the product phases. This contribution is concerned particularly with the role that nucleation kinetics play in promoting disequilibrium.

Nucleation kinetics

Nucleation is one of the most poorly understood of the processes involved in metamorphic reactions. Although there have been a number of studies of the kinetics of growth and dissolution during mineral reactions, studies of nucleation kinetics are rare. The few existing experimental studies have been concerned mainly with nucleation during the relatively simple aragonite–calcite (Liu & Yund 1993) and olivine–spinel (Rubie *et al.* 1990) polymorphic phase transformations.

The theory of nucleation was initially formulated to describe the condensation of water droplets from a vapour phase (see Christian (1975) and references therein). This theory was subsequently developed to describe nucleation during simple solid–solid (e.g. polymorphic) phase transformations (e.g. Christian 1975; Putnis & McConnell 1980; Porter & Easterling 1992; LeGoues & Aaronson 1984; LeGoues *et al.* 1984a, b; Rubie & Thompson 1985). A typical rate equation for homogeneous nucleation has the form:

$$\dot{N} = K_0 T \exp(-\Delta G_{\text{hom}}^*/kT) \times \exp(-\Delta H_a/RT) \quad (1)$$

with

$$\Delta G^* = \frac{16\pi\gamma^3}{3(\Delta G_v + \varepsilon)^2}$$

where \dot{N} is the nucleation rate, K_0 is a constant, ΔG^* is the activation energy for homogeneous nucleation, k is the Boltzmann constant, ΔH_g is the activation enthalpy for growth, γ is the

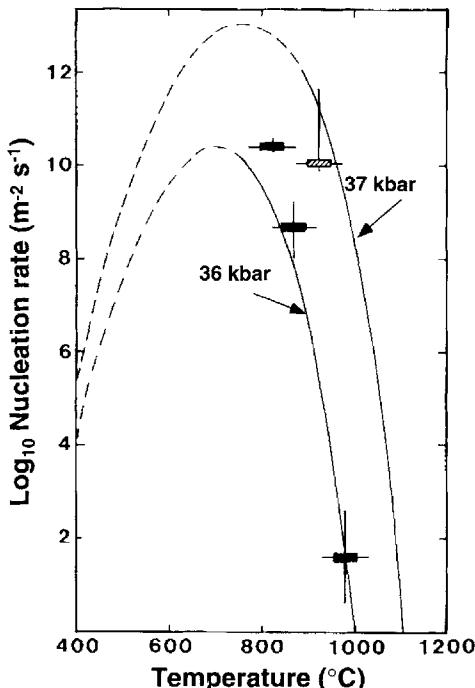


Fig. 1. Rates of nucleation during the polymorphic Ni_2SiO_4 olivine-spinel (α - γ) transformation at 36 kbar (filled symbols) and 37 kbar (shaded symbol) (after Rubie *et al.* 1990). These rates were estimated by fitting an appropriate rate equation to transformation-time data with rates of nucleation and growth as the fitting parameters. The lines are fits of equation (1) to the data. At 36 kbar, the equilibrium boundary for the transformation lies at about 1400°C. Therefore, these results indicate that a temperature understep of c. 400°C (equivalent to a pressure overstep of c. 4 kbar) is required to obtain observable nucleation rates on an experimental time scale. Because of the strong (exponential) dependence of the nucleation rate on the extent of overstepping/understepping (indicated by the steepness of the high-temperature parts of the fitted curves), these estimates will not be greatly reduced for a geological time scale when reaction occurs at relatively high temperature. Note that the extrapolation to low temperatures is very uncertain (dashed lines) because of uncertainties in the strain energy term in equation (1) (see Rubie *et al.* 1990; Liu & Yund 1993).

interfacial energy, ΔG_v is the free energy change of reaction per unit volume and ε is strain energy. The nucleation rate ($\dot{N} = dN/dt$) is defined as the number of nuclei N which form per unit time t either per unit volume or per unit area of grain boundary. According to equation (1), considerable overstepping (or understepping) of an equilibrium boundary is required before rates of nucleation become significant, even on a geological time scale (e.g. Fig. 1). This is because the negative value of the free energy change of reaction, ΔG_v , must be large enough to balance the positive strain energy and interfacial energy terms. Furthermore, according to equation (1) the nucleation rate increases extremely rapidly (by orders of magnitude) as the overstep (or understep) increases because of its exponential dependence on ΔG_v (Fig. 1). This rapid increase has the important consequence that when nucleation rates are extrapolated over orders of magnitude from a laboratory to a geological time scale, the amount of overstepping involved will not change significantly. However, this conclusion is applicable only to the high-temperature limb of the nucleation rate curves shown in Fig. 1. When an equilibrium boundary is crossed at relatively low temperature (during subduction, for example), the nucleation rate will be given by the low-temperature sections of the curves shown in Fig. 1. In general, nucleation rates cannot be determined experimentally at such low temperatures because growth rates are negligible on a laboratory time scale. In addition, the extrapolation of the high-temperature data to low temperatures (as shown by the dashed lines in Fig. 1) is highly uncertain (see Rubie *et al.* 1990).

The interfacial and strain energy terms in equation (1) are of considerable importance. The magnitudes of these terms control the overstepping which is required for nucleation and depend, at least partly, on the degree of mismatch between the crystal structures of the reactant and product phases. Coherent nucleation of a phase structurally similar to the reactant phase may require a relatively small overstep; on the other hand, incoherent nucleation of a structurally dissimilar phase may result in a high interfacial energy and will require a large overstep. In this context, structural similarities between the oxygen sub-lattices of the respective phases are likely to be particularly important (e.g. Brearley 1987; Worden *et al.* 1991, 1992).

Although the main approach to quantifying nucleation kinetics is through experimental studies, there is a potential problem in interpreting and extrapolating the resulting data. The

experimental procedure involves pressurizing and heating a polycrystalline aggregate in order to induce partial reaction (e.g. Rubie & Thompson, 1985; Brearley *et al.* 1992; Kerschhofer *et al.* 1996). When the crystals of the aggregate have anisotropic physical properties (i.e. compressibility and thermal expansivity), internal stresses will develop during pressurization and heating as a result of an increasing mismatch between the individual grains (Cleveland & Bradt 1978). As a result, stress concentrations will develop at grain boundaries (Raj & Ashby 1971) and, unless viscoelastic relaxation can occur on the experimental time scale (which requires high temperature), elastic strain energy will be concentrated in these regions. This strain energy may contribute significantly to the energy required for nucleation on the grain boundaries. Thus, nucleation rates determined experimentally might be much faster than those which would be observed in a fully relaxed aggregate and the overstepping required on geological time scales to produce nucleation may be significantly larger than in experiments. It should be possible to test the importance of this effect because the magnitude of the internal stresses increases with the grain size of the aggregate (Cleveland & Bradt 1978). Experimentally observed nucleation rates should therefore be faster in coarse-grained starting materials than in fine-grain aggregates; preliminary evidence for this dependence on grain size has been observed by Dupas *et al.* (1998) in a study of the $(\text{Mg},\text{Fe})_2\text{SiO}_4$ wadsleyite–ringwoodite (β – γ) transformation.

Nucleation during reactions involving multiple phases has not been studied quantitatively, either theoretically or experimentally. However, as discussed below, there are indications that it can be an extremely sluggish process even on the time scales of regional metamorphism. Based on field and experimental evidence, large oversteps of equilibrium conditions can be required for nucleation during a variety of solid–solid, dehydration and melting reactions. Some of the consequences of this behaviour are discussed below.

Reconstructive polymorphic phase transformations

Growth kinetics during the aragonite to calcite transformation were studied by Carlson & Rosenfeld (1981) at 1 bar and 375–455°C. The growth rate of individual calcite grains, which nucleated topotactically within aragonite single crystals, was measured directly using an optical

microscope fitted with a heating stage. The growth rate data were fitted using a rate equation for interface-controlled growth in which the rate-controlling step is the short-range thermally activated diffusion of atoms across the narrow interphase boundary (Turnbull 1956):

$$\dot{x} = k_0 T \exp(-\Delta H_a/RT) \times [1 - \exp(\Delta G_r/RT)] \quad (2)$$

Here \dot{x} is the growth rate of the new phase, k_0 is a constant, ΔH_a is the activation enthalpy for growth, ΔG_r is the molar free energy change of reaction, and R is the gas constant. The first exponential in this equation is an Arrhenius term which describes the thermally activated diffusion of atoms across the interphase boundary. The second part of the equation, in square brackets, is a thermodynamic term which describes the effect of the driving force (change in Gibbs free energy) for reaction. At equilibrium conditions, the driving force is zero ($\Delta G_r = 0$) so that the growth rate is also zero. Carlson & Rosenfeld (1981) used this equation, with parameter values determined from the fit to their experimental data, to model the growth of calcite grains along possible PTt paths followed during uplift of the Franciscan blueschist terrain in California. They concluded that, for reasonable uplift rates (0.1–10.0 mm a⁻¹), the Franciscan blueschists must have crossed the aragonite–calcite equilibrium boundary at a temperature between 125 and 175°C for the degree of observed transformation of aragonite to calcite to have occurred (Fig. 2). Their model was based on the assumption that nucleation occurs rapidly at all conditions in the calcite stability field including conditions very close to equilibrium, i.e. that the growth process is always the rate-controlling step.

Liu & Yund (1993) studied rates of both nucleation and growth during the aragonite to calcite transformation in polycrystalline aggregates at pressures ranging from 1 bar to 4 kbar in the temperature range 280–380°C. In polycrystalline samples, nucleation occurred incoherently on grain boundaries and growth was not topotactic. Growth rates were different and the activation enthalpy (ΔH_a) was higher than for the topotactic growth mechanism which occurred in Carlson & Rosenfeld's (1981) study. Extrapolations of Liu & Yund's nucleation rate data to higher pressures suggest that the equilibrium boundary needs to be understepped by about 2–4 kbar at 330°C for nucleation rates to become significant (the actual value depends on the magnitude of the strain energy, ϵ , in equation (1), which is poorly constrained). Liu & Yund (1993) also used their data to model the

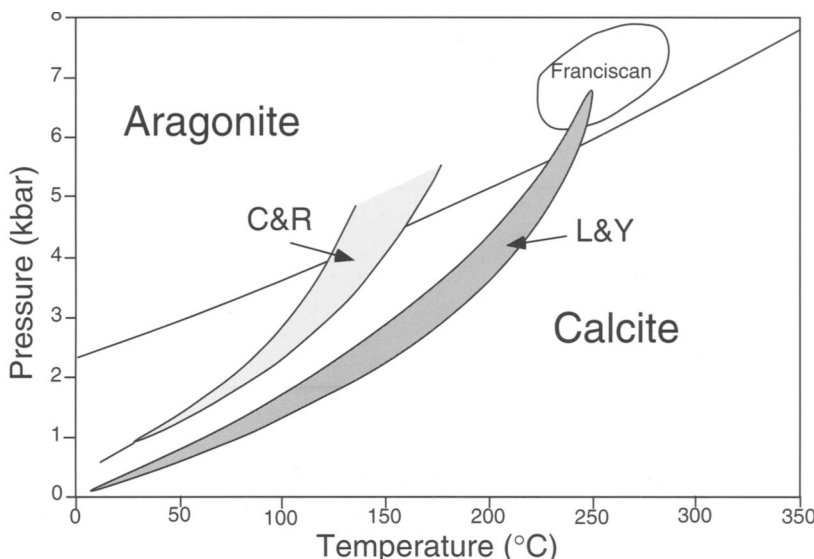


Fig. 2. CaCO_3 phase diagram showing the stability fields of calcite and aragonite. The conditions estimated for the Franciscan blueschist metamorphism are shown. P - T paths followed during the uplift of the Franciscan blueschists, constrained on the basis of experimental kinetic data for the aragonite to calcite transformation by Carlson & Rosenfeld (1981) (C&R) and Liu & Yund (1993) (L&Y), are shown. These paths were constrained by integrating kinetic rate equations along possible PTt paths and comparing the results with the extent of the calcite to aragonite reaction observed in the Franciscan blueschists. Both nucleation and growth kinetics were taken into account by Liu & Yund (1993), whereas Carlson & Rosenfeld (1981) only considered growth kinetics. Uplift rates in the range 0.1 to 10 mm per year were assumed in both studies.

aragonite to calcite transformation during uplift of the Franciscan blueschists and found that PTt paths which crossed the equilibrium boundary at c. 235°C are consistent with the observed extent of partial reaction (Fig. 2). This temperature is considerably higher than Carlson & Rosenfeld's (1981) estimate because (a) the nucleation barrier was incorporated in the kinetic model and (b) the growth rate parameters were different.

An experimental kinetic study of the calcite to aragonite transformation at 20–25 kbar shows that aragonite nucleates rapidly in the temperature range 600–800°C provided the equilibrium boundary is overstepped by c. 2 kbar or more (Hacker & Rubie, unpublished data). During the polymorphic Ni_2SiO_4 olivine to spinel transformation, an overstep of c. 4 kbar was estimated by Rubie *et al.* (1990) to be necessary for nucleation (Fig. 1). It must be emphasized, however, that extrapolations of nucleation rates in these systems to lower temperatures are very uncertain, particularly because the effect of temperature on the strain energy (ϵ) is unknown (Rubie *et al.* 1990). The oversteps/understeps required to obtain significant nucleation rates may therefore be larger at lower temperatures, even on geological time scales.

Multiphase solid–solid reactions

Plagioclase breakdown at high pressure

During high-pressure metamorphism of coarse-grained gabbroic and granitoid rocks in the absence of high-strain deformation, individual mineral grains often react in domains of local equilibrium, sometimes as nearly isochemical systems, due to slow rates of chemical diffusion (Mørk 1985; Koons *et al.* 1987; Rubie 1990). Plagioclase grains typically react to assemblages including jadeite, quartz, zoisite and kyanite. Under fluid-absent conditions and at pressures in excess of 18 kbar (at 600°C), plagioclase should be replaced by jadeite + kyanite + grossular + quartz, i.e. by a solid–solid reaction in which four new phases have to nucleate. The isothermal phase diagram of Fig. 3a shows the sequence of reactions which should occur under equilibrium conditions as pressure increases at c. 600°C during subduction. For plagioclase compositions with relatively high anorthite contents ($X_{\text{An}} > 0.4$), reaction is expected to occur initially at c. 13 kbar by a continuous reaction involving the formation of increasingly sodic plagioclase + grossular + kyanite + quartz. For equilibrium to

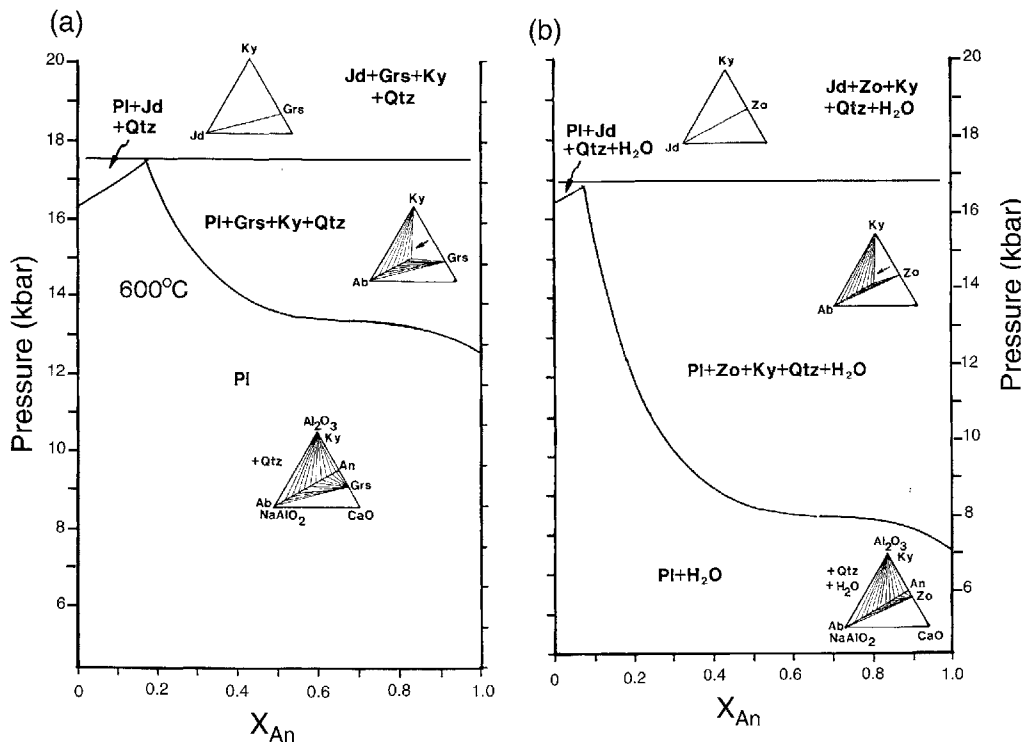


Fig. 3. Plagioclase phase diagrams calculated for $T = 600^\circ\text{C}$ showing breakdown reactions at high pressure under (a) anhydrous and (b) H_2O -saturated conditions. Note that these phase diagrams are semi-schematic and no account has been taken of thermodynamic complexities in plagioclase solid solutions (after Wayte *et al.* 1989).

be maintained, three new phases must nucleate and long-range $\text{NaSi}-\text{CaAl}$ interdiffusion in plagioclase is required. As this reaction proceeds with increasing pressure, the amount of residual plagioclase decreases. Finally, at $c. 18 \text{ kbar}$ the remaining plagioclase (composition $X_{\text{An}} \approx 0.2$) should disappear by a discontinuous reaction to jadeite + grossular + kyanite + quartz (Fig. 3a).

Allalin metagabbro

Information about the actual reaction behaviour of plagioclase during high-pressure metamorphism is provided by an example of partially reacted plagioclase from the Allalin gabbro, Western Alps (Wayte *et al.* 1989). The Allalin gabbro was metamorphosed at $>20 \text{ kbar}$ and 600°C during early-Alpine metamorphism (Chinner & Dixon 1973; Meyer 1983a, b) and consequently most of the original plagioclase ($X_{\text{An}} = 0.60-0.65$) was pseudomorphed by zoisite + jadeite + kyanite + quartz. However, rare examples of partially preserved plagioclase can be found in which little-altered plagioclase is cut

by extremely fine-grained, irregular veins (Fig. 4a). Transmission electron microscopy (TEM) shows that the least-altered regions consist of plagioclase containing small ($c. 0.2 \mu\text{m}$ long) oriented grains of clinozoisite; these regions contain no jadeite, grossular, kyanite or quartz (Fig. 4b). The irregular veins, on the other hand, consist of zoisite, jadeite, kyanite, quartz and sodic-plagioclase with a grain size of $c. 0.5 \mu\text{m}$ (Wayte *et al.* 1989, fig. 6; Rubie 1990, fig. 5.5). These observations indicate that plagioclase was able to survive at $>20 \text{ kbar}$ and 600°C for millions of years because the product phases of the fluid-absent reactions (Fig. 3a) failed to nucleate. At these conditions the equilibrium boundary was overstepped by $>7 \text{ kbar}$ (Fig. 3a) which means that plagioclase is able to survive metastably far outside of its stability field in the absence of hydrous fluid due to large nucleation barriers. However, even in the absence of nucleation barriers, $\text{NaSi}-\text{CaAl}$ interdiffusion in plagioclase is likely to be too slow for plagioclase breakdown reactions to occur under near-equilibrium conditions during subduction (Rubie 1990).

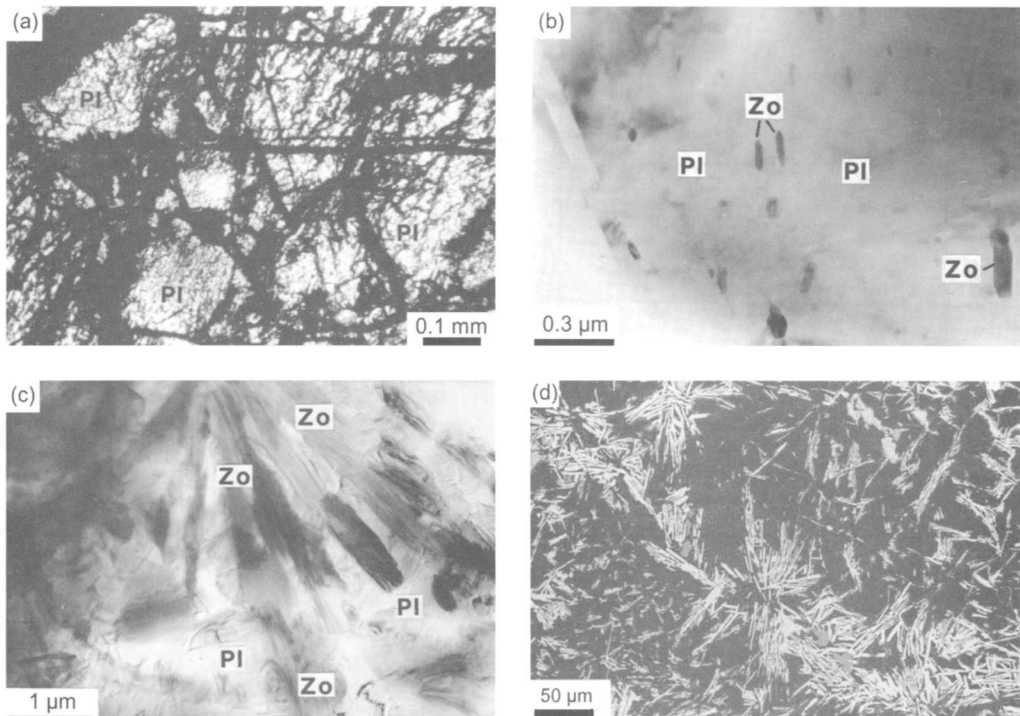


Fig. 4. Microstructures of plagioclase breakdown resulting from high-pressure metamorphism. (a) Optical micrograph showing partially reacted plagioclase from the Allalin metagabbro, Western Alps. The black veins, which contain extremely fine-grained zoisite, quartz and jadeite, as well as relict plagioclase, enclose islands of relatively unaltered plagioclase (PI). (b) TEM micrograph showing that only sub-micrometre zoisite grains (Zo) have nucleated in plagioclase (PI) in the least-altered regions seen in (a). (c) TEM image showing radiating zoisite prisms (Zo) in one of the black veins seen in (a); kyanite, quartz and jadeite can also be found in such regions. (d) Backscattered electron image of plagioclase from metaquartz diorite at Monte Mucrone (Sesia Zone) which has been completely pseudomorphed by jadite (grey), zoisite needles (white) and interstitial quartz (which cannot be resolved in this image). The distribution of zoisites (radiating from a linear feature which runs from top left to lower right) suggests that they have nucleated along a fluid-filled fracture as in (c).

The most likely explanation of the observed reaction (Fig. 4a) is that hydrous fluid infiltrated into fractures in the plagioclase at >20 kbar and $c. 600^\circ\text{C}$ allowing a hydration reaction to occur with zoisite, jadeite, kyanite and quartz as the product phases (Wayte *et al.* 1989; Rubie 1990). In this case, reaction occurred at a pressure >12 kbar above the equilibrium boundary at which plagioclase first becomes unstable in the presence of H_2O (Fig. 3b). Although under equilibrium conditions plagioclase breakdown is multivariant (Fig. 3), under disequilibrium conditions (involving a large overstepping) the reaction behaves as if it were univariant (at fixed water activity) as discussed by Rubie (1983). The localization of jadeite within the veins indicates that, even under conditions of large overstepping, jadeite was only able to nucleate within the fluid-filled fractures (possibly on the fracture

walls). The very fine grain size of the reaction products is consistent with this model in which rapid nucleation is triggered by fluid influx (cf. Rubie 1983).

Monte Mucrone metaquartz diorite

Another example of a plagioclase-bearing igneous protolith that underwent eclogite-facies metamorphism (>16 kbar and $c. 550^\circ\text{C}$) is the Monte Mucrone metaquartz diorite of the Sesia Zone, Western Alps (Oberhänsli *et al.* 1985; Koons *et al.* 1987). As in the case of the Allalin gabbro, the igneous textures are well preserved in bodies ($c. 100$ m across) which escaped high-strain deformation and reactions occurred within domains of local equilibrium which are geometrically defined by the original mineral

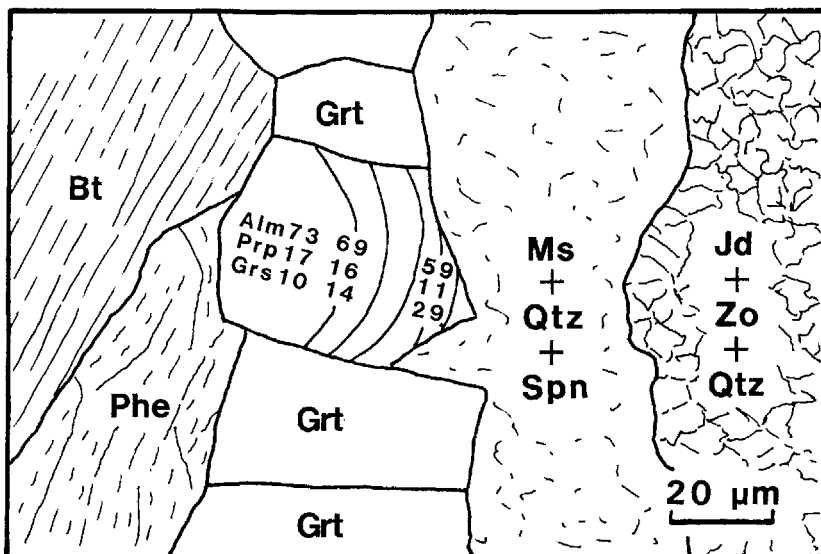


Fig. 5. Schematic sketch showing a typical corona structure from metaquartz diorite at Monte Mucrone. Jadeite + zoisite + quartz on the right has pseudomorphed plagioclase (as in Fig. 4d) and biotite (Bt) on the left has partly reacted to phengite (Phe). A corona consisting of layers of (a) garnet (Grt) and (b) muscovite + quartz + sphene (Ms + Qtz + Spn) has developed between the biotite and plagioclase sites. The zoning patterns in the garnet corona indicate that this layer grew in a region of high chemical potential gradients which existed between the biotite and plagioclase sites. Note that the jadeite is not in equilibrium with the mafic (biotite) components and there is also disequilibrium between the two white micas (after Koons *et al.* 1987).

grains (plagioclase + quartz + biotite \pm K-feldspar). The plagioclase ($X_{An} < 0.2$) was pseudomorphed by fine-grained jadeite + zoisite + quartz (but no kyanite). Biotite reacted to phengite and this reaction released components which contributed to the growth of a corona between the biotite and plagioclase sites. This corona consists of a layer of garnet ($c. 30 \mu\text{m}$ wide) adjacent to the biotite/phengite sites and a layer of fine-grained muscovite + quartz + sphene adjacent to the plagioclase sites (Fig. 5). Pronounced zoning patterns in the garnet, as well as compositional differences between the muscovite and phengite, indicate that the coronas formed in regions of high chemical potential gradients. As discussed by Joesten (1977), the growth of such layered structures is diffusion controlled.

The textures within the pseudomorphs after plagioclase suggest strongly that the reaction initiated along fluid-filled fractures as in the case of the Allalin plagioclase (Fig. 4d). Radiating clusters of zoisite needles typically originate from points which are located along linear features which are interpreted to have been fluid-filled fractures (Fig. 4d). Morphologically these are very similar to the smaller radiating

zoisite needles which occur close to the veins in the partially reacted Allalin plagioclase (Fig. 4c). It is therefore likely that plagioclase in the Monte Mucrone rocks also reacted directly to a jadeite-bearing assemblage due to the influx of fluid rather than by the equilibrium reactions shown in Fig. 3b (see also Koons *et al.* 1987). Again, this requires that plagioclase survived as a metastable phase well outside of its stability field because grossular, kyanite and quartz (the product phases of the fluid-absent reaction) were unable to nucleate in the absence of fluid. This behaviour has important consequences for the subsequent mineralogical evolution, as discussed in the next few paragraphs.

Consequences of sluggish nucleation for subsequent reaction behaviour

The reaction of albite to jadeite + quartz has been investigated experimentally at 600°C and a pressure overstep of 5 kbar (Hacker *et al.* 1993). In the presence of 1 wt% H_2O , the rate of reaction is fast on a laboratory time scale at these conditions. The conditions of high-pressure metamorphism in the Western Alps

were comparable to those of this experimental study. Therefore, assuming that reaction rates in plagioclase solid solutions are comparable to those of albite, the obvious conclusion is that the metastable plagioclase in the Allalin and Monte Mucrone rocks reacted extremely rapidly as soon as the influx of hydrous fluid occurred (perhaps on a time scale of days to months). The limited extent of reaction in some plagioclase grains of the Allalin gabbro was most likely due to limited available quantities of fluid which became consumed by the hydration reaction (Wayte *et al.* 1989; Rubie 1990).

In both the Allalin metagabbro and the Monte Mucrone metaquartz diorite, the stable pyroxene composition for the whole-rock compositions is omphacite (e.g. Koons *et al.* 1987). Therefore, the jadeite-rich pyroxenes which formed from the pseudomorphic breakdown of plagioclase (under conditions of local equilibrium) were strongly out of equilibrium (i.e. metastable) with the respective whole-rock compositions. The growth of metastable phases within the plagioclase pseudomorphs is the consequence of very rapid reaction rates at these sites which allowed no time for long-range equilibration to develop because of slow rates of diffusion between the different mineralogical domains. There is, however, a paradox with this model because the reaction of plagioclase at Monte Mucrone involved considerable mass-transport. The mineralogy of the pseudomorphs (especially the lack of kyanite) indicates significant loss of Al_2O_3 and CaO which diffused out to participate in the corona-forming reactions (Koons *et al.* 1987). Thus, mass-transport occurred over much larger length scales *within* the plagioclase sites than *between* the plagioclase and biotite sites. This behaviour may be related to several factors, such as the development of the garnet corona (which would inhibit mass-transport) and the large volume decrease during the plagioclase breakdown reaction (which might have enhanced mass-transport in the presence of fluid by producing a transiently high permeability).

It is generally assumed that high-strain deformation combined with fluid infiltration leads to equilibration (on a thin-section scale) in rocks such as those discussed above and that thermobarometric methods may be applied to such rocks in order to deduce the P - T conditions of equilibration. At Monte Mucrone, this was not the case and relicts of the early disequilibrium assemblages survived subsequent high-strain deformation and fluid infiltration (Koons *et al.* 1987; Frueh-Green 1994). Consequently, application of the garnet-clinopyroxene geothermometer to gneisses derived from the metaquartz

diorite leads to false temperature estimates in the range 730–1400°C (Koons *et al.* 1987). It must be strongly emphasized that direct textural evidence for disequilibrium mineral compositions in these deformed rocks is not apparent.

The persistence of disequilibrium assemblages during deformation and fluid influx at Monte Mucrone can be explained by the model of Koons *et al.* (1987) as being an indirect consequence of the prolonged metastable persistence of plagioclase. Because plagioclase reacted at conditions well outside of its stability field, nucleation rates of the product phases were high when fluid infiltration occurred. This caused the product phases to crystallize with a very small grain size. During the initial stages of ductile deformation, the jadeite + zoisite + quartz aggregates are inferred to have deformed by a diffusion-accommodated grain-boundary sliding mechanism because of the small grain size and were consequently very ductile (Rubie 1983). This deformation mechanism did not catalyse the normally slow cation diffusion rates in jadeite and the composition of individual pyroxene grains changed little during this stage of deformation. Simultaneously, garnet grains underwent pronounced growth, probably in equilibrium with coexisting crystallizing phenite but not with the metastable jadeite. As deformation progressed further, the grain size of the jadeite increased, due to grain growth, and caused a change in deformation mechanism to dislocation creep. The pyroxenes then became much more omphacitic, probably because diffusion rates were enhanced by the dislocation creep mechanism (experimental evidence for such an enhancement is given by Yund & Tullis (1991)). By this stage, garnet growth was complete and garnet compositions failed to adjust to the changing pyroxene compositions because of slow rates of lattice diffusion. The final result was complete disequilibrium between garnet and pyroxene, even in the case of grains in close spatial proximity.

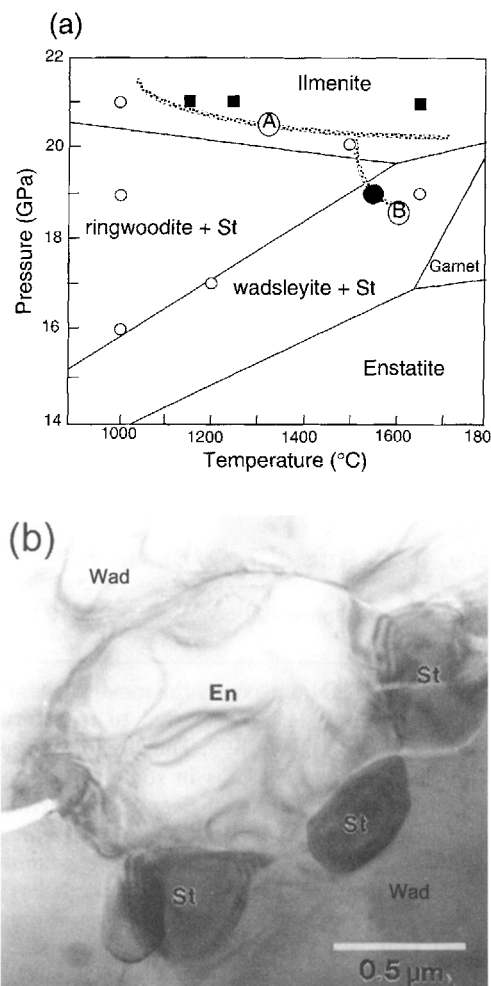
In the above examples, the occurrence of reactions is clearly controlled by the timing of fluid availability rather than by when equilibrium phase boundaries are crossed. The origin of such fluids is therefore of considerable interest. In the case of Monte Mucrone, an oxygen isotope study suggests that the fluids were locally derived, perhaps from dehydration reactions in the neighbouring paraglacials, and there is no evidence for significant fluxes of externally derived fluids (Frueh-Green 1994). A similar model has been used to explain the occurrence of retrograde hydration reactions in eclogites of the Adula nappe (Heinrich 1982).

Enstatite breakdown at high pressure

An experimental study of enstatite breakdown at high (mantle) pressures provides further evidence for large nucleation barriers during solid-solid reactions (Hogrefe *et al.* 1994). Under equilibrium conditions (at 1200–1500°C), MgSiO_3 enstatite should react first to $\beta\text{-Mg}_2\text{SiO}_4$ (wadsleyite) + stishovite at 15–16 GPa (160–170 kbar), then to $\gamma\text{-Mg}_2\text{SiO}_4$ (ringwoodite) + stishovite at higher pressure and at still higher pressures, MgSiO_3 ilmenite becomes the stable phase (Fig. 6a). Hogrefe *et al.* (1994) performed a series of experiments on hot-pressed forsterite + enstatite samples at 16–21 GPa and 1000–1650°C for times up to 30 h using a multianvil apparatus. The polymorphic transformation of the forsterite to wadsleyite or ringwoodite was rapid at all conditions, which meant that only stishovite nucleation was required for the enstatite grains to react. However, at pressures below 21 GPa stishovite only nucleated when the temperature exceeded 1500°C; nucleation was incoherent and the relatively wide spacing of stishovite grains at these conditions (Fig. 6b, see below) indicates that the stishovite nucleation rate was low. At lower temperatures, in the wadsleyite + stishovite stability field, enstatite survived as a metastable phase because stishovite failed to nucleate even though the conditions overstepped the equilibrium boundary by as much as 2–3 GPa (20–30 kbar). At higher pressure (21 GPa), the polymorphic transformation of enstatite directly

to ilmenite occurred and was kinetically much easier than the reactions involving stishovite nucleation. The ilmenite subsequently reacted to the lower-pressure assemblage of ringwoodite + stishovite (Hogrefe *et al.* 1994), possibly due to a localized pressure drop caused by the large volume decrease (c. 12%) of the enstatite-ilmenite transformation. In this case the new phases nucleated rapidly on ilmenite to form symplectites consisting of very closely spaced lamellae. Conclusions of these results are as follows. (1) The nucleation of stishovite on enstatite occurs incoherently because of large dissimilarities between the structures of the two phases; nucleation may be very sluggish because the structural dissimilarities cause the interfacial energy to be high. (2) The relatively rapid nucleation of stishovite on ilmenite may be due to structural similarities (e.g. Si is octahedrally

Fig. 6. (a) MgSiO_3 phase diagram showing that enstatite should break down to Mg_2SiO_4 wadsleyite + stishovite (St) at 14–16 GPa and $<1700^\circ\text{C}$ under equilibrium conditions (after Sawamoto 1987). The symbols show the P – T conditions of the kinetic experiments of Hogrefe *et al.* (1994) on hot-pressed enstatite + forsterite aggregates: open circles, no reaction of enstatite; filled circle, partial reaction to wadsleyite + stishovite; filled squares, polymorphic transformation of enstatite to MgSiO_3 ilmenite. The two thick grey lines delineate the minimum P – T conditions required for the nucleation of (A) ilmenite and (B) stishovite (one of the Mg_2SiO_4 polymorphs, either wadsleyite or ringwoodite, formed by transformation of forsterite in all experiments). These results show that metastable enstatite can survive at pressures as much as 40 kbar outside of its stability field because of the failure of stishovite to nucleate; stishovite nucleation was only observed in one experiment, at 1550°C and 19 GPa. (b) Transmission electron micrograph showing stishovite grains (St) which nucleated on enstatite (En) at 1550°C and 19 GPa. The surrounding Mg_2SiO_4 wadsleyite (Wad) has formed mainly by the transformation of forsterite (after Hogrefe *et al.* 1994).

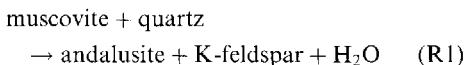


coordinated in both phases) which cause the interfacial energy to be low. These preliminary results emphasize the importance of structural similarities between reactant and product phases in controlling nucleation kinetics through the magnitudes of interfacial energy and/or strain energy (Worden *et al.* 1992).

Dehydration and melting reactions

Dehydration reactions

It is commonly believed that kinetic hindrance and metastability during dehydration and melting reactions is likely to be minimal during metamorphism, especially in comparison with solid-solid reactions. In addition to being based partly on intuition, such a belief has resulted from some experimental studies. For example, Schramke *et al.* (1987) studied the kinetics of the dehydration reaction:



and found that reaction rates are fast on an experimental time scale even at conditions close to the equilibrium phase boundary (Fig. 7). Based on an extrapolation of their experimental results, Schramke *et al.* (1987) concluded that this reaction would rapidly reach completion during metamorphism even when the equilibrium phase boundary is overstepped by only 2°C. This conclusion is the result of the experimental methodology used and is not supported by another experimental study, as discussed below. The starting materials in the experiments of Schramke *et al.* (1987) consisted of muscovite, quartz, andalusite, K-feldspar and water with the crystalline phases being in the form of sieved powders. The use of this starting material eliminates the need for nucleation because the product phases are already present at the start of each experiment; therefore the possibility that significant nucleation barriers might exist cannot be evaluated from these experiments. The fast reaction rates are a consequence of using powdered samples together with large quantities of H₂O (c. 20 wt%, which is equivalent to c. 45 vol%) which causes interface reactions between the crystalline phases and the hydrous fluid (i.e. dissolution or precipitation) to be rate-controlling (Schramke *et al.* 1987; see also Wood & Walther (1983) for a discussion of the kinetics of such processes).

The mechanisms and kinetics of the breakdown of muscovite + quartz have also been

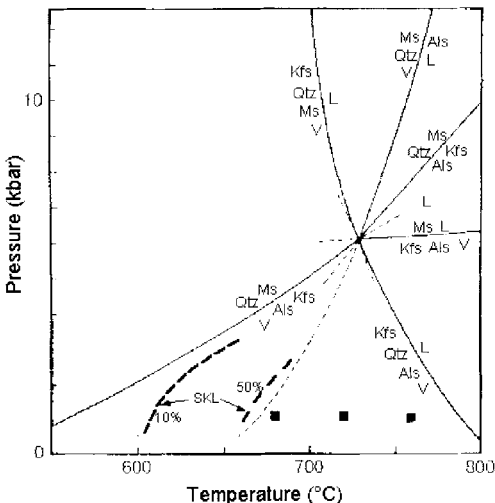
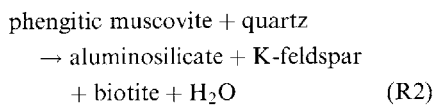


Fig. 7. Phase diagram for the system K₂O-Al₂O₃-SiO₂-H₂O showing the equilibrium phase boundary for the dehydration reaction: muscovite + quartz (Ms + Qtz) → K-feldspar + aluminosilicate + H₂O (Kfs + Als + V). The approximate position of the low-pressure metastable extension of the reaction Ms + Qtz → Als + liquid (L) is shown as a dashed line. The broken lines labelled 'SKL' show conditions estimated by Schramke *et al.* (1987) to be required for the dehydration of muscovite + quartz (by reaction R1) to reach 10% and 50% completion respectively in 4 days. The filled squares show the conditions of the experiments of Brearley & Rubie (1990) on muscovite + quartz; in this latter study, only trace amounts of metastable melt had formed after 2 months at 680°C (after Brearley & Rubie 1990).

studied using cylindrical cores of a quartz-muscovite schist (Fig. 8a) as the starting material (Rubie & Brearley 1987, 1990; Brearley & Rubie 1990). These experiments were performed at 1 kbar over the temperature range 680–760°C for times up to 5 months, both with and without the addition of 1 wt% H₂O (Fig. 7). Because the mica in the starting material was phengitic, the reaction which should occur at the experimental conditions is:



The direct and simultaneous nucleation of all the product phases was not observed in any of the experiments. In all cases, the first phase to nucleate was a silicate melt, which formed at muscovite-quartz grain boundaries (Fig. 8b)

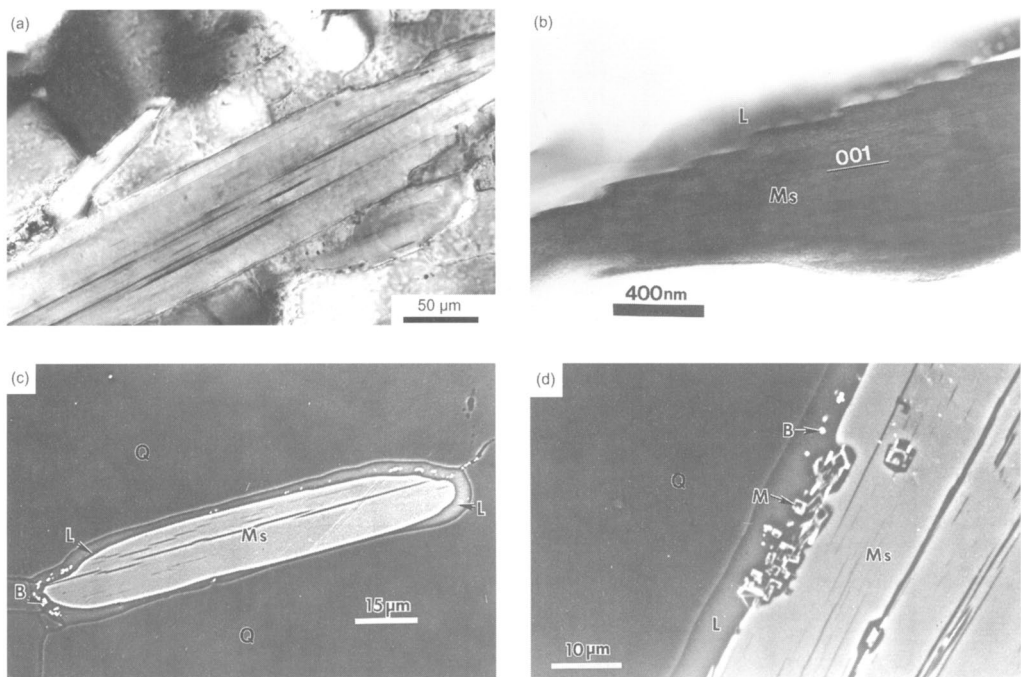


Fig. 8. Reaction of muscovite + quartz at 1 kbar (after Brearley & Rubie 1990). (a) Optical micrograph (crossed polarizers) of the quartz-muscovite schist starting material showing a grain of phenegitic muscovite (*c.* 0.5 mm long) enclosed in a quartz matrix. (b) Transmission electron micrograph showing an early stage of reaction in which a layer of melt, less than 1 μm wide, has formed along the grain boundary between quartz and muscovite. Note that the muscovite surface consists of segments parallel to (001) separated by distinct ledges; the dissolution of muscovite into the melt probably occurs by the lateral migration of these ledges. (c) Backscattered electron image (BSEI) showing a later stage of reaction in which the melt layer has widened and biotite grains (white) have started to nucleate. The nucleation of biotite is concentrated close to high surface energy regions of the muscovite boundary where the density of ledges (as seen in (b)) is high (29 h at 760°C and 1 kbar; H₂O-saturated). (d) BSEI showing the localized nucleation of mullite which occurs after biotite has nucleated (29 h at 760°C and 1 kbar; H₂O-saturated). Abbreviations: Ms, muscovite; Q, quartz; L, melt; B, biotite; M, mullite.

and also occasionally at intracrystalline sites in muscovite. In the experiments with 1 wt% H₂O added, K-feldspar was never observed as a product phase. Instead a metastable melting reaction occurred which produced melt, mullite and biotite (Rubie & Brearley 1987; Brearley & Rubie 1990). As discussed below, these phases nucleated sequentially and not simultaneously. At the lowest temperature (680°C), the melting reaction was extremely sluggish and after 6–8 weeks only a thin layer of melt, *c.* 0.3 μm wide, had formed along muscovite-quartz grain boundaries (Fig. 8b). At the highest temperature (760°C) the melting reaction reached completion after about 2 weeks (by consuming all the muscovite) and the metastable product phases persisted at these conditions for times up to 5 months. In the experiments without added H₂O, the reaction was also very sluggish. Silli-

manite, K-feldspar and biotite were observed as product phases but metastable melt was also always present. After 2 months at 680°C only a very thin melt layer was present, as in the H₂O-added experiments, whereas at 760°C it took several months before the muscovite was completely consumed by melt, sillimanite, mullite, K-feldspar and biotite.

With respect to reaction (R2), the study of Brearley & Rubie (1990) indicates that there is a very large energy barrier involved in the simultaneous nucleation of aluminosilicate + K-feldspar + biotite in low-porosity rocks with tight grain boundaries. Energetically it is much easier for metastable melt to nucleate first and then other phases (stable or metastable) to nucleate subsequently (and also sequentially, as discussed below). It is also energetically easier for metastable mullite to nucleate instead of

the stable aluminosilicate phase, as was also observed by Grapes (1986) in a study of muscovite breakdown in rapidly heated pelitic xenoliths from volcanic rocks. Once metastable phases form, they tend to persist (as in the high-pressure rocks from Monte Mucrone discussed above) because the driving force necessary to produce the stable equilibrium assemblage has been significantly reduced (Rubie & Brearley 1987).

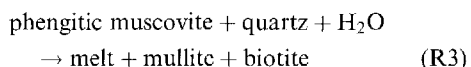
There is a huge difference between the reaction rates observed in the respective studies of Schramke *et al.* (1987) and Brearley & Rubie (1990). For example, at 680°C and 1 kbar (conditions which overstep the equilibrium boundaries R1 and R2 by 130–150°C), reaction (R2) did not even start in the latter study after 2 months; instead, very limited amounts of metastable melt formed (Fig. 8a). In contrast, the data of Schramke *et al.* (1987) suggest that more than 50% reaction should occur at these conditions within 4 days (Fig. 7). The experiments of the latter study did not require nucleation and the sluggishness of nucleation in the starting material of Brearley & Rubie (1990) was at least partly responsible for these contrasting results. Even if Schramke *et al.* (1987) had attempted to study nucleation by omitting one or more of the product phases from their starting materials, the results are unlikely to have been comparable. This is because nucleation occurs much more easily at surface–fluid interfaces than on grain boundaries (Rubie & Thompson 1985). In addition, growth kinetics are likely to be very different in the two types of starting materials. In the experiments of Schramke *et al.* (1987) growth was controlled by surface reactions between H₂O and the crystalline phases and was very fast. In a quartz–muscovite rock (e.g. Fig. 7a), if the product phases were able to eventually nucleate without metastable melt forming, growth would be controlled by grain-boundary diffusion (even in the H₂O-saturated case) and could therefore be orders of magnitude slower (Rubie 1986).

Not all dehydration reactions involve sluggish nucleation kinetics. For example, Rutter & Brodie (1988) observed experimentally that nucleation during the reaction serpentine → olivine + talc + H₂O occurs within a few degrees of the equilibrium boundary. Worden *et al.* (1991) also concluded that little overstepping is required from a study of the same reaction in a contact-metamorphic aureole. The very small oversteps required for nucleation during this reaction, compared with the large oversteps required for muscovite breakdown, may be related to differences in the strain and interfacial

energies. Such differences are likely to be caused by the degree of structural mismatch between the reactant and product phases in the respective reactions, as discussed above.

Melting reactions

The experimental study of Brearley & Rubie (1990) also provides an insight into the kinetics of nucleation during incongruous melting reactions, as discussed by Rubie & Brearley (1990). Under water-saturated conditions at 1 kbar, the observed reaction was:



The product phases of this reaction did not form simultaneously during melting but nucleated sequentially as shown in Figs 8 and 9. Melt was the first phase to nucleate and developed as a thin layer along quartz–muscovite grain boundaries. Biotite nucleated next after a time-dependent incubation period that consisted of a few hours at 760°C (Fig. 8c); however, at 680°C nucleation was not observed even after 2 months. The incubation period for mullite

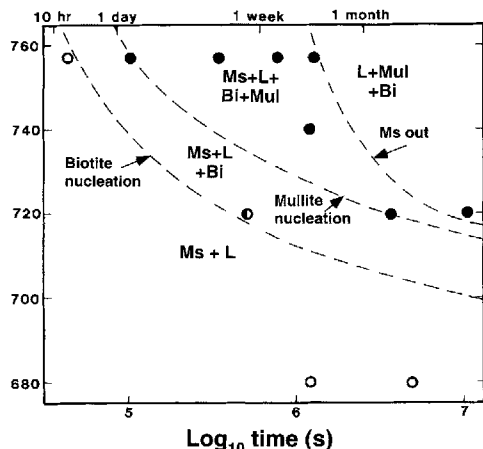


Fig. 9. Temperature–time–transformation (TTT) diagram showing the time-dependence of biotite and mullite reaction during the reaction phengitic muscovite + quartz → melt + mullite + biotite in the presence of excess quartz. Open circles, only melt present; half-filled circles, melt + biotite present; filled circles, melt + biotite + mullite present. At 680°C melt is the only phase to have nucleated after 2 months. Abbreviations: Ms, muscovite; Bi, biotite; Mul, mullite; L, melt (after Rubie & Brearley 1990).

nucleation was longer, was also temperature dependent, and varied from <30 h at 760°C to c. 1 month at 720°C (Fig. 8d); mullite nucleation was also never observed at 680°C. Although all three phases had nucleated after 6 weeks at the intermediate temperature of 720°C, the rarity of biotite and mullite grains indicates that the nucleation of these phases is very sluggish at this temperature. Even at the highest temperature (760°C), the initial nucleation of biotite and mullite generally occurs locally at high-energy sites, such as muscovite–melt interfaces which are oriented at a high angle to the (001) basal planes of muscovite. It is notable that at the lowest temperature (680°C), both biotite and mullite failed to nucleate even after 2 months, even though melt was present.

The sequential nucleation behaviour has an important effect on the kinetics of melting. Prior to mullite nucleation, the extent of melting is very limited because the melt becomes supersaturated in the mullite component and muscovite dissolution effectively ceases. Following mullite nucleation, the rate of melting becomes relatively fast and is controlled by multicomponent diffusion through the reaction zone of melt + crystals (Rubie & Brearley 1990).

A comparable reaction to (R3) in the K_2O – Al_2O_3 – SiO_2 – H_2O system (but with sillimanite as a product phase) is only stable at pressures above 5 kbar. At 1 kbar and 680–760°C the metastable extension of this reaction boundary must be overstepped (Fig. 7) in order to explain the observed melting reaction. Because the exact position of this metastable boundary is unknown, the amount of overstepping is also uncertain. However, assuming that the boundary lies at a slightly lower temperature than 680°C, the above results indicate that incubation periods are significant on a laboratory time scale even with an overstepping of 40°C (Fig. 9). The extrapolation of the nucleation curves shown in Fig. 9 to lower temperatures and longer time scales is highly uncertain. However, because the theoretical dependence of nucleation rates on overstepping is exponential (see above), the overstepping required for nucleation to occur on a geological time scale may not be significantly less than for nucleation on a laboratory time scale. In this case, incongruent melting reactions, involving the nucleation of new crystalline phases, might also require oversteps of tens of degrees in the Earth. The possibility of significant overstepping also being required for melt nucleation during eutectoid melting reactions has been discussed by Rubie & Brearley (1990); in this case the proposed mechanism for metastability under supersolidus conditions

involves a lack of mutual contact between the reactant phases.

Summary and discussion

The examples discussed above demonstrate that nucleation during a variety of solid–solid, dehydration and melting reactions can be a very sluggish process, even on geological time scales. This is particularly so when more than one new phase has to nucleate and when the structural differences between the reactant and product phases are large.

During polymorphic phase transformations (such as calcite to aragonite and olivine to silicate spinel) equilibrium boundaries typically need to be overstepped by 2–4 kbar for nucleation to occur experimentally. This estimate applies to well-annealed polycrystalline materials. Nucleation during high-pressure experiments in which the starting materials consist of powders may require smaller oversteps because of the high density of defects which develop during the pressurization and compaction of powders (Brearley *et al.* 1992). However, significant nucleation barriers still exist (e.g. Zhang *et al.* 1996). Even in annealed polycrystals, nucleation rates can be very sensitive to the grain-boundary structure and therefore to the extent of pre-transformation annealing (Mosenfelder 1996).

In the case of reactions with multiple product phases, much larger oversteps can be required for nucleation. Plagioclase, for example, can survive for millions of years at 20 kbar and 600°C, in the stability field of jadeite + grossular + kyanite + quartz, without any of these phases nucleating. This is in spite of a large thermodynamic driving force for reaction due to the initial plagioclase breakdown reaction being overstepped by >7 kbar at these conditions (Fig. 3a). Even when hydrous fluid becomes available, only zoisite is able to nucleate easily at intracrystalline sites in plagioclase. The other phases of the hydrous breakdown reaction – jadeite, kyanite and quartz – only nucleate at sites which are energetically favourable, such as the walls of fluid-filled fractures.

In an experimental investigation of the dehydration reaction phengitic muscovite + quartz → aluminosilicate + K-feldspar + biotite + H_2O at 1 kbar, the direct nucleation of the product phases was never observed. Even at temperature oversteps of >120°C, muscovite + quartz persisted as metastable phases for times up to 2 months, with only trace amounts of metastable silicate melt forming along muscovite–quartz grain boundaries. At higher oversteps (c. 200°C),

reaction was rapid but usually involved the nucleation and growth of metastable phases; when aluminosilicate, K-feldspar and biotite did nucleate, it was always via an intermediate metastable melt phase. In contrast, very small oversteps are required for nucleation during the dehydration reaction serpentine \rightarrow olivine + talc + H_2O (Rutter & Brodie 1988; Worden *et al.* 1991).

Even nucleation during melting reactions can require considerable overstepping in experimental studies, especially if multiple product phases have to form. The nucleation of product phases does not occur simultaneously but rather sequentially. Whether significant overstepping occurs on geological time scales is currently uncertain, although this is possible as a consequence of several different mechanisms (see Rubie & Brearley 1990).

The simultaneous nucleation of multiple phases requires the highly ordered separation of chemical components through diffusion to specific sites. However, until the phases have actually nucleated, there can be no well-defined chemical potential gradients that are required for these components to diffuse in the correct direction. The development of the correct concentration of components for the nucleation of one of the phases at a given site is a chance event to which, in principle, a statistical probability can be assigned. The chances of developing the critical component concentrations that are required for several different phases nucleating at multiple sites simultaneously is evidently extremely small.

When metamorphic reactions occur under marked disequilibrium conditions (i.e. at large pressure or temperature oversteps of equilibrium conditions), due to delayed nucleation, reaction rates can be very fast. This is at least partly because the driving force for transformation (ΔG_r) is large under such conditions. When nucleation is catalysed by fluid influx under disequilibrium conditions (as in the Allalin metababbro), the presence of fluid will also contribute to fast reaction rates. Delayed nucleation during metamorphism is also likely to result in rapid rates of partial melting during metamorphism. This is because under disequilibrium conditions, when the temperature significantly oversteps the equilibrium boundary, the melting rate becomes controlled by kinetic factors (e.g. diffusion) rather than by the rate of regional heat flow (see Rubie & Brearley 1990).

A consequence of rapid reaction rates occurring under disequilibrium conditions is that metastable phases are likely to form instead of the stable mineral assemblage, as predicted by the

Ostwald step rule (e.g. Putnis & McConnell 1980; Rubie & Brearley 1987). The formation of jadeitic pyroxenes in gabbros and quartz diorites during high-pressure metamorphism in the Western Alps is one example, as discussed above. A further example of such behaviour is the metastable melting of muscovite + quartz under sub-solidus conditions which occurs experimentally because the stable phases (K-feldspar + aluminosilicate + biotite) fail to nucleate.

Once metastable phases have formed, the thermodynamic driving force for forming the stable assemblage is reduced (because of the reduction in free energy). This means that the metastable phases may persist on long time scales even during high-strain ductile deformation in the presence of hydrous fluid. Metastable phases persisted in both examples mentioned in the previous paragraph. The orthogneisses at Monte Mucrone, which were derived from metaquartz diorite by deformation accompanied by fluid influx, are a particularly good example of the survival of phases (pyroxene and garnet) with metastable compositions through regional metamorphism (Koons *et al.* 1987). If such phases are not recognized as being metastable, the application of thermobarometric techniques will clearly result in incorrect estimates of the P - T paths followed during metamorphism.

I thank S. Chakraborty and M. Riedel for constructive reviews, S. Karato, L. Kerschhofer, J. Mosenfelder, P. O'Brien, T. Sharp and F. Seifert for helpful discussions, A. Brearley for providing Fig. 8b.

References

- BREARLEY, A. J. 1987. A natural example of the disequilibrium breakdown of biotite at high temperature: TEM observations and comparison with experimental data. *Mineralogical Magazine*, **51**, 93–106.
- & RUBIE, D. C. 1990. Effects of H_2O on the disequilibrium breakdown of muscovite + quartz. *Journal of Petrology*, **31**, 925–956.
- , — & ITO, E. 1992. Mechanisms of the transformations between the α , β and γ polymorphs of Mg_2SiO_4 at 15 GPa. *Physics and Chemistry of Minerals*, **18**, 343–358.
- CARLSON, W. D. & ROSENFIELD, J. L. 1981. Optical determination of topotactic aragonite calcite growth kinetics: metamorphic implications. *Journal of Geology*, **89**, 615–638.
- CHINNER, G. A. & DIXON, J. E. 1973. Some high-pressure parageneses of the Allalin gabbro, Valais, Switzerland. *Journal of Petrology*, **14**, 185–202.
- CHRISTIAN, J. W. 1975. *The Theory of Transformations in Metals and Alloys*. Pergamon, Oxford.

CLEVELAND, J. J. & BRADT, R. C. 1978. Grain size/microcracking relations for pseudobrookite oxides. *Journal of the American Ceramic Society*, **61**, 478–481.

DUPAS, C., SHARP, T. G., RUBIE, D. C. & DURHAM, W. B. 1998. Mechanisms of transformation and deformation in $Mg_{1.8}Fe_{0.2}SiO_4$ olivine and wadsleyite under non-hydrostatic stress. *Physics of the Earth and Planetary Interiors*, in press.

FRUEH-GRENF, G. L. 1994. Interdependence of deformation, fluid infiltration and reaction progress recorded in eclogitic metagranitoids (Sesia Zone, Western Alps). *Journal of Metamorphic Geology*, **12**, 327–343.

GRAPES, R. H. 1986. Melting and thermal reconstitution of pelitic xenoliths, Wehr Volcano, East Eifel, Germany. *Journal of Petrology*, **27**, 343–396.

HACKER, B. R., BOHLEN, S. R. & KIRBY, S. H. 1993. Albite \rightarrow jadeite + quartz transformation in albite. *EOS. Transactions of the American Geophysical Union, Fall Meeting Supplement*, **74**, 611.

HEINRICH, C. A. 1982. Kyanite-eclogite to amphibolite evolution of hydrous mafic and pelitic rocks, Adula Nappe, central Alps. *Contributions to Mineralogy and Petrology*, **81**, 30–38.

HOGREFE, A., RUBIE, D. C., SHARP, T. G. & SEIFERT, F. 1994. Metastability of enstatite in deep subducting lithosphere. *Nature*, **372**, 351–353.

JOESTEN, R. 1977. Evolution of mineral assemblage zoning in diffusion metasomatism. *Geochimica Cosmochimica Acta*, **41**, 649–670.

KERSCHHOFFER, L., SHARP, T. G. & RUBIE, D. C. 1996. Intracrystalline transformation of olivine to wadsleyite and ringwoodite under subduction zone conditions. *Science*, **274**, 79–81.

KOONS, P. O., RUBIE, D. C. & FRUEH-GREEN, G. 1987. The effects of disequilibrium and deformation on the mineralogical evolution of quartz diorite during metamorphism in the eclogite facies. *Journal of Petrology*, **28**, 679–700.

LEGOUES, F. K. & AARONSON, H. I. 1984. Influence of crystallography upon critical nucleus shapes and kinetics of homogeneous, f.c.c.–f.c.c. nucleation – IV. Comparisons between theory and experiment in Cu-Co alloys. *Acta Metallurgica*, **32**, 1855–1864.

—, — & LEE, Y. W. 1984a. Influence of crystallography upon critical nucleus shapes and kinetics of homogeneous f.c.c.–f.c.c. nucleation – III. The influence of elastic strain energy. *Acta Metallurgica*, **32**, 1845–1853.

—, LEE, Y. W. & AARONSON, H. I. 1984b. Influence of crystallography upon critical nucleus shapes and kinetics of homogeneous f.c.c.–f.c.c. nucleation – II. The non-classical regime. *Acta Metallurgica*, **32**, 1837–1843.

LIU, M. & YUND, R. A. 1993. Transformation kinetics of polycrystalline aragonite to calcite: new experimental data, modelling, and implications. *Contributions to Mineralogy and Petrology*, **114**, 465–478.

MEYER, J. 1983a. *Mineralogie und Petrologie des Allalin Gabbros*. PhD Thesis, University of Basel.

— 1983b. The development of the high pressure metamorphism in the Allalin metagabbro (Switzerland). *Terra Cognita*, **3**, 187.

MØRK, M. B. E. 1985. A gabbro to eclogite transition on Flemøy, Sunnmøre, western Norway. *Chemical Geology*, **50**, 283–310.

MOSENFELDER, J. L. 1996. *Kinetics of Metamorphic Reactions*. PhD Thesis, Stanford University.

OBERHÄNSLI, R., HUNZIKER, J. C., MARTINOTTI, G. & STERN, W. B. 1985. Geochemistry, geochronology and petrology of Monte Mucrone: an example of Eo-Alpine eclogitization of Permian granitoids in the Sesia-Lanzo Zone, Western Alps, Italy. *Chemical Geology*, **52**, 165–184.

PORTER, D. A. & EASTERLING, K. E. 1992. *Phase Transformations in Metals and Alloys*. Chapman and Hall, London.

PUTNIS, A. & MCCONNELL, J. D. C. 1980. *Principles of Mineral Behaviour*. Blackwell, Oxford.

RAJ, R. & ASHBY, M. F. 1971. On grain boundary sliding and diffusional creep. *Metal Transactions*, **2**, 1113–1127.

RUBIE, D. C. 1983. Reaction-enhanced ductility: the role of solid–solid univariant reactions in deformation of the crust and mantle. *Tectonophysics*, **96**, 331–352.

— 1986. The catalysis of mineral reactions by water and restrictions on the presence of aqueous fluid during metamorphism. *Mineralogical Magazine*, **50**, 399–415.

— 1990. Role of kinetics in the formation and preservation of eclogites. In: CARSWELL, D. A. (ed.) *Eclogite Facies Rocks*. Blackie, Glasgow, 111–140.

— & BREARLEY, A. J. 1987. Metastable melting during the breakdown of muscovite + quartz at 1 kbar. *Bulletin de Minéralogie*, **110**, 533–549.

— & — 1990. A model for rates of disequilibrium melting during metamorphism. In: ASHWORTH, J. R. & BROWN, M. (eds) *High-temperature Metamorphism and Crustal Anatexis*. Unwin Hyman, London, 57–86.

— & THOMPSON, A. B. 1985. Kinetics of metamorphic reactions at elevated temperatures and pressures: an appraisal of available experimental data. In: THOMPSON, A. B. & RUBIE, D. C. (eds) *Metamorphic Reactions: Kinetics Textures and Deformation*. Springer, New York, 27–79.

—, TSUCHIDA, Y., YAGI, T., UTSUMI, W., KIKEGAWA, T., SHIMOMURA, O. & BREARLEY, A. J. 1990. An in situ X ray diffraction study of the kinetics of the Ni_2SiO_4 olivine–spinel transformation. *Journal of Geophysical Research*, **95**, 15 829–15 844.

RUTTER, E. H. & BRODIE, K. H. 1988. Experimental ‘syntectonic’ dehydration of serpentinite under conditions of controlled water pressure. *Journal of Geophysical Research*, **93**, 4907–4932.

SAWAMOTO, H. 1987. Phase diagrams of $MgSiO_3$ at pressures up to 24 GPa and temperatures up to 2200°C: phase stability and properties of tetragonal garnet. In: MANGHINANI, M. H. & SYONO, Y. (eds) *High Pressure Research in Mineral Physics*. Geophysical Monograph **39**. AGU, Washington, 209–219.

SCHRAMKE, J. A., KERRICK, D. M. & LASAGA, A. C. 1987. The reaction muscovite + quartz = andalusite + K-feldspar + water. Part 1. Growth kinetics and mechanism. *American Journal Science*, **287**, 517–559.

TURNBULL, D. 1956. Phase changes. *Solid State Physics*, **3**, 225–306.

WAYTE, G. J., WORDEN, R. H., RUBIE, D. C. & DROOP, G. T. R. 1989. A TEM study of disequilibrium plagioclase breakdown at high pressure: the role of infiltrating fluid. *Contributions to Mineralogy and Petrology*, **101**, 426–437.

WOOD, B. J. & WALTHER, J. V. 1983. Rates of hydrothermal reactions. *Science*, **222**, 413–415.

WORDEN, R. H., DROOP, G. T. R. & CHAMPNESS, P. E. 1991. The reaction antigorite → olivine + talc + H_2O in the Bergell aureole, N. Italy. *Mineralogical Magazine*, **55**, 367–377.

—, — & — 1992. The influence of crystallography and kinetics of phengite breakdown reactions in a low-pressure metamorphic aureole. *Contributions to Mineralogy and Petrology*, **110**, 329–345.

YUND, R. A. & TULLIS, J. 1991. Compositional changes of minerals associated with dynamic recrystallization. *Contributions to Mineralogy and Petrology*, **108**, 346–355.

ZHANG, J., LI, B., UTSUMI, W. & LIEBERMANN, R. C. 1996. In situ X-ray observations of the coesite–stishovite transition: reversed phase boundary and kinetics. *Physics and Chemistry of Minerals*, **23**, 1–10.

Chemical and volume changes during deformation and prograde metamorphism of sediments

R. H. VERNON

School of Earth Sciences, Macquarie University, Sydney NSW 2109, Australia

Abstract: A long-standing problem is the extent of selective removal of chemical components and the amount of volume loss during the formation of slaty and crenulation cleavages during prograde metamorphism of sediments. Heterogeneous deformation leads to the formation of strongly deformed phyllosilicate-rich (P) domains and less deformed quartz-rich (Q) domains. The rocks generally show evidence of solution of quartz in P domains and addition of quartz in Q domains. The problem is whether the subtractions and additions balance or whether silica is lost from the system on the metre or broader scales. Structural studies tend to favour volume loss, whereas chemical studies tend to favour no volume loss. This review indicates that it is not yet possible to determine which of these views is correct. Deformation heterogeneity and fluid activity on a range of scales may play an important part in the development of slaty cleavage, suggesting the need for a detailed coordinated study, in which structural geologists and geochemists study identical material from the same sedimentary beds, in different parts of folds.

Local compositional changes may develop adjacent to quartz veins, and some aluminous ('pseudopelitic') mineral assemblages may develop in igneous rocks by base-cation leaching before or during metamorphism. However, broad chemical changes with metamorphic grade are difficult to determine, owing to protolith variation on all scales, although much more detailed chemical work with good geological control remains to be done. Marked local protolith variability may also hamper attempts to determine the chemical effects of cleavage formation.

As the density of metamorphic rocks increases generally with increasing grade, inferred conservation of mass on a regional scale implies loss of volume, which conceivably could be accommodated by collapse during deformation. Inferred volume loss implies a mass loss appropriate to the density increase. Inferred volume conservation implies regional mass gain, which is intuitively less probable. Marked chemical and volume changes occur when partial melts are removed at highest metamorphic grades.

Long-standing problems in the investigation of prograde metasedimentary rocks have been to determine: (1) the amount and scale of bulk chemical change and volume loss, if any, and (2) the relationship of such changes to metamorphism.

The controversy especially applies to slaty cleavage, but also to differentiated crenulation foliations at higher metamorphic grades. Most work has concentrated on slates, because (1) solution processes dominate at low metamorphic grades and (2) detrital grains and/or fossils commonly serve as markers of strain and degree of solution. However, crenulations at intermediate and high grades of metamorphism are commonly strongly compositionally differentiated, so that the possibility of solution transfer and selective volume loss must be considered at all metamorphic grades.

The problem is to determine with confidence whether material demonstrably dissolved from high-strain domains rich in layer silicates has been deposited in adjacent low-strain domains rich in quartz, or whether it has been removed from the local domainal system, at least on the

mesoscopic (metre) scale, perhaps to form the quartz veins that are so abundant in slate belts. The difficulty has not yet been resolved. The following questions will be addressed, both in general terms and with reference to specific areas.

- (1) What is the structural evidence for mass and/or volume loss? The underlying assumption is that the shapes and sizes of strain markers are well enough known.
- (2) What is the chemical evidence for mass and/or volume loss? The underlying assumption is that certain chemical elements are immobile enough to serve as constants when comparing the compositions of cleavage domains.

In an attempt to answer these questions, this review begins with a discussion and evaluation of the controversy about the formation of 'slaty cleavage' in low-grade rocks (slates and phyllites) and 'crenulation cleavage' in higher-grade rocks (schists and some gneisses). Detailed investigations of cleavage development in several areas will be reviewed, after which the present state of the controversy will be discussed. Then a

shorter discussion of problems involving crenulation cleavage in higher-grade schists is followed by a discussion of the evidence, scale and timing of bulk chemical changes not specifically related to foliation development. The review concludes with a brief discussion of local controls on chemical composition and consequent effects on local 'effective reaction volumes', as well as a mention of rocks hydrothermally altered before and during metamorphism to form 'pseudopelitic' compositions.

Deformation partitioning

Slates, phyllites and some schists typically have a lenticular, foliated domainal structure ('slaty cleavage') that reflects the tendency of deformation to be partitioned into high- and low-strain domains, called 'P' (or 'M') and 'Q' domains, respectively (Figs 1–6). The P domains are generally rich in aligned white mica, chlorite, and/or fine-grained, dark, carbonaceous and/or iron–titanium oxide aggregates, and anastomose around Q domains that commonly consist of detrital quartz grains, with feldspar in some

rocks, and less aligned phyllosilicate grains. This separation into compositionally distinct domains is generally called 'metamorphic differentiation' (Stillwell 1918). P domains may be intensified adjacent to larger clasts (e.g. Woodland 1985, figs 8a, 8b), presumably owing to greater stress and/or strain concentration at these sites. Some P domains consist largely of interlayered white mica–chlorite 'stacks' of controversial origin, possibly representing much-modified detrital clay or chlorite clasts in many instances (Beutner 1978; Roy 1978; Gregg 1986).

Also common in slates and phyllites, as well as higher-grade schists, is 'crenulation cleavage', which is similarly differentiated into Q and P domains (Figs 7–10), and develops in previously foliated rocks. The P domains in slaty cleavages tend to have sharper boundaries and anastomose more than crenulation cleavages (Williams 1990, p. 273). However, in many slates, the dominant, apparently first cleavage (identified as a 'slaty cleavage' in the field or hand specimen) is in fact a crenulation, either of a bedding-parallel foliation (Knipe & White 1977; Knipe 1981; Weber 1981) or an earlier tectonic foliation that is broadly sub-parallel to bedding, but in detail oblique to it (Powell & Rickard 1985). Gradations from slaty to crenulation cleavages and vice versa are common (e.g. Williams 1972, 1990; Bell & Rubenach 1983), and P domains rich in fine-grained dark material in some slates resemble stylolitic solution seams (e.g. Williams 1990). Figures 7 and 8 show folia (crenulation cleavage) rich in opaque material crenulating earlier folia (slaty cleavage) with similar dark concentrations, indicating that very similar or identical metamorphic differentiation processes can occur in both styles of cleavage development.

Therefore, both slaty and crenulation cleavages can be discussed in relation to the problem of compositional and volume changes. However, though some slaty cleavages may develop at very early or even premetamorphic conditions, most crenulation cleavages develop at metamorphic conditions of the greenschist facies and above. Consequently, crenulation cleavages in medium- to high-grade schists will be discussed separately from slaty cleavage in this review.

Generally, P domains are interpreted as insoluble residues resulting from the solution of quartz or carbonate (as discussed later), generally with evidence of neocrystallization of phyllosilicates (or sillimanite at highest grades of metamorphism) parallel to the foliation. Though some curvature of phyllosilicate grains at the edges of Q domains into P domains is common, old phyllosilicate grains statistically parallel to an earlier foliation or bedding generally appear



Fig. 1. Slate and siltstone beds with strong compositional layering approximately parallel to the axial surfaces of crenulation folds at Bermagui, SE Australia. The dark seams are concentrations of P domains in attenuated fold limbs. Knife is 9 cm long.

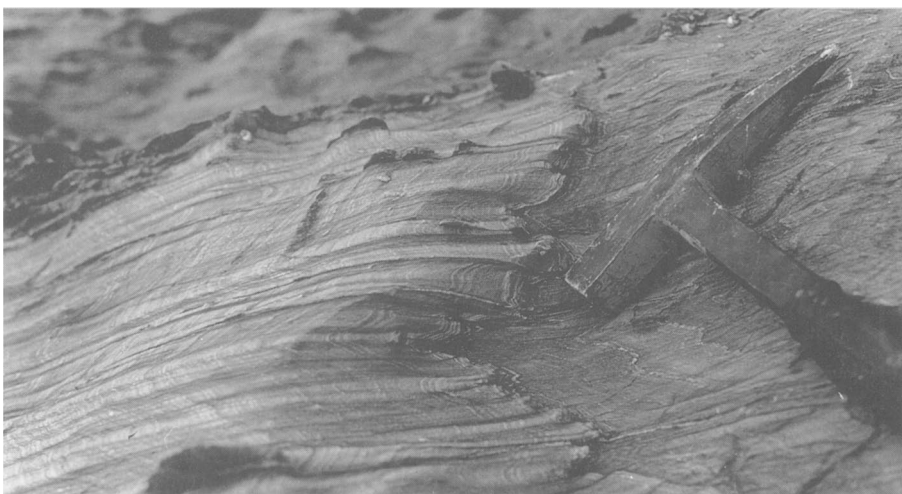


Fig. 2. Slate and silty slate beds with strong compositional layering approximately parallel to the axial surfaces of crenulation folds at Bermagui, SE Australia. The dark seams are concentrations of P domains in attenuated fold limbs.

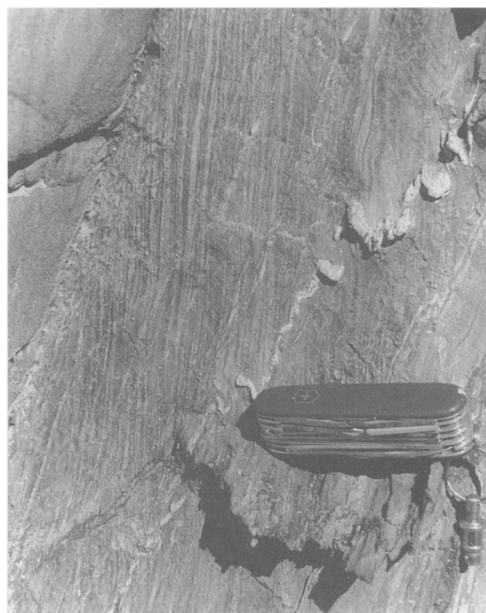


Fig. 3. Strong compositional layering oblique to bedding at Bermagui, SE Australia. The dark seams are concentrations of P domains in attenuated fold limbs, and remnants of quartz veins have been partly dissolved along the folia. Knife is 9 cm long.

to have been dissolved against the developing P domains (e.g. Lee *et al.* 1986).

In some slates and schists, the Q domains appear to be largely unmodified, showing detrital microstructures (e.g. Williams 1972; Etheridge

et al. 1983, fig. 2), as shown in Figs 5 and 6, whereas in other slates and some metasandstones, the quartz grains in the Q domains have overgrowths of quartz or of quartz–phyllosilicate ‘beards’ extending parallel to the cleavage (e.g. Powell 1969, figs 3, 5; Williams 1972; Brandon *et al.* 1994), as shown in Fig. 4. In many slates, the quartz clasts in Q domains are only weakly deformed or non-deformed, with only slight to no undulose extinction and little or no evidence of recrystallization; this indicates that their change into elongate shapes parallel to the cleavage is due largely to solution, rather than crystal-plastic processes (e.g. Williams 1972; Gray 1978; Bell 1978; Gregg 1985).

In slates in which detrital microstructures are preserved in Q domains, the metamorphic differentiation is dominated by grain rotation and diffusion processes (e.g. Williams 1972), whereas in other slates and phyllites, as well as in crenulation cleavages, recrystallization and neo-crystallization dominate (Beutner 1978; Bell 1978; Lee *et al.* 1986; Etheridge & Lee 1975), probably with some grain rotation. It appears that the process of metamorphic differentiation in these rocks involves diffusion through static fluid, fluid flow or both, because solid diffusion is too slow (e.g. Fyfe & Kerrich 1985).

Some slates have chlorite–white mica ‘stacks’ with their cleavages oriented obliquely to the slaty cleavage. Beutner (1978) suggested a primary origin, but the ‘stacks’ do not resemble typical unmodified detrital mica clasts (Gregg 1986), which tend to be very thin, owing to splitting along the cleavage during transport.

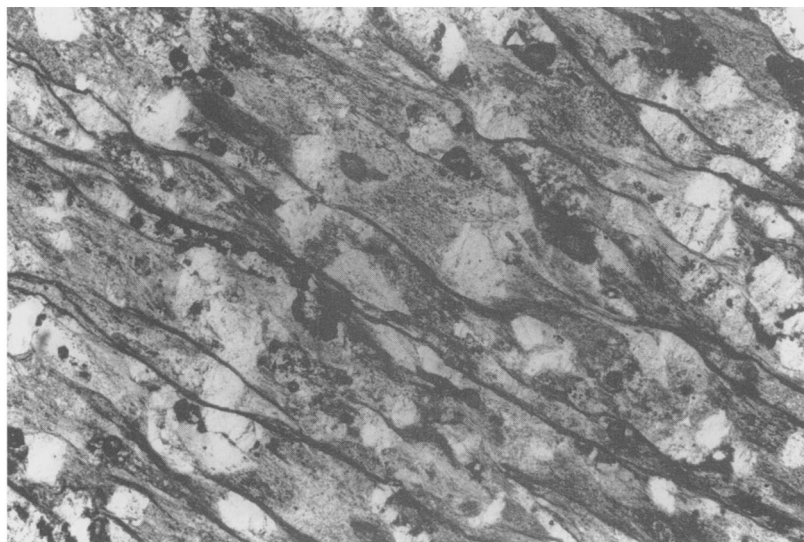


Fig. 4. Dark solution seams (P domains) between clay-rich, chert and recrystallized quartz clasts, which have been truncated by the seams and which have quartz-phyllosilicate 'beards' parallel to the foliation. Foothills terrane, central Sierra Nevada, California, USA. Plane-polarized light; base of photo 2.6 mm.

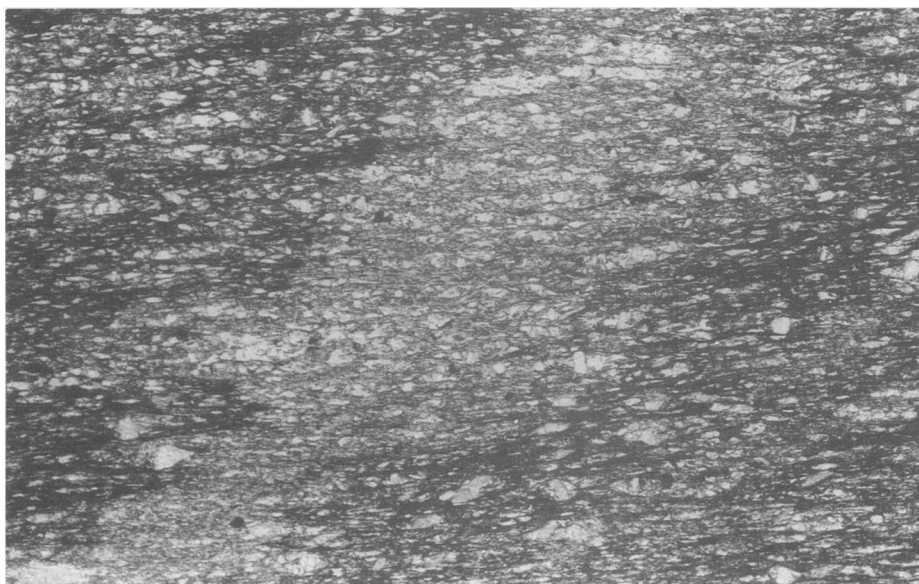


Fig. 5. Slate, with prominent slaty cleavage cutting obliquely an earlier, vaguely defined compositional layering (probably sedimentary bedding) marked mainly by variations in the concentration of fine-grained opaque (probably carbonaceous) material. Thin dark folia (P domains), composed mainly of phyllosilicates and (?)carbonaceous material, anastomose around detrital grains that are now lenticular and elongate in the cleavage, owing to solution; some have 'beards'. A marked domainal microstructure results from the compositional and microstructural contrasts between the folia (P domains) and the clast-rich lenses (Q domains). Plane-polarized light; base of photo 6 mm.

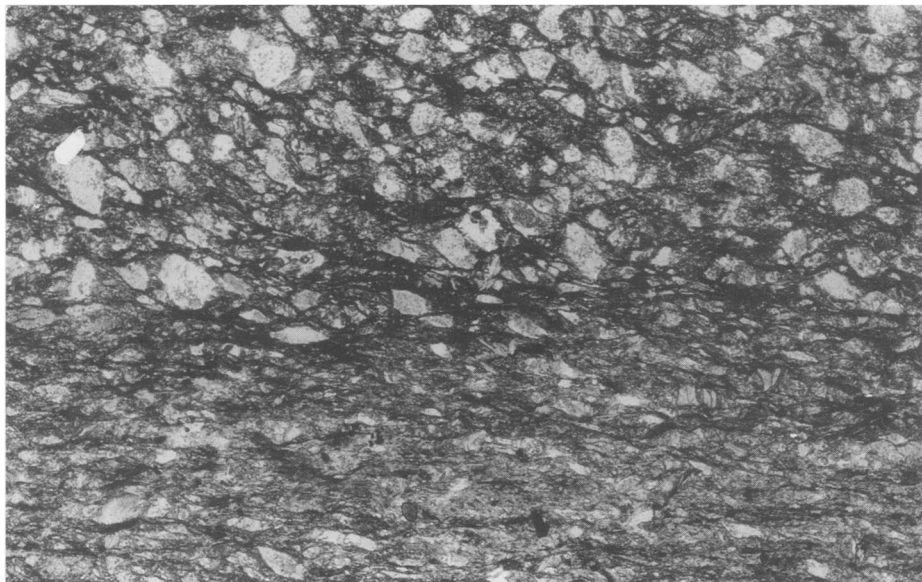


Fig. 6. Sandy siltstone (above) and silty shale (below), containing angular clasts of quartz, feldspar and phyllosilicates. A slaty cleavage is relatively well developed in the shale bed, but is more spaced in thin, anastomosing folia (P domains) in the siltstone bed. Quartz and feldspar clasts made lenticular by solution are parallel to the cleavage and bent detrital phyllosilicate grains are oblique to it. Plane-polarized light; base of photo 6 mm.

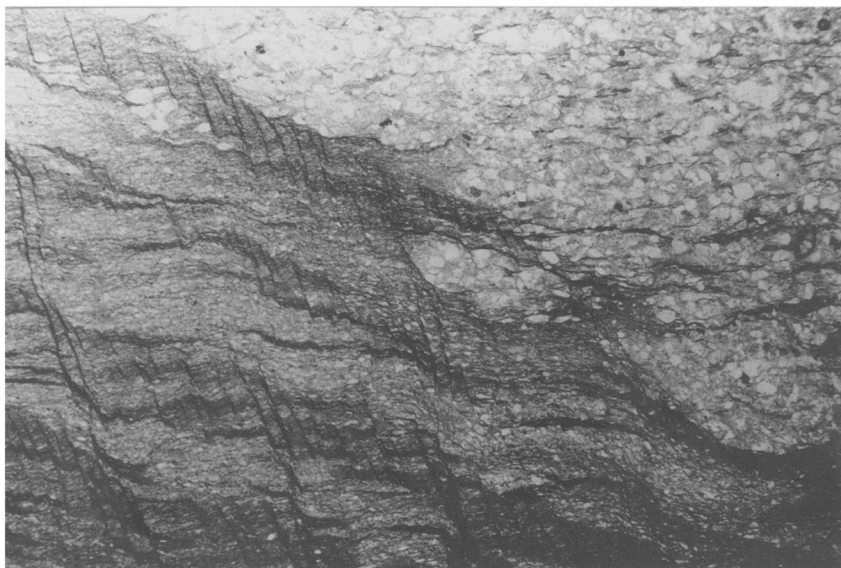


Fig. 7. Bed of siltstone (right) with weakly developed slaty cleavage and slate (left) with well-developed slaty and crenulation cleavages. Fine-grained, opaque, carbonaceous material has been concentrated as discontinuous folia in both the slaty and crenulation cleavages, indicating that similar processes operated in the formation of both. Foothills terrane, central Sierra Nevada, California, USA. Plane-polarized light; base of photo 6.3 mm.

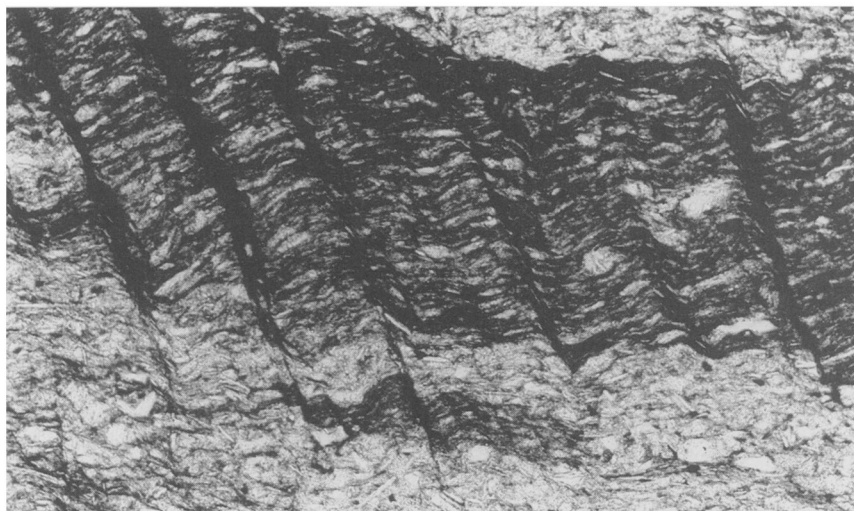


Fig. 8. Crenulated slate clast in metasiltstone, showing strong concentrations of opaque material in the attenuated limbs of the microfolds, and a finely domainal slaty cleavage preserved in the hinge zones. Foothills terrane, central Sierra Nevada, California, USA. Plane-polarized light; base of photo 0.9 mm.

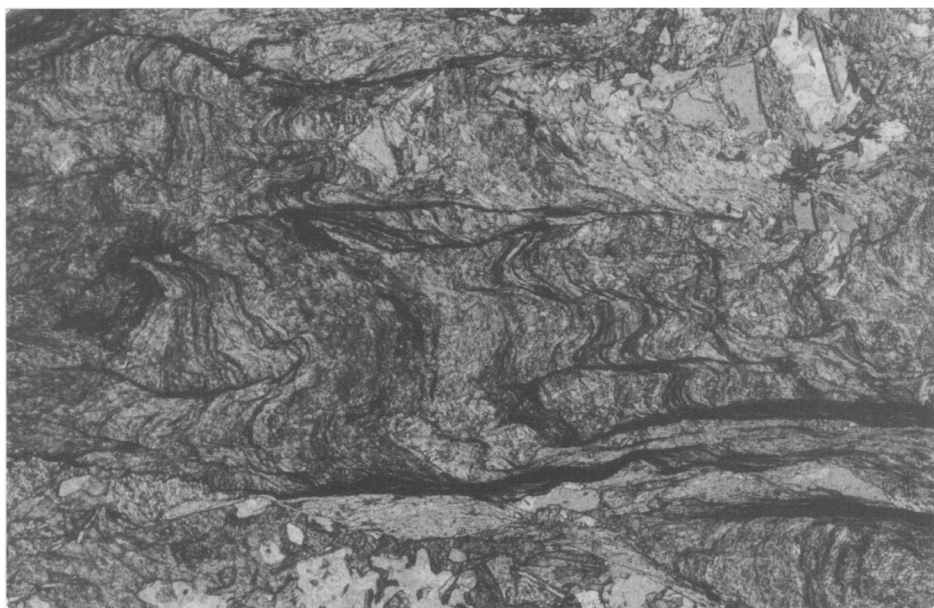


Fig. 9. Crenulation folds in a low-grade mica schist, with some strongly attenuated limbs, in which fine-grained mica-rich and opaque aggregates have been concentrated, forming a relatively spaced, discontinuous crenulation cleavage. These concentrations probably represent relatively insoluble material remaining after solution and removal of soluble minerals, especially quartz. Opaque material has been particularly concentrated in a high-strain zone (bottom). Plane-polarized light; base of photo 6 mm.

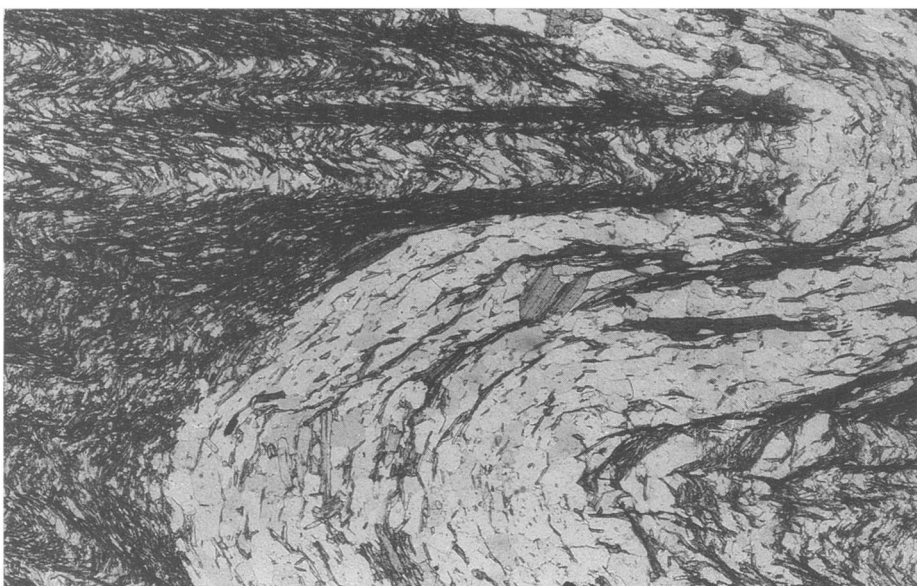


Fig. 10. Folded quartz-rich and mica-rich beds in a schist. A crenulation cleavage has been developed only in the mica schist (left and bottom-right). Mica has been concentrated in the attenuated limbs of the microfolds, implying removal of quartz. The earlier foliation, which has been crenulated, may be a bedding-parallel fissility, but is probably a slaty cleavage. Plane-polarized light; base of photo 6 mm.

In contrast, many 'stacks' are much thicker perpendicular to their cleavage than parallel to it, reflecting their growth in Q domains during development of the slaty cleavage. This interpretation implies that migration and deposition of phyllosilicate components into Q domains occurs during the development of slaty cleavage in some rocks. Several workers have interpreted the 'stacks' as primary clasts modified by fracturing and growth of secondary phyllosilicate (Roy 1978; van der Pluijm & Kaars-Sijpesteijn 1984; Milodowski & Zalasiewicz 1991; Clark & Fisher 1995). Clark & Fisher (1995) found that two chlorite compositions occur in the 'stacks', which they interpreted as reflecting clastic and secondary chlorite. This implies that the detrital chlorite compositions did not equilibrate at the conditions at which the cleavage was formed.

Slaty cleavage

Premetamorphic and early metamorphic changes

Sedimentary (pretectonic) compaction during dewatering can account for around 50%

volume loss in slates (Oertel 1970; Ramsay & Wood 1973; Beutner 1978; Beutner & Charles 1985; Paterson *et al.* 1995). Though cleavages may form in sedimentary slumps (e.g. Paterson & Tobisch 1993), compaction is not generally associated with cleavage development, unless it continues during the early stages of folding, as axial-surface cleavages initiate. If slaty cleavage can form mechanically during dewatering in this way, the consequent volume change should not result in bulk chemical change. Theoretically this could explain at least some of the discrepancy between structural and chemical studies, discussed later. However, once compositional differentiation between layers begins to develop, regardless of the mechanism, the question of mass and volume change arises.

As mentioned above, incipient cleavages have been observed in unconsolidated sediments (e.g. Moore & Geigle 1974; Paterson *et al.* 1995), especially in slumps (Williams *et al.* 1969; Maltman 1981; Paterson & Tobisch 1993), the foliation being formed mainly by rotation of existing phyllosilicates, which is a mechanism for forming slaty cleavage suggested by Sorby (1853). The problem is to determine how much of the volume loss associated with slaty cleavage formation inferred by some structural studies (discussed below) is related to premetamorphic

and early metamorphic stages of development, and how much to later stages that are typically regarded as being metamorphic (e.g. at greenschist facies conditions). Compaction dewatering is not relevant to the formation of crenulation cleavages at higher metamorphic grades.

Maxwell (1962) inferred that slaty cleavage in the Martinsburg Formation, New Jersey, was formed by bodily rotation of phyllosilicate grains during tectonic dewatering of unconsolidated pelitic sediments – a hypothesis subsequently applied by several others (e.g. Moench 1966; Carson 1968; Powell 1969; 1972a, b; Clark 1970; Alterman 1973; Moore 1973; Roy 1978). However, more recent work (e.g. Epstein & Epstein 1969; Boulter 1974; Geiser 1975; Etheridge & Lee 1975; Holeywell & Tullis 1975; Groshong 1976; Bell 1978; Williams 1983) has favoured solution of old grains and neocrystallization to form the cleavage in these and other rocks, although some grain rotation is usually accepted.

For example, Holeywell & Tullis (1975) inferred that slaty cleavage in the Martinsburg Formation at Lehigh Gap, Pennsylvania, could not have been formed by mechanical grain rotation because: (1) the orientations of phyllosilicate grains change abruptly from bedding-parallel to cleavage-parallel, and (2) individual bedding-parallel phyllosilicate grains may be truncated abruptly by cleavage folia. However, by combining scanning electron microscopy (SEM), X-ray diffraction, optical studies and X-ray texture goniometry, Ho *et al.* (1995) showed that the orientations of mica and chlorite grains change gradually from mudstone to slate in the Martinsburg Formation at Lehigh Gap. They suggested that mechanical reorientation of phyllosilicates, accompanied by solution-neocrystallization was important in the early stages of cleavage formation, whereas solution-neocrystallization dominated at later stages, accounting for the observations of Holeywell & Tullis (1975).

Bell (1985) calculated that deformed lapilli tuffs in the English Lake District were initially diagenetically compacted normal to bedding, after which cleavage developed tectonically, initially by uniaxial volume reduction normal to the incipient cleavage, which involved porosity reduction, clast rotation and early metamorphic dewatering reactions; this was incrementally replaced by plane-strain deformation, which conserved volume. However, Boulter (1986) showed that the data can also be explained by plane strain, with moderate incremental volume loss, superimposed on variable compaction strains. This discrepancy in interpretation illustrates the problem of inferring

strain histories and assigning ratios of prelithification to tectonic strain in cleavage formation. As stated by Paterson *et al.* (1995), 'strain paths in pelitic rocks always include early compaction, which may be followed by an episode of simultaneous compaction and plane strain in accretionary wedges and by a variety of other types of strain in other settings.'

Beutner (1978) suggested the following sequence of events for the development of slaty cleavage in the Martinsburg Slate in New Jersey, USA: (1) *sedimentary compaction*, accounting for about 50% volume reduction; (2) *layer-parallel shortening* of around 25% before and during the early stages of buckle folding, associated with around 10% volume loss accompanying an increase in density from 2.5 (shale) to 2.8 (slate), as discussed by Wood (1974), although some of the volume loss could have occurred later; (3) *limb rotation* and (4) *flattening* (of around 50%) and *cleavage development* as limb rotation was retarded and material was forced out of the fold cores. This last deformation was accomplished by (i) solution of quartz (Groshong 1976) and phyllosilicate minerals, especially where they impinged on growing cleavage films, and (ii) growth of new mica grains in the films (P domains) and new mica, chlorite and quartz grains between the films (Q domains). Because the average orientation of detrital chlorite grains remains parallel to bedding, and because fibrous 'beards' on the chlorite grains are parallel to each other and to the slaty cleavage, Beutner (1978) suggested that grain rotation during prelithification dewatering was not a major factor in the formation of the slaty cleavage, inferring that corrosion, diffusion transfer and neocrystallization were the controlling mechanisms.

Similarly, Bell (1978) suggested that slaty cleavage in the Adelaide Geosyncline was formed largely by solution of quartz and bedding-parallel phyllosilicates, coupled with growth of new mica parallel to the cleavage, though some grain rotation was inferred to have occurred also. Mancktelow (1979) agreed that the phyllosilicates in these rocks were not mechanically rotated, suggesting that the new biotite grains nucleated and grew in the cleavage.

Deformation of detrital, bedding-parallel phyllosilicate grains may produce kink bands parallel to the cleavage (Bell 1978; van der Pluijm & Kaars-Sijpesteijn 1984). Growth of these segments (van der Pluijm & Kaars-Sijpesteijn 1984) and/or nucleation of new mica grains parallel to them (Bell 1978) could lead to oriented mica aggregates in developing P domains. These interpretations of observations

of natural examples support models for mica preferred orientation suggested by Etheridge & Hobbs (1974) and Williams *et al.* (1977). Bell (1978, fig. 19) also observed mica aggregates that appeared to have grown along kink bands in detrital quartz grains. Norris & Rupke (1986) observed evidence of crenulation, kinking, bending and fracturing of detrital mica grains, and suggested that rotation of these grains provided nuclei in orientations suitable for growth of cleavage mica grains. They followed Knipe (1981) in suggesting that growth of the cleavage mica would be enhanced by strain energy and small size of the deformed detrital grains, and by greater ease of diffusion parallel to the aligned mica grains.

Knipe & White (1977), Knipe (1981) and Weber (1981) showed, from SEM studies on Welsh and German slates, respectively, that the earlier stages of cleavage formation may involve crenulation of earlier (e.g. bedding-parallel) foliations, after which syndeformational neocrystallization of phyllosilicates in the new foliation becomes the dominant mechanism. Evidence of the earlier crenulations may be largely obliterated as the cleavage develops, but some of the evidence of grain rotation in slates that mainly show evidence of neocrystallization conceivably could be preserved from this earlier stage of development. Maltman (1981) also described examples of the first cleavage involving crenulation of a strong bedding-parallel alignment of phyllosilicates.

In fact, many recent investigations (e.g. Williams 1972; Wood 1974; Gray 1978; Gregg 1985; Knipe 1981; White & Knipe 1978; Bell 1978; Beutner 1978; Woodland 1985; Lee *et al.* 1986) have inferred that most of the phyllosilicate alignment and cleavage development occurs by recrystallization and neocrystallization, as well as grain rotation, but essentially in the solid state, after most or all of the dewatering. Furthermore, chemical reactions are intimately involved with at least the later stages of the formation of slaty cleavage, which therefore cannot be regarded as a purely mechanical process.

Nevertheless, several studies have shown that cleavages may initiate mechanically during diagenesis and continue to develop by chemical-mechanical processes during low-grade metamorphism, in accretionary complexes (e.g. Williams *et al.* 1969; Spang *et al.* 1979; Mackenzie *et al.* 1987; Tranter 1992), tectonic mélanges (Hammond 1987) and thrust sheets (Boyer 1984). For example, cleavage in deformed sedimentary rocks can be formed entirely by mechanical rotation of detrital grains (e.g. Williams *et al.*

1969; Paterson & Tobisch 1993). Mackenzie *et al.* (1987, p. 355) related the early development of cleavage ('penetrative networks of shear zones') to dewatering, noting that spatial variations in rock type, porosity or degree of compaction between adjacent beds, or even within the same bed, could permit intergranular flow in one place and fracturing in another. They also noted that progressive burial would lead to more ductile deformation. Piqué (1982) related degree of strain and cleavage formation to intensity of metamorphism, and emphasized that cleavage formation may well be a complex and progressive mechanism, involving mechanical rotation and shape changes of detrital minerals (mostly by pressure solution at very low-grade metamorphism) and also syntectonic recrystallization. Tranter (1992) traced a progression from particulate flow and cataclasis in poorly lithified sediments, through the development of pervasive cleavages at greenschist and blueschist facies conditions, to local crystal-plastic deformation; he also noted that fluids were important, as evidenced by solution features and 'beards' on clastic grains. Spang *et al.* (1979) described evidence of solution of clasts, local deposition in strain shadows, and rotation and passive concentration of clay minerals in anastomosing cleavage seams, at 150–280°C. Lee *et al.* (1986) inferred that slaty cleavage formation in the Martinsburg Slate at Lehigh Gap, Pennsylvania, involved the destruction of metastable minerals and the formation of ordered, more stable minerals in a low-temperature (c. 225°C) metamorphic environment.

Gregg (1985) investigated the development of P domains in weakly cleaved rocks, showing that mica film segments nucleated in favourable locations along clastic grain boundaries, linked up, and gradually extended into more continuous folia. The films initiated as optically resolvable mica grains showing no evidence of the kinking or fraying that would be expected if they were mechanically rotated detrital grains; however, their optical similarity to mica grains aligned parallel to bedding in uncleaved rocks suggests that they may be former detrital grains recrystallized in the new orientation. The films were inferred to thicken by the solution of adjacent clastic grains and the residual accumulation of phyllosilicates (neocrystallized) and opaque minerals along the boundaries. The preferred orientation of mica progressively increased in the developing P domains until the later stages, when recrystallization produced more random, decussate aggregates. However, other authors have presented evidence of grain rotation, at least in the early stages of cleavage

formation (e.g. Knipe & White 1977; Roy 1978; Bell 1978; Gray 1979; Knipe 1979, 1981; White & Johnston 1981; van der Pluijm & Kaars-Sijpesteijn 1984).

Kisch (1989) has reviewed evidence that well-developed, closely spaced, continuous slaty cleavage initiates at very low grades of metamorphism, generally at low- to mid-'anchimetamorphic' grades, though in different areas it may appear at high diagenetic to 'epimetamorphic' grades. However, its appearance does not correlate well with the degree of metamorphism as indicated by illite 'crystallinity', which may reflect differences in initial fabric, pre-existing illite crystallinity or time relationships between deformation and metamorphism.

These observations indicate that (1) cleavages, with compositional differentiation, may begin to develop at sub-metamorphic temperatures, and continue to develop with prograde metamorphism, and (2) mechanical rotation of detrital grains may dominate in the earlier stages, whereas solution and neocrystallization dominate in the later, probably most important, stages of cleavage development.

Evidence of solution in and against P domains

Much mesoscopic and microscopic evidence exists for solution and transfer of material during the formation of foliations in metamorphic rocks (e.g. Plessman 1964; Williams

1972; Gray 1977, 1981; Vernon 1987). For example, the following primary structures may be partly removed by solution, the remnants being transected by dark seams of residual material: fossils (e.g. Siddans 1972, fig. 17), oolites (Durney 1972; p. 316), worm burrows (Wright & Henderson 1992), sand volcanoes and dewatering pipes (Wright & Henderson 1992), quartz and other detrital grains (Williams 1972; Gray 1978; Bell 1978), zoned plagioclase grains (Vernon *et al.* 1987), and early quartz veins (e.g. Wright & Henderson 1992). Figures 3, 4, 6, 11 and 12 show solution features.

Moreover, abrupt transitions from P to Q domains in many slates (e.g. Bell 1978; Beutner 1978; Lee *et al.* 1986) suggest that solution of strained old grains (quartz and phyllosilicates) and neocrystallization of cleavage phyllosilicates are the main processes involved, at least in the later stages of development of many slaty cleavages, rather than mechanical rotation (e.g. Etheridge & Lee 1975; Bell 1978; Gregg 1985; Woodland 1985; Lee *et al.* 1986).

Evidence of deposition in Q domains

Relatively clear features indicating deposition in Q domains include: 'beard structures' (Figs 4, 13), fibre growths (Gray & Willman 1991b; Gray & Wright 1984), and quartz overgrowths on detrital quartz grains (e.g. Williams 1972; Powell 1969; Gregg 1985; Sutton 1991). Mica layers in chlorite-mica 'stacks' in Q

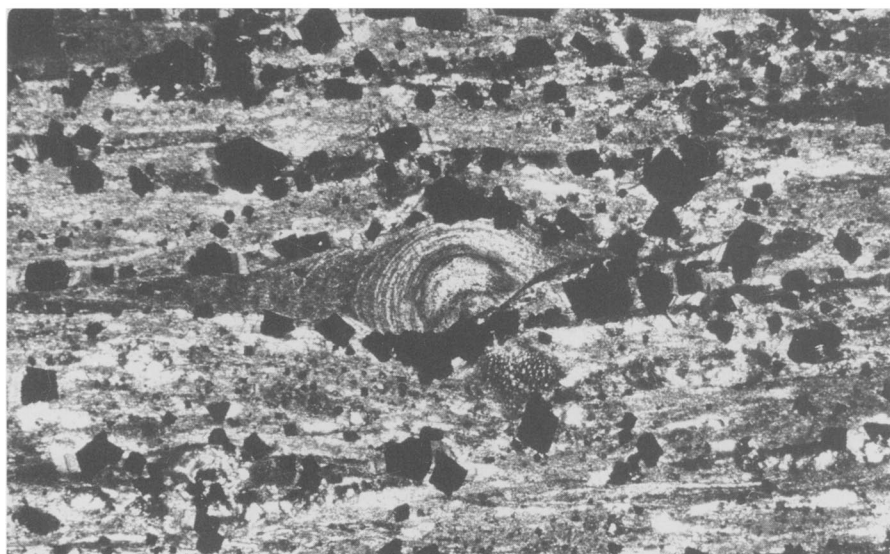


Fig. 11. Chlorite oolith partly removed by solution, Swiss Alps. Plane-polarized light; base of photo 3.5 mm.

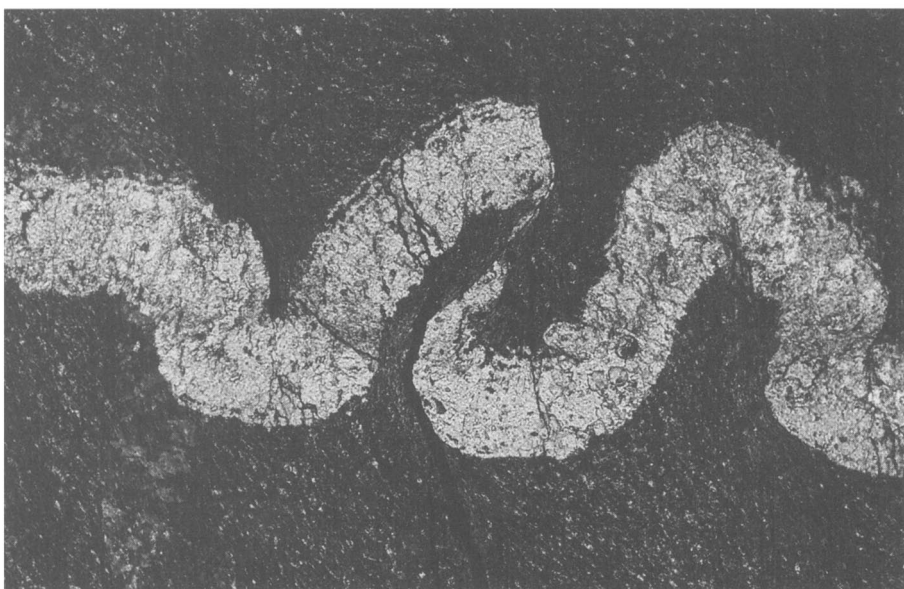


Fig. 12. Removal of part of folded quartz veins by solution along curved dark seam approximately parallel to the fine slaty cleavage. Plane-polarized light; base of photo 3.5 mm.

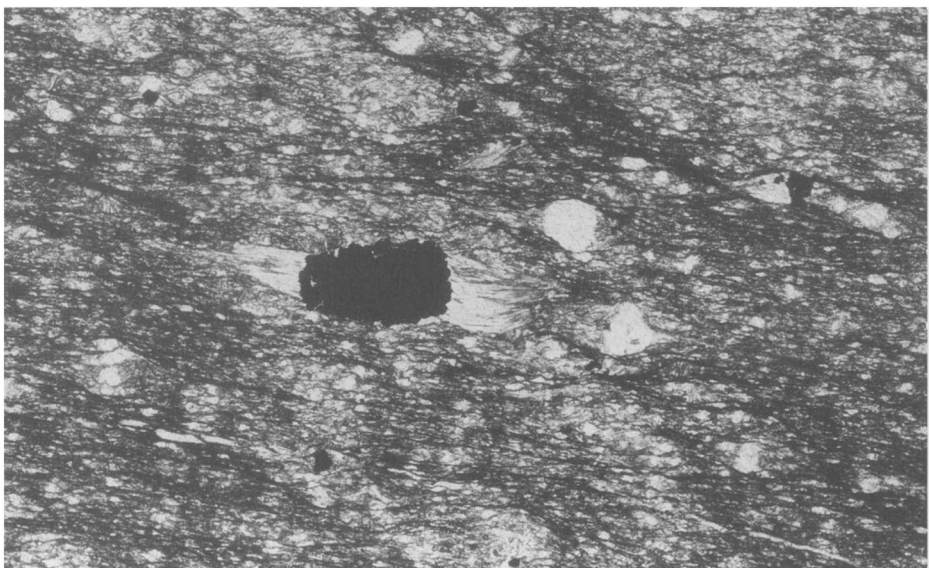


Fig. 13. Mica 'pressure shadows' parallel to slaty cleavage adjacent to a magnetite porphyroblast in a micaceous graphitic slate. The strongly heterogeneous (domainal) structure of the slaty cleavage is due to the marked contrast between thin, dark, relatively continuous folia and the more leucocratic lenses composed of clasts, their strain shadows and quartz–phyllosilicate ‘beards’, as well as poorly aligned phyllosilicate-rich aggregates. Plane-polarized light; base of photo 6 mm.

domains have also been attributed to deposition during slaty cleavage formation, as mentioned previously. Evidence of precipitation in some P domains has also been observed (e.g. Waldron & Sandiford 1988; Sutton 1991).

However, absence of these structures may not disprove deposition, if extensive recrystallization and obliteration of original grain shapes in the Q domains can be demonstrated. This applies especially to crenulation cleavages, but is less likely to apply to slaty cleavages, in which Q domains may have original detrital structures (e.g. Williams 1972).

Thus, slates show abundant evidence of solution, especially of silica-forming P domains, and some show evidence of deposition in Q domains. The question is whether the system is effectively closed (except for water) or whether volume and/or bulk chemical changes occur during slaty cleavage development, on the mesoscopic (metre) scale.

Local variations in mineral compositions

Chemical differences between phyllosilicates in P and Q domains have been observed (e.g. Boulter & Råheim 1974; Stephens *et al.* 1979; Knipe 1979, 1981; White & Johnston 1981; Lee *et al.* 1986; Sutton 1991). For example, White & Johnston (1981) found that the mica in P domains is more phengitic than that in Q domains, inferring that the mica in the P domains reflects metamorphic equilibration, whereas the mica in Q domains retains its diagenetic composition. This implies that the mica in Q domains did not equilibrate with mica in P domains and hence did not equilibrate with fluids during cleavage formation. This could be taken to suggest that solutions passing along the P domains generally do not enter the Q domains, which consequently remain essentially unmodified, or at least much less modified, during the cleavage-forming process; in fact, some of the phyllosilicates in the Q domains could be inherited or diagenetic, whereas those in P domains are metamorphic. This interpretation is supported by the occurrence of unmodified detrital structures in the Q domains of some slates (e.g., Williams, 1972, 1990, p. 275). However, local penetration of fluid from P to Q domains is suggested by growth of new mica in phyllosilicate 'stacks', as well as the abundant evidence of deposition on clastic quartz grains.

An alternative explanation to disequilibrium is that the phengitic mica occurs in P domains because it has a smaller molar volume than muscovite, so that its growth is favoured in

strongly shortened domains (C.V. Guidotti, pers. comm., work in progress).

The problem of compositional change and volume loss in slaty cleavage formation

Much controversy exists about the extent of compositional change and volume loss during the formation of slaty cleavage. From deformed reduction spots in Welsh slates, Sorby (1853) estimated 50% volume loss. More modern estimates range from little or no volume loss (e.g. Erslev & Mann 1984; Waldron & Sandiford 1988; Wintsch *et al.* 1991; Gray *et al.* 1991; Kanagawa 1991; Erslev & Ward 1993) to 20% (Ramsay & Wood 1973), 30–50% (Sutton & Land 1996), 33–55% (Brandon *et al.* 1994), 50% (Wright & Platt 1982; Beutner & Charles 1985), 55% (Goldstein *et al.* 1995) and 60% (Wright & Henderson 1992).

Estimates based on microstructures and geometrical features involving strain markers generally indicate large local volume losses, whereas estimates based on chemical ratios and isotopes generally indicate negligible losses, as discussed by Wright & Henderson (1992). This major dichotomy between interpretations resulting from structural and chemical approaches needs to be examined and hopefully resolved. Studies of slaty cleavage in some specific areas will be discussed first, and then the general problem will be addressed.

Bermagui, SE Australia

Williams (1972) described strongly compositionally differentiated, predominantly axial-surface foliations in Lower Palaeozoic greenschist facies metapelites (phyllites and slates) and metasandstones at Bermagui, NSW (Figs 1–3). Using the shapes of detrital quartz grains, he inferred that solution occurred in high-strain fold limbs producing very elongate quartz grain shapes in layer silicate-rich domains (P domains), leaving unmodified or only slightly modified detrital grain shapes in the hinge areas (microlithons or Q domains), which are richer in silica. The differentiated layering developed in slaty cleavage, crenulation cleavage and primary bedding laminations, so that the various foliation styles are gradational. Williams (1972) inferred that the compositional layering developed from originally homogeneous rock during deformation, and that transfer of silica dissolved from micaceous (P) domains was not restricted to

movement between adjacent domains, but occurred at least on the scale of individual mesoscopic folds.

Meguma Group, Nova Scotia

Wright & Henderson (1992) presented a very detailed analysis of strain and volume loss in lower greenschist facies (chlorite grade) slates of the Meguma Group, Nova Scotia, Canada. They used silt-filled worm burrows as 'palaeoplumbines' that originally were at large angles to bedding. On bedding surfaces, the burrows show elliptical sections, with the long axes of the ellipses parallel to the trace of the slaty cleavage. Their aspect ratios average more than 2:1, regardless of bedding dip, indicating that the bedding-plane distortion accompanying cleavage formation occurred before flexural folding. To avoid the non-coaxial strain accumulation that has occurred on the limbs of the later folds, observations were confined to the hinge regions, where bedding and cleavage are at right angles, and where the layer-parallel cleavage formation was unaffected by the folding. Assuming that the original separation of the burrows was linearly related to the burrow diameter, the normalized centre-to-centre distances between paired burrows indicate bedding-parallel shortening of 60% ($Z = 0.4$).

Wright & Henderson (1992) used buckled, early tectonic, bedding-parallel quartz veins and carbonate beds to provide estimates of layer-parallel shortening in rocks showing abundant other evidence of 'pressure solution'. Comparison of initial and final bed lengths (assuming no homogeneous layer-parallel shortening) indicated bedding-parallel shortening of 40–60% ($Z = 0.6–0.4$), which is similar to the amount of shortening indicated by deformed worm burrows.

The observations indicated 60% bedding-parallel shortening (Z) by solution-transfer, without evidence of any extension parallel to fold hinges (Y). Estimation of tectonic vertical extension (X) in the cleavage plane is complicated by corrections for diagenetic compaction that need to be made to primary strain markers, but it is insufficient to compensate for the 60% shortening in Z . The suggestion is that 40–60% volume loss occurred during the formation of slaty cleavage.

Wright & Henderson (1992, p. 289) pointed out an apparent paradox, in that they inferred 60% bedding-parallel shortening by solution-transfer in slates that had subsequently undergone buckle folding. The former implies no or

low competence contrast between beds, whereas the latter requires relatively high contrast. However, if solution-transfer occurs at lower local stresses than those required to cause buckling instabilities, the local stresses may be relieved entirely by solution-transfer and the rocks could shorten without folding, despite high competence contrasts between the layers. Once it becomes too difficult to remove material by solution-transfer, stress could locally rise to the level at which buckling occurs, and folding may take over as the main shortening process.

NW Cascades and San Juan Islands, Washington, USA

Brandon *et al.* (1994) carried out a detailed microstructural analysis of deformed fine- and medium-grained sandstones in the NW Cascades and San Juan Islands, Washington, USA, with a view to determining volume strain and mass loss associated with the development of solution-mass-transfer cleavage, using detrital grains as strain markers.

The sandstones show truncated detrital grains, discontinuous anastomosing folia, and directed fibre overgrowths of quartz, chlorite and phengite. First-cycle quartz clasts of volcanic provenance show no undulose extinction or sub-grains, indicating that dislocation glide was unimportant and suggesting that solution-mass-transfer was the dominant deformation mechanism. Grains were shortened by grain-boundary solution and extended by precipitation of the directed fibre overgrowths. Brandon *et al.* (1994) inferred that, because the fibres are parallel to the folia, the deformation was approximately coaxial and so the cleavage did not form by simple shear.

Brandon *et al.* (1994) made a three-dimensional study of grain shapes, determining modes with an automated micrometre-stepping microscope. Both the XY and XZ sections show well-organized fibre overgrowths oriented in the same direction. They inferred that the maximum extensional stretch is related to the modal abundance of fibre overgrowths, and determined that local strains have a prolate symmetry and are weakly constrictional. The largest distortion is associated with shortening in the Z direction. The volume loss was calculated to be 33–55%.

Castlemaine Supergroup, SE Australia

Lower Ordovician slates and metapsammites in the Bendigo-Ballarat zone of the Lachlan Fold

belt in central Victoria, Australia, have been intensely investigated, in an attempt to determine the extent of volume loss during foliation development. The rocks of the Lachlan Fold Belt have been shortened 50–70% by folding, cleavage development and faulting (Gray & Willman 1991a). A strong slaty cleavage occurs in metapelites (slates) and a spaced cleavage occurs in metapsammites.

Evidence and arguments in favour of volume loss during cleavage development have been presented by Stephens *et al.* (1979) and Cox *et al.* (1983), whereas the opposite viewpoint has been presented by Waldron & Sandiford (1988), Binns & Eames (1989), Gray *et al.* (1991) and Tan *et al.* (1995). An attempt to rationalize these diametrically opposed interpretations has been made by Cox *et al.* (1991).

Stephens *et al.* (1979) compared chemical analyses of P and Q domains in metamorphically differentiated slates from Clunes. The results imply volume losses of more than 40% from P domains. If these were losses from the bulk rock, the implication is that 15–20% of the total volume was lost on the hand-specimen scale. The shapes of detrital quartz and albite grains are better preserved in Q domains, which is inconsistent with addition of quartz and albite to these domains. Corroded boundaries of quartz grains in Q domains, as well as absence of overgrowths on albite clasts, are also inconsistent with transfer of material from P to Q domains; in fact, grain shapes suggest limited removal, rather than addition of material in Q layers.

Trains of Ti-rich oxide grains along P layers may have been passively accumulated by removal of more soluble material, following interpretations of Plessman (1964) and Gray (1977). Veins of quartz (\pm chlorite) and carbonate have been regarded as logical 'sinks' for expelled material. The development of P domains depends on positions in mesoscopic folds in the metasiltstones and metapelites, but is independent of fold position in the metasandstones, in which folds are generally absent at the scale of observation.

The P layers are richer than the Q layers in all elements except Si, Na and Mn. Calculations suggest that formation of the P domains involved $\geq 40\%$ losses of Na, Si, Mn and Ca, 15–40% losses of P, total Fe, Mg and Al, < 15% losses of Zr and Y, and < 15% addition of K, assuming that Ti was completely immobile; Stephens *et al.* (1979) inferred that this was so, as Ti shows the highest enrichment factor of the more immobile elements: Ti, Zr, Al and Y. Stephens *et al.* (1979) argued that since the P layers occupy 10–20% of the rock volume, and

since the Ti values indicate a loss of about 50% from each P layer, the total volume loss was around 10–20% of the original rock volume. This is a minimum estimate, because of probable removal of some material from Q layers as well as P layers.

White & Johnston (1981) examined the microstructure of metapelites and metasiltstones with dark, anastomosing P domains from the Wattle Gully gold mine in the Chewton area, finding that the dark colour may be due to 'staining' rather than concentration of opaque material, as some P domains have fewer opaque grains than some Q domains. The Q domains show no optical evidence of quartz deformation, although transmission electron microscopy shows some deformed and recrystallized grains. Quartz overgrowths are common in the Q domains.

Chlorite–mica 'stacks' suggest growth of chlorite during cleavage development. The cleavage developed from microcrenulations, mainly by crystallization processes, supported by 'pressure solution' and mechanical rotation. In the P domains, some phyllosilicate grains are deformed and strongly aligned, whereas others are not deformed and are commonly transgressive, suggesting growth of new grains. Thus, it appears that phyllosilicates in P domains were concentrated by localized metamorphic reactions rather than by passive accumulation. White & Johnston (1981) observed that mica and chlorite have different compositions in P and Q domains, as discussed previously.

Gray & Willman (1991b) carried out strain determinations on slates containing graptolites on bedding planes and 'pressure shadows' on frambooidal pyrite, which indicated plane-strain deformation on the hand-specimen scale, with volume losses of < 10%. However, small errors in the estimation of strain in the Y direction can change volume loss estimates from small to zero (Gray *et al.* 1991).

From a combination of chemical and microstructural criteria, Waldron & Sandiford (1988) concluded that no volume loss occurred during cleavage formation in metasandstones of the Ballarat slate belt. They found that the deformation involved plane strain on the hand-specimen scale. Evidently, the deformation mainly involved solution transfer, as quartz shows optical evidence of only minor plastic deformation in the form of slight undulose extinction and rare recrystallization. In both XZ and YZ sections, detrital quartz grains are elongate in both P and Q domains, but the mean aspect ratios of grains in P domains is twice that in Q domains, i.e. solution occurred in both domains, but much more in P domains.

Waldron & Sandiford (1988) isolated and analysed separate P and Q domains for major and trace elements. They followed Stephens *et al.* (1979) in proposing that Ti and Zr were chemically inert during cleavage development, so that the relative concentration of these elements in P and Q domains should provide an independent estimate of strain partitioning by solution-transfer. They found that Ti, Y, Nb, Hf, Th, Zr and REE are concentrated in P domains by a factor of two, owing to passive accumulation of zircon, rutile and apatite, and so inferred that these elements were immobile during cleavage formation. They concluded that Si, Sr, Na, Fe, Mg and possibly Al were partitioned into Q domains, relative to the inert elements, whereas K, Rb and V were partitioned into P domains.

On the basis of microstructural evidence, Waldron & Sandiford (1988) estimated that the bulk shortening in P domains is approximately twice that in Q domains. They stated that solution was more rapid in P domains, leading to a net volume loss, whereas precipitation occurred more rapidly than solution in Q domains, leading to a net volume gain. They also stated that all the rocks show evidence of extension in X. For example, fibrous quartz-chlorite overgrowths on detrital quartz grains, elongate in X, are abundant in both P and Q domains. In addition, Waldron & Sandiford (1988) inferred that chlorite overgrowths occur on 'pulled-apart' detrital muscovite grains. They also observed rare quartz fringes ('pressure shadows') elongate in X around pyrite porphyroblasts. Though the inferred extension in X could be quantified in only one sample, using quartz overgrowths on pyrite, the finite extension associated with cleavage development was estimated to have been more than 100%, which agrees with the amount of extension predicted for constant-volume plane-strain deformation dominated by solution-transfer. This conclusion contrasts markedly with the inference of Stephens *et al.* (1979) and Etheridge *et al.* (1983) that extension is negligible. A corollary of this interpretation is that if the Q domains have received considerable addition of material, they should be richer in quartz than typical non-foliated sandstones of this region, which requires verification.

Binns & Eames (1989) found that bulk-rock compositions of both metasandstones and metapelites in more and less cleaved positions on the Clunes anticline have uniform compositions, suggesting internal redistribution, with negligible net loss from the system. Durney & Gray (unpublished data, reported by Gray *et al.*

(1991) and Tan *et al.* (1995)) carried out strain determinations on three orthogonal sections of a metapsammite with striped cleavage that was originally used by Stephens *et al.* (1979), employing a modified centre-to-centre (Ramsay & Huber 1983) method on quartz grains; they found effectively zero volume loss ($-0.4 \pm 6.0\%$).

An attempt to reconcile the divergent observations and interpretations on cleaved rocks of the Castlemaine Supergroup has been made by Cox *et al.* (1991), whose observations in the Castlemaine area indicated that volume loss is particularly important in the inner arcs of arenite units in fold-hinge zones, but may be less important in arenite units in fold-limb zones; any association between volume losses and their structural position in the slates was not apparent. Their conclusion does not agree with that of Binns & Eames (1989), mentioned previously.

Cox *et al.* (1991) found that in the Castlemaine area, Q domains generally show little microstructural evidence of sufficient extension in the cleavage plane to balance volume decrease due to solution and removal of material from adjacent P domains. For example, for well-developed solution cleavage in interlaminated metapelite and semipelite, at least 30% shortening has occurred by removal of quartz from P domains. Constant-volume plane-strain deformation requires at least 40% extension at high angles to bedding and parallel to the cleavage plane. However, fibrous 'beards' on clastic grains in Q domains are generally absent, which implies several tens of percent volume loss, at least on a scale comparable to bed thickness. Though some slates have well-developed, short, fibrous quartz-mica overgrowths that indicate approximately constant-volume deformation, others have no overgrowths on pyrite frambooids, despite the presence of a discrete solution cleavage.

Martinsburg Formation, eastern USA

In the Ordovician Martinsburg Formation, central Appalachians, eastern USA, Wright & Platt (1982) found that passively deformed graptolites record maximum shortening perpendicular to the slaty cleavage, but are little distorted parallel to the cleavage. At large bedding/cleavage angles, the shortening is 50 to 70%, but as acute bedding/cleavage angles decrease, this apparent shortening in the bedding plane decreases according to the sine of the bedding/cleavage angle, whereas dimensions parallel to cleavage remain unchanged. Where bedding and cleavage are parallel on fold limbs, the apparent shortening decreases to nearly zero; yet there is no evidence for extension in any

direction. These observations are consistent with a material volume loss of 50%. The loss was inferred to have resulted from pressure solution of calcite and silicate minerals, as indicated by crumpled and broken precleavage veins and insoluble residues on cleavage surfaces. However, Gray & Wright (1984) reported fibrous chlorite overgrowths on pyrite framboids that are consistent with some extension parallel to X, and Tan *et al.* (1995) commented that the variably deformed samples described by Wright & Platt (1982) are from widely separated areas, which implies unrealistically homogeneous strain.

In the Hamburg sequence, along strike from the Martinsburg Formation in Pennsylvania, Beutner & Charles (1985) measured strain in red slates with pale green ellipsoidal reduction spots. They assumed that the spots were originally spherical and that the elongation is due to deformation; this is reasonable, as X, Y and Z are all different, whereas X and Y should be equal if reduction was mimetic in a pre-existing foliation, unless grain alignment parallel to X is strong enough to promote elongation of the reduction spots. Conodonts occur inside the reduction spots, and their spine-like denticles and cusps have been pulled apart, providing independent true measures of extension in various directions inside the spots (which themselves provide only strain ratios). The gaps in the conodont fragments are filled with fibrous quartz, indicating a mean stretch of 141%. Comparison of extensions indicated by the boudinaged conodonts with the shapes of the reduction spots on fold limbs and hinges indicated that compaction of 44% preceded tectonic strain associated with cleavage formation. The tectonic strain was estimated as 141% extension in X, no change in Y, and 50–59% shortening in Z. The tectonic volume loss was estimated as 29–42%. The inferred large volume loss is reflected in a general lack of directed overgrowths on clasts. On the other hand, Beutner (1978) found that shortening normal to the cleavage was balanced by shortening parallel to the cleavage, indicating no volume change.

Deformation without volume loss in the same region has also been inferred by Wintsch *et al.* (1991), who made mass-balance calculations based on chemical analyses and relative density measurements of 48 mudstones and 26 greywackes across a 130 m strain gradient in the mudstone-to-slate transition in the Martinsburg Formation at Lehigh Gap, Pennsylvania. Unfortunately, the transition from mudstone to slate is oblique to the bedding (Ho *et al.* 1995), so that direct comparison of strain variation in an

individual bed cannot be made. Using minimum-strain samples and Al_2O_3 as references, the analyses show no loss of SiO_2 , but large losses of CaO , Na , Ba and Sr that are directly proportional to inferred total strain, reflecting open-system behaviour on the kilometre scale for these elements. However, large losses in SiO_2 , Na_2O and total volume in greywacke/metagreywacke are balanced by opposite changes in adjacent mudstone/slate, reflecting silica mobility only on the centimetre scale. Ratios of Al_2O_3 , TiO_2 , total Fe as FeO , MgO , MnO , Y, V and Zr remain constant. The inferred inertness of most major components (especially SiO_2) over the outcrop requires (1) that the fluid composition was buffered by the local mineral assemblage (quartz–albite–muscovite–chlorite), (2) a small fluid volume, and (3) a gentle P – T gradient, down which the fluid travelled.

Again, the contrast in interpretations made from structural and chemical studies is marked, although Beutner and co-workers have found evidence for volume loss in some places and no volume loss in others. Perhaps the suggestion of Beutner & Charles (1985, p. 805), that the geochemical systems may vary along the Martinsburg Formation, may help resolve the conflict. They commented that, although position in the orogenic belt and amount of tectonic shortening are comparable, the magnitudes of associated extensions differ greatly. They suggested that this variation in the character of the strain may be related to differences in the chemical systems involved. At sub-greenschist and low-greenschist facies conditions, where 'pressure solution' appears to be the dominant deformation mechanism, large tectonic volume losses may correlate with large fluid fluxes and low (near-hydrostatic) fluid pressure in open systems, whereas small or no volume losses, marked by large extensions, may be favoured by higher fluid pressures in more nearly closed systems.

Torlesse Terrane, New Zealand

Cox (1993) has described the transition from non-foliated greywackes through greywacke–semischists, to intensely deformed greenschist and amphibolite facies schists in the Torlesse Terrane, New Zealand. The parent rocks are apparently compositionally uniform quartzofeldspathic greywackes and subordinate argillites. Solution-transfer deformation dominated foliation development at lower metamorphic grades (prehnite–pumpellyite and pumpellyite–actinolite facies), whereas crystal-plastic mechanisms occurred at highest grades (greenschist and

lower amphibolite facies). Norris & Bishop (1990) estimated 50% shortening accompanying the development of slaty cleavage in the semischists and 70% shortening accompanying the development of segregation lamination in the schists. Quartz-rich symmetamorphic veins are abundant, indicating that silica was highly mobile during deformation and metamorphism. Mass-balance analysis is consistent with the veins being derived from material dissolved from P domains during cleavage formation.

Lower-grade metapelites generally record volume losses (-39%) and metapsammites record volume gains (+24%), based on hand specimen mass-balance analysis, the proportions of veins, selvedges and host rock indicating that mass was generally conserved at the outcrop scale. Average volume changes determined from 332 hand specimens over the whole terrane show a general tendency for volume loss, increasing from -4.7% in semischists to -8.3% in schists to -9.1% in the highest-grade rocks. The hand specimen losses are balanced by, or are smaller than, the proportions of outcropping quartz veins. Cox (1993) concluded that deposition generally accompanied solution and that silica transfer was only local, most remaining in the hand-specimen volume.

At lower metamorphic grades, relatively short source-sink distances during solution transfer, coupled with relatively small degrees of deformation, resulted in mass conservation at the hand-sample scale. However, at lower greenschist facies conditions, extensive element mobility conserved mass at the outcrop or slightly broader scale. At upper greenschist facies and above, crystal-plastic deformation tends to homogenize effects caused by solution-transfer, so that mass is again conserved at the hand-sample scale. Thus, despite the abundance of quartz veins, mass was approximately conserved at least at the outcrop scale, and relatively small fluid-rock ratios were involved in the deformation (Cox 1993).

This study integrates the structural and chemical approaches, and confirms expectations that if mass is conserved during prograde metamorphism, volume must be lost, in order to accommodate the general increase in density that accompanies the change from low- to high-grade metamorphic rocks.

Evaluation of controversy regarding volume loss during slaty cleavage formation

As mentioned previously, structural studies generally indicate volume loss during foliation

development, whereas chemical studies commonly do not. As noted by Wright & Henderson (1992, p. 289)

'Just as assumptions about the shape and size of strain markers affect geometric methods, assumptions about original compositions of starting materials affect the chemical approach. The approach taken by Erslev & Mann (1984) and Wintsch *et al.* (1991) can only measure present compositions of deformed material and relies on one or more elements being immobile to provide a means of determining the original composition. The measured low differential mobility of the "immobile" elements is equated to actual immobility. However if, these elements are removed at an equal rate during cleavage development, an undetectable bias could cause the volume loss to be underestimated.'

The problem has not been satisfactorily resolved, but the following points need to be kept in mind when evaluating the problem of volume loss in the formation of slaty cleavage.

(1) Slates commonly show clear evidence of solution and volume loss in P domains.

(2) Many rocks show no evidence of addition of material in Q domains and no extension in X, suggesting removal of material on the scale of the observed sample. On the other hand, many slates show evidence of quartz overgrowths and quartz-phyllosilicate 'beards', generally only in Q domains, but also in P domains in some examples (e.g. Waldron & Sandiford 1988, Sutton 1991). Generally, the evidence for overgrowths and 'beards' is optical and so may be indistinct in such fine-grained material, but back-scattered scanning electron microscopy can show clearer evidence of overgrowths (Sutton 1991).

(3) Chemical studies assume that cleavage is planar, whereas P domains anastomose around lenticular Q domains. Therefore, assuming that the original rock is non-domainal, more material must be removed from the ends of Q lenses than their centres.

(4) The structural (geometrical) approach assumes that the shapes and sizes of strain markers are well enough known; fossils are probably the most reliable strain markers, as their predeformation shapes are generally obtainable, though the effects of pre-tectonic deformation may be difficult to detect in readily deformable fossils such as graptolites. Reduction spots should provide relatively reliable markers, but only if they predate the cleavage. To be certain of this, a transition from undeformed spots or spots slightly flattened parallel to

bedding by compaction, to spots tectonically elongated parallel to cleavage, should ideally be observed. The local occurrence of vein-like reduction patches in some Welsh slates suggests that post-cleavage reduction is a possibility, at least in some areas. An important problem is the extent to which compaction during dewatering can account for deformation of strain markers in such a way that volume loss during cleavage formation could be overestimated. As mentioned previously, Beutner & Charles (1985) estimated pre-tectonic compaction by comparing conodont extensions with the shapes of reduction spots. They presented evidence that the reduction spots were not formed mimetically in a foliation, and that the conodont extension along with the slaty cleavage was post-compaction. However, even if the spots were originally spherical, as inferred by Beutner & Charles (1985) and Goldstein *et al.* (1995), some of their deformation could have occurred during the early stages of folding, perhaps before the cleavage was initiated. If so, the amount of strain accompanying cleavage formation would be overestimated by an unknown amount. The probability of compaction and early indeterminate complex strain was acknowledged by Goldstein *et al.* (1995), but they inferred that most of the ellipsoid deformation was due to a strong-late tectonic overprint. The problem of prelithification strain could also apply to the use of deformed graptolites as strain markers.

(5) The chemical approach assumes that certain chemical elements (especially Ti, but also Zr and Al) are immobile enough to serve as constants. Relative immobility of Ti is suggested by concentrations of Ti-rich minerals in some P domains in slates and schists, but mobility of Ti is indicated by some studies of low-temperature alteration in mafic rocks (e.g. Hart 1970; Hellman & Smith 1979; Philipott & Selverstone 1991) and felsic volcanic rocks (Schandl *et al.* 1990), as well as by single-grain veinlets of sphene and ilmenite forming folia in some high-temperature mylonites (Lafrance & Vernon 1993). Solubility of Ti at metamorphic conditions is also indicated by the experiments of Ayers & Watson (1993). Al has also been mobile in many places (e.g. Sykes & Moody 1978; Vernon 1979; Vernon *et al.* 1987; Kerrick 1988). Other elements commonly assumed to be relatively immobile may also be mobile, e.g. REE at sub-greenschist to greenschist facies conditions (Hellman & Smith 1979), Zr at low-temperature conditions (Philipott & Selverstone 1991) and Zr at high-temperature conditions (Altenberger 1996).

(6) As noted by Wright & Henderson (1992, p. 289), the accepted low differential mobility of the 'immobile' elements is equated to actual

immobility in chemical studies of mass and volume change. However, if these elements are removed at an equal rate during cleavage development, an undetectable bias could be introduced, and so volume loss could be underestimated. If the rocks show constant Al/Ti ratios, immobility of both elements may be more confidently inferred (Wintsch *et al.* 1991), because it is difficult to imagine the mobilities of both elements maintaining constant ratios. However, in the Lehigh Gap succession referred to by Wintsch *et al.* (1991), the rocks compared are from different sedimentary beds (Ho *et al.* 1995, fig. 2), presumably reflecting differences in quartz-clay mineral ratios. Thus, constant Ti/Al ratios could simply reflect the restriction of both elements to the quartz-poor fraction, regardless of variation in the quartz-clay ratio, and so would not be a reliable standard for comparing silica loss or gain in deformed and less deformed rocks.

(7) Even if immobility of an element is established beyond reasonable doubt, caution is needed, because, for example, if the protolith contains more than one Al-rich component (e.g. clay and chlorite-white mica), 'the ratios of individual elements to Al_2O_3 in the protolith are...not constant, so element concentrations normalized to Al_2O_3 (or perhaps to other immobile elements) in metamorphic rocks need not be a sensitive indicator of mobility of those elements' (Moss *et al.* 1996, p. 503). If so, studies that suggest mobility during cleavage formation, based on such ratios, may be in error.

(8) Distinguishing between the effects of protolith variation and possible metamorphic changes appears to be impractical on all scales (except where marked local metasomatism is obvious), as emphasized later, and so the bulk chemical approach to possible compositional changes due to cleavage formation may be confronted by similarly insurmountable sampling problems.

(9) Structural and chemical comparisons of individual domains assume that the P domains originally had the composition of the Q domains (e.g. Cox 1993), whereas both could have been modified during cleavage formation.

(10) Local volume loss could help accommodate boundary difficulties where slates are strongly deformed and shortened against relatively undeformed metasandstones that show sedimentary structures. Fold strain incompatibilities relieved by volume loss in cleavage formation have been discussed by Goldstein *et al.* (1995).

(11) Cox *et al.* (1991) suggested that the amount of volume loss may depend on a rock's

position in a fold, but Binns & Eames (1989) found uniform compositions in more and less cleaved rocks. Perhaps volume loss on the hand-specimen scale is controlled by a rock's position in mesoscopic folds (e.g. Williams 1972), whereas as this variation is obscure on the scale of macroscopic folds, owing to broader original (sedimentary) compositional variations.

(12) Engelder (1984) suggested that open systems with volume loss deformation occurred higher in the Appalachian succession, and closed systems with no volume loss deeper in the succession. The evidence of volume loss for the Martinsburg Formation presented by Wright & Platt (1982) argues against this suggestion, at least in its simplest form. However, Beutner & Charles (1985) agreed that local variations in closed versus open system behaviour could account for variations in the evidence for and against volume loss. This could explain inconsistencies in the same small area, but only if variation in the openness of the system can vary very locally, which is possible. Beutner & Charles (1985) implied that some parts of a deforming unit may be open at the same time as other parts are effectively closed, and that this is not necessarily related to structural position or amount of shortening. This could explain the conflict between detailed, evidently reputable investigations, referred to previously, that found a virtual lack of extension and those that found enough extension to preclude volume loss. Tan *et al.* (1995) suggested that the greatest mass loss should occur in areas of higher and/or more focused fluid flow. Cox *et al.* (1991) suggested that structural position may be the controlling factor, though Binns & Eames (1989) inferred that structural position has no effect on the mesoscopic fold scale. However, the problem is to find out what determines whether a system is open or closed, and it would be surprising if local structural setting did not exert some control on this.

(13) Deformation heterogeneity on all scales may play an important part in the development of slaty cleavage. If so, the material collected may need to be very closely controlled. For example, rocks have been sampled from different areas, different parts of folds, and folds of different sizes and amplitudes. A major, coordinated study, in which structural geologists and geochemists study identical material from the same sedimentary beds, examining rocks deformed at different scales and in different parts of folds, is needed.

(14) Too few studies have combined the structural and chemical approaches in an even-handed way, a notable exception being that of Cox (1993). Variation in the amount of volume

change between and within areas is to be expected, but at this stage, agreement between the structural and chemical approaches has not been reached for any locality in the classical slate belts.

Crenulation foliations in schists

Partitioning of deformation into compositionally differentiated high- and low-strain domains is also a feature of crenulation cleavages (e.g. Voll 1960; Nicholson 1966; Williams 1972; Cosgrove 1976; Talbot 1964; Hobbs *et al.* 1976; Gray 1977, 1978, 1979), which occur in some slates and phyllites, but which are most characteristic of intermediate- and high-grade metapelitic schists. The high-strain (P) domains are rich in mica, graphite or sillimanite, and form in the limb zones of crenulation folia, whereas the low-strain (Q) domains are richer in quartz and form in the hinge zones of crenulation folia (Figs 7–10). The P domains may be relatively planar, but typically anastomose around lenticular Q domains (Fig. 9). Studies of the progressive development of crenulation folia have shown that mica and/or graphite progressively concentrate in the high-strain zones, possibly owing to their ability to deform by intergranular slip, whereas minerals with less anisotropic structures tend to be dissolved and removed from these zones (e.g. Bell & Rubenach 1983).

In crenulated schists, P domains may transect partly dissolved porphyroblasts, such as garnet (e.g. Vernon 1978; Hara *et al.* 1984) and plagioclase (Hara *et al.* 1984). The main question is: where does the dissolved material go? A bulk chemical change (e.g. increase in Al and K) is implied if it is removed from the system (e.g. on the mesoscopic scale), but if it is redeposited in the Q domains, no bulk chemical change would occur.

Marlow & Etheridge (1977) traced microstructural, chemical and mineralogical changes from non-crenulated, non-differentiated schist to crenulated, differentiated schist, over approximately 2 cm, in an amphibolite facies schist of the Cambrian Kanmantoo Group, South Australia. The rocks show no microscopic evidence of plastic deformation. The long limbs (P domains) of the microfolds are richer in muscovite at the expense of biotite, quartz and feldspar, reflecting a large increase in Al and a smaller increase in K at the expense of Si, Mg and Fe. The compositional changes in the short limbs are somewhat complementary, but comparison with non-crenulated rock 2 cm away suggests that the

formation of the differentiated layering involved bulk chemical change, mainly depletion in Mg and Fe. The most notable change is the marked increase in muscovite in the P domains.

The main problem is that the microstructure of the non-crenulated to weakly crenulated area looks very similar or identical to that of the P domains in the crenulated areas. Moreover, mineral grains are larger and more equidimensional in the Q domains than in the non-crenulated rock. Therefore, if this really is a change from non-differentiated to differentiated schist, the Q domains must have been modified much more than the P domains and, if so, the Q domains must have developed by *addition* of material. An alternative explanation is that the P domains and the non-crenulated zones represent more deformed material (possibly reactivated zones), whereas the Q domains are less deformed relicts. In any event, the non-crenulated zones probably should not be regarded as unmodified, pre-crenulation material.

Mancktelow (1994) compared the bulk chemical composition of isolated zones of crenulation cleavage and adjacent relatively homogeneous slate from three localities. He showed that the crenulated and uncrenulated zones are generally compositionally similar, and inferred that marked bulk volume change is not a prerequisite for the development of crenulation cleavage, although a volume loss of 35–40%, by removal of silica, occurred in the formation of the crenulated zone in a sample from the Mosel

Valley. The problem with this investigation, as with that of Marlow & Etheridge (1977), is that absence of simultaneous deformation (e.g. shearing and/or flattening) in the non-crenulated zones cannot be assumed, in which case chemical composition and volume may have been affected in both crenulated and non-crenulated zones.

Glen (1982) examined in detail the shapes, sizes and proportions of minerals in Q and P domains in a crenulated schist in the Broken Hill area, Australia. He measured both XZ and YZ sections, finding that quartz was dissolved from both domains. However, silica did not migrate from P into Q domains. Though some silica was used to form muscovite from biotite, the rest was inferred to have left the system on the hand-specimen scale.

Sillimanite folia

Sillimanite folia are common in high-grade metapelites (Figs 14, 15). Some may represent deformed pseudomorphs of andalusite, but many appear to be residual concentrations in high-strain zones (P domains) in crenulation limbs (Vernon 1987). Thus, they may be analogous to mica concentrations in crenulated schists. If so, they could reflect local selective removal of components, perhaps by base-cation leaching (Vernon 1979, 1987), though the possibility of some addition of Al to the folia cannot be dismissed.

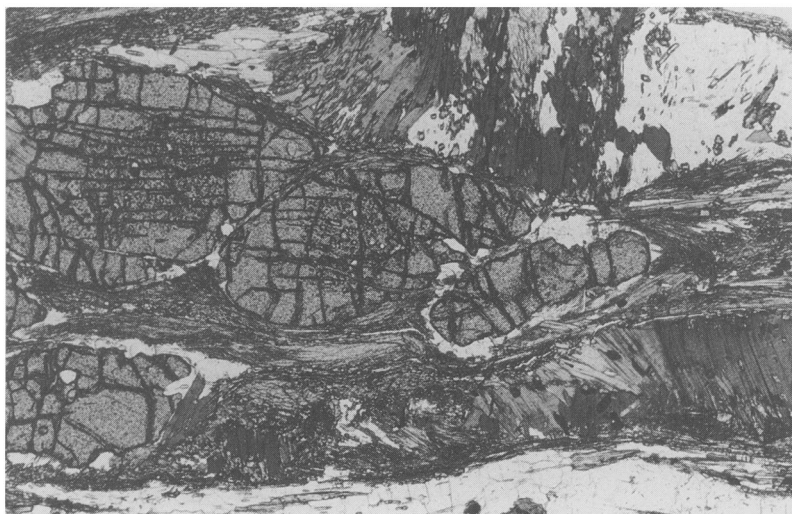


Fig. 14. Folia of sillimanite (P domains) anastomosing around lenticular Q domains containing variable proportions of garnet, quartz, K-feldspar and cordierite, with sillimanite and biotite that tend to be aligned oblique to the main foliation. Biotite–sillimanite–garnet gneiss, Broken Hill, Australia. Plane-polarized light; base of photo 4.4 mm.

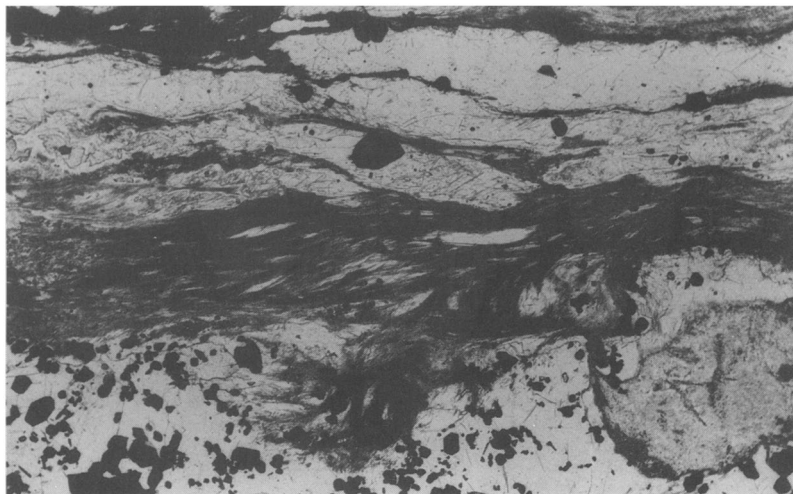


Fig. 15. Folia of fibrous sillimanite (P domains) anastomosing around Q domains in a quartz-andalusite-sillimanite-sulphide schist, Big Bell Mine, Western Australia. Plane-polarized light; base of photo 12 mm.

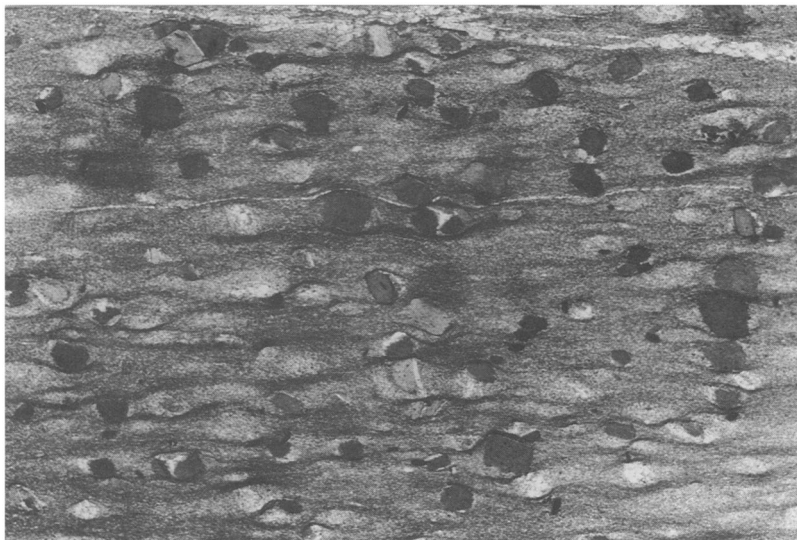


Fig. 16. Dark, anastomosing, relatively discontinuous micaceous-carbonaceous folia concentrated around biotite porphyroblasts in a schist from the Picuris Range, New Mexico, USA. The folia may have nucleated on the porphyroblasts and have since been intensified by strain and solution of quartz adjacent to them. Plane-polarized light; base of photo 12 mm.

Localization and intensification of P domains by porphyroblasts

Gratier (1979) showed by electron microprobe analysis that quartz, calcite and dolomite were preferentially dissolved and removed from more intensely deformed parts of crenulated metasediments (i.e. adjacent to relatively strong objects

and in tight to pinched fold hinges), leaving behind concentrations of relatively insoluble chlorite and illite. Volume decreases accompany the compositional changes (Gratier 1983). Similar effects are common around porphyroblasts, dark, mica-rich seams occurring where the matrix foliation is most strongly compressed against the porphyroblasts (Figs 16–18). The



Fig. 17. Dark, anastomosing, relatively continuous micaceous-carbonaceous folia (P domains) anastomosing around Q domains consisting of andalusite porphyroblasts and their strain shadows, some of which show residual crenulations, in a schist from the Pyrenees, Spain. The P domains have been intensified around the porphyroblasts, owing to concentrated strain and consequent solution of quartz. Plane-polarized light; base of photo 13 mm.

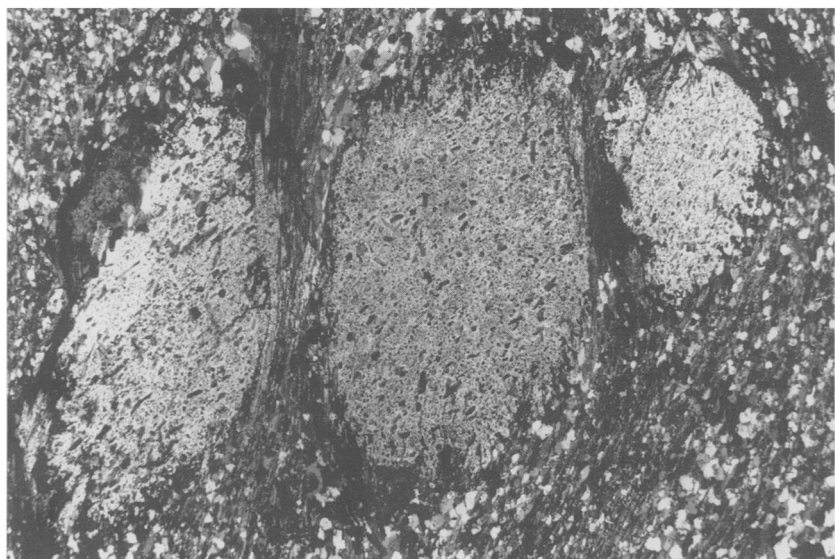


Fig. 18. Mica-rich concentrations (P domains) adjacent to and between porphyroblasts of cordierite in a schist from the Foothills terrane, central Sierra Nevada, California, USA. Plane-polarized light; base of photo 6 mm.

seams appear to be the result of pressure solution and selective removal of components, leaving residual mica and graphite, as in the formation of many crenulation cleavages. This has metamorphic implications, as discussed below.

Effective reaction volumes in prograde metamorphism

When a volume of rock becomes isolated from reaction, either by growth of porphyroblasts that do not take part in later prograde reactions or by solution and removal of selective chemical components from P domains, the remaining volume of the rock becomes the potential 'effective reaction volume' for subsequent prograde reactions. Thus, prograde metamorphism need not be isochemical, as far as the effective reactive system is concerned, even if no bulk chemical changes occur.

Porphyroblasts of minerals such as cordierite, garnet, staurolite, andalusite and K-feldspar commonly grow during prograde metamorphism of metapelitic rocks. Because of their high strength and large size, porphyroblasts force deformation to be partitioned into the matrix, because they tend to resist deformation/recrystallization. Therefore, they may escape participation in later prograde reactions (except perhaps for solution, recrystallization and change in mineral composition at their margins), thereby altering the chemical composition of the effective reacting system. On the other hand, reactions may become localized within porphyroblasts, especially in retrograde metamorphism. For example, Clarke *et al.* (1995) observed evidence for the reaction andalusite + biotite + water = staurolite + chlorite + muscovite + corundum being restricted to andalusite porphyroblasts devoid of quartz inclusions, so that corundum grew despite the presence of quartz in the matrix.

In addition, porphyroblasts of strong minerals can reverse the deformability of metamorphosed graded beds, in that previously weaker metapelitic parts may become much stronger than the quartz-rich metapsammitic parts, owing to preferential growth of large, strong porphyroblasts of aluminous minerals in the metapelitic fractions. This may allow preferred development of foliations in the metapsammitic fractions, as at Cooma, SE Australia (e.g. Johnson *et al.* 1994). As a result, bulk compositional changes due to foliation development, if any, could occur preferentially in metapsammitic, rather than metapelitic, layers at higher metamorphic grades.

Bulk chemical changes not specifically related to foliation development

If dissolved components are removed during progressive deformation and prograde metamorphism of sediments, the chemical composition of the effective reacting system changes, so that prograde metamorphism of metapelites is not isochemical. However, if the main change is generally postulated to be removal of silica, the changes may not be sufficient to produce very unusual or non-sedimentary compositions, so that the metamorphic mineral assemblages probably would not be altered, but only the mineral proportions.

As pointed out by Roser & Nathan (1997), many chemical studies of metasedimentary rock suites and collections of analyses have indicated that regional metamorphism is isochemical, apart from water and carbon dioxide (e.g. Shaw 1956; Butler 1965; Atherton 1977; Yardley 1977). However, other studies have suggested allochemical metamorphism. For example, the work of Haack *et al.* (1984) indicated loss of a number of elements from metapelites during prograde metamorphism above the biotite isograd.

Recent detailed work by Ague (1991, 1994a, b, 1997a) has produced evidence in favour of allochemical regional metamorphism. Ague (1991) compared chemical analyses of pelites and metapelites in Barrovian metamorphic settings, and also examined analyses of rocks of the Littleton Formation, eastern USA. He found that the whole-rock concentration of lower-solubility elements, Al and Ti, varies with metamorphic grade. He inferred this to be a residual enrichment caused by removal of more soluble elements, especially Si, but also Na, K and Ca. Moreover, mass-balance calculations indicated that the average metapelite loses up to 30% of its mass and volume from greenschist to amphibolite facies. Calculated volume strains are -16 to -20% for medium- and high-grade metapelites of the Littleton Formation (relative to their low-grade equivalents) and -20 to -31% for average amphibolite facies metapelites (relative to average shales and slates). Ague (1991) noted that although these strain estimates provide no direct information about mechanisms, much of the volume loss probably occurs parallel to penetrative foliations.

The assumptions underlying the study of Ague (1991) are: (1) the average metapelite composition is a fair indication of protolith compositions, and (2) the chosen reference elements, Al and Ti, are effectively immobile, at least to a first approximation (see below). Ague (1991) added that if both Al and Ti behave

as perfectly immobile components, the percentage change in total mass based on each of these elements should be the same. However, mass loss based on immobile Ti is greater than mass loss based on immobile Al, suggesting that Al may be somewhat more mobile than Ti, as indicated by kyanite in quartz veins.

Ague (1994a, b) observed quartz veins surrounded by aluminous selvedges rich in staurolite \pm kyanite + mica, and poor in quartz and plagioclase, suggesting wall-rock alteration adjacent to the veins. Kyanite and staurolite are absent further away from the veins, and Ague (1994b) inferred that they were formed by reactions destroying quartz, plagioclase and mica adjacent to the veins, in an environment with reduced Na/Al and locally also K/Al, as well as loss of silica. Silica loss from local metapelites can account for only 70% of the quartz in the veins, suggesting that the remaining 30% was externally derived. Ague (1994b) argued that the alteration accompanied regional metamorphism because the quartz veins cut garnet porphyroblasts, which show post-vein garnet overgrowths, and kyanite occurs in some veins, either as bladed crystals or replacing plagioclase.

A synmetamorphic origin is more difficult to argue for alteration selvedges adjacent to quartz veins in some metasedimentary rocks from the Barrovian garnet zone in NE Scotland, described by Ague (1997a). At the locality investigated, the veins constitute around 13 vol% of the rock, and the veins plus alteration zones constitute nearly 40 vol% of the rock. The alteration selvedges have more plagioclase, larger plagioclase porphyroblasts, more calcic plagioclase, and higher plagioclase/muscovite, Na/K, Ca/K, Sr/Rb, (Na + Ca + K)/Al, Mg/Fe^T, (Mg + Fe^T)/Al and Ti/Si ratios than the less altered rock. Also, some selvedges have garnet + biotite + chlorite instead of chloritoid + biotite + chlorite further away. This contrast illustrates the well-known control of bulk chemical composition on mineral assemblages, and is attributed by Ague (1997a) to open-system transport during regional metamorphism of non-volatile elements through a regional network of fractures. The fractures are now represented as quartz veins with alteration selvedges, the silica having been derived locally.

Though the effect of hydrothermal alteration on metamorphic mineral assemblages is well shown by this example, the problem of its timing is more difficult to resolve. Ague (1997a) suggested alteration during metamorphism because the plagioclase porphyroblasts 'grew over the steep cleavage and over preexisting

chloritoid crystals' with the same orientation as those in the matrix. However, this interpretation is very doubtful, because both the plagioclase and chloritoid could have nucleated simultaneously, but with very different nucleation rates, so that the plagioclase (with a low nucleation rate) incorporated many crystals of chloritoid (with a high nucleation rate) as both grew together. This interpretation problem has been emphasized by Vernon (1977, 1996a). Moreover, the quartz vein illustrated by Ague (1997a) is strongly folded, which is consistent with a premetamorphic origin. Therefore, the hydrothermal alteration responsible for the chemical and mineralogical variation could have been premetamorphic, which is a common situation, as discussed in the next section.

In contrast to the observations and interpretations of Ague (1994a, b, 1997a), Yardley & Bottrell (1992) described quartz veins without alteration zones in a wide variety of upper amphibolite facies metasedimentary rocks in Connemara, Ireland. Because the oxygen isotopic compositions of quartz in the veins and adjacent rocks are similar, Yardley & Bottrell (1992) inferred that the quartz segregated locally and that large-distance fluid transport did not accompany regional metamorphism.

Also, in contrast to the studies of Ague, Moss *et al.* (1995), in a reassessment of the data of Shaw (1956), found that although differences in element concentrations relative to Ti and Al exist, they are not systematically related to metamorphic grade, and that the evidence for large gains and losses is hampered by statistical uncertainties. Similarly, in a statistical study of the compositions of schists in a roof pendant in the Sierra Nevada Batholith, Cardenas *et al.* (1996) found that element variations could be explained by metamorphic and/or diagenetic redistribution, as well as original protolith variability.

Roser & Nathan (1997) found little evidence for metasomatism in a detailed investigation of a turbidite succession in New Zealand, and concluded that the regional metamorphism was essentially isochemical. The compositional uniformity of the succession and the use of both pelitic and psammitic compositions, treated separately, minimized some of the problems of previous investigations, especially uncertainty about protoliths and their variability across a metamorphic terrane. Simple comparisons of average compositions at 2% Al₂O₃ intervals showed little contrast between greenschist to amphibolite facies equivalents, except for 'progressive and marked enrichment' in Ca and Sr and loss of Ba, Rb and As, especially in the

sandier rocks. The enrichment in Ca was attributed to redistribution of Ca from calcareous nodules observed in some low-grade rocks. Some exchange of K and Rb between metapsammites and metapelites occurred in the amphibolite facies, and some Si was lost from the metapsammites and gained by the metapelites. Some samples show variation in other elements, but this was inferred to be due to protolith variability.

Uncertainty about the degree and scale of elemental mobility, bulk compositional change and volume loss during regional metamorphism may be due to: (1) variation between different terrains, e.g. strong veining, obvious alteration and a more complex mineral assemblage in the regions studied by Ague (1991, 1994a, b, 1997a) compared with weak veining, simple mineral assemblage, relatively evolved bulk composition and paucity of aluminosilicate minerals in the region studied by Roser & Nathan (1997); (2) uncertainties in the timing of alteration zones (pre- versus synmetamorphic); and (3) initial protolith variability, with the consequent difficulty of ensuring uniformity of protolith composition across a regional prograde metamorphic succession. For example, though Bebout & Barton (1989) detected consistent metasomatic changes in mafic and ultramafic rocks, they found that 'pervasive compositional alteration in metasedimentary rocks is more difficult to document because of variable protolith compositions and extensive mechanical mixing (\pm local chemical redistribution) accompanying ductile deformation. For the most part, chemical changes are unambiguous only in vein envelopes and igneous clasts.'

As pointed out by Roser & Nathan (1997), the large spread of shale and slate analyses in the literature highlights the difficulty of using average compositions of pelites as reference data sets for low-grade rocks; even the assignment of analyses to the category 'pelite' can be doubtful, in the absence of clear criteria for making such an assignment (Roser & Nathan 1997). This problem has been strongly emphasized by Moss *et al.* (1996), who studied in detail outcrops of the low-grade Littleton Formation (New Hampshire) and the equivalent Carrabassett Formation (Maine), and found that the rocks are compositionally variable on the macroscopic to mesoscopic scales, even down to smaller than hand-specimen scale, and even in visually homogeneous rocks. They interpreted this variation as being inherited from the sedimentary protolith, and detected no evidence of alteration over distances greater than the centimetre scale (e.g. to form porphyroblasts,

veins and compositional layering). All the compositional variations could be modelled as mixtures of clay, quartz and chlorite-mica. Compositional variations in hand-specimen size samples from the higher-grade parts of the Littleton Formation are the same as for the low-grade samples, and so can be interpreted as being due to protolith variation. Because the low-grade rocks are so compositionally variable, a simple average with a small standard deviation cannot be obtained. Therefore, the effect of possible metamorphic variation cannot be separated with certainty from the protolith variation.

Moss *et al.* (1996) concluded that 'if differences among average compositions of rocks of different metamorphic grade are the principal means of determining whether there has been large-scale gain or loss of an element, then representative sampling is crucial but may be virtually impossible in practice'. They went further, and suggested that variation in composition on the hand-specimen scale in high-grade metamorphic rocks, such as they observed, may be used to infer the nature of sedimentary protoliths over intermediate and large distances – the ultimate position on isochemical metamorphism!

However, Ague (1997b) has pointed out serious deficiencies in the studies of Moss *et al.* (1995, 1996). For example, mass balance calculations using their data and based on immobile Zr fail to detect volatile loss, even for the strongly dehydrated, highest grade rocks. Calculations based on immobile Al do detect volatile loss in medium- and high-grade rocks, as well as loss of silica – equivalent to a rock volume loss of -20% – in the highest grade rocks. Ague (1997b) suggested that the outcrops selected are spaced too far apart (one per 350 km^2 on average) to detect mass transport phenomena, which commonly occur over distances of $1\text{--}10\text{ km}$. He concluded that, regardless of the reference element selected, the Littleton Formation data of Moss *et al.* (1995, 1996) cannot be used to support isochemical metamorphism.

The foregoing discussion emphasizes the great difficulty of sampling rocks supposed to be low- and high-grade equivalents and the care that must be taken with sampling and statistical analysis of the results. Possibly contact metamorphic environments may be better for tracing single sedimentary units up-grade, though the duration of heating may be insufficient to produce much element mobility.

Future emphasis should be placed on (1) accurate identification of lithotypes, and (2) tighter control on protolith variation across the terrane

to be investigated, caused, for example, by provenance variations. As pointed out by Ague (1997b), definitive resolution of the problem will require studies that take into account the detailed geological contexts of low-, medium- and high-grade samples. For example, if veins and their selvedges are not sampled, but intervein rocks are, the amount of chemical and volume change would be seriously underestimated. Ague (1997b) suggested that some regional metamorphic terranes may be 'closed' and others 'open'. Perhaps future detailed investigations will reveal characteristic terrane differences with regard to mass and volume changes during prograde metamorphism and deformation.

The common extreme compositional variability on the local scale (Moss *et al.* 1996) also highlights the difficulty of using chemical studies to argue against mass and volume changes in the formation of slaty cleavage.

Pseudopelitic compositions formed by pre- and synmetamorphic alteration of igneous rocks

Hydrothermal alteration involving base-cation leaching (hydrogen metasomatism) of a variety of igneous rock types can result in aluminous metamorphic assemblages containing minerals such as pyrophyllite, cordierite, andalusite and sillimanite, which are more typical of metapelites (e.g. Espenshade & Potter 1960; Gresens 1971; Gustafson & Hunt 1975; Lowder & Dow 1978; Sykes & Moody 1978; Carpenter & Allard 1980; Allard & Carpenter 1981; Valiant *et al.* 1983; Watanabe & Hasegawa 1986). Generally the alteration is relatively local, for example in fault or shear zones, adjacent to quartz veins, and/or around sulphide gold concentrations, commonly in subvolcanic or porphyry copper settings. Regional and contact metamorphism of such rocks produces aluminous schists and gneisses that could be mistaken as representing pelitic protoliths, in the absence of evidence to the contrary. In some examples, residual igneous microstructures (e.g. deformed plagioclase laths) may remain to indicate a non-sedimentary parentage.

For example, Vernon *et al.* (1987) described metamorphosed felsic igneous plutonic and shallow intrusive rocks that underwent base-cation leaching, promoting the formation of cordierite, andalusite and sillimanite; the alteration was at least partly metamorphic, though some premetamorphic leaching may also have

occurred. Another example is at the Big Bell Mine, Western Australia, where high-grade regional metamorphism has been superimposed on intense premetamorphic alteration of rocks of mafic composition, resulting in assemblages that include cordierite + sillimanite + K-feldspar + garnet + biotite + quartz (Phillips & de Nooy 1988), as shown in Fig. 15. Such apparently anomalous aluminous assemblages may indicate zones of former hydrothermal alteration and so assist ore exploration in high-grade metamorphic terranes (e.g. Stanton & Vaughan 1979; Vernon 1996b).

Conclusions

The following are the main conclusions of this review.

(1) Grain rotation may be a dominant mechanism in the early stages of slaty cleavage development. If dewatering can produce a rudimentary slaty cleavage by removal of all minerals in zones of high fluid flow, some volume reduction perpendicular to the cleavage may be achieved without bulk chemical change.

(2) Variation in the degree of compositional change and volume loss between and within areas is to be expected, depending on variations in deformation and/or the extent of openness of the local system to fluids. However, the first step is to try to achieve agreement between the structural and chemical approaches in at least one small area in at least one of the classic slate belts. Ideally, a structural geologist and geochemist should investigate together in detail the same bed in different structural settings, for example around a fold.

(3) Elements generally taken to be immobile, such as Ti, Al and Zr, may be relatively mobile in some circumstances, and so are not necessarily reliable when comparing the compositions of less and more deformed rocks.

(4) Extreme, local compositional variation in sedimentary protoliths (even those that appear homogeneous) hampers chemical comparisons between rocks that have undergone different degrees of deformation and metamorphism.

(5) The most detailed statistical evaluations have indicated no systematic variation of chemical composition with metamorphic grade, so that prograde metamorphism may be regarded as being effectively isochemical, at least until removal of partial melts at high metamorphic grades. However, effective reaction volumes are not necessarily isochemical, owing to potential preferential isolation of components by porphyroblasts (a form of metastable persistence).

(6) If mass is inferred to have been conserved during regional prograde metamorphism, volume also must have been lost, in order to accommodate the general increase in density that accompanies the change from low- to high-grade metamorphic rocks. A good example of this effect has been discussed by Cox (1993). The volume loss could be accommodated by shortening without removal of material, owing to the higher density of the higher-grade minerals. Studies inferring volume loss by removal of material on the regional scale necessarily also infer mass loss appropriate to the density increase. Unfortunately, much of the evidence is for very local volume loss, which is difficult to translate to the regional scale. Studies inferring no regional volume loss must infer mass gain, which is intuitively less likely than mass conservation or loss. Marked chemical and volume changes occur when partial melts are removed at highest metamorphic grades.

(7) Local bulk chemical changes in rocks of igneous composition may be caused by hydrothermal alteration (especially base-cation leaching) in subvolcanic/porphyry copper areas, especially adjacent to veins, faults, shear zones and gold and/or sulphide deposits. Metamorphism of the resulting aluminous compositions can produce rocks with unexpected Al-rich minerals, which could be mistaken for pelitic assemblages, in the absence of residual igneous microstructures. Such anomalous assemblages are potential indicators of mineral resources in medium- and high-grade metamorphic terranes.

I thank A. Barker, S. Johnson and B. Yardley for helpful comments, and acknowledge financial support from a Macquarie University Research Grant.

References

AGUE, J. J. 1991. Evidence of major mass transfer and volume strain during regional metamorphism of pelites. *Geology*, **19**, 855–858.

— 1994a. Mass transfer during Barrovian metamorphism of pelites, south-central Connecticut. I: Evidence for changes in composition and volume. *American Journal of Science*, **294**, 989–1057.

— 1994b. Mass transfer during Barrovian metamorphism of pelites, south-central Connecticut. II: Channelized fluid flow and the growth of staurolite and kyanite. *American Journal of Science*, **294**, 1061–1134.

— 1997a. Crustal mass transfer and index mineral growth in Barrow's garnet zone, northeast Scotland. *Geology*, **25**, 73–76.

— 1997b. Compositional variations in metamorphosed sediments of the Littleton Formation – discussion. *American Journal of Science*, **297**, 440–449.

ALLARD, G. O. & CARPENTER, R. H. 1981. Alteration in the Otake geothermal field – a model for interpreting certain metamorphic assemblages in metamorphosed volcanic terranes. *1981 IAVCEI Symposium: Arc Volcanism, Tokyo-Hakone*, 1–2 (abstract).

ALTENBERGER, U. 1996. Material transport in channelized fluids – examples from high-temperature shear zones in the Central-European Variscan belt. *Mineralogy and Petrology*, **57**, 51–72.

ALTERMAN, I. B. 1973. Rotation and dewatering during slaty cleavage formation: some new evidence and interpretations. *Geology*, **1**, 33–36.

ATHERTON, M. P. 1977. The metamorphism of the Dalradian rocks of Scotland. *Scottish Journal of Geology*, **13**, 331–370.

AYERS, J. C. & WATSON, E. B. 1993. Rutile solubility and mobility in supercritical aqueous fluids. *Contributions to Mineralogy and Petrology*, **114**, 321–330.

BEABOUT, G. E. & BARTON, M. D. 1989. Fluid flow and metasomatism in a subduction zone hydrothermal system: Catalina Schist terrane, California. *Geology*, **17**, 976–980.

BELL, A. 1985. Strain paths during slaty cleavage formation – the role of volume loss. *Journal of Structural Geology*, **7**, 563–568.

BELL, T. H. 1978. The development of slaty cleavage across the Nackara Arc of the Adelaide Geosyncline. *Tectonophysics*, **51**, 171–201.

— & RUBENACH, M. J. 1983. Sequential porphyroblast growth and crenulation cleavage development during progressive deformation. *Tectonophysics*, **92**, 171–194.

BEUTNER, E. C. 1978. Slaty cleavage and related strain in Martinsburg Slate, Delaware Water Gap, New Jersey. *American Journal of Science*, **278**, 1–23.

— & CHARLES, E. G. 1985. Large volume loss during cleavage formation, Hamburg sequence, Pennsylvania. *Geology*, **13**, 803–805.

BINNS, R. A. & EAMES, J. C. 1989. *Geochemistry of wall rocks at the Clunes gold deposit, Victoria*. Economic Geology Monograph, **6**, 310–319.

BOULTER, C. A. 1974. Tectonic deformation of soft sedimentary clastic dikes from the Precambrian rocks of Tasmania, Australia, with particular reference to their relations with cleavages. *Bulletin of the Geological Society of America*, **85**, 1413–1420.

— 1986. Strain paths during slaty cleavage formation – the role of volume loss: Discussion. *Journal of Structural Geology*, **8**, 719–720.

— & RÄHEIM, A. 1974. Variation in Si^{4+} -content of phengites through a three stage deformation sequence. *Contributions to Mineralogy and Petrology*, **48**, 57–71.

BOYER, S. E. 1984. Origin and significance of compositional layering in Late Precambrian sediments, Blue Ridge Province, North Carolina, USA. *Journal of Structural Geology*, **6**, 121–133.

BRANDON, M. T., COWAN, D. S. & FEEHAN, J. G. 1994. Fault-zone structures and solution-mass-transfer cleavage in Late Cretaceous nappes, San Juan Islands, Washington. In: SWANSON, D. A. &

HAUGERUD, R. A. (eds) *Geologic Field Trips in the Pacific Northwest*, 1994 Geological Society of America Annual Meeting, Seattle, Washington, **2**, 2L1–2L19.

BUTLER, B. C. M. 1965. A chemical study of some rocks of the Moine Series of Scotland. *Quarterly Journal of the Geological Society of London*, **121**, 163–208.

CARDENAS, A. A., GIRTY, G. H., HANSON, A. D., LAHREN, M. M., KNAACK, C. & JOHNSON, D. 1996. Assessing differences in composition between low metamorphic grade mudstones and high-grade schists using logratio techniques. *Journal of Geology*, **194**, 279–293.

CARPENTER, R. H. & ALLARD, G. O. 1980. Mineralization, alteration and volcanism in the Lincolnton-McCormick district, Georgia and South Carolina. *Geological Society of America Abstracts with Programs*, **7**, 398–399.

CARSON, W. P. 1968. Development of flow-cleavage in the Martinsburg Slate, Port Jervis South area, (northern New Jersey). *Tectonophysics*, **5**, 531–541.

CLARK, B. R. 1970. Origin of slaty cleavage in the Coeur d'Alene district, Idaho. *Bulletin of the Geological Society of America*, **81**, 3161–3176.

CLARK, M. B. & FISHER, D. M. 1995. Strain partitioning and crack-seal growth of chlorite-muscovite aggregates during progressive noncoaxial strain: an example from the slate belt of Taiwan. *Journal of Structural Geology*, **17**, 461–474.

CLARKE, G. L., POWELL, R. & VERNON, R. H. 1995. Reaction relationships during retrograde metamorphism at Olary, South Australia. *Journal of Metamorphic Geology*, **13**, 715–726.

COSGROVE, J. W. 1976. The formation of crenulation cleavage. *Journal of the Geological Society of London*, **132**, 155–178.

COX, S. C. 1993. Fluid-rock interaction and the source of gold in metamorphic belts: an example from the Torlesse Terrane and Otago Schist of New Zealand. *Irish Association for Economic Geology Annual Review*, **1993**, 44–51.

—, CEPELCHA, J., WALL, V. J., ETHERIDGE, M. A., CAS, R. A. F., HAMMOND, R. & WILLMAN, C. E. 1983. Lower Ordovician Bendigo Trough sequence, Castlemaine area, Victoria – deformation and implications for the tectonic evolution of the Lachlan Fold Belt. *Geological Society of Australia Abstracts*, **9**, 41–42.

—, ETHERIDGE, M. A., CAS, R. A. F. & CLIFFORD, B. A. 1991. Deformational style of the Castlemaine area, Bendigo-Ballarat Zone: implications for evolution of crustal structure in central Victoria. *Australian Journal of Earth Sciences*, **38**, 151–170.

DURNEY, D. W. 1972. Solution-transfer, an important geological deformation mechanism. *Nature*, **235**, 315–317.

ENGELDER, T. 1984. The role of pore water circulation during the formation of foreland fold and thrust belts. *Journal of Geophysical Research*, **89**, 4319–4325.

EPSTEIN, J. B. & EPSTEIN, A. G. 1969. Geology of the Valley and Ridge province between Delaware Water Gap and Lehigh Gap, Pennsylvania. In: SUBITZKY, S. (ed.) *Geology of Selected Areas in New Jersey and Eastern Pennsylvania, and Guidebook of Excursions*. Rutgers University, New Brunswick, New Jersey, 132–205.

ERSLEV, E. & MANN, C. 1984. Pressure solution shortening in the Martinsburg Formation, New Jersey. *Proceedings of the Pennsylvania Academy of Science*, **58**, 84–88.

— & WARD, D. J. 1993. Non-volatile element and volume flux in coalesced slaty cleavage. *Journal of Structural Geology*, **16**, 531–553.

ESPENSHADE, G. H. & POTTER, D. B. 1960. *Kyanite, sillimanite and andalusite deposits of the southeastern States*. United States Geological Survey Professional Paper, **336**.

ETHERIDGE, M. A. & HOBBS, B. E. 1974. Chemical and deformational controls on recrystallization of mica. *Contributions to Mineralogy and Petrology*, **43**, 111–124.

— & LEE, M. F. 1975. Microstructure of slate from Lady Loretta, Queensland, Australia. *Bulletin of the Geological Society of America*, **86**, 13–22.

— WALL, V. J. & VERNON, R. H. 1983. The role of the fluid phase during regional metamorphism and deformation. *Journal of Metamorphic Geology*, **1**, 205–226.

FYFE, W. S. & KERRICH, R. 1985. Fluids and thrusting. *Chemical Geology*, **49**, 353–362.

GEISER, A. 1975. Slaty cleavage and the dewatering hypothesis – an examination of some critical evidence. *Geology*, **3**, 717–720.

GLEN, R. A. 1982. Component migration patterns during the formation of a metamorphic layering, Mount Franks area, Willyama Complex, N.S.W., Australia. *Journal of Structural Geology*, **4**, 457–467.

GOLDSTEIN, A., PICKENS, J., KLEPEIS, K. & LINN, F. 1995. Finite strain heterogeneity and volume loss in slates of the Taconic Allochthon, Vermont, USA. *Journal of Structural Geology*, **17**, 1207–1216.

GRATIER, J.-P. 1979. Mise en évidence de relations entre changement de composition chimique et intensité de déformation dans les roches à schistosité. *Bulletin de la Société géologique de France*, **21**, 95–104.

— 1983. Estimation of volume changes by comparative chemical analyses in heterogeneously deformed rocks (folds with mass transfer). *Journal of Structural Geology*, **5**, 329–339.

GRAY, D. R. 1977. Differentiation associated with discrete crenulation cleavages. *Lithos*, **10**, 89–101.

— 1978. Cleavages in deformed psammitic rocks from southeastern Australia: their nature and origin. *Bulletin of the Geological Society of America*, **89**, 577–590.

— 1979. Microstructure of crenulation cleavages: an indicator of cleavage origin. *American Journal of Science*, **279**, 97–128.

— 1981. Compound tectonic fabrics in singly folded rocks from southwest Virginia, USA. *Tectonophysics*, **78**, 229–248.

— & WILLMAN, C. E. 1991a. Deformation in the Ballarat slate belt, central Victoria and implications for crustal structure across SE Australia. *Australian Journal of Earth Sciences*, **38**, 171–201.

— & — 1991b. Thrust-related strain gradients and thrusting mechanisms in a chevron-folded sequence, southeastern Australia. *Journal of Structural Geology*, **13**, 691–710.

— & WRIGHT, T. O. 1984. Problems of volume loss, fabric development, and strain determination in low-grade pelitic rocks, Martinsburg Formation, USA. *Journal of Structural Geology*, **7**, 492.

—, GREGORY, R. T. & DURNEY, D. W. 1991. Rock-buffered fluid–rock interaction in deformed quartz-rich turbidite sequences, eastern Australia. *Journal of Geophysical Research*, **96**, 19 681–19 704.

GREGG, W. J. 1985. Microscopic deformation mechanisms associated with mica film formation in cleaved psammitic rocks. *Journal of Structural Geology*, **7**, 45–56.

— 1986. Deformation of chlorite-white mica aggregates in cleaved psammitic and pelitic rocks from Islesboro, Maine, USA. *Journal of Structural Geology*, **8**, 59–68.

GRESENS, R. L. 1971. Application of hydrolysis equilibria to the genesis of pegmatite and kyanite deposits in northern New Mexico. *Mountain Geology*, **8**, 3–16.

GROSHONG, R. H. 1976. Strain and pressure solution in the Martinsburg Slate, Delaware Water Gap, New Jersey. *American Journal of Science*, **276**, 1131–1146.

GUSTAFSON, L. B. & HUNT, J. P. 1975. The porphyry copper deposit at El Salvador, Chile. *Economic Geology*, **70**, 857–912.

HAACK, U., HEINRICHS, H., BONESS, M. & SCHNEIDER, A. 1984. Loss of metals from pelites during regional metamorphism. *Contributions to Mineralogy and Petrology*, **85**, 116–132.

HAMMOND, R. L. 1987. The influence of deformation partitioning on dissolution and solution transfer in low-grade tectonic mélange. *Journal of Metamorphic Geology*, **5**, 195–211.

HARA, I., SHIITE, T. & HIDE, K. 1984. Pressure solution of plagioclase and garnet during Naghma folding in the Sambagawa Belt of central Shikoku. *Journal of the Geological Society of Japan*, **90**, 33–42.

HART, R. 1970. Chemical exchange between sea water and deep ocean basalt. *Earth and Planetary Science Letters*, **9**, 269–279.

HELLMAN, P. L. & SMITH, R. E. 1979. The mobility of the rare earth elements: evidence and implications from selected terrains affected by burial metamorphism. *Contributions to Mineralogy and Petrology*, **71**, 23–44.

HO, N.-C., PEACOR, D. R. & VAN DER PLUIJM, B. A. 1995. Reorientation mechanisms of phyllosilicates in the mudstone-to-slate transition at Lehigh Gap, Pennsylvania. *Journal of Structural Geology*, **17**, 345–356.

HOBBS, B. E., MEANS, W. D. & WILLIAMS, P. F. 1976. *An Outline of Structural Geology*. Wiley, New York.

HOLEYWELL, R. C. & TULLIS, T. E. 1975. Mineral reorientation and slaty cleavage in the Martinsburg Formation, Lehigh Gap, Pennsylvania. *Bulletin of the Geological Society of America*, **86**, 1296–1304.

JOHNSON, S. E., VERNON, R. H. & HOBBS, B. E. 1994. *Deformation and metamorphism of the Cooma Complex, southeastern Australia*. Specialist Group in Tectonics & Structural Geology, Geological Society of Australia, Field Guide 4.

KANAGAWA, K. 1991. Change in dominant mechanisms for phyllosilicate preferred orientation during cleavage development in the Kitakami slates of NE Japan. *Journal of Structural Geology*, **13**, 927–943.

KERRICK, D. M. 1988. Al_2SiO_5 -bearing segregations in the Lepontine Alps, Switzerland: Aluminium mobility in metapelites. *Geology*, **16**, 636–640.

KISCH, H. J. 1989. Discordant relationship between degree of very low-grade metamorphism and the development of slaty cleavage. In: DALY, J. S., CLIFF, R. A. & YARDLEY, B. W. D. (eds) *Evolution of Metamorphic Belts*. Geological Society, Special Publication, **43**, Blackwell, Oxford, 173–185.

KNIPE, R. J. 1979. Chemical changes during slaty cleavage development. *Bulletin de Minéralogie*, **102**, 206–209.

— 1981. The interaction of deformation and metamorphism in slates. *Tectonophysics*, **78**, 249–272.

— & WHITE, S. H. 1977. Microstructural variation of an axial plane cleavage around a fold – a HVEM study. *Tectonophysics*, **39**, 355–380.

LAFRANCE, B. & VERNON, R. H. 1993. Mass transfer and microfracturing in gabbroic mylonites of the Guadalupe Igneous Complex, California. In: BOLAND, J. N. & FITZ GERALD, J. D. (eds) *Defects and Processes in the Solid State: Geoscience Applications. The McLaren Volume*. Elsevier, Amsterdam, 151–167.

LEE, J. H., PEACOR, D. R., LEWIS, D. D. & WINTSCH, R. P. 1986. Evidence for syntectonic crystallization for the mudstone to slate transition at Lehigh Gap, Pennsylvania, USA. *Journal of Structural Geology*, **8**, 767–780.

LOWDER, G. G. & DOW, J. A. S. 1978. Geology and exploration of porphyry copper deposits in North Sulawesi, Indonesia. *Economic Geology*, **73**, 628–644.

MACKENZIE, J. S., NEEDHAM, D. T. & AGAR, S. M. 1987. Progressive deformation in an accretionary complex: An example from the Shimanto belt of eastern Kyushu, southwest Japan. *Geology*, **15**, 353–356.

MALTMAN, A. J. 1981. Primary bedding-parallel fabrics in structural geology. *Journal of the Geological Society of London*, **138**, 475–483.

MANCKTELOW, N. S. 1979. The development of slaty cleavage, Fleurieu Peninsula, South Australia. *Tectonophysics*, **58**, 1–20.

— 1994. On volume change and mass transport during the development of crenulation cleavage. *Journal of Structural Geology*, **16**, 1217–1231.

MARLOW, P. C. & ETHERIDGE, M. A. 1977. Development of layered crenulation cleavage in mica schists of the Kanmantoo Group near Macclesfield, South Australia. *Bulletin of the Geological Society of America*, **88**, 873–882.

MAXWELL, J. C. 1962. Origin of slaty and fracture cleavage in the Delaware Water Gap area, New Jersey and Pennsylvania. In: ENGEL, A. E. J., JAMES, H. L. & LEONARD, B. F. (eds) *Petrologic Studies – a Volume in Honour of A. F. Buddington*. Geological Society of America, Boulder, Colorado, 281–311.

MIŁODOWSKI, A. E. & ZALASIEWICZ, J. A. 1991. The origin and sedimentary, diagenetic and metamorphic evolution of chlorite-mica stacks in Llandovery sediments of central Wales, U.K. *Geological Magazine*, **128**, 263–278.

MOENCH, R. 1966. Relation of S_2 schistosity to metamorphosed clastic dikes, Rangeley-Phillips area, Maine. *Bulletin of the Geological Society of America*, **77**, 1449–1462.

MOORE, J. C. 1973. Complex deformation of Cretaceous trench DEPOSITS, N. W. Alaska. *Bulletin of the Geological Society of America*, **84**, 2005–2020.

— & GEIGLE, J. E. 1974. Slaty cleavage: incipient occurrences in the deep sea. *Science*, **183**, 509–510.

Moss, B. E., HASKIN, L. A. & DYMEK, R. F. 1995. Redetermination and reevaluation of compositional variations in metamorphosed sediments of the Littleton Formation, New Hampshire. *American Journal of Science*, **295**, 988–1019.

—, — & — 1996. Compositional variations in metamorphosed sediments of the Littleton Formation, New Hampshire, and the Carrabassett Formation, Maine, at sub-hand specimen, outcrop, and regional scales. *American Journal of Science*, **296**, 473–505.

NICHOLSON, R. 1966. Metamorphic differentiation in crenulated schists. *Nature*, **209**, 68–69.

NORRIS, R. J. & BISHOP, D. G. 1990. Deformed conglomerate and textural zones in the Otago Schists, New Zealand. *Tectonophysics*, **174**, 331–349.

— & RUPKE, N. A. 1986. Development of slaty cleavage in a mudstone unit from the Cantabrian Mountains, northern Spain. *Journal of Structural Geology*, **8**, 871–878.

OERTEL, G. 1970. Deformation of a slaty, lapillar tuff in the Lake District, England. *Bulletin of the Geological Society of America*, **81**, 1173–1188.

PATERSON, S. R. & TOBISCH, O. T. 1993. Prelithification structures, deformation mechanisms, and fabric ellipsoids in slumped turbidites from the Pigeon Point Formation, California. *Tectonophysics*, **222**, 135–149.

—, YU, H. & OERTEL, G. 1995. Primary and tectonic fabric intensities in mudrocks. *Tectonophysics*, **247**, 105–119.

PHILIPOTT, P. & SELVERSTONE, J. 1991. Trace-element-rich brines in eclogitic veins: implications for fluid composition and transport during subduction. *Contributions to Mineralogy and Petrology*, **106**, 417–430.

PHILLIPS, G. N. & DE NOOV, D. 1988. High-grade metamorphic processes which influence Archaean gold deposits, with particular reference to Big Bell, Australia. *Journal of Metamorphic Geology*, **6**, 95–114.

PIQUE, A. 1982. Relations between stages of diagenetic and metamorphic evolution and the development of a primary cleavage in the northwestern Moroccan Meseta. *Journal of Structural Geology*, **4**, 491–500.

PLESSMAN, W. 1964. Gesteinslösun, ein Hauptfaktor beim Schieferungsprozess. *Geologische Mitteilungen*, **4**, 69–82.

POWELL, C. M. 1969. Intrusive sandstone dykes in the Siamo Slate near Negaunee, Michigan. *Bulletin of the Geological Society of America*, **80**, 2585–2594.

— 1972a. Tectonic dewatering and strain in the Michigamme Slate, Michigan. *Bulletin of the Geological Society of America*, **83**, 2149–2158.

— 1972b. Tectonically dewatered slates in the Ludlovian of the Lake District, England. *Geological Journal*, **8**, 95–110.

— & RICKARD, M. J. 1985. Significance of the early foliation at Bermagui, N.S.W., Australia. *Journal of Structural Geology*, **7**, 385–400.

RAMSAY, J. G. & HUBER, M. I. 1983. *The Techniques of Modern Structural Geology. Volume 1: Strain Analysis*. Academic Press, London.

— & WOOD, D. S. 1973. The geometric effects of volume change during deformation processes. *Tectonophysics*, **13**, 263–277.

ROSER, B. P. & NATHAN, S. 1997. An evaluation of elemental mobility during metamorphism of a turbidite sequence (Greenland Group, New Zealand). *Geological Magazine*, **134**, 219–234.

ROY, A. B. 1978. Evolution of slaty cleavage in relation to diagenesis and metamorphism: a study from the Hunsrückschiefer. *Bulletin of the Geological Society of America*, **89**, 1775–1785.

SCHANDL, E. S., DAVIS, D. W. & KROGH, T. E. 1990. Are the alteration halos of massive sulfide deposits syngenetic? Evidence from U-Pb dating of hydrothermal rutile at the Kidd volcanic center, Abitibi subprovince, Canada. *Geology*, **18**, 505–508.

SHAW, D. M. 1956. Geochemistry of pelitic rocks. Part III: Major elements and general geochemistry. *Bulletin of the Geological Society of America*, **67**, 919–934.

SIDDANS, A. W. 1972. Slaty cleavage – a review of research since 1815. *Earth Science Reviews*, **8**, 205–232.

SORBY, H. C. 1853. On the origin of slaty cleavage. *Edinburgh New Philosophical Journal*, **55**, 137–148.

SPANG, J. H., OLDERSHAW, A. E. & STOUT, M. Z. 1979. Development of cleavage in the Banff Formation at Pigeon Mountain, Front Ranges, Canadian Rocky Mountains. *Canadian Journal of Earth Sciences*, **16**, 1108–1115.

STANTON, R. L. & VAUGHAN, J. P. 1979. Facies of ore formation: a preliminary account of the Pegmont deposit as an example of potential relations between small 'iron formations' and stratiform sulphide ores. *Proceedings of the Australasian Institute of Mining and Metallurgy*, **270**, 25–38.

STEPHENS, M. B., GLASSON, M. G. & KEAYS, R. R. 1979. Structural and chemical aspects of metamorphic layering development in metasediments from Clunes, Australia. *American Journal of Science*, **279**, 129–160.

STILLWELL, F. L. 1918. The metamorphic rocks of Adelie Land. *Australasian Antarctic Expedition 1911–14 Scientific Report, Series A*, **3**, 1–320.

SUTTON, S. J. 1991. Development of domainal slaty cleavage at Ocoee Gorge, Tennessee. *Journal of Geology*, **99**, 789–800.

— & LAND, L. S. 1996. Postdepositional chemical alteration of Ouchita Shales. *Geological Society of America Bulletin*, **108**, 978–99.

SYKES, M. L. & MOODY, J. B. 1978. Pyrophyllite and metamorphism in the Carolina slate belt. *American Mineralogist*, **63**, 96–108.

TALBOT, J. L. 1964. Crenulation cleavage in the Hunsrück-schiefer of the Middle Moselle region. *Geologische Rundschau*, **54**, 1026–1043.

TAN, B. K., GRAY, D. R. & STEWART, I. 1995. Volume change accompanying cleavage development in graptolitic shales from Gisborne, Victoria, Australia. *Journal of Structural Geology*, **17**, 1387–1394.

TRANTER, T. H. 1992. Underplating of an accretionary prism: An example from the LeMay Group of central Alexander Island, Antarctic Peninsula. *Journal of South American Earth Sciences*, **6**, 1–20.

VALIANT, R. I., BARNETT, R. L. & HODDER, R. W. 1983. Aluminum silicate-bearing rock and its relation to gold mineralization, Bousquet Mine, Bousquet Township, Quebec. *CIM Bulletin*, **76**, 81–90.

VAN DER PLUIJM, B. A. & KAARS-SIJPESTEIJN, C. H. 1984. Chlorite-mica aggregates: morphology, orientation, development and bearing on cleavage formation in very low-grade rocks. *Journal of Structural Geology*, **6**, 399–407.

VERNON, R. H. 1977. Relationships between microstructures and metamorphic assemblages. *Tectonophysics*, **39**, 439–452.

— 1978. Porphyroblast-matrix microstructural relationships in deformed metamorphic rocks. *Geologische Rundschau*, **67**, 288–305.

— 1979. Formation of late sillimanite by hydrogen metasomatism (base-leaching) in some high-grade gneisses. *Lithos*, **12**, 143–152.

— 1987. Growth and concentration of fibrous sillimanite related to heterogeneous deformation in K-feldspar–sillimanite metapelites. *Journal of Metamorphic Geology*, **5**, 51–68.

— 1996a. Problems with inferring *P-T-t* paths in low-*P* granulite facies rocks. *Journal of Metamorphic Geology*, **14**, 143–153.

— 1996b. Structural evidence of parent rocks in high-grade metamorphic areas – especially Broken Hill. In: PONGRATZ, J. & DAVIDSON, G. (eds) *New Developments in Broken Hill Type Deposits*. Centre for Ore Deposit and Exploration Studies, University of Tasmania, Special Publication **1**, 17–20.

—, FLOOD, R. H. & D'ARCY, W. F. 1987. Sillimanite and andalusite produced by base-cation leaching and contact metamorphism of felsic igneous rocks. *Journal of Metamorphic Geology*, **5**, 439–450.

VOLL, G. 1960. New work on petrofabrics. *Liverpool and Manchester Geological Journal*, **2**, 503–567.

WALDRON, H. M. & SANDIFORD, M. 1988. Deformation volume and cleavage development in metasedimentary rocks from the Ballarat slate belt. *Journal of Structural Geology*, **10**, 53–62.

WATANABE, J. & HASEGAWA, K. 1986. Borosilicates (datolite, schorl) and aluminosilicates (andalusite, sillimanite) in the Oketo Rhyolite, Hokkaido. *Journal of the Faculty of Science, Hokkaido University, Series IV*, **21**, 583–598.

WEBER, K. 1981. Kinematic and metamorphic aspects of cleavage formation in very low-grade metamorphic slates. *Tectonophysics*, **78**, 291–306.

WHITE, S. H. & JOHNSTON, C. 1981. A microstructural and microchemical study of cleavage lamellae in a slate. *Journal of Structural Geology*, **3**, 279–290.

— & KNIFE, R. J. 1978. Microstructure and cleavage development in selected slates. *Contributions to Mineralogy and Petrology*, **66**, 165–174.

WILLIAMS, P. F. 1972. Development of metamorphic layering and cleavage in low grade metamorphic rocks at Bermagui, Australia. *American Journal of Science*, **272**, 1–47.

— 1983. Timing of deformation and the mechanism of cleavage development in a Newfoundland mélange. *Maritime Sediments and Atlantic Geology*, **19**, 31–48.

— 1990. Differentiated layering in metamorphic rocks. *Earth-Science Reviews*, **29**, 267–281.

—, COLLINS, A. R. & WILTSHERE, R. G. 1969. Cleavage and penecontemporaneous deformation structures in sedimentary rocks. *Journal of Geology*, **77**, 415–425.

—, MEANS, W. D. & HOBBS, B. E. 1977. Development of axial-plane slaty cleavage and schistosity in experimental and natural materials. *Tectonophysics*, **42**, 139–158.

WINTSCH, R. P., KVALE, C. M. & KISCH, H. D. 1991. Open-system, constant volume development of slaty cleavage, and strain-induced replacement reactions in the Martinsburg Formation, Lehigh Gap, Pennsylvania. *Bulletin of the Geological Society of America*, **103**, 916–927.

WOOD, D. S. 1974. Current views of the development of slaty cleavage. *Annual Reviews of Earth and Planetary Sciences*, **2**, 369–401.

WOODLAND, B. G. 1985. Relationship of concretions and chlorite-muscovite porphyroblasts to the development of domainal cleavage in low-grade metamorphic deformed rocks from north-central Wales, Great Britain. *Journal of Structural Geology*, **7**, 205–215.

WRIGHT, T. O. & HENDERSON, J. R. 1992. Volume loss during cleavage formation in the Meguma Group, Nova Scotia, Canada. *Journal of Structural Geology*, **14**, 281–290.

— & PLATT, L. B. 1982. Pressure dissolution and cleavage in the Martinsburg Shale. *American Journal of Science*, **282**, 122–135.

YARDLEY, B. W. D. 1977. Relationships between the chemical and modal compositions of metapelites from Connemara, Ireland. *Lithos*, **10**, 235–242.

— & BOTTRELL, S. H. 1992. Silica mobility and fluid movement during metamorphism of the Connemara schists, Ireland. *Journal of Metamorphic Geology*, **10**, 435–464.

The role of microcracking and grain-boundary dilation during retrograde reactions

ANDREW J. BARKER & XING ZHANG

Department of Geology, University of Southampton, Southampton Oceanography Centre, Southampton, SO14 3ZH, UK

Abstract: Under conditions of sub-greenschist and low greenschist facies retrogression, both intragranular microcracking and grain-boundary dilatancy are important processes for facilitating fluid access into domains between fractures in metamorphic rocks. Both processes play a crucial role in promoting retrogression of high-temperature minerals. In a quartz-rich schist from Norway, garnet retrogression is clearly linked to microcracking in the vicinity of a minor fracture. Intense microcracking of quartz extends up to 12 mm from the fracture, and permits fluid infiltration. This causes extensive (70–100%) garnet retrogression to chlorite. At distances >16 mm from the fracture there is no sign of fluid infiltration and garnets are entirely unaltered.

The spatial distribution of grain-boundary reaction products in a scapolite-dominated rock from Scotland provides evidence for the significant role played by transient grain-boundary dilatancy in promoting grain-scale fluid access and resultant retrogression. By applying distinct element modelling (UDEC code) the geometrical differences in distribution of grain-boundary reaction products are directly related to subtle differences in the magnitude and orientation of applied stresses and patterns of transient grain-boundary dilatancy.

Veined metamorphic rocks are common, and are taken as evidence of fracture-controlled fluid flow (e.g. Fyfe *et al.* 1978; Ramsay 1980; Yardley 1983, 1986; Rumble 1989). However, the processes involved in fluid infiltration in domains between fractures are rarely well established. Reaction products which are concentrated at grain margins give an indication that diffusion of elements along grain boundaries may be important, and, in addition, linear arrays of fluid inclusions provide evidence of intragrain-scale microcracking. Despite these common observations, the relative importance of grain-boundary processes and microcracking at different metamorphic grades is not well characterized.

A transmission electron microscope (TEM) study by White & White (1981) established that the grain boundaries of metamorphic rocks comprise a number of small (nanometre to micrometre scale) voids (or ‘bubbles’), and that at grain triple-junctions larger ‘tubules’ are present. White & White (1981) also noted a 10–30 nm zone of preferential electron beam damage at certain grain boundaries. They considered this to indicate the presence of a thin film of fluid, which effectively gave complete fluid connectivity along the grain boundary region. By contrast, Etheridge *et al.* (1983) have suggested that the cohesive strength of most grain boundaries would prohibit such areas being permanently occupied by a continuous fluid film. They argue that grain boundary regions are much tighter structures,

and that features such as the zone of preferential electron beam damage described by White & White (1981) may relate to post-metamorphic (e.g. weathering) processes.

Etheridge *et al.* (1983) developed a metamorphic porosity model comprising the grain boundary ‘bubbles’ and ‘tubules’ of White & White (1981), but also incorporating tensile cracks. At low pressure conditions, variations in the local stress state within a polycrystalline aggregate are likely to initiate transient microcracking and grain-boundary dilatancy. This will promote enhanced porosity, permeability and grain-scale fluid infiltration. The extent to which retrogression occurs will depend on the degree of connectivity of the dilatant cracks and grain boundaries, and whether, for particular P–T–X conditions, the infiltrating fluid is at equilibrium (or not) with the host being infiltrated.

An important aspect of the Etheridge *et al.* (1983) model was the recognition that the geometrical arrangement of the grain aggregate and the crystallographic and mechanical properties of individual minerals greatly influence which boundaries dilate (grain boundary tensile cracks, C_b), and which grains develop intragrain tensile cracks (C_g). Etheridge *et al.* (1983) emphasize the importance of deformation in promoting metamorphic porosity due to intergranular stress variations. The opening of intergranular (C_b) and intragranular (C_g) cracks

leads to greatly enhanced transient connected porosity and resultant permeability (also see Bauer & Johnson 1979). Etheridge *et al.* (1983) examined the case of quartz–mica aggregates, with a fluid phase in grain-edge tubules and grain-boundary cavities. They considered a starting situation of $\sigma_3 < P_f < (\sigma_3 + T)$, where σ_3 is the minimum compressive stress, P_f is fluid pressure, and T is the tensile strength of the grain or grain boundary adjacent to a fluid-filled cavity. As deformation proceeds, should P_f of any of the fluid-filled cavities along a grain boundary exceed $\sigma_3 + T$, then a crack will initiate and propagate along the boundary, thus forming a dilatant grain boundary or effectively a grain-boundary microcrack. Material may precipitate along the dilatant grain boundary, but if P_f is maintained at an elevated level then Etheridge *et al.* (1983) argue that a steady-state microcrack porosity will result. Further elevation of differential stress, especially at low temperatures, will initiate intragranular microcracking (C_g) of the harder phases. Emphasizing the importance of microcracking, Etheridge *et al.* (1983) conclude that microcracking rates may influence reaction rates.

Aims

The principal aims of the present study are to examine: (a) the contributions made by microcracking and grain-boundary dilatancy in facilitating fluid access in domains between fractures under low greenschist facies, and sub-greenschist facies conditions; and (b), the extent to which such fluid infiltration promotes retrogression of high-temperature assemblages. After petrographic analysis by transmitted light microscopy and scanning electron microscopy (SEM) back-scattered electron imaging, the nature and extent of grain-boundary reaction products has been established, and the pattern of grain-scale fluid infiltration mapped out.

The first part of the paper examines the role of microcracking with specific reference to a quartz-rich garnet schist from north Norway. The second section focuses on grain-boundary dilatancy with reference to a granoblastic polygonal aggregate of a scapolite gneiss from Scotland. The geometrical arrangement of reaction products at specific grain boundaries is considered in terms of fluid infiltration by grain-boundary dilatancy, and 2D distinct-element modelling is undertaken in an attempt to evaluate the conditions required to produce the observed pattern, and to assess the role of grain-boundary dilation

in promoting fluid access and retrogression of seemingly unfractured rocks.

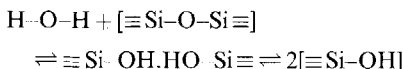
Microcracking

Numerous workers (e.g. Bauer & Johnson 1979; Etheridge *et al.* 1983; Oliver *et al.* 1990; Lespinasse & Cathelineau 1990) have recognized the importance of microcracking in promoting fluid access through rocks. The evidence for microcracking is usually in the form of planar fluid inclusion arrays. These are interpreted as healed microcracks, and have been most frequently studied in quartz-rich assemblages such as vein quartz, granitoid rocks, and low greenschist or sub-greenschist facies arenitic to pelitic rocks (e.g. Tapponier & Brace 1976; Krantz 1983; Lespinasse & Cathelineau 1990; Onasch 1990, 1994; Onasch & Dunne 1993; Craw & Norris 1993). Controls on crack initiation, opening, propagation and orientation in relation to local stresses have been examined by authors such as Tapponier & Brace (1976), Krantz (1983), Atkinson (1984), Reches & Lockner (1994) and Moore & Lockner (1995).

In pure shear, the vast majority of microcracks form perpendicular to the minimum compressive stress axis (σ_3). In other words they are microscopic extensional fractures (Mode I cracks; e.g. Lawn & Wilshaw 1975; Pollard *et al.* 1982; Atkinson 1984; Reches & Lockner 1994), and represent grain-scale brittle failure. Pécher *et al.* (1985) have linked the nature of infiltrating fluid to particular fracturing directions and stress orientations. When examining the microcracking of quartz and feldspar in granite, Lespinasse & Cathelineau (1990) found that the abundance and spatial distribution of cracks in quartz and feldspar was much the same, and that the cleavage of feldspar seemingly did not affect the formation and orientation of microcracks.

Crack initiation occurs at sites of stress concentration, and is influenced by features such as grain size, mineral assemblage, grain-boundary configuration and other pre-existing heterogeneities. A crack will propagate once a critical stress intensity factor (K_c) at the crack tip has been exceeded, but experiment (e.g. Atkinson, 1980, 1984) has shown that significant crack extension can occur substantially below K_c , and this is known as sub-critical crack growth. Atkinson (1984) identified stress corrosion, dissolution, diffusion, ion exchange and microplasticity as possible mechanisms for crack growth. For shallow crustal levels (<15–20 km; low greenschist and sub-greenschist facies), he considered stress corrosion of Si–O–Si bonds involving chemical

action by an agent (e.g. water) at the crack tip to be the most significant mechanism for crack growth in silicates. Atkinson (1984) envisaged strained Si–O bonds at crack tips to be probably more reactive than unstrained bonds, since a strain-induced reduction of atomic orbital overlap would arise, producing a weakened (activated) state. For silicate glasses and quartz rocks in the presence of aqueous fluid, a general expression for weakening has been given (Scholz 1972; Atkinson 1979, 1984) as:



Prior (1993) examined fractured garnets in mylonites of the Alpine Fault, New Zealand. Several types of fracture were recorded, of which Prior's Type 2 fractures, described as mostly 1–100 μm width with a retrogressive fill of Qtz + Chl + Pl \pm Bt \pm Ms \pm Cal (rare) \pm Ep (rare), are most relevant to the present study (see below). Prior (1993) argued that the retrogressive fracture fill precipitated during fracture propagation, and that dissolution was an important crack-tip process. Individual garnets are traversed by many cracks, and all fractures have at least one end terminating at the garnet margin, suggesting that fluid infiltration is an essential part of the fracturing process. More recently, Zhao & Saruwatari (1997) have examined fracturing of garnets in granulite facies quartz-feldspathic mylonites. These tensile microfractures in garnet are developed normal to the mylonitic foliation, and lack retrogressive fill. They are interpreted to have developed at $T > 300^\circ\text{C}$ ($< 15\text{ km}$ depth for a thermal gradient of 20°C km^{-1}), and to form as a result of stress release (horizontal extension) during exhumation and cooling. Such microfracturing, whilst also present in quartz and feldspar (fig. 3d of Zhao & Saruwatari, 1997) is most extensively developed in garnet, since garnet is a harder (more brittle) phase than quartz and feldspar at the conditions under consideration. Zhao & Saruwatari (1997) also found that larger garnet grains and those with greater aspect ratio were more heavily fractured. They recorded almost complete absence of fracturing in grains $< 200\text{ }\mu\text{m}$ diameter and with aspect ratio less than 2. So during exhumation of quartz-rich garnet-bearing rocks it is expected that microfracturing of garnet should initiate at low greenschist facies conditions, whereas microcracking of quartz should not normally develop until lower temperature ($< 300^\circ\text{C}$) sub-greenschist facies conditions. This means that should a fluid infiltrate at the time of quartz microcracking, then assuming temperatures are

high enough for chlorite development it is highly likely that the heavily fractured garnets will become retrogressed.

Example of the role of microcracking

A sample (324/81) from near the Grønfjellet thrust, north Norway (Fig. 1) has been chosen for detailed examination since it shows clear evidence of the role of microcracking during low greenschist facies retrogressive fluid infiltration. Polydeformed metamorphic nappes of Troms (Norway) were emplaced southeastwards during the Scandian (430–370 Ma) phase of the Caledonian Orogeny, to produce a broadly inverted metamorphic sequence (Barker 1986, 1989; Anderson *et al.* 1992). The sequence comprises greenschist and sub-greenschist facies nappes at the base of the pile and mid- to upper amphibolite facies (Ky–Sil) nappes at the top. At a late stage in the Caledonian evolution, the amphibolite facies nappes experienced greenschist facies retrogression. This is especially well developed in the vicinity of thrusts such as the Grønfjellet thrust (Fig. 1), and has resulted in localized intense retrogression of garnet and other peak metamorphic porphyroblasts such as kyanite and staurolite (Barker 1986, 1989, 1995a; Bennett & Barker 1992). Fluids associated with the retrogression are generally hypersaline, although some CO_2 -rich inclusions are also recorded (Bennett & Barker 1992; Barker 1995b).

Petrography

Sample 324/81 is a quartz-rich garnet–mica schist with a peak metamorphic assemblage of Qtz (55–60%) + Ms (15–20%) + Bt (10%) + Czo (7%) + Grt (4%) + Pl (1%) + Spn (1%) + opaques (Mag, Ilm 0.5%). Grain size of matrix minerals is chartacteristically 20–400 μm , and up to 1.8 mm for garnet. The size variation for different phases is as follows: Qtz (50–200 μm), Ms (20–400 μm), Bt (20–400 μm), Czo (50–150 μm), Grt (80 μm –1.8 mm), Pl (50–250 μm), Spn (20–100 μm) and opaques (20–100 μm).

Fluid infiltration by a combination of secondary minor brittle fractures (centimetre scale) and microcracks (micrometre scale) was primarily responsible for the heterogeneous sub-greenschist or low greenschist facies retrogression of garnets within the sample. Many garnets (e.g. Fig. 2a) display fractures parallel to the fluid inclusion trails defining healed microcracks in matrix quartz. Indeed, in many cases, fractures in garnet (now filled with retrograde

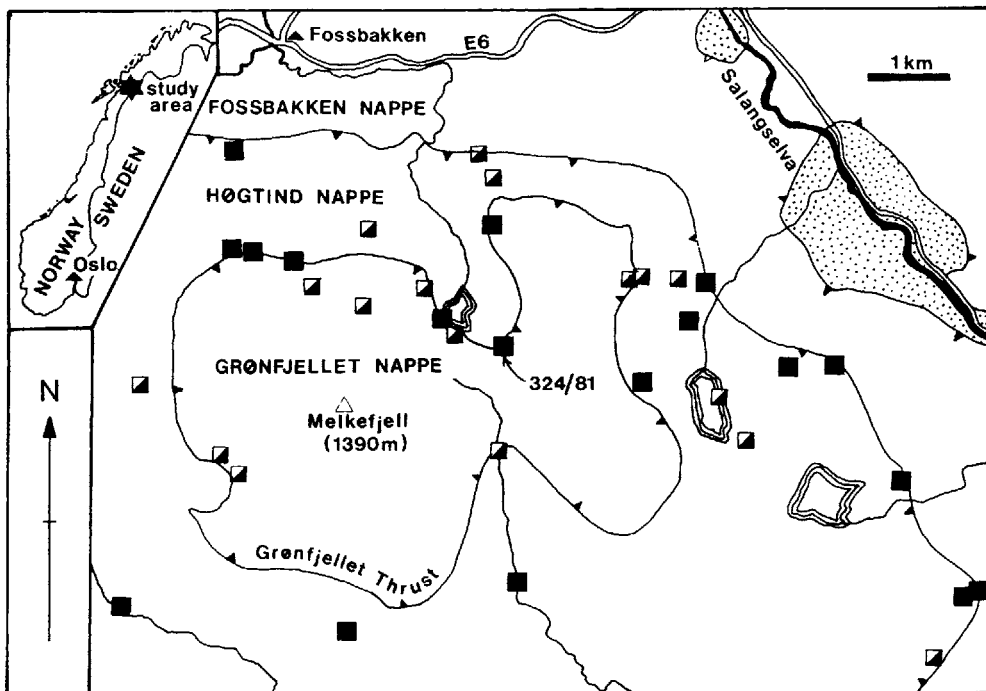


Fig. 1. Location map showing the position of sample 324/81 in relation to the Grønfjellet Thrust, Troms, Norway (modified after Barker, 1986). In the area shown, three Caledonian nappes (Fossbakken, Høgtind, Grønfjellet) have been emplaced over Precambrian basement rocks, which are exposed as 'windows' (stippled) in the Salangselva area. Thrusts = single lines with 'teeth'; roads = parallel lines; rivers = single line (no teeth); lakes = three parallel lines (closed circuit); mountain summit = open triangle; village = filled triangle; schist with totally retrogressed garnets = filled square; partially retrogressed garnets = square with diagonal split.

chlorite) show direct continuation with fluid inclusion trails in matrix quartz. This intimate association shows that the microcracks in quartz were a significant aid to fluid infiltration and greatly contributed to garnet retrogression. This partial and complete pseudomorphic replacement of garnet (Fig. 2a) is best represented by the divariant reaction $\text{Grt} + \text{Bt} + \text{H}_2\text{O} \rightarrow \text{Chl} + \text{Qtz} + \text{Ms}$ (KFMASH system; Spear 1993). Because the almanditic garnets of the sample have a significant grossular component (typically 30% (core), 27% (rim)), and since the infiltrating fluid is a $\text{H}_2\text{O}-\text{CO}_2$ mix, sparse, patchy development of retrograde calcite is seen in the matrix. Therefore, the reaction is more accurately described as $\text{Grt} + \text{Bt} + \text{H}_2\text{O} + \text{CO}_2 \rightarrow \text{Chl} + \text{Qtz} + \text{Ms} + \text{Cal}$ (KFMCAH-HCO system). Calcite probably constitutes 1% (by volume) of the rock, and retrogressive chlorite less than 1%. To maintain mass, the retrograde reaction will involve a volume increase since chlorite is less dense than garnet. However, since garnet constitutes less than 4 vol% of the modal assemblage, any volume increase would

be negligible. Further to this, since a fluid has infiltrated the rock to cause the retrogression (i.e. the system is not isochemical), it is quite likely that mass does not balance, and that some material released from the garnet is lost from the local system.

Fluid inclusions defining healed microcracks have either $\text{H}_2\text{O}-\text{CO}_2$ or hypersaline aqueous chemistries, typical of retrogressive fluids of the region. Quantitative thermometric studies on fluid inclusions in matrix quartz have not been attempted due to their generally small ($<5\text{ }\mu\text{m}$) size. However, studies of comparable fluid inclusions from retrogression-related quartz veins of the area (Bennett 1991; Bennett & Barker 1992; Barker 1995b) have confirmed that the fluids are principally hypersaline aqueous fluids, but with a subsidiary population of CO_2 -rich fluid inclusions.

Figure 3 shows the thin-section scale distribution of partial and complete garnet pseudomorphs in relation to a minor fracture (max. 1 mm displacement) and associated intense microcracking on each side. Whilst most

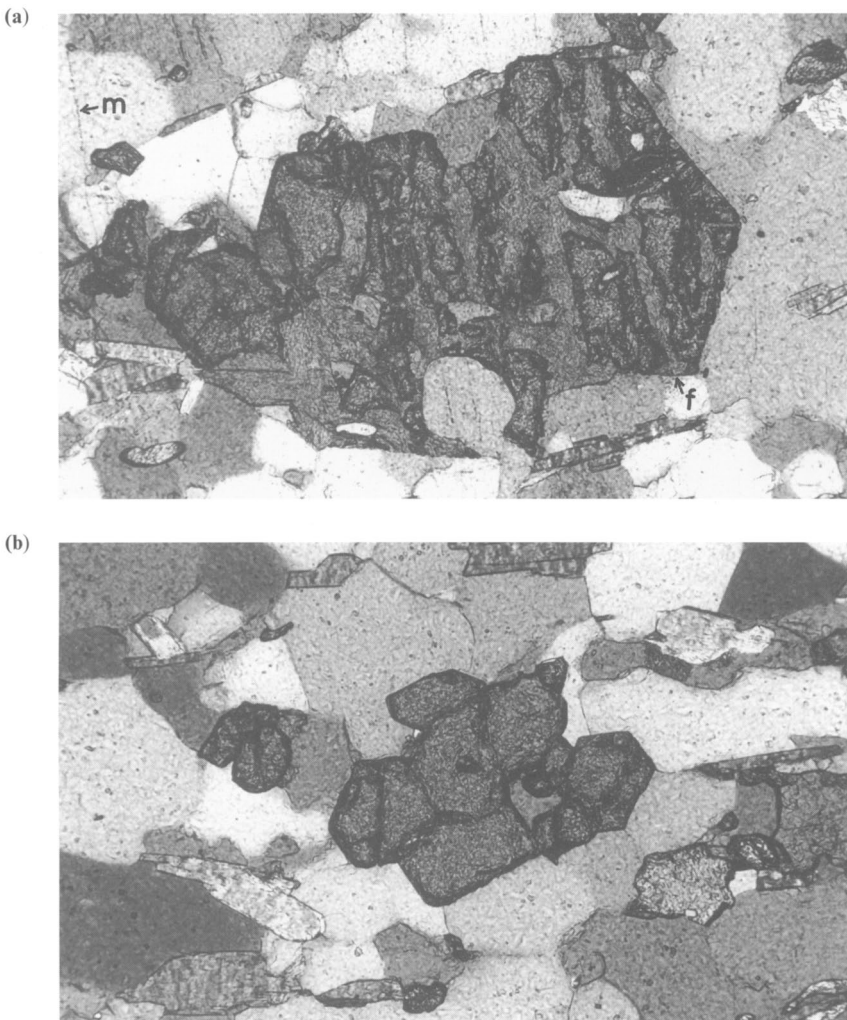


Fig. 2. Almanditic garnets from sample 324/81: (a) 70% retrogressed garnet from within intensely microcracked zone close to minor fracture. Note the faint sub-vertical lines (m) in quartz. These represent healed microcracks defined by fluid inclusion trails (fluid inclusions typically 1–5 µm). Also note the chlorite-filled fractures (f) traversing the garnet. These are sub-parallel to the microcracks and represent fluid pathways through garnet that promoted retrogression; (b) unaltered garnet from outside the microcracked zone. See Fig. 3 for location of garnets photographed. Width of view in both photographs = 1 mm (partial cross-polarized light).

quartz grains in the immediate vicinity of the minor fractures show evidence of microcracking, towards the outer part of the 'zone of microcracking', microcracks are only seen in a few quartz crystals. Usually, it is those crystals that are larger than average, or have a higher aspect ratio in the plane of the schistosity. The microcracks in quartz (Fig. 4) are systematically arranged sub-perpendicular to the schistosity, defined by aligned micas, making an angle of about 55–60° to the principal fracture depicted. This geometric relationship is readily related to

the stresses about the minor fracture in a pure shear regime (Fig. 3). Where the dip of the principal fracture shallows towards the top of the area illustrated, the microcracks also change, so that they form an angle of about 75° to the schistosity, whilst maintaining an angle of about 60° to the fracture. Whilst it is linear trails of fluid inclusions in quartz that give the clearest picture of the nature and extent of microcracking, minor phases such as garnet, sphene and clinozoisite also show well developed microcracking. Unfortunately 324/81 was not an

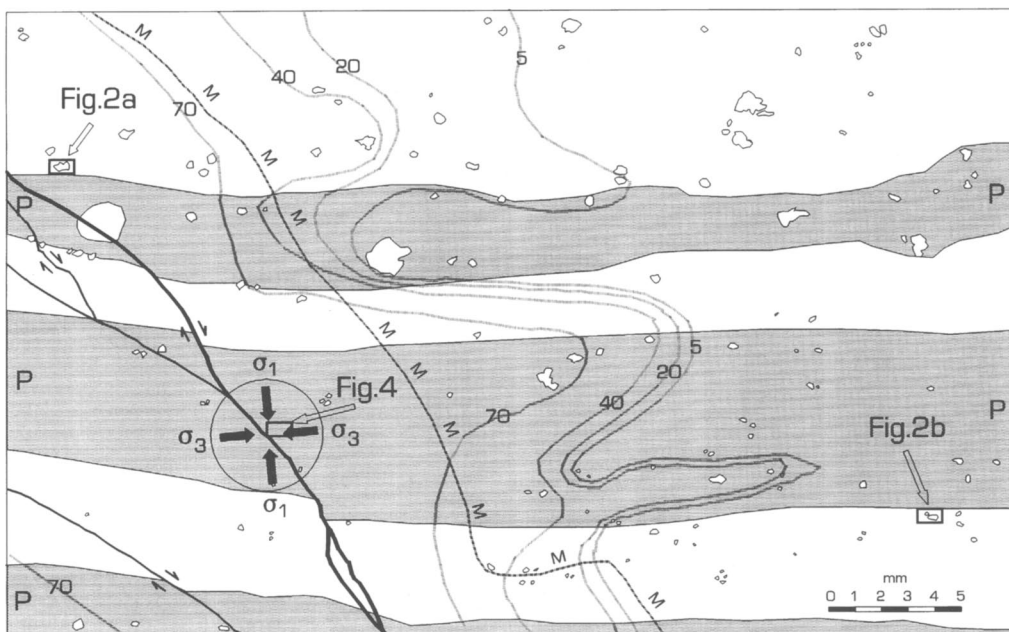


Fig. 3. Detailed line drawing of a thin section showing part of sample 324/81. Although the sample is essentially a quartz-rich garnet–mica schist, there is some compositional layering defined by horizons that are slightly richer in phyllosilicate minerals, principally muscovite. These horizons are shaded, and marked with P at each end. The regional schistosity (S_2), defined by mica and epidote (clinozoisite) in this specimen is sub-parallel to the compositional layering. Minor brittle fracturing associated with late orogenic brittle reactivation of the Grønfjellet Thrust has produced a minor fracture and associated splays in this sample, which are oblique to the compositional layering (left side of drawing). The stress field about this minor extensional fracture is indicated by the labelled arrows. The dashed line labelled with M's marks the outer limit of visible microcracking to the right of the fracture. The entire area to the left of the fracture shows extensive microcracking, no doubt due in part to the series of minor splays off the main fracture (see Fig. 5 for detail).

Garnets range in size up to 2 mm diameter, but many are less than 0.5 mm diameter. All garnets are accurately marked on the line drawing, and appear as numerous irregular to sub-rounded shapes across the field of view. The extent of retrogression of each garnet was carefully recorded, based on visual estimates from the thin section. A clear pattern of retrogression exists, and shows a strong correlation with the intense zone of microcracking and minor fractures. Contour lines (5%, 20%, 40% and 70%) refer to the percentage alteration of individual garnets. Note that garnets in the microcracked zone generally show 70–100% retrogression, whereas garnets in the right-hand third of the diagram (well outside the microcracked zone) are totally unaltered.

oriented sample, so it is not possible to say which is the footwall and hanging wall side of the fracture illustrated. To the left of the fracture (as illustrated) intense microcracking of quartz (15–50 microcracks/mm) extends at least 12 mm perpendicular from the main fracture (Fig. 5). By contrast, on the right-hand side, such microcracking (Figs 4, 5) extends only 2–3 mm, then diminishes rapidly, and is entirely absent when >5 –6 mm from the fracture. This asymmetrical pattern of microcracking in relation to the minor fracture has much in common with that expected in association with Mode II fractures (i.e. fractures with in-plane shear). Lockner *et al.* (1991) and Reches & Lockner (1994) have shown by modelling and experiment that as a

fault propagates, the ‘damage zone’ defined by microcracks is much more extensively developed on one side of the fault than the other, and can be used to determine the direction of fracture propagation. Experiment G3 of Lockner *et al.* (1991) on a sample of Westerly Granite shows this feature particularly well (also see fig. 14 of Reches & Lockner 1994). Indeed, the asymmetrical nature of microcracking and even the width of the microcracking zone each side of the fracture has much in common with that seen in sample 324/81 of this study.

Almanditic garnets in the heavily microcracked zone of sample 324/81 are 70–100% retrogressed to chlorite (Fig. 2a), according to the divariant reaction described above. Even

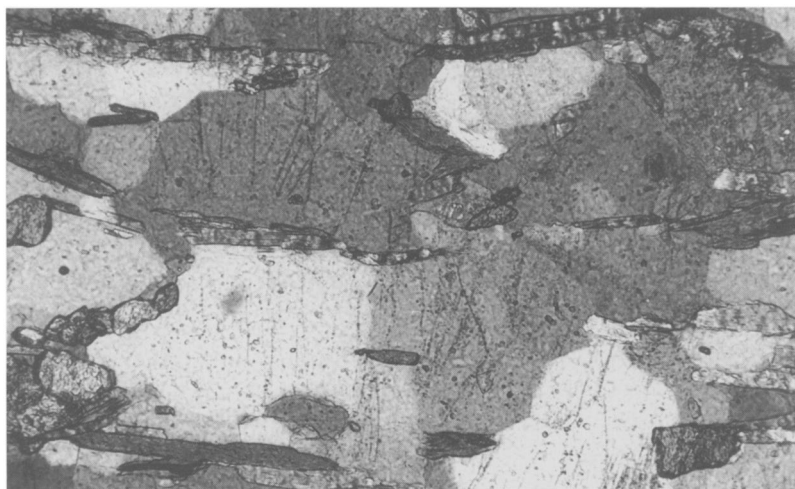


Fig. 4. Detail of microcracking within quartz grains in the most intensely microcracked zone (see Fig. 3 for photograph location). Note that the microcracks (seen as faint vertical lines defined by fluid inclusion trails) are approximately perpendicular to the regional (S_2) schistosity defined by micas aligned 'sub-horizontal' across the field of view. Field of view (width) = 1 mm (partial cross-polarized light).

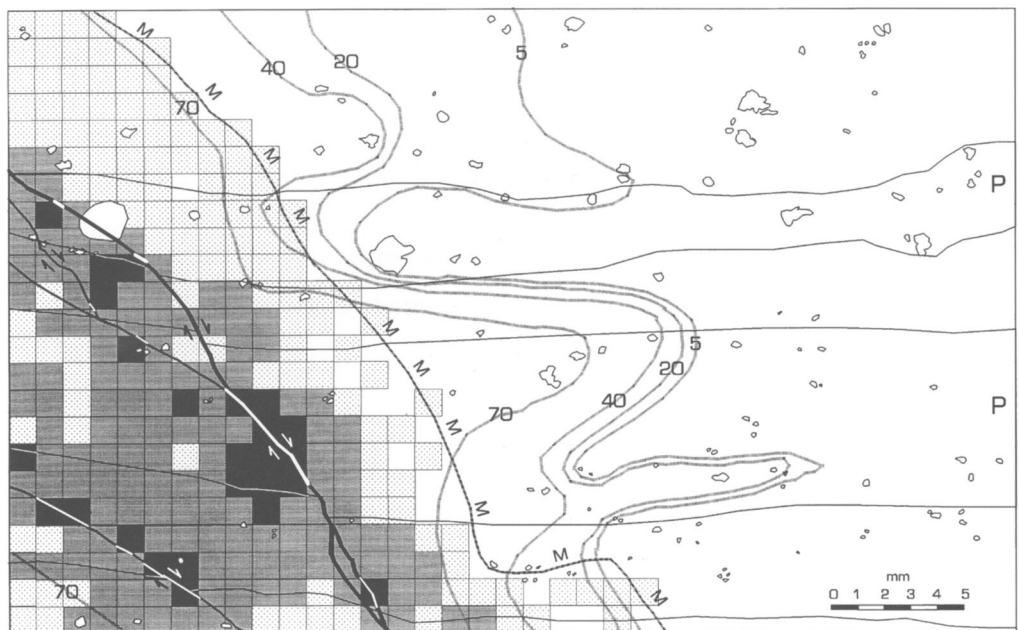


Fig. 5. Map of microcrack densities (324/81) for the area shown in Fig. 3. The area was sub-divided into a $1\text{ mm} \times 1\text{ mm}$ grid, and for each square the number of microcracks in quartz along a horizontal traverse was recorded. There are no microcracks to the right of the gridded area, so although this part of the sample was examined in the same detail, for clarity the grid has been omitted. The grey-scale shading of individual squares reflects the density of microcracking: white = 0 microcracks/mm (i.e. everything to the right of the gridded area, and a few squares in the outer part of the gridded area); light stipple = 1–14 microcracks/mm; mid-grey = 15–29 microcracks/mm; black = 30–50 microcracks/mm. Note that the outermost squares of the gridded area generally have just 1–2 microcracks/mm. For clarity the phyllosilicate-rich layers have not been shaded in this diagram, but in all other respects, the symbols, contour lines and annotations are the same as in Fig. 3.

when microcracking in quartz diminishes to <5 microcracks/mm, partial pseudomorphs with 50–70% garnet retrogression are typical. Biotite is likely to have experienced a decrease in Mg/Fe ratio as the divariant reaction progressed, whilst plagioclase, although not directly involved in the garnet retrogression, is likely to have become more sodic in composition as it equilibrated from low amphibolite facies to low greenschist facies conditions. Detailed studies of changing mineral chemistry during the reaction are a part of ongoing research.

In the first 1–3 mm beyond the limit of visible microcracking (Fig. 3) many garnets show >40% alteration, and up to 10 mm beyond the limit of microcracking there is a highly patchy distribution of garnets showing 0–50% retrogression. At distances greater than 10 mm from the limit of microcracking (>16 mm from the fracture) all garnets are entirely unaltered (Fig. 2b).

The fact that significant garnet retrogression occurred outside the 'zone of microcracking' indicates that microcracking was not the only process that facilitated fluid access. Quartz infill of microfractured sphene, clinozoisite and, rarely, garnet suggests that localized pressure solution occurred, and thus grain-boundary diffusion may have played a role in the transfer of material and retrogression of garnet. Even in the 'zone of microcracking' multiple processes are likely to have operated. Nevertheless, there is a good correlation between the 'zone of microcracking' and the area of most extensive garnet retrogression. This suggests that grain-scale microcracking enhanced the effective permeability, promoted fluid ingress, and thus made a significant contribution to garnet retrogression.

Grain-boundary dilatancy (see below), combined with permeability differences between layers, may have contributed to enhanced fluid access and the heterogeneous pattern of retrogression outside the 'zone of microcracking'. However, there is no obvious correlation between extent of fluid penetration within the P-layers (phyllosilicate-rich; Qtz (50–55%), Ms + Bt (32–37%)) or the Q-layers (quartz-rich; Qtz (65%), Ms + Bt (20–23%)), since each horizon type records both reduced and enhanced fluid penetration. A further complication in the pattern of alteration could be the 3D distribution of any additional minor fractures. However, serial sections do not reveal fractures other than the ones illustrated.

It is rare to preserve such detailed evidence of retrogression due to fluid infiltration by microcracking, because both dynamic and static recrystallization of quartz usually destroys much of the evidence. Uniquely preserved are the

precise fluid pathways (healed microcracks) into and out of retrogressed garnets. Microfractures traversing garnets pass directly into surrounding quartz and are represented by healed microcracks defined by fluid inclusion trails. The fluids involved are predominantly hypersaline aqueous fluids (30–35 wt% NaCl equiv.), and are interpreted as residual fluid after the phyllosilicate-forming hydration reactions have proceeded (Bennett 1991; Bennett & Barker 1992; Barker 1995b). Utilizing chlorite geothermometry (calibration of Cathelineau 1988) and fluid inclusion microthermometry (quartz veins), Bennett (1991) and Bennett & Barker (1992) have estimated the conditions of retrogression for rocks in the near vicinity of sample 324/81 as $T = 330\text{--}370^\circ\text{C}$ / $P = 1.0\text{--}3.0$ kbar. Such temperatures are not entirely compatible with the observation of extensive microcracking in quartz, since such brittle behaviour of quartz and quartz rocks is usually confined to $T < 300^\circ\text{C}$ at crustal strain rates of 10^{-12} to 10^{-14} s^{-1} and a typical geothermal gradient of say 30°C km^{-1} (e.g. Sibson 1983). At greenschist facies conditions of $350\text{--}400^\circ\text{C}$, quartz deforms largely by crystal-plastic process; specifically, dislocation glide and creep become important, by basal slip in the $(c)\langle a \rangle$ direction to give undulose extinction. At such temperatures quartz is not expected to show extensive intragranular microcracking. In an attempt to resolve this apparent incompatibility between the conditions at which extensive microcracking in quartz is expected, and the temperatures of retrogression deduced by chlorite geothermometry for nearby samples, a small population of chlorites from sample 324/81 were analysed using a JEOL 6400 SEM with EDS attachment. Chlorite geothermometry (after Cathelineau 1988) based on analyses of ten individual chlorites from this rock gave temperature estimates ranging from 283 to 338°C , with a mean of 313°C . These lower temperature estimates for the conditions of garnet retrogression in this specific sample are consistent with the onset of brittle behaviour of quartz (namely microcracking) being important in promoting fluid infiltration. Since quartz grain size in 324/81 is $50\text{--}200\text{ }\mu\text{m}$, the upper limit for brittle fracturing could perhaps be as high as 325°C , as illustrated by Sibson (1983). Considering the various lines of evidence and available data, it seems reasonable to conclude that for the sample in question, microcracking, fluid infiltration and resultant retrogression occurred at approximately $T = 300\text{--}325^\circ\text{C}$, and probably at a depth not exceeding $10\text{--}15$ km. These new temperature estimates suggest that garnet retrogression to chlorite in the vicinity of the Grønfjellet Thrust

occurred over a much broader range of temperature conditions than had previously been thought.

This study suggests that in the more brittle sub-greenschist to low greenschist facies conditions of the upper crust, connected networks of fractures and microcracks can play a vital role in grain-scale fluid infiltration and resultant retrograde metamorphism. Indeed, for the sample studied, fluid infiltration by microcracking extended several millimetres away from the nearest visible fracture, to cause extensive garnet retrogression. At higher temperatures of the mid- and lower crust, linear fluid inclusion trails are uncommon and suggest that microcracking is unimportant under such conditions, or that the evidence has been lost due to extensive annealing and recrystallization. For most rock types at amphibolite facies (c. 530–680°C), grain-boundary and intracrystalline diffusive processes assume greater importance for facilitating ionic transfer and reaction progress (e.g. Yardley 1977; Joesten 1983; Walther & Wood 1984).

Grain-boundary dilatancy

Previous work on grain boundaries

Grain boundaries have often been identified as areas where fluid inclusions are concentrated (e.g. White & White 1981; Craw & Norris 1993). Because of this, grain boundaries have been interpreted as important pathways for intergranular diffusive mass transfer (e.g. Walther & Orville 1982; Walther & Wood 1984), assisted by the presence of a grain-boundary fluid (e.g. Rutter 1976; White & White 1981; Watson & Brenan 1987). Fluid-absent diffusion along grain boundaries (Coble creep) involves diffusion of vacancies in the crystal lattice. However, this is an inefficient process for the transfer of soluble species at low metamorphic grades (e.g. Chen & Peterson 1981; Joesten 1983; Walther & Wood 1984) since with decreasing temperature, diffusive processes in silicate aggregates become very slow. In contrast, fluid-present diffusive mass-transfer along grain boundaries (pressure solution) operates widely at low greenschist facies and sub-greenschist metamorphic conditions (Rutter 1976, 1983).

Grain-boundary dilatancy (often in conjunction with intragranular microcracking) is an important process that greatly enhances permeability, and thus fluid infiltration and retrograde reactions in domains between fractures (e.g. Etheridge *et al.* 1983; Cox & Etheridge

1989). Grain boundaries are defined on the basis of crystallographic mismatch and misorientation. For different minerals there is clearly crystallographic mismatch where they meet, and where grains of the same mineral are in contact, a grain boundary is defined where $>10^\circ$ crystallographic misorientation exists. In an aggregate of silicate phases, grain boundaries are complex, often highly disordered areas. White & White (1981) reviewed data for grain boundary width (δ) based on diffusion experiments in metals and ceramics (e.g. Gleiter & Chalmers 1972; Mistler & Coble 1974). They concluded that grain boundaries of metals may be as little as two atom spacings (2b) wide, whereas for ceramics values range from 10–30 nm (c. 20–60b) to as much as 1–2 μm (2000–4000b). White & White (1981) emphasize that δ , referred to as grain-boundary width, is more specifically *the width of the zone of enhanced diffusion rates parallel to the grain boundary*. In other words, the zone of lattice mismatch between grains (i.e. the physical width of the grain boundary) is significantly less than the values quoted for δ . Although there is a lack of data for grain-boundary width in natural rocks, TEM evidence suggests that in silicate aggregates the width of grain boundaries is probably on the nanometre scale.

In polygonal grain aggregates, a higher degree of ordering may exist, and the surface energy of grain boundaries may be significantly lower than less ordered aggregates. Although the bonding across grain boundaries between silicate phases may be relatively strong, the grain boundaries within a rock aggregate are generally weaker than the ordered internal structure of individual mineral grains. When a rock is subject to some superimposed stress, the different crystallographic and mechanical properties of individual minerals produce strain rate incompatibilities between adjacent grains and consequent development of intergranular stresses. Some grain boundaries will be subject to compressional stress, whilst others will be under tension. Whether a grain boundary fails or not will depend on the strength of the bonding. The presence of a fluid phase along grain boundaries, whether as isolated 'bubbles' or a continuous film, may contribute significantly to the weakening of a grain boundary, and if fluid pressure (P_f) exceeds $\sigma_3 + T$ (tensile strength), a crack will initiate and propagate along a grain boundary. In effect, this is grain-boundary dilatancy, and will be most likely in those boundaries oriented at a high angle to σ_3 (i.e. under tension), and least likely in those boundaries at a high angle to σ_1 .

Experimentally produced grain-boundary dilatancy

Means (1989) and Ree (1990, 1994) have shown the significance of deformation-induced grain-boundary opening and void development in experiments on octachloropropane (OCP). More recently, Peach & Spiers (1996) have demonstrated the widespread development of intergranular (grain-boundary) microcracking during crystal plastic deformation of synthetic rock-salt. They found that minor bulk rock dilatancy (<0.2 vol%) during plastic deformation of rock-salt produced permeability increases of several orders of magnitude, and concluded that the very small dilatancies recorded in their experiments may be common in natural rock deformation at low effective confining pressures.

The pattern of grain-boundary dilatancy observed in the experimental deformation of OCP and synthetic rock-salt is consistent with behaviour expected for grain-boundary sliding. However, in natural rocks, grain-boundary sliding (i.e. movement in the plane of the grain boundary) is associated with fine-grained aggregates, generally at high temperatures and/or high strains (e.g. Knipe 1989; Walker *et al.* 1990; Gilotti & Hull 1990), so it is not relevant for medium-grained rocks that have experienced low strain at greenschist facies conditions, as in the present study. However, the case described below, and subsequent modelling, will examine transient grain-boundary opening or dilation on the scale of a few micrometres, for an aggregate with grain size 300–700 µm. We argue that such transient *elastic* opening or dilatancy of grain boundaries is feasible at low confining pressure with subtle variations in differential stress and P_f , but difficult to detect in natural rocks because of the lack of any perceptible evidence of deformation once the superimposed stress subsides and the grain boundary relaxes to its residual (nanometre-scale) aperture. With the strong possibility that pressure solution processes have operated either simultaneously or subsequently, the evidence for grain-boundary dilatancy will be further masked.

Grain-boundary dilatancy in natural rocks

Etheridge *et al.* (1983) described grain-boundary dilatancy as a potentially significant process in fluid infiltration at high crustal levels, and Cox & Etheridge (1989) discussed coupled grain-scale dilatancy and mass transfer during deformation at high fluid pressures in a sequence of sub-greenschist/low greenschist silicic metavolcanic

rocks. In particular, they emphasized how grain-boundary dilatancy during regional metamorphism can significantly enhance permeability and that episodic grain-scale dilatancy could have important implications for mass transfer processes during rock deformation. They concluded that grain-scale dilatancy indicates deformation at low differential stress, and low effective stress in the presence of a high-pressure intergranular fluid. In response to transient fluctuations in fluid pressure (P_f), Cox & Etheridge (1989) considered that grain-scale dilatancy driven pumping would have been significant for mass-transfer processes. In their example, openings of 50 µm or more were recorded, and crack-seal development of fibrous minerals in dilatant microcracks was a key feature.

Whilst grain-boundary dilatancy is an attractive (more efficient) mechanism in promoting fluid access at low metamorphic grades compared to passive grain-boundary processes, it is rare to find evidence that it has occurred in natural rocks. Grain-boundary dilatancy on the micrometre scale is likely, but difficult to prove. The presence of fluid inclusions along grain boundaries indicates that fluid was present or moved through the grain boundary region, but does not give evidence for the mechanism involved. Reaction products at grain boundaries can provide some of the best evidence for grain-boundary dilatancy, but could also indicate that pressure solution processes have operated. For grain-boundary dilatancy, it is necessary to demonstrate a systematic arrangement that is not linked to particular mineral–mineral contacts (i.e. mineralogical/chemical control), but shows a spatial relationship that can be interpreted in terms of the stress field, perhaps corroborated by the presence of microcracks. In the example below we believe the criteria necessary to prove grain-boundary dilatancy are satisfied and, as such, this represents one of the few cases, if not the first case, where grain-boundary dilatancy has been identified and documented in some detail as the cause of retrogression at specific grain boundaries.

Example of the role of grain-boundary dilatancy

A sample from the Rodil District, South Harris, Scotland (Fig. 6) provides a good illustration of the role of grain-boundary dilatancy in facilitating fluid access into the rock matrix and promoting grain-boundary retrograde reactions. The Rodil District comprises amphibolite to

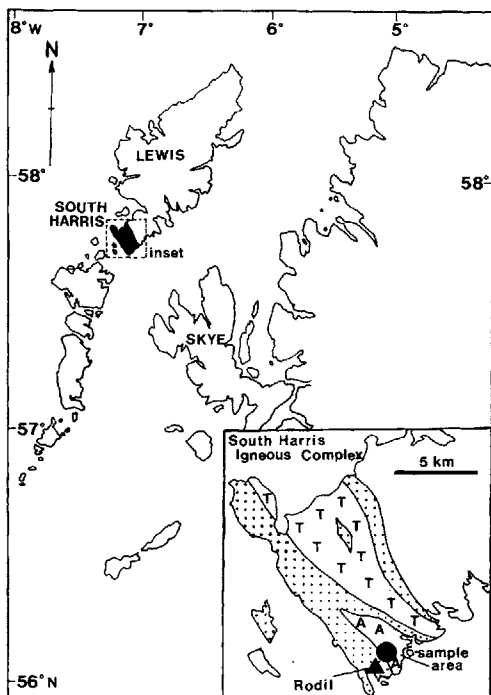


Fig. 6. Map showing the location of the Rodil District, South Harris (simplified after Dearnley, 1963). Key to inset: T = tonalite; A = anorthosite; stipple = metagabbro, amphibolite, pyroxene granulite and paragneiss (psammite, quartzite, pelitic schist, marble). Filled circle = approximate position of sample locality (sample 34079).

granulite facies metasedimentary and metigneous rocks of the Precambrian Lewisian Complex (see Davidson 1943; Dearnley 1963; Fettes & Mendum 1987).

Petrography

The particular sample studied (sample 34079) comes from the anorthositic gneiss unit, within the South Harris Igneous Complex. It displays a medium-grained (typically 0.3–0.7 mm) polygonal aggregate, dominated by anorthitic plagioclase and scapolite, in an assemblage of: Scp (20–50%) + An (40–60%) + Hbl (15–20%) + Ms (2%) + opaques (0.5%) + Kfs (tr.) + Qtz (0.5%). Detailed examination by both transmitted light optical microscopy and SEM (back-scattered electron imaging and X-ray element mapping) coupled with EDS spot analyses has confirmed the chemistry of various phases in

selected areas of the granoblastic polygonal aggregate, as well as the nature of fine-grained reaction products at grain boundaries.

Davidson (1943) described scapolite-bearing assemblages from the area in terms of metasomatic alteration of a primary granulite facies anorthitic gneiss. However, such scapolitic assemblages are also well known from calc-silicate gneisses of granulite facies terrains (e.g. von Knorring & Kennedy 1958; Harley 1989; Yardley *et al.* 1990). Since scapolite of the sample under consideration occurs as polygonal grains (Fig. 7) in equilibrium with anorthitic plagioclase (An₆₅), it seems likely that the scapolite of this rock forms part of the peak metamorphic granulite facies assemblage. Analyses by JEOL 6400 SEM (with EDS attachment) confirmed the scapolites as mizonitic in composition (typically Me_{60–65}). Calc scapolites such as these, with a high meionite (Me) component, are typical of high-grade terrains. For example, Deer *et al.* (1992) describe scapolites (Me_{65–72}) from calc-gneisses and granulite facies rocks of the Scourie Complex, northwest Scotland, which is indeed the same province from which the present sample comes. The scapolites in sample 34079 are unzoned and lack undulose extinction or other obvious signs of deformation.

The scapolite-dominated assemblage (locally scapolite 80–90%) shows variable grain-boundary alteration, with fine-grained aggregates of epidote (±Fe-oxides) along some grain boundaries (1–2%), fine-grained phyllosilicates and quartz along other grain boundaries (1–2%), yet with other boundaries seemingly devoid of alteration products. These fine-grained aggregates form zones typically 5–20 µm wide along grain boundaries. Because of their fine grain size (generally <5 µm) it is difficult to obtain good analyses and establish with any precision the phase proportions in the alteration assemblages. For the phyllosilicate + quartz aggregates, EDX data (normalized to 100%) have yielded mixed analyses approximating to SiO₂ = 60–70 wt%, Al₂O₃ = 24–28 wt%, K₂O = 5.3–6.5 wt%, Na₂O < 0.2 wt%, CaO = 0.25–0.56 wt%, FeO = 2.2–5.0 wt%. This confirms the aggregate as probably a quartz + muscovite (sericite) (±illite?) mix. The small but significant amount of iron suggests that the white mica is phengitic, or else that Fe-oxides are present. Analyses of the products along other grain boundaries indicate the presence of epidote and Fe-oxides, supporting the interpretations made by transmitted light optical microscopy.

It is the alteration products described above that are of special interest in this study. The fact

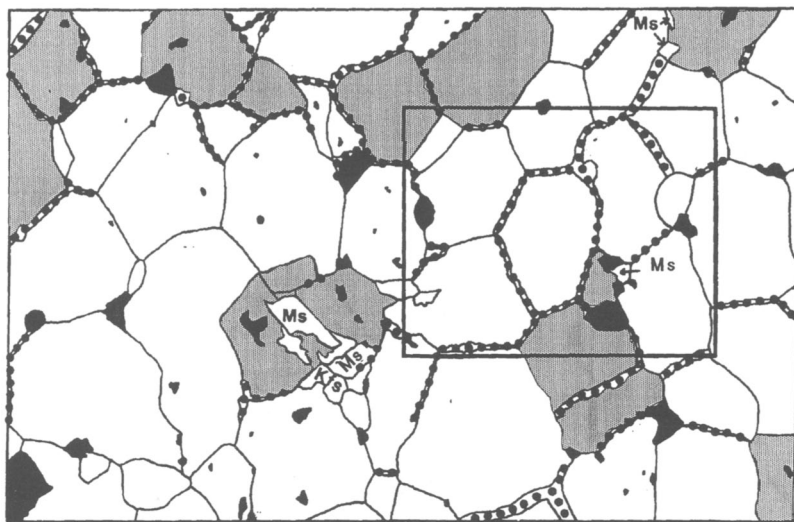


Fig. 7. Line drawing of scapolite-dominated polygonal aggregate (sample 34079) showing inter-relationships between various mineral phases, and distribution of grain-boundary reaction products. White = scapolite; grey = anorthite; black = opaque (Fe-oxide) phases; Ms = muscovite, Kfs = K-feldspar. Black dots = grain-boundary reaction products (Qtz, Ep, Ms(sericite), Fe-oxides), undifferentiated. Field of view (long axis) is 3 mm. Box outlined to right of centre is the area shown in Fig. 8.

that the fine-grained mineral aggregates are concentrated at certain grain boundaries at first impression may be considered to reflect a mineralogical control. That is to say, boundaries between different minerals are no longer in equilibrium and show a fine-grained reaction assemblage at their mutual contacts. However, this does not explain the pattern of reaction

products in this particular example, because most of the mutual contacts are scapolite-scapolite (Fig. 7), and since 'sericite' is a key phase in one type of grain-boundary aggregate, the potassium required to form sericite must have been derived from an external source, or else from dissolution of muscovite or K-feldspar of the primary assemblage. Whatever the case, there must have been diffusive mass-transfer of material. But, was it by localized pressure solution processes, or by a process such as grain-boundary dilatancy? The latter would have enhanced permeability, promoted fluid infiltration and in turn resulted in deposition of fine-grained reaction products in the dilatant grain boundaries.

Figure 8 shows a back-scattered electron image of part of one of the samples, illustrating the uneven distribution of reaction products, and a difference in the orientation of those grain boundaries along which Fe-oxides + epidote (white/light grey) are distributed (approximately N-S in field of view), compared to the boundaries along which sericite + quartz (dark grey) occur (approximately E-W and NE-SW in field of view). Although Fig. 8 only depicts one small portion of the aggregate (to show the fine detail), much the same distribution pattern for reaction products is seen throughout the thin section.

The distinctive difference in the arrangement of reaction products, seemingly uninfluenced by any

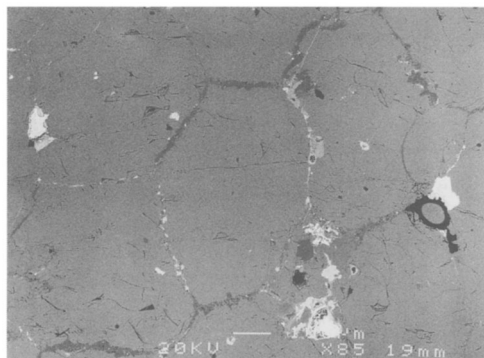


Fig. 8. SEM back-scattered electron image showing distribution of reaction products around an individual scapolite grain within the aggregate illustrated in Fig. 7. Scale (lower centre) = 100 μ m (width of field of view = 1.25 mm). Medium grey = scapolite, dark grey = sericite (+ illite) + quartz, pale grey to white = Fe-oxides + epidote.

mineralogical control, gives a strong indication that geometrically controlled grain-boundary dilatancy may have occurred. The relationship can be interpreted in terms of subtle grain-scale dilatancy at greenschist facies or lower temperature conditions, allowing fluid access into grain boundaries oriented approximately perpendicular to principal extension, whilst tightening (closing) those boundaries perpendicular to principal compression. The differential stress responsible for this grain-boundary dilatancy is considered relatively small since there is almost no evidence of intragrain tensile microcracking or undulose extinction in the plagioclase and scapolite grains of the aggregate. The contrast between the medium to coarse-grained granoblastic polygonal Scp-An aggregate compared with the ultra-fine grain-boundary reaction products serves to emphasize that the polygonal aggregate crystallized at high temperature conditions, whereas the fine-grained reaction products developed at much lower temperature conditions.

Pressure solution can occur over a wide range of temperatures, but for rocks dominated by silicate minerals with a grain size between 0.1 and 1.0 mm, it is a process that commonly operates in the temperature range 200–400°C. It could reasonably be held responsible for the pattern of reaction products and microstructures seen in the sample being considered. The process of pressure solution (e.g. Durney 1972; Rutter 1976, 1983) involves diffusive mass transfer via an intergranular (typically aqueous) fluid. Material at high-stress grain boundaries goes into solution, then moves down a stress-induced chemical potential gradient to be deposited at low-stress sites. The types of features that provide evidence for pressure-solution processes having operated include: (a) truncated surfaces or grain boundaries, indicating sites of dissolution; (b) cleavage surfaces enriched in phyllosilicate phases and fine carbonaceous/opaque material, representing pressure-solution seams; (c) stylolites; (d) fibrous overgrowths of the same or different mineral phase on an existing grain; (e) new optically continuous overgrowths of the same phase on a pre-existing grain. None of these features is observed in the sample under consideration, thus pressure solution is not considered as the main process responsible for the fine-grained reaction products seen at many grain boundaries. In addition to the lack of features normally associated with pressure solution, other points that favour grain-boundary microcracking or dilatancy as an explanation for the fine-grained alteration products at grain boundaries include: (1) evidence of material

deposited at grain boundaries in a wide range of orientations; (2) pronounced angular triple-junctions, rather than rounding/smoothing of selective boundaries (a feature of pressure solution); (3) the presence of sericite-rich aggregates along grain boundaries. These would not be expected for pressure solution in a calc-silicate rock, and suggest infiltration of fluid from an external source.

Grain-scale modelling of rock deformation

Previous research

To date, the focus of grain-scale modelling has been on fabric development, including both lattice preferred orientations and grain-shape fabrics. The Taylor–Bishop–Hill (TBH) model (Taylor 1938; Bishop & Hill 1951) has been an important basis for many subsequent studies, especially in the simulation of quartz polycrystal aggregates (e.g. Lister *et al.* 1978). The TBH model simulates the development of crystallographic preferred orientation (CPO) in a deforming polycrystal aggregate, in which grains deform by dislocation glide. The model has been thoroughly discussed and evaluated by Lister *et al.* (1978) and Lister & Paterson (1979), so rather than consider all aspects of the model, we will simply state the basic assumptions, and consider some of the merits and limitations of the model. The fundamental assumptions of the TBH model are: (1) deformation takes place solely by dislocation glide; (2) deformation occurs uniformly throughout the sample; (3) deformation within each grain occurs by simultaneous operation of several glide systems, each approximated to simple shear parallel to the glide plane; (4) gliding obeys a rigid-plastic flow law; (5) there is no intergranular fluid (i.e. the deforming polycrystal aggregate is dry).

The initial assumption of deformation solely by dislocation glide means that the TBH model cannot be applied to the full range of geological conditions and materials. Even so, dislocation glide operates in many natural polycrystal aggregates over a broad range of conditions (e.g. Rutter 1976, Knipe 1989), so the TBH model offers considerable potential for simulating natural rock deformation. However, the TBH model cannot be used to model deformation of natural polycrystal aggregates where grain-boundary diffusional processes (e.g. Coble creep, pressure solution) are dominant, or where deformation is achieved primarily by movement of grains relative to each other (e.g. cataclastic

flow, grain-boundary sliding). Additionally, the effects of recrystallization are not considered.

The second assumption of the TBH model is that of homogeneous deformation. This is necessary to ensure that all grains remain in contact along the entire length of their boundaries. This assumption has the disadvantage that it is necessary for 'hard' grains to deform as much as 'soft' grains, since different mechanical properties of adjacent grains would produce significant strain gradients at their boundaries. This means that multiphase polycrystal aggregates cannot be suitably modelled (unless the phases have similar mechanical properties), so the TBH model is of primary use for monomineralic polycrystal aggregates (e.g. quartzite). In order for the model to achieve homogeneous strain solely by dislocation glide, the third assumption requires the simultaneous operation of several glide systems. Five linearly independent slip systems are needed (Von Mises 1928), but in any given grain it is likely that deformation would be achieved by the simultaneous operation of fewer glide systems. Lister *et al.* (1978) note from their modelling that the bulk of the strain can usually be achieved by three systems. The fourth assumption, that the material obeys a rigid-plastic flow law, means the material behaves rigidly as deviatoric stress rises, until a critical value of shear stress at which yield occurs. This means that elastic strains are neglected, and glide on a particular plane will only take place once the critical resolved shear stress (τ_c) for yield on that plane has been exceeded (Lister *et al.* 1978). The fifth assumption of fluid-absent deformation simplifies the modelling, but means that the TBH model is not a reliable simulation of deformation in fluid-present natural polycrystal aggregates.

Utilizing the TBH model, Lister *et al.* (1978), Lister & Paterson (1979) and Lister & Hobbs (1980) examined fabric development during ductile deformation, and its application to quartzite. Their simulations, based on a refined TBH model, produced fabrics showing considerable similarity with natural examples. But since the modelling assumes homogeneous deformation by dislocation glide, and the coexistence of five independent slip systems, there are limitations when drawing comparisons with observed fabrics in heterogeneous natural polycrystalline rock aggregates. The self-consistent modelling of Molinari *et al.* (1987) and Wenk *et al.* (1989) is perhaps a better approximation since it requires fewer slip systems, and allows a degree of inhomogeneous deformation. Other studies of note include the geometrical modelling of Etchocopar (1977) and Etchocopar & Vasseur (1987), and the

modelling of Jessell (1988a, b) which permitted grain-boundary migration during fabric development in a recrystallizing aggregate. Finite element modelling was employed by Harren & Asaro (1989) and Tharp (1989) to overcome some of the problems of previous models, but requires specially arranged slip systems not particularly analogous to natural rock aggregates.

More recently, Zhang *et al.* (1994a, b), using the FLAC (Fast Langrangian Analysis of Continua) computer code of Cundall & Board (1988), have modelled grain deformation behaviour and fabric development in simulated polycrystalline aggregates involving a single slip system. Zhang *et al.* (1994a) used the 'ubiquitous joint model' which considers each 'grain' of the polycrystal aggregate as an elastic-perfectly-plastic matrix comprising an infinite number of parallel slip surfaces. Their numerical polycrystalline aggregate comprised 49 hexagonal grains, each with 36 internal elements. In the initial aggregate, the orientation of the slip planes, whilst constant in any given grain (i.e. single slip system), varied between adjacent grains. The models of Zhang *et al.* (1994a, b) allow heterogeneous, essentially ductile deformation, whilst maintaining strain compatibility and overall stress equilibrium (Zhang *et al.* 1994a). Deformation is achieved by slip on the single slip system of a given grain, and by deformation of the grain matrix. The dominant process is a function of the values of critical resolved shear stress (τ_c) for slip planes, and the strength of the grain matrix, according to the yield limit (σ_0). Zhang *et al.* (1994a) set the angle of friction as zero for both the slip planes and the matrix, so τ_c is completely a function of slip plane cohesion (C_s), and the value of σ_0 is entirely controlled by matrix cohesion (C_m). By setting C_m at a value (2×10^{10} Pa) considerably larger than the value (2×10^5 Pa) for C_s , Zhang *et al.* (1994a) ensured that σ_0 would be much larger than τ_c , and thus deformation would be dominated by dislocation glide rather than matrix flow within individual grains. Zhang *et al.* (1994a) showed that the spatial pattern of grain boundaries changed as the individual grains deformed, and that strain heterogeneities developed at both inter- and intragrain scale. Even so, the fact that grain boundaries remain in contact demonstrates that strain compatibility was maintained (Zhang *et al.* 1994a). The values used were not based on any real slip system or material, but were simply chosen to achieve the effect described. However, values for most parameters were chosen to be those of quartz, and thus the modelling results could be considered to approximate to the behaviour of quartz polycrystal

aggregates during low-temperature deformation. It should be noted that quartz has at least three independent slip systems, but at sub-greenschist and low greenschist facies conditions and low differential stress it is only basal slip in the $(c)<a>$ direction that is likely to be important. With this in mind, it is reasonable to approximate quartz to a single slip system under the specific conditions outlined. However, this approximation would be invalid at higher temperatures and higher differential stress.

Modelling with significant intracrystalline ductile deformation is not particularly relevant to the present study, since at the low greenschist and sub-greenschist facies conditions the principal minerals of the aggregate (scapolite and anorthitic plagioclase), if deformed, will have become so by brittle fracturing rather than dislocation glide or other crystal-plastic intracrystalline deformation. We have not documented or accounted for any pressure solution in our modelling, since, for the reasons given above, we do not see any convincing petrographic evidence that pressure solution has played a significant role in the microstructural development of the rock in question. Similarly, we do not consider static or dynamic recrystallization to be important. Undoubtedly, the highly polygonal aggregate has experienced extensive high-temperature recrystallization, but for the conditions of interest, when the fine-grained grain-boundary aggregates formed, the fine grain size ($<5\text{ }\mu\text{m}$) and mineral phases present (e.g. epidote, sericite \pm illite) suggests low temperatures and little or no recrystallization.

2D distinct-element modelling using the Universal Distinct Element Code (UDEC) of Cundall (1971, 1980), and usefully summarized by Zhang & Sanderson (1996a) and Homberg *et al.* (1997).

UDEC modelling (which is two-dimensional) has primarily been used for analysis of fracture patterns, fault behaviour, fluid flow and permeability of large rock masses (e.g. Last & Harper 1990; Peacock & Zhang 1994; Zhang & Sanderson 1996a, b; Homberg *et al.* 1997) and, until now, analysis of grain-scale processes in largely monomineralic aggregates has not been attempted.

In UDEC modelling, the deformation of the fractured rock (or in our case, polycrystal aggregate) involves elastic and plastic deformation of coherent blocks (in our case, grains), coupled with displacement along and across the boundaries. The area under consideration is subdivided into a finite number of blocks, delimited by discontinuities such as faults. In our new application of UDEC modelling to grain-scale analysis, the blocks are individual grains and the discontinuities are grain boundaries. Calculation of incremental normal and shear forces ($\partial F_n, \partial F_s$), given by $\partial F_n = K_n \partial U_n$ and $\partial F_s = K_s \partial U_s$, enables evaluation of normal and shear forces between individual blocks or grains. In these equations, ∂U_n and ∂U_s are relative incremental normal and shear displacements, and K_n and K_s are the normal and shear stiffness for the boundary. The deformability of the interface between blocks (in our case, grain boundary) and the frictional characteristics at such boundaries are represented by a spring-slider system with prescribed force-displacement relations permitting shear and normal forces between blocks to be evaluated (Zhang & Sanderson 1996b).

UDEC modelling, which proceeds by a series of time-step increments, allows simulation of deformation both within grains and at grain boundaries, whilst permitting fluid flow between interfaces. A fully coupled mechanical-hydraulic analysis is performed in which mechanical deformation influences interface connectivity, but is itself influenced by interface hydraulic pressure (e.g. Last & Harper 1990; Zhang & Sanderson 1996b). Within the aggregate of blocks (grains), a pressurized fluid forms an interconnected network at the interfaces. If a fluid pressure differential ΔP_f exists between adjacent domains, flow will take place down the pressure gradient. The flow rate (described more fully by Zhang & Sanderson 1996b) is a function of boundary permeability, hydraulic aperture, ΔP_f and distance. The hydraulic aperture (a),

UDEC modelling

The common feature of the models described above is that they are all 'dry' (i.e. no pore fluid). The other key feature is that they are dominated by intracrystalline 'plastic' deformation, which for the conditions and phases of the present study is inappropriate. Only the modelling of Zhang *et al.* (1994b) permits grain-boundary dilatancy and void development, which is vital for our study.

For the present study we wanted to model grain-boundary dilation of a largely 'monomineralic' (scapolite-dominated) polycrystal aggregate under more brittle conditions, in the presence of a suprathydrostatic fluid to simulate the low greenschist facies, low strain, brittle conditions relevant to the sample. None of the models described in the previous section are appropriate for this, so we have applied

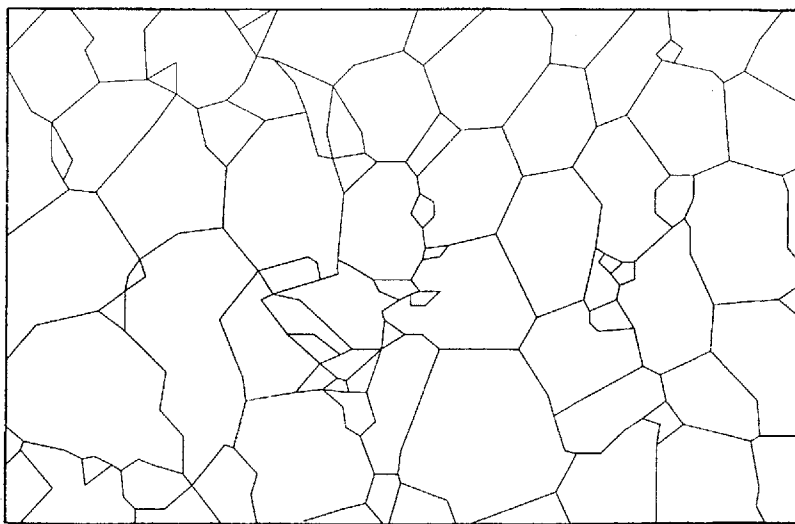


Fig. 9. Digitized polygonal aggregate shown in Fig. 7.

which is of particular importance to the present study, is given by:

$$a = a_0 + u_n$$

in which a_0 is the width of the aperture (in our case, grain boundary aperture) at zero normal effective stress, and u_n is the displacement normal to the boundary, which is a function of normal stress and grain and grain-boundary properties. It is assumed that all interfaces have a residual aperture (a_{res}), below which mechanical closure has no effect on contact permeability (Zhang & Sanderson 1996b). Should P_f exceed the normal stress at a given boundary, the aperture will dilate to a value greater than a_0 , thus a tensile effective stress will cause aperture opening (dilatancy), whilst compressive effective stress will give closure.

To simulate conditions that may account for the geometrical arrangement of reaction products seen in the sample under investigation, the 3 mm section of the polygonal scapolite-plagioclase-dominated aggregate illustrated in Fig. 7 was digitized (Fig. 9), and then UDEC modelling applied. Since the grain-boundary alteration products include fine-grained sericite and epidote, it is likely that these minerals formed under low greenschist or even sub-greenschist facies conditions. At such temperatures, both plagioclase and scapolite are likely to deform by brittle fracturing rather than crystal-plastic processes. If slip does occur it is likely that a single slip system will dominate.

Models

The models we have used set vertical stress (σ_2 in our models) at 300 MPa (3 kbar), a value appropriate for low greenschist facies conditions. Maximum horizontal stress, σ_3 was arbitrarily set at 330 MPa (= 1.1 times vertical stress), and minimum horizontal stress, σ_1 , at 270 MPa (= 0.9 times vertical stress). Therefore mean stress ($P_{\text{confining}}$) = 300 MPa. These values are

Table 1. Material properties used in UDEC modelling

Property	Value	Units
Grain		
Density	2700	kg m^{-3}
Shear modulus	0.88	GPa
Bulk modulus	3.28	GPa
Tensile strength	2.5	MPa
Cohesion	27.2	MPa
Frictional angle	35	degree
Bond		
Shear stiffness	1.0×10^5	GPa m^{-1}
Normal stiffness	2.5×10^5	GPa m^{-1}
Tensile strength	1.5	MPa
Cohesion	2.0	MPa
Frictional angle	30	degree
Aperture at zero stress	100×10^{-9}	m
Residual aperture	10×10^{-9}	m
Fluid		
Density	1000	kg m^{-3}
Viscosity	3.5×10^{-4}	Pas

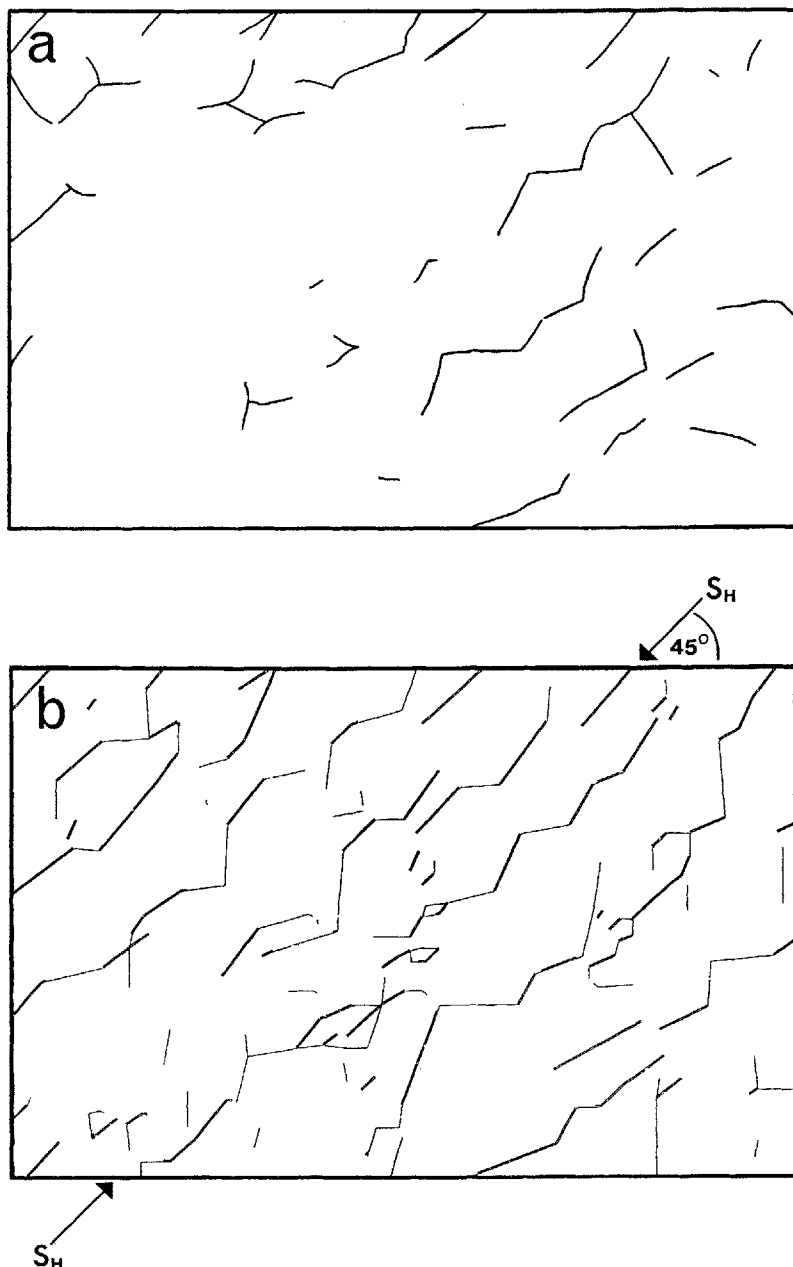


Fig. 10. (a) Line drawing showing distribution of sericite (+ illite) + quartz reaction products based on SEM back-scattered imaging and standard optical microscopy. (b) Result of UDEC modelling run using digitized polygonal aggregate of Fig. 9, and the following specifications: vertical stress (σ_2) = 300 MPa, maximum horizontal stress (σ_1) = 330 MPa; minimum horizontal stress (σ_3) = 270 MPa; pore fluid pressure P_0 = 240 MPa. Based on this, maximum horizontal effective stress $S_H = 90$ MPa (330–240 MPa), minimum horizontal effective stress $S_h = 30$ MPa (270–240 MPa). S_H at 45° as indicated. Material properties used are given in Table 1. UDEC model run to an upper limit of aperture opening = 10 μm . Lower aperture limit shown on plot = 2 μm .

considered realistic estimates of the stress variations commonly encountered by rocks at low greenschist conditions, and give the magnitude of differential stress appropriate for our modelling of grain-boundary dilatancy. Initial pore fluid pressure (P_0) was set at 240 MPa (i.e. $0.8 \times$ mean stress). This represents suprathydrostatic pressure (i.e. not quite lithostatic pressure), and is considered to be a reasonable approximation of low greenschist or sub-greenschist facies conditions (e.g. Sibson 1994). On the basis of these settings, S_H (maximum horizontal effective stress, $= \sigma_1 - P_0$) is 90 MPa (i.e. 330–240 MPa) and S_h (minimum horizontal effective stress, $= \sigma_3 - P_0$) is 30 MPa (i.e. 270–240 MPa), and S_v (vertical effective stress, $= \sigma_2 - P_0$) is 60 MPa (i.e. 300–240 MPa). The full range of material properties for scapolite–anorthite aggregates are not known, but having set appropriate values (Table 1) for grain strength and grain-boundary stiffness, to give a dominance of grain-boundary opening rather than intracrystalline fracturing, the UDEC models were run. The maximum grain-boundary aperture was set at $10 \mu\text{m}$, so that once some grain boundaries had opened by $10 \mu\text{m}$ the run stopped. The lower aperture limit shown on the plots is $2 \mu\text{m}$. To approximate to natural grain boundaries in silicate aggregates, the grain-boundary aperture at zero stress was set at 100 nm, and the residual aperture set at 10 nm.

Results

Figure 10b is a plot for $2\text{--}10 \mu\text{m}$ aperture (grain-boundary) opening produced during one of the runs, using the starting polygonal aggregate based on the digitized field of view of Fig. 9. The conditions that operated during the run are specified in the caption. Accepting the limitations of 2D modelling of a 3D aggregate, comparison of Figs 10a and 10b indicates that there is reasonable agreement between the plot of boundaries that dilated by $2\text{--}10 \mu\text{m}$ under the conditions specified in the model and the map of boundaries showing sericite (+ illite) + Qtz reaction products in the natural sample. By rotating the orientation of the minimum and maximum effective horizontal stresses through 90° (i.e. switching them round), it is not surprising that the grain boundaries previously experiencing minimum extensional stress (effectively compression) are now under conditions of maximum extension, and thus dilate. Consequently the grain boundaries that dilated during this UDEC run (Fig. 11b) are approximately perpendicular to the previous run (Fig. 10b).

There is reasonable agreement with the pattern of epidote and Fe-oxide reaction products in the natural sample (Fig. 11a), but more boundaries are predicted to open than the number of boundaries showing reaction products. We interpret the cause of the reaction products in two distinct orientations to be the result of two separate events of fluid infiltration and alteration due to grain-boundary dilatancy, whilst at low greenschist or sub-greenschist facies conditions. The different geometrical arrangement of alteration products we consider largely to reflect the orientation of maximum and minimum effective stresses at the time of a particular event. In this particular case, the pattern of reaction products would suggest that the maximum and minimum effective stresses switched through 90° from one event to the next. It has not proved possible to establish the order of the two events.

Discussion

The results from these studies may not directly equate to the behaviour of the scapolite–anorthite aggregate under consideration, since not all of the material properties are known, and estimates have been made. A further limitation is that UDEC models are 2D, whereas the material being studied is a slice through a 3D polygonal aggregate. Undoubtedly, the boundaries of any polygonal aggregate will cut the plane of the section at a wide range of angles, but of necessity the 2D UDEC model assumes all boundaries to be vertical. Clearly the nature of boundaries in 3D will be important, but the point of our analysis is to show that, in principle, the pattern of grain-boundary dilatancy in a polycrystal aggregate under an imposed differential stress, and given P_f , can give a reasonable indication of the pattern of grain-boundary opening and connectivity according to the orientation of maximum and minimum horizontal stresses. Despite the limitations and assumptions made, this pilot study has given promising results to suggest that UDEC modelling of grain-boundary dilatancy and fluid infiltration is feasible, and can lead to an enhanced understanding of subtle stress-induced fluid infiltration, transient permeability enhancement, and resultant retrograde reaction processes that may operate in natural rocks at greenschist or sub-greenschist facies conditions. We realize that at present there are significant limitations to the modelling we have undertaken, but with increased knowledge of the input parameters, especially the material and grain-boundary properties, we believe that future modelling of this

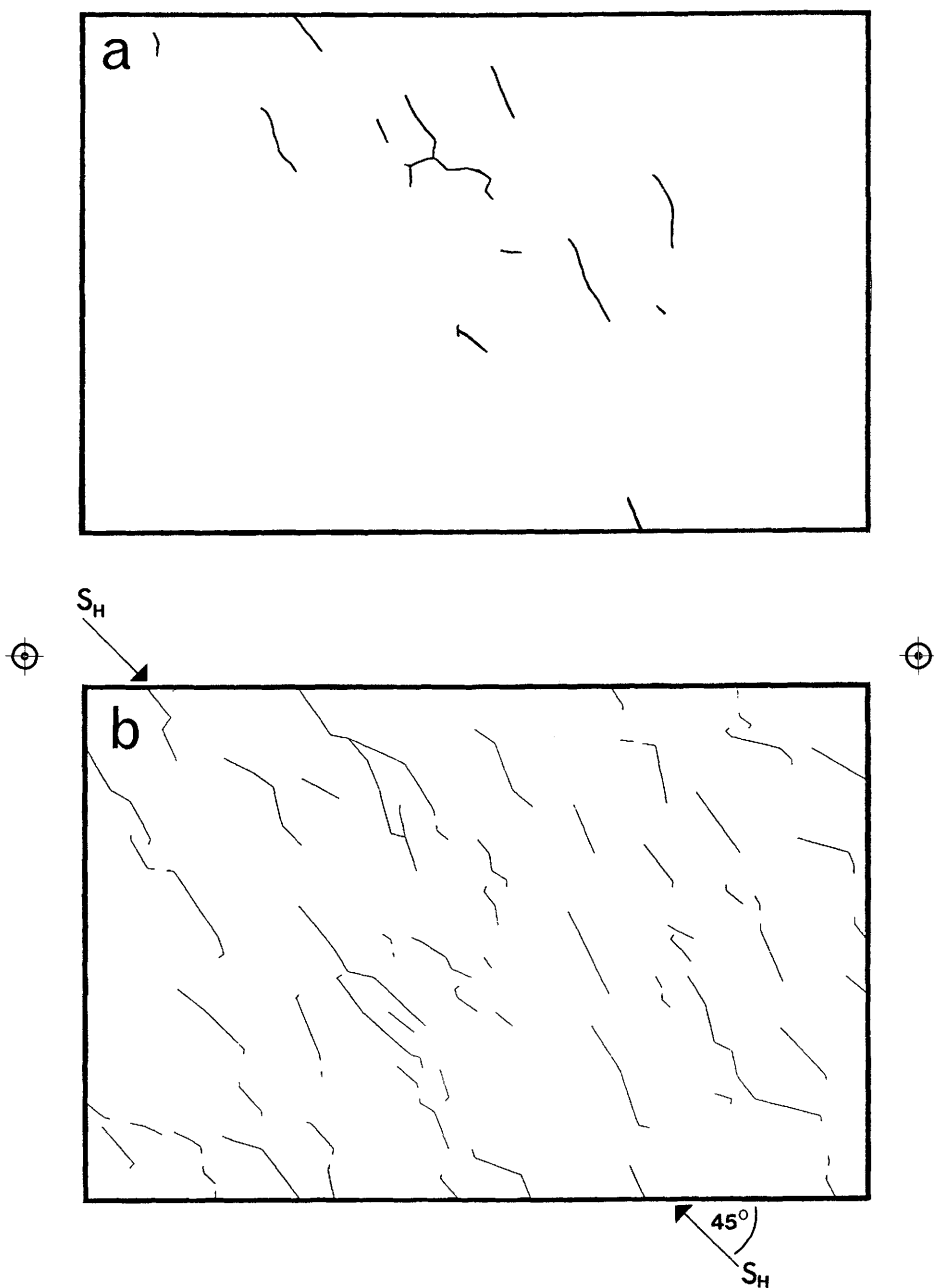


Fig. 11. (a) Line drawing showing distribution of epidote and Fe-oxide reaction products based on SEM back-scattered imaging and standard optical microscopy. (b) Result of UDEC modelling run using digitized polygonal aggregate of Fig. 9. All specifications are the same as given for Fig. 10b run, except that S_H and S_h have been swapped around so that aperture opening develops at approximately 90° to that of the previous run.

type can make a major contribution to the understanding of grain-scale fluid infiltration and retrogression at low P-T conditions.

Conclusions

This study has shown that both microcracking and grain-boundary dilatancy can be crucial processes in promoting fluid access into seemingly unfractured domains of metamorphic rocks, and consequently promoting retrograde alteration of higher P-T mineral assemblages. This work has also emphasized the considerable potential offered by UDEC modelling for understanding how subtle differences in magnitude and orientation of applied stresses can have an important influence on microscale grain-boundary dilatancy during metamorphism at greenschist facies and sub-greenschist facies conditions. The connectivity of dilatant grain boundaries can greatly enhance and control the pattern of grain-scale fluid infiltration in domains between fractures and thus control the pattern of retrograde reactions and the spatial distribution of reaction products.

The sample from South Harris is from the departmental teaching collection. The precise location and original collector are not known. We would like to thank D. Sanderson, P. Treloar and T. Fliervoet for their thorough and incisive reviews of an earlier draft of this paper. Their suggestions have led to significant improvements in the manuscript. Correspondence to A. J. Barker (email: ajb1@soc.soton.ac.uk).

References

- ANDERSON, M. W., BARKER, A. J., BENNETT, D. G. & DALLMEYER, R. D. 1992. A tectonic model for Scandian terrane accretion in the northern Scandinavian Caledonides. *Journal of the Geological Society*, **149**, 727-741.
- ATKINSON, B. K. 1979. A fracture mechanics study of subcritical tensile cracking of quartz in wet environments. *Pure and Applied Geophysics*, **117**, 1011-1024.
- 1980. Stress corrosion and the rate-dependent tensile failure of a fine-grained quartz rock. *Tectonophysics*, **65**, 281-290.
- 1984. Sub-critical crack growth in geological materials. *Journal of Geophysical Research*, **89**, 4077-4114.
- BARKER, A. J. 1986. The geology between Salangsålen and Gratangensfjord, Troms, Norway. *Norges geologiske undersøkelse*, **405**, 41-56.
- 1989. Metamorphic evolution of the Caledonian nappes of north central Scandinavia. In: GAYER, R. A. (ed.) *The Caledonide Geology of Scandinavia*. Graham & Trotman, London, 193-204.
- 1995a. Diachronous fluid release and veining associated with out-of-sequence thrusts in the north Scandinavian Caledonides. *Australian Journal of Earth Sciences*, **42**, 311-320.
- 1995b. Post-entrapment modification of fluid inclusions due to overpressure: evidence from natural samples. *Journal of Metamorphic Geology*, **13**, 737-750.
- BAUER, S. J. & JOHNSON, B. 1979. Effects of slow uniform heating on the physical properties of the Westerley and Charcoal granites. *Proceedings of the 20th US Symposium on Rock Mechanics*, 7-15.
- BENNETT, D. G. 1991. *The role of fluids during retrograde metamorphism, associated with thrust zones; the Caledonides of north Norway*. PhD thesis, University of Southampton.
- & BARKER, A. J. 1992. High salinity fluids: the result of retrograde metamorphism in thrust zones. *Geochimica et Cosmochimica Acta*, **56**, 81-95.
- BISHOP, J. F. W. & HILL, R. 1951. A theory of plastic distortion of a polycrystalline aggregate under combined stresses. *Philosophical Magazine*, **42**, 414-427.
- CATHELINEAU, M. 1988. Cation site occupancy in chlorites and illites as a function of temperature. *Clay Minerals*, **23**, 471-485.
- CHEN, W. K. & PETERSON, N. L. 1981. Grain-boundary diffusion of ^{60}Co and ^{51}Cr in NiO. *Journal of the American Ceramic Society*, **63**, 566-570.
- COX, S. F. & ETHERIDGE, M. A. 1989. Coupled grain-scale dilatancy and mass transfer during deformation at high fluid pressures: examples from Mount Lyell, Tasmania. *Journal of Structural Geology*, **11**, 147-162.
- CRAW, D. & NORRIS, R. J. 1993. Grain boundary migration of water and carbon dioxide during uplift of garnet-zone Alpine Schist, New Zealand. *Journal of Metamorphic Geology*, **11**, 371-378.
- CUNDALL, P. A. 1971. A computer model for simulating progressive large scale movements in blocky rock systems. *Proceedings of the Symposium of the International Society of Rock Mechanics, Nancy*, paper II-8.
- 1980. *UDEC, a generalised distinct element program for modelling jointed rock*. US Army European Research Office and Defence Nuclear Agency, Contract Report DAJA 37-39-C-0548.
- & BOARD, M. 1988. A microcomputer program for modelling large-strain plasticity problems. In: SWOBADA, C. (ed.) *Numerical Methods in Geomechanics: Proceedings of the 6th International Conference on Numerical Methods in Geomechanics*. Balkema, Rotterdam, 2101-2108.
- DAVIDSON, C. F. 1943. The Archean rocks of the Rodil district, South Harris, Outer Hebrides. *Transactions of the Royal Society of Edinburgh*, **61**, 71-112.
- DEARNLEY, R. 1963. The Lewisian Complex of South Harris. *Quarterly Journal of the Geological Society of London*, **119**, 243-312.
- DEER, W. A., HOWIE, R. A. & ZUSSMAN, J. 1992. *An Introduction to the Rock-forming Minerals*. Longman, Harlow.

DURNEY, D. W. 1972. Solution-transfer, an important geological deformation mechanism. *Nature*, **235**, 315–317.

ETCHOCOPAR, A. 1977. A plane kinematic model for the progressive deformation in a polycrystalline aggregate. *Tectonophysics*, **39**, 121–139.

— & VASSEUR, G. 1987. A 3-D kinematic model of fabric development in polycrystalline aggregates: Comparisons with experimental and natural examples. *Journal of Structural Geology*, **9**, 705–717.

ETHERIDGE, M. A., WALL, V. J. & VERNON, R. H. 1983. The role of the fluid phase during metamorphism and deformation. *Journal of Metamorphic Geology*, **1**, 205–226.

FETTES, D. J. & MENDUM, J. R. 1987. The evolution of the Lewisian complex in the Outer Hebrides. In: PARK, R. G. & TARNEY, J. (eds) *Evolution of the Lewisian and Comparable Precambrian High Grade Terrains*. Geological Society, Special Publication, **27**, 27–44.

FYFE, W. S., PRICE, N. J. & THOMPSON, A. B. 1978. *Fluids in the Earth's Crust*. Elsevier, Amsterdam.

GILOTTI, J. A. & HULL, J. M. 1990. Phenomenological superplasticity in rocks. In: KNIFE, R. J. & RUTTER, E. H. (eds) *Deformation Mechanisms, Rheology and Tectonics*. Geological Society, Special Publication, **54**, 229–240.

GLEITLER, H. & CHALMERS, B. 1972. High-angle grain boundaries. *Progress in Materials Science*, **16**, 1–272.

HARLEY, S. L. 1989. The origin of granulites: a metamorphic perspective. *Geological Magazine*, **126**, 215–247.

HARREN, S. V. & ASARO, R. J. 1989. Nonuniform deformation in polycrystals and aspects of the validity of the Taylor model. *Journal of the Mechanics and Physics of Solids*, **37**, 191–233.

HOMBERG, C., HU, J. C., ANGELIER, J., BERGERAT, F. & LACOMBE, O. 1997. Characterization of stress perturbations near major fault zones: insights from 2-D distinct-element numerical modelling and field studies (Jura mountains). *Journal of Structural Geology*, **19**, 703–718.

JESSELL, M. W. 1988a. Simulation of fabric development in recrystallizing aggregates – I. Description of the model. *Journal of Structural Geology*, **10**, 771–778.

— 1988b. Simulation of fabric development in recrystallizing aggregates – II. Example model runs. *Journal of Structural Geology*, **10**, 779–793.

JOESTEN, R. 1983. Grain growth and grain-boundary diffusion in quartz from the Christmas Mountains (Texas) contact aureole. *American Journal of Science*, **283A** (Orville), 233–254.

KNIFE, R. J. 1989. Deformation mechanisms – recognition from natural tectonites. *Journal of Structural Geology*, **11**, 127–146.

KRANTZ, R. L. 1983. Microcracks in rocks; a review. *Tectonophysics*, **100**, 449–480.

LAST, N. C. & HARPER, T. R. 1990. Response of fractured rock subject to fluid injection. Part I: Development of a numerical model. *Tectonophysics*, **172**, 1–31.

LAWN, B. R. & WILSHAW, T. R. 1975. *Fracture of Brittle Solids*. Cambridge University Press.

LESPINASSE, M. & CATHELINÉAU, M. 1990. Fluid percolations in a fault zone: a study of fluid inclusion planes in the St. Sylvestre granite, northwest Massif Central, France. *Tectonophysics*, **184**, 173–187.

LISTER, G. S. & HOBBS, B. E. 1980. The simulation of fabric development during plastic deformation and its application to quartzite: the influence of deformation history. *Journal of Structural Geology*, **2**, 355–370.

— & PATERSON, M. S. 1979. The simulation of fabric development during plastic deformation and its application to quartzite: Fabric transitions. *Journal of Structural Geology*, **1**, 99–115.

— & HOBBS, B. E. 1978. The simulation of fabric development during plastic deformation and its application to quartzite: the model. *Tectonophysics*, **45**, 107–158.

LOCKNER, D. A., BYERLEE, J. D., KUKSENKO, V., PONOMAREV, A. & SIDRIN, A. 1991. Quasi-static fault growth and shear fracture energy in granite. *Nature*, **350**, 39–42.

MEANS, W. D. 1989. Synkinematic microscopy of transparent polycrystals. *Journal of Structural Geology*, **11**, 163–174.

MISTLER, R. E. & COBLE, R. L. 1974. Grain-boundary diffusion and boundary widths in metals and ceramics. *Journal of Applied Physics*, **45**, 1507–1509.

MOLINARI, A., CANAVA, G. R. & AHZI, S. 1987. A self-consistent approach of the large deformation polycrystal viscoplasticity. *Acta Metallurgica*, **35**, 2983–2994.

MOORE, D. E. & LOCKNER, D. A. 1995. The role of microcracking in shear-fracture propagation in granite. *Journal of Structural Geology*, **17**, 95–114.

OLIVER, N. H. S., VALENTA, R. K. & WALL, V. J. 1990. The effect of heterogeneous stress and strain on metamorphic fluid flow, Mary Kathleen, Australia, and a model for large-scale fluid circulation. *Journal of Metamorphic Geology*, **8**, 311–331.

ONASCH, C. M. 1990. Microfractures and their role in deformation of a quartz arenite from the central Appalachian foreland. *Journal of Structural Geology*, **12**, 883–894.

— 1994. Assessing brittle volume-gain and pressure solution volume-loss processes in quartz arenite. *Journal of Structural Geology*, **16**, 519–530.

— & DUNNE, W. M. 1993. Variation in quartz arenite deformation mechanisms between a roof sequence and duplexes. *Journal of Structural Geology*, **15**, 465–475.

PEACH, C. J. & SPIERS, C. J. 1996. Influence of crystal plastic deformation on dilatancy and permeability development in synthetic salt rock. *Tectonophysics*, **256**, 101–128.

PEACOCK, D. C. P. & ZHANG, X. 1994. Field examples and numerical modelling of oversteps and bends along normal faults in cross-section. *Tectonophysics*, **234**, 147–167.

PÉCHER, A., LESPINASSE, M. & LEROY, J. 1985. Relations between fluid inclusion trails and regional stress field: a tool for fluid chronology – An example of an intragranitic uranium ore deposit (northwest Massif Central, France). *Lithos*, **18**, 229–237.

POLLARD, D. D., SEGALL, P. & DELANEY, P. T. 1982. Formation and interpretation of dilatant echelon cracks. *Bulletin of the Geological Society of America*, **93**, 1291–1303.

PRIOR, D. J. 1993. Sub-critical fracture and associated retrogression of garnet during mylonitic deformation. *Contributions to Mineralogy and Petrology*, **113**, 545–556.

RAMSAY, J. G. 1980. The crack-seal mechanism of rock deformation. *Nature*, **284**, 135–139.

RECHES, Z. & LOCKNER, D. A. 1994. Nucleation and growth of faults in brittle rocks. *Journal of Geophysical Research*, **99**, 18159–18173.

REE, J.-H. 1990. High temperature deformation of octachloropropane: dynamic grain growth and lattice reorientation. In: KNIPE, R. J. & RUTTER, E. H. (eds) *Deformation Mechanisms, Rheology and Tectonics*. Geological Society, Special Publication, **54**, 363–368.

— 1994. Grain boundary sliding and development of grain boundary openings in experimentally deformed octachloropropane. *Journal of Structural Geology*, **16**, 403–418.

RUMBLE, D. (III). 1989. Evidences of fluid flow during regional metamorphism. *European Journal of Mineralogy*, **1**, 731–737.

RUTTER, E. H. 1976. The kinetics of rock deformation by pressure solution. *Philosophical Transactions of the Royal Society of London*, **283A**, 203–219.

— 1983. Pressure solution in nature, theory and experiment. *Journal of the Geological Society of London*, **140**, 725–740.

SCHOLZ, C. H. 1972. Static fatigue of quartz. *Journal of Geophysical Research*, **77**, 2104–2114.

SIBSON, R. H. 1983. Continental fault structure and the shallow earthquake source. *Journal of the Geological Society of London*, **140**, 741–767.

— 1994. Crustal stress, faulting and fluid flow. In: PARRELL, J. (ed.) *Geofluids: Origin, Migration and Evolution of Fluids in Sedimentary Basins*. Geological Society, Special Publication, **78**, 69–84.

SPEAR, F. S. 1993. *Metamorphic phase equilibria and pressure-temperature-time paths*. Mineralogical Society of America Monograph, Washington.

TAPPONIER, P. & BRACE, W. F. 1976. Development of stress-induced microcracks in Westerly granite. *International Journal of Rock Mechanics and Mineral Science*, **13**, 103–112.

TAYLOR, G. I. 1938. Plastic strain in metals. *Journal of the Institute Metals*, **62**, 307–324.

THARP, T. M. 1989. Crystal rotation by mechanical interaction between plastically anisotropic crystals. *Journal of Structural Geology*, **11**, 613–623.

VON KNORRING, O. & KENNEDY, W. Q. 1958. The mineral paragenesis and metamorphic status of garnet-hornblende-pyroxene-scapolite gneiss from Ghana (Gold Coast). *Mineralogical Magazine*, **31**, 846–859.

VON MISES, R. 1928. Mechanik der plastischen Formänderung von Kristallen. *Zeitschrift für angewandte Mathematik und Mechanik*, **8**, 161–184.

WALKER, A. N., RUTTER, E. H. & BRODIE, K. H. 1990. Experimental study of grain-size sensitive flow of synthetic, hot-pressed calcite rock. In: KNIPE, R. J. & RUTTER, E. H. (eds) *Deformation Mechanisms, Rheology and Tectonics*. Geological Society, Special Publication, **54**, 259–284.

WALTHER, J. V. & ORVILLE, P. M. 1982. Volatile production and transport in regional metamorphism. *Contributions to Mineralogy and Petrology*, **79**, 252–257.

— & WOOD, B. J. 1984. Rate and mechanism in prograde metamorphism. *Contributions to Mineralogy and Petrology*, **88**, 246–259.

WATSON, E. B. & BRENNAN, J. M. 1987. Fluids in the lithosphere. I. Experimentally-determined wetting characteristics of CO_2 - H_2O fluids and their implications for fluid transport, host-rock physical properties, and fluid inclusion formation. *Earth and Planetary Science Letters*, **85**, 497–515.

WENK, H.-R., CANOVAR, G., MOLINARI, A. & KOCKS, U. F. 1989. Viscoplastic modelling of texture development in quartzite. *Journal of Geophysical Research*, **94B**, 17895–17906.

WHITE, J. C. & WHITE, S. H. 1981. On the structure of grain boundaries in tectonites. *Tectonophysics*, **78**, 613–628.

YARDLEY, B. W. D. 1977. The nature and significance of the mechanism of sillimanite growth in the Connemara Schists, Ireland. *Contributions to Mineralogy and Petrology*, **65**, 53–58.

— 1983. Quartz veins and devolatilization during metamorphism. *Journal of the Geological Society of London*, **140**, 657–663.

— 1986. Fluid migration and veining in the Connemara schists, Ireland. In: WALTHER, J. V. & WOOD, B. J. (eds) *Fluid-rock Interaction during Metamorphism. Advances in Physical Geochemistry*, **5**. Springer-Verlag, New York, 109–131.

—, MACKENZIE, W. S. & GUILFORD, C. 1990. *Atlas of Metamorphic Rocks and their Textures*. Longman, Harlow.

ZHANG, X. & SANDERSON, D. J. 1996a. Numerical modelling of the effects of fault slip on fluid flow around extensional faults. *Journal of Structural Geology*, **18**, 109–119.

— & — 1996b. Effects of stress on the two-dimensional permeability tensor of natural fracture networks. *Geophysical Journal International*, **125**, 912–924.

ZHANG, Y., HOBBS, B. E. & ORD, A. 1994a. A numerical simulation of fabric development in polycrystalline aggregates with one slip system. *Journal of Structural Geology*, **16**, 1297–1313.

—, — & JESSELL, M. W. 1994b. The effect of grain-boundary sliding on fabric development in polycrystalline aggregates. *Journal of Structural Geology*, **16**, 1315–1325.

ZHAO, S., JI, P. & SARUWATARI, K. 1997. Fracturing of garnet crystals in anisotropic metamorphic rocks during uplift. *Journal of Structural Geology*, **19**, 603–620.

Making movies: phase diagrams changing in pressure, temperature, composition and time

BRENTON WORLEY* & ROGER POWELL

*School of Earth Sciences, The University of Melbourne, Parkville,
Victoria 3052, Australia*

* Present address: *Department of Geology and Geophysics,
University of Adelaide, S.A. 5005, Australia*

Abstract: Quantitative phase diagrams, and in particular phase diagram movies, offer a powerful and versatile forward approach to modelling the P - T - x - t relationships of natural mineral assemblages. Phase diagram movies are ideal for illustrating the continuous way in which mineral compositions and assemblages evolve with changing P - T - x conditions. A feature of the animation process, is that it also enables an extra variable to be represented by the running time of the movie. A methodology for producing quantitative phase diagram movies is illustrated using the example of the AFM compatibility diagram. This approach involves the calculation of phase equilibria at critical values of the animating variable (in this case temperature), with interpolation of the data between these values. Phase equilibria calculations were performed using Thermocalc v2.5, and data interpolation and construction of the individual phase diagrams (or movie frames) was achieved in *Mathematica*® v2.2.2 using purpose-written code. Although the details of the technique, and the code, have been designed for use with this particular application, the approach is quite general.

When performing thermodynamic calculations the first aim of metamorphic petrologists is generally the computation of the peak metamorphic temperature experienced by the rocks of interest. However, this temperature maximum only represents a single point in the P - T - t history experienced by the rocks, and therefore the constraint of this P - T - t path, either qualitatively or quantitatively, is of considerably more interest. Peak metamorphic conditions are traditionally calculated using thermobarometry, either by the use of directly calibrated single-reaction thermometers and barometers (e.g. Ferry & Spear 1978; Ghent & Stout 1981), or internally consistent datasets (Berman 1991; Powell & Holland 1994). Similarly, segments of P - T - t paths have been calculated by thermobarometry of inclusion suites (e.g. St. Onge 1987), and modelling of mineral zonation profiles (e.g. Spear & Selverstone 1983; Young 1989; Spear *et al.* 1990). These techniques are inverse approaches in that observed mineral assemblages and, in particular, measured mineral compositions form the starting point for the calculations. A disadvantage in such an approach is a reliance on the recognition and analysis of equilibrium assemblages, as mineral compositions may fail to equilibrate at the metamorphic peak, and may continue to equilibrate along the retrograde portion of the P - T - t path (e.g. Powell 1985; Fitzsimons & Harley 1994; Pattison and Bégin 1994; Okay 1995). Therefore, although it is usually possible to identify the phases involved

in equilibrium assemblages, determination of the equilibrium compositions of these phases is often impossible.

The interpretation of mineral textures, assemblages and compositions in terms of phase diagrams (e.g. Clarke *et al.* 1989; Connolly *et al.* 1994; Vance & Holland 1993) offers an additional, powerful and versatile forward modelling approach. Early petrogenetic grids were essentially qualitative, constructed from a combination of petrographic observations, compositions of coexisting phases and sub-system experimental results (e.g. Albee 1965; Hess 1969; Harte & Hudson 1979). More recently, the development of internally consistent thermodynamic datasets (Holland & Powell 1985, 1990; Berman 1988) has enabled the calculation of quantitative grids (e.g. Powell & Holland 1990; Xu *et al.* 1994; Worley & Powell 1998) and the forward modelling of P - T - x relationships of natural mineral assemblages (Connolly *et al.* 1994; Vance & Holland 1993).

One of the fundamental difficulties associated with the presentation of phase diagrams has always been the reduction of the effective dimensions of the *total phase diagram* so that it can be illustrated on a two-dimensional piece of paper, or screen. The total phase diagram contains all of the phase assemblage and composition information for a given system. The dimension, or number of axes, of this diagram is related to the size of the system, i.e. the number of components. For a system with n components, there

will be axes for pressure (P), temperature (T) and $n - 1$ compositional (x) terms. There are only $n - 1$ compositional terms as the n th term can always be determined by difference, and hence is not independent. Therefore, the total phase diagram has $2 + (n - 1) = n + 1$, dimensions.

This description is the normal geological one in which the system is considered to be closed, and under constant superimposed P and T . Other descriptions, involving instead enthalpy (instead of T), volume (instead of P), or chemical potential (instead of x), still involve a total phase diagram of $n + 1$ dimensions.

Considering the six-component KFMASH system, its total phase diagram has a dimension of seven. The effective dimension can be made to be two, and AFM compatibility diagrams constructed, by holding P and T constant, and treating muscovite, quartz and H_2O as 'in excess' (Thompson 1957). Although the resulting ternary diagram has three components as its apices, there are only two independent axes, in the same way as the total phase diagram has only $n - 1$ independent x terms. This dimension problem is obviously compounded as the number of components in the model system is increased, for example to more closely approximate natural systems. Therefore, one of the important features of phase diagram movies is that the animation process allows an extra dimension to be represented, i.e. the variable with respect to which the diagrams are animated is portrayed by the running time (t) of the movie.

The choice of what the time (t dimension) of the movie (as well as the two dimensions portrayed in the individual phase diagram frames) will represent, is dependent upon the specific problem of interest. The most obvious choice is to animate with respect to intensive variables, such as P or T , an approach which is applicable to sections (e.g. compatibility diagram movies) and pseudosections (e.g. T - x and P - x movies). It is also possible to portray extensive, or compositional, variables with the

t dimension. For example, pseudosection movies can be constructed where t represents a changing bulk composition (P - T pseudosections) or bulk compositional line (T - x and P - x pseudosections). Another interesting possibility is where t corresponds to the real t dimension, so that, for example, a compatibility diagram movie shows relationships along a chosen P - T - t path to reflect P - T variations during orogenesis.

Phase diagram movies, represent a significant advance in our ability to portray the results of phase equilibria calculations. Such an advance should improve our understanding of quantitative phase equilibria and ultimately our ability to interpret metamorphic reactions and complex reaction textures.

General approach

All of the phase equilibria calculations were performed with THERMOCALC v2.5 (Powell *et al.* 1998) and the 20 April 1996 update of the Holland & Powell dataset (Holland & Powell 1990). When run in phase diagram mode, THERMOCALC produces a large amount of output, including values for P , T and x variables for all of the possible equilibria. Conventional THERMOCALC output includes all of the calculated variables; however, the application can be instructed (by the use of a script; Powell *et al.* 1998) to produce a secondary output file, named say '*th math*', which contains the results of the calculations in an appropriate form to be used in *Mathematica*®. As THERMOCALC does not distinguish between stable and metastable equilibria, it is necessary to edit the output before producing individual phase diagrams and movies.

Generation of a phase diagram movie involves construction of a series of phase diagrams, which form the individual frames of the movie, for a range of values of the variable chosen for animation. An effective movie requires on the order of 10–20 frames per second, so the calculation of

Table 1. Mineral formulae and abbreviations

Mineral	Abb.	Structural formula
staurolite	st	$(Mg,Fe)_4Al_{18}Si_{7.5}O_{48}H_4$
garnet	g	$(Mg,Fe)_3Al_2Si_3O_8$
chlorite	chl	$(Mg,Fe)_4(Mg,Fe,Al)_2Si_2[Al, Si]_2O_{10}(OH)_8$
biotite	bi	$K(Mg,Fe)(Mg,Fe,Al)_2Si_2[Al, Si]_2O_{10}(OH)_8$
muscovite	mu	$K\Box(Mg,Fe,Al)_2Si_2[Al, Si]_2O_{10}(OH)_2$
chloritoid	ctd	$(Mg,Fe)Al_2SiO_5(OH)_2$
aluminosilicate	als	Al_2SiO_5
quartz	q	SiO_2
water	H_2O	H_2O

each frame is impractical. A practical approach is to calculate the necessary equilibria at critical values of the animating variable (the exact choice dependent upon the system and diagram of interest, as well as sophistication of the interpolation technique), and interpolate the data between these points. The approach that we have used here is to perform the data interpolation and construction of the individual phase diagram frames in *Mathematica* v2.2.2 using purpose-written code (see also Powell *et al.* 1998). Initial animation is also undertaken in *Mathematica* with built-in functions. Although various versions of the *Mathematica* code are presented here and in Powell *et al.* (1998), anyone can design code for their own specific purposes, for use in either *Mathematica*, or other suitable software; THERMOCALC for example, can be instructed to produce tab-delimited output.

The general approach, outlined above, is illustrated in the next section with some simple code, specifically designed for constructing compatibility diagram movies. All of the examples have been produced using an Apple Macintosh computer; however, IBM-compatible versions of the critical software (i.e. THERMOCALC and *Mathematica*) are available. The explanations and commands presented here are for Macintosh applications.

The AFM compatibility diagram

It is simplest to illustrate the calculation and construction steps necessary to produce a movie by following a worked example. For this purpose we have chosen the AFM (+ mu + q + H₂O) compatibility diagram in the model KFMASH system, which will be animated with respect to

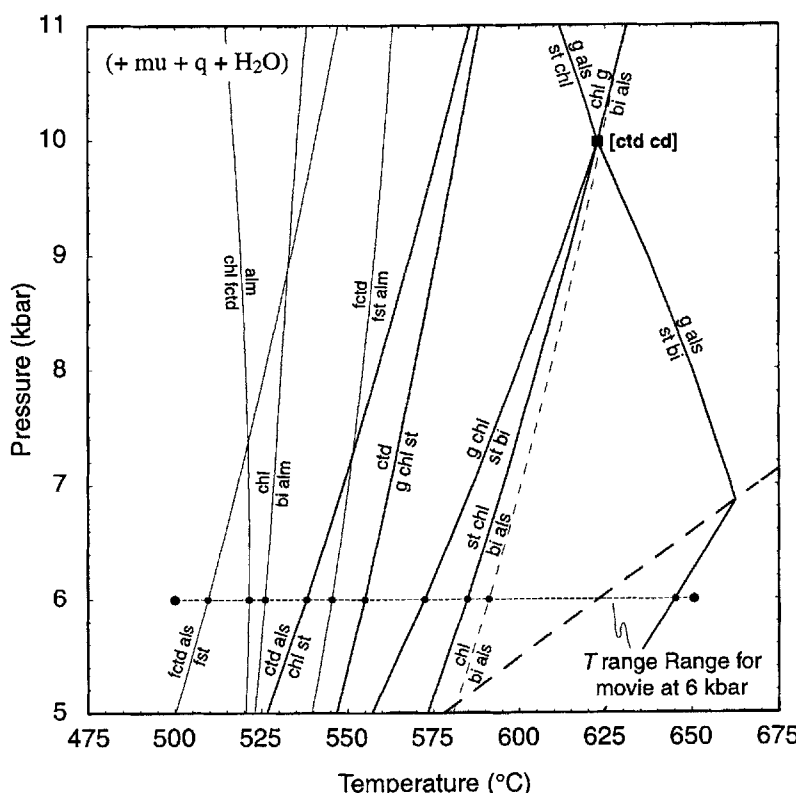


Fig. 1. *P-T* projection for the system KFMASH + mu + q + H₂O. Full-system univariants are represented by heavy solid lines, KFASH sub-system univariants by light solid lines, and KMASH sub-system univariants by dashed lines. The finely dashed horizontal line, at 6 kbar, represents the temperature range over which 'Movie 1', has been calculated. Filled circles on this line are the temperatures at which divariant assemblages were calculated for the construction of the movie.

temperature at constant pressure (mineral abbreviations are given in Table 1). This example was chosen because of its relative simplicity, as well as a widespread familiarity with both the system and the AFM diagram (Thompson 1957, and many papers since). The KFMASH, KFASH and KMASH datafiles used for the calculations are presented in Powell *et al.* (1998).

P-T projection

Before calculating and constructing a movie it is generally helpful firstly to calculate, or have access to a previously calculated, petrogenetic

grid for the P - T range of interest, as this will indicate exactly which equilibria need to be calculated. In this case the P - T projection has been constructed for a P - T window of 475–675°C and 5–11 kbar (Fig. 1). The KFASH and KMASH sub-system information is included in Fig. 1, because the example code requires coordinates for each temperature at which the topology of the diagram changes, i.e. whenever KMASH, KFASH or KFMASH univariant reactions are encountered. The main AFM movie used as an example has been calculated over a temperature range of 500–650°C at $P = 6$ kbar, as indicated by the horizontal dashed line in Fig. 1. Also illustrated along this

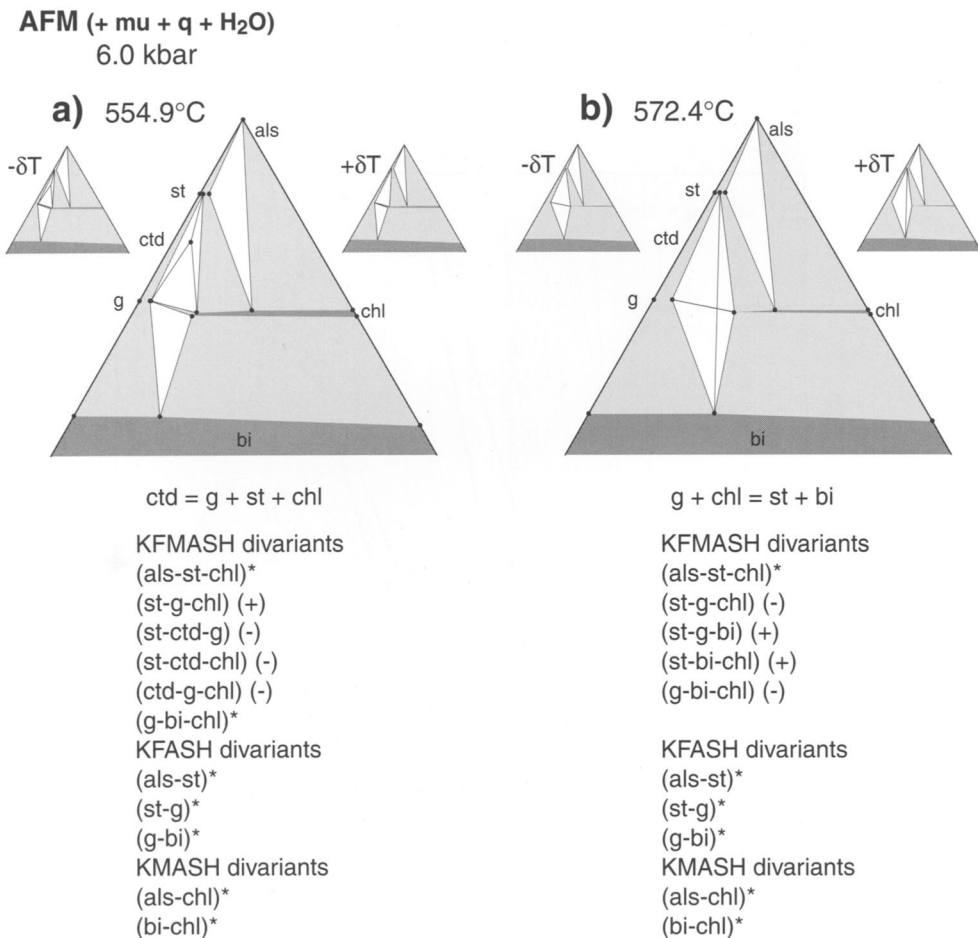


Fig. 2. AFM + mu + q + H₂O compatibility diagrams at (a) 554.9°C and (b) 572.4°C illustrating the divariant equilibria which need to be calculated at two univariant reactions. The inset diagrams drawn at $T_R - \delta T$ and $T_R + \delta T$ show how the stable divariants change as a univariant reaction is crossed. Assemblages which are introduced at the reaction are labelled (+), those which are removed are labelled (-), and unaffected assemblages are denoted by (*).

line (by the filled circles) are all of the temperatures at which divariant equilibria were calculated, where the line intersects the sub- and full-system univariant reactions.

A feature of the grid which should be noted is the discrepancy between the calculated partitioning of Fe and Mg between garnet and staurolite and that generally observed in nature. Although the difference is very small – actually within the uncertainties of the data – the predicted Fe/Mg ratio of garnet is less than that of coexisting staurolite, which is the converse of that observed in the majority of natural assemblages. The main consequence of this reversed partitioning is that the final consumption of staurolite is predicted to occur via the KFASH sub-system reaction, $st = g + als$, rather than the full-system terminal reaction, $st = g + bi + als$. This discrepancy sug-

gests that the thermodynamic descriptions of staurolite and/or garnet are not quite correct. The likely culprit is staurolite (Powell & Holland 1990), but given our relatively limited understanding of staurolite crystal chemistry, the attractiveness and effectiveness otherwise of the simple models used, as well as the natural system observations being in a Fe_2O_3 -bearing system, we feel that, at this stage, it is justifiable to present the results as they are.

Divariant equilibria for AFM (+ mu + q + H_2O) compatibility diagram

At each of the univariant equilibria there is a change in the stable divariant equilibria, the

Table 2. *AFM coordinates for KFMASH, KFASH and KMASH divariants*

(*)-----*)	(*)-----*)
KFMASH	KFMASH
{ {6.000, 554.93},	{ {6.000, 572.42},
{ "st", 0.6923, 0.2959, 0.0118},	{ "st", 0.6923, 0.2882, 0.0195},
{ "g", 0.2500, 0.7086, 0.0414},	{ "ch1", 0.1976, 0.4845, 0.3178},
{ "ch1", 0.1989, 0.5684, 0.2327} },	{ "bi", -0.2216, 0.7670, 0.4547} }
{ { "st", 0.6923, 0.2959, 0.0118},	{ { "st", 0.6923, 0.2882, 0.0195},
{ "ctd", 0.5000, 0.4363, 0.0637},	{ "g", 0.2500, 0.6831, 0.0669},
{ "ch1", 0.1989, 0.5684, 0.2327} },	{ "bi", -0.2216, 0.7670, 0.4547} }
{ { "ctd", 0.5000, 0.4363, 0.0637},	{ { "g", 0.2500, 0.6831, 0.0669},
{ "g", 0.2500, 0.7086, 0.0414},	{ "ch1", 0.1976, 0.4845, 0.3178},
{ "ch1", 0.1989, 0.5684, 0.2327} },	{ "bi", -0.2216, 0.7670, 0.4547} }
{ { "st", 0.6923, 0.2959, 0.0118},	{ { "g", 0.2500, 0.6831, 0.0669},
{ "ctd", 0.5000, 0.4363, 0.0637},	{ "ch1", 0.1976, 0.4845, 0.3178},
{ "g", 0.2500, 0.7086, 0.0414} },	{ "bi", -0.2216, 0.7670, 0.4547} }
{ { "st", 0.6923, 0.2761, 0.0316},	{ { "st", 0.6923, 0.2882, 0.0195},
{ "ch1", 0.2080, 0.3648, 0.4272},	{ "g", 0.2500, 0.6831, 0.0669},
{ "ky", 1.0000, 0, 0} },	{ "ch1", 0.1976, 0.4845, 0.3178} }
{ { "g", 0.2500, 0.7121, 0.0379},	{ { "st", 0.6923, 0.2695, 0.0382},
{ "ch1", 0.1873, 0.5922, 0.2205},	{ "ch1", 0.2050, 0.3343, 0.4607},
{ "bi", -0.2294, 0.9178, 0.3116} },	{ "ky", 1.0000, 0, 0} } }.
(*)-----*)	(*)-----*)
KFASH	KFASH
{ {6.000, 554.93},	{ {6.000, 572.42},
{ "bi", -0.2258, 1.2258},	{ "bi", -0.2217, 1.2217},
{ "alm", 0.2500, 0.7500} },	{ "alm", 0.2500, 0.7500} }},
{ { "fst", 0.6923, 0.3077},	{ { "fst", 0.6923, 0.3077},
{ "alm", 0.2500, 0.7500} },	{ "alm", 0.2500, 0.7500} }},
{ { "fst", 0.6923, 0.3077},	{ { "fst", 0.6923, 0.3077},
{ "ky", 1.0000, 0} } },	{ "ky", 1.0000, 0} } }.
(*)-----*)	(*)-----*)
KMASH	KMASH
{ {6.000, 554.93},	{ {6.000, 572.42},
{ "bi", -0.2705, 1.2705},	{ "bi", -0.2541, 1.2541},
{ "ch1", 0.1798, 0.8202} },	{ "ch1", 0.1907, 0.8093} }},
{ { "ch1", 0.2080, 0.7920},	{ { "ch1", 0.2050, 0.7950},
{ "ky", 1.0000, 0} } },	{ "ky", 1.0000, 0} } }.

reactions, as written, representing the change. For example the reaction $\text{ctd} = \text{g} + \text{st} + \text{chl}$, which occurs at 554.9°C at 6 kbar, results in the three divariant equilibria, (st-ctd-g), (st-ctd-chl) and (ctd-g-chl) being replaced by the single equilibrium (st-g-chl) (Fig. 2a). This is illustrated in the two inset AFM diagrams drawn at $T_R - \delta T$ and $T_R + \delta T$ which show the stable divariant configurations immediately prior to and following the reaction with increasing temperature. Similarly, at the reaction $\text{g} + \text{chl} = \text{st} + \text{bi}$ (Fig. 2b), at 572.4°C at 6 kbar, the (st-g-bi) and (st-bi-chl) equilibria are stabilized at the expense of the (st-g-chl) and (g-bi-chl) equilibria. The relevant THERMOCALC results for these two univariant reactions are given in Table 2. The coordinates for all of the stable divariant equilibria are given, including the incoming (denoted by (+) in Fig. 2), outgoing (-) and unaffected (*) divariants.

In the AFM compatibility diagram, muscovite is the only projecting phase which exhibits solid solution, the range of which is essentially negligible over the P - T range of interest. This contributes to the trivariant-quadravariant boundaries on these diagrams being straight; this simplification is followed in constructing the diagrams and movies. This linearity is in contrast to results in the NCKFMASH system NCFM (+ plagi + bi + mu + q + H_2O) compatibility diagrams, which involve projection from plagioclase and biotite solid solutions (Worley & Powell 1998; Powell *et al.* 1998). A result of this simplification is that it is not necessary to calculate explicitly the trivariant or quadravariant equilibria; instead they can be constructed by simply joining corresponding pairs of phases in the divariants. This also leads to a significant simplification of the *Mathematica* code; for example, compare the code presented here to the general compatibility diagram code, which includes input data for trivariant equilibria, given in Powell *et al.* (1998).

Mathematica code

The *Mathematica* code used to construct all of the compatibility diagrams and movies in this paper is given in Tables 3 and 4. Each line in the code has been numbered to enable discussion and explanation in the text. It is useful to subdivide the code into two parts, as many of the functions are quite general and can be used in the construction of compatibility diagrams for other systems. The general code is given in Table 3 and specific details, such as plot ranges, the definition of variables, labelling and the data

Table 3. *Mathematica* code for performing data interpolation and constructing AFM compatibility diagrams

```

1 Off[General::spell]; Off[General::spell1]; Off[Interpolation::inhr];
2 SetOptions[Position, Heads -> False];
3 <>Graphics`Animation`;
4 varyTatP = True;

```

Function for interpolating the divariant data

```

5 Clear[interpolateddivariant];
6 interpolateddivariant[phase_, info_, v_] :=
7  (info1 = Fold[(k = #2; pm = phase[[k]];
8    pp = Position[#, 1, -?(&==pm)&];
9    MapAt[kk, #1, pp]&), info, Range[Length[phase]]];
10  info2 = Map[#[[1]], Map[Sort[#, (#1[[1]] < #2[[1]])&],
11    Drop[#, 1]]]&], info1];
12  vv = Map#[[1,vpos1]]&, info];
13  kki = Flatten[Position[vv, _?(Abs[v - #]<diffv)&]];
14  If[Length[kki] == 1, info2[[kkk[[1,1]],2]],
15  k2 = Flatten[Position[vv, _?(v < #)&]][[1]]; k1 = k2 - 1;
16  If[k1 == 0, {},
17    vprop = (v - vv[[k1]])/(vv[[k2]] - vv[[k1]]);
18    d1 = Map[Transpose[#[[1]]]&, Drop[info2[[k1]],1][[1]]];
19    d2 = Map[Transpose[#[[1]]]&, Drop[info2[[k2]],1][[1]]];
20    dic = Intersection[d1,d2];
21    Map[(idik = #
22      pk1 = Position[d1, _?(&==idik)&][[1,1]];
23      pk2 = Position[d2, _?(&==idik)&][[1,1]];
24      q1 = info2[[k1,2,pk1]]; q2 = info2[[k2,2,pk2]];
25      q1 + vprop (q2 - q1)&, dic]]];

```

Drawing the trivariant fields

```

26 Clear[drawtrivariant];
27 drawtrivariant :=
28  (c = Map[Transpose[#[[1]]]&, allinfo];
29  ic = Intersection[Flatten[c]];
30  lic = Length[ic];
31  gr = Flatten[Map[(k = #; Map[#[k, #]&,
32    Range[k+1, lic]]&), Range[lic-1, 1]];
33  a = Map[(k1,k2) = #
34    plc = Flatten[Position[Map[Length,
35      Map[Intersection[{{k1,k2}, #}&, c]], _?(&#==2)&]];
36    cc = Map[allinfo][[#, Flatten[Position[c[[#1], _?(&#==k1)&],
37      Position[c[[#1], _?(&#==k2)&]]]]]&, plc];
38    occ = Map[Drop[#, 1][[1]]&, Sort[Map[#[[1,2], #]&, cc]]];
39    cocc = Map[Map[conv, #]&, occ];
40    Map[Join[occ[[#][[1]]], Reverse[cocc[[#][[2]]]]],
41      {occ[[#][[1]], #]}]&,
42    Partition[Range[Length[plc]], 2]]&, Map[ic[[#]&, gr]];
43  {Hue[0,0.15,1], Map[Map[Polygon[#, #]&, a],
44  GrayLevel[0], Map[Map[Line[#, #]&, a], GrayLevel[0]]];

```

Drawing divariant fields

```

45 Clear[drawdivariant];
46 drawdivariant[{{}, _}] :=
47  {GrayLevel[1], Map[conv[Polygon[#, #]&, a],
48  GrayLevel[0], Map[conv[Line[#, #]&, a], GrayLevel[0]]];

```

Setting parameters

```

49 Clear[setup];
50 setup[s_] :=
51  (vstring = s;
52  If[TrueQ[varyTatP],
53    diffv = 0.01; vpos1 = 2; vlow = info[[1,1,2]];
54    vhigh = info[[-1,1,2]];
55    diffv = 0.0001; vpos1 = 1; vlow = info[[1,1,1]];
56    vhigh = info[[-1,1,1]]];

```

Function for constructing the diagrams

```

57 Clear[compatibilitytriangle];
58 compatibilitytriangle[vk_] :=
59  (assemble[vk];
60  Show[Graphics[{ Hue[0,0.45,1], Polygon[shape], GrayLevel[0],
61    Line[shape],
62    labelling[vk],
63    drawtrivariant,
64    drawdivariant[infok]],
65    AspectRatio->Automatic,
66    PlotRange->plotrange} ] /;vk >= vlow && vk <= vhigh];
67 compatibilitytriangle[___] :=
68  If[TrueQ[varyTatP], Print["T outside range"],
69  Print["P outside range"]];

```

Table 4. Specific functions and data

Functions
1 Clear[conv]; 2 conv[f_,t_]:=p=Map[{Mg = #[[4]]; Fe = #[[3]]; 3 Mg - Fe} / Sqrt[3], {-Mg - Fe}] &, t]; 4 f[Join[p,{p[[1]]}]];
5 conv[t_]:= (Mg = t[[4]]; Fe = t[[3]]; 6 Mg - Fe) / Sqrt[3], -(Mg + Fe)];
7 fontsize1 = 12; fontsize2 = 16; 8 third = 1/3; sqrtthird = 1/Sqrt[3]; twothird = 2/3; 9 ll = 1.36; lla = ll sqrtthird; dd = 0.03;
10 shape = {{lla - dd sqrtthird, -11 - dd}, {0, 0}, 11 {lla + dd sqrtthird, -11 - dd}};
12 xlow0 = -1; xhigh0 = 1; ylow0 = -1.8; yhigh0 = 0.1; 13 plotrange = {{xlow0,xhigh0},{ylow0,yhigh0}}; 14 plotrangef = plotrange;
15 xsc = -0.9; ysc = -0.1; p1 = 2; 16 plotvscale[v_] := Text[FontForm[Round[10^Ap1 v]/10^Ap1, {"Helvetica", fontsize2}], {xsc, ysc}]
17 Clear[labelling]; 18 labelling[p_,t_]:=
19 {{Text[FontForm[p, {"Helvetica", 16}], {-0.7, -0.11}], 20 Text[FontForm["Ap", {"Helvetica", fontsize2}], {-0.7, 0}], 21 Text[FontForm["ky", {"Helvetica", fontsize2}], {0, 1, 0}], 22 Text[FontForm["st", {"Helvetica", fontsize2}], {-0.27, -0.3}], 23 Text[FontForm["ctd", {"Helvetica", fontsize2}], {-0.38, -0.5}], 24 Text[FontForm["g", {"Helvetica", fontsize2}], {-0.52, -0.75}], 25 Text[FontForm["ch1", {"Helvetica", fontsize2}], {0.52, -0.78}], 26 Text[FontForm["bi", {"Helvetica", fontsize2}], {0.52, -0.75}], 27 Text[FontForm["Symbol", 12]], {0.3, -1.34}, {-1, 0}], 28 Text[FontForm["bw/rp 1996", {"Helvetica", 12}], 29 {0.36, -1.34}, {-1, 0}]}];
30 Clear[assemble]; 31 assemble[tk_]:=
32 (infok = interpolateddivariant[phase, info, tk]; 33 infosubfk = Map[Insert[#, 0, -1] &, 34 interpolateddivariant[phasesubf, infosubf, tk]]; 35 infosubmk = Map[Map[Insert[#, 0, 3] &, #]&, 36 interpolateddivariant[phasesubm, infosubm, tk]]; 37 allinfo = Join[infok, infosubfk, infosubmk]);
Coordinates
KFMASH system
38 phase = {"ch1", "bi", "g", "st", "ctd", "ky"}; 39 info = { 40 {{6.000, 500.00}, 41 {"ctd", 0.5000, 0.3392, 0.1608}, 42 {"ch1", 0.2180, 0.3193, 0.4627}, 43 {"ky", 1.0000, 0, 0}}, 44 {{6.000, 650.00}, 45 {"st", 0.6923, 0.3012, 0.0065}, 46 {"g", 0.2500, 0.7282, 0.0218}, 47 {"bi", 1.0000, 0, 0}, 48 {"ctd", 0.2500, 0.6563, 0.0937}, 49 {"ch1", -0.1990, 0.6990, 0.5000}, 50 {"ky", 1.0000, 0, 0}}};
KFMASH subsystem
51 phasesubf = {"ch1", "bi", "alm", "fst", "fctd", "ky"}; 52 infosubfk = { 53 {{6.000, 500.00}, 54 {"ch1", 0.1477, 0.8523}, 55 {"bi", -0.2368, 1.2368}, 56 {"ch1", 0.1843, 0.8157}, 57 {"fctd", 0.5000, 0.5000}, 58 {"fctd", 0.5000, 0.5000}, 59 {"ky", 1.0000, 0}}, 60 {{6.000, 650.00}, 61 {"bi", -0.2044, 1.2044}, 62 {"alm", 0.2500, 0.7500}, 63 {"fst", 0.6923, 0.3073}, 64 {"alm", 0.2500, 0.7500}, 65 {"fst", 0.6923, 0.3073}, 66 {"ky", 1.0000, 0}}};
KMASH subsystem
67 phasesubm = {"ch1", "bi", "py", "mst", "mctd", "ky"}; 68 infosubm = { 69 {{6.000, 500.00}, 70 {"bi", -0.3598, 1.3598}, 71 {"ch1", 0.1427, 0.8573}, 72 {"ch1", 0.2180, 0.7820}, 73 {"ky", 1.0000, 0}}, 74 {{6.000, 650.00}, 75 {"bi", -0.3407, 1.3407}, 76 {"ky", 1.0000, 0}}};
Calling function to plot compatibility diagram
77 varyTatP = True; 78 setup["6.0 kbar"]; 79 Off[Set::shape]; 80 compatibilitytriangle[560]; 81 Map[compatibilitytriangle, Range[555, 572, 0.5]];

themselves are given in Table 4. In practice, these two tables may occur as separate *Mathematica* files.

The overall function of the code is: (1) to interpolate the coordinates between the critical temperatures for which data has been calculated with THERMOCALC, which is achieved by making the assumption that the variations are linear with respect to T over the range of interest; and (2) to construct the phase diagrams from the interpolated coordinates. In the following discussion each block of *Mathematica* code will be explained briefly.

General functions (Table 3):

- Lines 1–3 consist of globals relating to the general running of *Mathematica*. Line 4 conveys to later functions that T is the animating variable rather than P .
- An ‘**interpolateddivariant**’ function is defined in lines 5–25 which performs the interpolation of divariant field coordinates. Lines 7–11 order the data and normalize the labelling of the phases (i.e. equate the sub-system names with those from the full system). The situation where there is an exact match in T (i.e. constructing a diagram at T_R) is dealt with in lines 12–16; the interpolation, if necessary, is actually performed by the code in lines 17–25.
- A ‘**drawtrivariant**’ function is defined in lines 26–44 which draws the trivariant fields by joining up the appropriate divariant phases by pairs, where (a) (defined in lines 33–42) refers to the divariant coordinates. The polygons defined by (a) are constructed by the code in lines 43–44.
- A ‘**drawdivariant**’ function is defined in lines 45–48 which draws polygons from the interpolated divariant coordinates.
- The ‘**setup**’ function in lines 49–56 deals with the different positions and magnitudes of the P and T variables in the input data.
- Individual diagrams (at $T = v_k$) are constructed using the ‘**compatibilitytriangle**’ function defined in lines 57–69.

Specific functions and data (Table 4):

- The ‘**conv**’ functions in lines 1–6 convert the ternary coordinates output by THERMOCALC to x - y coordinates for plotting.
- A number of parameters required in the functions given in Tables 3 and 4 are defined in lines 7–16.
- The ‘**labelling**’ function (lines 17–29) produces the labelling for the final diagrams/movies.

- The ‘assemble’ function, in lines 30–37, applies the interpolation function, defined in Table 3 (5–25), to the full- and sub-system data.
- Lines 38–76 contain examples of the input data for the full- and sub-systems. Only data for the upper and lower temperature limits of the example movie have been included.
- The command for plotting a single compatibility diagram is given in line 80, and the resulting diagram is illustrated in Fig. 3. Similarly, the command for constructing a series of diagrams at small temperature intervals is given on Line 81; this applies the ‘compatibilitytriangle’ function across the temperature range 555–572°C at an interval of 0.5°.

Animation of phase diagrams

Within *Mathematica*, the animation of a contiguous series of phase diagrams (in a single ‘cell’), as would be produced by the command in Table 4, line 81, is a trivial exercise. The phase diagrams are selected and then the inbuilt ‘Convert to QuickTime’ function, found in the *Graph* menu (Fig. 4), is used to construct a multi-platform QuickTime™ movie. In principle it would be possible to construct a full movie over the temperature range of interest using this simple approach. However, in practice, to obtain a smooth result it is necessary to use a small temperature interval (<0.5°C) which results in a very large number of individual diagrams (frames). For example, the AFM

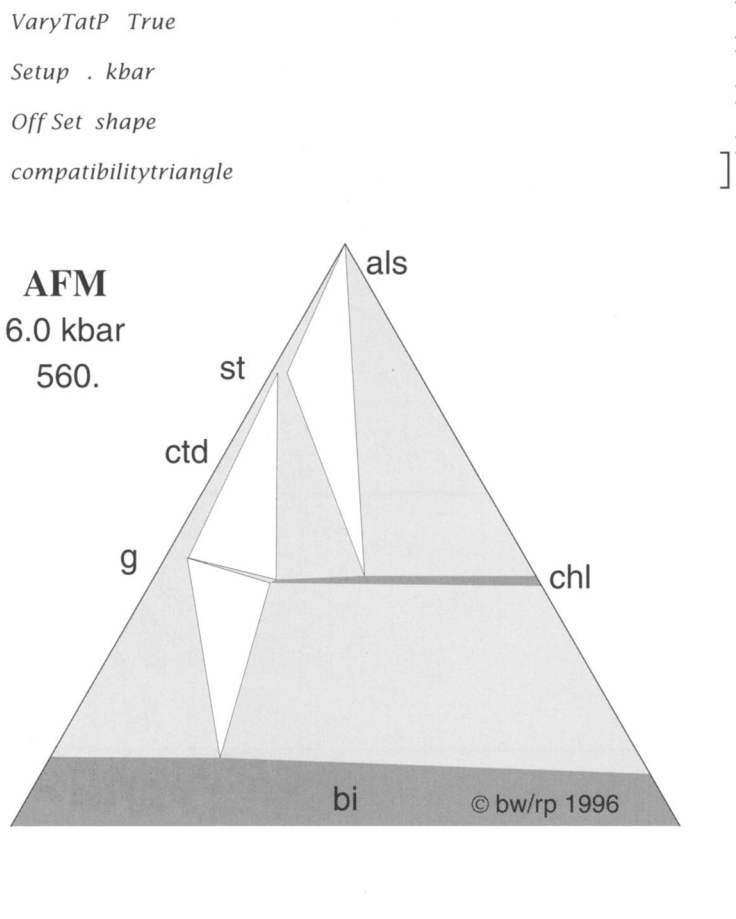


Fig. 3. AFM + mu + q + H₂O compatibility diagram at 560°C and 6 kbar, as output from *Mathematica*.

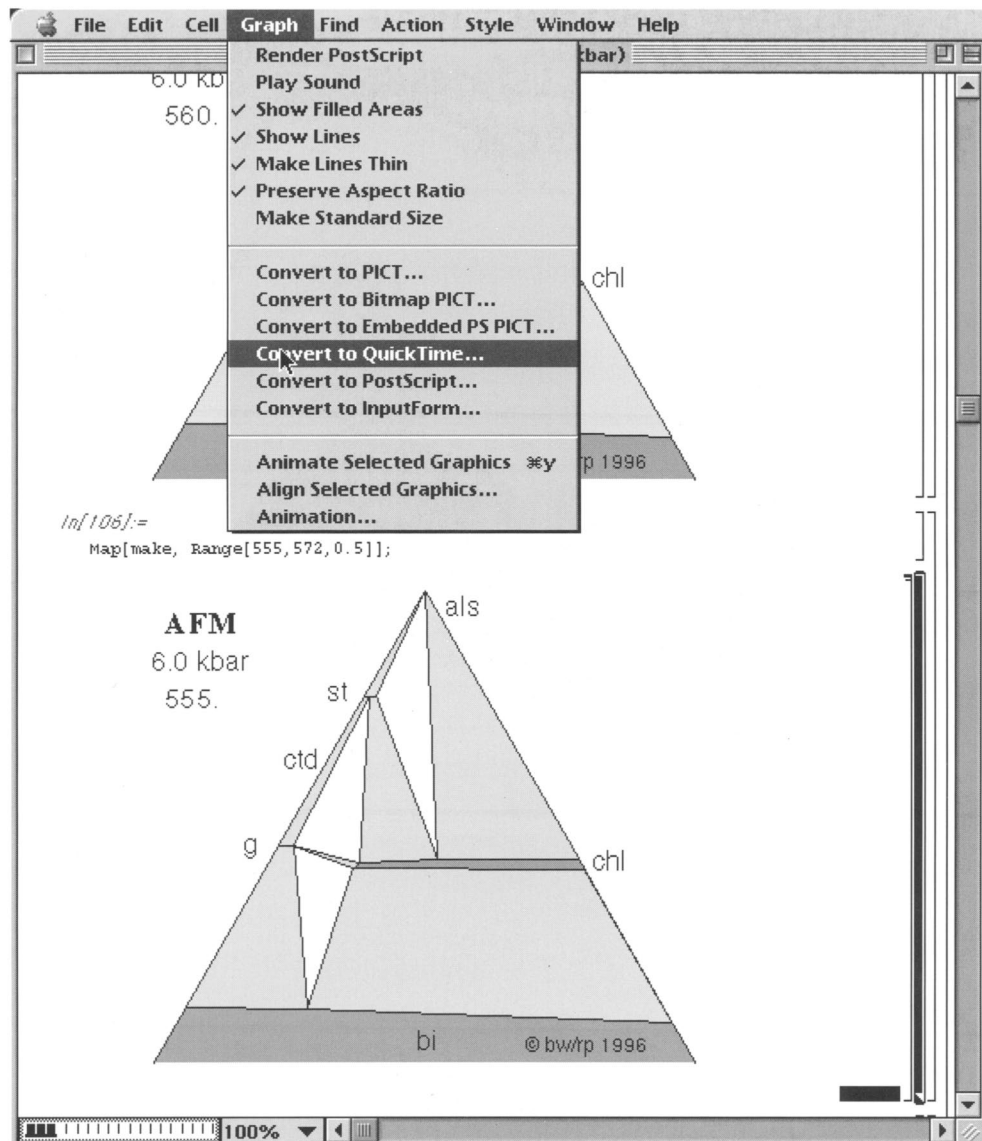


Fig. 4. Conversion of a series of phase diagrams (frames) to a QuickTime movie using a built-in function in *Mathematica*.

compatibility diagram movie from 500 to 650°C contains in excess of 350 frames. Because each diagram is drawn in PostScript format, and uses approximately 200–300 kb of the RAM assigned to the *Mathematica* FrontEnd, it is obvious that memory problems are going to arise if a movie of say 350 frames (requiring >70 Mb of RAM!) is calculated in one step. Therefore, all but the most simple movies need to be constructed as a series of *clips* which can then be joined together. This 'bolting' of the clips can be achieved using a

multimedia software package like Adobe Premiere v4.0, in which the clips are imported into a *Sequence* window and the final movie constructed using the 'Movie' command in the *Make* menu (Fig. 5).

Results: examples of movies

As an example of the results which can be achieved using the approach outlined above,

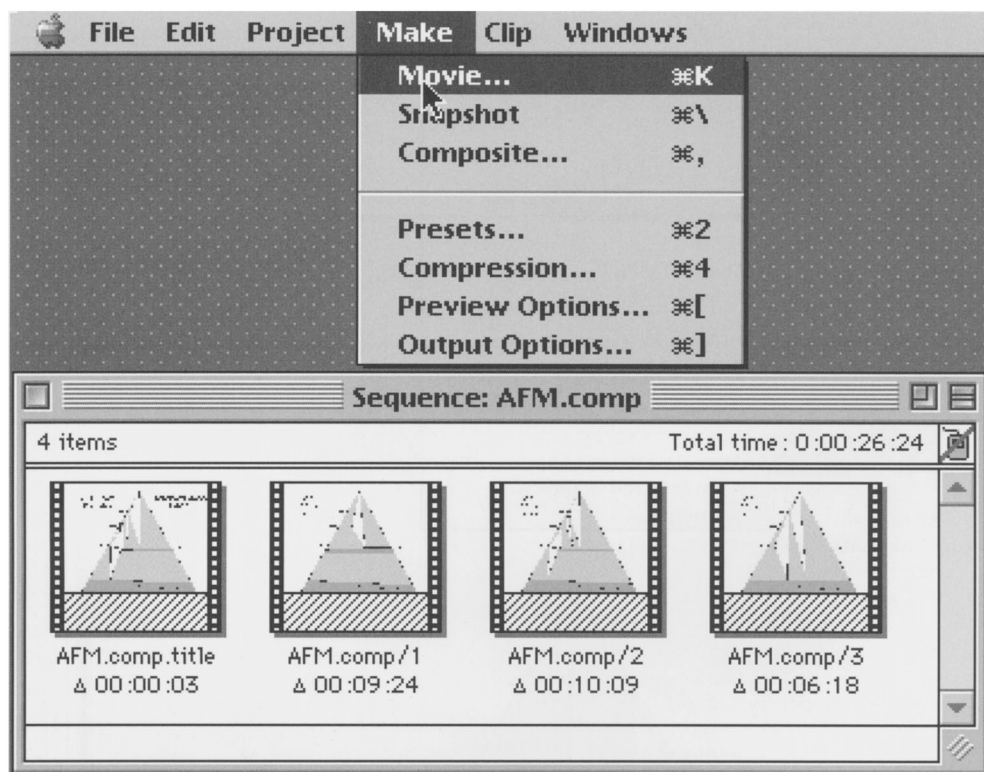


Fig. 5. Compilation of a movie in Adobe Premiere v4.0, from a series of QuickTime clips. The clips are imported into the *Sequence* window, and then the *Make Movie* command is used to construct the final movie.

two AFM compatibility diagram movies are available for downloading from the World Wide Web. In addition to the examples presented here, other movies, including an animated T - x pseudosection, can be found in Powell *et al.* (1998) and Worley & Powell (1998).

The movies associated with this paper can be accessed directly at the following URL:

<http://rubens.its.unimelb.edu.au/~RPOWELL/SMG/Movies/making.movies.html>.

The movies are in QuickTime format and can be viewed on Macintosh, IBM-compatible PC (Windows) and UNIX platforms using a Web Browser, such as Netscape Navigator with the appropriate QuickTime plugin, or a stand-alone application such as MoviePlayer (for the Mac) or PLAY32.EXE (for Windows 95/NT). The latest versions of QuickTime, the QuickTime plugins, and applications for playing QuickTime multimedia files can be downloaded, free of charge, from the Apple QuickTime Home Page at:

<http://www.quicktime.apple.com/>.

The first movie presented here (Movie 1) is the one referred to above, i.e. the AFM ($+ \text{mu} + \text{q} + \text{H}_2\text{O}$) compatibility diagram movie at 6 kbar for the temperature range 500–650°C. Also included is an expansion of a small portion of the diagram over the temperature range 544–557°C, focusing on the disappearance of chloritoid (Movie 2). These movies illustrate a number of fundamental features of the KFMASH system and phase equilibria in general.

1. Individual phases and divariant assemblages are primarily stabilized in the KFMASH subsystem and the mineral compositions become progressively more Mg-rich with increasing temperature as the result of continuous net-transfer reactions.
2. The evolution of the divariant equilibria as univariant reactions are approached and then crossed are elegantly illustrated, especially in Movie 2 where the (st-ctd-g), (st-ctd-chl) and (ctd-g-chl) divariants converge with increasing temperature, resulting in the disappearance of chloritoid in a classic terminating reaction.

3. A specific point which is highlighted in the full movie is the speed at which the compositions of biotite and chlorite, in equilibrium with aluminosilicate, change once the reaction $st + chl = bi + als$ has been crossed with increasing temperature. This results in the predicted disappearance of chlorite via the KMASH reaction, $chl = bi + als$, within 6°C of the full-system reaction.

Discussion

The dynamic nature of metamorphism makes the animation of phase diagrams a logical step in their development as a research tool in metamorphic petrology. The phase diagram movies presented here indicate the power of this approach, in particular their illustration of the continuous evolution of mineral assemblages and compositions with changing conditions. One of the most important features of the animation process is the ability to represent an additional variable, which will become critical as petrologists attempt to investigate increasingly more complex model systems (e.g. Worley & Powell 1998).

In addition to improving our understanding of such model systems, we can visualize several specific directions for the future development of this research. The animation of phase diagrams introduces the possibility of calculating compatibility diagram movies for individual $P-T$ paths (cf. the AFM movie presented here for increasing T at constant P). These movies would constitute a powerful tool for predicting the way in which mineral assemblages change along $P-T-t$ paths, which could then be compared with textural observations from natural samples. Pseudosections can be animated not only with respect to P or T , but also compositional variables. For example, $T-x$, $P-x$ and $P-T$ pseudosections can be animated with respect to a range of important substitutions (i.e. Tschermak's exchange in KFMASH and $CaAlNa_{1-x}Si_x$ in NCKFMASH (Worley & Powell 1998)). Alternatively, the range of bulk compositions for which the animation is performed can be chosen so as to model the path of a particular process.

We would like to acknowledge financial support for this research from the Australian Research Council. F. Spear and N. Hudson are thanked for their positive reviews. Thanks must also go to P. Treloar and P. O'Brien for their hard work in both organizing the original meeting and editing this volume.

References

ALBEE, A. L. 1965. A petrogenetic grid for the Fe–Mg silicates of pelitic schists. *American Journal of Science*, **263**, 512–536.

BERMAN, R. G. 1988. Internally consistent thermodynamic data for minerals in the system Na_2O – K_2O – MgO – FeO – Fe_2O_3 – Al_2O_3 – SiO_2 – TiO_2 – H_2O – CO_2 . *Journal of Petrology*, **29**, 445–522.

— 1991. Thermobarometry using multi-equilibrium calculations: a new technique, with petrological applications. *Canadian Mineralogist*, **29**, 833–855.

CLARKE, G. L., POWELL, R. & GUIRAUD, M. 1989. Low pressure granulite facies metapelitic assemblages and corona textures from MacRobertson Land, East Antarctica: the importance of Fe_2O_3 and TiO_2 in accounting for spinel-bearing assemblages. *Journal of Metamorphic Geology*, **7**, 323–336.

CONNOLLY, J. A. D., MEMMI, I., TROMMSDORFF, V., FRANCESCHELLI, M. & RICCI, C. A. 1994. Forward modeling of calc-silicate microinclusions and fluid evolution in a graphitic metapelite, northeast Sardinia. *American Mineralogist*, **79**, 960–972.

FERRY, J. M. & SPEAR, F. S. 1978. Experimental calibration of the partitioning of Fe and Mg between biotite and garnet. *Contributions to Mineralogy and Petrology*, **66**, 113–117.

FITZSIMONS, I. C. W. & HARLEY, S. L. 1994. Disequilibrium during retrograde cation exchange and the recovery of peak metamorphic temperatures: a study of granulites from East Antarctica. *Journal of Petrology*, **35**, 534–576.

GHENT, E. D. & STOUT, M. Z. 1981. Geobarometry and geothermometry of plagioclase–biotite–garnet–muscovite assemblages. *Contributions to Mineralogy and Petrology*, **76**, 92–97.

HARTE, B. & HUDSON, N. F. C. 1979. Pelitic facies series and the pressures and temperatures of Dalradian metamorphism in eastern Scotland. In: HARRIS, A. L., HOLLAND, C. H. & LEAKE, B. E. (eds) *The Caledonides of the British Isles Reviewed*. Geological Society of London, Special Publication, **8**, 323–337.

HESS, P. C. 1969. The metamorphic paragenesis of cordierite in pelitic rocks. *Contributions to Mineralogy and Petrology*, **24**, 191–207.

HOLLAND, T. J. B. & POWELL, R. 1985. An internally consistent thermodynamic dataset with uncertainties and correlations: 1: Data and results. *Journal of Metamorphic Geology*, **3**, 343–370.

— & — 1990. An enlarged and updated internally consistent thermodynamic dataset with uncertainties and correlations: the system K_2O – Na_2O – CaO – MgO – MnO – FeO – Fe_2O_3 – Al_2O_3 – TiO_2 – SiO_2 – CH_2O_2 . *Journal of Metamorphic Geology*, **8**, 89–124.

OKAY, A. I. 1995. Paragonite eclogites from Dabie Shan, China: re-equilibration during exhumation? *Journal of Metamorphic Geology*, **13**, 449–460.

PATTISON, D. R. M. & BÉGIN, N. J. 1994. Zoning patterns in orthopyroxene and garnet in granulites: implications for geothermometry. *Journal of Metamorphic Geology*, **12**, 387–410.

POWELL, R. 1985. Geothermometry and geobarometry: a discussion. *Journal of the Geological Society of London*, **42**, 29–38.

— & HOLLAND, T. J. B. 1990. Calculated mineral equilibria in the pelite system KFMASH (K_2O - FeO - MgO - Al_2O_3 - SiO_2 - H_2O). *American Mineralogist*, **75**, 367–380.

— & — 1994. Optimal geothermometry and geobarometry. *American Mineralogist*, **79**, 120–133.

—, — & WORLEY, B. 1998. Calculating phase diagrams with Thermocalc. *Journal of Metamorphic Geology*, in press.

SPEAR, F. S & SELVERSTONE, J. 1983. Quantitative P - T paths from zoned minerals: Theory and tectonic applications. *Contributions to Mineralogy and Petrology*, **83**, 348–357.

—, HICKMOTT, D. D. & SELVERSTONE, J. 1990. Metamorphic consequences of thrust emplacement, Fall Mountain, New Hampshire. *Geological Society of America Bulletin*, **102**, 1344–1360.

ST. ONGE, M. R. 1987. Zoned poikiloblastic garnets: P - T paths and syn-metamorphic uplift through 30 km of structural depth, Wopmay Orogen, Canada. *Journal of Petrology*, **28**, 1–22.

THOMPSON, J. B. JR 1957. The graphical analysis of mineral assemblages in pelitic schists. *American Mineralogist*, **42**, 842–858.

VANCE, D. & HOLLAND, T. 1993. A detailed isotopic and petrological study of a single garnet from the Gassetts Schist, Vermont. *Contributions to Mineralogy and Petrology*, **114**, 101–118.

WORLEY, B. & POWELL, R. 1998. Singularities in NCKFMASH (Na_2O - CaO - K_2O - FeO - MgO - Al_2O_3 - SiO_2 - H_2O). *Journal of Metamorphic Geology*, **16**, 169–188.

XU, G., WILL, T. M. & POWELL, R. 1994. A calculated petrogenetic grid for the system K_2O - FeO - MgO - Al_2O_3 - SiO_2 - H_2O , with particular reference to contact-metamorphosed pelites. *Journal of Metamorphic Geology*, **12**, 99–119.

YOUNG, E. D. 1989. Petrology of biotite–cordierite–garnet gneiss of the McCullough Range, Nevada II. P - T - a_{H_2O} path and growth of cordierite during late stages of low- P granulite-grade metamorphism. *Journal of Petrology*, **30**, 61–78.

Index

Page numbers in *italics* are to Figures or Tables

Abukuma belt 145
deformation 151
geochronology 151–2
metamorphism 152–3
P–T path 154
ridge subduction evidence 155
setting 148–51
Acadian metamorphism 24
accretionary prism and ridge–trench interaction 141–2
Adula nappe 206
advective heating 178
AFM compatibility diagrams 271–3
divariant equilibria 273–4
Alaska gold mineralization 141
Alboran Sea *P–T* path study 56
Aldan Shield (Siberia) 83, 84
Allalin metagabbro 203–4, 206
Alpine case studies
Allalin 203–4
Monte Mucrone 204–5
Alpine Fault (New Zealand) 249
amphibolite facies 126
Anabar massif 83
Anakapelle 82
Annapurna Range 11, 12
anatexis
heating models 178–9
Himalayan 173–4
melt extraction models 179
protolith evidence 176–8
relation to deformation 11–12
Sr behaviour 174–6
Anatolide belt 54–6
andalusite–sillimanite transition 57
animation *see* movies
Anmatjira Range 110
anorogenic magmatism and low pressure metamorphism 119, 121
Vredefort Dome 129–32
Antarctica 83, 101
apatite in metapelitic 184
Appalachians terrain *P–T* path study 57
aragonite–calcite transformation 199, 201, 202
Araku 82
Archaean metamorphism 85
see Slave Province
Arunta Inlier (Australia) 109–10, 140, 158
asthenospheric magma and heat transfer 3
attractor states 8
Australia
Arunta Inlier 109–10, 140, 158
Bermagui 226–7
Big Bell Mine 240
Castlemaine Supergroup 227–9
Cooma 237
Proterozoic HPLT terranes
heat flow data 109–11
modelling heat production
equation application 112–13
equations 111–12
results 113–17
results discussed 118–19
autocatalysis in orogeny 12–14
back-exchange calculations 93–4
Bamble 83
baric approach 1
Barrovian metamorphism
characteristics 23
thermal–mechanical modelling
application 28–9
parameters 26, 27
results
crustal tarm effects 42–6
mantle tarm effects 33–42
reference model 29–33
results discussed 46–9
basin evolution and ridge–trench interaction 141
Belousov–Zhabotinsky (BZ) reaction 13–14
Bermagui (Australia) compositional layering 226–7
Betic Cordillera, *P–T* path study 56
Big Bell Mine (Australia) 240
biotite
dehydration in KFMASH system 89–90
in FMAS system 85
in metapelitic 184
Bushveld Complex magmatothermal event 121, 123, 129–32
calc-silicates in UHT province 93
Caledonian orogeny
retrogressive metamorphism 249
schist petrography 249–55
Canada
Labrador 82, 84, 94, 99
Nova Scotia 227
St Maurice 83, 101, 102
Slave Province 158–60
Cascades 227
Castlemaine Supergroup (Australia) 227–9
catalysis in orogeny 12–14
Central Anatolide Crystalline Complex (CACC) 54–6
chalcopyrite in metapelitic 184
chemically stabilized lithosphere (CSL) 115–17
Chichibu belt 145, 146
Chile triple junction 144
Chugach complex 157
coesite 81, 1212
collision-related processes 137
compositional layering
case studies
Bermagui 226–7
Cascades and San Juan 227
Castlemaine Supergroup 227–9
Martinsburg Formation 229–30
Nova Scotia 227
Torlesse Terrane 230–1

conductive heating 179
 conductivity of crust 109
 convergent margin processes 137
 triple junction effects 140–2
 Cooma (Australia) 237
 cordierite
 in FMAS system 85
 in KFMASH system 86–9
 in metapelite 184
 crack initiation 248
 crenulation cleavage 216, 219, 220, 221
 crenulation foliation 215, 233–4
 Cretaceous metamorphism
 Abukuma belt 145–55
 Hidaka belt 158
 Ryoke belt 145–55
 Shimanto belt 157–8
 Cretaceous plate settings 153–5
 crustal behaviour
 conductivity 109
 melting
 effect on Sr isotopes 171–3
 mechanisms 178–9
 thickening 2
 crystallographic preferred orientation (CPO),
 modelling of 259–61
 Cycladic Islands 54
P–*T* path study 56–7

Dalradian 138
 decompression melting 12, 179
 deformation
 effect on *P*–*T* path 58–9
 modelling
 application
 methods 262–4
 results 264
 results discussed 264–6
 evaluation
 TBH model 259–60
 UDEC model 261–2
 dehydration reactions 208–10
 D'Entrecasteaux Islands *P*–*T* path study 57
 depth–temperature relationship 1
 diamonds 81
 dilatancy of grain boundaries 255
 experimentally produced 256
 naturally occurring 256
 role in retrograde metamorphism 256–7
 modelling
 methods 262–4
 results 264
 results discussed 264–6
 petrography 257–9
 disequilibrium of isotopes *see* Sr
 disequilibrium reactions 199
 Sr isotopes 171–3
 Himalayan orogeny 174–6
 dislocation glide, role in deformation 259–60
 dissipative heating 2, 179
 dissipative structures 13
 Dominion Group 123, 124

ductile deformation 260
 dynamothermal metamorphism 1

Eastern Ghats (India) 82, 84, 89, 90, 91, 94–5, 99–100, 102
 eclogite hydration 206
 effective reaction volume 237
 energy budgets of orogenesis 14–17
 enstatite reactions, high pressure 207–8
 Eohimalayan event 9
 epizonal division 1
 equilibration of isotopes
 Sr in crustal melting 171–3
 Himalayan orogeny 174–6
 erosion and exhumation 2, 3
 effect on *P*–*T* path 59
 Üçkapılı pluton 56
 experimental petrology, role of 1
 extensional phase, reconstruction of 53

Farallon–Izanagi spreading centre 145, 153–5
 Fe–Ti oxides 92
 feldspar 93
 in KFMASH system 86–9
 fluid flow and circulation
 at grain boundaries 255
 via microcracks 248–9
 petrographic evidence 249–55
 in ridge–trench interaction 141
 fluid inclusions 248, 250
 FMAS system 85
 FMASH system 85–6
 Forefinger Point 83, 101
 fracture propagation and melt extraction 179
 Franciscan blueschist 201
 frictional heating 179

gahnite 190
 Galicia *see* Ollo de Sapo gneiss
 Ganguvarpatti 82
 garnet
 in FMAS system 85
 fracture behaviour 249
 in KFMASH system 86–9
 in metapelite 184
 in retrogressive metamorphism 250–5
 geotherms and heat flow modelling 113, 114, 115
 Gokarvaram 82
 gold mineralization 141
 Golfo de Peñas Basin 144
 Gonto La 11
 grain boundary processes 247–8
 dilatancy observations 256–7
 modelling, methods 262–4
 modelling results 264
 results discussed 264–6
 petrographic evidence 257–9
 fluid flow 255
 granites, role in Ryoke Belt 146–7
 granulite facies 84
 Vredefort Dome 126

granulite petrology 82–3, 84
 Greater Himalayan zone 8, 9
 chronology of development 11–12
 energy budgets of orogenesis 14–17
 equilibrium conditions 17–18
 inversion 10–11
 leucogranites 10
 metamorphic evolution 8–10
 orogeny and thermodynamics 12–14
 greenschist facies reactions
 role of grain boundary dilatancy 256–7
 modelling, methods 262–4
 modelling results 264
 results discussed 264–6
 petrographic evidence 257–9
 role of microcracks 249
 petrographic evidence 249–55
 Vredefort Dome 124–5
 Grønsjellet thrust (Norway) 249
 petrography of schists 249–55
 Gruf Complex (Italy) 83

Hakurutale 83
 heat production models 24
 Australian terranes 110–1
 equation application 112–13
 equations 111–12
 results
 chemically stabilized lithosphere 115–17
 thermally stabilized lithosphere 113–15
 results discussed 118–19
 heat sources 1
 role in melting crust 178–9
 hematite 92
 hemoilmenite 92
 hercynite 190
 Hidaka belt 145, 158
 Himalayan orogeny 3
 anatexis 173–4
 heating models 178–9
 melt extraction models 179
 protolith evidence 176–8
 Sr behaviour 174–6
 Himalayas 8, 9
 Greater Himalayan zone
 chronology of development 11–12
 energy budgets of orogenesis 14–17
 equilibrium conditions 17–18
 inversion 10–11
 leucogranites 10
 metamorphic evolution 8–10
 orogeny and thermodynamics 12–14
 Nanga-Parbat-Haramosh massif
 AFM diagram 190–1
 KFMASH petrogenetic grid 191–3
 mineral chemistry 184–90
 petrography 183–4
 spinel stability 190
 thermobarometry 193–5
 hornfelsic texture 141
 HTLP metamorphism 138
 causes 109, 139–40
 P–T paths 140

triple junction effects 140–2
 Mesozoic–Cenozoic examples
 Arunta Inlier 109–10, 140, 158
 Chugach Complex 157
 Japanese Islands 146, 157–8
 Slave Province 158–60
 modern examples 144
 slab windows 142–3
 hydrogen metasomatism 240
 hydrothermal alteration 240
 hydrothermal overprinting and ridge–trench interaction 141
 hypersolvus feldspar 93

Iberian Peninsula *see* Ollo de Sapo gneiss
 igneous bodies, as heat sources 1
 igneous characters in UHT province 93
 ilmenite 184, 207
 In Hihaou 82
 Indus suture zone 8, 9
 inversion of isograds 10–11
 ironstone in UHT province 93
 isobaric cooling (IBC) 1, 3, 87
 regional studies 95–9
 isopleth diagrams, KFMASH 92–4
 isothermal decompression (ITD) 1, 3, 99–102
 isotopes *see* Nd *also* Sr
 Izanagi–Farallon spreading centre 145, 153–5
 Izumi belt 145, 146

jadeite 206
 Japanese Islands
 Cretaceous evolution 145
 Abukuma belt 148–51
 deformation 151
 geochronology 151–2
 metamorphism 152–3
 P–T path 154
 ridge subduction evidence 155
 Hidaka belt 158
 Ryoke belt *see*
 deformation 145–6
 geochronology 147
 granites 146–7
 metamorphism 147–8
 P–T path 148
 ridge subduction evidence 155
 Shimanto belt 157–8
 Cretaceous plate setting 153–5
 HTLP belts 146
 paired metamorphic belts 3
 tectonic interpretation 155–7

K-feldspar in metapelite 184
 Kaapvaal Craton 98, 121
 Karoo Supergroup 123, 124
 katazonal division 1
 KFMASH system 86–90, 270
 animation of
 methods 271–7
 results 277–9
 results discussed 279

KFMASH system (*continued*)
 petrogenetic grid 191–93
 spinel stability 190

kinematic–thermal coupling 24–5

kink bands 222, 223

Kitakami batholith 145, 155

Kula–Farallon spreading centre 144–5

Labwor Hills (Uganda) 82, 84, 92, 95, 99

Lace Kimberlite (South Africa) 82, 98

Lebowa Granite Suite 121, 130

Lesser Himalayan zone 8, 9

leucogranites
 Greater Himalayan zone 10
 anatexis 11–12

Lewisian gneiss 93

Lhochag–La Kang 11

Limpopo 83

Liquine–Ofqui fault 144

lithosphere
 role in heat production modelling
 equation application 112–13
 equations 111–12
 results
 chemically stabilized lithosphere 115–17
 thermally stabilized lithosphere 113–15
 results discussed 118–19

Littleton Formation (USA) 237

Long Point (Antarctica) 83, 101

Losberg Complex 121, 123

Lugo dome 63, 70

Lutzow Holm Bay 101

M domains 216
see also P domains

magnetic signatures in ridge–trench interaction 141

magmatism
 association with metamorphism 109
 effect on *P–T* path 57–8
 role in HTLP 139
 role in low pressure metamorphism 121
 Vredefort Dome 129–32

magnetite 92, 184

Main Boundary Thrust (MBT) system 8, 9

Main Central Thrust system 8, 9
 chronology of development 11–12

Manaslu leucogranite 11, 177

mantle plume and Bushveld Event 130–2

mantle processes, role of 3

Martinsburg Formation (USA) 222, 229–30

Mathematica Code 274–6

mechanical–thermal coupling 24–5

Meguma Group 227

melting reactions 210–11
 crustal
 effect on Sr isotopes 171–3
 mechanisms 178–9
 extraction modelling 179

Menderes Massif *P–T* path study 56

Mendocino Triple Junction 144

mesozonal division 1

metagreywacke protolith 177

metamorphic belt classification 138

metamorphic differentiation 216

metapelite study 177
 AFM diagram 190–1
 KFMASH petrogenetic grid 191–3
 mineral chemistry 184–90
 petrography 183–4
 spinel stability 190
 thermobarometry 193–5

meteorite impact, Vredefort Dome 123, 127–9

MgSiO₃ phase diagram 207

mica
 composition variation 226
see also biotite *also* muscovite

microcracking
 development of 248–9
 role of 249
 petrography of schists 249–55

microplate development 142

migmatite and thrusting 12

mineral data
 Abukuma belt 152–3
 Ryoke belt 147–8

mineralogy
 amphibolite facies 126
 granulite facies 126
 greenschist facies 124–5

modelling
 deformation and *P–T* path 58–9
 application
 methods 262–4
 results 264
 results discussed 264–6
 evaluation
 TBH model 259–60
 UDEC model 261–2

heat flow and Barrovian metamorphism 28–9

parameters 26, 27

results
 crustal tarm effects 42–6
 mantle tarm effects 33–42
 reference model 29–33
 results discussed 46–9

Moine 138

Molopo Farms Complex 121, 129

monazite in metapelite 184

Monte Mucrone diorite 204–5, 206

Mosendo 63

movies in phase diagram studies 270
 application to KFMASH system
 methods 271–7
 results 277–9
 results discussed 279
 principles of animation 270–1

Mt Isa 109–20

Mt Painter Inlier 110

multiple thermal peaks in *P–T* paths 53
 locations studied 54–7
 parameters studied
 role of deformation 58–9
 role of exhumation 59
 role of magmatism 57–8

Murás 63

muscovite at high pressure
 dehydration 208–10
 melting 210–11
 mylonite 249

Namaqua Event 123
 Nanga–Parbat–Haramosh massif metapelite
 AFM diagram 190–1
 KFMASH petrogenetic grid 191–3
 mineral chemistry 184–90
 petrography 183–4
 spinel stability 190
 thermobarometry 193–5
 Napier Complex (Antarctica) 82, 84, 85, 87, 93, 94, 95–8
 Nd isotopes 178
 Neogene metamorphism 158
 Neohimalayan event 9, 17
 Nepal leucogranites 174
 New Zealand 230–1
 Niğde massif
 multiple thermal peaks study 54–6
 role of magmatism 57–8
 Nova Scotia 227
 nucleation kinetics
 dehydration reactions 208–10
 melting reactions 210–11
 polymorphic phase transformation 201–2
 rate equation 199–201
 solid–solid reactions 202–8

obduction and heating 178
 ocean basin closure 138
 olivine–spinel transformation 199
 Ollo de Sapo gneiss 61–2
 mineralogy and petrology 63, 64–70
 P–T evolution 70–74
 omphacite 206
 ophiolite emplacement
 mechanism 142
 in ridge–trench interaction 141–2
 orogens and first order spatial patterns 7–8
 orthopyroxene
 in FMAS system 85
 in KFMASH system 86–9
 osumilite in KFMASH system 86–9
 Ourol 63
 Ouzzal Complex (Algeria) 82, 84, 94, 100–1
 oxygen effects on spinel 92–3

P domains 216, 218, 223–4
 effect of porphyroblasts 235–7
 case studies
 Bermagui 226–7
 Castlemaine Supergroup 227–9
 mineral composition 226
 in schists 233–4
 solution evidence 224
 P–T diagrams
 FMAS 86, 96
 KFMASH 87, 88, 272–3

P–T paths
 clockwise–anticlockwise 138, 140
 conditions for UHT metamorphism 84
 factors affecting
 role of deformation 58–9
 role of exhumation 59
 role of magmatism 57–8
 locations studied 54–7
 Abukuma Belt 153
 Ryoke Belt 148
 Vredefort Dome 126–7

P–T–t paths 17
 Barrovian 23
 model output
 crustal tarm effects 42–6
 mantle tarm effects 33–42
 reference 29–33
 Pacific Islands P–T study 57
 Pacific Ocean plate interactions 153–5
 Pacific–Farallon spreading centre 144–5
 Paderu 82
 paired metamorphic belts 3, 138, 154
 Pakistan *see* Nanga Parbat–Haramosh massif
 Palaeogene metamorphism
 Chugach 157
 Shimanto 157–8
 Pan–African Event 123
 Papua–New Guinea P–T study 57
 peak metamorphism 269
 pelite grids as UHT indicators
 FMAS 85–6
 KFMASH 86–90
 petrogenetic grids 191–3, 269
 petrography, metapelite 183–4
 Phalaborwa alkaline complex 122
 phase diagrams
 KASH 208
 MgSiO₃ 207
 problems of presentation 269–70
 use of movies 270
 animation 270–1
 application to KFMASH system
 methods 271–7
 results 277–9
 results discussed 279

phase transformation, polymorphic 201–2
 phyllite, deformation partitioning 216–21
 pigeonite 93
 plagioclase reactions
 high pressure 202–3
 case studies
 Allalin 203–4
 Monte Mucrone 204–5
 in metapelite 184
 Playa de Abrlea 63
 Playa de San Roman 63
 plutons as heat sources 1
 polymorphic phase transformation 201–2
 porphyroblasts 2
 and effective reaction volume 237
 and P domains 235–7
 Precambrian metamorphism *see* Arunta Inlier 157
 pressure shadows 225
 Proterozoic metamorphism 85

protolith character, Sr evidence 176–8
 Punta Anchousa 63
 Pyrenees *see* Ollo de Sapo gneiss
 pyrite in metapelite 184
 pyroxene reactions under high pressure 206, 207–8

Q domains 216, 217, 218
 deposition evidence 224–6
 case studies
 Bermagui 226–7
 Castlemaine Supergroup 227–9
 mineral composition 226
 in schists 233–4

Qomolangma 11

quartz
 in FMAS system 85
 in KFMASH system 86–9
 in metapelite 184
 veins 215

quartzite in ductile deformation 260

radioactive elements
 effect of distribution 24, 25
 see also tectonically accreted radioactive material

radiogenic heat production 1, 2, 139
 see also heat production

rare earth element (REE) diffusivity 178

Rashoop Granophyre Suite 121, 122

Rauer Group 93

reduction spots 226

retrieval calculations 93–4

retrogressive reactions
 role of grain boundary dilatancy 256–7
 modelling
 methods 262–4
 results 264
 results discussed 264–6
 petrographic evidence 257–9

role of microcracks 249
 petrographic evidence 249–55

Reynolds Range 110

rheology
 role in tectonic evolution 24–5
 role in thrusting 12

ridge–trench interaction 3, 138
 effect on overriding plate 142
 Mesozoic–Cenozoic systems *see* Japanese Islands
 modern systems 144
 role in paired metamorphic belts 138–9
 triple junction effect 140–1

rift-drift delamination in HTLP 139

ringwoodite 207

Rivera Triple Junction 144

Rooiberg Group 121, 122, 130

Rundvagshetta (Antarctica) 83, 101

Rustenburg Layered Suite 121, 122, 129, 130

rutile in metapelite 184

Ryoke belt 145
 deformation 145–6
 geochronology 147
 granites 146–7
 metamorphism 147–8
 P–T path 148
 ridge subduction evidence 155

St Maurice (Canada) 83, 101, 102

Sambagawa belt 145

San Andreas Fault 144

San Juan Islands 227

sapphirine in FMAS system 85

Scandian 249

scapolite 93, 257–9

Schiel alkaline complex 122

schists, deformation partitioning 216–21, 233–4

Scotland
 Dalradian and Moine blocks 138
 South Harris Igneous Complex 257
 modelling retrogressive metamorphism
 methods 262–4
 results 264
 results discussed 264–6
 petrography 257–9
 Scourie 93
 shear heating in HTLP 139

Shimanto belt 145, 146, 157–8

sillimanite
 in FMAS system 85
 in KFMASH system 86–9
 in metapelite 184, 234

Sipiwek Lake 82, 85, 94, 98

Sixto 63

slab window development 142

slaty cleavage 215, 216, 219
 domain effects 224–6

early metamorphic changes 223–4

case studies
 Bermagui 226–7
 Cascades and San Juan 227
 Castlemaine Supergroup 227–9
 Martinsburg Formation 229–30
 Nova Scotia 227
 Torlesse Terrane 230–1
 pre-metamorphic changes 221–23
 volume loss evidence 231–33

Slave Province (Canada) 158–60

solution transfer 224
 case studies
 Bermagui 226–7
 Cascades and San Juan 227
 Castlemaine Supergroup 227–9
 Martinsburg Formation 229–30
 Nova Scotia 227
 Torlesse Terrane 230–1

South Africa *see* Vredefort Dome

South Harris Igneous Complex 257
 modelling retrogressive metamorphism
 methods 262–4
 results 264
 results discussed 264–6
 petrography 257–9

South Tibetan detachment (STD) 8, 9
 chronology of development 11–12
 slip rate 17

Spain *see* Ollo de Sapo gneiss

spinel
 domains in metapelite 184–90
 effects of oxygen 92–3
 in FMAS system 85

Sr isotope disequilibrium 171–3
 Himalayan orogeny 174–6
 Sri Lanka 83, 101
 Stanovoy 83
 stishovite 123
 subduction-related processes 137
 role in low pressure metamorphism 121
 Subhimalayan zone 8, 9
 Sutam Block (Siberia) 83, 84, 85

Taitao ophiolite 144
 TBH model 259–60
 tectonic thickening
 role in HTLP 139
 role in low pressure metamorphism 121
 tectonic thinning, role in low pressure metamorphism 121
 tectonically accreted radioactive material (tarm) 25
 role in Barrovian metamorphism
 crustal 42–6
 mantle 33–42
 temperature field control in Barrovian metamorphism 23–4
 thermal conductivity of crust 109
 thermal–mechanical coupling 24–5
 thermally stabilized lithosphere (TSL) 113–15
 thermobarometry 93–5, 193–5
 thermodynamics of orogenesis 12–14
 thermometers, Fe/Mg 93
 Tibetan zone 8, 9
 Tokskii (Siberia) 101
 Torlesse Terrane (New Zealand) 230–1
 Transhimalayan zone 8, 9
 Transvaal Supergroup 121, 123, 124, 129
 trench–ridge interaction *see* ridge–trench
 triple junctions
 at convergent margins 140–42
 classification 140
 slab windows 142–3
 Turkey
 Anatolide belt 54–6
 metamorphic setting 54–6
 Niğde massif
 multiple thermal peaks study 54–6
 role of magmatism 57–8

Ubendian Event 122, 123
 Üçkapılı pluton
 metamorphic setting 55–6
 role of magmatism 57–8
 UDEC model 261–62
 ultra-high pressure (UHP) metamorphism 81
 ultra-high temperature (UHT) metamorphism 3
 isopleth diagrams 90–2
 locations studied
 Aldan Shield 83, 84
 Eastern Ghats 82, 84, 89, 90, 91, 94–5, 99–100, 102
 Forefinger Point 83, 101
 Gruf Complex 83, 101
 Labwor Hills 82, 84, 92, 95, 99
 Lace Kimberlite 82, 98
 Long Point 83, 101
 Lutzow Holm Bay 101

Napier Complex 82, 84, 85, 87, 93, 94, 95–8
 Ouzzal Complex 82, 84, 94, 100–1
 Rundvagshetta 83, 101
 St Mauric 83, 101, 102
 Sipiwers Lake 82, 85, 94, 98
 Sri Lanka 83, 101
 Sutam Block 83, 84, 85
 Tokskii 101
 Wilson Lake 82, 84, 94, 99
P–*T* fields 84
 pelite grids
 FMAS 85–6
 KFMASH 86–90
 oxygen effects 92–3
 signatures in rocks 93
 thermobarometry 93–4
 underplating, role of 3
 Universal Distinct Element Code model 261–2
 unroofing *see* exhumation
 unroofing rate evidence 17–18
 USA
 Littleton Formation 237
 Martinsburg Formation 222, 229–30

Variscan event *see* Ollo de Sapo gneiss
 veins, role in melt extraction 179
 Ventersdorp Supergroup 123, 124
 Villalba 63
 Viso 63
 Vivero fault zone 67, 68, 69
 volume losses
 in crenulation cleavage 233–4
 effect of porphyroblasts 235–7
 in slaty cleavage
 Bermagui 226–7
 Cascades and San Juan 227
 Castlemaine Supergroup 227–9
 evidence evaluated 231–33
 Martinsburg Formation 229–30
 Nova Scotia 227
 pre-metamorphic 221
 reduction spots 226
 Torlesse Terrane 230–1

Vredefort Dome 3, 122
 amphibolite facies 126
 geological setting 123–4
 granulite facies 126
 greenschist facies 124–5
 magmatism
 impact of 129–30
 origins of 130–32
P–*T* path 126–7
 timing of metamorphism 127–9
 Vredefort Event 123

wadsleyite 207
 water and crack growth 248–9
 Wilson Lake (Labrador) 82, 84, 94, 99
 Witwatersrand Supergroup 123, 124
 wollastonite 93

Xuan Blanco 63

zircon in metapelitic 184

What Drives Metamorphism and Metamorphic Reactions?

edited by

P. J. Treloar

(Kingston University, UK)

and

P. J. O'Brien

(Universität Bayreuth, Germany)

Although it has long been recognized that what ultimately drives metamorphism and metamorphic reactions is heat, what was less certain is the distribution of heat within the crust, the type and location of major heat sources and the rates of heat flux through crustal rocks. This book explores the factors that control metamorphism and rates of metamorphic processes.

- 288 pages
- 14 chapters
- 120 illustrations
- index

Cover picture: A tourmaline–spinel symplectite rimming a zoned tourmaline cored by biotite and hosted by grandidierite. Grandidierite–kornerupine–tourmaline rock from high grade gneisses of the Mesoproterozoic Magondi orogenic belt of Northern Zimbabwe.

ISBN 1-86239-009-6



9 781862 390096 >